



UnB



TESE DE DOUTORADO EM COTUTELA ENTRE  
UNIVERSIDADE DE BRASÍLIA E SORBONNE UNIVERSITÉ

Área de concentração :

FÍSICA – ED 564: PHYSIQUE EN ILE-DE-FRANCE  
FÍSICA EXPERIMENTAL – PPGFIS: PROGRAMA DE PÓS-GRADUAÇÃO EM FÍSICA

---

**Ferrofluidos e Dots de Carbono como exemplos de  
nanomateriais multifuncionais para a conversão de energia**

---

apresentada por

**Thiago Fiuza Lima da Silva**

para a obtenção do título de  
Doutor da Sorbonne Université e Doutor da Universidade Brasília

Tese defendida em 22 de dezembro de 2020

Diante da banca composta por:

Dr. Antonio M. FIGUEIREDO NETO	Universidade de São Paulo	Relator
Dr. Julian OBERDISSE	Université de Montpellier	Ralator
Dr. Geraldo José DA SILVA	Universidade de Brasília	Examinador
Dr. Michel GOLDMANN	Sorbonne Université	Examinador
Dra. Régine PERZYNSKI	Sorbonne Université	Orientadora
Dr. Jérôme DEPEYROT	Universidade de Brasília	Orientador

Brasília - DF

2020



UnB



PHD THESIS IN CO-TUTORSHIP BETWEEN  
THE UNIVERSIDADE DE BRASÍLIA AND SORBONNE UNIVERSITÉ

Concentration area:

PHYSICS – ED 564: PHYSIQUE EN ILE-DE-FRANCE  
EXPERIMENTAL PHYSICS – PPGFIS: PROGRAMA DE PÓS-GRADUAÇÃO EM FÍSICA

---

## **Ferrofluids and Carbon Dots as examples of multifunctional nanomaterials for energy conversion**

---

presented by

**Thiago Fiuza Lima da Silva**

in order to obtain the title of  
Doutor da Universidade de Brasília and Docteur de Sorbonne Université

Thesis defended in the 22<sup>nd</sup> of December of 2020

In front of the jury composed by:

Antonio M. FIGUEIREDO NETO	Universidade de São Paulo	Referee
Julian OBERDISSE	Université de Montpellier	Referee
Geraldo José DA SILVA	Universidade de Brasília	Examiner
Michel GOLDMANN	Sorbonne Université	Examiner
Régine PERZYNSKI	Sorbonne Université	Thesis Director
Jérôme DEPEYROT	Universidade de Brasília	Thesis Director

Brasília - DF

2020

*In memory of my father Antonio Donizetti.*

# Acknowledgements

I would like to thank first my family and friends for all the support throughout these years, in special 2020 which was a very difficult year for all of us.

My gratitude goes to Jérôme Depeyrot and Régine Perzynki who gave me an immense support in my research project. I am grateful for all the opportunities, trust, dedication and freedom that they have given me and for the knowledge that I will surely carry for the rest of my life.

I would also like to thank all the researchers who collaborated directly or indirectly to this work, in special Fabrizio Messina. Without them this work would have never been possible.

I also acknowledged the financial support of this work by the European Union Horizon 2020 research and innovation program under the grant number 731976 (MAGENTA), the Brazilian agency CNPq by the Doutorado Sanduíche - SWE grant number 202009/2018-1 and the PhD scholarship from CAPES.

This research used resources of: the Brazilian Synchrotron Light Laboratory (LNLS), an open national facility operated by the Brazilian Centre for Research in Energy and Materials (CNPEM) for the Brazilian Ministry for Science, Technology, Innovations and Communications (MCTIC); the Laboratoire Léon Brillouin and SOLEIL (shareholding of the French public centers CNRS and CEA) with the SAXS, SANS and synchrotron radiation experiments. The facilities staff is acknowledged for the assistance during the all the experiments.

# Abstract

Material science has been gathering worldwide attention due to its broad range of applications and solutions to current global issues. Ferrofluids (FFs) and Carbon Nanodots (CDs) stand out as promising energy harvesters of renewable sources (e.g. thermal or solar). In this context, the first main objective of this thesis was to investigate the thermodiffusive properties of ferrofluids based on room temperature ionic liquids (RTILs). This peculiar class of solvents composed purely of ions presents multiple advantages such as high thermal stability, low vapor pressure and modest conductivity, making them highly suitable for fluid-based thermoelectric devices. The explored RTILs are ethylammonium nitrate (EAN) and 1-Ethyl-3-methylimidazoliumbistriflimide (EMIM-TFSI). Here, it was analysed the role of the nature of counterions, the water content and the application of magnetic field in the colloidal stability and, most importantly in the thermodiffusive parameters, namely the Soret and diffusion coefficients. The theoretical approach applied to these systems showed to satisfactorily model, describe and adjust the experimental data. Further on, into a different perspective, little was known about the stability, surface charge development and local ordering of nitrogen-rich carbon nanodots (N-CDs). Along those lines, the second objective was to deeply analyse these properties for two kinds of N-CDs – differing by their nitrogen/carbon ratios ( $N/C=0.14$  and  $0.74$ ) – via a multi-scale and multi-technique approach. The results shed new light on the importance of the pH of the carrier fluid in N-CDs aqueous dispersions. Finally, the third objective was to design and produce a novel fluorescent magnetic liquid combining the two previously mentioned classes of colloids: ferrofluids and N-CDs. The achieved colloïdally stable aqueous hybrid nanofluid presents a homogeneous visual aspect, while largely preserving the magnetic and fluorescent properties of each one of the nanocomponents, unlocking the possibility of use in multiple forms of applications.

**Keywords:** Magnetic Fluids. Thermodiffusion. Ionic Liquids. Carbon Nanodots. Colloidal Stability. Fluorescent Magnetic Liquids. Energy conversion.

# Résumé

La science des matériaux apporte une large gamme d'applications et de solutions aux problèmes mondiaux actuels. Les ferrofluides (FF) et les nanodots de carbone (CD) se distinguent comme de prometteurs collecteurs d'énergie renouvelable thermique ou solaire, par exemple. Dans ce contexte, le premier objectif de cette thèse était d'étudier les propriétés thermodiffusives des ferrofluides à base de liquides ioniques à température ambiante (RTIL). Cette classe particulière de solvants composés uniquement d'ions présente de multiples avantages tels qu'une stabilité thermique élevée, une faible pression de vapeur et une conductivité modeste, ce qui les rend parfaitement adaptés aux dispositifs thermoélectriques à base de fluide. Les RTIL explorés ici sont le nitrate d'éthylammonium (EAN) et le 1-éthyl-3-méthylimidazoliumbistriflimide (EMIM-TFSI). Nous avons analysé le rôle de la nature des contre-ions, de la teneur en eau et de l'application du champ magnétique sur la stabilité colloïdale et, surtout, sur les coefficients thermodiffusifs, à savoir le coefficient Soret et le coefficient de diffusion. L'approche théorique appliquée à ces systèmes a montré qu'elle modélisait, décrivait et ajustait de manière satisfaisante les données expérimentales. Ensuite, dans une perspective différente, parce qu'on en savait peu sur la stabilité, le développement de la charge de surface et l'ordre local des nanodots de carbone riches en azote (N-CD), nous avons analysé en profondeur ces propriétés pour deux types de N-CD - différant par leurs rapport azote/carbone ( $N/C = 0,14$  et  $0,74$ ) - via une approche multi-échelles et multi-techniques. Les résultats jettent un éclairage nouveau sur l'importance du pH du fluide porteur dans les dispersions aqueuses de N-CD. Enfin, le troisième objectif était de concevoir et de produire un nouveau liquide magnétique fluorescent combinant les deux classes de colloïdes précédemment mentionnées : les ferrofluides et les N-CD. Le nanofluide hybride aqueux, stable au plan colloïdal, qui est obtenu, présente un aspect visuel homogène, tout en préservant largement les propriétés magnétiques et fluorescentes de chacun des nanocomposants, ouvrant la possibilité d'une utilisation dans de multiples formes d'applications.

Un [Résumé Long en Français](#) se trouve dans la page 183.

**Mots-clés** : Fluides magnétiques. Thermodiffusion. Liquides ioniques. Nanodots de carbone. Stabilité Colloïdale. Liquides magnétiques fluorescents. Conversion de l'Énergie.

# Resumo

A ciência de materiais tem atraído atenção mundial devido à sua ampla gama de aplicações e soluções para problemas globais atuais. Ferrofluidos (FFs) e Nanodots de carbono (CDs) se destacam como promissores coletores de energia de fontes renováveis (por exemplo, térmica ou solar). Nesse contexto, o primeiro objetivo principal desta tese foi investigar as propriedades termodifusivas de ferrofluidos à base de líquidos iônicos à temperatura ambiente (RTILs). Esta classe peculiar de solventes compostos puramente por íons apresenta múltiplas vantagens, como alta estabilidade térmica, baixa pressão de vapor e modesta condutividade, tornando-os altamente apropriados para dispositivos termoelétricos à base de fluidos. Os RTILs explorados são o nitrato de etilamônio (EAN) e a bistriflimida de 1-etil-3-metilimidazólio (EMIM-TFSI). Aqui, foi analisado o papel da natureza dos contra-íons, do teor de água e da aplicação do campo magnético na estabilidade coloidal e, principalmente, nos parâmetros termodifusivos, isto é, os coeficientes Soret e de difusão. A abordagem teórica aplicada a estes sistemas mostrou modelar, descrever e ajustar os dados experimentais de forma bem satisfatória. Mais adiante, em uma perspectiva diferente, pouco se sabia sobre a estabilidade, desenvolvimento de carga superficial e ordem local de nanodots de carbono ricos em nitrogênio (N-CDs). Nesse sentido, o segundo objetivo foi analisar profundamente essas propriedades para dois tipos de N-CDs – diferindo por suas razões de nitrogênio/carbono ( $N/C = 0,14$  e  $0,74$ ) – por meio de uma abordagem multi-escala e de múltiplas técnicas experimentais. Os resultados lançam uma nova luz sobre a importância do pH do fluido carreador em dispersões aquosas de N-CDs. Finalmente, o terceiro objetivo era projetar e produzir um novo líquido magnético fluorescente combinando as duas classes de coloides mencionadas anteriormente: ferrofluidos e N-CDs. O nanofluido híbrido aquoso e coloidalmente estável apresenta aspecto visual homogêneo, preservando em grande parte as propriedades magnéticas e fluorescentes de cada um dos nanocomponentes, dessa forma criando a possibilidade de uso em múltiplas formas de aplicações.

Um [Resumo Estendido em Português](#) encontra-se na página 163.

**Palavras chave:** Fluidos magnéticos. Termodifusão. Líquidos Iônicos. Nanodots de carbono. Estabilidade Coloidal. Líquidos magnéticos fluorescentes. Conversão de Energia.

# Contents

<b>Introduction</b> . . . . .	<b>10</b>
<b>I Ferrofluids</b>	<b>17</b>
<b>1 Magnetic Nanoparticles (MNPs)</b> . . . . .	<b>18</b>
1.1 Synthesis . . . . .	19
1.2 Morphology and Size . . . . .	21
1.3 Internal Structure and Surface Properties . . . . .	23
<b>2 Colloidal Dispersions of MNPs</b> . . . . .	<b>27</b>
2.1 Peptization in Weak Electrolyte Solvents . . . . .	28
2.1.1 Acidic Medium with $\text{NO}_3^-$ Counterions . . . . .	28
2.1.2 Neutral pH and Citrate Functionalization . . . . .	29
2.2 Peptization in Ionic Liquids . . . . .	29
2.2.1 SMIM $^\pm$ -TFSI $^-$ coated MNPs dispersed in EMIM-TFSI . . . . .	29
2.2.2 Citrate coated MNPs dispersed in EAN . . . . .	30
2.3 Interparticle Interactions . . . . .	31
2.3.1 Stability of MNPs in EMIM-TFSI . . . . .	33
2.3.2 Stability of MNPs in EAN with $\text{Na}^+$ , $\text{Rb}^+$ and $\text{Li}^+$ Counterions . . . . .	35
2.3.3 Ionic Layering around the NPs in FF-EAN . . . . .	38
2.3.4 Stability of MNPs in EAN/Water Mixtures with $\text{Na}^+$ Counterions . . . . .	40
2.4 Conclusions on the Colloidal Stability of the Studied Systems . . . . .	43
<b>3 Thermodiffusive Properties</b> . . . . .	<b>44</b>
3.1 Theoretical Background . . . . .	45
3.1.1 Thermodiffusion in Charged Colloids . . . . .	45
3.1.2 Under-Field Model for MNPs . . . . .	48
3.2 Forced Rayleigh Scattering Experiment (FRS) . . . . .	50
3.2.1 Experimental Setup . . . . .	50
3.2.2 Experimental Determination of ( $S_T$ ) and ( $D_m$ ) . . . . .	52
3.3 Water-EAN Mixtures: Inversion of Thermodiffusive Properties . . . . .	55
3.3.1 Thermodiffusion measurements in EAN with various counterions . . . . .	55
3.3.2 Analysis of $S_T$ Measured in EAN with $\text{Na}^+$ Counterions at 22 °C . . . . .	59
3.3.3 Thermodiffusion in EAN-water mixtures with $\text{Na}^+$ counterions . . . . .	60
3.4 EMIM-TFSI: Thermodiffusion Under Magnetic Field . . . . .	65
3.4.1 Zero-Field Results . . . . .	65
3.4.2 Under-Field Results . . . . .	67
3.5 Conclusions on the Thermodiffusion Measurements . . . . .	73

<b>Conclusions on ferrofluids based in Ionic Liquids</b> . . . . .	<b>75</b>
<b>II Carbon Nanodots</b>	<b>80</b>
<b>4 Nitrogen-Rich Carbon Nanodots (N-CDs)</b> . . . . .	<b>81</b>
4.1 Synthesis . . . . .	82
4.2 Morphology and Size . . . . .	84
4.3 Internal Structure and Surface Groups . . . . .	89
4.4 Density . . . . .	91
<b>5 Colloidal Dispersions of N-CDs</b> . . . . .	<b>94</b>
5.1 Dispersion in Different pH Aqueous Media . . . . .	94
5.2 Visual Aspects and Short Term Aging . . . . .	95
5.3 Surface Charge Development in Aqueous Media . . . . .	99
5.3.1 Zeta Potential . . . . .	101
5.3.2 Potentiometric-Conductimetric Titrations . . . . .	104
5.3.3 Surface Charge . . . . .	107
5.4 Nanoscale Organization . . . . .	111
5.4.1 Transmission Electron Microscopy . . . . .	111
5.4.2 Dynamic Light Scattering (DLS) . . . . .	113
5.4.3 Small Angle X-ray Scattering (SAXS) . . . . .	114
<b>6 Photoluminescence (PL)</b> . . . . .	<b>123</b>
6.1 Nitrogen/Carbon Ratio Effect in Optical Properties . . . . .	124
6.2 Optical Absorption and Fluorescence in Highly Alkaline Medium . . . . .	126
<b>Conclusions on N-CDs Aqueous Dispersions</b> . . . . .	<b>130</b>
<b>III Fluorescent Magnetic Liquids</b>	<b>133</b>
<b>7 Magneto-Photoluminescent Systems based on Nanoparticles</b> . . . . .	<b>134</b>
7.1 General Context and State of the Art . . . . .	135
<b>8 N-CDs MNPs Hybrid Nanocolloid</b> . . . . .	<b>138</b>
8.1 Overview: Acidic, Neutral and Alkaline Medium Conditions . . . . .	138
8.2 Combining N-CDs and Magnetic Fluids . . . . .	140
8.2.1 Colloidally Unstable Acidic Hybrid MNP N-CD Suspension . . . . .	141
8.2.2 Colloidally Stable Fluorescent Magnetic Liquid . . . . .	142
8.3 Nanoscale Ordering . . . . .	144
8.3.1 Acidic Hybrid MNP N-CD Suspension . . . . .	144
8.3.2 Fluorescent Magnetic Liquid . . . . .	148
8.4 Magnetic and Photoluminescent properties . . . . .	149
8.4.1 Magnetization and Magnetohypertermia . . . . .	149
8.4.2 Photophysical effects . . . . .	151

Conclusions on Fluorescent Magnetic Liquids . . . . .	155
<b>General Conclusions and Perspectives</b>	<b>158</b>
<b>Extended Abstracts</b>	<b>163</b>
Resumo Estendido em Português . . . . .	163
Résumé Long en Français . . . . .	183
Bibliography . . . . .	203
<b>Annex</b>	<b>222</b>
ANNEX A Open-Access Published Paper - On the Colloidal Stability of Nitrogen-Rich Carbon Nanodots Aqueous Dispersions . . . . .	223
ANNEX B Article to be submitted - Colloidal and thermal stabilities of iron oxide nanoparticle dispersions in EMIM TFSI stabilised with sulfonate based imidazolium ions . . . . .	236
ANNEX C Article submitted - Thermodiffusion anisotropy under magnetic field in ionic liquid-based ferrofluid . . . . .	247
ANNEX D Patent - Nanofluidos Mágneticos Fluorescentes e seu processo de obtenção . . . . .	258

# Introduction

The unceasing increase in materials science research is responsible for a significant share of the technological development achieved in the past decades. The emerging class of nanomaterials investigated in this thesis gathered conspicuous attention due to its broad range of applications such as: in current worldwide issues as the reduction of environmental contamination [1,2], treatment and diagnosis of diseases [3–7]; and in technological advances as hyperthermic or heat transfer fluids [8], sensors [9], photocatalytic and optoelectronic components [10–12].

In this sense, an outstanding problem faced by modern civilization is obtaining energy in a sustainable and increasing manner, thereby, nanotechnology might provide substantial assist uncovering solutions to this matter. The usual path to solve the problem is investing in renewable energy sources (e.g. solar, wind, hydraulic and biomass), nevertheless it might not be the solely alternative. As one study [13] published in 2015 points out, thermal energy/heat reached 47% of the total energy consumption worldwide, largely by industrial applications, which significant amounts of it can be lost by rejection to the environment via exhaustion gases and water cooling systems. These circumstances open a great opportunity for the implementation of thermoelectric devices with which residual heat can be converted into electricity. The recovered energy could be stored, used directly to improve the efficiency of the primary process or redirected to another purpose. Following this reasoning, a reduction in energy waste of global proportions could have a massive economical and environmental impact, even though the efficiency of thermoelectricity is still in need of crucial improvement. This scenario highlights the relevance of profoundly investigating the fundamentals of the thermodiffusive and thermoelectric properties, which has been showing a step-wise increase in performance over the past years [14].

The most efficient converters are still the conventional solid-state thermoelectric devices [15], however liquid thermocells present rising interest as promising alternatives to low-grade waste heat recovery due to their reduced cost and scalability. Further, it has been shown that in liquid thermocells, the inclusion of magnetic particles could increase the thermoelectric energy conversion efficiency in comparison to conventional electrolytes [16], evidently, under controlled and particular physico-chemical conditions. In this given context emerges the interest of this thesis in exploring the thermodiffusive properties of ferrofluids

based on ionic liquids.

Generally speaking, ferrofluids (FFs) or magnetic fluids (MFs) are colloidal dispersions of magnetic nanoparticles (MNPs) in non-magnetic liquid media. In the context of this work, the investigated media are aqueous solutions and room temperature ionic liquids (RTILs). The latter is a category of solvents composed purely of ions, typically defined as molten salts at near room temperature. RTILs present many convenient properties such as nonflammability, high thermal and electrochemical stability, negligible vapor pressure and high ionic conductivity, as well as the advantage of being considered a “green” alternative to replace the classical and more dangerous organic solvents [17]. Consequently, these features make this class of ferrofluids based on ionic liquids (FF-ILs) strong candidates to produce cutting-edge thermocells. In addition, these systems accomplish the non-trivial achievement of conferring unique and reversible properties to liquids in the presence of an external magnetic field [18], providing an extra parameter that can be implemented to manipulate the nanomaterial.

At the current state of the art, it is not obvious to predict in which physical-chemical conditions such as surface functionalization, temperature range and nanoparticles concentration the dispersions in RTILs are colloidally stable. Consequently, a lot of effort is directed into experimentally determine the set of parameters in which the nanoparticles could remain well dispersed in a certain ionic liquid. Previous studies identified two promising ionic liquids based ferrofluids: citrate-coated nanoparticles dispersed in ethylammonium nitrate (EAN) with sodium (Na) counterions [18]; and hydroxyl-coated nanoparticles initially dispersed in water with SMIM<sup>±</sup>-TFSI<sup>-</sup> (deprotonated 1-(4-sulfobutyl)-3-methylimidazolium bistriflimide) counterions then transferred to EMIM-TFSI (1-ethyl-3-methylimidazolium bistriflimide) [19, 20]. Reliable information on the limits of the colloidal stability of those systems were probed using an association of different experimental techniques, as well as essential groundwork of their thermodiffusive properties. Along those lines, in [Part I](#) of this study it was possible to go a few steps further and investigate more complex phenomena:

- Electric double layered ferrofluids (EDL-FFs) dispersed in aqueous media are charged colloids (electrostatically stabilized) in which as the concentration of electrolytes in solution increases (e.g. the addition of a salt) the system typically undergoes a destabilization after a certain point. This well studied effect [21–23] is predominantly due to shielding of the repulsive electrostatic potential by the excessive amount of counterions in the vicinity of the nanoparticles, inducing phase separations and possibly irreversible particle aggregation. With that in mind, what would happen if water was gradually substituted by an ionic liquid, meaning a progressive increment in ionic strength, until the complete removal of the water<sup>1</sup>? The evolution of a

---

<sup>1</sup> Note however that the very notion of ionic strength does not exist anymore in an Ionic Liquid, which is a medium fully constituted of ions

stable colloid is usually impossible to follow on the whole range of water proportion, because, as said above, a phase separation of the aqueous colloid usually happens at large ionic strength. However, surprisingly, with ethylammonium counterions ( $\text{EA}^+$ ), the system remains monophasic on the whole range of  $[\text{EA}^+]$  if NPs are small enough and at a volume fraction not too large. In this part, it is proposed the mix<sup>2</sup> of two stable ferrofluids in the extreme cases. A single synthesis of citrate-coated magnetic nanoparticles is separated in two aliquots (at the same NP's volume fraction  $\Phi$ ): one is dispersed in water and the other in EAN (a well behaved ferrofluid as mentioned previously). This mixed system is stable from a colloidal point of view through the whole range of mixture proportions and continuously evolves from an aqueous electrolyte to a pure ionic liquid, EAN (at least at  $\Phi$  not too large, here  $\leq 3\%$ ). Hence, [subsection 2.3.4](#) is focused in elucidating the evolution of the interparticle interaction along the different  $\text{H}_2\text{O}/\text{EAN}$  proportions. For its part [section 3.3](#) analyzes the evolution of the thermodiffusive properties, such as the diffusion coefficient, the viscosity, the sign-inversion of the Soret coefficient, the role of temperature and nanoparticle concentration.

- Ionic ferrofluids are not only of great interest in thermoelectricity due to their behavior in a temperature gradient, but also for bearing an extra parameter granted by the magnetic nature of the nanoparticles. Recently, the thermodiffusive response of the fluid to the application of an external magnetic field in association with a temperature gradient has been studied in FFs based on polar solvents [[25](#), [26](#)]. Besides, the improvement of the thermoelectric properties has been attested in under-field conditions [[26](#)]. Although, the effectiveness of the theoretical model used in polar media [[25](#)] in adjusting the under-field experimental data in ionic liquids is not completely clear, we thus evaluate in [section 3.4](#) the development of the thermodiffusive properties under-field in an ionic liquid based ferrofluid. The FF-ILs of choice was the one dispersed in EMIM-TFSI and surface-covered by SMIM<sup>±</sup>-TFSI<sup>-</sup>, as mentioned above. This system raises two novel topics of discussion to be evaluated by the evoked theoretical model: first, if it properly contemplates the thermodiffusion effects imposed by the unconventional nanoscale structuration of the solvent; second, as an ionic liquid presents a wider thermal stability over aqueous media, a broad range of temperatures are probed in order to attest the under-field effect in both parallel and perpendicular directions.

Likewise, carbon nanodots (CDs) are a recently emerging class of nanomaterials with high research interest to be implemented in energy conversion applications, specially in solar harvesting [[27](#)] due to their broad absorption spectra, large absorption coefficients

---

<sup>2</sup> A similar approach was used by [Sarkar et al.\[24\]](#) mixing dimethyl sulfoxide and water, however the nature of the resulting media is completely different in this case.

and good solubility in polar solvents. Currently, they are a viable alternative to the traditional semiconductor quantum dots presenting substantial advantages such as simpler, direct and low-cost synthesis [28], low toxicity [29] and being environmental friendly [30]. Beyond that, CDs offer exceptional bright [31] and tunable photoluminescence in the visible range [32] expanding even further their field of applications. Besides their high application potential, they still present fairly low power conversion efficiency, for instance, their usage in solar cells reached an efficiency value just close to 1% in a recent study [33].

CDs are likely to exhibit promising thermodiffusive properties to be implemented in thermocells, and as a matter of fact, a preliminary test was carried out with a dispersion of CDs in aqueous media. Unfortunately, the thermodiffusive parameters measured were on the limit of the experimental resolution, most likely due to the considerably low nanoparticle concentration. If so, why not just increase the nanodots concentration? First of all, the post-synthesis CDs investigated in this work are initially in powder form, then later subjected to a straight forward dispersion protocol (detailed in [section 5.1](#)) consisted essentially of adding a certain mass of the solid sample to a chosen liquid medium. This means that increasing nanoparticle concentration is a simple matter of supplementing more powder to the aqueous solution, yet, the colloidal stability of the final dispersion is not guaranteed. That being said, it is of crucial importance for thermodiffusion applications to have a stable and consistent product. Moreover, realizing the nanoscale organization of the dispersion as function of the physical-chemical parameters is not only fundamental to perform a reliable data analysis, but it should present critical implications to their photoluminescent properties. Since very little is known over this subject for CDs, specially the class here investigate, the main focus of [Part II](#) was directed in elucidating the following queries:

- In general, hydrophilic carbon nanodots are considered to demonstrate great water “solubility” as a direct consequence of their surface functionalization, typically, with polar carboxyl or hydroxyl groups [27, 29, 34–36]. In this study the nanoparticles are initially aggregated in a dried powder, thereafter in aqueous media these surface groups might undergo hydrolysis reactions conferring the nanodots a negative surface charge. Accordingly, the surface charge of the nanodots are certainly strongly dependent on the  $\text{H}_3\text{O}^+/\text{OH}^-$  concentration of the aqueous solutions in which they are dispersed. Similar to the FFs, these dispersions are also charged colloids, therefore in aqueous media the effective surface charge plays the leading role in maintaining long-term colloidal stability and forming/dismantling aggregates. Hence, the first main goal in order to understand the overall interparticle interactions is to probe the surface charge development as function of the pH. Thus [section 5.1](#) describes the dispersion of nanodots in a wide pH-range of aqueous solutions acidified by nitric acid ( $\text{HNO}_3$ ) and alkalized by sodium hydroxide ( $\text{NaOH}$ ). The macroscopical

stability was checked by visual observations in the [section 5.2](#), later linked with the progression of the surface charge properties deeply analyzed in the [section 5.3](#). Subsequently, a general panorama of the nanoscale ordering was probed in [section 5.4](#) by scattering techniques as function of nanoparticles concentrations, pH of the media and size separation via centrifugation.

- The photoluminescence of carbon nanodots has been intensively studied in the past decade, yet, the underlying electronic transitions behind their bright photoluminescence are strongly debated. It has been shown that the fluorescence greatly depends on the medium's factors such as the pH and the nature of solvents [[34](#)], as well as CDs intrinsic characteristics as size, surface groups and crystalline structure [[37](#)]. In this thesis, two types of nitrogen enriched carbon nanodots (N-CDs) [[38](#)] are investigated differing in structure and photoluminescence properties: one presents a predominantly blue fluorescence and the other a green emission. The arguments for the difference in emissions between the two have been justified by [Sciortino et al.](#) [[38](#)], yet they were not probed in different pH conditions. For the green emitter, it was observed a considerable blue shift in the emission band in an alkaline aqueous medium. Specifically, the shift occurs in a sufficiently high pH, in which the signal transition is time dependent and irreversible. Then [section 6.2](#) discusses a possible explanation for this intriguing effect.

Ferrofluids and carbon dots share multiple similarities, oftentimes being employed in the same field of applications. Notwithstanding, they present very distinct and unique features: the magnetic and fluorescence properties. In this sense, magneto-photoluminescent systems have been intensively investigated considering their versatility by unifying two very compelling characteristics in a single adaptive and responsive smart material. The combination of these properties provides enhanced applications such as associated targeting, labeling and sorting [[39,40](#)], simultaneous bioimaging and therapy [[41](#)] and multimodal contrast agents (fluorescent and magnetic resonance imaging) [[42,43](#)].

The benefits of multifunctional nanocomposites usually come along with an increase in complexity of the system and a restriction of the conditions in which the material maintains its desirable properties. In the literature, different mechanisms are employed in order to combine magnetic and photoluminescent components such as coating by chemisorption [[44](#)], encapsulating various nanobjects by a polymer shell [[7,45](#)] or confining one type of nanoparticle inside another [[46](#)]. In all of these cases the interactions between the components are restricted, as well as the nanoparticles with the medium. In addition, the layering increases significantly the resulting nanostructure size, thereupon preventing an adequate colloidal stability with or without the appliance of an external magnetic field. These matters may not present a problem depending on the desired application (they might even be very useful), however, allowing different regimes of particle-particle and

particle-solvent interactions enables us to explore a wider variety of nanoscale ordering. Specially in the case of carbon nanodots (ferrofluids) in which the photoluminescent (magnetic) properties are greatly dependent on the interface between the medium and the nanoparticles' surface, the interparticle electric and magnetic interactions and the degree of ordering/aggregation. This ensemble of assets indicate a strong potential in sensor applications from biomedicine to industry.

These factors motivated the conception of an unprecedented fluorescent magnetic liquid realized by combining the two types of nanocolloids here studied. [Part III](#) is dedicated to establish the implications of dispersing both N-CDs and MNPs in two distinct aqueous conditions:

- In acidic medium (around pH 2.0) MNPs present a saturated positive surface charge while N-CDs exhibit a low negative surface charge, therefore, a global attractive electrostatic potential is established between N-CDs/MNPs. A priori, the system will present a strong aggregation and subsequent destabilization, however, depending of the particle proportion and concentration, the size and effective charge of the agglomerates and acidity of the medium the final colloid could present different degrees of instability. The [subsection 8.3.1](#) presents the visual aspects of an acidic condition with two different sizes of MNPs with and without an applied magnetic field. The study is complemented by a nanoscale scale analysis performed by small angle X-ray scattering providing a multiscale overview of the mixture stability status.
- In alkaline medium both nanoparticles present negative surface charge, although repulsive electric forces are expected to exist in all nanoparticle interactions, the resulting potential may be globally attractive due to Van der Waals and dipolar interactions. Since the green emitting N-CD presents irreversible surface alterations in highly alkaline medium, in attempt to preserve their fluorescence properties another strategy was implemented. The MNPs present a point of zero charge at pH 7.0, however a citrate coating procedure can ensure a negative charge at this condition. This way, in [subsection 8.3.2](#) it is presented a fluorescent magnetic liquid in neutral pH simultaneously presenting both properties and maintaining a long term colloidal stability. A detailed investigation of the impacts on the fluorescence of the N-CDs due to the presence of the MNPs is presented in [subsection 8.4.2](#).

In sum, the content of the thesis, which has been prepared in the context of the long lasting collaboration between Universidade de Brasilia and Sorbonne Université, is composed of three parts, each dedicated to a nanomaterial and its main studied properties:

**Part I Ferrofluids:** This first part details the thermodiffusion properties of ionic liquid based ferrofluids. It initially describes the synthesis and characterization of the

magnetic nanoparticles, as well as the dispersion procedure in different media, responsible for achieving long-term stable colloids. As follows, well-established FF-ILs systems are investigated probing two different phenomena: the inversion of the Soret coefficient as function of the water content in EAN-water mixtures and the anisotropic thermodiffusive effect under the application of an external magnetic field in ferrofluids based on EMIM-TFSI.

**Part II Carbon Nanodots:** The colloidal stability and surface properties of nitrogen-enriched carbon nanodots are investigated in this part. Firstly, the synthesis and structural characterization of the carbon-based nanoparticles are established, focusing on the surface charge development when dispersed in different pH aqueous solutions. Further, the macroscopical observations are associated with the nanoscale ordering and an unexpected photoluminescence blue-shift is linked with the modifications of the surface in highly alkaline conditions.

**Part III Fluorescent Magnetic Liquids:** A novel fluorescent magnetic liquid is presented by the association of the fluids investigated in the preceding parts. The system is combined in two distinct interaction regimes: attractive and repulsive electrostatic potentials between the N-CDs and MNPs. Finally, the photophysical and magneto hyperthermia effects of the repulsive particle-particle interactions are investigated.

Part I

Ferrofluids

This work on magnetic fluids, also called ferrofluids, based on Room Temperature Ionic Liquids (RTIL) has been done in the framework of the European Union Horizon 2020 research and innovation program MAGENTA, under the grant number 731976 (MAGnetic nanoparticle based liquid ENergy materials for Thermoelectric device Applications) joining together 10 different European teams. The work presented here has been done in close collaboration between Chemists and Physicists. In particular, I have been closely working with a German PhD student in Chemistry, in PHENIX laboratory - SU, Dr. Jesse Cornelius Riedl, who has defended his PhD on September 25, 2020 in SU - Paris under the responsibility of Dr. Emmanuelle Dubois and Dr. Véronique Peyre. The chemical synthesis of the various samples studied in Sorbonne University (SU) in the context of MAGENTA has been done by Jesse C. Riedl. We have realized in collaboration the study of the colloidal properties of the synthesized samples by SAXS and SANS. A common paper on various types of stability in EMIM-TFSI (1-Ethyl-3-methylimidazolium bistriflimide), which is submitted to publication, is joined in Annex and is not detailed in the present text. I have driven myself the thermodiffusion measurements by Forced Rayleigh Scattering which are described here, in collaboration with the team of Physicist in PHENIX. [Part I](#) of the present thesis mainly focuses on two physico-chemical problems in two model-systems: - Under-field anisotropy of thermodiffusion in a moderately concentrated sample based on EMIM-TFSI as a function of temperature and - Evolution as a function of temperature and of the water content of NP dispersions in mixtures of water and EAN (Ethylammonium nitrate).

## Chapter 1

# Magnetic Nanoparticles (MNPs)

Combining the magnetic properties of solids with the peculiar characteristics of fluids generating a unique product is a non-trivial task. The solution to the issue lies in the remarkable effects that arise when matter is controlled at the nanometric level.

The first reported method to successfully produced a fluid that could be manipulated by magnetic fields was designed by [Papell](#)[47]. He was interested in solving the problem of undesired and unconstrained movement of propellant inside the fuel tanks of rockets caused by the microgravity environment experienced in space. The basis of the invention

consisted in developing a fluid upon which an artificial gravity condition could be imposed via magnetic forces as well as maintaining the propelling properties. The smart material was achieved by grinding bulk magnetite in the presence of a propellant and a grinding agent until the material fragmented in particles sufficiently small to enter in suspension and do not separate from the liquid phase in the presence of an applied magnetic field. This idea established the current understanding of magnetic fluids (MFs) as colloidal suspensions of magnetic nanoparticles (MNPs) dispersed in a carrier liquid [48].

The initial process of nanoparticle production was since then improved, expanded and diversified. Throughout the years, it transitioned from the initial *top-down* approach consisted of breaking down bulk materials into smaller particles to the *bottom-up* method in which the nanoparticles are synthesized via crystallization promoted by chemical reactions.

The class of MNPs based in spinel ferrites studied in this work have been extensively investigated in the past decades, like so, the synthesis and characterization methods employed here are well-established and deeply detailed in the literature. Therefore, this chapter briefly describes and specifies the characteristics of the samples investigated here, ensuring future reproducibility of the obtained experimental results and providing support to the main focus of this study, namely the thermodiffusion effects.

## 1.1 Synthesis

The ferrofluid (FF) samples were produced by a two-step protocol: step 1 consists in the chemical synthesis of the MNPs by the widely employed coprecipitation method in an aqueous medium; step 2 refers to the peptization in more complex solvents and the used particle functionalization depending on the characteristics of the carrier fluid. The first step concerning just the synthesis of the nanoparticles is described below, while the second step is detailed in [section 2.1](#) and [section 2.2](#).

Maghemite ( $\gamma\text{-Fe}_2\text{O}_3$ ) nanoparticles were chemically synthesized using the well-known Massart method [49,50]. The MNPs synthesis can be divided in four substeps (a,b,c and d) illustrated in [Figure 1](#):

- a) *Coprecipitation*: the nucleation and crystal growth processes that form the iron oxide NPs occur when an acidic solution of  $\text{Fe}^{3+}$  and  $\text{Fe}^{2+}$  ions is alkalized. Thus, the precursor solution is prepared by dissolving  $\text{FeCl}_3$  and  $\text{FeCl}_2$  in HCl in a 2:1 concentration ratio in a beaker. At room temperature, ammonia ( $\text{NH}_3$ ) is rapidly added to the acidic solution reacting under vigorous stirring for 30 minutes. The mixed solution turns into a black-brownish color due to the formation of magnetite ( $\text{Fe}_3\text{O}_4$ ) nanoparticles. At this point, the particles present a negative surface charge, however, the high ionic strength allows the dark solid phase to be precipitated with

the assistance of a magnet placed underneath the beaker.

- b) *Acidification*: An acidic medium is necessary before the next reaction can be performed. The alkaline supernatant is removed and the precipitate covered with a nitric acid ( $\text{HNO}_3$ ) solution (2 mol/L). This procedure also inverts the particle surface charge to positive values.
- c) *Particle treatment*: In order to completely oxidize the  $\text{Fe}_3\text{O}_4$  nanoparticles into  $\gamma\text{-Fe}_2\text{O}_3$  a solution of 0.5 mol/L ferric nitrate ( $\text{Fe}(\text{NO}_3)_3$ ) is added. Immediately after, the temperature is raised to 80 °C and the system is let to react for another 30 minutes.
- d) *Washing*: Finally, the nanoparticles are chemically stable, still, one last procedure is required before the direct dispersion or surface functionalization. In order to remove the excess of unwanted ions and water, the precipitate is repeatedly washed with acetone/ether. After this process, the MNPs are ready to be fully dispersed. It is important to mention that the particles can never be completely dried or otherwise the system undergoes irreversible particle aggregation which prevents the development of proper colloidal suspensions in the following peptization protocols.

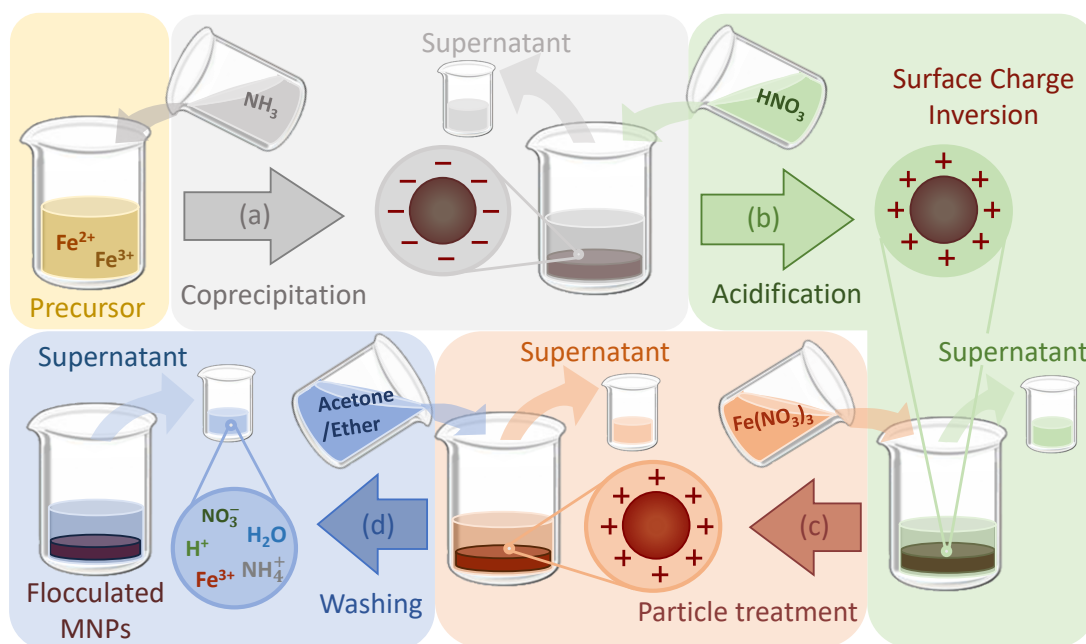


**Figure 1** – Diagram of the four substeps in the MNP synthesis process: (a) coprecipitation; (b) acidification; (c) particle treatment and (d) washing. The addition of solutions are represented by the arrows pointing inwards and the removal of the supernatants as arrows pointing outwards. The change in color of the MNPs represents the fully oxidation of the internal structure.

The morphology, size and crystalline structure of the studied MNPs produced by this method are indicated in the following sections of this chapter. In addition, key information regarding the MNPs surface features is provided for a better understanding of the achieved stability in the studied solvents.

Before proceeding further to the characterizations, it is worth acknowledging a variation of the presented synthesis method proposed by [Gomes et al.](#)[51]. This alternative process allows the synthesis of *core-shell* MNPs, in which the structural composition can be diversified by substituting the  $\text{Fe}^{2+}$  source by an equivalent salt of a desired divalent metal  $\text{M}^{+2}$ . The produced core can be formed by a variety of ferrites (e.g.  $\text{MFe}_2\text{O}_4$  with  $\text{M} = \text{Co}, \text{Cu}, \text{Ni}$  or  $\text{Zn}$ ) and the mentioned  $\text{Fe}(\text{NO}_3)_3$  treatment generates a maghemite shell. This way, the magnetic properties of the sample can be tuned and peculiar magnetic effects appear due to the additional core/shell interface. This variation of the synthesis method produced the cobalt based nanoparticles employed in the mixtures reported in [Part III](#) of this work.

## 1.2 Morphology and Size

It is well known that the mentioned coprecipitation method produces roughly spherical iron oxide nanoparticles with mean diameters typically  $\sim 10$  nm [52, 53]. A downside of the presented method is the high polydispersity index ( $s$ ), which can reach up to  $s \sim 0.4$ . Although the size of the nanoparticles can be controlled by the synthesis parameters [54], the polydispersity cannot be drastically reduced [55]. The shift towards a monodisperse system is highly desired, that is because the magnetic properties are strongly size dependent and modeling the fluid becomes much more complex with a broad size distribution.

From the many different methods that have been developed in order to control the polydispersity, it was applied here a low-cost size sorting process that can be performed on significant amounts of fluid and it is fairly efficient as it allows  $s$ -values to reach as low as 0.1. The details on the size sorting procedure<sup>1</sup> can be found in references [56, 57].

The nanoparticles here studied have been already deeply characterized in previous studies [18–20, 58, 60]. As an example to illustrate their morphological and size characteristics after the sorting process, [Figure 2](#) presents transmission electron microscopy (TEM) images of the “rock-like shape” nanoparticles that were size sorted in two different size populations: (a) with mean diameter  $\sim 7$  nm and (b)  $\sim 11$  nm. In this thesis, we focus on investigating only **sample (a)**. These smaller nanoparticles are surface coated with citrate, and later, dispersed in water (neutral pH) and EAN (check [subsection 2.1.2](#) and [subsection 2.2.2](#)).

TEM experimental data is analyzed by pixel measuring the diameters ( $d$ ) of a large number of nanoparticles and creating the histograms presented in [Figure 2c](#). The data is

<sup>1</sup> In short the method is based on the destabilization of a MNP colloidal suspension via the increment of the ionic strength by the addition of an electrolyte. A phase separation is induced by taking advantage of the fact that the larger nanoparticles are more susceptible to sedimentation as the surface potentials are screened.

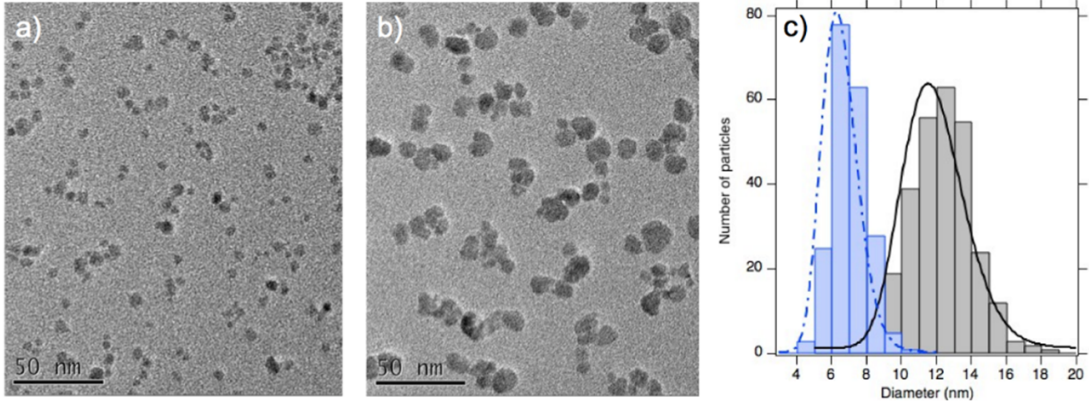


**Figure 2** – Transmission electron microscopy (TEM) of size-sorted samples previously characterized: (a) a TEM image of the sample chosen to be investigated in this thesis, that was studied by Mamusa et al.[58]. (b) a TEM image of a larger particle size sample studied in [59]. (c) the size distribution of both samples deduced by several TEM images fitted by Equation 1.1. Figure reproduced from ref. [18].

adjusted using the lognormal function

$$P_{\ln}(d, d_0, s_0) = \frac{1}{ds_0\sqrt{2\pi}} \exp\left[-\frac{\ln^2(d/d_0)}{2s_0^2}\right] \quad (1.1)$$

where the median diameter  $d_0$  and  $s_0$  are the fitting parameters. The values obtained by the fitting in Figure 2c for sample (a) are  $d_{0,\text{TEM}} = 6.5$  nm and  $s_{0,\text{TEM}} = 0.22$ .

Taking advantage of the magnetic properties of the NPs, the values of  $d_0$  and  $s_0$  can also be estimated from measurements performed in a vibrating sample magnetometer (VSM). The magnetization ( $M$ ) measured as function of an applied magnetic field  $H$  at a given temperature  $T$  can be expressed by the Langevin model as

$$M(x, d_{0,\text{mag}}, s_{0,\text{mag}}) = m_s \Phi \frac{\int d^3 L(x) P_{\ln}(d, d_{0,\text{mag}}, s_{0,\text{mag}}) dd}{\int d^3 P_{\ln}(d, d_{0,\text{mag}}, s_{0,\text{mag}}) dd}, \quad (1.2)$$

which is adjusted using the first Langevin function

$$L(x) = \coth(x) - \frac{1}{x} \quad \text{with} \quad x(H, T, d_{0,\text{mag}}) = \frac{\mu_0 \mu_{\text{NP}} H}{kT}, \quad (1.3)$$

where  $\mu_{\text{NP}} = V_{\text{NP}} m_s$  is the NP's magnetic moment. The parameters  $V_{\text{NP}}$ ,  $m_s$  and  $\Phi$  are respectively the NP's volume, NP's saturation magnetization and NP's volume fraction. Lastly,  $x$  is the Langevin parameter,  $\mu_0$  is the vacuum permeability and  $k$  is the Boltzmann constant.

Figure 3 presents examples of room temperature superparamagnetic magnetization curves, where two experimental results are shown: one obtained for the sample initially dispersed in acidic aqueous medium and another after transferred to EMIM-TFSI. The particle diameter and polydispersity remains unchanged as a result of the curves overlapping, which indicates that the performed solvent interchange process does not sensibly alter the size distribution. The size parameters obtained by the Langevin function fit are the

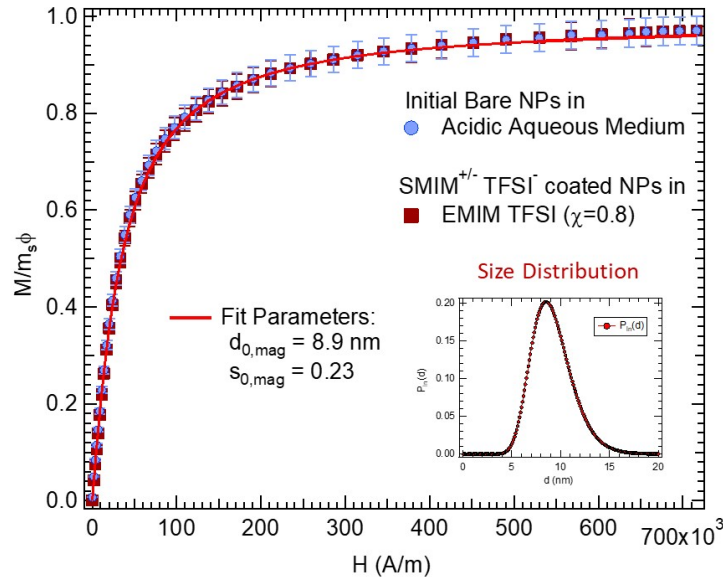


**Figure 3** – *Main figure*: Room temperature magnetization ( $M$ ) curves as function of the applied magnetic field ( $H$ ). The data is normalized by the volume fraction of nanoparticles ( $\Phi_{\text{aq}} = 1.53 \pm 0.03$  vol% in aqueous medium and  $\Phi_{\text{(EMIM-TFSI)}} = 0.96 \pm 0.03$  vol% in EMIM-TFSI) and by the saturation magnetization ( $m_{s(\text{aq})} = 278 \pm 17$  kAm $^{-1}$  and  $m_{s(\text{EMIM-TFSI})} = 292 \pm 18$  kAm $^{-1}$ ). *Inset*: lognormal size distribution (Equation 1.1) of the fitted parameters by the Langevin model (Equation 1.2). Figure adapted from ref. [19].

magnetic median diameter  $d_{0,\text{mag}} = 8.9$  nm and the polydispersity  $s_{0,\text{mag}} = 0.23$ . This magnetic size distribution leads to the volume-averaged diameter ( $d_{\text{NP}}$ ) [61] standardly used ahead in the analysis of interparticle interaction and thermodiffusion in chapter 2 and chapter 3.

**Table 1** – Experimental size determinations (from [18,19]) obtained by TEM ( $d_{0,\text{TEM}}$ ,  $s_{0,\text{TEM}}$ ) and by room temperature magnetization ( $d_{0,\text{mag}}$ ,  $s_{0,\text{mag}}$ ,  $d_{\text{NP}}$ ) of the samples dispersed in various media: EMIM-TFSI, EAN and water.

Sample	$d_{0,\text{TEM}}$ (nm)	$s_{0,\text{TEM}}$	$d_{0,\text{mag}}$ (nm)	$s_{0,\text{mag}}$	$d_{\text{NP}}$ (nm)
Water and EAN [18]	6.5	0.22	6.9	0.21	7.4
EMIM-TFSI [19]	8.7	0.3	8.9	0.23	9.6

Finally, Table 1 sums up the size characterizations performed by TEM and room temperature magnetization for the both samples investigated throughout this Part I.

### 1.3 Internal Structure and Surface Properties

Initially, magnetite ( $\text{Fe}_3\text{O}_4$ ) nanoparticles are formed in substep 1(a) of the synthesis process (see Figure 1). Nonetheless, this structure is not chemically stable as it evolves in acidic medium in response to acid attack and oxidizes in the presence of oxygen [62]. Therefore, after step 1(c), the internal structure is fully oxidized and converted into maghemite ( $\gamma\text{-Fe}_2\text{O}_3$ ), where the  $\text{Fe}^{2+}$  ions are substitute by  $\text{Fe}^{3+}$ .

Both materials belong to the class of spinel ferrites, named after the mineral spinel ( $\text{MgAl}_2\text{O}_4$ ) due to the resemblance of the crystalline structure. The spinel structure is a cubic close-packed lattice (CCP) expressed by the space group  $\text{Fd}\bar{3}\text{m}$  n° 227 as illustrated in Figure 4. The unit cell is composed of a face-centered cubic array of 32 oxygen atoms forming 64 tetrahedral sites and 32 octahedral ones. In the ideal maghemite structure, the  $\text{Fe}^{3+}$  metallic ions occupy 1/8 of the tetrahedral sites and 5/12 of the octahedral sites, where the distribution of these vacancies can be ordered or disordered [63]. For the standard maghemite synthesis, the presence of a single phase spinel structure is routinely confirmed by X-ray diffraction of the powdered samples [58].

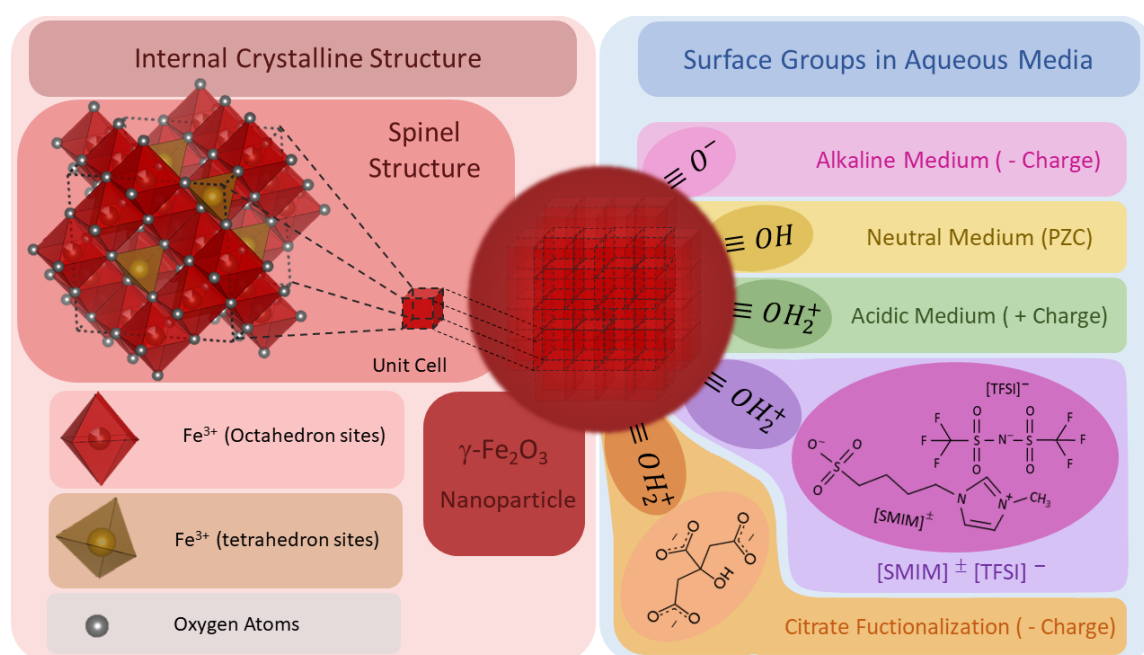
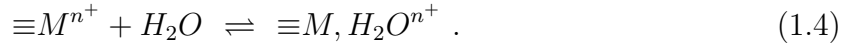


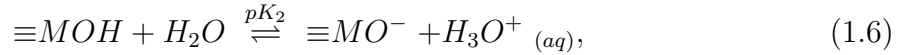
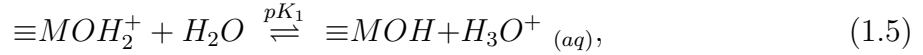
**Figure 4** – *Left red side:* Internal spinel crystalline structure of the MNPs exhibiting the octahedron (red) and tetrahedron (yellow) sites. Structure visualization generated using ref. [64]. *Right blue side:* Surface group development in different aqueous media: alkaline, neutral and acidic. The addition of two different anions (citrate and  $[\text{SMIM}]^+[\text{TFSI}]^-$ ) to a solution where the nanoparticles are highly positively charged can induce surface functionalization.

The magnetic properties of the NPs originate from this crystalline structure. Maghemite belongs to the ferrite class which, as the name might suggest, exhibits ferrimagnetic properties. Ferrimagnetism is also known as “uncompensated antiferromagnetism” due to the anti-parallel alignment of the spins but with a resulting non-zero dipole moment as consequence of the structural arrangement. As a result of the nanoscale size reduction and of the rock-like shape of the NPs, the nanoparticles can be considered as uniaxial magnetic monodomains and, therefore, present a high magnetic moment, however with a low anisotropy energy (reaching the order of magnitude of thermal energy  $\sim kT$ ). This combination of characteristics allows the manifestation of peculiar effects, such as Néel’s superparamagnetism [52], observed in the magnetization response presented in previous section (Figure 3).

Now, we turn ourselves to the surface properties, more specifically the surface charge development. First, we have to acknowledge that the particle's surface is going to be immersed in an aqueous medium in the subsequent step 2 of the synthesis. At this condition two charging mechanisms might emerge: ionization/dissociation of surface groups or adsorption of ions available in the solution [65]. In particular, the case of surface charge generation in bare iron oxide nanoparticles has been already well documented in the literature [66–68]. The principle behind the formation of a surface charge in bare oxide nanoparticles dispersed in aqueous medium is based on *aquation reactions* [69] that affect metal ions ( $M^{n+}$ ) located on the surface in direct contact with water, simplified as



Therefore, the protonation and deprotonation of the hydrated surface is conventionally represented by the following hydrolysis pH-dependent reactions [70]:



where  $K_1$  and  $K_2$  are the corresponding thermodynamic constants, following the definition  $pK = -\log K$ . This way, the surface of the nanoparticle acts as a weak diprotic Brønsted<sup>2</sup> acid with the pH of the aqueous medium favoring the formation of the  $\equiv MOH_2^+$  sites in case of an acidic medium, the amphoteric<sup>3</sup>  $\equiv MOH$  in an intermediary condition and the sites  $\equiv MOH^-$  in more alkaline conditions.

It is experimentally determined [71, 72] that the point of zero charge (PZC) of these NPs, characterized by the complete dominance of the sites  $\equiv MOH$ , is observed close to neutral medium ( $pH_{PZC} \approx 7.0$ ). The surface gradually charges positively for  $pH < pH_{PZC}$ , as a consequence of the equilibrium being dislocated towards the formation of  $\equiv MOH_2^+$  sites, until it reaches a saturated surface charge density ( $\sigma_0^{\text{sat}}$ ) certainly after  $pH < 2$ . As expected, for  $pH > pH_{PZC}$ , the particle becomes negatively charged reaching surface charge saturation for  $pH > 12$ . In both senses, the surface charge can reach up to  $\sigma_0^{\text{sat}} = 0.3 \text{ C/m}^2$ , where a limiting factor is the particle size, as it correlates with the proportion of available/dead charging sites [73].

The introduction of ions to the aqueous solution where the nanoparticles are charged can induce surface functionalization by physical adsorption. Here two different anion species are employed as surface complexants: citrate (2-hydroxypropane-1,2,3-tricarboxylate) and [SMIM]<sup>±</sup>-[TFSI]<sup>-</sup> (deprotonated 1-(4-sulfobutyl)-3-methyl imidazolium bistriflimid). The surface coating is possible in acidic situations due to attractive electrostatic forces, since

<sup>2</sup> In the theory of Brønsted-Lowry acids and bases are classified, respectively, by their capacity to donate or receive protons ( $H^+$ ).

<sup>3</sup> The amphoteric character is determined as the capacity of a compound or ion to react both as an acid or a base.

the large positive structural charge of the NPs (around 2 elementary charges per  $\text{nm}^2$ ) induces the condensation of anions (that have at least one available negative charge) around the particle. In the case of the citrate functionalization the anion becomes attached to the surface sites by any of the three carboxylate groups, while the remaining ones will provide additional negative charge (one or both, depending on the pH of the medium). For  $[\text{SMIM}]^\pm\text{-}[\text{TFSI}]^-$ , the electric bounding occurs by the zwitterion  $[\text{SMIM}]^\pm$ , while the  $[\text{TFSI}]^-$  compensates the remaining positive and no additional charge is generated.

Conclusively, it is possible to achieve stable ferrofluids with bare nanoparticles in the pH extremes (with a controlled ionic strength) due to their high structural charge. In addition, citrate coating will produce a negative surface charge in water as the pH shifts towards alkaline, allowing effective particle dispersion for  $\text{pH} \geq 7$ , and also, in several ionic liquids (with specific positive counter-ions). Although the surface functionalization with  $[\text{SMIM}]^\pm\text{-}[\text{TFSI}]^-$  remains flocculated in water, it enables adequate dispersions in several ionic liquids that otherwise would not be possible [19]. The dispersion process and fluid structuralization is discussed in the next chapter.

## Chapter 2

# Colloidal Dispersions of MNPs

Colloids are systems composed of at least two phases, where one of them is in the sub-microscopic region but greater than the atomic size range [74]. Ferrofluids belong to the colloid class of dispersions of solid particles in a continuous liquid, also known as *Sols*. This kind of colloids present a uniform visual aspect at the macroscopic scale, even though at the nano to micrometric level the fluid is heterogeneous.

Several forces are involved in order to prevent the complete phase separation of the dispersed particles and the solvent. The colloidal stability can be lost at different scales, from nanometric condensation, to microscopical density fluctuations, until it reaches macroscopic separation. Moreover, the mentioned destabilization may be reversible or irreversible depending on the physico-chemical process.

By the presented colloid definition, the first limiting factor is already established as the particle size. Maintaining the particles in suspension relies on the preponderance of the diffusive Brownian motion promoted by the thermal agitation, over the sedimentation impelled by the gravitational force. For this reason, the density of the components, the viscosity of the solvent and the temperature are the dominant parameters regulating the critical size limit [75]. As a result, aggregation/flocculation/coagulation is one of the most preponderant causes of colloidal instabilities.

The attractive forces that tend to promote particle agglomeration are typically van der Waals (Keeson, Debye and London), magnetic dipole-dipole and dipole-field<sup>1</sup> to the system. interactions. Many different strategies are developed in order to overcome these attractive forces, which are mainly built up on the generation of repulsive interparticle forces such as electric and/or steric repulsion.

As mentioned before, we are dealing with charged MNPs where the standard approach to realize the interparticle interactions in standard polar solvent is of electrostatic origin. Then the DLVO theory [76,77] gives a good understanding of the colloidal stability

---

<sup>1</sup> Evidently, when an external magnetic field  $\vec{H}$  is applied

and the system's phase diagram. This theory assembles the resulting potential of the system as the sum of the vdW and electrostatic potentials, that was even expanded to a X-DLVO model [72] to accommodate the magnetic interactions. It is heavily based on the establishment of an electric double layer (EDL), in which the surface electrical potential in standard polar media, such as water or DMSO, can be mathematically developed by the Poisson-Boltzmann equation (PB)[65] considering the Gouy-Chapman model [78,79]. This approach leads to insightful qualitative and quantitative results [80] in standard polar media, however, it presents several limitations in more intricate circumstances, mostly related to simplifications adopted in order to solve the PB equation.

The ionic liquid based sols studied here are an example of systems for which the DLVO theory is not at all applicable, due to critical features that arise from the fact that the solvent composition is solely composed of ions, the ionic concentration is far too large. Nonetheless, multiple studies [17, 19, 20, 58, 60, 81] in the past years shed light on the particle interactions and colloidal stability of the ferrofluids here investigated. In such ionic liquids, the colloidal stability of ferrofluids is ensured by an ionic structuration around the NPs (see [subsection 2.3.1](#)).

The step 2 of the synthesis process is described in the following sections, detailing the procedures required to disperse the MNPs in the different aqueous and ionic liquids media. It is also provided essential information regarding the particle interactions and local ordering, as demanded for the thermodiffusion analysis in [chapter 3](#).

## 2.1 Peptization in Weak Electrolyte Solvents

### 2.1.1 Acidic Medium with $\text{NO}_3^-$ Counterions

After the subsequently washing of the NPs with acetone and ether, as described in the final procedure of step 1 in [section 1.1](#), the flocculated nanoparticles can then be satisfactorily dispersed by the direct addition of an aqueous nitric acid solution. The pH of the ferrofluid is then regulated between 1.5 and 2.0, setting an ionic strength of  $10^{-1.5} \sim 10^{-2.0}$  M, whereas the remaining organic solvents are removed by evaporation. As previously mentioned, this condition guarantees a saturated positive surface charge balanced by  $\text{NO}_3^-$  counterions, which prevents phase separations in sufficiently low ionic strength. The sample can be diluted using a nitric acid solution (adjusted at the appropriate pH) until the desired NP's volume fraction is reached. This standard stable acidic ferrofluid is the starting point to further manipulations that will be performed to achieve the following dispersions, however, itself is not going to be the object of study in this part of the thesis.

### 2.1.2 Neutral pH and Citrate Functionalization

Ferrofluids dispersed at a  $\text{pH} \sim 7$  can be obtained by functionalization with citrate ligand. First, the acidic ferrofluid obtained previously (set at 1.0 % volume fraction) can be destabilized by adding sufficient amounts of citric acid<sup>2</sup>, in which the increased ionic strength precipitates the nanoparticles as the electrostatic potential is heavily screened. The precipitation process is accelerated with the help of magnets placed at the bottom of the beaker. Next, the supernatant is removed and the sedimented nanoparticles are washed with an aqueous solution of citric acid prepared at  $10^{-2.5}$  M. This washing process is repeated several times ensuring the complete removal of the  $\text{NO}_3^-$  counterions, covering the NP's surface with citrate and adjusting the free citric acid concentration to  $\approx 10^{-2.5}$  M.

Finally, a 1 mol/L base of the type  $(\text{X}^+, \text{OH}^-)$ , with  $\text{X}^+ = \text{Li}^+, \text{Na}^+$  or  $\text{Rb}^+$  is carefully added till a  $\text{pH} \approx 7$  is reached by substituting the  $\text{H}^+$  ions by the  $\text{X}^+$  cations in the process. The final product is a sol at neutral pH thanks to the negatively charged citrate coating balanced by the X counter-ions introduced by the base. The particle concentration can be reduced by the addition of a  $\text{pH} = 7.0$  solution of  $10^{-2.5}$  M of citric acid neutralized by the respective base.

These two weak electrolyte solvents are the foundation of the dispersions in ionic liquids, and also, of the mixtures with carbon nanodots performed in [Part III](#). Despite the fact that in the latter case, the investigated MNPs present a cobalt ferrite core instead of being constituted uniquely of maghemite.

## 2.2 Peptization in Ionic Liquids

### 2.2.1 $\text{SMIM}^\pm\text{-TFSI}^-$ coated MNPs dispersed in EMIM-TFSI

Before actually describing the transfer process from the typical acidic ferrofluid to EMIM-TFSI, first, it is indicated a few important features of this room temperature ionic liquid (RTIL). EMIM-TFSI (here supplied by Solvionic [83]) presents a viscosity ranging from  $4 \times 10^{-2}$  Pa s at 294 K down to  $3 \times 10^{-3}$  Pa s at 460 K (following [84]). It presents a low vapor pressure, a low flammability, a high ionic conductivity and a wide electro-chemical window [84–86]. It is also chemically stable up to high temperature (long-term  $\sim 500$  K and up to  $\sim 700$  K for shorter times [85]), making it a good candidate for thermoelectrical applications [87].

The preparation details of the dispersions in EMIM-TFSI are given extensively in ref.[19]. Here is a short summary of the process. First, an aqueous solution of NaOH 1 M is added to 1.0% volume fraction of the acidic ferrofluid, till the pH reaches the point of

<sup>2</sup> Previously, the procedure was performed by adding a given citrate salt, incurring in several technical disadvantages if compared to the enhanced method applied here, proposed and described in [82].

zero charge ( $\text{pH}_{\text{PZC}} \approx 7$ ). The uncharged nanoparticles are magnetically precipitated and the supernatant is removed. Next, the particles are washed several times with ultra-pure water, removing the  $\text{NO}_3^-$  ions until the free concentration is reduced to values below  $10^{-6}$  M. An acidic aqueous solution of 1-(4-sulfobutyl)-3-methyl imidazolium bistriflimide (HSMIM TFSI) is added, reducing the pH back to a value close to 1.5. At this condition, the surface of the NPs are recharged and a structural charge  $Z_{\text{struc}} \sim +400 \pm 100$  is reintroduced, but now the species compensating their charge are deprotonated 1-(4-sulfobutyl)-3-methylimidazolium bistriflimide ( $\text{SMIM}^{\pm}\text{-TFSI}^-$ ), which has been shown to be close to the interface [19]. At this step, the particles remain flocculated.

Finally, EMIM-TFSI is added and the water removed by freeze-drying<sup>3</sup>, leading to a stable ferrofluid in a pure ionic liquid. The volume of the added EMIM-TFSI is adjusted such as the volume fraction of NPs is settled around 1%.

Increasing the volume fraction of the samples till  $\sim 12.0\%$  was achieved by ultracentrifugation (Optima MAX-XP Ultracentrifuge from the company Beckman Coulter, USA) at  $250,000\times g$  and  $25^\circ\text{C}$ . The duration usually varies between 16 to 32 hours. This technique promotes a reversible phase separation, where the clear supernatant is removed and the remaining liquid is homogenized. Then, the volume fractions can be determined by two methods: i) tracking the mass of the material during the sensible stages, (before/after) freeze-drying and (before/after) ultracentrifugation; ii) Iron titration by inductively coupled plasma mass spectrometry (ICP-MS) (Thermo Scientific ICAP Q apparatus). Both methods were in good agreement.

### 2.2.2 Citrate coated MNPs dispersed in EAN

Ferrofluids composed of maghemite nanoparticles dispersed in Ethylammonium Nitrate (EAN) are recognized as a model system, since both components have been extensively studied in the literature. Its viscosity is known as a function of temperature ( $37.4\text{ mPa}\cdot\text{s}$  at  $22^\circ\text{C}$ ) [88], a stand out feature considering thermophoretic applications. Another advantage is that a pH scale can be defined [89, 90] and some electrical properties can be determined at room temperature, such as the permittivity (26.2) and its Bjerrum length (2.1 nm) [18].

Regarding the local ordering, it is known that EAN molecules form a network of hydrogen bonds (similar to that of water [91]) and the small ethyl chain induces a sponge-like structure in the bulk EAN with polar and apolar domains [92]. Close to a negatively charged surface, the sponge-like structure of EAN becomes lamellar, where at the first layer, the charged polar heads of  $\text{EA}^+$  remain close to the negative charges on the surface and the tails associate together. Several, less organized layers are formed above the

<sup>3</sup> Note that a very small amount of water, difficult to quantify exactly, always remains in the RTIL.

first one until the bulk sponge structure is recovered, as seen experimentally for example by atomic force Microscopy [93].

The details on the preparation of dispersions in EAN are given extensively in [18]. The process is simple and direct. EAN is added to the aqueous dispersions of citrate coated nanoparticles with the counterion of choice ( $\text{Na}^+$ ,  $\text{Rb}^+$  or  $\text{Li}^+$ ), in a 50/50 vol% proportion of EAN and water. Water is (almost - see the previous footnote) completely removed by freeze-drying, leading to dispersions in pure EAN with a volume fraction close to the initial 1.0 %. This process produces visually stable samples and optical microscopy shows no heterogeneities at the micron scale.

Thereafter, a series of samples at various volume fractions, between 3.5% and 25%, have been produced by ultracentrifugation of the initial dispersion. The same process detailed previously for the EMIM-TFSI sample was here applied.

EAN and water are miscible in the whole range of proportions. Considering that the water and EAN ferrofluids are prepared stemming from the same initial sample, the production of dispersions with different water contents can be readily performed by direct mixing both fluids, at the same volume fraction, adjusting only the mass proportions.

## 2.3 Interparticle Interactions

In the previous sections, it was established that the studied systems are constituted of particles performing Brownian motion inside a liquid medium. They present attractive interactions due to van der Waals forces (which are isotropic and are present in any colloid) and dipolar magnetic interactions (which are anisotropic and attractive on average). In addition, they may also develop repulsive interactions if an electric surface charge is generated. One last effective “interaction” of entropic origin is the hard core repulsion (or volume exclusion), which emerges from the fact that the particles are completely solid and cannot interpenetrate each other.

These features make the interparticle potential of sols very similar to that of atomic systems<sup>4</sup> despite the difference in scale. In such a way, the phases of a colloidal system are comparable to the states of matter [94]: *Gas* is characterized by low particle concentration; *Liquid* is attributed to large particle concentration; *fluid* is reached above a critical point; Finally, *Solid* is an extremely dense amorphous or crystalline phase.

In general, the parameters controlling the transitions between these phases are temperature, ionic strength and pH in aqueous media, and applied magnetic field. These are responsible for the regulation of the electrostatic and magnetic interactions, altering the surface charge, the screening of the electric potential and the fluid structure (e.g. the

---

<sup>4</sup> The interaction of a pair of atoms can be approximated by the Lennard-Jones potential (potential 6-12), which is comparable to the potential experienced by the NPs.

interparticle distance). The thermodynamic quantities in the colloidal conjuncture are the osmotic pressure  $\Pi$ , the volume fraction  $\Phi$  and the temperature  $T$ . The relationship of these variables can be approximated by reinterpreting the virial expansion.

The virial expansion is a generalization of the ideal gas law carried out by a power series of the form:

$$P V = NkT \left( 1 + a_2 \frac{N}{V} + a_3 \left( \frac{N}{V} \right)^2 + \dots \right), \quad (2.1)$$

where  $V$  and  $P$  are the volume and pressure of a gas containing  $N$  molecules at temperature  $T$ ,  $a_n$  (with  $n = 1, 2, 3..$ ) are the virial coefficients<sup>5</sup> and  $k$  is the Boltzmann constant. For sufficiently diluted systems, it is possible to construct the virial expansion for colloidal dispersions [95] as

$$\frac{\Pi V_{\text{NP}}}{kT} = \Phi + A_2 \Phi^2 + \dots, \quad (2.2)$$

where the original development for pressure ( $P$ ) was adapted to the osmotic pressure ( $\Pi$ ) and the number of molecules per volume ( $N/V$ ) was substituted by the number density of nanoparticles ( $n_{\text{NP}} \equiv N_{\text{NP}}/V$ ). In fact, Equation 2.2 was written in a more useful fashion, i.e., in terms of the nanoparticle volume fraction

$$\Phi = n_{\text{NP}} \cdot V_{\text{NP}} \quad (2.3)$$

and the dimensionless virial coefficients  $A_n \equiv a_n/(V_{\text{NP}})^n$ , where  $V_{\text{NP}}$  is the nanoparticle volume.

The  $A_n$  coefficients are closely related to the global interactions and an approximation till the second order is often enough to achieve a reasonable representation of the system in a wide range of  $\Phi$ . Therefore, if  $A_2 = 0$ , the conventional form of the ideal gas law is obtained, featuring a system of non-interacting particles depending only on the linear relation between the thermodynamic quantities  $\Pi V_{\text{NP}} = \Phi kT$ . If  $A_2 > 0$  the interparticle interactions are globally repulsive, while if  $A_2 < 0$  the interaction regime is effectively attractive.

The second virial coefficient  $A_2$  can be experimentally determined by a  $\Pi$  vs  $\Phi$  phase diagram or it can be estimated via the osmotic compressibility  $\chi$ . At low  $\Phi$ 's, the relation between  $\chi$ ,  $\Pi$  and  $A_2$  can be written as follows [82]:

$$\chi(\Phi) = \frac{kT}{\left( \frac{\partial \Pi V_{\text{NP}}}{\partial \Phi} \right)_T} \approx \frac{1}{(1 + 2A_2 \Phi)}, \quad (2.4)$$

this approximation assuming that the particle concentration is low enough for higher orders to be neglected (i.e.  $2A_2 \Phi \ll 1$ ).

At larger volume fractions, Carnahan and Starling has proposed for Hard Spheres (for which  $A_2 = 4$ ) a model allowing to describe the  $\Phi$ -dependence of the osmotic pressure

<sup>5</sup> The first virial coefficient is equal to 1, corresponding to the first term in parenthesis in Equation 2.1.

$\Pi$  and of the compressibility  $\chi$ , which is valid up to very high volume fractions (of the order of 40%)[96].

Along those lines, we can experimentally estimate  $\chi(\Phi)$  by Small Angle X-ray Scattering (SAXS), where the determination of the intensity at low scattering vector ( $q \rightarrow 0$ ) leads to the osmotic compressibility  $\chi$  at a certain  $\Phi$ . The measurements were carried out with the XEUSS 2.0 (Xenocs) of LLB-Saclay at room temperature on dispersions in a broad range of volume fractions. Complementary Small Angle Neutron Scattering (SANS) experiments were performed at PAXY spectrometer in Orphée - LLB - Saclay at various  $T$ 's ranging between 293 K and 473 K. All these experiments were performed without applied magnetic field.

The theoretical approach applied here to adjust the  $\Phi$ -dependency of the compressibility  $\chi(\Phi)$  is the same used in references [82, 97]. The model, valid for repulsive interparticle interaction ( $A_2 > 0$ ), is based on the Carnahan-Starling formalism [96, 98], where the particles are considered as hard spheres with an effective volume fraction  $\Phi_{\text{eff}}$  (determined by an effective particle volume  $V_{\text{eff}}$  with an adapted diameter  $d_{\text{eff}} = d_{\text{NP}} + 2\kappa^{-1}$ ) taking into account an effective screening length<sup>6</sup>  $\kappa^{-1}$  as:

$$\chi(\Phi) = \chi_{\text{cs}}(\Phi_{\text{eff}}) = \frac{(1 - \Phi_{\text{eff}})^4}{1 + 4\Phi_{\text{eff}} + 4\Phi_{\text{eff}}^2 - 4\Phi_{\text{eff}}^3 + \Phi_{\text{eff}}^4}. \quad (2.5)$$

Further,  $\Phi_{\text{eff}}$  can be expressed as function of  $\Phi$  and the volume-averaged diameter  $d_{\text{NP}}$  by noting that the number of particles per volume ( $n_{\text{NP}} = n_{\text{eff}}$ ) is conserved:

$$\frac{\Phi_{\text{eff}}}{V_{\text{eff}}} = \frac{\Phi}{V_{\text{NP}}} \Rightarrow \Phi_{\text{eff}} = \Phi \left( 1 + \frac{2\kappa^{-1}}{d_{\text{NP}}} \right)^3. \quad (2.6)$$

Lastly, the coefficient  $A_2$  can be determined as a function of the effective volume fraction for example by applying the approximation done in Equation 2.4 to Equation 2.5:

$$\frac{1}{(1 + 2A_2\Phi)} = \frac{1}{(1 + 2A_2^{\text{HS}}\Phi_{\text{eff}})} \Rightarrow A_2 = A_2^{\text{HS}} \frac{\Phi_{\text{eff}}}{\Phi} = 4 \frac{\Phi_{\text{eff}}}{\Phi} \quad (2.7)$$

where  $A_2^{\text{HS}}$  is the the second virial coefficient of hard spheres, which (as said before) is equal to 4 [96].

This method allows, for systems in repulsive interaction, to determine the coefficient  $A_2$  with samples at volume fractions well outside the linear limit of Equation 2.4.

### 2.3.1 Stability of MNPs in EMIM-TFSI

The experimental results of  $\chi(\Phi)$  obtained with ferrofluids based on EMIM-TFSI by SAXS and SANS experiments at room temperature and zero magnetic field are shown in Figure 5a.  $\chi(\Phi)$  is a decreasing function of  $\Phi$  and the global particle interaction is thus

<sup>6</sup> which is not a Debye length

repulsive with  $A_2 > 0$ . The theoretical fit (red line) is performed by Equation 2.5, where the adjusted parameters are the effective volume fraction  $\Phi_{\text{eff}} = 1.82 \Phi$  and the second virial coefficient  $A_2 = 7.3$ . Taking into consideration that in this system the generation of a Debye electric double layer is not feasible, the repulsive component has to be attributed to another effect.

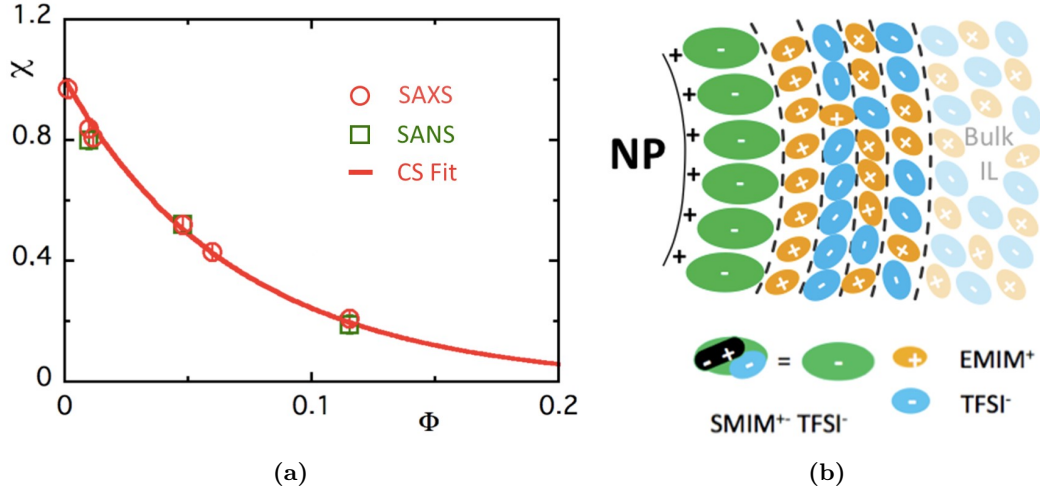


**Figure 5** – (a) Osmotic compressibility  $\chi$  of the NPs in the colloidal dispersions as based on EMIM-TFSI a function of their volume fraction  $\Phi$  - Open symbols: Experimental determinations at room temperature by SAXS (open circles) and SANS (open squares) - Full line: Carnahan-Starling adjustment with effective hard spheres [96, 98] of volume fraction  $\Phi_{\text{eff}} = 1.82 \Phi$  leading to  $A_2 = 7.3$ ; (b) Sketch of the ionic layering around the NPs responsible for the colloidal stability of the dispersion. The first layers close to NPs figure the hydroxyl ionic NP surface and some condensed SMIM<sup>±</sup>-TFSI<sup>-</sup> counterions, they initiate the long-range IL layering.

It has been proven both experimentally [93, 99, 100] and by numerical simulations [101–105] that along a flat and charged interface, ILs can organize themselves as layers of ions of alternating sign. Along a curved interface such as that of the present charged NPs [106, 107], long-range charge-density oscillations can be also formed, for given geometrical and charged conditions of the IL anions and cations [19, 104, 108]. If the number of organized layers is large enough, they are able to overcome the attractive components of the interparticle interaction and stable colloidal dispersions can be obtained [19, 81, 107]. The colloidal stability of the present NPs in EMI-TFSI is thus proposed to come here from the “effective” interparticle repulsion, due to the regular layering of ions, of alternate sign, around the NPs (see the sketch in Figure 5b), which dominates both van der Waals and magnetic dipolar interparticle attractions. Here the resultant screening  $\kappa^{-1}$  of the repulsive (on average) interparticle interaction can be extracted from the Equation 2.6. It leads to  $\kappa^{-1} \sim 1.1$  nm, which means that the structure of the liquid is modified on few  $\kappa^{-1}$ , typically up to  $5 \kappa^{-1}$ , which corresponds to 6-7 layers of anions and cations from the IL [109].

The effect of temperature on the colloidal stability is analysed at  $\Phi = 1.0$  vol% by SANS measurements. The experimental results are shown in Figure 6, where the curves

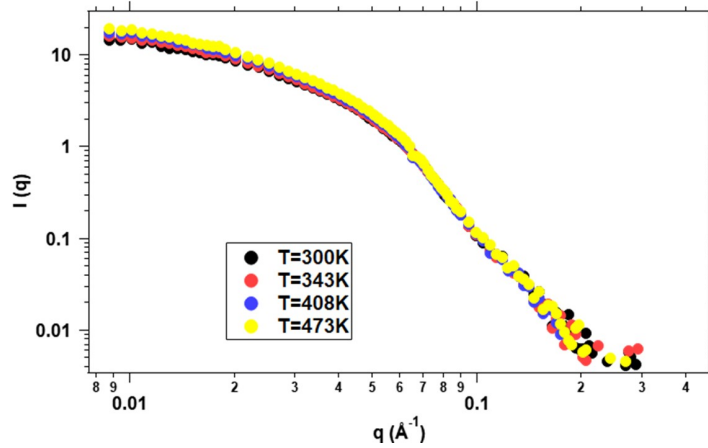


**Figure 6** – SANS intensity as a function of the scattering vector  $q$  for a sample dispersed in EMIM-TFSI at  $\Phi = 1.0\%$  measured in four different temperatures.

indicate a meager shift of the intensity as function of temperature. At this level, the colloidal stability remains unaffected and  $\chi$  is nearly independent of  $T$ . The colloidal stability of the samples was also examined under-field up to  $H = 716 \text{ kA m}^{-1}$  ( $= 9\,000 \text{ Oe}$ ). It has been checked optically, looking at the scattering pattern of a non-absorbing laser beam, as described in [19, 110], indicating no perceptible destabilization.

The colloidal stability of the sample, both in zero field and under-field, confirms that a strong interparticle repulsion exists, that persists in a broad range of particle concentrations and temperatures.

### 2.3.2 Stability of MNPs in EAN with $\text{Na}^+$ , $\text{Rb}^+$ and $\text{Li}^+$ Counterions

The nanostructure of the colloidal dispersions in EAN were studied by SAXS (SWING beamline of SOLEIL Synchrotron, France). The measurements were performed with a beam energy of  $14\,666 \text{ eV}$  and two sample-detector distances were used to reach a range of the scattering vector  $q$  between  $3.2 \times 10^{-3}$  and  $4.0 \times 10^{-1} \text{ \AA}^{-1}$ . Figure 7 shows the evolution of the  $\Phi$ -normalized scattered intensity  $I(q)/\Phi$  for the three counterions. The measurements correspond to the available stable samples of each concentration series. This scattered intensity can be written as:

$$I(q, \Phi) = (\Delta\rho)^2 \Phi V_{\text{NP}} P(q) S(q, \Phi), \quad (2.8)$$

where  $\Delta\rho$  is the scattering length contrast between NPs and solvent,  $\Phi$  is the NPs' volume fraction,  $V_{\text{NP}}$  their volume,  $P(q)$  is the form factor and  $S(q)$  the structure factor. An extrapolation of the measurements at zero volume fraction enabled us to determine the experimental form factor, also plotted in Figure 7, which corresponds to  $S(q) = 1$  in Equation 2.8. The comparison of  $I(q \rightarrow 0)$  of other samples to the value for the form factor thus tells us if interparticle interactions are repulsive or attractive.

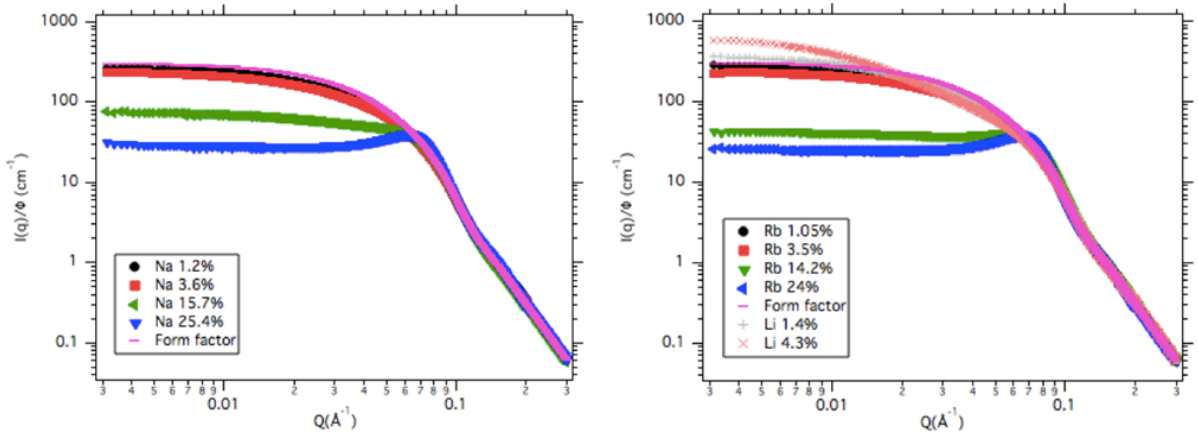


**Figure 7** – Small angle X-ray Scattering (SAXS) of several dispersions with sodium counterions (left) and rubidium or lithium counterions (right) for several volume fraction indicated in the captions. The intensity is normalized by the volume fraction (in %). The reference form factor which corresponds to the pure geometric contribution of the nanoparticles (no interparticle interaction) is plotted on each graph in pink.

Figure 7 clearly shows that the global interparticle interaction is repulsive ( $A_2 > 0$ ) for sodium and rubidium ( $I(q \rightarrow 0) < I_{\text{Form factor}}(q \rightarrow 0)$ ), while it is attractive ( $A_2 < 0$ ) for lithium ( $I(q \rightarrow 0) > I_{\text{Form factor}}(q \rightarrow 0)$ ). Figure 7 also illustrates the fact that it is possible to obtain stable colloids up to a  $\Phi$  of the order of 25.0% with  $\text{Na}^+$  and  $\text{Rb}^+$  counterions, while with  $\text{Li}^+$  counterions only a maximal volume fraction of the order of 4.0% can be achieved.

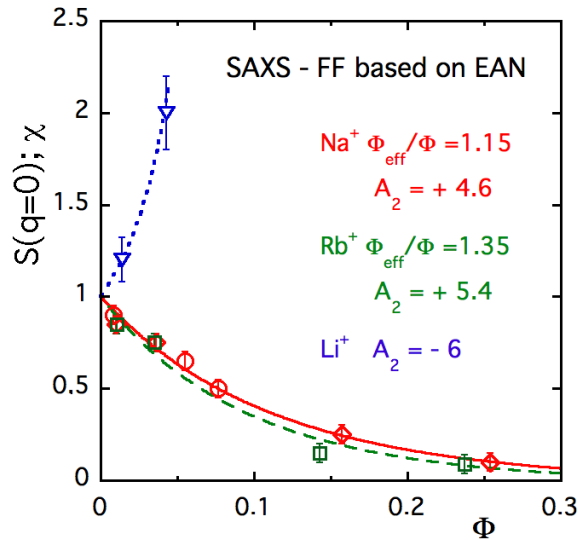


**Figure 8** – Compressibility  $\chi$  of the NP's system as determined by  $S(q=0)$  in SAXS experiments for EAN-based dispersions with  $\text{Na}^+$  (red circles, this work and red diamonds from ref [58]) and  $\text{Rb}^+$  (green squares) counterions - Fits of the data with Equation 2.5 are obtained using  $\Phi_{\text{eff}}/\Phi = 1.15$  for  $\text{Na}^+$  (full line,  $A_2 = 4.6$ ) and  $\Phi_{\text{eff}}/\Phi = 1.35$  for  $\text{Rb}^+$  (dashed line,  $A_2 = 5.4$ ). For  $\text{Li}^+$  (blue symbols) the linear development of Equation 2.4 is used (dotted line,  $A_2 = -6$ ).

The obtained compressibility assuming  $S(q=0) = \chi$  is plotted in Figure 8 for the different counterions  $\text{Na}^+$ ,  $\text{Rb}^+$  and  $\text{Li}^+$ . The analysis with equation Equation 2.5 gives

$A_2 = 4.6 \pm 0.5$  for  $\text{Na}^+$  counterions and  $5.4 \pm 1$  for  $\text{Rb}^+$ , both values being very close to the hard sphere value  $A_2 = 4$ , meaning that the associated “screening length”  $\kappa^{-1}$  is extremely small  $\sim 0.2$  nm for  $\text{Na}^+$  and  $\sim 0.4$  nm for  $\text{Rb}^+$  (using a volume-averaged NP diameter  $d_{\text{NP}} = 7.4$  nm). On the contrary for  $\text{Li}^+$  counterions the values of  $\chi$  are larger than 1, which can be associated either to individually dispersed NPs with a negative  $A_2 = -6$  or to the presence of small aggregates (also due to attractive interparticle interactions). This attraction also explains why stable colloids with  $\Phi$  larger than 4.0% cannot be obtained. Note that these results are comparable to previous ones [58] on the same kind of samples with  $\text{Na}^+$  counterions – but also with  $\text{Li}^+$  counterions which produced some weakly attractive interaction leading to small aggregates stable in the long run for higher  $\Phi$  [58].

By Small Angle Neutron Scattering, it has been checked on a ferrofluid sample based on EAN with  $\text{Na}^+$  counterions at  $\Phi = 5.0\%$ , that the scattered intensity does not depend – at the first order within the error bar – on temperature for  $300 \text{ K} \leq T \leq 360 \text{ K}$ , above which EAN is no longer stable. This fact is illustrated by Figure 9, which also shows that the scattered intensity remains the same at 300 K after a stay of several hours at 360 K (during the SANS measurement). This implies that (at the first order) the interparticle interaction and the compressibility  $\chi$  do not depend on  $T$  in the dispersion, nor the local ionic organization around the NPs. We can assume that the same behavior is also true for  $\text{Rb}^+$  counterions, as they present very similar interparticle interactions (see Figure 8).

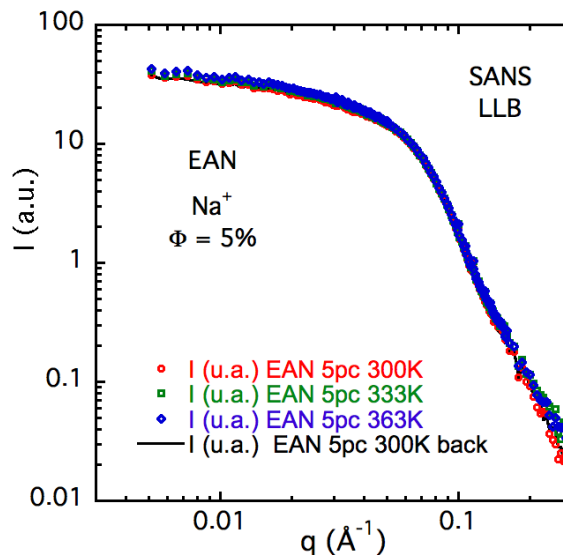


**Figure 9** – Small Angle Neutron Scattering (SANS) of a dispersion in EAN with  $\text{Na}^+$  counterions at  $\Phi = 5.0\%$  at three temperatures 300 K, 330 K and 360 K, and then back at 300 K.

### 2.3.3 Ionic Layering around the NPs in FF-EAN

The achievement of stable colloidal dispersions in EAN follows analogous interpretation as proposed for FFs in EMIM-TFSI, arising from a surface induced ionic layering around the NPs [58, 59]. The difference in colloidal stability between the three kinds of ferrofluids in EAN – based on the different initial ions ( $X^+ = \text{Na}^+$ ,  $\text{Rb}^+$  or  $\text{Li}^+$ ) used during the NP's synthesis in water – proves that at least some of these ions remain close to the NP's interface. Table 2 collects the concentration, measured with ICP-MS (Inductively Coupled Plasma Mass Spectroscopy) by Véronique Peyre, of these alkaline ions in the colloidal FF-EAN dispersions and in the supernatant obtained by ultracentrifugation (containing no NP). Some cations remain localized at the NPs interface<sup>7</sup>, staying close to the NPs, instead of diluting randomly in the solvent. They are thus not all replaced by most numerous ethylammonium cations ( $\text{EA}^+$  ions) in the NPs vicinity. Moreover  $\text{Na}^+$ ,  $\text{Rb}^+$  and  $\text{Li}^+$  do not remain in the same quantity close to the NPs. This has to be associated to their ionic diameter and to their chemical properties.

**Table 2** – FF based on EAN for the three studied counterions: Second virial coefficient  $A_2$ , diffusion coefficient  $D_m$  from DLS at room temperature for  $\Phi = 1\%$  in dry samples, free concentration of  $X^+$  cations in the EAN (not localized on the NPs), number of  $X^+$  cations per surface unit of NPs (localized on the NPs), ionic radius of these cations from ref. [111].

Initial counterion	$A_2$	$D_m$ ( $10^{-12} \text{ m}^2\text{s}^{-1}$ )	$[X^+]_{\text{free}}$ in EAN (mol/L)	$X^+/\text{nm}^2$	Ionic radius (Å)
$\text{Li}^+$	$-6 \pm 1$	1.2	0.075	2.7	0.6
$\text{Na}^+$	$4.6 \pm 0.5$	1.2	0.110	0.6	1.02
$\text{Rb}^+$	$5.6 \pm 1$	1.4	0.097	0.25	1.65

The concentration of free alkaline cations equals the initial value in water for  $\text{Li}^+$  ( $[\text{Li}_3\text{Citrate}] = 0.025 \text{ mol/L}$  according to the preparation, thus  $[\text{Li}^+] = 0.075 \text{ mol/L}$ , see subsection 2.1.2 and Table 2). This means that the amount of lithium linked to the NPs is similar in EAN and in water. On the contrary, this number of linked ions decreases for  $\text{Na}^+$  and for  $\text{Rb}^+$ , increasing the concentration of free cations compared to its initial value. This cation localization had already been seen in previous studies for sodium and lithium ions [59] with less precise values obtained formerly by Atomic Absorption Spectroscopy (AAS). Note that, whatever the technique used, the titration of sodium remains more difficult due to its ubiquitous presence. This effect of localization is here extended to rubidium as a newly studied counterion.

Therefore, the mechanism explaining the colloidal stability in ILs is expected to result from the organization of all the ions close to the charged surface (see Figure 10),

<sup>7</sup> The titrations of the alkaline ions enable to determine the concentration of the free cationic counterions (not localized on the NPs) in the solvent (EAN) from the measurements in the supernatant. Comparing it to the titration of the total alkaline cations in the colloidal dispersions allows to extract the amount of counterions linked to the nanoparticles in EAN. It can be converted to an amount of alkaline cations per surface of iron oxide.

as already portrayed for case of EMIM-TFSI. In the case of EAN, the small ethyl chain induces a sponge like structure in the bulk EAN with polar and apolar domains [92]. Addition of salts in the EAN, such as lithium nitrate [112, 113], zinc chloride [114] or cerium nitrate [115] shows that they are located in the polar domains and surrounded by nitrate anions. Among alkaline ions, mainly lithium was studied in literature and it was shown that lithium is a structure breaker for EAN [112]. Close to a negative surface, the sponge-like structure of EAN becomes lamellar. In the first layer, the charged polar head of  $EA^+$  is close to the negative charges on the surface and the tails associate. Several layers less organized are formed above the first one until the bulk sponge structure is recovered as seen experimentally, for example by Atomic Force Microscopy (AFM) [116].

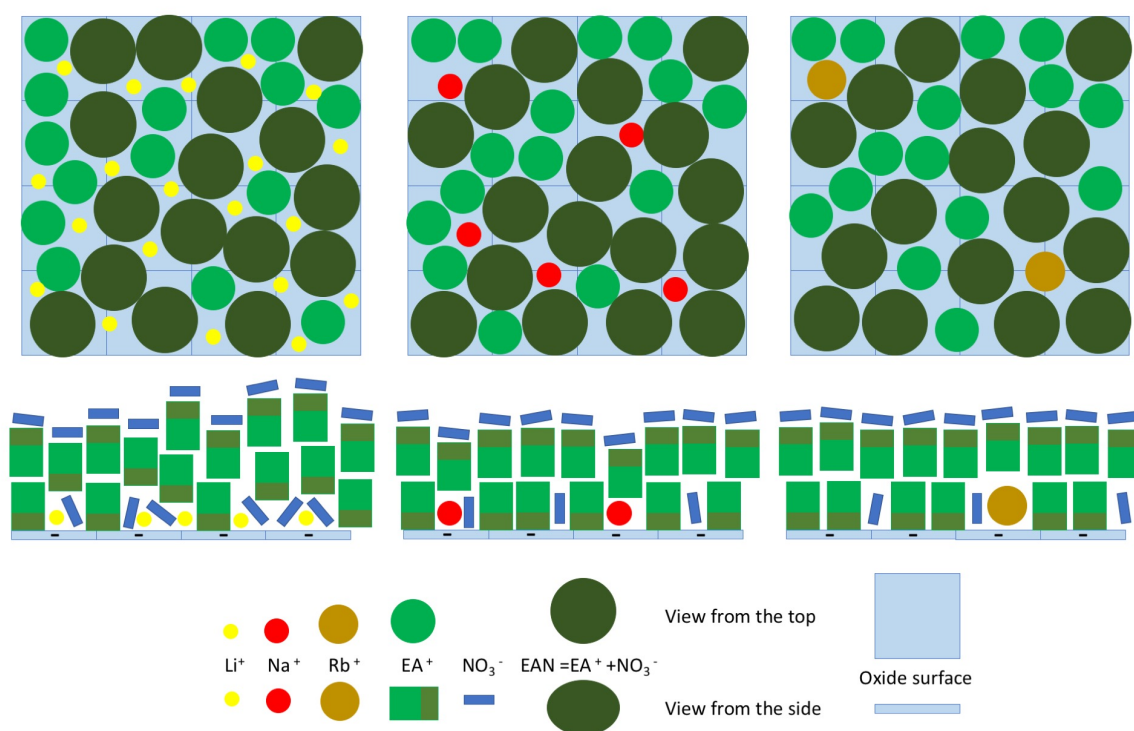


**Figure 10** – *Top*: Tentative sketches of the organization of the first ionic layer on the oxide surface viewed from above; From left to right with  $Li^+$  counterions close to the surface, with  $Na^+$  counterions and with  $Rb^+$  counterions (for symbols see the bottom of the figure); *Middle*: Tentative sketches of a lateral view of the first two ionic layers in the three cases ( $Li^+$ ,  $Na^+$  and  $Rb^+$ ). The  $Li^+$  ions which are small are far numerous than  $Na^+$  and  $Rb^+$  close to the surface. These  $Li^+$  ions disturb more the local lamellar organisation of  $EA^+/EAN$  close to the surface than  $Na^+$  and  $Rb^+$ . The size of  $Na^+$  and  $Rb^+$  is closer to that of  $EA^+/EAN$  and they less disturb the lamellar organization. And on the contrary they may help to fill some “holes” in the first layer of  $EA^+/EAN$  onto the NP surface, as shown in [Figure 10](#) top (view of the first layer from above).

[Figure 10](#) proposes a sketch of the local ionic organization close to the negative oxide surface of the NPs (viewed perpendicular and parallel to the particle surface), taking in account the chemical determinations of [Table 2](#). The side view of [Figure 10](#) depicts the conceptualized interpretation that  $Li^+$  ions – which are a structure breaker of EAN and much more numerous close to the surface than  $Na^+$  and  $Rb^+$  – are more disturbing in the

organization of the first layer, leading to less stable dispersions as attested by the SAXS analysis.

The adequate evaluation of the effective charge of the NPs is a difficult issue. Let us come back here to the detail of the solid/liquid interface. In water, the NPs are charged thanks to the adsorbed citrate molecules. The structural charge  $Z_{\text{str}}$  is known to be around 2 elementary charges per  $\text{nm}^2$  [22], which corresponds here to  $Z_{\text{str}} = 315$  for one NP ( $32 \mu\text{C}/\text{cm}^2$ ). Note that this charge is similar to the one for mica surfaces, used in many AFM studies with ILs, which can thus reasonably be compared with our results. However, NPs differ from mica due to the curvature of the interface and of their higher roughness. Still in water, the high structural charge of the maghemite NPs induces a condensation of lots of counterions on the surface causing a significant screening effect. As a consequence, the static effective charge  $Z_0^{\text{eff}}$  as well as the dynamic one  $\xi_0^{\text{eff}}$  determined from electrophoresis is in reality close to 15 [98]. This effective charge and the diffuse layer around the NP are responsible for the electrostatic repulsion enabling colloidal stability in water or classical polar solvents.

While transferring the NPs to EAN, the citrate molecules stay on the surface and free citrate remains in the surrounding EAN, as the  $\text{X}_3\text{Citrate}$  salts are soluble in the IL. The charge to compensate at the solid/liquid interface is thus still 2 per  $\text{nm}^2$  and this counterbalance can be ensured by  $\text{EA}^+$  cations or by  $\text{X}^+$  cations. Our results show that this compensation is at least partly due to  $\text{X}^+$  cations, which stay localized close to the NPs' interface (See Table 2 and Figure 10).

Even knowing the apparent charge on the top of each layer, we would ignore the effective charge  $\xi_0^{\text{eff}}$  of the moving objects when applying a force as in thermodiffusion and in thermoelectric measurements. Indeed, as in water, the NP moves with the highly bound species around it, which defines a shearing plane, location where  $\xi_0^{\text{eff}}$  is defined. Nevertheless, we do not know its extension and no study of literature is able to answer this question as far as we know. We can expect that at least the first layer close to the NPs moves with it as it is strongly linked on the surface (according to AFM studies), but it could as well be possible that more layers are also carried along. Therefore, values of  $\xi_0^{\text{eff}}$  with a modulus between 0 and  $|Z_{\text{str}}|$  or even a bit larger appear possible, which the charge signal could be either negative or positive. We thus consider in the following that  $\xi_0^{\text{eff}}$  can be taken between 0 and  $\pm 350$  to fit the data,  $Z_{\text{str}}$  being chosen as a good order of magnitude of the maximum possible  $\xi_0^{\text{eff}}$ .

### 2.3.4 Stability of MNPs in EAN/Water Mixtures with $\text{Na}^+$ Counterions

SAXS measurements have also been performed on samples with  $\text{X}^+ = \text{Na}^+$  at  $\Phi = 1.0\%$  of NPs with  $w_{\text{water}} = 5.0$  weight% of water added in order to estimate its influence, which is important as EAN is hygroscopic and as the samples were manipulated

either in a glovebox (thermoelectric measurements) or in a protected but less perfect inert atmosphere (all other experiments). The  $I(Q)$  are similar to the ones without water (data not shown), meaning that interactions are not modified. However, the change can be seen from Dynamic Light Scattering (DLS) performed on these same samples (with a Vasco, from Cordouan Technologies, device built for dark media) and also by relaxation of FRS (see subsection 3.2.2). The hydrodynamic diameter does not change if a few w% of water is added, only the viscosity is modified. The water uptake is reversible by freeze drying, nevertheless, if some water molecules still locate at the interface, is for the moment an open question.

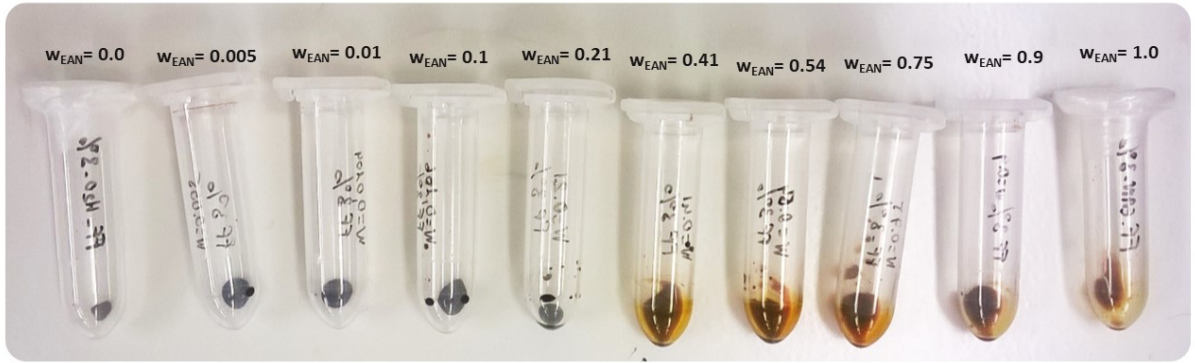


**Figure 11** – Macroscopic observation at room temperature of ferrofluid samples based on mixtures of EAN and water with  $X^+ = \text{Na}^+$ , at  $\Phi = 3\%$  and various different weight % of EAN ( $w_{\text{EAN}}$ ). A wetting transition is observed in the Eppendorfs at  $w_{\text{EAN}}$  between 0.21 and 0.41 of EAN

Besides these observations, EAN and water are miscible in any proportions at room temperature which can lead to macroscopically stable FFs with  $X^+ = \text{Na}^+$  and  $d_{\text{NP}} = 7.4$  nm up to  $\Phi = 3.0\%$  (in fact, this is not true for larger diameters, where macroscopic phase separation are then observed). The macroscopic stability is attested by the photo in Figure 11 showing such ferrofluids with  $X^+ = \text{Na}^+$  in Eppendorfs with increasing mass fraction of EAN ( $w_{\text{EAN}}$ ). Note a wetting transition between  $w_{\text{EAN}} = 21$  w% and 41 w% of EAN in the carrier fluid.

SAXS measurements performed at  $\Phi = 1\%$  in the whole range of  $w_{\text{EAN}}$  allows the evaluation of  $\chi$  (as equal to  $S(Q = 0)$ ). It shows that the interparticle interaction is repulsive at low and large weight% of EAN in the carrier fluid, while it is slightly attractive in between  $0.1 < w_{\text{EAN}} < 0.75$ . We can deduce  $A_2$  with the Carnahan-Starling formalism of Equation 2.5 when the interparticle interaction is repulsive ( $A_2 > 0$ ) and with the linear development of Equation 2.4 if  $|A_2| \leq 5$  in the whole range of  $w_{\text{EAN}}$  at  $\Phi = 1\%$ . This is shown in Figure 12.

If we now look at the SAXS measurements at  $\Phi = 3.0\%$  and compare them to those of Figure 12, we observe in Figure 13a that the values of  $S(Q = 0)$  are much larger in the  $w_{\text{EAN}}$  range where  $A_2$  is found negative at  $\Phi = 1.0\%$ . Even if the development of Equation 2.4 is not really valid (we obtain values of  $|A_2|$  larger than  $0.17 (= 0.1/(2\Phi))$ ) we

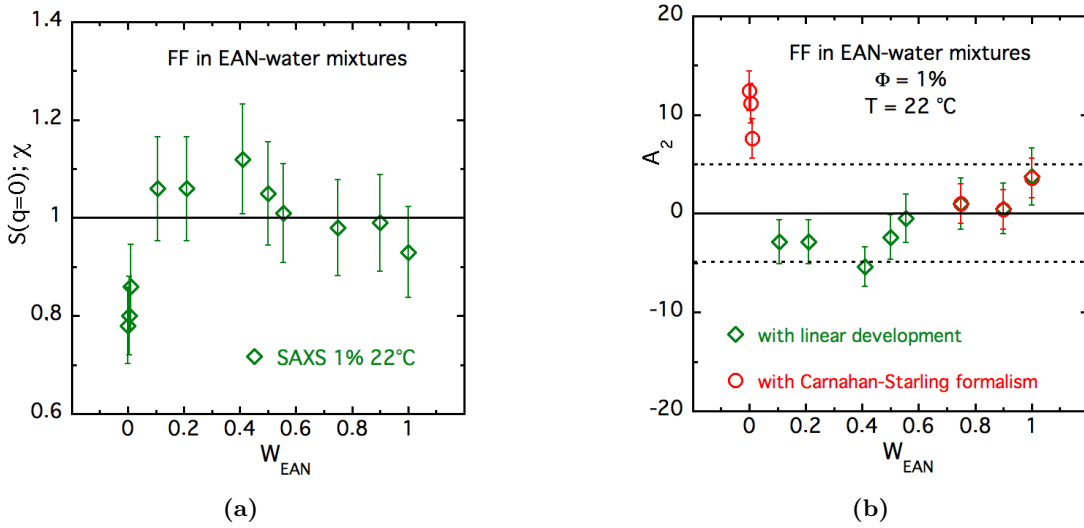


**Figure 12** – (a) Compressibility  $\chi$  of the NP's system as determined by SAXS  $S(Q = 0)$  for samples based on EAN/water mixtures with  $X^+ = \text{Na}^+$  at different weight% of EAN ( $w_{\text{EAN}}$ ) at  $\Phi = 1\%$  and  $T = 22^\circ\text{C}$ ; (b) Second virial coefficient deduced from  $\chi$  values of figure (a) with Equation 2.4 and 2.5. Dotted lines figure the limits of the linear development of Equation 2.4.

tentatively use it to deduce  $A_2$ , without giving any error bar. This is shown in Figure 13b. Anyway, this confirms that  $A_2$  is positive for  $w_{\text{EAN}}$  close to 0<sup>8</sup> and 1, as well as there is an inversion in between where  $A_2$  becomes negative. It also shows that  $|A_2|$  is maximal for  $w_{\text{EAN}}$  of the order of 0.3, where the wetting transition of Figure 11 occurs.

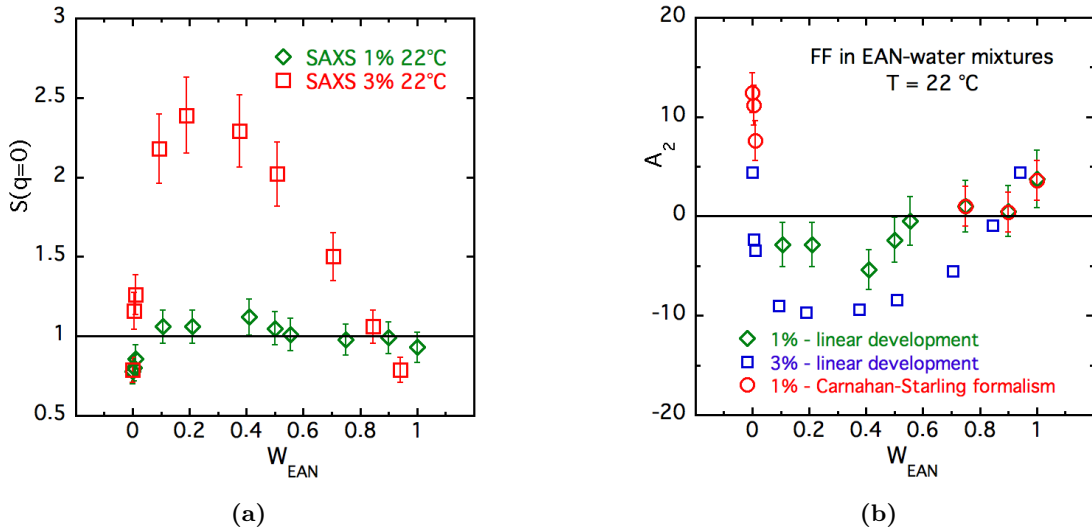


**Figure 13** – (a) Values  $S(Q = 0)$  assimilated to the compressibility  $\chi$  of the NP's system as determined by SAXS for samples based on EAN/water mixtures with  $\text{Na}^+$  counterions at different weight% of EAN ( $w_{\text{EAN}}$ ) at  $T = 22^\circ\text{C}$  for  $\Phi = 1.0\%$  and  $3.0\%$ . (b) Second virial coefficient deduced from figure (a) with Equation 2.4 – Open red circles are deduced at  $\Phi = 1.0\%$  from Equation 2.5 as in Figure 12b.

<sup>8</sup> Note that at  $\Phi = 3.0\%$  in water, the found value of  $A_2$  should be the same as at  $1.0\%$ , within the error bar. It is not the case, meaning that the concentration of free  $\text{Na}^+$  in water was probably different at  $\Phi = 1.0\%$  and  $\Phi = 3.0\%$ . A more detailed study of the influence of the concentration (and nature) of the free counterions at low  $w_{\text{EAN}}$  should be driven in the future.

## 2.4 Conclusions on the Colloidal Stability of the Studied Systems

In the general framework of dispersing magnetic NPs in Room-Temperature Ionic Liquids (RTILs), we have here focused our studies on two well-known model-systems. The first one, EMIM-TFSI (1-Ethyl-3-methylimidazolium bistriflimide) because this RTIL is stable up to rather high temperatures (more than 460 K) and could be useful in thermoelectric applications. The second one EAN (EthylAmmonium Nitrate) because it is miscible with water in any proportions, which may allow to study the evolution of the ionic structural organization in NP's colloidal dispersions when the fluid carrier goes from a standard electrolyte (water a low concentration of  $\text{EA}^+$  and  $\text{NO}_3^-$  ions) to an Ionic Liquid (at very low water concentration).

Stable colloidal dispersions of maghemite NPs in EMIM-TFSI, EAN and mixtures of water and EAN are obtained with an adapted NP's coating. In EMIM-TFSI, the coating is realized with  $\text{SMIM}^\pm\text{-TFSI}^-$  zwitterions while a NP's citrate-coating is used in EAN, water and in their mixtures. The interparticle interaction, which is here found either repulsive or weakly attractive, is well characterized in all these dispersions by SANS and/or SAXS experiments, allowing an evaluation of the second coefficient  $A_2$  of the virial development of the osmotic pressure. In the probed RTIL (EMIM-TFSI and EAN) the stability of the dispersions is ensured by an ionic layering around the NPs, contrasting with the usual Debye-Huckel description of standard electrolytes.

If in EMIM-TFSI a strong repulsion is here observed ( $A_2 = +7.3$ ), in EAN it is shown that the nature of the initial counter-ions used during the initial synthesis in water is of paramount importance for the inter-particle interaction. It is repulsive with  $\text{Na}^+$  and  $\text{Rb}^+$  counter-ions ( $A_2 = +4.6$  and  $+5.4$ ), while it is attractive with  $\text{Li}^+$  counter-ions ( $A_2 = -6$ ). It shows that at least some of these initial counter-ions remain close to the NP's surface when they are ultimately dispersed in the ionic Liquid, demonstrating the utmost significance of the ionic layering close to the NP's interface. With  $\text{Na}^+$  counter-ions, if the interparticle interaction is here repulsive both in pure water ( $A_2 = +13$ ) and in pure EAN ( $A_2 = +4.6$ ), it is weakly attractive in their mixtures at intermediate proportions, traducing a progressive evolution in the NP's stabilization mode. A complementary study by Forced Rayleigh Scattering is devoted to this point in the next Chapter.

## Chapter 3

# Thermodiffusive Properties

The *Ludwig-Soret effect* is a non-equilibrium thermodynamic phenomenon characterized by the internally forced movement of the constituents of a multi-component liquid system in response to a temperature gradient. This thermally induced effect is a particular case of a much broader class entitled *phoretic motions*. Thereupon, multiple agents can promote particle movement such as: electric field (electrophoresis), concentration gradient (diffusiophoresis), magnetic field (magnetic separation) or gravity (sedimentation).

In a colloid of charged nanoparticles dispersed in molecular solvents or ionic liquids, the thermodiffusive properties are highly dependent on the particle-solvent interface. The reason behind it lies on the mechanism in which the temperature gradient acts indirectly in the particle displacement. The applied temperature difference promotes the rearrangement of the different ions in the medium that produces additional inhomogeneities at the layer of fluid surrounding the nanoparticles. In certain circumstances, this asymmetrical condition causes pressure variations that drive the NPs in a predominant direction. Therefore, the generated mass flux and the preferred concentration region (hot or cold) comprehensively depends on the surface forces and ion organization/concentration in the vicinity of the particle.

In this chapter, we investigate the thermodiffusion properties, Soret coefficient  $S_T$  and mass diffusion coefficient  $D_m$ , of magnetic NPs dispersed in two well known RTILs, that can be considered as model systems, EMIM-TFSI and EAN. EAN being miscible with water in any proportion we also explore the evolution of thermodiffusion properties when the water content is increased, the system evolving from an aqueous electrolyte towards a pure RTIL. Varying the temperature and changing the particle concentration enables us to achieve a deeper analysis by altering in a different manner the viscosity (which influences  $D_m$ ) and the extent of the interparticle interactions (which influences both  $S_T$  and  $D_m$ ). Using EMIM-TFSI allows us to explore the thermodiffusive properties up to very high temperatures, the colloidal system being stable (at least) up to 200 °C. These extreme temperatures can only be achieved with certain RTILs in rather pure conditions

(it would be impossible to avoid water boiling in such dispersions). Thanks to a home made apparatus, we analyse the implications of applying an external magnetic field to this system in a broad range of temperatures.

## 3.1 Theoretical Background

This section provides a theoretical development of the thermodiffusion of charged colloids dispersed in RTIL, and develops specially the case of dispersions of magnetic nanoparticles submitted to a magnetic field. We present hereby the models and approximations that are employed in the analysis of the experimental data obtained with the FRS apparatus described in [subsection 3.2.1](#). Thermodiffusion results obtained with the different systems are presented and discussed in [section 3.3](#) and [section 3.4](#).

### 3.1.1 Thermodiffusion in Charged Colloids

We start by determining the macroscopical total mass flux ( $\vec{J}_{\text{NP}}$ ) experienced by a colloidal dispersion in a restricted case, where the predominant effects are the thermophoresis and diffusiophoresis, while the other phoretic contributions will be initially neglected. The modeling of the phenomenon is based in the premise that as the temperature gradient ( $\vec{\nabla}T$ ) induces a temperature driven mass flux ( $\vec{J}_{\text{TD}}$ ). The latter develops a mass concentration gradient ( $\vec{\nabla}w$ ), which is counteracted by a reactive concentration driven mass flow ( $\vec{J}_{\text{D}}$ ) described by Fick's law. Ergo, the total mass flow can be written as the following expression [117]:

$$\vec{J}_{\text{NP}} = \vec{J}_{\text{D}} + \vec{J}_{\text{TD}} = -\rho D_{\text{m}} \vec{\nabla}w - \rho w(1-w) D_{\text{T}} \vec{\nabla}T, \quad (3.1)$$

where  $D_{\text{m}}$  is the diffusion coefficient,  $\rho$  the fluid density,  $w$  is the NP's mass fraction and the phenomenological quantity  $D_{\text{T}}$  is generally called thermal diffusion coefficient, however, a more suitable name would be thermophoretic mobility [118]. In diluted dispersions of charged ionic NPs, the approximation  $(1-w) \approx 1$  can be assumed and the equation is conveniently rearranged as

$$\vec{J}_{\text{NP}} = -\rho D_{\text{m}} \left( \vec{\nabla}w - w \frac{D_{\text{T}}}{D_{\text{m}}} \vec{\nabla}T \right). \quad (3.2)$$

This expression for the mass flux is implicitly time-dependent, nonetheless, by considering a uniform thermal gradient and avoiding convective effects, the net mass flow vanishes ( $\vec{J}_{\text{NP}} = 0$ ) after a sufficiently long period of time, reaching a steady-state concentration profile. The Soret coefficient at this stationary condition is defined as

$$S_{\text{T}} \equiv \frac{D_{\text{T}}}{D_{\text{m}}} \quad (3.3)$$

and links the applied temperature gradient to the induced volume fraction<sup>1</sup> gradient ( $\vec{\nabla}\Phi$ ) in the following way:

$$\vec{\nabla}\Phi = -\Phi S_T \vec{\nabla}T. \quad (3.4)$$

By this approach the Soret signal is defined such as: if  $S_T > 0$  it corresponds to the nanoparticles moving towards the cold region (thermophobic NPs), whereas the opposite situation which  $S_T < 0$  corresponds to the nanoparticles concentrating on the hot region (thermophilic NPs).

The studied charged colloid systems have a diversity of charged species (nanoparticles, counterions, co-ions, etc), therefore, in addition to the mass flux, the thermal gradient will also generate a charge current. Since the phoretic response to the applied temperature gradient is different depending on the nature of the components (i.e. the heat of transport of each ionic species), a separation of the positive and negative charge carriers might be established creating an electromotive force. This thermoelectric phenomenon named *Seebeck effect* is characterized by the development of an electric field ( $\vec{E}$ ) as function of the temperature gradient such as

$$\vec{E} = S_e \vec{\nabla}T, \quad (3.5)$$

where  $S_e$  is the Seebeck coefficient. In stationary conditions, the Seebeck coefficient also becomes time-independent and it will be denoted here by  $S_e^{\text{St}}$ .

Considering that the nanoparticles also bear a significant amount of surface charge, they will not only be locally subjected to a force stemming from the NP's chemical potential, but also to an electromagnetic force (Lorentz Force) arising from the Seebeck electric field. The development [25, 98] of the resulting force in terms of the osmotic pressure  $\Pi$ , the Eastman entropy of transfer  $\hat{S}_{\text{NP}}$  and the effective dynamic charge (electrophoretic charge)  $e\xi_0$  enables the establishment of the following relation between the Soret and Seebeck coefficients:

$$S_T = \chi \left[ \frac{1}{\Phi kT} \frac{\partial \Pi V_{\text{NP}}}{\partial T} + \frac{\hat{S}_{\text{NP}}}{kT} - e\xi_0^{\text{eff}} \frac{S_e^{\text{St}}}{kT} \right] \approx \chi \left[ \frac{\hat{S}_{\text{NP}}}{kT} - e\xi_0^{\text{eff}} \frac{S_e^{\text{St}}}{kT} \right], \quad (3.6)$$

where the compressibility  $\chi$  is given by Equation 2.4 and can be experimentally determined by SAS experiments. The first term  $[(1/\Phi kT)(\partial \Pi V_{\text{NP}}/\partial T)]$  corresponds to thermodynamic contributions, that are usually neglected in first approximations [118–121]. For each ionic species  $\{i\}$ , the Eastman entropy of transfer is defined [122] as  $\hat{S}_i \equiv Q_i^*/T$ , where  $Q_i^*$  is the heat of transport of the ionic species  $\{i\}$ . Therefore, the second term  $\hat{S}_{\text{NP}}$  refers to the NP's Eastman entropy of transfer, which is characteristic of the interaction between the charged nanoparticles and the solvent [82, 121, 123, 124]. The last term presents the thermoelectric contribution, which can be experimentally measured in thermogalvanic cells (thermocells) or theoretically developed. Here we use a model for polar systems [25, 98],

<sup>1</sup> The mass fraction can be directly converted into volume fraction ( $\Phi$ ) since the left-hand side of Equation 3.2 is zero at the steady state.

also employed in an ionic liquid system[18], that determines a relation between  $eS_e^{\text{St}}$  and the nanoparticles concentration ( $\Phi$ ) by assuming: First, the electro-neutrality principle

$$Z_0^{\text{eff}} n_{\text{NP}} + \sum_i n_i z_i = 0, \quad (3.7)$$

where  $Z_0^{\text{eff}}$  is the static NP's effective charge,  $n_{\text{NP}} = \Phi/V_{\text{NP}}$  is the number of NPs per unit of volume,  $V_{\text{NP}}$  the particle volume, the index  $\{i\}$  corresponds in the present RTILs to ionic species with charge  $z_i = \pm 1$  and number per volume  $n_i = n_{\pm}$ ; Second, the total flux of each species is null

$$\vec{J}_{\text{NP}} = \vec{J}_i = 0 \quad (3.8)$$

whatever  $\{i\}$ . It is also assumed that  $Z_0^{\text{eff}}$  is of the same order of magnitude as  $\xi_0^{\text{eff}}$ . Since the nanoparticle can have either positive or negative surface charge the relation can be expressed in two different ways

$$eS_e^{\text{St}}(\Phi)_{\pm} = \frac{\hat{S}_+ - \hat{S}_- + Z_0^{\text{eff}} \left(\frac{n_{\text{NP}}}{n_{\pm}}\right) (\chi \hat{S}_{\text{NP}} - \hat{S}_{\mp})}{2 + Z_0^{\text{eff}} \left(\frac{n_{\text{NP}}}{n_{\pm}}\right) (\chi \xi_0^{\text{eff}} \pm 1)}, \quad (3.9)$$

where the upper sign corresponds to  $Z_0^{\text{eff}} > 1$  and the lower sign  $Z_0^{\text{eff}} < 1$ . In this expression the entropy of transfer ( $\hat{S}_+$  and  $\hat{S}_-$ ) of the very small ions can be neglected if compared with the huge NPs value and the  $\pm$  equations can be merged into a single one as function of  $|Z_0^{\text{eff}}|$  as

$$eS_e^{\text{St}}(\Phi) = \frac{i |Z_0^{\text{eff}}| n_{\text{NP}} \chi \hat{S}_{\text{NP}}}{2n_i + |Z_0^{\text{eff}}| n_{\text{NP}} (1 + \chi |\xi_0^{\text{eff}}|)} \quad (3.10)$$

where  $i$  controls the sign of  $Z_0^{\text{eff}}$ . Finally, we can rearrange Equation 3.6 and substitute the Seebeck term by Equation 3.10 obtaining

$$\frac{TS_{\text{T}}}{\chi} = \frac{1}{k} (\hat{S}_{\text{NP}} - e \xi_0^{\text{eff}} S_e^{\text{St}}) = \frac{\hat{S}_{\text{NP}}}{k} \left[ \frac{2n_i + |Z_0^{\text{eff}}| n_{\text{NP}}}{2n_i + |Z_0^{\text{eff}}| n_{\text{NP}} (1 + \chi |\xi_0^{\text{eff}}|)} \right]. \quad (3.11)$$

For the sake of simplicity, when adjusting the data we can assume  $|Z_0^{\text{eff}}| = |\xi_0^{\text{eff}}|$ , since they are of the same order of magnitude and  $\Phi$ -independent. As a consequence, once it is possible to experimentally determine  $S_{\text{T}}(\Phi)$  and  $\chi(\Phi)$ , Equation 3.11 allows us to evaluate  $\hat{S}_{\text{NP}}$ ,  $|Z_0^{\text{eff}}| = |\xi_0^{\text{eff}}|$  and  $n_{\pm}$  by fitting the data, yet, the actual sign cannot be inferred by this method and further information is required.

So far the attention has been focused on the Soret and Seebeck coefficients, however, while the diffusion coefficient has not showed up explicitly in the equations, it is an equally important parameter in the thermodiffusive properties. The isotropic mass diffusion coefficient  $D_{\text{m}}$  can be written as function of the derivative of the osmotic pressure and the viscous friction ( $\zeta$ ) experienced by the NPs in the fluid medium by the generalized Stokes-Einstein equation [125]

$$D_{\text{m}}(\Phi, T) = \frac{(1 - \Phi)}{\zeta} \frac{\partial \Pi V_{\text{NP}}}{\partial \Phi} = \frac{(1 - \Phi) kT}{\zeta} \frac{1}{\chi} \sim \frac{kT}{\zeta \chi} \quad \text{if } \Phi \ll 1, \quad (3.12)$$

where the  $\Pi$ -dependence has been transposed as a function of  $\chi$  by using [Equation 2.4](#). In the absence of interparticle correlations ( $\chi = 1$  and  $\Phi \rightarrow 0$ ), the friction writes as:

$$\zeta(\Phi \rightarrow 0, T) = \zeta_0(T) = 3\pi\eta_0(T) d_H \quad (3.13)$$

where  $\eta_0(T)$  is the solvent viscosity and  $d_H$  the NP's hydrodynamic diameter. The mass diffusion coefficient  $D_m(\Phi \rightarrow 0, T)$  can then be expressed as:

$$D_m(\Phi \rightarrow 0, T) = \frac{kT}{\zeta_0(T)} = \frac{kT}{3\pi\eta_0(T)d_H} \quad (3.14)$$

In the presence of interparticle correlations  $\chi \neq 1$  and  $\zeta(T) \neq \zeta_0(T)$ , these correlations modify  $D_m(\Phi, T)$ . An expression for the friction  $\zeta(T)$  experienced by hard spheres in hydrodynamic interaction at a volume fraction  $\Phi_{HS}$  has been proposed in [\[126\]](#) for  $\Phi_{HS} \ll 1$ :

$$\zeta(\Phi_{\text{eff}}, T) = \zeta_0(T) (1 + k_F \Phi_{\text{eff}}) \quad \text{with} \quad k_F = 6.55 \quad (3.15)$$

Finally, it is then possible to rewrite [Equation 3.12](#) using [Equation 3.15](#) as

$$D_m(\Phi_{\text{eff}}, T) = \frac{kT}{\zeta(\Phi_{\text{eff}}, T)\chi} = \frac{kT}{3\pi\eta_0(T)d_H(1 + k_F \Phi_{\text{eff}})\chi}, \quad (3.16)$$

assuming  $\Phi_{\text{eff}} = \Phi_{HS}$  and  $(1 - \Phi_{\text{eff}}) \approx 1$ , where the effective volume fraction  $\Phi_{\text{eff}}$  was defined in the previous chapter by [Equation 2.6](#).

### 3.1.2 Under-Field Model for MNPs

Until this point, the magnetic character of the nanoparticles was disregarded in the development of the theoretical description of the thermodiffusive phenomenon. In the under-field model considered from now on [\[127\]](#), the system components are divided in two categories: 1) the diamagnetic solutes, ions or neutral species (all  $< 1$  nm in size) are treated as an ideal gas; 2) the charged MNPs are considered to behave as hard-spheres following the presented Carnahan-Starling formalism (see [Equation 2.5](#), [2.6](#) and [2.7](#)) with their interparticle magnetic interactions in zero magnetic field included inside the global interparticle potential. Under-field, we propose to describe them with mean-field approach [\[128–130\]](#). In this mean-field framework, the magnetic interparticle interaction is described using the effective Langevin parameter  $x_e$  of the FFs written as:

$$x_e = x + \lambda\gamma L(x_e), \quad (3.17)$$

where  $L(x)$  is the Langevin function and  $x$  the Langevin parameter, both already described in [Equation 1.3](#),  $\lambda$  the mean-field parameter and

$$\gamma = \frac{\mu_0 m_S \mu_{NP} \Phi}{kT} \quad (3.18)$$

is the magnetic dipolar interaction parameter of the MNPs with a saturation magnetization  $m_S$  and a magnetic moment  $\mu_{NP} = m_S V_{NP}$ . Note that at low  $\Phi$ ,  $\gamma \ll 1$  and  $\lambda\gamma L(x_e) \ll x$ ,

then  $x_e \sim x$  is recovered. Here we use  $\lambda = 0.22$  as in [128, 129, 131], a value confirmed by numerical simulations in water [130].<sup>2</sup> Under-field, in this mean field approach the chemical potential of the dispersion contains a supplementary additive term [129, 135]

$$\mu_H = -kT \cdot \ln[\sinh(x_e)/x_e] \quad (3.19)$$

As a consequence, this mean-field approach allows us to evaluate the modifications caused by the introduction of the external magnetic field  $\vec{H}$  to the two main thermodiffusive parameters, namely,  $S_T$  and  $D_m$  in terms of the variables presented in Equation 3.17.

In our experiments the induced gradient of particle concentration always occurs in the same direction as that of the temperature gradient, i.e.  $\vec{\nabla}T \parallel \vec{\nabla}\Phi \vec{O}y$ , although, the magnetic field can be applied either perpendicular ( $\vec{H}_\perp$ ) or parallel ( $\vec{H}_\parallel$ ) to them. For this reason, the in-field diffusion coefficient  $D_m(\vec{H})$  writes for each configurations as

$$D_m^{\vec{H}_\perp} = \frac{kT}{\zeta} \left( \frac{1}{\chi} - \alpha_\lambda \right) = D_m^* [1 - \chi \alpha_\lambda] \quad (3.20)$$

and

$$D_m^{\vec{H}_\parallel} = \frac{kT}{\zeta} \left( \frac{1}{\chi} + \beta_\lambda - \alpha_\lambda \right) = D_m^* [1 + \chi (\beta_\lambda - \alpha_\lambda)] \quad (3.21)$$

where  $D_m^* = D_m(H=0, \Phi, T) = kT/\zeta\chi$  is the zero-field condition, as written in Equation 3.12. The parameters  $\alpha_\lambda$  and  $\beta_\lambda$  are given by [129]:

$$\alpha_\lambda = - \left( \frac{\Phi}{kT} \right) \left( \frac{\partial \mu_H}{\partial \Phi} \right)_H = \frac{\lambda \gamma L^2(x_e)}{1 - \lambda \gamma L'(x_e)} \quad (3.22)$$

and

$$\beta_\lambda = - \left( \frac{\Phi}{kT(\partial\Phi/\partial y)} \right) \cdot \left( \frac{\partial \mu_H}{\partial \Phi} \right)_\Phi = \frac{\gamma L^2(x_e)}{[1 - \lambda \gamma L'(x_e)] [1 + (1 - \lambda) \gamma L'(x_e)]}. \quad (3.23)$$

The parameter  $\alpha_\lambda$  is associated with the mean-field dipolar interaction, which is attractive on average and is present in both orientations of the applied field. On the other hand, the term  $\beta_\lambda$  is anisotropic emerging from the discontinuity of  $\vec{H}_\parallel$  in Maxwell equations along the spatial inhomogeneities<sup>3</sup> of concentration over the y axis [127–129, 137]. Consequently,  $\beta_\lambda$  is maximum in the field direction parallel to  $\vec{\nabla}\Phi$  and null perpendicularly. This anisotropic behavior becomes progressively more significant as the the volume fraction  $\Phi$  increases, taking into account that the magnetic dipolar parameter  $\gamma$  and the coefficient  $\beta_\lambda$  gets increasingly larger.

<sup>2</sup> Up to  $\gamma \sim 5$ , it has been shown (at room temperature) in refs. [132, 133] that the simple mean-field model of Equation 3.17 gives the same initial magnetic susceptibility as the second order perturbation model of Ivanov and Kuznetsova[134] with  $\lambda = 1/3$  and as the mean-spherical model of Morozov and Lebedev[88], all the three being in good agreement with experiments.

<sup>3</sup> Such under-field inhomogeneities of concentration are also present at the local scale as attested by small angle scattering [131, 136].

The in-field anisotropy of the Soret coefficient  $S_T(\vec{H})$  can be expressed in the same framework as that of Equation 3.20 and 3.21 for  $D_m(\vec{H})$  but including derivatives of the NP's chemical potential with respect to temperature [25, 127]:

$$S_T^{\vec{H}_\perp} = \frac{1}{\frac{1}{\chi} - \alpha_\lambda} \left[ \frac{S_T^*}{\chi} + \frac{S_1}{T} \right] \quad (3.24)$$

and

$$S_T^{\vec{H}_\parallel} = \frac{1}{\frac{1}{\chi} + \beta_\lambda - \alpha_\lambda} \left[ \frac{S_T^*}{\chi} + \frac{S_1 - S_2}{T} \right], \quad (3.25)$$

where  $S_T^* = S_T(H=0, T)$  and the parameters  $S_1$  and  $S_2$  are given by:

$$S_1 = \frac{x_e L(x_e)}{1 - \lambda \gamma L'(x_e)} - \ln \frac{\sinh x_e}{x_e} \quad (3.26)$$

and

$$S_2 = \beta_\lambda \frac{x_e L'(x_e)}{L(x_e)}. \quad (3.27)$$

These equations for the Soret coefficient involve the same parameters as Equation 3.20 and 3.21 for the diffusion coefficient, besides the additional parameters  $S_1$  and  $S_2$ . Still, these extra terms depend on the same parameters as  $\alpha_\lambda$  and  $\beta_\lambda$ .

This ensemble of equations imposes a substantial restriction to the curve fitting parameters of  $D_m(\vec{H}, T)$  and  $S_T(\vec{H}, T)$ . That is because the adjustment has to be performed concomitantly and still remain valid in several different temperatures.

## 3.2 Forced Rayleigh Scattering Experiment (FRS)

The thermodiffusion effect is here probed by the Forced Rayleigh Scattering<sup>4</sup> (FRS) experiment, which have been successively applied in many different systems and largely developed throughout the years by the scientific community [138–143]. In this section, we provide a short description of our experimental setup together with a brief explanation of the method used to experimentally determine the Soret  $S_T$  and diffusion  $D_m$  coefficients.

### 3.2.1 Experimental Setup

The setup we use for these (FRS) measurements (see Figure 14) has been initially presented in ref. [141]. Recently, several improvements were implemented in this home-made apparatus [24] allowing us to work with more viscous systems, at a wide range of temperatures (from 20°C to 200°C), with and without an external magnetic field and easily/rapidly alternating to a portable dynamic light scattering device (DLS Vasco Kin - Cordouan Technologies).

<sup>4</sup> Forced Rayleigh scattering implies forced inhomogeneities with respect to the spontaneous fluctuations observed in a classical Rayleigh scattering experiment [138].

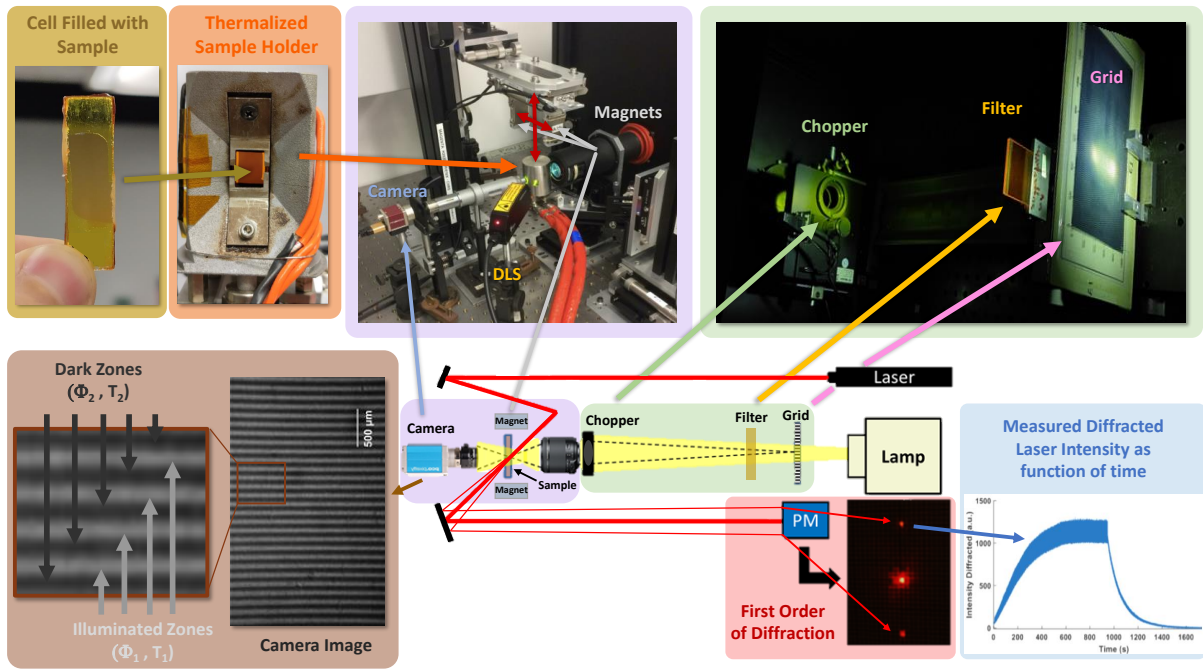


**Figure 14** – Forced Rayleigh scattering device: *Center*: the Experimental set-up, seen from above; *Top-right*: The Hg-lamp illuminates a grid creating an image that is filtered and modulated periodically at a few Hz by a chopper. *Top-left*: The image is then focalized in the thermalized sample inside a glass optical cell with a Kapton sheet spacer. If needed, the sample can also be submitted to a horizontal magnetic field  $\vec{H}$ ; Both a thermal and a concentration arrays are induced in the sample; *Bottom-left*: A direct observation of the image of the grid projected in the cell can be captured by a camera located behind the sample; Their temporal evolution is observed by the diffraction of a He-Ne laser beam; *Bottom-right* the diffracted pattern of the He-Ne laser beam is generated by the temperature and concentration arrays. The intensity of the first order diffraction as a function of time is recorded by a photomultiplier (PM). When the heating lamp is turned off, the recorded intensity relaxes towards zero as observed in the graph in blue.

The main principle behind this experiment is the induction of alternating cold and hot zones in the sample using a powerful light source, while the generated optical index gradients can be probed by the intensity variation of a diffracted laser beam.

First, a high power lamp (Oriel 6285 - 500 W - Hg Arc Lamp) illuminates a grid generating equally spaced dark and light fringes. For ferrofluids with citrate coated NPs an UV filter is necessary to preserve the integrity of the colloidal dispersion, since at such wavelengths, a chemical reaction between iron, citrate and the glass cell might induce a sample degradation when exposed for long periods of time. The generated image of the grid passes through a chopper which modulates the light source to a few Hertz ( $\sim 4.0 - 8.0$  Hz). The flashing image of the grid is focused on the liquid sample inside a thermalized<sup>5</sup> home-made optical cell (of thickness  $e = 25 \mu\text{m}$ ). Because of the strong optical absorption of the maghemite NPs, a thermal grating of time-dependent amplitude  $\Delta T(t)$  and spatial period  $\Lambda$  (ranging between 88 and 145  $\mu\text{m}$ ) is generated throughout the

<sup>5</sup> The temperature of the cell is adjusted by a sample holder which receives a circulating flow of oil coming from a thermoregulated bath.

dispersion. Eventually, a stationary concentration grating of amplitude  $\Delta\Phi(t)$  with the same spatial period  $\Lambda$  is induced thanks to the Ludwig-Soret effect [144, 145]. A camera located behind the sample allows us to evaluate precisely the extent of the gratings by measuring the image in pixels, after an initial calibration with known grids printed on glass windows, substituted to the sample cell.

In under-field conditions, a set of permanent magnets are loaded to a mechanical arm, which is then positioned such as a homogeneous magnetic field is generated inside the cell. The magnitude of the applied field can be varied by changing the number/type of magnets, as well as the distance between them. The magnitude  $H$  of this horizontal magnetic field  $\vec{H}$ , homogeneous at the scale of the sample, may vary from 0 up to  $100 \text{ kA m}^{-1}$ , making possible to determine both  $S_T(H, T)$  and  $D_m(H, T)$  in a large range of temperature and magnetic field. The under-field anisotropy of  $S_T(H, T)$  and  $D_m(H, T)$  is probed by orienting the temperature gradient (and thus also the concentration gradient) either horizontally or vertically, optical cell and grating being both in the vertical plane.

Both the thermal and the concentration gratings are here probed with a He-Ne laser beam ( $\lambda = 632 \text{ nm}$ ), which is poorly absorbed by these dispersions. The refractive index difference created by the mentioned gratings will cause the diffraction of the probing laser beam. The intensity of the first order diffraction is recorded as a function of time by a photomultiplier, initially, in the presence of the light source until the system eventually reaches the stationary state. At this condition, the lamp can be switched off and the system gradually relaxes, as presented in the graph in the bottom-left of [Figure 14](#). In the next section, we briefly describe the method to evaluate  $S_T$  and  $D_m$  by this FRS technique.

### 3.2.2 Experimental Determination of ( $S_T$ ) and ( $D_m$ )

$S_T$  and  $D_m$  can both be evaluated by experimentally determining the temperature  $\Delta T(t)$  and concentration  $\Delta\Phi(t)$  difference between the alternating hot and cold zones as a function of time. As a direct consequence of [Equation 3.4](#), the Soret coefficient writes

$$S_T = -\frac{\Delta\Phi_{\text{St}}}{\Phi\langle\Delta T\rangle}, \quad (3.28)$$

where  $\Delta\Phi_{\text{St}}$  is the spatial modulation of the volume fraction ( $\Phi$ ) in stationary conditions and  $\langle\Delta T\rangle$  being the time-averaged spatial modulation of temperature. Here we follow the same convention assumed previously, in which  $\Delta T$  is always taken positive, thus  $\Delta\Phi$  is positive if the MNPs go towards hot regions (meaning  $S_T < 0$ ) and  $\Delta\Phi$  is negative if the MNPs go towards cold regions (meaning  $S_T > 0$ ).

The mass diffusion coefficient  $D_m$  of the MNPs can be determined exclusively by the exponential decay of  $\Delta\Phi(t)$  starting from the steady state and once the heat source is turned off evolves as

$$\Delta\Phi_{\text{off}}(t) = \Delta\Phi_{\text{St}}e^{-q^2D_m t}, \quad (3.29)$$

with  $q = 2\pi/\Lambda$ , where  $\Lambda$  is the spatial period.

The temperature and concentration differences are actually very subtle, as an example, for the FF dispersed in EMIM-TFSI at  $\Phi = 5.95\%$ , we obtain  $|\Delta\Phi_{\text{St}}|/\Phi \leq 10^{-2}$  and  $\langle\Delta T\rangle \leq 0.1$  K whatever the amplitude and the direction of the applied field  $\vec{H}$  and whatever  $T$ . Nevertheless, these variations are large enough to produce a significant change in refractive index  $\Delta n$  between the regions. In fact, it is possible to establish a direct relation between the two parameters as in [141]:

$$|\Delta\Phi| = \frac{|\Delta n_{\Phi}|}{\partial n/\partial\Phi} \quad (3.30)$$

and

$$\Delta T = \frac{|\Delta n_T|}{|\partial n/\partial T|}, \quad (3.31)$$

where  $|\Delta n_{\Phi}|$  and  $|\Delta n_T|$  are the change in refractive index caused by the variation in particle concentration and by the temperature difference, respectively. The values of the partial derivatives for this type of particles and for the studied solvents have already been determined in the literature. For maghemite nanoparticles [24, 98] the derivative  $\partial n/\partial\Phi = 0.97$  as calculated from [146]. The derivative  $\partial n/\partial T$  for: 1) EMIM-TFSI is taken equal  $-2.82 \times 10^{-4} \text{ K}^{-1}$  and independent of  $T$  in our range of  $T$  from the optical index measurement of [147] (even if only measured up to 353 K); 2) EAN is taken equal  $-2.50 \times 10^{-4} \text{ K}^{-1}$  and independent of  $T$  in our range of  $T$  from the optical index measurement of Fig.5 in [148] (even if only measured up to 313 K); 3) water is temperature dependent evolving from  $-8.49 \times 10^{-5} \text{ K}^{-1}$  at  $T = 294$  K down to  $-2.095 \times 10^{-5} \text{ K}^{-1}$  at  $T = 353$  K, following [149] and S.I. of [98].

The modulation of the refractive index  $\Delta n$  can be experimentally determined by the probing laser intensity  $I_0$  and by the intensity of the first-order diffracted  $I_d$  through:

$$\Delta n = \pm \frac{\lambda \cos \theta}{\pi e} \sqrt{\frac{I_d}{I_0}}, \quad (3.32)$$

here for all experiments the incidence angle  $\theta = 38^\circ$ , the beam wavelength  $\lambda = 632$  nm and the sample thickness  $e = 25 \mu\text{m}$ .

Experimentally, at the steady state with a constant thermal grating, the refractive index modulation is actually a linear sum of both contributions:

$$\Delta n_{T\Phi} = \Delta n_T + \Delta n_{\Phi}. \quad (3.33)$$

For this reason, in order to separate the two contributions we consider a two time-scale model described in detail in ref. [141]. Based on the fact that the thermal response of the system is orders of magnitude faster than the concentration one, we use a chopper to repeatedly switch on and off the light of the Hg lamp focused on the sample. Consequently,

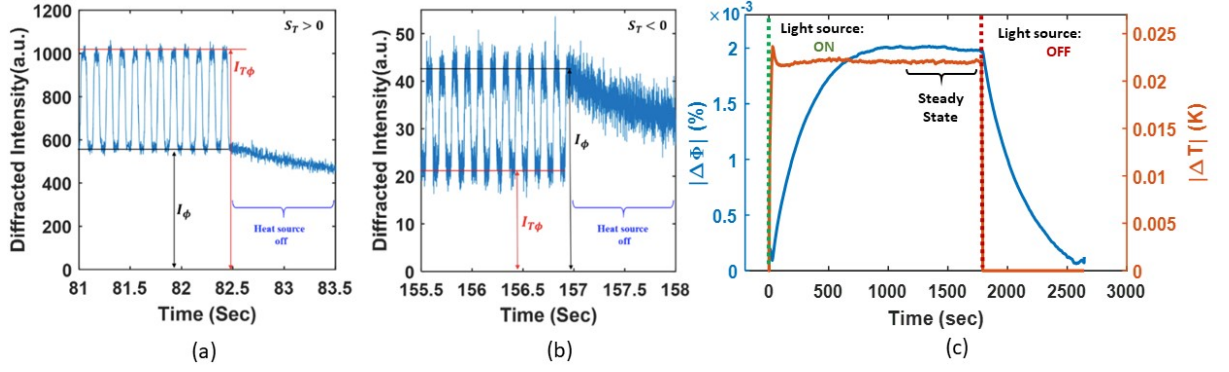


**Figure 15** – Examples of experimental curves obtained by measuring the intensity of the first-order diffracted intensity of the laser beam: (a) for a positive Soret coefficient (when particles move to regions with lower temperatures) the temperature and volume fraction modulations are in antiphase. This causes  $I_{T\Phi} > I_{\Phi}$ ; (b) for negative Soret coefficient (particles move to higher temperatures) they are in phase resulting in  $I_{T\Phi} < I_{\Phi}$ . (c) An example of a calculated  $|\Delta\Phi|$  and  $|\Delta T|$  before the heat source is on, after the source is shut down and finally when the system relaxes. Figure adapted from the E.S.I of ref. [24].

at 4 – 8 Hz the heat source alternates slowly enough that the thermal response can periodically vanish, but fast enough that the concentration gradient cannot relax.

Figure 15a and b shows the recorded signal of the laser first-order diffracted intensity for a positive and a negative  $S_T$ . Both graphs start at the steady state, where the contribution of the thermal grating to the diffracted signal exhibits the same periodicity as the heating light. When the chopper allows the light pass through, we have access to the intensity  $I_{T\Phi}$  associated to  $\Delta n_{T\Phi}$ , on the other hand, when the chopper blocks the heat source we have just  $I_{\Phi}$ . Finally, when the heat source is permanently shut down the laser intensity proceeds to decay exponentially due to the relaxation of the enforced concentration gradient.

The temperature and concentration difference shown in Figure 15c can be calculated by applying Equation 3.32 and 3.33 to Equation 3.30 and 3.31 resulting in

$$|\Delta\Phi| = \frac{\lambda \cos \theta}{\pi e \partial n / \partial \Phi} \sqrt{I_{\Phi} / I_0} \quad (3.34)$$

and

$$\Delta T = \frac{|\Delta n_{T\Phi} - \Delta n_{\Phi}|}{|\partial n / \partial T|} = \frac{\lambda \cos \theta}{\pi e |\partial n / \partial \Phi|} \left| \sqrt{I_{T\Phi} / I_0} - \sqrt{I_{\Phi} / I_0} \right|, \quad (3.35)$$

$\Delta\Phi$  being the same sign of  $I_{\Phi} - I_{T\Phi}$ . As a result, these equations can be directly applied to Equation 3.28 in order to determine the experimental value of  $S_T$ , considering that the duty cycle of the chopper is 50% and thus at the steady state  $\langle \Delta T \rangle = \Delta T^{\text{St}} / 2$ . It is checked that the measured  $S_T$  is independent of  $\Lambda$  and of the power of the Hg lamp (the experimental range is limited to the power linear regime [150]).

In-field measurements are performed at ratios of the sample thickness  $e$  over spatial period  $\Lambda$ , such that  $0.17 < e/\Lambda < 0.28$ , thus in the 2D-array conditions. The experiments are also performed at magnetic fields  $\vec{H}$  below the threshold of 2D magnetoconvection [151, 152].

The diffusion coefficient  $D_m$  is determined by adjusting the relaxation of  $|\Delta\Phi(t)|$  after the heat source is turned off by an exponential fit  $e^{-t/\tau}$  with  $\tau = q^{-2}D_m^{-1}$  (see Equation 3.29).

### 3.3 Water-EAN Mixtures: Inversion of Thermodiffusive Properties

In this section we investigate the thermodiffusion effects on ferrofluids based in ethylammonium nitrate (FF-EAN), where the thermodiffusive parameters are first used to analyse the general context of the colloidal stability as a function of different counterions – here introducing the novel results for the  $\text{Rb}^+$  ion – supporting the scenario drawn in subsection 2.3.2. Secondly, aqueous ferrofluids can be well described by the DVLO approach allowing the determination of an effective surface charge via electrophoretic mobility that can be later compared with values obtained by thermodiffusion [25,98]. Yet, the same is not viable for ILs and thus we present a brief thermodiffusion characterization of ferrofluids in EAN with  $\text{Na}^+$  counterions, as proposed by Bhattacharya et al.[18], which sets the order of magnitude of the effective charge for this system.

Lastly, as the aqueous and EAN systems have been comprehensively characterized independently, we are able to explore the impacts in the thermodiffusion properties at different proportions of these solvents, in two different particle concentrations and a broad range of temperatures.

#### 3.3.1 Thermodiffusion measurements in EAN with various counterions

Let us first elucidate the thermodiffusion in pure EAN with various counterions. As mentioned previously, FFs in EAN could be dispersed with  $\text{Na}^+$ ,  $\text{Rb}^+$  and  $\text{Li}^+$  counterions, while the first two present a globally repulsive regime the latter shows attractive interparticle interactions, thus limiting the range of particle concentration. These contrasting behaviors indicate that the thermodiffusion is certainly to exhibit notable differences. So in this context arises our interest in probing these distinct conditions aiming to trace a general panorama of the EAN system.

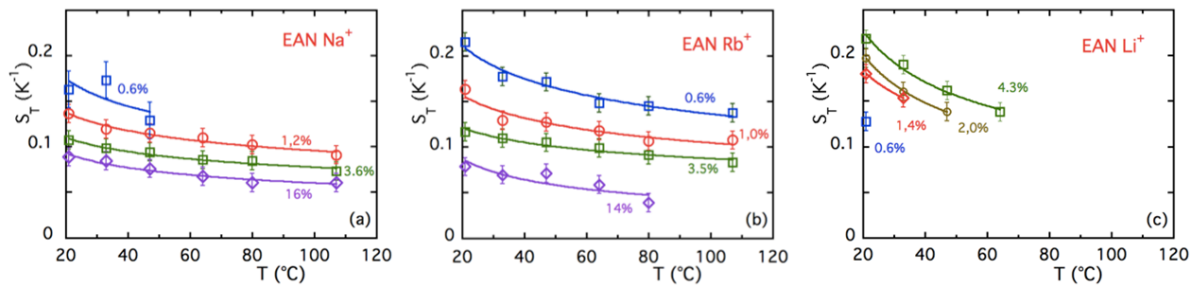


**Figure 16** – Soret coefficient as a function of the temperature and particle concentration for the three studied counterions  $\text{Na}^+$ ,  $\text{Rb}^+$  and  $\text{Li}^+$  in EAN. Full lines are guide to the eyes.

As follows, [Figure 16](#) shows the Soret coefficient  $S_T$  obtained by FRS as a function of temperature  $T$  for the three different counterions  $\text{Na}^+$ ,  $\text{Rb}^+$  and  $\text{Li}^+$  at various  $\Phi$  from 0.6% till 16.0%. If in any case  $S_T$  decreases with temperature, different behaviors of  $S_T$  as a function of  $\Phi$  are observed for dispersions with interparticle attraction ( $A_2 < 0$ , here with  $\text{Li}^+$ ) and with interparticle repulsion ( $A_2 > 0$ , here with  $\text{Na}^+$  and  $\text{Rb}^+$ , for which the results are quite similar). At any temperature it can be seen that  $S_T$  is an increasing function of  $\Phi$  for the attractive NP's system with  $\text{Li}^+$  counterions, while it is a decreasing one for the repulsive NP's system with  $\text{Na}^+$  and  $\text{Rb}^+$  counterions.

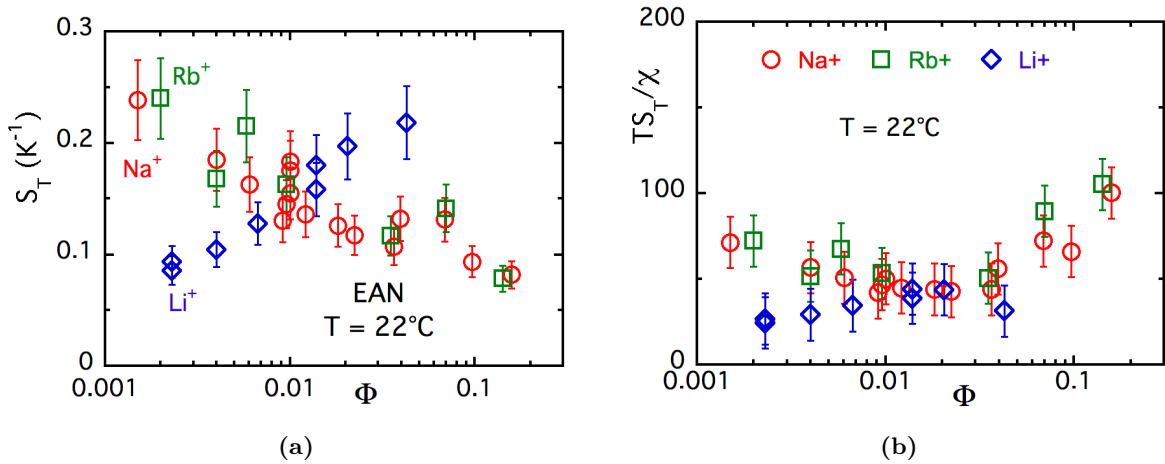


**Figure 17** – (a) Volume fraction dependence of the Soret coefficient ( $S_T$ ) of NPs dispersions with the various counterions  $\text{Na}^+$ ,  $\text{Rb}^+$  and  $\text{Li}^+$  at  $T = 22^\circ\text{C}$ . (b) Associated  $\Phi$ -variations of  $TS_T/\chi$ .

These trends are even more clear if  $S_T$  is presented as a function of  $\Phi$  at room temperature, as shown in [Figure 17a](#). This plot illustrates the fact that in [Equation 3.6](#) the Soret coefficient  $S_T$  is directly proportional to the compressibility  $\chi$  of the NP system which comprehends to a certain extent the response of the system interactions to the  $\Phi$ -variations. Indeed  $\chi$  is lower than 1 for  $A_2 > 0$  and decreases with  $\Phi$  for a repulsive system – see the red circles and green squares trend in [Figure 8](#); while for  $A_2 < 0$  the opposite behavior occurs as  $\chi$  is larger than 1 and increases with  $\Phi$  (in the narrow range of  $\Phi$ 's where the system remains a stable colloid) – see the blue triangles trend in [Figure 8](#).

[Figure 17b](#) presents  $TS_T/\chi$  as a function of  $\Phi$ , in order to normalize  $S_T$  by its  $\chi$ -dependence. We can note that if the obtained variations for  $\text{Na}^+$  and  $\text{Rb}^+$  are close to one another, there is a mismatch for  $\text{Li}^+$  in opposition, particularly at low  $\Phi$ 's.

We now look at the diffusion coefficient  $D_m$  measured by FRS at room temperature. As seen in [Figure 18](#),  $D_m$  does not present a strong dependence on  $\Phi$  in the explored range for  $\text{Na}^+$  and  $\text{Rb}^+$  counterions. On the contrary, it seriously decreases for  $\text{Li}^+$ . In the following we try to understand these  $\Phi$ -dependencies also as a function of  $T$ .

In general,  $D_m$  strongly depends on temperature through the viscosity  $\eta_0(T)$  of the carrier fluid accordingly to [Equation 3.16](#), which also contains the hydrodynamic diameter

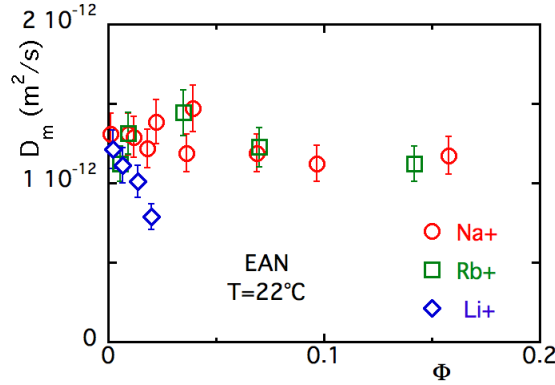


**Figure 18** – Diffusion coefficient  $D_m$  as a function of the NP's volume fraction  $\Phi$  at  $T = 22^\circ\text{C}$  in ferrofluids based on EAN with the different initial counterions  $\text{Na}^+$ ,  $\text{Rb}^+$  and  $\text{Li}^+$ .

$d_H$ , the compressibility  $\chi$  (here measured by SAXS) and the  $\Phi$ –dependence of the friction  $\zeta$ . Let us first focus in a set of measurements realized on different samples all with  $\text{Na}^+$  counterions and  $\Phi$ 's close to 1.0%. The diffusion coefficients were obtained as a function of  $T$  ranging from 295 K to 380 K. They are presented in [Figure 19a](#) together with the respective adjustment performed using [Equation 3.16](#) in which  $\eta_0(T)$  was taken from ref. [153],  $d_H = 8.7$  nm,  $\Phi_{\text{eff}} = 1.15\%$  (obtained by SAXS and SANS) and  $\chi$  was deduced from [Equation 2.5](#). Note that at  $\Phi = 1.0\%$ , the  $\Phi$ –dependence of  $\chi$  almost cancels that of  $[1 + k_f\Phi_{\text{eff}}]$  at room temperature, remaining true for the whole experimental range of  $T$  [18]. Another equivalent way to analyse these results is presented in [Figure 19b](#), by directly comparing an effective viscosity  $\eta_{\text{eff}}(T)$  – extracted from the  $D_m$  measured by FRS using the same parameters  $d_H$  and  $\Phi_{\text{eff}}$  – to the viscosity  $\eta_0(T)$  of EAN from the literature [153]. In both cases, the experimental data obtained from the FRS measurements is in good agreement with the expected values for this medium.

The development of [Equation 3.15](#) has a limited  $\Phi$ –range of validity. To check it let us go back to measurements with the different counterions  $\text{Na}^+$ ,  $\text{Rb}^+$  and  $\text{Li}^+$  in the whole range of  $\Phi$  and  $T$ . We deduce the reduced friction  $\zeta/\zeta_0$  experienced by the nanoparticles (see [Figure 20](#)) from  $D_m$  measurements using [Equation 3.14](#) and [3.16](#) resulting in

$$\frac{\zeta(\Phi_{\text{eff}}, T)}{\zeta_0} = \frac{kT}{3\pi\eta_0(T)d_H D_m \chi(\Phi)}, \quad (3.36)$$

where again  $\eta_0(T)$  is taken from ref. [153],  $d_H = 8.7$  nm and  $\chi$  is deduced from [Equation 2.5](#) with  $\Phi_{\text{eff}}$  deduced from SAXS and SANS measurements with the corresponding counterions (see [Figure 8](#) in [subsection 2.3.2](#)).

These results presented in [Figure 20](#) organize themselves on a master curve which is at the first order independent on  $T$  and on the nature of the counterions, departing from the [Batchelor](#)[126] development of [Equation 3.15](#) for  $\Phi$  larger than 4.0%. Below  $\Phi = 4.0\%$ , the development seems to match the experimental results, however, above this concentration a strong interparticle interaction enters in play in  $\zeta$  which multiplies the

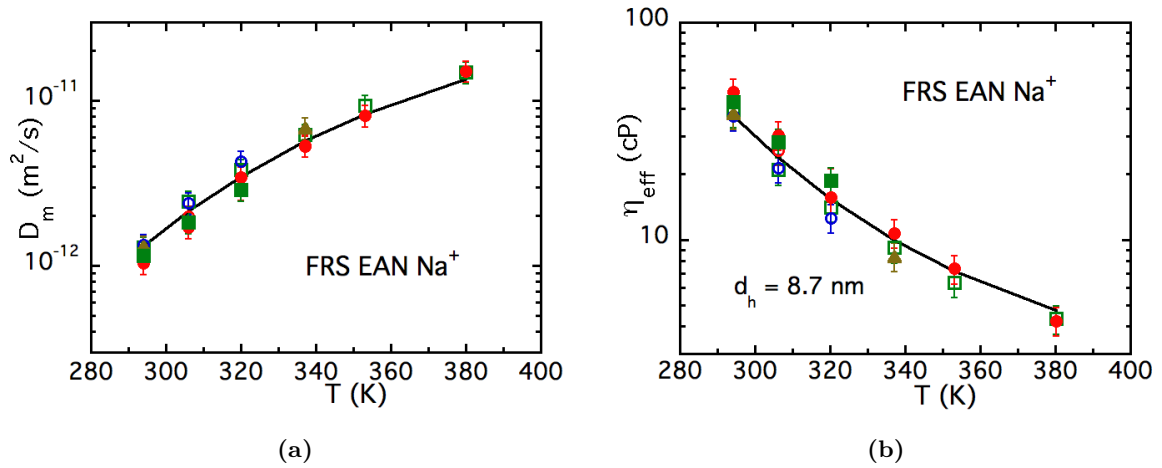


**Figure 19** – (a) Diffusion coefficient  $D_m$  as a function of temperature  $T$  for six different samples in EAN with  $\text{Na}^+$  counterions at  $\Phi = 1.2\%$  (Open green squares),  $0.91\%$  (open red discs),  $0.96\%$  (full brown triangles) and  $1.0\%$  (open blue discs, full green squares and full red discs). The full line corresponds to the adjustment by Equation 3.16 using  $\eta_0(T)$  from [153],  $d_H = 8.7 \text{ nm}$ , with  $\Phi_{\text{eff}} = 1.15\%$  and  $\chi$  deduced from Equation 2.5 (b) Effective viscosity  $\eta_{\text{eff}}$  deduced from FRS measurements of Figure 19a as a function of  $T$ , using the same parameters  $d_H$  and  $\Phi_{\text{eff}}$ . Same symbols as in Figure 19a. Full line  $\eta_0(T)$  of EAN from ref. [153]

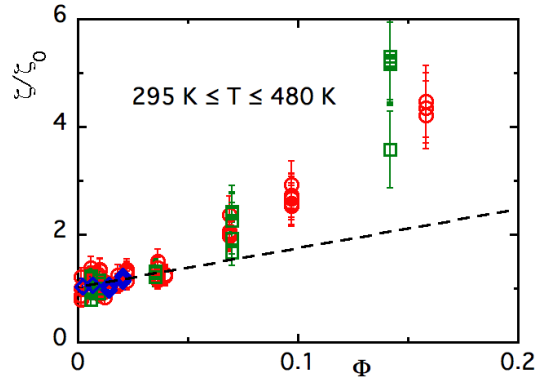


**Figure 20** – Reduced friction  $\zeta/\zeta_0$  experienced by the NPs as a function of their volume fraction  $\Phi$  for the three counterions (red circles correspond to  $\text{Na}^+$ , green squares to  $\text{Rb}^+$  and blue diamonds to  $\text{Li}^+$ ) in the whole experimental range of temperature. The dotted line corresponds to Equation 3.15 in the case of  $\text{Na}^+$  counterions ( $\Phi_{\text{eff}} = 1.15\Phi$ ).

friction by a factor 5 at  $\Phi$  of the order of  $15.0\%$ . This is necessary related to the ionic organization in EAN and to the layering around the NPs. Withal, we have no theoretical description to describe the friction at large  $\Phi$ .

Conclusively, the presented thermodiffusion results corroborate the stability variations due to the two different regimes of interparticle interactions caused by the nanoscale organization of the three different counterions around the NPs. From this point on, we focus the attention in the EAN sample with  $\text{Na}^+$  counterions as it presents great colloidal stability and it was possible to estimate its effective surface charge (see next section). For this reason, it is the optimal available candidate to investigate the modifications on the thermodiffusion properties as a function of the water content, since the system has been vastly characterized in both solvents.

### 3.3.2 Analysis of $S_T$ Measured in EAN with $\text{Na}^+$ Counterions at 22 °C

We limit here our analysis to the case of  $\text{Na}^+$  counterions (as in ref. [18]), some more work being needed to quantify precisely the ionic organization of Figure 10 in the case of  $\text{Rb}^+$  and  $\text{Li}^+$ .

In the referred study, it was proposed that at least the first layer (above the citrate layer) close to the NPs moves with it, as it is strongly linked on the surface according to AFM studies [154], but maybe more layers move with the NP as well. If solely the first layer moves with the particle one can expect a positive effective charge  $\xi_0^{\text{eff}}$  with a modulus around  $0.2|Z_{\text{str}}|$  (here structural charge  $Z_{\text{str}}$  is of the order of  $-300$ ). If more than one layer of ions moves with the NPs, the effective charge sign could then invert to negative with a lower absolute value as the screening is progressively increased. These considerations give some limits to the adjustment of the  $\Phi$ -dependence of  $S_T$  when applying Equation 3.7 at a given temperature by Equation 3.11.

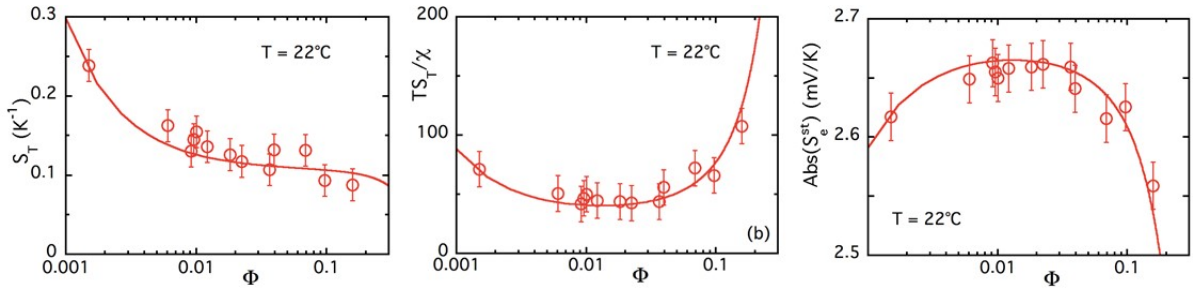


**Figure 21** – (Left)  $\Phi$ -dependence of Soret coefficient  $S_T$  (left) and of  $TS_T/\chi$  (center) for EAN-based dispersions with  $\text{Na}^+$  counterions at room temperature - full line adjustment with Equation 3.10 using  $|Z^{\text{eff}}| = \xi_0^{\text{eff}} = \pm 55$ ,  $\hat{S}_{\text{NP}} = +6.0 \text{K}^{-1}$  and  $[i = \pm]_{\text{dis}} = 0.4 \times 10^{-3} \text{mol/L}$ ; index  $i = \{\pm\}$  corresponding to dissociated  $\text{NO}_3^-$  species if  $Z^{\text{eff}}$  is negative and to dissociated  $\text{EA}^+$  species if  $Z^{\text{eff}}$  is positive (for details see subsection 3.1.1 and [18]). (Right)  $\Phi$ -dependence of the absolute value of the obtained Seebeck coefficient  $S_e^{\text{st}} = (\hat{S}_{\text{NP}} - kTS_T/\chi)/(e\xi_0^{\text{eff}})$  as obtained from the FRS data (circles) and from their adjustments with Equation 3.10 (full line) using the values of  $Z^{\text{eff}} = \xi_0^{\text{eff}} = \pm 55 \pm 15$ ,  $\hat{S}_{\text{NP}} = +6 \pm 1.6$  and  $[i = \pm]_{\text{dis}} = 0.4 \pm 0.1 \times 10^{-3} \text{mol/L}$ . According to Equation 3.10,  $S_e^{\text{st}}$  has the same sign as  $Z^{\text{eff}} = \xi_0^{\text{eff}}$ , all the other quantities entering in the expression of  $S_e^{\text{st}}$  being positive. Figure reproduced from ref. [18].

Equation 3.11 implies that the adjustments of  $S_T$  and  $TS_T/\chi$  presented in Figure 21 left and center (except through the meaning of index  $i$ ) do not analytically depend on the sign of  $Z^{\text{eff}} = \xi_0^{\text{eff}}$ . Thus, independently of the sign of the NP charge,  $\hat{S}_{\text{NP}}/kT$  is found to be positive and equal to  $0.11|Z^{\text{eff}}| = 6.0 \pm 1.6 \text{K}^{-1}$  for  $|Z^{\text{eff}}| = \pm 55 \pm 15$ . This absolute value is close to 20% of the structural charge mentioned above, nonetheless, its sign still cannot be precisely determined from this experiment. Then, the meaning of the mute parameter  $n_i$  in Equation 3.10 is the unique difference in interpretation when the sign of  $Z^{\text{eff}} = \xi_0^{\text{eff}}$  is reversed, which corresponds either to the concentration of dissociated  $\text{EA}^+$  or dissociated  $\text{NO}_3^-$  following the same sign as the NP's charge. The concentration of the dissociated complementary ions counterbalancing the  $n_i$ 's and the NP's charges depends on  $\Phi$ . They can be readily obtained from the electro-neutrality relation written

in Equation 3.7. It typically ranges between  $0.4 \times 10^{-3}$  and  $6.9 \times 10^{-3}$  mol/L in our  $\Phi$  range [18]. Thus, whatever the sign of the effective charge,  $n_+$  and  $n_-$  are still rather small.

Finally, let us incorporate this quantitative result to the schematics presented previously in Figure 10 and discuss how this effective surface charge could be achieved through the structured/built up exclusively of ions along the NP's surface. First of all,  $\xi_0^{\text{eff}}$  is the charge close to the surface that passively accompanies the particle movement under the action of the temperature gradient. As mentioned several times, at the very least, the first layer of the condensed ions at the NP surface moves along with the particle. In this case,  $\xi_0^{\text{eff}}$  would be positive in direct opposition to the negatively charged particle surface. If  $\xi_0^{\text{eff}}$  includes the second layer of condensed ions, then it will have a negative sign, following the same principle as described in the first case. In both situations the order of magnitude of  $|\xi_0^{\text{eff}}|$  would be approximately the same, therefore not being possible with this dataset alone to discriminate between the two solutions of  $Z_0^{\text{eff}} = \xi_0^{\text{eff}} = +55$  and  $-55$ . As the sign of  $\hat{S}_{\text{NP}}$  was precisely known from the presented thermodiffusion measurements, a positive value of  $\xi_0^{\text{eff}}$  was only determined by thermoelectric measurements, discriminating between the two signs for the case of  $\text{Na}^+$ [18].

### 3.3.3 Thermodiffusion in EAN-water mixtures with $\text{Na}^+$ counterions

In mixtures of water and ethylammonium nitrate (EAN), it has been shown in subsection 2.3.4 that ferrofluids based on MNPs with  $\text{Na}^+$  counterions and a volume-averaged diameter  $d_{\text{NP}} = 7.4$  nm form stable colloidal dispersions at any weight proportion  $w_{\text{EAN}}$  of EAN/water at  $\Phi = 1.0\%$  and  $3.0\%$ . SAXS measurements have shown that the overall interparticle interaction is repulsive at large and low  $w_{\text{EAN}}$ , and attractive for medium values. At  $\Phi = 1.0\%$ , it is possible to deduce the second virial coefficient  $A_2$  from SAXS measurements (see Figure 12). Let us note that as  $w_{\text{EAN}}$  increases, the ionic dispersion is evolving from a colloid in a standard aqueous electrolyte at very low  $w_{\text{EAN}}$  (that could be described by a DLVO-like model) to a dispersion in an ionic liquid at large  $w_{\text{EAN}}$ , purely constituted of ions (see Figure 10). We try to probe here this evolution by Forced Rayleigh Scattering.

We first focus on the measurements of the diffusion coefficient  $D_m$  at  $\Phi = 1.0\%$  where both  $\chi$  and  $A_2$  are known. Figure 22a presents  $D_m$  as a function of  $w_{\text{EAN}}$  at the two extreme temperatures probed here, namely room temperature ( $T = 295$  K) and  $T = 353$  K ( $= 80$  °C). At a given  $T$ ,  $D_m$  reduces by more than one order of magnitude between  $w_{\text{EAN}} = 0$  (water) and  $w_{\text{EAN}} = 1$  (EAN). Increasing  $T$  from 295 K to 353 K produces an increase of  $D_m$  whatever  $w_{\text{EAN}}$ . These effects are both mainly due (but not only) to the variations of the solvent viscosity  $\eta_0$  as a function of  $w_{\text{EAN}}$  and  $T$ . As  $\eta_0$  is not known in our whole range of  $T$  and  $w_{\text{EAN}}$ , we propose as in subsection 3.3.1 to deduce an effective viscosity  $\eta_{\text{eff}}$  from  $D_m$  measurements using here also Equation 3.16. This is

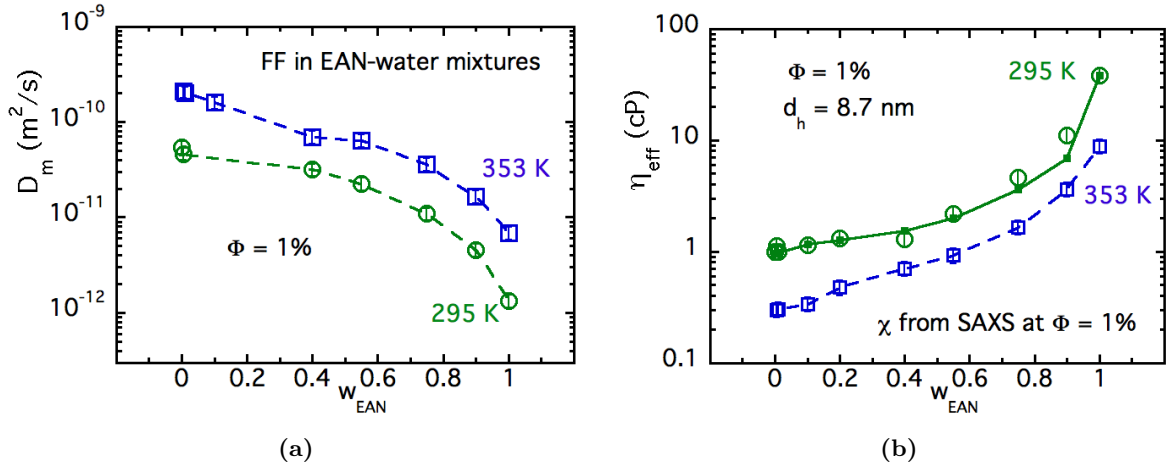


**Figure 22** – (a) Diffusion coefficient  $D_m$  determined by FRS at  $\Phi = 1.0\%$  as a function of  $w_{\text{EAN}}$  at the two extreme experimental temperatures. Dashed lines are guides for the eye; (b) Effective viscosity  $\eta_{\text{eff}}$  deduced from these  $D_m$  determinations as a function of  $w_{\text{EAN}}$  at  $T = 295 \text{ K}$  and  $353 \text{ K}$  (open symbols - see text for details). Full line and close squares correspond to the viscosity  $\eta_0$  of mixtures water-EAN at  $295 \text{ K}$  from ref. [155]. Dashed line is a guide for the eye.

presented in Figure 22b. The adjustment is performed with  $d_H = 8.7 \text{ nm}$ ,  $\chi$  from the SAXS measurements of Figure 12a and using the linear development of the friction  $\zeta$  of Equation 3.15, where  $\Phi_{\text{eff}}$  is taken equal to  $\Phi A_2/4$  (see Equation 2.7 extended here to the weakly attractive regime). The interparticle interaction parameters,  $\chi$  and  $\Phi_{\text{eff}}$ , are here supposed independent of temperature. Figure 22b compares this effective viscosity  $\eta_{\text{eff}}$  to the values reported by Zarrougui, Dhahbi and Lemordant [155] at room temperature. There is a good agreement between ref. [155] and our determinations.

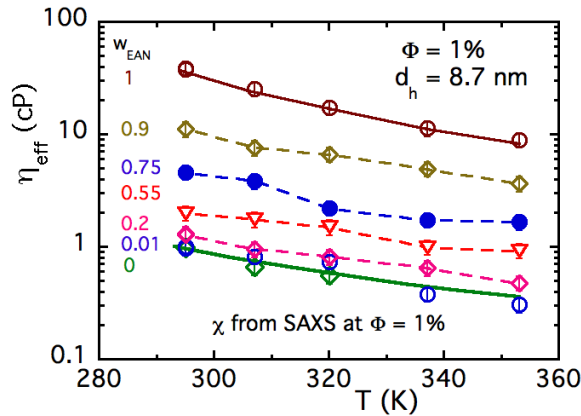


**Figure 23** – Effective viscosity  $\eta_{\text{eff}}$  deduced from  $D_m$  determinations at  $\Phi = 1.0\%$  of Figure 22a as a function of  $T$  at several  $w_{\text{EAN}}$  - Some values are interpolated. Full lines are  $\eta_0$  for EAN (brown line from ref. [153]) and for water (green line). Dashed lines are guides for the eye.

The effective viscosity  $\eta_{\text{eff}}$  is also presented as a function of  $T$  in Figure 23 at several  $w_{\text{EAN}}$  (some missing values were deduced from interpolations of the experimental results). They are in good agreement – for  $w_{\text{EAN}} = 0$  and  $1.0$  – with the known values of  $\eta_0(T)$  for water and EAN, confirming the validity of our hypothesis of interparticle interaction

independent of  $T$  at the first order.

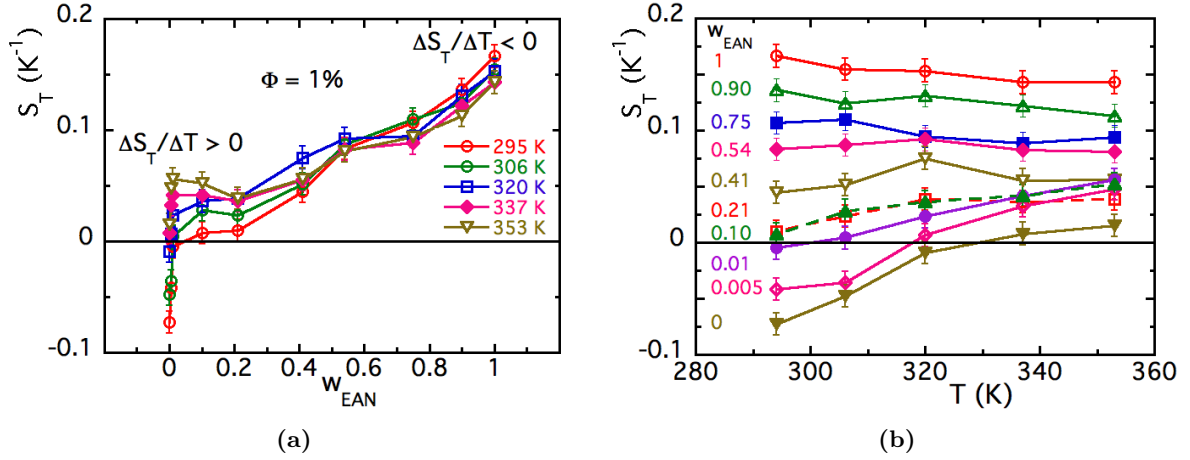


**Figure 24** – (a) FRS measurements of Soret coefficient  $S_T$  at  $\Phi = 1.0\%$  as a function of  $w_{\text{EAN}}$  at the various probed temperatures – Full lines are guide for the eye; (b) Same measurements as a function of  $T$  at constant  $w_{\text{EAN}}$  - Full and dashed lines are guides for the eye.

FRS also allows to determine the Soret coefficient  $S_T$  in the dispersions based on EAN/water mixtures. Figure 24a presents the obtained results at  $\Phi = 1.0\%$  as a function  $w_{\text{EAN}}$  for the various probed temperatures between 295 K and 353 K. We can notice that at low  $w_{\text{EAN}}$ ,  $S_T$  is an increasing function of temperature from a negative value towards a positive one, as it has been previously noticed in citrated water based ferrofluids with  $\text{Na}^+$  counterions (see Figure 27 further on). On the contrary, at large  $w_{\text{EAN}}$ ,  $S_T$  is positive and is a decreasing function of  $T$ , as previously observed in pure EAN, as shown in Figure 16. This is more obvious in Figure 24b, where the same results for these various samples with different EAN/water proportions are plotted as a function of  $T$  at constant  $w_{\text{EAN}}$ .

Now looking at the  $S_T$  measurements at  $\Phi = 3.0\%$  in Figure 25a, this trend<sup>6</sup>  $\Delta S_T / \Delta T > 0$  at low  $w_{\text{EAN}}$  and  $\Delta S_T / \Delta T < 0$  at large  $w_{\text{EAN}}$  is even more pronounced. At  $\Phi = 3.0\%$ , the inversion point at which  $\Delta S_T / \Delta T$  is of the order of 0 can be located at  $w_{\text{EAN}}$  of the order of 0.6.

Comparing these results at  $\Phi = 1.0\%$  and  $3.0\%$  for the two extreme experimental temperatures in Figure 25b, another trend can be evidenced.  $\Delta S_T / \Delta \Phi$  is negative at large  $w_{\text{EAN}}$ , as it is observed in pure EAN with  $\text{Na}^+$  counterions, marking a repulsive interparticle interaction (see Figure 17a).  $S_T$  then becomes almost independent of  $T$  and  $w_{\text{EAN}}$  at proportions in the order of 0.5 – 0.7. For  $w_{\text{EAN}}$  ranging between 0.1 and 0.5,  $\Delta S_T / \Delta \Phi$  is positive. In a pure IL it would be a mark of attractive interparticle interaction. SAXS measurements shows that it is really the case,  $S(Q = 0)$  is larger than 1 in this range of  $w_{\text{EAN}}$  (see Figure 13a). The dispersion thus already behaves as an Ionic Liquid in this range of  $w_{\text{EAN}}$ . Below  $w_{\text{EAN}} < 0.1$ ,  $S_T$  presents an abrupt variation that could be

<sup>6</sup> In aqueous dispersions of proteins,  $\Delta S_T / \Delta T$  is considered as a marker of the hydrophilicity/hydrophobicity of proteins [156]. The hydrophilicity of the solute (i.e. its solvation) decreases when  $\Delta S_T / \Delta T$  decreases.

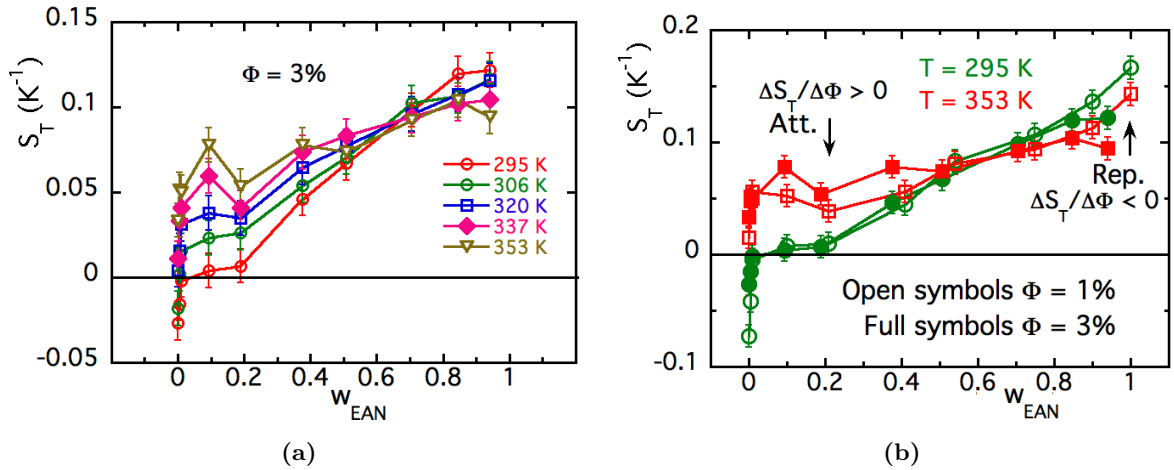


**Figure 25** – (a) FRS measurements of Soret coefficient  $S_T$  at  $\Phi = 3.0\%$  as a function of  $w_{\text{EAN}}$  at the various probed temperatures - Full lines are guide for the eye; (b) Comparison at  $T = 295 \text{ K}$  and  $353 \text{ K}$  between  $S_T$  measurements as a function of  $w_{\text{EAN}}$  at  $\Phi = 1.0\%$  and  $3.0\%$  - Full lines are guides for the eye.

associated to the behavior of a more standard electrolyte. This is confirmed when plotting as in Figure 26, the reduced quantity  $TS_T/\chi$ <sup>7</sup> as a function of  $w_{\text{EAN}}$  at room temperature. Whatever  $\Phi$ , the value of  $TS_T/\chi$  is very close to zero for  $0.01 \leq w_{\text{EAN}} \leq 0.2$ , positive for  $w_{\text{EAN}} > 0.2$  and negative for  $w_{\text{EAN}} < 0.01$ .

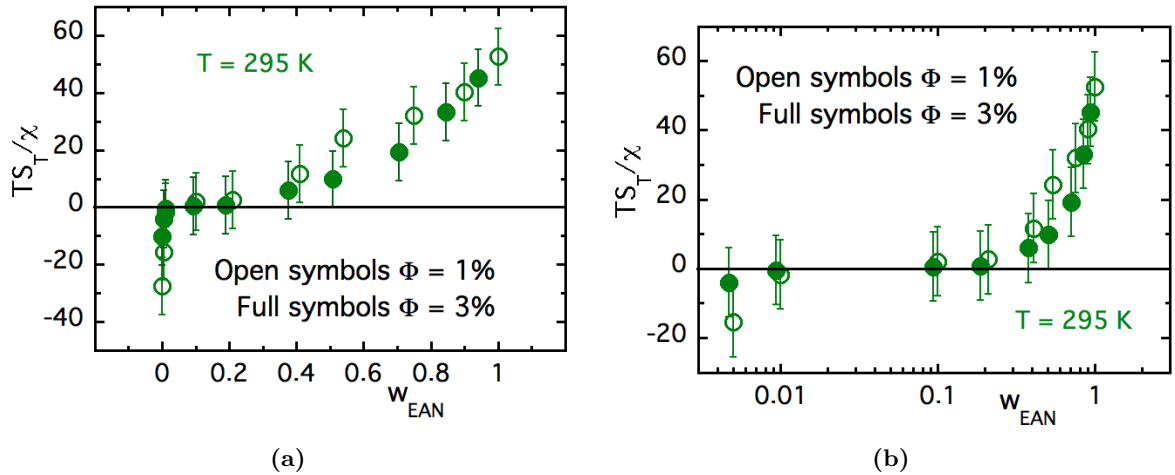


**Figure 26** –  $TS_T/\chi$  as a function of  $w_{\text{EAN}}$  in a linear representation (a) and a semi-log representation (b) at room temperature for  $\Phi = 1.0\%$  and  $3.0\%$

Let us recall (see Figure 17b) that in pure EAN  $TS_T/\chi$  is positive and of the order of 50 at  $\Phi = 1.0 - 3.0\%$ , similar to the values obtained here. This was associated to a positive  $\hat{S}_{\text{NP}}/kT = 6 \text{ K}^{-1}$  and a positive  $\xi_0^{\text{eff}} = +55$  in the adjustments of subsection 3.3.2.

In water with citrated NPs as used here, on the contrary, Kouyaté et al.[25] found that at room temperature the sign of the Soret coefficient depends on the nature of

<sup>7</sup> Following Equation 3.11 this quantity equals  $(\hat{S}_{\text{NP}} - e\xi_0^{\text{eff}}S_e^{\text{St}})/k$ ,  $\hat{S}_{\text{NP}}$  and  $\xi_0^{\text{eff}}$  being characteristics of the NPs in the solvent and  $S_e^{\text{St}}$  being the stationary Seebeck coefficient.

the counterions (see Figure 27a). Its value also depends on the concentration of free citrate [98]. With  $\text{Na}^+$  counterions,  $S_T$  is negative, as we find here both at  $\Phi = 1.0\%$  and  $3.0\%$ . Moreover, it is found (with the same MNPs as in [25], which have a diameter of  $d_{\text{NP}} = 8.5$  nm, thus slightly larger than the present ones) that for  $\text{Na}^+$  counterions  $S_T$  is an increasing function of temperature (see Figure 27b). This behavior is very similar to the one observed in Figure 24b for the unmixed water sample ( $w_{\text{EAN}} = 0$ ). Whatever the nature of the counterions, the effective charge of the citrated NPs is negative in water. Its measured value for  $\text{Na}^+$  counterions in ref. [25] is  $\xi_0^{\text{eff}} = -30$  and the adjustments of  $S_T$  leads to  $\hat{S}_{\text{NP}}/kT = -0.13 \text{ K}^{-1}$ . Therefore, we expect values of the same order of magnitude here.

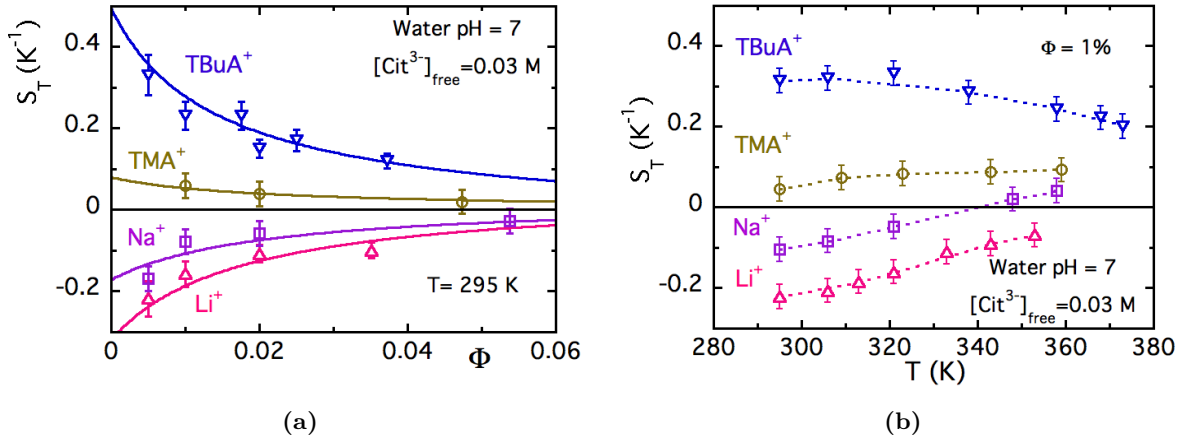


**Figure 27** – Citrated NPs in water with different counterions from ref. [25] – (a)  $S_T$  as a function of  $\Phi$  at room temperature – data and full line adjustments from figure of ref. [25]; (b)  $S_T$  as a function of  $T$  at  $\Phi = 1.0\%$  (unpublished data) with dotted lines as guides for the eye. Figure reproduced from ref.[25].

Thus in the water-EAN mixtures, both the effective charge  $\xi_0^{\text{eff}}$  and  $\hat{S}_{\text{NP}}/kT$  evolve from a negative value to a positive one while  $w_{\text{EAN}}$  increases from 0 to 1. We can imagine that the evolution of the effective charge of the NPs is progressive, being almost zero in the intermediate range  $0.01 \leq w_{\text{EAN}} \leq 0.2$ . For  $0.2 \leq w_{\text{EAN}} \leq 0.5 - 0.7$ , it becomes slightly positive but not yet large enough to produce an interparticle repulsion. For  $0.7 \leq w_{\text{EAN}} \leq 1$ , the effective charge becomes large enough to produce an interparticle repulsion as in the pure Ionic Liquid. For  $w_{\text{EAN}} \leq 0.01$ , the system is in the regime of a more standard electrolyte, where the ionic strength, the nature and concentration of all the free ions are important [25, 98].

A deeper study in this “electrolyte regime” ( $w_{\text{EAN}} \leq 0.01$ ) should be undertaken in the future, in particular replacing  $\text{Na}^+$  free counterions by  $\text{EA}^+$  ones in the dispersions. A preliminary test performed with  $\text{EA}^+$  counterions in water at  $\Phi = 2.7\%$  and  $[\text{cit}]_{\text{free}} = 1.3 \times 10^{-2} \text{ mol/L}$  shows that  $S_T$  is positive and equal to  $+0.01 \text{ K}^{-1}$  at room temperature with the NPs of ref. [25]. Thus using  $\text{EA}^+$  ions instead of  $\text{Na}^+$  counterions should sensibly modify the shape of  $S_T$  as a function of  $w_{\text{EAN}}$  (cf Figure 24 and Figure 25), at least at low

$w_{\text{EAN}}$  (where the effective charge of the NPs should still be negative), as  $S_{\text{T}}$  is expected to remain positive in the “ionic liquid regime”<sup>8</sup>. But with  $\text{EA}^+$  counterions what would be the value of  $\xi_0^{\text{eff}}$  in pure EAN? If we know from refs. [58, 59, 81] that a stable colloid can be obtained in the case of pure EAN, we have yet no proof that  $\xi_0^{\text{eff}}$  would still be positive.

## 3.4 EMIM-TFSI: Thermodiffusion Under Magnetic Field

The under-field effects are investigated using a ferrofluid dispersed in EMIM-TFSI to benefit from some appealing characteristics of this system. First, the magnetically determined particle size of  $d_{0,\text{mag}} = 8.9$  nm with polydispersity index  $s_{0,\text{mag}} = 0.23$  leads to a volume-averaged diameter [61] of  $d_{\text{NP}} = \langle d_0^3 \rangle^{1/3} = 9.6$  nm, which is large enough to produce a substantial magnetically induced anisotropy in the thermodiffusion. Second, it exhibits a considerable interparticle repulsion demonstrated by the second virial coefficient  $A_2 = 7.3$ .

In addition, the colloidal stability is preserved in a broad range of temperatures, exhibiting only a negligible disturbance at the nanometric level. This set of assets makes this type of FF-RTIL a strong candidate for future applications utilizing thermodiffusive properties under-field.

### 3.4.1 Zero-Field Results

Let us first address the behavior of  $D_{\text{m}}$  and  $S_{\text{T}}$  without the presence of an external magnetic field. The evolution of the experimentally determined  $D_{\text{m}}(\Phi, T)$  as a function of  $T$  in zero magnetic field is plotted in Figure 28a for  $\Phi = 1.0$  % and 5.95 %, while the development of  $S_{\text{T}}(\Phi, T)$  as a function of  $\Phi$  is exhibited in Figure 28b for three different temperatures (294 K, 358 K and 441 K).

Serving as a guideline, the full line in Figure 28a corresponds to the computation of the diffusion coefficient  $D_{\text{m},0}(\Phi \rightarrow 0, T)$  defined by Equation 3.14, taking  $\eta_0(T)$  as given by [84] and  $d_{\text{H}} = 13.6$  nm. As shown by this graph, the strong temperature dependence of  $D_{\text{m}}(T)$  can be ascribed to the large decrease of the solvent viscosity  $\eta_0(T)$  as  $T$  increases. However, note that here, the NPs present strong interparticle repulsion (as shown by the Carnahan-Starling fit in Figure 5a) and the interparticle correlations cannot be forgotten in the expression of  $D_{\text{m}}$  to take in account the NP’s volume fraction influence. Hence,  $D_{\text{m}}(\Phi_{\text{eff}}, T)$  is presented as obtained from the general expression Equation 3.16 for  $\Phi = 1.0\%$  (long dashed pink line) and for  $\Phi = 5.95\%$  (dashed green line), using SAXS and SANS experimental  $\chi$  values with  $\Phi_{\text{eff}} = 1.82 \Phi$  as an effective volume fraction.

<sup>8</sup> For any NPs dispersions in the different Ionic Liquids (see ref. [20]) probed in PHENIX lab. the Soret coefficient  $S_{\text{T}}$  has always been found positive.

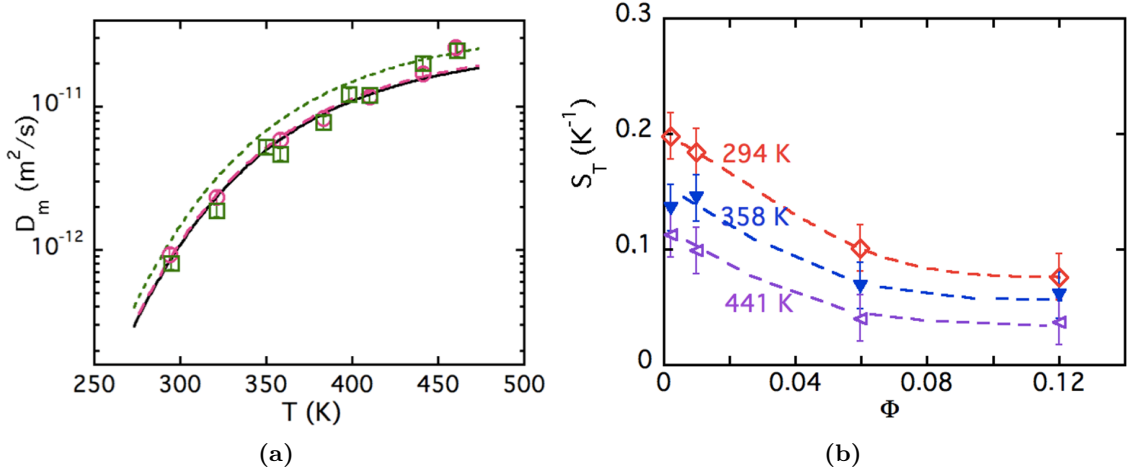


**Figure 28** – Zero-field results: (a) Diffusion coefficient  $D_m$  at various  $\Phi$  as a function of  $T$ . The symbols are experimental determinations at  $\Phi = 5.95\%$  (open squares) and  $\Phi = 1.0\%$  (open circles). The full line corresponds to the ideal case  $D_m(\Phi \rightarrow 0, T)$  given by Equation 3.14. The green dashed line corresponds to the general case of Equation 3.16 for  $\Phi = 5.95\%$  and the pink long dashed for  $\Phi = 1.0\%$ , taking into account the interparticle correlations with  $\chi = 0.86$  at  $\Phi = 5.95\%$  and  $0.43$  at  $\Phi = 1.0\%$  with the hard sphere volume fraction  $\Phi_{\text{eff}} = 1.82 \Phi$ . (b) Soret coefficient  $S_T$  at various  $T$  as a function of  $\Phi$ . Dashed lines are guide for the eye.

The general expression matches correctly the experimental results at  $\Phi = 1.0\%$ , which are close to the ideal case  $D_m(\Phi \rightarrow 0, T)$  due to a compensation between  $\chi(\Phi = 1.0\%)$  and  $\zeta(\Phi = 1.0\%, T)/\zeta_0(T)$  – except at  $T \geq 450$  K, and so, it should be necessary to check that the viscosity values deduced from the calculations of Paduszynski and Domanska[84] are completely reliable in this range of  $T$ . On the other hand, a systematic discrepancy (by a factor ranging from 1.4 at room temperature down to 1.2 at 450 K) is found at  $\Phi = 5.95\%$ , meaning that the friction  $\zeta$  is 40% to 20% larger than what is given by the development of Equation 3.15 at this volume fraction in this temperature range.

In regard to the Soret coefficient, one can first note that whatever  $\Phi$  and  $T$ , the measured  $S_T$  is here always positive, contrary to what is sometimes observed for ferrofluids in water [25, 140] and similarly to what was observed in the FF-RTIL in pure EAN. But this similarity is not a given, it is important to recall that EAN is hydrophilic and totally miscible with water, although EMIM-TFSI is hydrophobic. Therefore, note that the NP/liquid interface is not constituted of the same species and H-bonds can occur with EAN while only weaker ones can exist with EMIM-TFSI.

Moreover,  $S_T$  is a decreasing function of  $\Phi$ . This behavior is expected as it has been experimentally shown in [98] and can be theoretically predicted by Equation 3.6 that

$$|S_T| \propto \chi, \quad (3.37)$$

which is here a decreasing function of  $\Phi$  – see Figure 5a.  $S_T$  is also a decreasing function of  $T$ , as also observed in EAN. For a deeper analysis of the behavior of  $S_T(\Phi, T)$  (as in [18] for example), a larger number of samples at various  $\Phi$  should be investigated. It will

be left as a future work perspective as we focus hereafter on the under-field behavior of the sample at  $\Phi = 5.95\%$  in the whole accessible  $T$ -range of the experiment.

### 3.4.2 Under-Field Results

At this  $\sim 6\%$  volume fraction, it was possible to observe an anisotropy of both the diffusion coefficient  $D_m$  (see [Figure 29](#)) and of the Soret coefficient  $S_T$  (see [Figure 30](#)) whatever  $T$  ranging between 295 K and 460 K, if an external magnetic field  $\vec{H}$  is applied to the sample during the FRS measurement ( $0 \leq H \leq 100 \text{ kA m}^{-1}$ ). As expected,  $D_m$  and  $S_T$  both depend on the amplitude of the applied field and on its direction, akin to previous results for  $D_m$  and/or  $S_T$  in non-ionic magnetic fluids [[157–159](#)] and in aqueous ferrofluids [[25, 128–130](#)] at room temperature. We limited ourselves here to gradients of temperature ( $\vec{\nabla}T$ ) and of concentration ( $\vec{\nabla}\Phi$ ) either horizontal (and thus parallel ( $\parallel$ ) to the applied field – direction denoted  $\vec{H}_{\parallel}$ ) or vertical (and thus perpendicular ( $\perp$ ) to the field – direction denoted  $\vec{H}_{\perp}$ ).

As previously shown in [Figure 28a](#), the zero field value of  $D_m$  increases with  $T$ . Under-field  $D_m$  is anisotropic with  $D_m(H_{\perp}) < D_m(H=0) < D_m(H_{\parallel})$  and this anisotropy decreases with  $T$ . In an opposite manner (as also previously shown in [Figure 28b](#)), the zero field value of  $S_T$  decreases with  $T$  with the under-field induced anisotropy, with  $S_T(H_{\parallel}) < S_T(H=0) < S_T(H_{\perp})$ . Let us note that, in the experimental range, whatever the amplitude of  $\vec{H}$  and whatever its direction with respect to  $\vec{\nabla}\Phi$  and  $\vec{\nabla}T$ ,  $S_T(H)$  remains always positive, as  $S_T(H=0)$ .

The adjustments of  $D_m^{\vec{H}_{\perp}}$  and  $D_m^{\vec{H}_{\parallel}}$  at room temperature are both presented in [Figure 29](#). They are made, assuming as in refs. [[128, 129, 131](#)] that  $\chi$  and  $\zeta$  keep under-field their zero field value. The fit is performed using [Equation 3.20, 3.21, 3.22 and 3.23](#) with  $\chi = 0.43$ ,  $m_S = 3.2 \times 10^5 \text{ A m}^{-1}$  and letting  $d_{\text{NP}}$  and  $D_m^*$  as a free parameters.  $D_m^*$  is found within the experimental error bar of  $D_m(H=0)$  and we obtain  $d_{\text{NP}} = 13.2 \text{ nm}$ , leading to  $\gamma = 2.3$  at room temperature.

In the monodisperse model used here for the adjustment, the polydispersity in NP's diameter is not taken in account and the value of  $d_{\text{NP}}$  obtained is 30% larger than the volume average diameter obtained from magnetization measurements. It is anyway reasonable as it corresponds to a reduced dipolar parameter  $\Psi_{\text{dd}} = \gamma/\Phi = 39$ , quite comparable to those previously obtained experimentally for aqueous samples based on maghemite NPs similar in diameter [[132, 133](#)].

Still at room temperature, we use in [Figure 30a](#) the same mentioned values to fit the Soret coefficient, however, in this case  $S_T^*$  is kept as the free parameter that is adjusted within the experimental error bar of  $S_T(H=0)$ .

At higher temperatures than 295 K, the osmotic compressibility  $\chi$ , as determined

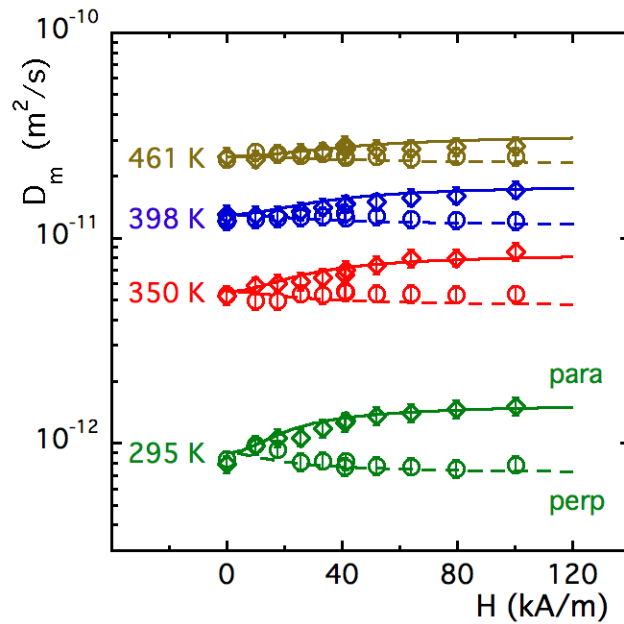


**Figure 29** – Under-field diffusion coefficient  $D_m$  as a function of the applied field for different temperatures  $T$  (from bottom to top: 295, 350, 398 and 461 K); The label perp (resp. para) and open discs (resp. open diamonds) mean measurements in  $H_{\perp}$  direction (resp.  $H_{\parallel}$ ); Symbols correspond to FRS measurements, dashed lines (resp. full lines) correspond to adjustment of the data in  $H_{\perp}$  direction (resp. in  $H_{\parallel}$  direction with Equation 3.21). See the text for the detailed values of the parameters used.

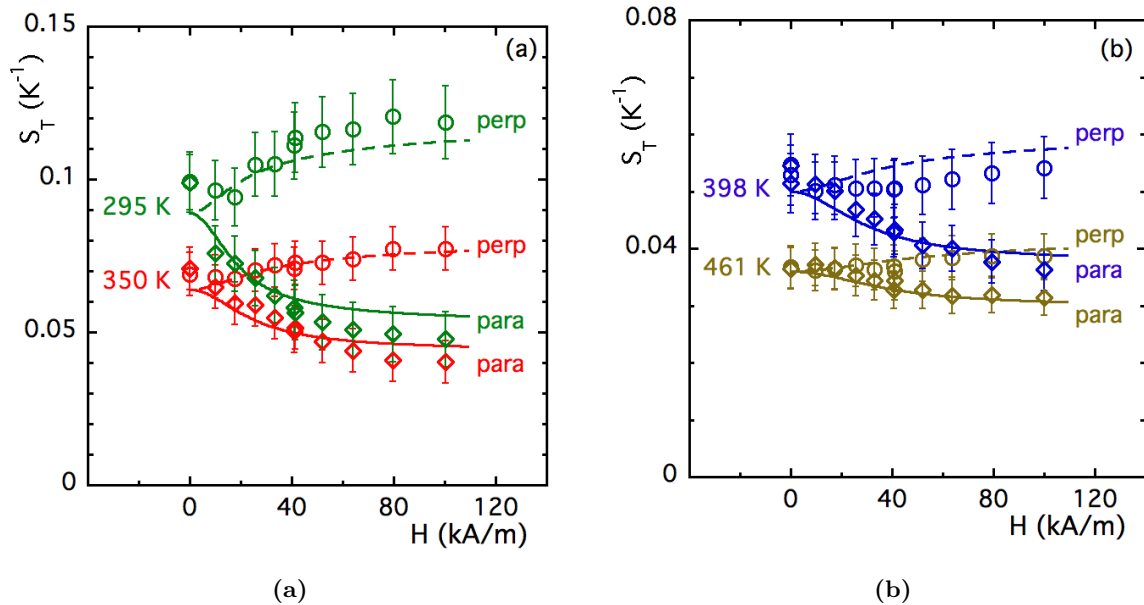


**Figure 30** – Under-field Soret coefficient  $S_T$  as a function of the applied field for different temperatures  $T$  (Figure 30a at 295 and 350 K, Figure 30b at 398 and 461 K); The label perp (resp. para) and open discs (resp. open diamonds) means measurements in  $H_{\perp}$  direction (resp.  $H_{\parallel}$ ); Symbols correspond to FRS measurements, dashed lines (resp. full lines) correspond to adjustment of the data in  $H_{\perp}$  direction (resp. in  $H_{\parallel}$  direction with Equation 3.25). See the text for the detailed values of the parameters used in the adjustments.

by SANS measurements at  $H=0$ , is observed to be independent of  $T$ . The temperature dependence of  $\zeta(T)$  enters inside the fitting parameter  $D_m^*(T)$ , still kept within the experimental error bar of  $D_m(H=0)$  at the given  $T$ . However, two other parameters have to be modified in the model because of their  $T$ -dependence and that of the NP's magnetization  $m_S(T)$ . Namely these two parameters are the Langevin parameter

$$x \propto \frac{\mu_{NP}}{T} \propto \frac{m_S(T)}{T} \quad (3.38)$$

and the dipolar parameter

$$\gamma \propto \frac{m_S \mu_{NP}}{T} \propto \frac{m_S^2(T)}{T}. \quad (3.39)$$

In a first approximation, it is here proposed to approximate the temperature dependence of  $m_S$  with the following Bloch law of bulk maghemite [160–163] as finite-size effects and interface effects on the magnetization are small at the present NP diameters [164–167]:

$$m_S(T) = 390 \left(1 - 3.3 \times 10^{-5} T^{\frac{3}{2}}\right), \quad (3.40)$$

where  $m_S$  is expressed in  $\text{kA m}^{-1}$  and  $T$  in K. Note that this equation is only valid up to 723 K, temperature above which maghemite transforms in hematite [160, 161].

As a result, for the presented adjustments in Figure 29 of the in-field anisotropy at different temperatures,  $\chi$  is kept independent of  $\vec{H}$  and  $T$  as said above, while  $D_m^*$  is the only  $T$ -dependent fitting parameter. At each  $T$ , the shape of the anisotropy of  $D_m$  is well adjusted with the model with a dipolar interaction parameter  $\gamma(T)$  derived from Equation 3.18 and 3.40 given in Table 3. The model quite nicely reproduces the anisotropy of  $D_m$  in the experimental range of  $T$  and  $\vec{H}$ .

Once again, the analogous approach is applied to the Soret coefficient in which the same values of all mentioned parameters are used to incorporate the  $T$ -dependency. The fits for  $S_T$  are presented in Figure 30a and b, where in this condition  $S_T^*(T)$  is the only  $T$ -dependent fitting parameter. A quite reasonable agreement with the experimental variation of the in-field anisotropy of  $S_T(\vec{H})$  is obtained in the whole range of  $T$  and  $\vec{H}$ .

**Table 3** – Evolution of some fit parameters as a function of  $T$  (see text).

$T$ (K)	$\gamma$	$D_m(H=0)$ ( $\text{m}^2/\text{s}$ )	$D_m^*$ ( $\text{m}^2/\text{s}$ )	$\frac{D_m^* - D_m(H=0)}{D_m^*}$	$S_T(H=0)$ ( $\text{K}^{-1}$ )	$S_T^*$ ( $\text{K}^{-1}$ )	$\frac{S_T^* - S_T(H=0)}{S_T^*}$
295	2.3	$8.06 \cdot 10^{-13}$	$9.0 \cdot 10^{-13}$	+ 10 %	0.099	0.089	– 11 %
350	1.7	$5.24 \cdot 10^{-12}$	$5.5 \cdot 10^{-12}$	+ 6 %	0.070	0.064	– 9 %
398	1.3	$1.21 \cdot 10^{-11}$	$1.3 \cdot 10^{-11}$	+ 8 %	0.054	0.050	– 8 %
461	0.92	$2.45 \cdot 10^{-11}$	$2.5 \cdot 10^{-11}$	+ 4 %	0.037	0.036	– 3 %

$D_m^*$  and  $S_T^*$  which have been left free because of the substantial experimental error bars on the direct experimental determinations of  $D_m$  and  $S_T$  in zero field at  $T$ , present however a systematic small shift with respect to these values (see Table 3). This shift,

which always remains within the experimental error bar, is positive for  $D_m^*$  and negative for  $S_T^*$ .

Let us go deeper into the analysis of each of the terms entering in the adjustments, to try to separate their respective influences. In the under-field analysis the two main contributions to  $D_m(\vec{H})$  and  $S_T(\vec{H})$  come from the two parameters  $\alpha_\lambda$  and  $\beta_\lambda$ , which are null in zero magnetic field. The term  $\alpha_\lambda$  is related to the under-field dipolar interaction, modeled in the framework of a mean field approximation. It decreases as  $T$  increases. In this framework, it is isotropic and thus exists in both directions  $\vec{H}_\perp$  and  $\vec{H}_\parallel$ . In the model, the under-field anisotropic contribution to  $D_m(H)$  comes from the under-field inhomogeneities of concentration, modeled by  $\beta_\lambda$ . This anisotropic term, which is also proportional to the magnetic dipolar parameter  $\gamma(T)$ , becomes weaker as  $T$  increases. Let us first briefly have a deeper look on these two terms  $\alpha_\lambda$  and  $\beta_\lambda$  and on their influence on the under-field variations of  $D_m(\vec{H})$  and  $S_T(\vec{H})$ . We then will focus on the influence of the two terms  $S_1$  and  $S_2$ .

It is possible to compare the theoretical expressions of  $\alpha_\lambda$  and  $\beta_\lambda$  given by [Equation 3.22](#) and [3.23](#) to direct experimental determinations, namely<sup>9</sup>:

$$-\alpha_\lambda = \frac{1}{\chi} \frac{D_m^{\vec{H}_\perp} - D_m^*}{D_m^*} \quad (3.41)$$

and

$$\beta_\lambda = \frac{1}{\chi} \frac{D_m^{\vec{H}_\parallel} - D_m^{\vec{H}_\perp}}{D_m^*}. \quad (3.42)$$

as the anisotropy of  $D_m$  is solely influenced by  $\beta_\lambda$ .

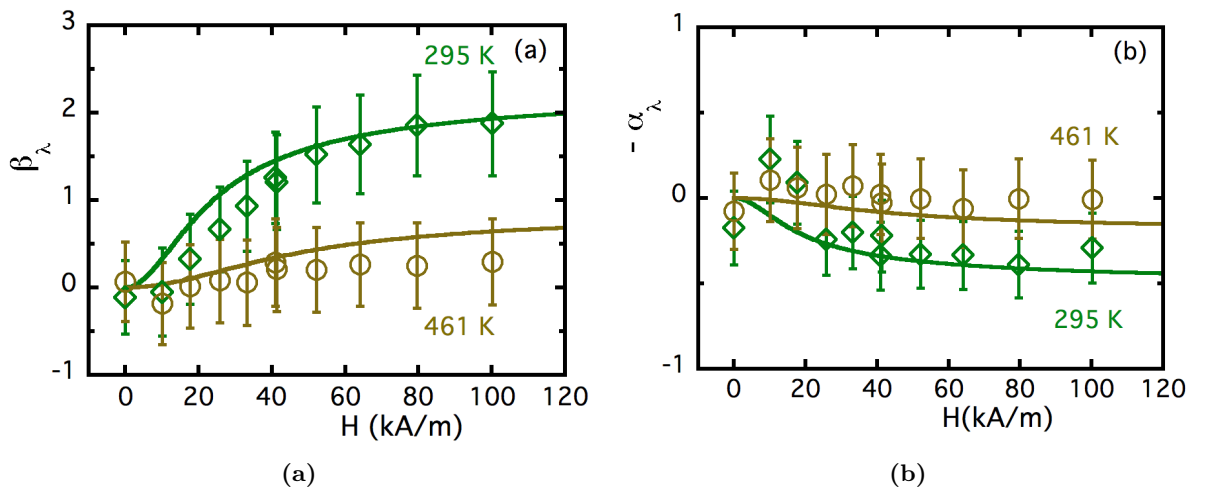


**Figure 31** – Field-dependence of parameters  $\beta_\lambda$  (a) and  $-\alpha_\lambda$  (b) at  $T = 295$  K and  $461$  K. Experimental values (see text for details) are obtained from [Equation 3.41](#) and [3.42](#) (open diamonds at  $T=295$  K; open discs at  $T=461$  K). Theoretical adjustments (full lines) are deduced from [Equation 3.22](#) and [3.23](#), using the same parameters values as in [Figure 29](#).

<sup>9</sup> We use here the adjusted value of  $D_m^*$  and not the corresponding experimental value  $D_m(H=0)$  to reduce the error bar in [Figure 31](#)

Figure 31 presents at  $T= 295$  K and 461 K the experimental values of  $-\alpha_\lambda$  and  $\beta_\lambda$  deduced from Equation 3.41 and 3.42 using  $\chi = 0.43$  and  $D_m^*$  values obtained in Figure 29 adjustments (see Table 3). Figure 31 also compares these experimental determinations to the theoretical expressions of  $-\alpha_\lambda$  and  $\beta_\lambda$  deduced from Equation 3.22 and 3.23, using the same parameters values as in Figure 29. There is a very good agreement between the theoretical and the experimental expressions of  $-\alpha_\lambda$  and  $\beta_\lambda$  as a function of  $H$  and  $T$ , within the error bar of the experiment.

For its part, the anisotropy of  $S_T$  is also mainly related to the terms  $\alpha_\lambda$  and  $\beta_\lambda$ , which bring large contributions, even larger than  $S_1$  and  $S_1 - S_2$ . In order to probe more precisely the influence of the terms  $S_1$  and  $S_1 - S_2$ , we can remark that when looking at the product  $S_T D_m$  both  $\alpha_\lambda$  and  $\beta_\lambda$  contributions vanish. We obtain<sup>10</sup>:

$$\frac{S_T^{\vec{H}_\perp} D_m^{\vec{H}_\perp}}{D_m^*} = S_T^* + \chi \frac{S_1}{T} \quad (3.43)$$

and

$$\frac{S_T^{\vec{H}_\parallel} D_m^{\vec{H}_\parallel}}{D_m^*} = S_T^* + \chi \frac{S_1 - S_2}{T}. \quad (3.44)$$

Figure 32 presents, at the various  $T$ 's, the experimental values of  $S_T^{\vec{H}_\perp} D_m^{\vec{H}_\perp} / D_m^*$  (open discs) and  $S_T^{\vec{H}_\parallel} D_m^{\vec{H}_\parallel} / D_m^*$  (open diamonds), using  $D_m^*$  values obtained in Figure 29 adjustments (see Table 3). Figure 32 also presents the expressions  $S_T^* + \chi S_1 / T$  (full lines) and  $S_T^* + \chi(S_1 - S_2) / T$  (dotted lines), using  $S_T^*$  values obtained in Figure 30 adjustments (see Table 3),  $\chi = 0.43$  and theoretical expressions of  $S_1$  and  $S_2$ , given by Equation 3.26 and 3.27. The first conclusions from this representation are that:

$$\chi \frac{S_1(H, T)}{T} \ll S_T^*(T) \quad \text{and} \quad \chi \frac{[S_1(H, T) - S_2(H, T)]}{T} \ll S_T^*(T), \quad (3.45)$$

which means that almost no under-field anisotropy is predicted in Equation 3.43 and 3.44 from a theoretical point of view, as well as a very weak field dependence of  $S_T D_m / D_m^*$ , weaker than the experimental error bar.

From an experimental point of view, similar conclusions are obtained. If a subsidiary field anisotropy of  $S_T D_m / D_m^*$  is observed (mainly at 295 K and 350 K), it however always remains smaller than the error bar. So within the error bar, which is here much larger than  $\chi S_1 / T$  and  $\chi(S_1 - S_2) / T$  variations, experimental values of  $S_T D_m / D_m^*$  can thus be adjusted by Equation 3.43 and 3.44. Then, the main contribution to the under-field anisotropy of  $S_T$  is coming, as for  $D_m$ , from the term  $\beta_\lambda$ , which is associated to the under-field inhomogeneities of concentration.

Note that the small shift at  $H=0$  between experimental and adjusted values of  $D_m$  and  $S_T$ , almost completely compensate in  $D_m S_T$  representation of Figure 32. It is

<sup>10</sup> We use here the adjusted value of  $S_T^*$  and not the corresponding experimental value  $S_T(H=0)$  to reduce the error bar in Figure 32

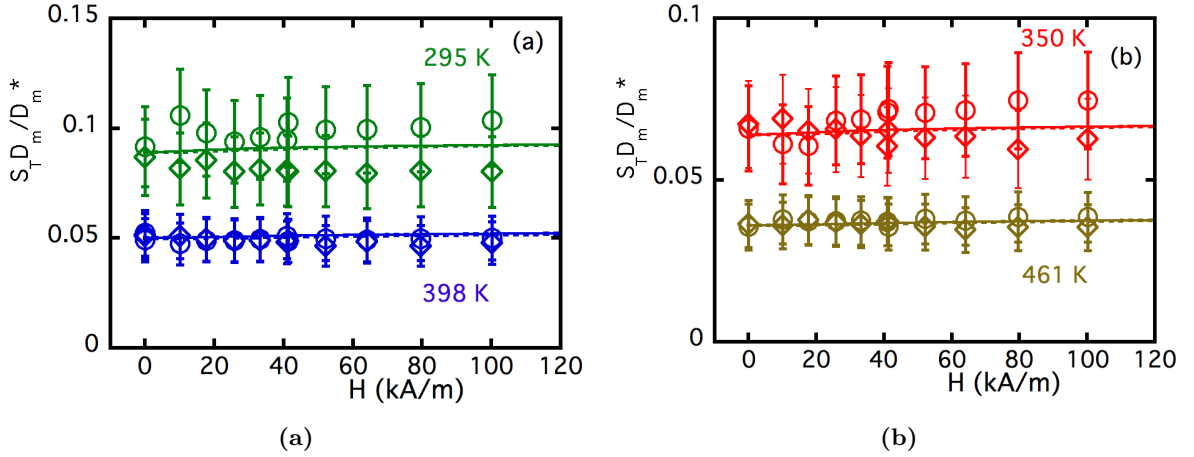


**Figure 32** – Under-field anisotropy of  $S_T D_m / D_m^*$  at various  $T$ 's; Experimental determinations (open discs symbols correspond to measurements in  $H_\perp$  direction and open diamonds to measurements in  $H_\parallel$  direction) are compared with theoretical expressions of Eqs. 3.43 (full line) and 3.44 (dotted line) - for details see text.

also true for  $\beta_\lambda$  in Figure 31a. On the contrary the term  $\alpha_\lambda$  in Figure 31b, present small distortions at very low fields. This isotropic term  $\alpha_\lambda$ , associated to the modeling of the average magnetic dipolar interaction, is in fact responsible for the small, but systematic, positive shift obtained between  $D_m^*$  and the direct experimental value of  $D_m$  in zero field at the same temperature. It is as well responsible for the negative shift obtained between  $S_T^*$  and the direct experimental value of  $S_T$  in zero field at the same temperature.

We propose the following explanation: In Equation 3.20 contributions of magnetic dipolar interparticle interactions appear in two places (i) inside the compressibility  $\chi$  measured in zero field by SAXS and SANS, through a contribution  $\chi_{\text{dip}}$  (here supposed additive) and also (ii) in mean-field expression  $\alpha_\lambda$ , which equals zero without the presence of the field. The approximation of Equation 3.20 is in fact very rough in very low fields as the zero-field contribution  $\chi_{\text{dip}}$  should vanish in the presence of field. Equation 3.20 is thus strictly valid only in the limit of  $\chi_{\text{dip}} \ll \chi$  (condition which is here verified see ahead).

At the first order, in zero field,  $D_m^*$  can be seen as the extrapolation of  $D_m(\vec{H})$  at  $H = 0$  in the absence of magnetic dipolar interparticle interaction,  $D_m^* \sim kT / [\zeta(\chi - \chi_{\text{dip}})]$  while experimentally we measure  $D_m(H = 0) = kT / \chi$ . The conclusion is equivalent for  $S_T^*$ ; following Equation 3.37  $S_T^* \propto (\chi - \chi_{\text{dip}})$  and  $S_T(H = 0) \propto \chi$ .

We can then roughly evaluate here at  $T = 295$  K the contribution  $\chi_{\text{dip}}$  in zero field of the magnetic dipolar interparticle interaction to the total compressibility  $\chi$  of the NPs' system to  $\sim 10\%$  of  $\chi$  as

$$\frac{(D_m^* - D_m(H = 0))}{D_m^*} \sim \frac{(S_T(H = 0) - S_T^*)}{S_T^*} \sim 10\%, \quad (3.46)$$

corresponding to  $\chi_{\text{dip}} \sim +0.04$ , which is of the order of magnitude of the error bar on  $\chi$  measurements at 295 K. This contribution would be smaller than the error bar at higher  $T$ .

In conclusion, we confirmed that a ferrofluid based in EMIM-TFSI shows the under-field anisotropy of both  $S_T$  and  $D_m$  coefficients, demonstrating that the thermophoretic behavior in the presence of an applied magnetic field observed for aqueous FFs can be also applied for FF-RTILs. The importance of this outcome is that such feature has been shown to be promising for thermoelectric applications [168]. As theoretically predicted,  $S_T$  is larger when  $\vec{\nabla}T$  and  $\vec{\nabla}\Phi$  are perpendicular to  $\vec{H}$ , while  $D_m$  reduces in this configuration. The main cause of the thermodiffusion anisotropy can be attributed to the under-field spatial inhomogeneities of NP's concentration, associated here to  $\beta_\lambda$  coefficient in the model. When  $T$  increases, the NP's magnetization  $m_S$ , the magnetic dipolar interaction parameter  $\gamma$  and  $\beta_\lambda$  coefficient decrease, the under-field anisotropy of both  $S_T$  and  $D_m$  coefficients drastically reduces, as it is, in fact, observed in the experiment. The under-field anisotropy of  $S_T$  and  $D_m$  is well described, at the first order, by the model from [25, 127] here applied for the first time for a FF-RTIL in a vast range of  $T$  and  $\vec{H}$ . The effectiveness of the model is demonstrated by correctly adjusting the experimental data using fitting parameters inside the error bar for both  $S_T$  and  $D_m$  as a function of the multiple values of  $\vec{H}$  and  $T$ .

### 3.5 Conclusions on the Thermodiffusion Measurements

Thermodiffusion measurements have been performed in a wide range of temperatures  $T$  and NP's concentrations  $\Phi$  on the various colloidal systems previously studied in chapter 2. The technique used here is Rayleigh Forced Scattering. It leads to the determination of the diffusion coefficient  $D_m$  and of the Soret coefficient  $S_T$ . The anisotropy of these two coefficients have also been probed under-field up to  $H = 100$  kA/m with the EMIM-TFSI system up to 460 K.

In all the dilute probed systems, the diffusion coefficient  $D_m$  shows that the NPs experience locally the macroscopic viscosity of the fluid carrier, whatever  $T$ . This viscosity is always large in RTILs. It demonstrates that in all the present synthesized dispersions in RTILs, there could not exist a layer of fluid-water, locally surrounding the NP's, inside which the diffusion would occur. This is also shown in water-EAN mixtures, whatever the EAN content at room temperature (to our knowledge it exists no measurements of viscosity at higher temperatures in these mixtures to compare to our measurements).

While increasing the concentration, interparticle interaction becomes increasingly important. It influences  $D_m$  from a thermodynamic point of view (compressibility  $\chi$ , which is known from SAXS, SANS measurements) and from an hydrodynamic point of view (friction  $\zeta$  which is here determined). It is shown that the friction is initially correctly described by Batchelor formalism for effective hard spheres, however it becomes stronger at  $\Phi$  typically larger than 4.0% in EAN dispersions. A similar effect (data not shown) is

observed for EMIM-TFSI.

With respect to the Soret coefficient  $S_T$ , the main conclusions are :

- A positive  $S_T$  and a decrease of  $S_T$  while  $T$  increases are both obtained in all the probed RTILs (even those not presented here), while in water both signs of  $S_T$  can be obtained with either an increase or a decrease with  $T$ , depending on the hydrophilicity of the counterions (see [Figure 27](#));
- A systematic correlation between the sign of the  $\Phi$ -dependence of  $S_T$  and that of  $\chi$  is observed in RTIL (in particular in EAN with different initial counterions) while in water this correlation exists for  $|S_T|$ ;
- In water-EAN mixtures, with  $\text{Na}^+$  counterions, the system behaves as an aqueous electrolyte at low  $w_{\text{EAN}}$  ( $< 1$  weight %) with NPs bearing an effective negative charge (as attested by direct measurements) in repulsive interaction. At large  $w_{\text{EAN}}$  ( $> 90$  weight %), this effective charge is positive (as deduced from FRS and thermoelectric measurements in ref [18]) also in repulsive interaction. In between we can deduce from [Figure 26](#), that this charge seems to pass through zero for  $0.01 < w_{\text{EAN}} < 0.1$  (an area which is not explored in full details in [subsection 2.3.4](#)) and then becomes positive, but not large enough to produce an interparticle repulsion up to  $w_{\text{EAN}}$  of the order of 0.5-0.7 (following [Figure 12](#)), above which the interaction is repulsive.
- Under-field the developed model well describes the experimental anisotropy of both  $D_m$  and  $S_T$  in the whole range of  $T$ , the main influence coming for both  $D_m$  and  $S_T$  from the term  $\beta_\lambda$  associated to the under-field spatial inhomogeneities of NP's concentration.

# Conclusions on ferrofluids based in Ionic Liquids

In this part we have investigated two well characterized ferrofluids based in room temperature ionic liquids, namely EAN [18] and EMIM-TFSI [19]. The synthesis of maghemite magnetic nanoparticles (MNPs), their morphology, size distribution and structure have already been evaluated in previous works, therefore, we could here focus on the colloidal features of the dispersions and their thermodiffusive properties.

The protocol of transfer of the MNPs from the initial aqueous dispersions to the various RTILs allows us to control important parameters such as the surface coating and the presence of initial counterions close to the NP's interface. Along those lines, the MNPs dispersed in EAN were surface coated with citrate ions and different initial counterions, while the particles in EMIM-TFSI had a SMIM<sup>±</sup>-TFSI<sup>-</sup> surface functionalization. In EAN, the different initial counterions which were probed, are Na<sup>+</sup> and Li<sup>+</sup> already used in previous works, and Rb<sup>+</sup>, never investigated before. Compressibility measurements by SAXS and SANS allow to determine in each of these cases the second coefficient  $A_2$  of the virial development of the osmotic pressure. And by combining various chemical titrations, in particular by mass spectroscopy, to geometrical ionic considerations, it has been possible to propose an arrangement of ions surrounding the MNPs case by case.

These results show that the global interparticle interactions are repulsive for the SMIM<sup>±</sup>-TFSI<sup>-</sup> coated MNPs dispersed in EMIM-TFSI (typically up to 11 vol% of NPs) and for EAN with Na<sup>+</sup> and Rb<sup>+</sup> counterions (up to 25 vol% of NPs). On the other hand, ferrofluids in EAN with Li<sup>+</sup> counterions present a weak attractive interaction preventing the achievement of stable dispersions in high particle concentrations. The experimental data associated with the current understanding of ILs structuration suggests that the repulsive interactions arise from an ionic layering of the counterions and co-ions induced by the NPs surface. Lithium being a structure breaker of EAN and being in large number in the vicinity of the particle disturbs the organization of the first layer, thus resulting in less stable dispersions.

Going one step further, we introduce an additional parameter to the EAN dispersion: water content. Macroscopic and microscopic observations show that dispersions of citrate

coated MNPs with  $\text{Na}^+$  counterions remain stable at least up to  $\Phi = 3.0\%$  with NPs of mean diameter of the order of 7.4 nm, in the whole range of EAN and water proportions, and even in the presence of an external magnetic field. Note that this colloidal stability on the whole range of mass fraction  $w_{\text{EAN}}$  would not be observed with NPs of the same size as the one used in EMIM-TFSI - mean diameter 9.6 nm. Nonetheless, with the present NPs, the transition between an aqueous medium to a pure ionic liquid was shown to include a range of proportions in which the interparticle interactions change from repulsive to attractive, and vice versa. This result was inferred from SAXS measurements in which  $A_2$  is negative in the intermediary range of mass fractions  $w_{\text{EAN}}$  and  $A_2$  is positive in the extremes.

Thanks to this comprehensive groundwork, we could then deeply analyse the thermodiffusion of these samples by a forced Rayleigh scattering experiment (FRS).

First we have analysed the influence of the nature of the counterions in ferrofluids based on EAN as a function of the NP volume fraction  $\Phi$  and temperature  $T$ . As expected from theoretical developments on thermodiffusion, and as it is observed in any ferrofluid based on RTILs up to now, the Soret coefficient  $S_T$  is always positive and reduces with the increase in temperature  $T$ , independently of the interparticle interaction. In EAN it is observed that  $S_T$  is also positive but presents various behaviors depending on the interparticle interaction: in the repulsive systems – where  $A_2 > 0$ , the compressibility  $\chi < 1$  decreasing with the increment of  $\Phi$  –  $S_T$  decreases with the increase of  $\Phi$ ; In a system with globally attractive interparticle interaction –  $A_2 < 0$ ,  $\chi > 1$  increasing as the sample concentrates – the Soret coefficient  $S_T$  actually increases with  $\Phi$ , at least in the available concentration range. This experimental result illustrates the fact that  $S_T$  is directly proportional to  $\chi$ .

The diffusion coefficient  $D_m$  is also affected by the different regimes of interaction and by temperature. The  $T$ -dependence of  $D_m$  is strongly related with the viscosity of liquid medium  $\eta_0(T)$ , while the  $\Phi$ -dependence is largely encapsulated in  $\chi(\Phi)$ . At low NPs concentration, it is shown that the effective viscosity experienced by the NPs is the macroscopic viscosity of the fluid carrier. While  $D_m$  remains mostly unchanged for the repulsive  $\text{Na}^+$  and  $\text{Rb}^+$  systems (up to  $\Phi \sim 15\%$ ),  $D_m$  significantly reduces for  $\text{Li}^+$  as the volume fraction  $\Phi$  slightly increases. For  $\text{Li}^+$  this can be associated with the augmentation of  $\chi$ -values as  $D_m \propto 1/\chi$ . Yet,  $D_m$  depends on the friction  $\zeta(T, \Phi)$  which can then be deduced from  $D_m$  and  $\chi$  measurements. The friction obtained in diluted FFs ( $\Phi < 4.0\%$ ) is compatible with the linear Batchelor development, however, at higher concentrations the friction is shown to largely increase. Although we have no theoretical description for this deviation, it is certainly related to the ionic local organization in EAN and the mentioned layering around the MNPs.

The EAN-FF with  $\text{Na}^+$  counterions can be considered to be a versatile model

system, thereupon being suitable to evaluate the effects of the water content. This way,  $D_m$  and  $S_T$  were both experimentally determined by FRS as a function of the weight proportion of  $w_{\text{EAN}}$  of EAN in water,  $\Phi$  and  $T$ . At  $\Phi = 1.0\%$ ,  $D_m$  increases as a function of temperature and decreases with respect to  $w_{\text{EAN}}$ . This behavior can mostly – but not exclusively as the NP’s compressibility clearly depends on  $w_{\text{EAN}}$  – be attributed to an increase of the macroscopic viscosity  $\eta_0$  of the carrier fluid as the amount of EAN is increased and, contrarily, a reduction in  $\eta_0$  takes place when  $T$  is increased. Moreover, since an effective viscosity  $\eta_{\text{eff}}$  can be calculated from the measured  $D_m$  at low  $\Phi$ , we could compare the values determined via FRS with the data currently reported in the literature [153]. The obtained results are in good agreement for  $w_{\text{EAN}} = 1$  and 0 in the whole range of accessible  $T$ ’s and at any  $w_{\text{EAN}}$  at room temperature. At higher temperatures for these intermediary  $w_{\text{EAN}}$  values,  $\eta_{\text{eff}}$  follows the tendency mentioned previously ( $\eta_{\text{eff}}$  reduces with  $T$  and increases with  $w_{\text{EAN}}$ ) but no values yet exist in literature to compare with these results.

In these water-EAN mixtures, at low  $w_{\text{EAN}}$  and for both  $\Phi = 1.0\%$  and  $\Phi = 3.0\%$ ,  $S_T$  is observed to increase with temperature from a negative value towards a positive one, as it is observed in water based ferrofluids with citrate-coated NPs and  $\text{Na}^+$  counterions. On the contrary, at large  $w_{\text{EAN}}$ ,  $S_T$  is measured positive and a decreasing function of  $T$ , as previously observed in pure EAN. At  $\Phi = 3.0\%$  the two opposite behaviors clearly met at an inversion point located around  $w_{\text{EAN}} \sim 0.6$ , while this observation is less precise at  $\Phi = 1.0\%$ . Another inversion can also be evidenced by FRS in terms of the  $\Phi$ -dependence of  $S_T$ . At large  $w_{\text{EAN}}$ ,  $\Delta S_T/\Delta\Phi$  is negative (as characteristic of repulsive IL systems), while between  $w_{\text{EAN}} = 0.1$  and 0.5 it is found positive (a mark of attractive interactions in ILs systems). This sign inversion of  $\Delta S_T/\Delta\Phi$  can indeed be associated to the shift between repulsive and attractive interparticle interactions observed in SAXS measurements in water-EAN mixtures.

An analysis in terms of  $TS_T/\chi$  as a function of  $w_{\text{EAN}}$  shows a behavior close to that of a ferrofluid in a standard electrolyte with repulsive interparticle interactions is only observed for  $w_{\text{EAN}}$  below 0.01 – 0.1. This range of  $w_{\text{EAN}}$  would deserve in the future a more systematic analysis. Moreover in aqueous ferrofluids based on citrate-coated NPs (thus at  $w_{\text{EAN}} = 0$ ) at room temperature, the sign of the Soret coefficient  $S_T$  has been shown to invert depending on the hydrophilicity of the free counterions. In particular if only  $\text{EA}^+$  counterions were present and no  $\text{Na}^+$ ,  $S_T$  would be positive at  $w_{\text{EAN}} = 0$ . Still, in this case the surface charge in water is always negative independently of the type of counterions.

The sign inversion of  $S_T$  occurring with the increase of  $w_{\text{EAN}}$  may thus be related to the increasing number of  $\text{EA}^+$  ions in the vicinity of the NPs. But interestingly the data might also suggest that it could be further associated with an effective charge inversion from

negative at  $w_{\text{EAN}} = 0$  (as measured experimentally) to positive at  $w_{\text{EAN}} = 1$  (as deduced for  $\text{Na}^+$  counterions from a crossed analysis of FRS and thermoelectric measurements). A possible track could comply with the following line: the negative effective charge  $\xi_0^{\text{eff}}$  of the NPs at  $w_{\text{EAN}} = 0$  progressively decreases in absolute value with  $w_{\text{EAN}}$ , down to almost zero in the intermediate range  $0.01 \leq w_{\text{EAN}} \leq 0.2$ ; For  $0.2 \leq w_{\text{EAN}} \leq 0.5 - 0.7$ , it becomes slightly positive but not yet capable of producing a sufficiently strong interparticle repulsion; for  $0.7 \leq w_{\text{EAN}} \leq 1$ , the positive effective charge becomes large enough to produce a global interparticle repulsion, arising from an efficient ion layering.

Finally, the under-field anisotropy of the thermodiffusion was investigated in an IL based ferrofluid for the first time. The broad range of  $T$  in which the FF based in EMIM-TFSI is stable allowed us to probe the magnetic response from 295 K till 461 K at moderate concentration of  $\Phi = 5.95\%$ . In the absence of an external magnetic field,  $D_{\text{m}}$  and  $S_{\text{T}}$  behave as a typical FF-RTILs with repulsive interactions:  $D_{\text{m}}$  increases with the temperature as the macroscopic viscosity  $\eta_0$  of the fluid carrier decreases. As for EAN based FF with  $\text{Na}^+$  counterions, the friction is larger than theoretically predicted by the Batchelor development (by 20% to 40%), likely due to the ionic structural organization around the MNPs. Moreover, the experimental values of  $S_{\text{T}}$  decrease as  $\Phi$  and  $T$  increase, following the characteristic tendency ferrofluids based on RTIL with globally repulsive interparticle interactions.

An under-field anisotropy of both  $D_{\text{m}}$  and  $S_{\text{T}}$  is observed at all the probed temperatures. As expected, the under-field response depends on the direction (parallel  $\vec{H}_{\parallel}$  or perpendicular  $\vec{H}_{\perp}$  to  $\vec{\Delta}\Phi$ ) and the amplitude ( $0 \leq H \leq 100 \text{ kA m}^{-1}$ ) of the applied magnetic field  $\vec{H}$ . Under-field the diffusion coefficient  $D_{\text{m}}$  persists in increasing with  $T$  as in zero field, however, the magnetically induced anisotropy results in  $D_{\text{m}}(H_{\perp}) < D_{\text{m}}(H=0) < D_{\text{m}}(H_{\parallel})$ , where this effect progressively reduces as the temperatures increases. Contrarily,  $S_{\text{T}}$  reduces as a function of  $T$  and the anisotropy effect results in  $S_{\text{T}}(H_{\parallel}) < S_{\text{T}}(H = 0) < S_{\text{T}}(H_{\perp})$ , with here also a progressive reducing of the effect as  $T$  increases.

The experimental data are well adjusted as a function of  $H$  and  $T$  by the theoretical model described in refs. [25, 127] that has been already shown to properly describe the anisotropy effect in aqueous ferrofluids at room temperature. Here we observe that the modeling is also valid for non-DLVO systems and at high  $T$ 's. The fit used values of  $\chi$  determined by SANS,  $m_{\text{s}}(T)$  using Bloch law and letting  $d_{\text{NP}}$  and two zero-field coefficients,  $D_{\text{m}}^*(T)$  and  $S_{\text{T}}^*(T)$  as free parameters. It is here assumed that  $\chi$  and  $\zeta$  kept their zero field values as in refs. [128, 129, 131]. A deeper look was applied to the different terms of the model. The parameter  $\alpha_{\chi}$  is related to the under-field dipolar interaction and is modeled here in the framework of a mean field approximation; It is isotropic and thus exists in both directions  $\vec{H}_{\perp}$  and  $\vec{H}_{\parallel}$ . The coefficient  $\beta_{\chi}$  which models the under-field anisotropic contribution coming from the under-field inhomogeneities of concentration.

Both coefficients are proportional to the magnetic dipolar parameter  $\gamma(T)$ , therefore becoming weaker as  $T$  increases. The two next parameters  $S_1$  and  $S_2$  of the model have almost no under-field contribution to the anisotropy from a theoretical point of view, which was mostly confirmed in the experimental results. The main contribution to the anisotropy of  $D_m$  and  $S_T$  thus comes from the parameter  $\beta_\lambda$ .

The small systematic shift, within the experimental error bar, between the coefficients  $D_m^*(T)$  and  $S_T^*(T)$  and their experimental zero-field values  $D_m(T, H = 0)$  and  $S_T(T, H = 0)$  is attributed to the weakness of the mean-field approximation in very low fields in  $\alpha_\lambda$  (as attested by small experimental distortions of  $\alpha_\lambda$  with respect to the model below  $H = 10$  kA/m - they remain however within the experimental error bar). This leads to an evaluation of the (small) dipolar magnetic contribution  $\chi_{\text{dip}}$  to the experimental compressibility in zero-field conditions ( $\chi_{\text{dip}} \sim 0.1\chi$  at room temperature).

All these results show that this ferrofluid based on EMIM-TFSI is indeed a promising candidate for thermoelectric applications under magnetic field.

## Part II

# Carbon Nanodots

## Chapter 4

# Nitrogen-Rich Carbon Nanodots (N-CDs)

Bulk carbon materials are more often than not associated with their well-known allotropes: diamond and graphite. Thereupon, until recently, it was inconceivable that this sort of materials could be “soluble” in water or even exhibit high fluorescence. Nonetheless, when carbon structures are downsized to nanoscale particles, their properties dramatically differ from the macroscopic materials [169]. Carbon nanodots (CDs) are a subclass of carbonaceous nanomaterials considered to be zero-dimensional (0D) due to their considerably small nanoparticle size ( $< 10$  nm) [170] compared to the related carbon-based nanostructures such as the one-dimensional (1D) carbon nanotubes and the two-dimensional (2D) graphene sheets.

The chemical composition of CDs is not restricted to carbon atoms. The nanodots often bear hydrogen and high amounts of oxygen (20-50%) [171], largely located on the surface where it plays a crucial role in the dispersion mechanism in polar media. The introduction of doping agents is a commonly employed procedure to tweak the photophysics of the nanomaterial. In particular, the focus of this thesis was concentrated in the so called nitrogen-rich carbon nanodots (N-CDs) in which nitrogen-doping has been shown to strongly enhance the quantum yield [34]. The here investigated N-CDs not only show increased brightness, but also present the possibility of tailoring the emission color by varying the nitrogen content of the synthesis protocol [38].

In previous studies [38, 170–172], the structural and photoluminescent properties of N-CDs were extensively investigated, however, very limited information is reported on the extent of the colloidal stability of these nanoparticles in aqueous dispersions. The evaluation of the stability of the system presents major importance in order to appraise effects as local variations in nanoparticle concentration, changes in interparticle interactions, aggregation and sedimentation processes. Understanding these phenomena should provide needful assistance, not only in the dispersibility, but also in the interpretation of the photoluminescence emission. As an example of the significance of this research, the origin of the CDs emission tunability has been a theme of intense debate in the literature

[37], where aggregation effects are given a significant role on the data interpretation [173]. In addition, the aggregation/dissaggregation effect is a well-established mechanism to turn the emission on and off by the so called aggregation-caused signal change [174]. Typically, the disaggregation that turns on the emission, nonetheless – in specific conditions that depend on the nature of the aggregation unit and the environmental conditions – induced aggregation has been shown to actually promote emission enhancement [175]. In this context, addressing the impact of physico-chemical parameters in surface properties would aid to clarifying interparticle interactions and ordering. Also, it could serve as an alternative or complementary procedure to the existing sorting methods (e.g. size exclusion chromatography [172] and ultracentrifugation [176]) to obtain more homogeneous characteristics making use of well-controlled induced phase separations.

The samples described and analysed in the following sections were prepared by a group of collaborators from the physics department of the *Università degli Studi di Palermo* in Italy – professor Fabrizio Messina and his team. They have been previously characterized by the Italian researches, notwithstanding, to augment and compare the results already established in the literature we also performed a few similar characterizations in the University of Brasilia. Alongside, this thesis provides novel results regarding the dispersions of these nanoparticles in aqueous media unraveling, qualitatively and quantitatively, their surface charge development as function of the pH and its relation with the observed macroscopical visual aspects of the system. Furthermore, it is presented the implications of the different interparticle interaction regimes in the nanoscale organization as well as possible explanations for the variations observed in the colloidal stability and fluorescence emission in the different pH conditions.

## 4.1 Synthesis

The synthesis of CDs greatly expanded and advanced from their initial publications in early 2000s [31, 177, 178]. The production of the nanodots are generally classified as physical or chemical methods, in which various techniques are employed such as: laser ablation of carbonaceous materials [31], irradiation of nanodiamonds by a proton beam [178], deposition of soot [179], chemical immersion of carbon nanotubes [177], eletrochemical oxidation of graphite [180] and thermal oxidation of molecular precursors [181].

The nitrogen enriched carbon nanodots studied here are synthesized following a microwave-induced thermal decomposition of organic precursors performed in a household microwave oven. This synthesis protocol is consolidated in the literature [29, 171, 182, 183] as a direct, simple and low-cost method constituted of just one step with ordinary equipment. This method also allows the usage of a variety of organic precursors, consequently, changing the properties of the resulting nanoparticles.

Sciortino et al.[38] describe the synthesis parameters that produced the samples here investigated, in which urea is used as the nitrogen doping source and citric acid adjusts the quantity of carbon. In this manner, the original study analysed a broad range of nitrogen and carbon nominal atomic ratios (N/C) shifting the molar concentrations of the reagents<sup>1</sup> in the precursor aqueous solution. The N/C was varied from 0.14 till 1.5, in which range a transition of the inner crystalline structure of the N-CDs was observed between the ratios of 0.34 and 0.58. Increasing the nitrogen content also promoted a shift of the fluorescence emission from blue to green. Further information on the difference in structure is detailed in section 4.3 and the photoluminescence effect disclosed in section 6.1. Else, for values above 0.74 the reaction produced small molecular side products, therefore the final sample presented high amounts of impurities.

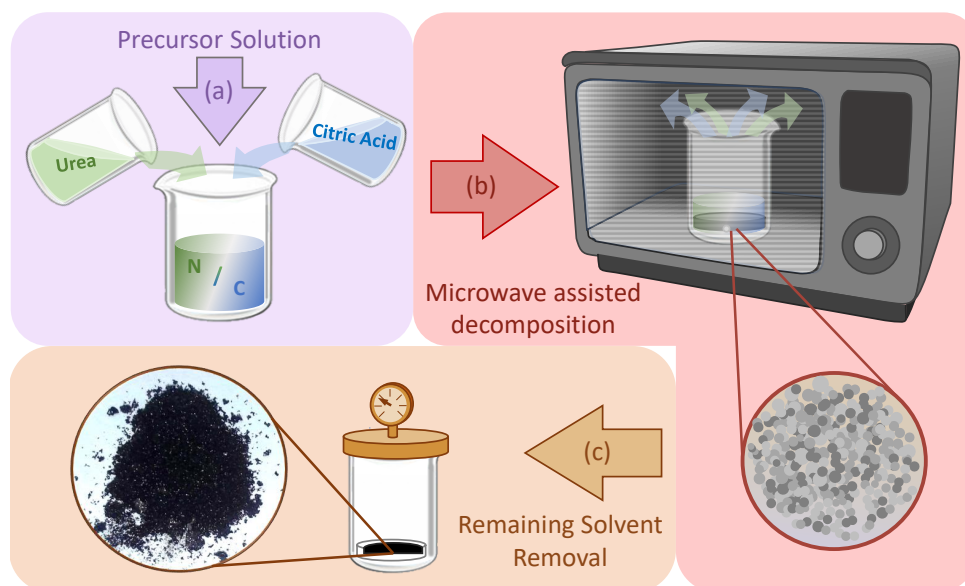


**Figure 33** – Diagram of the synthesis process of nitrogen-rich carbon nanodots: (a) Precursor solution preparation; (b) Microwave assisted decomposition and (c) Remaining Solvent Removal. The typical dark black powder produced after the carbonization process consisting of aggregated N-CDs is shown at the end.

In this context, the N/C lower and upper bounds (0.14 and 0.74) were chosen to be here investigated in depth. In order to simplify the nomenclature of the samples the N/C = 0.14 will be referred as *CD1* and the N/C = 0.74 as *CD7*. The synthesis protocol of these samples is performed as follows:

- a) *Precursor solutions*: The organic aqueous precursor is prepared by completely dissolving in 10 ml of type 1 water 3 g of citric acid monohydrate and 0.39 g (3 g) of urea, so that a 0.14 (0.74) nominal atomic ratio of nitrogen and carbon is established.

<sup>1</sup> The following pro analyse (P.A.) grade reagents supplied by Sigma-Aldrich were used for the synthesis of the nanoparticles: citric acid monohydrate ( $C_6H_8O_7 \cdot H_2O$ ; M= 210.14 g/mol), urea ( $CH_4N_2O$ ; M= 60.06 g/mol) and deionized water Type I (Millipore Milli-Q Gradient quality).

- b) *Microwave assisted decomposition:* The solution is heated in a standard household microwave oven (power set to 700 W) until the complete evaporation of the liquid phase. This carbonization process requires only a few minutes and produces a black powder. The yield can reach up to 30% in weight of the initial precursors.
- c) *Remaining Solvent Removal:* Since the dark material is strongly hygroscopic, after being brought back to room temperature, it is dried in vacuum for 90 minutes. The final product is a fine dry powder consisting of aggregates of N-CDs as shown in [Figure 33](#). Thenceforth, the powder can be dispersed in different aqueous solutions with well controlled physico-chemical parameters.

Before describing the properties of the colloidal dispersion, a careful characterization of the nanodots is presented determining particle morphology, size, the main surface groups and density, thus guaranteeing a systematic and substantiated analysis.

## 4.2 Morphology and Size

Carbon dots are typically described as quasi-spherical nanoparticles with mean diameter in the 1–10 nanometers range [171]. These characteristics are strongly dependent on the synthesis procedure, therefore, the size and morphology of the N-CDs were analysed by multiple techniques and compared to the results previously reported in the literature.

One of the most commonly adopted techniques for this purpose is the nanoscale imaging, which allows a direct observation of the nanoparticles. In this work, the N-CDs were probed by high resolution transmission electron microscopy (HRTEM) performed in a JEM2100 electron microscope (JEOL) using an ultra thin carbon type-A 400 mesh Cu substrate (TED PELLA). The technique demands the deposition of the N-CDs on a substrate, where the particles should ideally be spread out to facilitate the image analysis. For this reason, the N-CDs were first dispersed<sup>2</sup> in deionized water type I (Millipore) and subsequently diluted in ethanol (P.A) in order to accelerate the drying process when deposited over the carbon-based substrate. The obtained HRTEM images were able to resolve both synthesized N-CDs as shown in [Figure 34](#).

The images indicate the synthesis successfully produced nanoparticles with almost-circular outlines. The presented result is in strong agreement with data reported in previous studies with the same synthesis protocol [170–172] in which HRTEM images attested similar morphology, therefore endorsing the efficacy and reproducibility of the method.

Registering high-quality images of these N-CDs is a challenging task due to the low contrast of carbon and reduced thickness due to the small particle size. In addition, there are also agglomeration and stacking effects as a consequence of the solvent evaporation.

<sup>2</sup> The complete dispersion procedure is detailed step-by-step in [section 5.1](#).

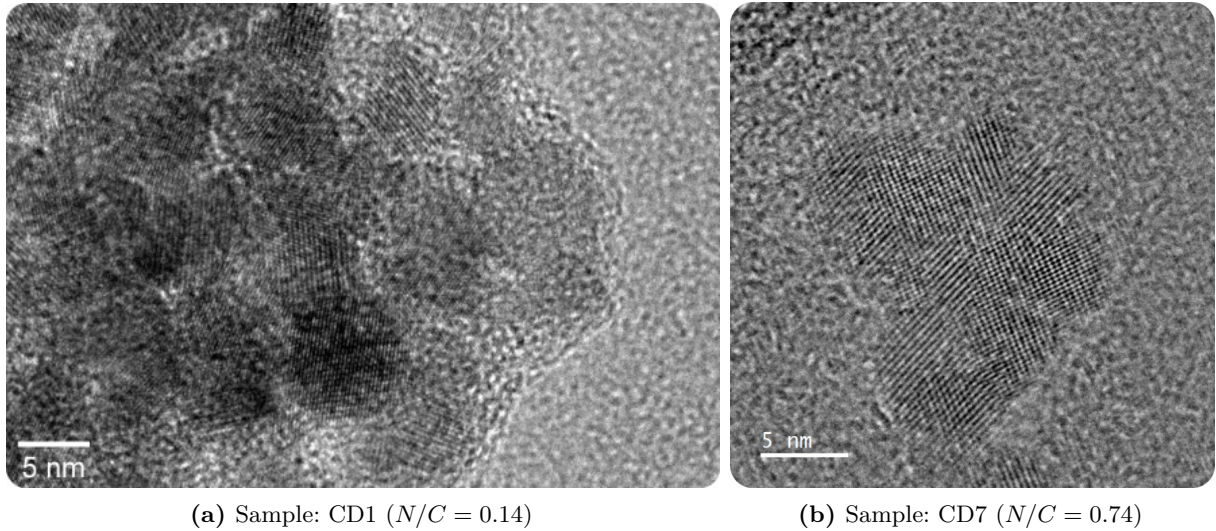


**Figure 34** – High-resolution transmission electron microscopy of the studied samples, evidencing the shape and internal crystalline structure of the dots.

Regardless these difficulties, tracing boundaries was eventually feasible by carefully adjusting the contrast and recognizing the lattice fringes generated by the internal crystalline structure of the N-CDs. An overlap of the multi-oriented lattice patterns and the different high contrast circular zones can be readily observed in Figure 34a and 34b, thus indicating monocrystalline nanoparticles, as also pointed out in reference [38]. A rough estimation of the nanoparticles size was achieved by pixel measuring the diameter of the N-CDs that could be properly outlined.

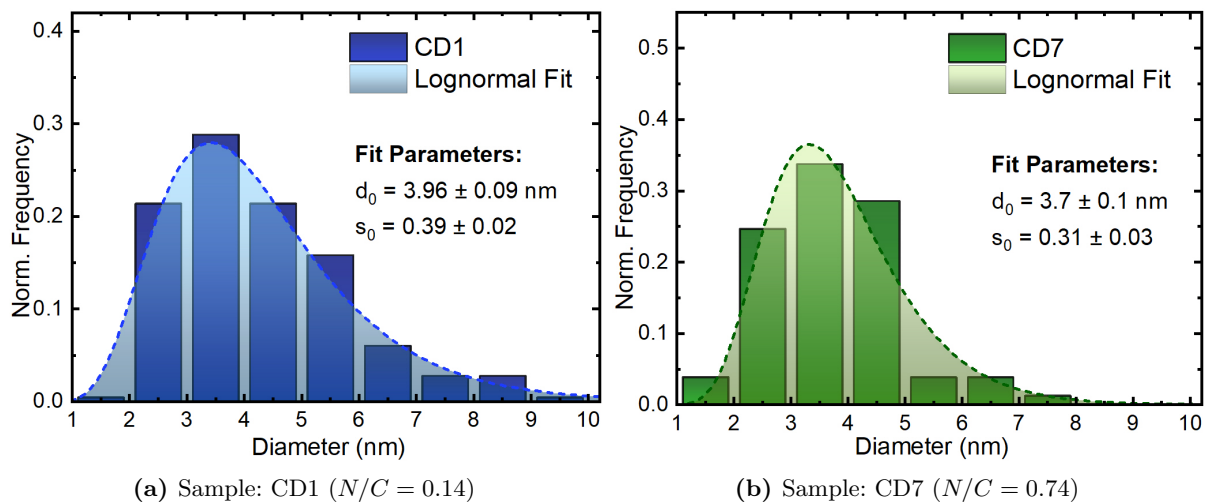


**Figure 35** – Particle size histograms deduced from transmission electron microscopy images. The adjustment of the data was performed using the lognormal distribution presented in Equation 1.1.

Naturally, these nanoparticles present a non-uniform dispersion in diameter, which would only be fully captured with relevant statistical confidence in a sufficiently large sample size. The total number of particles counted was a few hundreds, yet it was possible to obtain plausible histograms as shown in Figure 35.

The experimental data was analyzed fitting the lognormal distribution, already presented in Equation 1.1, where the median diameter obtained for sample CD1 was  $d_0 = 3.96 \pm 0.09$  nm and a similar value of  $d_0 = 3.7 \pm 0.1$  nm was found of sample CD7. Thus, at first, it seems that the difference in the N/C ratio does not have a great impact in the size of these nanodots, specially in the most probable value ( $d_{mp} = d_0 \exp(-s_0^2)$ ) which is located at 3.4 nm in both cases. These results should be interpreted with caution since particles smaller than 2 nm are extremely difficult to be identified in the measured resolution, therefore, inducing an observer bias. These measured median diameters ( $\sim 4$  nm) are in accordance with the values reported in references [38, 170, 183]. The PDI of CD1 is  $s_0 = 0.39 \pm 0.02$ , slightly higher than the value fitted for CD7 of  $s_0 = 0.31 \pm 0.03$ . The lower evaluation for CD7 can be mostly attributed to the lack of particles observed with diameters around 5 nm, where the histogram presents an abrupt reduction of counts deviating from the theoretical curve. Since HRTEM presents certain limitations due to the nature of these nanoparticles, which can incur in systematic errors, other techniques were employed pursuing an increased reliability in estimating the nanodots size.

Powder X-ray diffraction (XRD) is a convenient approach to achieve a reasonable mean diameter estimation, since it is a non-destructive method, independent of nanoparticle aggregation and less susceptible to statistical bias. The XRD measurements were performed on post-synthesis dried powder, prior to any dispersion in aqueous media. The measurements were carried out in a D8 Focus (Bruker) diffractometer with Cu K $\alpha$  radiation (wavelength  $\lambda_{XR} = 1.5406$  Å). The sample was probed in a  $10^\circ - 90^\circ$  range of  $2\theta$  with a  $0.05^\circ$  step at  $0.1^\circ/\text{min}$ . A Si standard was used to obtain the instrumental line broadening  $\beta_{ins} = 0.001921$  rad. The nanoparticles mean diameter ( $d_{XRD}$ ) can be estimated by Scherrer's equation [184]:

$$d_{XRD} = \frac{k\lambda_{XR}}{\beta \cos \theta_c}, \quad (4.1)$$

where  $k$  is the correlation factor (0.9 for spheres),  $\theta_c$  half of the peak position in the diffratogram (i.e. the incidence angle at the local maximum) and

$$\beta = \sqrt{(FWHM)^2 - \beta_{ins}^2}, \quad (4.2)$$

represents the broadening of the peak coming from the nanodots finite crystalline dimensions. The full width at half maximum ( $FWHM$ ) and the center of the peak ( $2\theta_c$ ) is obtained by a adjusting one or multiple Lorentzian functions<sup>3</sup>

$$L(2\theta) = \frac{2}{\pi} \left( \frac{(FWHM)}{4(2\theta - 2\theta_c)^2 + (FWHM)^2} \right). \quad (4.3)$$

The experimental curves exhibit a considerable background signal, hence a polynomial of high degree (six or higher) is adjusted as a baseline to be later subtracted in order to assist the peak fitting by removing the undesired contribution.

<sup>3</sup> In this form the function is normalized so that the area is unity and the offset is zero.

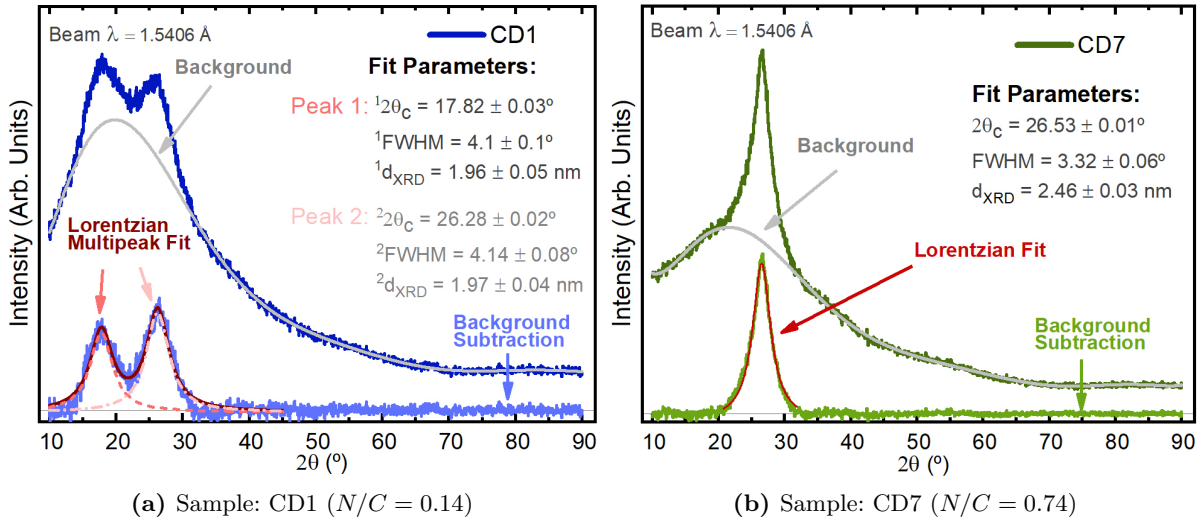


**Figure 36** – X-ray diffractograms of the investigated samples. A background subtraction was performed by the adjustment of a polynomial baseline. The treated curves were fitted using a Lorentzian multipole fit. The fit parameters (peak center  $2\theta_c$  and full width at half maximum  $FWHM$ ) determined the X-ray diameters  $d_{XRD}$  via Scherrer's equation (see text).

The diffractograms and fits are presented in Figure 36. The profile of the CD1 sample shows two intense peaks, while for CD7 only one very intense peak can be realized. Both samples present some lower intensity contributions that were not analysed since they are just slightly above noise level and they can not be resolved from a quantitative point of view. The absence of very sharp peaks assures that microcrystalline structures were not formed, an issue observed by Sciortino et al.[38] in higher N/C ratios.

The mean diameter determined by the XRD technique emerges as an average of the internal crystalline core size of the particles, this means that the polydispersity is embedded in the estimation and it does not take into account the extent of the surface groups. For the two analysed peaks found in CD1's profile, the diameter determined using Scherrer's equation provides extremely close values of  $^1d_{XRD} = 1.96 \pm 0.05$  nm and  $^2d_{XRD} = 1.97 \pm 0.04$  nm. The similarity of the obtained values indicates the diffraction peaks originate from the same crystalline structure and reinforces the accuracy of the evaluated diameter. The fitted parameters for the CD7 peak results in  $d_{XRD} = 2.46 \pm 0.03$  nm

The obtained crystallite sizes are 1.5–2.0 nm smaller than the diameters determined by HRTEM, which relatively represents up to a 50% reduction. As mentioned previously, the HRTEM images provided evidence that a nanodot is formed by a single crystal, thus it is reasonable to rule out the possibility of multiple smaller domains per particle. Also, the cause of the discrepancy does not appear to be largely associated to the disordered surface, since the fringes generally cover almost the entire dark region generated by the NPs in HRTEM images, as evidenced in Figure 34b. Further, the extent of the surface layer cannot be appropriately determined due to their very low density and consequently really poor contrast.

Therefore, the diminished particle size is likely to be induced by a considerable number of dots with diameters  $< 2$  nm that cannot be identified by HRTEM, bearing in mind that a reduction in diameter means also a lower contrast as a result of less matter absorbing and scattering. One way around this problem is the use of atomic force microscopy (AFM) that acquires a topographic height distribution of the nanodots deposited in a substrate by scanning the surface with a metallic tip (nano-antenna). The images presented in Figure 37 were generated at the Brazilian Synchrotron Light Laboratory (LNLS) in the infrared line IR1.

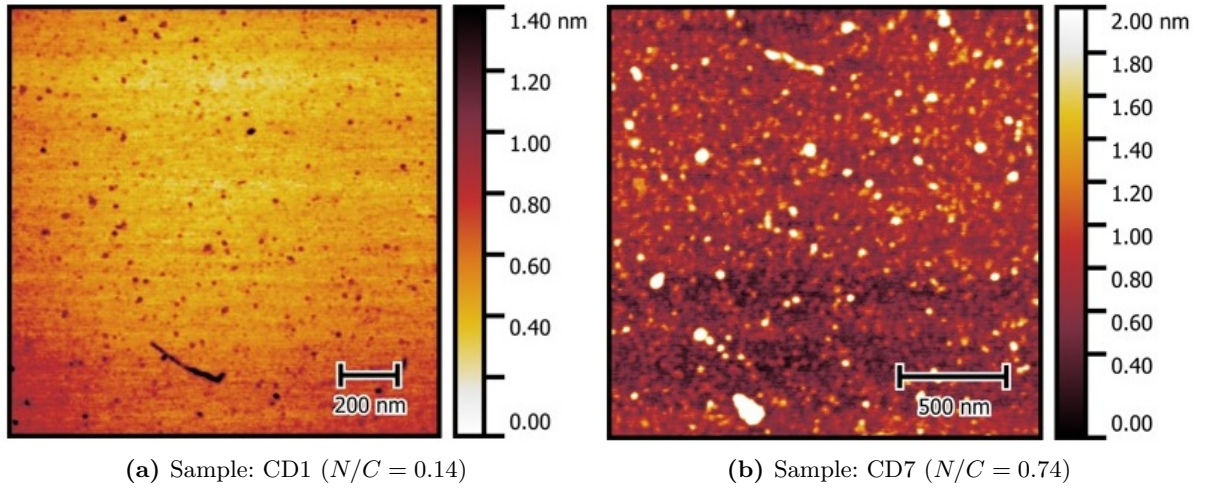


**Figure 37** – Atomic Force Microscopy of the studied samples evidencing the presence of under 2.0 nm particles.

In fact, numerous nanoparticles in the sub 2 nm range can be observed by this technique. These results were possible due to an ultracentrifugation process, which induced a concentration gradient and a size separation. After this procedure, the supernatant was collected and deposited over the substrate to be analysed. This means that producing a histogram of these images would be strongly biased and would not reflect the actual size distribution of the samples. In addition, a high number of CDs with diameters  $\leq 2$  nm can be observed in ref. [170] (HRTEM histogram and AFM image). Therefore, the here presented AFM data supports the suggested hypothesis and will provide relevant aid to the analysis of the nanoscale ordering. As an extra, HRTEM and XRD are insufficient to determine the spherical nature of the N-CDs, as it could be intricate to distinguish them from graphene quantum dots (GQDs). The AFM technique approach allows the validation of the isotropy of the dots by probing the sample in a different axis.

**Table 4** – Experimental size determinations obtained by TEM ( $d_{0,TEM}$ ,  $s_{0,TEM}$ ) and by XRD ( $d_{XRD}$ ) of the samples CD1 and CD7.

Sample	$d_{0,TEM}$ (nm)	$s_{0,TEM}$	$^1d_{XRD}$ (nm)	$^2d_{XRD}$ (nm)
CD1	$3.96 \pm 0.09$	$0.39 \pm 0.02$	$1.96 \pm 0.05$	$1.97 \pm 0.04$
CD7	$3.7 \pm 0.1$	$0.31 \pm 0.03$	$2.46 \pm 0.03$	-

The presented results are summarized in [Table 4](#), reinforcing the already well-established characterization of these nanoparticles as dots (i.e. really reduced particle size presenting a spherical symmetry). Unfortunately, it was not possible to accurately evaluate a comprehensive size distribution, anyhow, the mean diameter can be at least narrowed down to values smaller than 4 nm. Thence, in the next section we explore the N-CDs' structural features, in view that they play a crucial role in the colloidal stability of the system.

### 4.3 Internal Structure and Surface Groups

The general chemical composition of CDs varies widely depending on the synthesis process, yet, they are basically composed of carbon, oxygen, nitrogen, hydrogen and eventually sodium or sulfur [185]. Its structure varies from amorphous to crystalline, and may present diverse quantities of each one [37]. The carbon atoms may be arranged in different degrees of hybridization ( $sp^2$  and  $sp^3$ ), whose proportion and combination varies case by case [186]. Thus, CDs are generally composed of a distinct crystalline/amorphous core enveloped by a surface layer bearing small or long atomic chains of polar or apolar moieties, which the most commonly found functional groups are carboxyl ( $-COOH$ ), hydroxyl ( $-OH$ ) and carbonyl ( $-C=O$ ) [35].

The nitrogen enriched N-CDs here investigated – synthesized via the hydrothermal route – are no exception to the described general features. Yet, this process presents a useful perk regarding the internal crystalline structure formation. [Sciortino et al.\[38\]](#) observed a transition from the fairly common hexagonal-close-packed (HCP) C-graphite structure (space group P63/mmc, space group n° 194  $a = b = 2.460 \text{ \AA}$   $c = 6.704 \text{ \AA}$ ) to the unexpected, but also hexagonal,  $\beta-C_3N_4$  (space group P63/m, space group n° 176  $a = b = 6.380 \text{ \AA}$   $c = 2.395 \text{ \AA}$ ) [187], when surpassing a certain N/C threshold. [Figure 38](#) illustrates both structures.

In fact, the graphitic structure is not purely formed of carbon atoms, instead, some of them are substituted within the ideal structure by N atoms. Therefore, a low nitrogen content results in the N-doping of the inner crystalline structure of the CDs, however, it is not enough to considerably modify the HCP C-graphite structure itself. Only when the nitrogen to carbon nominal molar ratio exceeds somewhere between 0.34 and 0.58 that the structural transition actually occurs.

Several techniques had to be implemented in order to attest these structures. The X-ray diffraction curves presented in [Figure 36](#) are in very good agreement with the results using the same technique reported in the E.S.I of ref. [38]. The number and position of the most intense peaks match for both samples, although, their positions show a certain ambiguity if compared with the expected theoretical values. Therefore, [Sciortino et al.\[38\]](#)

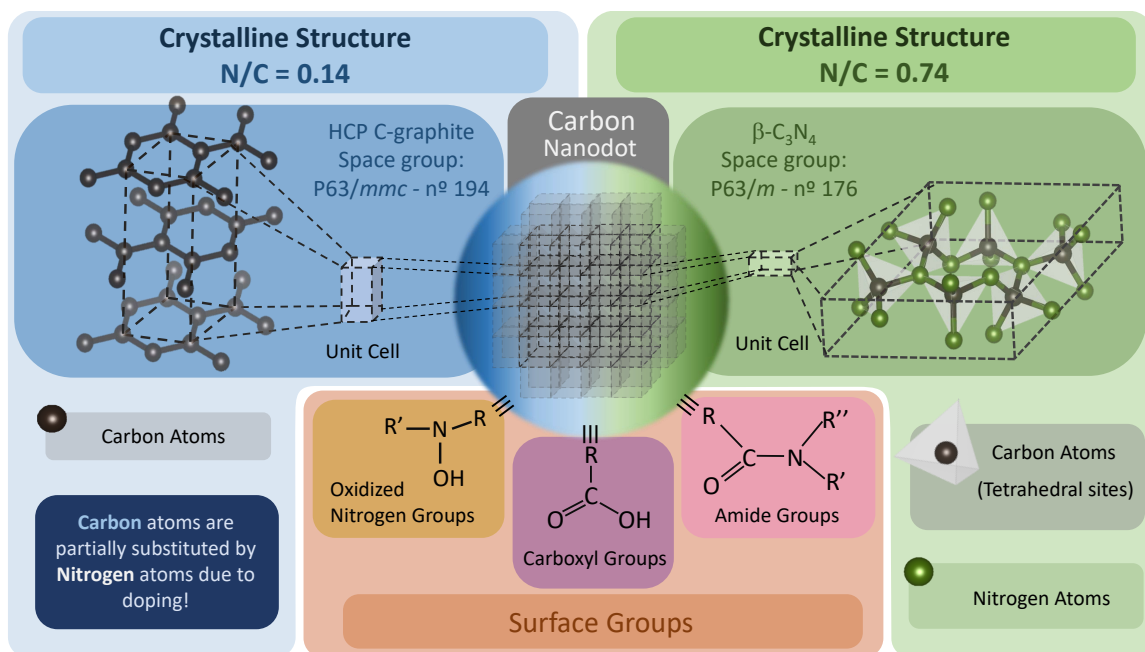


**Figure 38** – Diagram of the core and surface characteristics of the studied N-CDs. The presented internal crystalline structures correspond to the two variants of the hydrothermal synthesis with different N/C ratios, named here CD1 (*left* - N/C=0.14) and CD7 (*right* - N/C=0.74). The crystalline structures were deduced from multiple techniques (see text for references). Structure visualization generated using ref. [64]. The surface groups were inferred from the FTIR spectra exhibited in Figure 39, where all the presented surface groups are observed in both types of N-CDs. R, R' and R'' represent organic groups or – R' and R'' – may be single hydrogen atoms.

presented two additional techniques: (a) the Fourier Transform (FT) analysis of HRTEM images confirms the crystallinity of both N-CDs by comparing with calculated diffraction patterns and further demonstrate the N-doping by the existence of some forbidden reflection; (b) Raman spectra attest the graphitic structure for N/C = 0.14 by the presence of peaks that are characteristic of these systems, while distinctive vibrational fingerprints associated to the  $\beta$ -C<sub>3</sub>N<sub>4</sub> are observed for N/C = 0.74. In addition, the carbon nitride structure was characterized in ref. [170] using selected-area electron diffraction (SAED) and X-ray photoelectron spectroscopy (XPS), altogether corroborating the previously reported findings.

To gather deeper insights about the surface composition of the N-CDs, fourier transform infrared spectroscopy (FTIR) measurements were performed using a Perkin Elmer FTIR spectrometer (model Frontier). Pellets of KBr+sample were prepared by mixing the powder sample and potassium bromide then pressing at 10 tons on a hydraulic press (Auto-CrushIR, Pike Technologies). The spectra were recorded in absorbance mode from 4000 to 400 cm<sup>-1</sup> using 8 scans at 4 cm<sup>-1</sup> resolution.

The mid-FTIR spectrum of the N-CDs is shown in Figure 39 and reveals their complex surface chemistry. The large broad band between 2600 and 3400 cm<sup>-1</sup> (A) are due to O–H, N–H and possibly C–H stretching vibrations. The peaks at 1712 cm<sup>-1</sup> (B) and

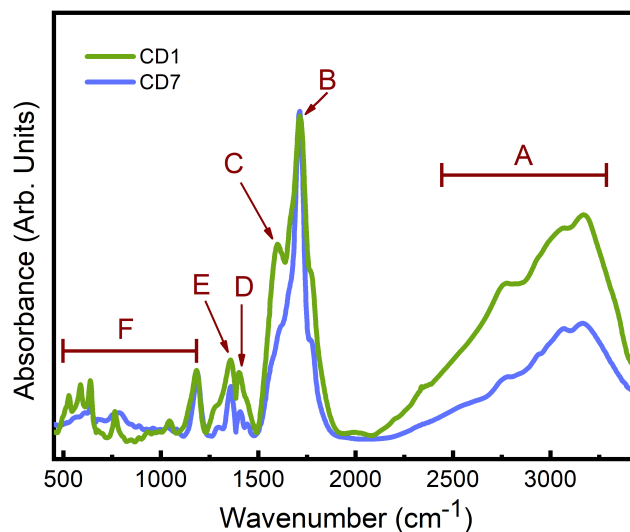


**Figure 39** – FTIR spectra of the investigated samples (CD1 in blue and CD7 in green). The A-G areas illustrate the different regions of interest described in the text.

$1600\text{ cm}^{-1}$  (C) can be respectively attributed to carboxylic and amide C=O stretchings. The peak at  $1401\text{ cm}^{-1}$  (D) is characteristic of the O–H in plane bend while that at  $1357\text{ cm}^{-1}$  (E) can be assigned to the C–N stretching. Finally, the spectrum still shows characteristic H–O and H–N out of plane vibrations (F).

The reduction of the peak (C) attributed C=O stretchings can indicate a lower amount of amide surface groups in CD1 if compared with CD7, which makes sense considering that the nitrogen content is significantly diminished in the first case. These results are in conformity with the FTIR data presented in ref. [170], where the general behavior of the curves are greatly alike, even comprehending the intensity reduction observed for the amide related vibration. Lastly, in addition to the pointed out carboxyl and amide groups, we should address the likelihood of oxidized nitrogen functionalities being present onto the N-CDs surface, as N–O bounds were revealed using XPS in ref. [170]. The presence of such surface functional groups are far from atypical, as it was observed multiple times for similar carbon materials [188–190].

Figure 38 summarizes the realized crystalline and surface structure of the N-CDs based on the ensemble of the presented experimental results achieved through the extensive multi-technique combination.

## 4.4 Density

In section 4.2 we were able to roughly determine the mean diameter of the core by XRD due to its crystalline nature. Further on, the nanodots' core and surface structures were detailed in the previous section, but the extent of the surface layer remains unclear. Sadly, the accurate and precise distinction of the crystalline core and the disordered surface

via direct observation through the presented HRTEM images were not feasible due to low contrast and insufficient resolution.

Therefore, experimentally determining the density of the N-CDs powder sample might indicate the relevance of the surface layer in relation to the core by comparing the measured value to the expected density of the inner crystalline structure exclusively. The theoretical density for the HCP C-graphite is  $2.266 \text{ g/cm}^3$ , but due to the N-doping it should be appropriate to consider a value in between pure graphite and the slightly lower density value of  $2.02 \text{ g/cm}^3$  for the graphitic carbon nitride (g-C<sub>3</sub>N<sub>4</sub>) [191]. Regarding the  $\beta$ -C<sub>3</sub>N<sub>4</sub> crystal, the density of  $3.57 \text{ g/cm}^3$  was experimentally determined in ref. [192]. As an extra, experimentally estimating the N-CDs density will also be useful to perform a mass to volume conversion, which is occasionally necessary depending on the technique.

Let us first define the density of the powder and the solvent as

$$\rho_p = \frac{m_p}{V_p} \quad \text{and} \quad \rho_{\text{solv}} = \frac{m_{\text{solv}}}{V_{\text{solv}}}, \quad (4.4)$$

where  $V_p$  and  $V_{\text{solv}}$  are the volumes corresponding, respectively, to the mass  $m_p$  of the powdered N-CDs and the mass  $m_{\text{solv}}$  of aqueous solvent. In this context, it is fairly easy to experimentally evaluate the mass and the volume of the liquid solvent, however, determining the volume of the solid N-CDs samples is quite intricate. For this reason, when working with N-CDs dispersions the concentration is typically expressed as mass per volume (usually g/L) or by the mass fraction

$$w = \frac{m_p}{m_p + m_{\text{solv}}}. \quad (4.5)$$

In order to determine the powder density, we measured the density of various N-CDs aqueous dispersions<sup>4</sup> at five different mass concentrations using a DMA 38 Anton Paar digital densimeter. The density  $\rho_{\text{disp}}$  of the aqueous dispersion can then be written as

$$\rho_{\text{disp}} = \frac{m_p + m_{\text{solv}}}{V_p + V_{\text{solv}}}. \quad (4.6)$$

Moreover, it can be expressed in terms of  $\rho_p$ ,  $\rho_{\text{solv}}$  and  $w$  by applying Equation 4.4 and 4.5 to 4.6 resulting in

$$\rho_{\text{disp}} = \frac{\rho_{\text{solv}}\rho_p}{\left(\rho_{\text{solv}}w + \rho_p(1 - w)\right)}. \quad (4.7)$$

Figure 40 presents the measured density values as a function of the mass fraction of both CD1 and CD7. The fit is performed using Equation 4.7, where the adjusted parameters are  $\rho_p$  and  $\rho_{\text{solv}}$ . The adjusted solvent density was in agreement to the measured values at  $w = 0$  and within the error bar considering the different N-CDs dispersions.

<sup>4</sup> The samples were dispersed in alkaline medium to obtain a microscopically homogeneous fluid avoiding particle sedimentation and substantial density fluctuations. See section 5.1 for the dispersion protocol.

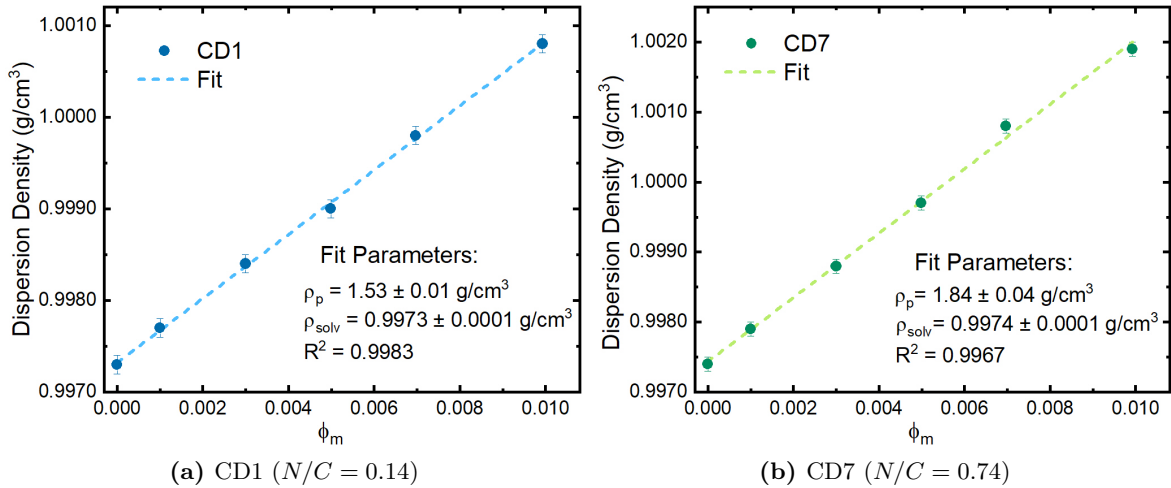


**Figure 40** – Measured density of N-CDs dispersions in aqueous medium as a function of the mass fraction. Figure (a) shows to the data of CD1 sample (N-doped C-graphite core) and (b) the CD7 sample ( $\beta$ -C<sub>3</sub>N<sub>4</sub> core). The dashed lines correspond to the fits using Equation 4.7.

The fitted value of  $\rho_p$  for CD1 is  $1.53 \pm 0.01$  g/cm<sup>3</sup> and for CD7 it is equal to  $1.84 \pm 0.04$  g/cm<sup>3</sup>. The obtained densities are lower in both cases, in which for CD1 it corresponds to an approximate 24 – 33% reduction while for CD7 it is a more substantial value of  $\sim 48\%$ . Even though the reduction is larger for CD7 it remains denser than CD1, following the tendency of the inner structure density. These results show a considerable variation with respect to the core densities alone, suggesting a highly populous surface layer. In fact, the vast surface passivation is a very common feature found in carbon dots, in particular cases, it can reach be as thick as a few nanometers [193]. Unfortunately, it is not possible to experimentally resolve the density solely of the surface layer by this method, which prevents the proper estimation of its actual size.

It is important to address that the decrease in density should be taken carefully, since it cannot be attributed exclusively to the surface functional groups. Some other factors could also influence in the density of the powder, such as residual amounts of water adsorbed from the ambient and small molecules generated during the synthesis along with the CDs that can get attached to their surface [194–196].

## Chapter 5

# Colloidal Dispersions of N-CDs

Hydrophilic CDs are frequently considered to be water-soluble nanoparticles [29, 35, 36] since they are easily dispersed in the polar solvent exhibiting high colloidal stability. In particular, the investigated N-CDs have been known to form suspensions (up to at least 15 g/L in pure water) which can remain stable for months and could not be separated by centrifugation up to 12000 rpm [171].

One of the key factors for stability in charged colloids is the development of the nanoparticles surface charge depending on the medium characteristics. Given the nature of the N-CDs charge mechanism in aqueous medium, we focused our attention on the pH-dependency, reasonably the most important parameter to monitor the surface charge. The limited range of studies on the stability of this material led us to develop a quantitative and qualitative analysis by applying a coupled experimental technique to evaluate the surface charge density and link the results with the evolution over time of the macroscopical visual aspect of the samples.

### 5.1 Dispersion in Different pH Aqueous Media

The dispersion medium is primarily deionized Type I water with  $\text{pH} \approx 7$ . The pH is then regulated to a specific value by either adding concentrated nitric acid ( $\text{HNO}_3$ ) as the acidifying agent or sodium hydroxide ( $\text{NaOH}$ ) as the alkalizing agent. If necessary, sodium nitrate ( $\text{NaNO}_3$ ) is added to the solutions as a background electrolyte to impose a particular ionic strength. The salt was chosen such as the added co-ions/counterions are limited to  $\text{NO}_3^-$  and  $\text{Na}^+$ , which are already present in the system as a result of the adopted acid/base reagents. Finally, the pH of the solutions are measured with a pH meter (913 pH Meter Metrohm).

The dispersion is performed by the direct combination of the solid material with liquid medium, in which the N-CDs concentration is controlled by weighing a certain mass of powder and the dispersion total volume is set by the addition of the pH-adjusted

aqueous solution. If performed under UV light, the fluorescent emission is immediately observed as the CDs are added to the medium. In Figure 41 it is presented the addition of N-CDs to pure water: (a) before the addition of the carbon dots; (b) a few seconds after the powder is added to the solution and (c) after the tubes are given a gentle shake.

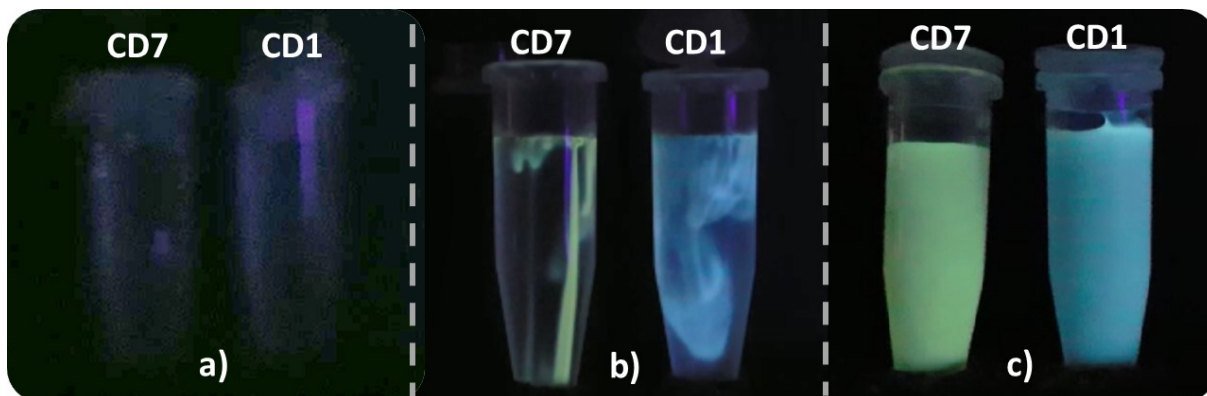


**Figure 41** – Dispersion of N-CDs into pure water under UV light: (a) before the addition of the carbon dots; (b) a few seconds after the powder is added to the solution; (c) after gently shaking the tubes.

Although the vast majority of the nanopowder gets in suspension fairly easily, a considerable amount of aggregates are still visible. Therefore, the dispersion procedure is finalized by sonicating the sample in an ultrasound bath (Eco-Sonics) at 50 °C for at least 12 hours until the macroscopic visual aspect looks as homogeneous as possible. In highly acidic and/or concentrated conditions, the described procedure with the mentioned equipment cannot always fully homogenize the sample (even for a period longer than 24 hours inside the ultrasound bath) leaving persistent microscopic clusters that are hardly perceived by the naked eye in freshly prepared circumstances.

Observing the behavior of the peptization in the different aqueous media, it is clearly noted that a substantial portion of the added powder effortlessly enters in suspension, which endorses the widespread strong hydrophilic character of water-soluble nanodots. However, a significant portion of the powder requires additional energy to break apart and – depending on the medium conditions – the clusters can be very persistent. Consequently, the dispersion mechanism is presumably a heterogeneous process which not only depends on the solvent affinity, but shall also be profoundly impacted by the interparticle interactions. A deeper analysis regarding these visual observations is found in the following sections.

## 5.2 Visual Aspects and Short Term Aging

The visual aspects of the dispersed samples will provide valuable preliminary information regarding some features of these colloids, despite the fact that the results were analyzed only qualitatively. Figure 42 presents a series of photos of the sample CD7 where three parameters were probed: the N-CD's concentration, the pH of the precursor solution

and the time elapsed after the dispersion procedure. Here we present the images solely for CD7, but the results and conclusions can be comprehensively extended to CD1 as it presents analogous behavior.

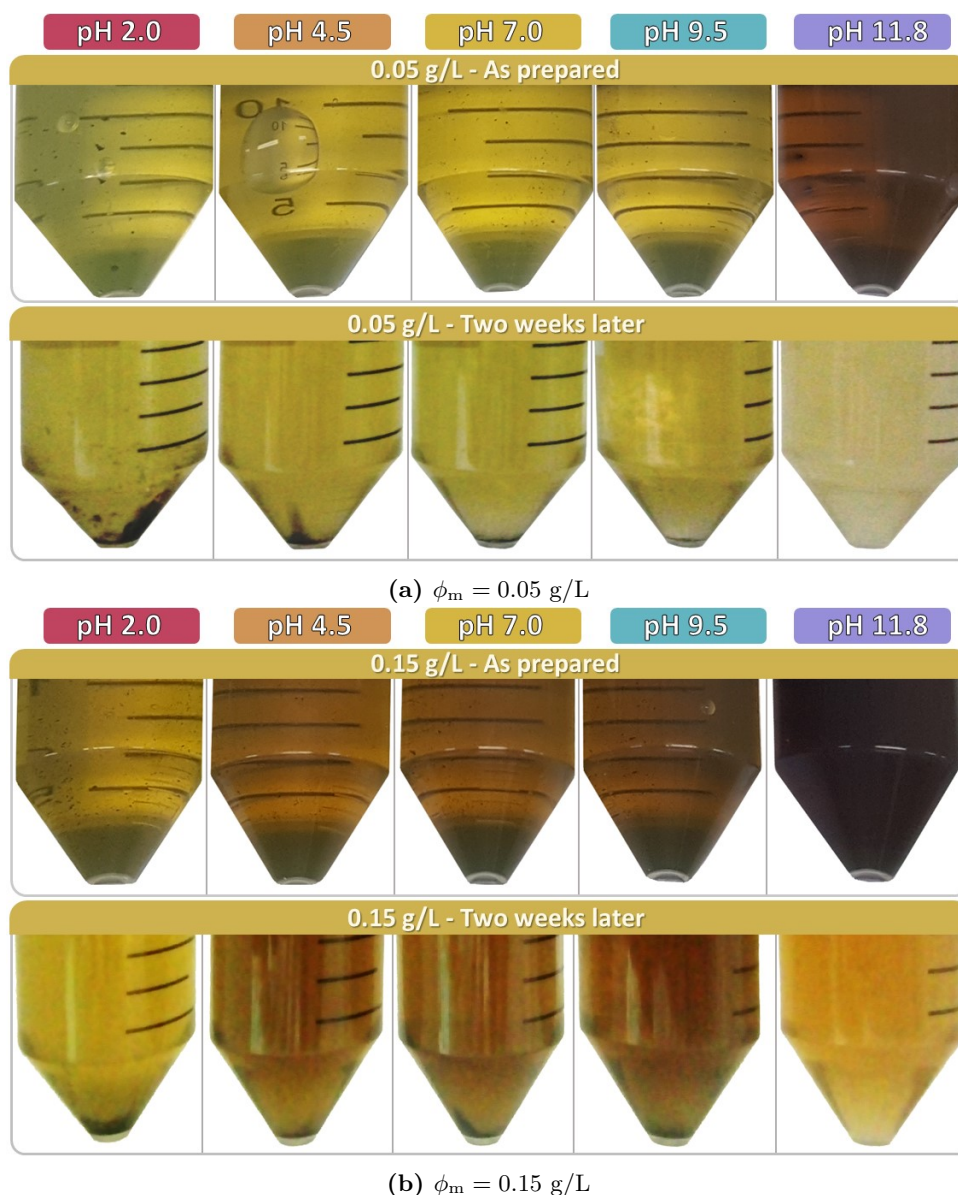


**Figure 42** – Visual aspects of CD7 dispersed in different pH solutions and in two different mass concentrations ( $\phi_m$ ): **a)** 0.05 g/L and **b)** 0.15 g/L. First row refers to photos taken subsequently to the dispersion protocol and second row after the sample was left immobilized for two weeks.

The concentration of N-CDs was set to 0.05 g/L and 0.15 g/L, rather diluted circumstances, since these are the typical range of values adopted in studies of fluorescence properties. The aqueous medium varied from acidic to alkaline conditions, such as the  $\text{pH}_i$ <sup>1</sup> of the precursor solution was set to five different values: 2.0, 4.5, 7.0, 9.5 and 11.8. At last, the observation took place in two points in time: the first row images of each concentration

<sup>1</sup> The mentioned values refer to the pH of the solutions measured prior to the addition of the CDs. In general, these values are shifted as the nanoparticles are introduced as a result of reactions on the interface particle/solvent.

were captured immediately after the dispersion procedure and the second row shows the evolution suffered after they were let at rest for two weeks at room temperature.

Starting from the as prepared samples, first point to be noted is that increasing the concentration promotes a general increase in darkness, shifting the color from yellow to brown, meaning a higher absorption coefficient. This should indicate that as the concentration increases the number of particles in dispersion also raise, at least until a certain concentration limit. It might seem obvious, however, it is observed in the extremes that the sample looks slightly lighter at  $\text{pH}_i$  2.0 and undoubtedly darker at  $\text{pH}_i$  11.8. This can be associated with a better homogenization of the dispersion, hence as the  $\text{pH}_i$  increases the aggregated CDs are easier to dismantled, allowing the particles to become more spread apart throughout the liquid and thus increasing the overall absorption of the fluid. This hypothesis is supported by the photos taken two weeks later, in which a progressive reduction of the precipitate is observed with the increment of the  $\text{pH}_i$ .

At this scale, it is not clear if the precipitate is formed just by the slow settling of clusters that could not be disaggregated or if there is a flocculation process that increases the aggregate size due to attractive forces, thenceforth causing sedimentation. Therefore, optical microscopy images were taken using a Zeiss Microscope to reduce the probing scale. The images obtained for the precipitate observed in the sample at 0.15 g/L are presented in [Figure 43](#) indicating that it is most likely a combination of both.

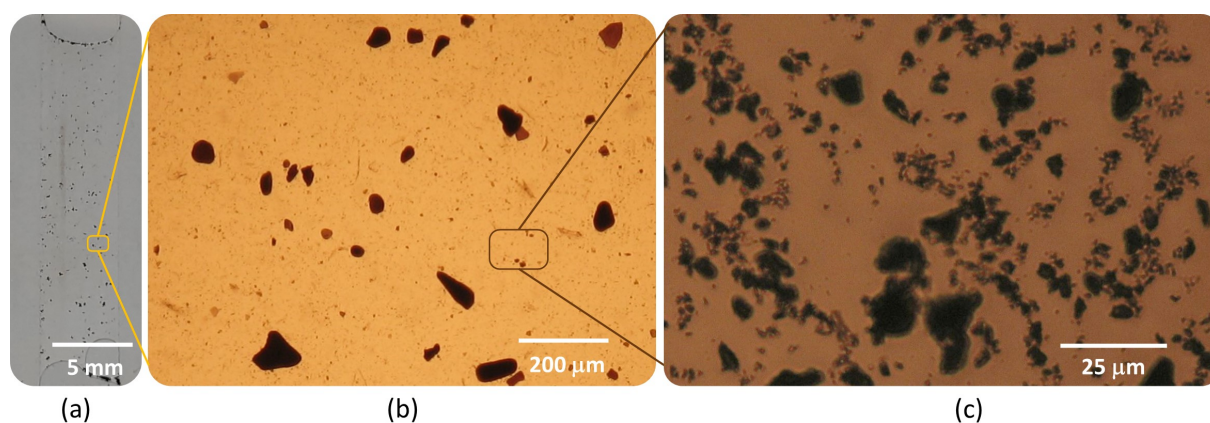


**Figure 43** – Visual aspects of the precipitate of sample CD7 at 0.15 g/L dispersed in  $\text{pH}_i$  2.0 solution: (a) photo of the sample inside microscopy slides. The borders are stripes of parafilm; (b) optical microscopy image taken with a 5x objective lens and (c) optical microscopy image taken with a 40x objective lens.

An aliquot of the bottom section of the tube of the dispersion at  $\text{pH}_i$  2.0 was collected containing high amounts of the precipitate. [Figure 43a](#) shows the visual aspect of the sample placed in the microscopy slides. At the microscopical level, it is observed in [Figure 43b](#) the presence of fairly spread apart flakes with size ranging from  $\sim 50$ – $150 \mu\text{m}$ . These lamellar structures present various geometrical shapes and differences in thickness can be noticed by the change in contrast. [Figure 43b](#) zooms in the minor objects, where aggregates as small as  $1 \mu\text{m}$  interact to generate agglomerated structures of higher orders.

Even though most of the observed particles are in direct contact with others, there are still a certain amount of them (typically the smaller ones) detached from the rest, free to move inside the fluid by performing Brownian motion. These images indicate that in low pH conditions, dense aggregates – reaching up to a few hundred microns – cannot be easily broken apart. One potential reason behind the persistence of these highly contrasting objects is the particle arrangement across the aggregate, which could make it difficult for the solvent to extensively wet the dots inside the highly packed structure, demanding extra energy and/or time. Note that it is assured that these objects are not microcrystalline structures considering the absence of sharp peaks in the XRD results (see [Figure 36](#)). Further, at a smaller scale, lower density fractal-like structures self-assemble due to attractive forces. The dynamic observation at this scale suggests that the chain-like configuration is time-dependent and can be easily reversed by agitating the sample, since the aggregates show to be loosely interconnected.

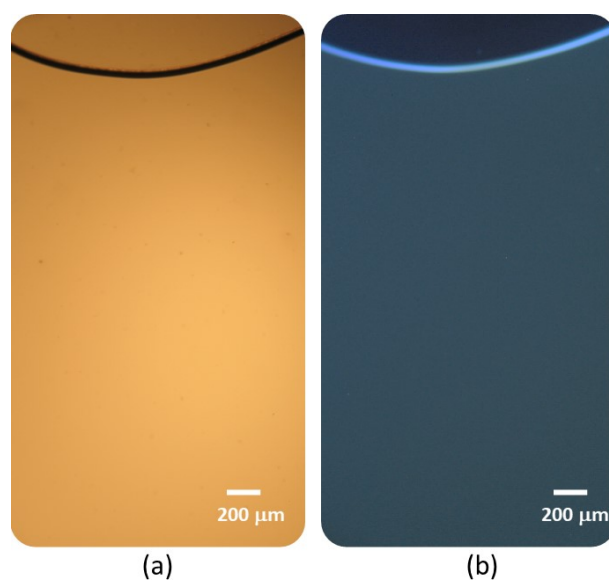


**Figure 44** – Optical microscopy image of the homogeneous supernatant of sample CD7 at 0.15 g/L dispersed in  $\text{pH}_i$  2.0 solution. Image (a) is taken under visible light and (b) under a commercial UV light.

Now, let us analyze the microscopical aspect of the supernatant. Even in  $\text{pH}_i$  2.0, indisputably the worst stability condition, the supernatant exhibits exceptional visual homogeneity, as presented in [Figure 44a](#). The yellowish color exhibited in the visible light indicates the presence of N-CDs in the dispersion and, indeed, in [Figure 44b](#) it can be confirmed by the green fluorescence emission observed under UV light. This observation demonstrates that part of the N-CDs can be properly dispersed generating long-term stable colloids even in highly acidic conditions, without the presence of microscopic aggregates.

At  $\text{pH}_i$  11.8 an astonishing colloidal stability is attested by the complete absence of any sediment, even in optical microscopy images. However, note that the absorption spectrum clearly has been extremely altered in both concentrations. The reduction of the

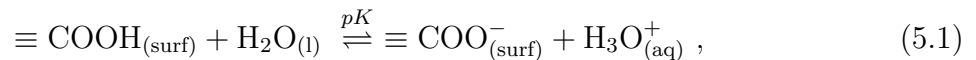
visible light absorption cannot be attributed to a reduction of particle concentration, since no precipitate was formed. Further on, if the liquid is evaporated the carbon dots can be retrieved again as powder, meaning that the particles were not completely destroyed. In [section 6.2](#) it is presented a possible explanation for this effect.

We can conclude that in aqueous dispersions the aggregates tend to spontaneously break apart due to the hydrophilic surface, although the discrepancy between the well-dispersed supernatant and the flocculated precipitate – combined with the absorption increase with concentration – suggests a heterogeneous solubility of the powder. The distinct behaviors are likely to be attributed to interface effects, such as variations on the CD's surface properties and the initial degree of aggregation. These visual observations indicate that the stability of the dispersion highly depends on the pH of the medium, since the results show a progressive reduction of aggregation as the pH increases. The fact that the surface hosts carboxyl groups, which can develop a negative surface charge in aqueous medium – introducing a repulsive electrostatic component – led us to investigate the surface charge mechanism to understand in-depth the stability enhancement.

### 5.3 Surface Charge Development in Aqueous Media

A comprehensive description of the relations between colloidal stability and interparticle interactions was given in [chapter 2](#) focusing on ferrofluids dispersed in ionic liquids. On the contrary of what was ascertained for the FF-RTILs, here it is viable to adopt the conventional approach for charged colloids by considering the framework of the DLVO theory [[76, 77](#)].

When the CD's powder is introduced to an aqueous media, the surface of the NPs becomes hydrated by the solvent allowing protonation/deprotonation reactions to come in play. The most commonly reported charge mechanism considers the pH-dependent equilibrium reaction of carboxyl surface groups, which can provide a negative surface charge as a consequence of the following equation [[197](#)]



where  $K$  is the corresponding thermodynamic constant ( $pK = -\log K$ ). This assumption is here supported by the presented FTIR results that recognized the presence of such functional groups.

Then, the generated negative surface charge density  $\sigma_0$  will establish an electrostatic surface potential  $\Psi_0$  that – in an aqueous electrolyte solution – will promote a condensation of the counterions near the particle surface creating the well-known Electric Double Layer (EDL).

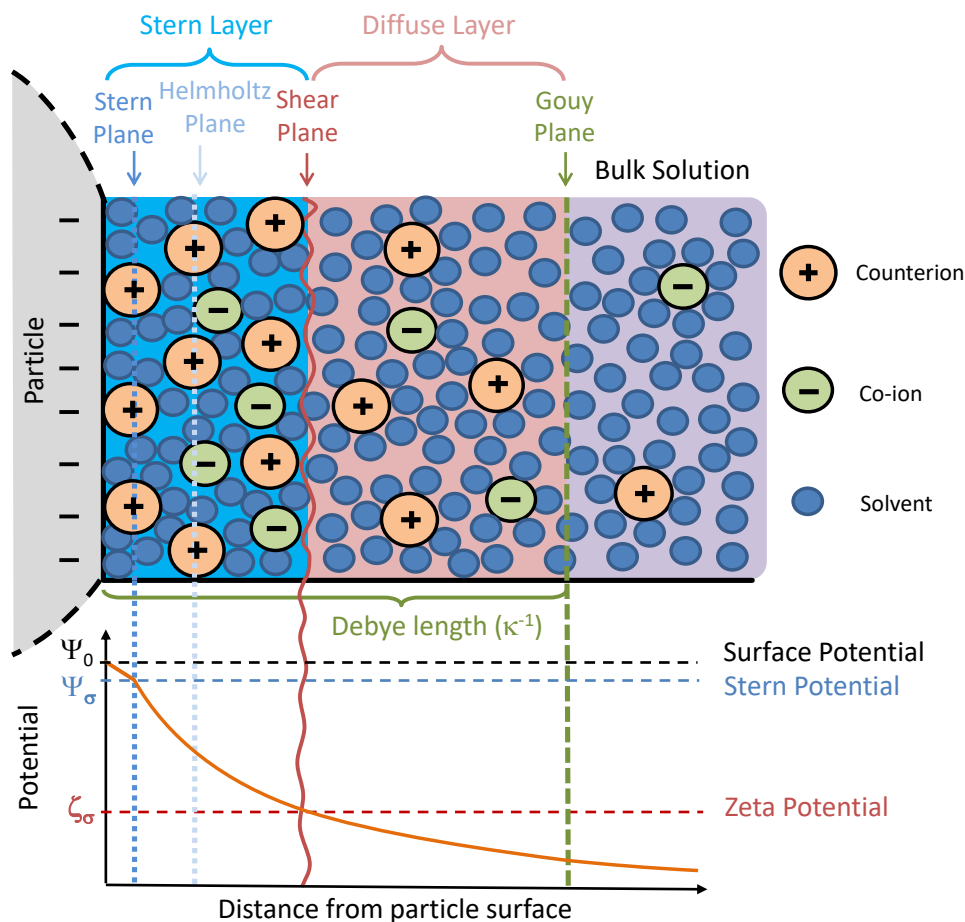


**Figure 45** – Schematic representation of an electric double layer (EDL) and the potential decay due to the counterion condensation near the particle surface.

Figure 45 exhibits a schematic representation of a typical EDL based on the model of Stern-Grahame [198], where the surface potential produced by the negatively charged particle surface is characteristically screened by the counterions in solution. Three different regions can be observed in representation: the region located the closest to the particle surface entitled Stern/Helmholtz layer is frequently subdivided in a first group of counterions that are directly adsorbed on the particle surface creating the internal Stern plane and a second group of hydrated counterions that outlines the external Helmholtz plane. This first layer extends from the particle surface until the shear (or slipping) plane, which is characterized by the interface delimiting where the fluid accompanies to the surface displacement. The second region denominated diffuse (or Gouy) layer still presents an increased concentration of counterions, but they experience rapid random motion due to thermal agitation and do not consistently follow the nanoparticle movement path. Finally, the bulk solution is reached after crossing the Gouy plane, where the electrical potential of the surface is negligible and the concentration of counterions and co-ions is equally balanced.

Two important concepts arise from this approach: the Zeta potential and the Debye length. The Zeta potential can be understood for colloids as the electrokinetic potential of

the nanoparticles evaluated as the effective surface potential at the shear plane. The Debye length represents the extent of the EDL and can be calculated by the expression [65]

$$\kappa^{-1} = \left( \frac{\varepsilon_0 \varepsilon_r kT}{2N_A e^2 I} \right)^{1/2}, \quad (5.2)$$

where  $\varepsilon_0$  is the vacuum permittivity,  $kT$  is the Boltzmann constant and temperature,  $\varepsilon_r$  is the dielectric constant of the solvent,  $N_A$  is the Avogadro constant,  $e$  is the elementary charge and  $I$  is the ionic strength of the dispersion.

Under these modeling circumstances, we explore the development of the N-CDs' surface charge in the next sections. We combine zetametry and potentiometric-conductimetric titrations to access independent quantitative results allowing us to associate the pH-dependency of the surface charge with the evolution of the visual aspect observed in the previous section.

### 5.3.1 Zeta Potential

The Zeta potential measurements were taken using a ZetaSizer (model NanoZS 90, Malvern Panalytical) with a disposable folded capillary cell (DTS 1070). The same sample preparation performed for the visual aspects observation was used, thus, the N-CDs were dispersed in the five pH<sub>i</sub>  $\sim$  2.0, 4.5, 7.0, 9.5, 12.0 aqueous solutions, but additionally, an ionic strength of 0.01 mol/L was imposed by adding NaNO<sub>3</sub> as a background electrolyte, avoiding the introduction of different ions to the system. In order to preserve the 0.05 g/L nanoparticles mass concentration<sup>2</sup>, no adjustment of the physical-chemical parameters was performed after combining the N-CDs and the suited medium. The adopted particle concentration was enough to obtain a strong signal and sufficiently diluted as the measurement technique requires. Temperature variations were evaded by performing all measurements at 25 °C.

The electrophoretic mobilities  $\mu^{el}$  are obtained by measuring the particle velocity using Laser Doppler Velocimetry (LDV). Then, the corresponding zeta potentials ( $\zeta_\sigma$ ) are calculated using Henry's equation [199]

$$\mu^{el} = \frac{2}{3} \frac{\varepsilon_0 \varepsilon_r \zeta_\sigma}{\eta} f(\kappa r_{NP}), \quad (5.3)$$

where  $\eta$  and  $\varepsilon_r$  are respectively the viscosity and dielectric constant of the solvent and  $\varepsilon_0$  is the vacuum permittivity. Henry's function  $f(\kappa r_{NP})$  depends on both the Debye length  $\kappa^{-1}$  expressed by Equation 5.2 and the particle average radius  $r_{NP}$ . The function  $f(\kappa r_{NP})$  varies from 1.0, for low values of  $\kappa r_{NP}$  (Hückel model), to 1.5 as  $\kappa r_{NP}$  approaches infinity

<sup>2</sup> The measurements were also performed in a concentration 3× higher, namely 0.15 g/L, resulting in similar values situated inside the error bar, hence, no significant concentration effect was observed in highly diluted conditions.

(Smoluchowski model). For the transition range between low and high  $\kappa r_{\text{NP}}$ , Ohshima [200] has provided an approximate analytical expression of  $f(\kappa r_{\text{NP}})$  as

$$f(\kappa r_{\text{NP}}) = 1 + \frac{1}{2} \left[ 1 + \frac{2.5}{\kappa r_{\text{NP}} (1 + 2e^{-\kappa r_{\text{NP}}})} \right]^{-3}. \quad (5.4)$$

The obtained zeta potential values for the N-CDs dispersions at different  $\text{pH}_i$  are presented in Table 5. The determined zeta potentials of both N-CDs are negative throughout the whole measured range and strongly pH-sensitive. This behavior is in conformity with the commonly assumed charge mechanism attributed to the deprotonation of carboxyl groups (see Equation 5.1). By increasing the  $\text{pH}_i$ , the equilibrium is dislocated towards the production of  $\text{COO}_{(\text{surf})}^-$ , resulting in a higher concentration of negatively charged surface groups, and consequently, increasingly negative values of zeta potential are generated.

**Table 5** – Zeta potential values calculated by Equation 5.3 obtained by electrophoretic mobility measurements at different pH precursor aqueous solutions for samples CD1 and CD7 at 0.05 g/L.

CD1			CD7		
$\text{pH}_i$	$\text{pH}_f$	$\zeta_\sigma(\text{mV})$	$\text{pH}_i$	$\text{pH}_f$	$\zeta_\sigma(\text{mV})$
2.0	2.0	$-16.9 \pm 0.6$	2.0	1.9	$-22.5 \pm 0.8$
4.2	3.5	$-18.0 \pm 0.5$	4.5	4.6	$-26.2 \pm 0.8$
7.2	3.9	$-19.8 \pm 0.8$	7.0	5.2	$-27.9 \pm 1.2$
9.4	4.3	$-21.4 \pm 2.1$	9.5	6.4	$-31.6 \pm 2.9$
11.4	10.4	$-28.9 \pm 7.1$	11.8	11.8	$-53.6 \pm 3.2$

In charged colloids, as N-CDs, it is generally assumed that a zeta potential higher than  $|30 \text{ mV}|$  indicates good stability against aggregation because of the sufficiently strong electrostatic repulsion between particles [201, 202]. This is consistent with the macroscopic observations, in which the highly negative zeta potential ensures a very stable sol and no phase separation is observed at  $\text{pH}_i > 11.0$ .

On the other hand, the zeta potential gradually becomes less negative as the  $\text{pH}_i$  shifts towards lower values, as a consequence of the equilibrium in Equation 5.1 being shifted towards the left-hand side, which favors the generation of neutral  $\text{COOH}_{(\text{surf})}$  surface groups. Thus, a correlation between the surface charge and the amount of precipitate can now be established, as the most pronounced sediment is observed at  $\text{pH}_i = 2.0$ , corresponding to the minimum of measured zeta values.

Considering the visual aspects and these Zeta results, the general behavior suggests that particle hydration alone is not enough to guarantee a fully dispersed system. Consequently, the surface charge development plays a major role in disassembling clusters and generating effective interparticle repulsion to prevent posterior re-aggregation. One should also keep in mind that the measured potential is a mean value over the heterogeneous particle distribution, which means that certain N-CDs might present higher or

lower surface charge density depending on the number and type of moieties per surface area. This assumption is supported by the work of Deng et al.[176], in which the CDs' hydrophilicity was shown to depend on their size, interestingly, in a non-linear behavior. Therefore, we can assume that the many degrees of aggregation observed in Figure 43 is likely a consequence of the particular hydrophilicity and surface charge state of the heterogeneous N-CD's surface structures. This heterogeneity assumption for the presented N-CDs is supported by using size exclusion chromatography (SEC) [172, 203, 204], where three different size populations could be separated (2.6 nm, 4 nm and 6 nm). The surface heterogeneity was confirmed by FTIR, and even dot-to-dot variations could be inferred via surface-dependent photophysical properties.

In spite of clear flocculation in acidic conditions, it was visually noted in Figure 44a that a substantial portion of nanoparticles must remain in suspension by the color of the supernatant, enforced by the fluorescent emission presented in Figure 44b. This behavior can be correlated with the persisting non-zero zeta potential, even in  $\text{pH}_i = 2.0$ , as observed in Table 5. It is unlikely to attribute the retaining surface charge to solely carboxyl moieties considering that the pK of these species are typically between 2.0 and 5.0 [205]. Nonetheless, the presence of oxidized nitrogen functionalities that could provide such negative charge has already been observed onto N-CDs surface of similar carbon materials [188–190]. As a matter of fact, XPS studies of the here studied N-CDs [170] revealed the presence of N-O bonds on the surface, assuring the present assumption.

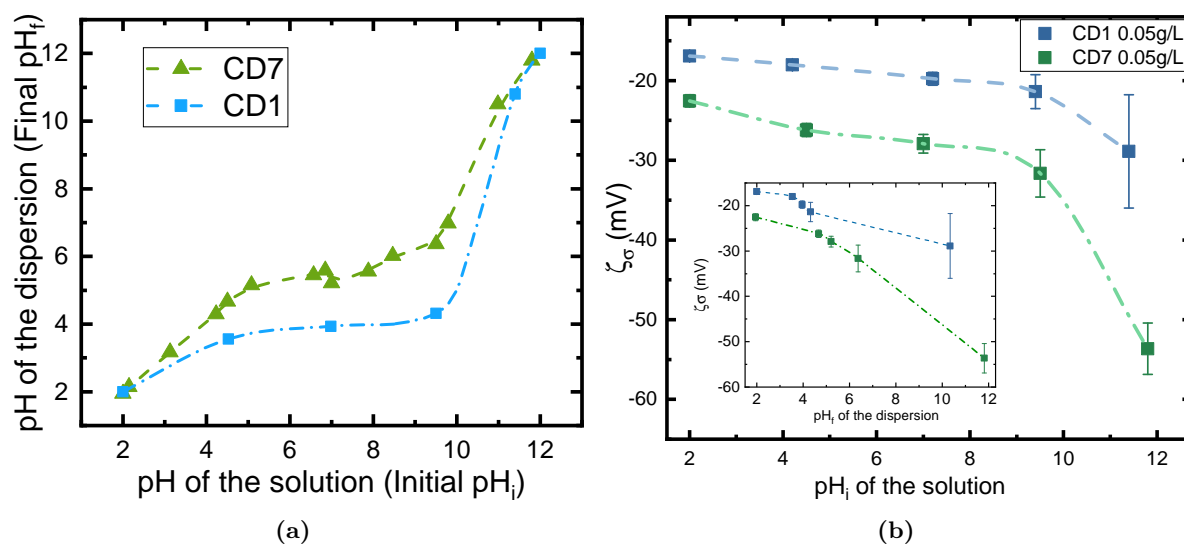


**Figure 46** – (a) Relation between the pH of the precursor aqueous solution ( $\text{pH}_i$ ) and the measured value after 24h of the dispersion protocol ( $\text{pH}_f$ ) of samples CD1 (Blue squares) and CD7 (green triangles) at 0.05 g/L. (b) Calculated Zeta potential values in different pH aqueous solutions with the addition of  $\text{NaNO}_3$  as a background electrolyte – ionic strength of  $10^{-2}$  mol/L. Inset: Values of Zeta potential as a function of the pH of the sample after 24h of the dispersion protocol. Dashed Lines are guides to the eye.

Table 5 also presents the change of the initial  $\text{pH}_i$  of the solution and the final  $\text{pH}_f$  of the dispersion. The fact that the addition of the N-CDs causes a reduction of

the  $\text{pH}_f$  confirms the acidic character of these nanoparticles, a direct consequence of the deprotonation of the surface groups. A more detailed correspondence between  $\text{pH}_i$  and  $\text{pH}_f$  is presented in Figure 46a. Note that a buffering behavior is observed for both samples, but the location of the plateau is different, while for CD1 the flat region is found somewhere between  $3.5 < \text{pH}_f < 4.5$ , for CD7 it is realized at higher value between  $4.5 < \text{pH}_f < 6$ . These values are close to the mentioned  $\text{pK}$  range for carboxyl moieties, confirming once again the presence of this presumed surface charge source. The difference between the samples indicates that the nature of the surface is in fact also changed by the N/C ratio, as previously suggested considering the intensity variations observed in FTIR profiles (see Figure 39). Thus, the increase in nitrogen content seems to shift the overall  $\text{pK}$  of the surface towards higher values, but deeper information can only be achieved via titration curves.

Back to the Zeta potential, Figure 46b exhibits a more visual representation of the evolution of  $\zeta_\sigma$  as a function of the solution  $\text{pH}_i$  and final dispersion  $\text{pH}_f$ . CD7 presents a higher zeta potential than CD1 throughout the whole  $\text{pH}$ -range. For this reason, it is very likely that CD7 bears a higher surface charge in comparison to CD1 since the samples were prepared in equal physico-chemical conditions, nonetheless, we should keep in mind that even though the behavior of the Zeta potential is quantitatively relevant, further analysis is often required considering that the values are related to the average effective screened electric potential. Besides that, it is also noticeable that at  $\text{pH} \sim 12.0$  both curves display a more prominent variation, which is much more expressive for CD7. This disparity could be associated to a few factors such as chemical alterations of the surface functional groups or the reduction of the aggregates.

Whereas the Zeta potential does not entirely comprehend the complexity of the structural surface charge mechanism, combined potentiometric-conductimetric titrations were carried out to clarify and expand the understanding of the surface properties.

### 5.3.2 Potentiometric-Conductimetric Titrations

The electrochemical measurements were acquired with a 713 Metrohm  $\text{pH}$ meter with a  $\text{pH}$  glass double-junction electrode, a 712 Metrohm Conductimeter with a conductometer using a conductivity cell specially designed for colloidal dispersions and an electronic burette 665 Metrohm Dosimat. Potentiometric and conductimetric titrations were simultaneously performed on 35 ml of N-CDs dispersions at 0.15 g/L mass concentration in acidified ( $\text{pH} \sim 2.0$ ) and alkalized ( $\text{pH} \sim 12.0$ ) aqueous medium. This mass fraction was selected in order to generate a well-resolved conductimetric curve where the distinction of strong and weak acids is evident. The titrations were performed in both directions, namely, acidic route from  $\text{pH}$  2.0 to 12.0 and alkaline route from  $\text{pH}$  12.0 to 2.0, by controlling

the titrant<sup>3</sup> addition with an electronic burette. Both potentiometer and conductometer were gauged using appropriate templates. Upon addition of the titrant, the pH and the conductivity of the sample medium are measured after equilibrium is reached. Thermal compensation is automatically applied in the measured conductivity. The titrations were performed in triplicate as usual in analytical chemistry and the results of equivalence points determinations present very low standard deviations. The titration analysis were performed by considering the deprotonation equilibrium of surface carboxyl groups according to Equation 5.1.

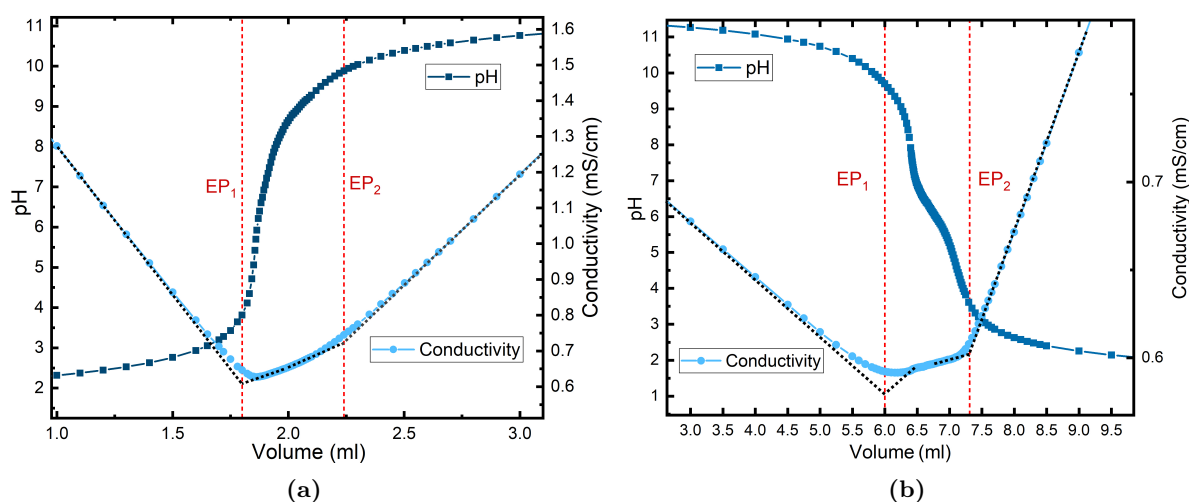


**Figure 47** – Potentiometric-conductometric titrations of CD1 sample showing the pH (dark blue squares) and conductivity (in light blue circles) as a function of titrant volume. Vertical red dashed lines indicate the equivalence points as determined from the conductivity curves and black dashed are direction lines.

Typical potentiometric-conductometric titration curves of N-CDs sample are presented in Figure 47 and 48, where the equivalence points EP<sub>1</sub> and EP<sub>2</sub> were determined by using direction lines applied to the conductometric curve [66, 73, 206]. These equivalence points delimit three distinct regions whose meaning can be described as follows. The first one corresponds to the strong acid/base titration (free H<sub>3</sub>O<sup>+</sup>/OH<sup>-</sup> ions from HNO<sub>3</sub>/NaOH in the bulk dispersion). The sharp decrease of the conductivity indicates the neutralization of H<sub>3</sub>O<sup>+</sup>/OH<sup>-</sup> ions, gradually substituted by Na<sup>+</sup>/NO<sub>3</sub><sup>-</sup> ions from the titrant solution, which present lower specific molar conductivity [207]. After EP<sub>2</sub>, the third region is related to the excess of titrant reagent, which increases the conductivity strongly due to the high specific molar conductivity of OH<sup>-</sup>/H<sub>3</sub>O<sup>+</sup> ions. The second region, between EP<sub>1</sub> and EP<sub>2</sub>, corresponds to the titration of N-CDs, i.e. the deprotonation of surface groups. The contribution of N-CDs to the conductivity is negligible due to the mass of the particles, and the slight increase in conductivity can be more appropriately assigned to the increase of Na<sup>+</sup>/NO<sub>3</sub><sup>-</sup> ions concentration from the titrant.

<sup>3</sup> The titrants were standardized HNO<sub>3</sub> and NaOH solutions, close to 0.01 mol/L, stirred and degassed by purified nitrogen during 10 minutes to avoid carbonation.

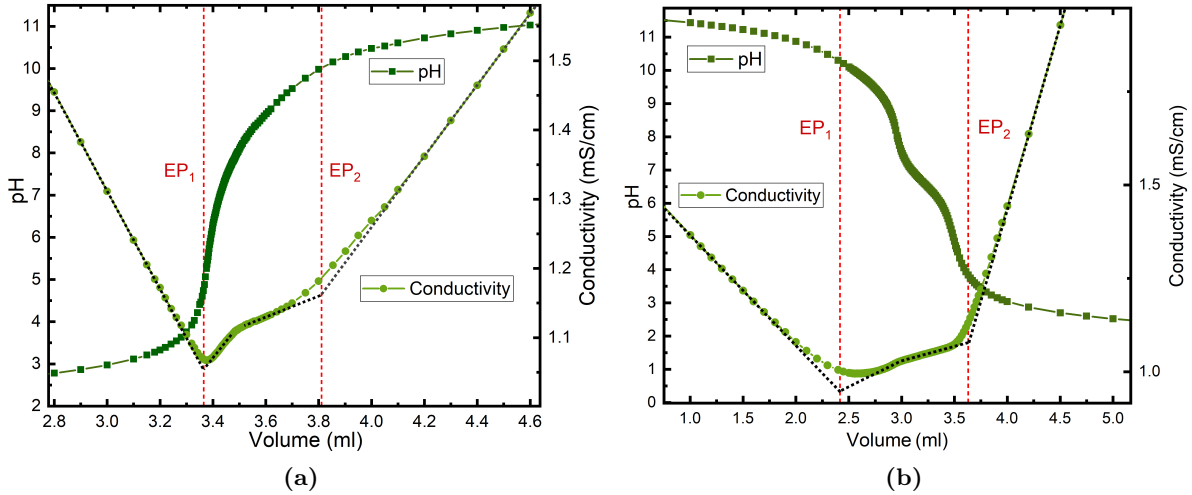


**Figure 48** – Potentiometric-conductometric titrations of CD7 sample showing the pH (dark green squares) and conductivity (in light green circles) as a function of titrant volume. Vertical dashed lines indicate the equivalence points as determined from the conductivity curves.

It can also be observed for the acidic to alkaline route exhibited in [Figure 47a](#) and [48a](#) that the potentiometric curve does not exhibit sharp changes in second region, which is consistent with the presence of different surface carboxyl groups associated to various acidic constants [208–210]. Moreover, the protons of N–H and O–H bonds related to amide and hydroxyl groups present at N-CDs surface are not titratable in the investigated pH range [211]. However, the alkaline towards acidic route presents a major change on the curve profile in comparison to the opposite route, indicating that some surface alteration might have happened.

Let us first consider the acidic to alkaline route exhibited in [Figure 47a](#) and [48a](#), the total titratable acidity of the N-CDs surface can be calculated in terms of moles of  $H_{\text{add}}^+$  per gram of sample by using the determined equivalence points and the mass of N-CDs leading to  $8.2 \pm 0.3$  mmol/g for CD1 and  $9.8 \pm 0.2$  mmol/g for CD7, values similar to the ones observed for other carbon materials [212]. Further, the charge density ( $\sigma_0$ ) can be calculated by

$$\sigma_0^{\text{sat}} = \frac{H_{\text{add}}^+ N_A}{A_p}. \quad (5.5)$$

where  $N_A$  is Avogadro's constant. However, we do not know precisely the surface area  $A_p$  of a given solid sample mass  $m_p$ . We can perform a rough estimation to have some idea of the order of magnitude of  $\sigma_0$  by theoretically calculating the surface area per gram using

$$A_p = \frac{n_{\text{NP}} A_{\text{NP}}}{m_p}, \quad (5.6)$$

where the area  $A_{\text{NP}} = \pi d_{\text{NP}}^2$  of one CD can be estimated by the average diameter  $d_{\text{NP}}$  and the number of particles per unit of volume  $n_{\text{NP}}$  can be determined by  $n_{\text{NP}} = V_{\text{NP}}/V_p$ . The particle volume  $V_{\text{NP}} = \pi d_{\text{NP}}^3/6$  and the solid sample volume  $V_p = m_p/\rho_p$  is approximated<sup>4</sup>

<sup>4</sup> It was applied the mean diameter determined in [section 4.2](#) and the density estimated in [section 4.4](#).

using the average nanoparticles diameters  $d_{\text{NP}} = d_{\text{NP}}^{\text{CD1}} = 2.0$  nm and  $d_{\text{NP}}^{\text{CD7}} = 2.5$  nm and the particle density  $\rho_p = \rho_p^{\text{CD1}} = 1.53$  g/cm<sup>3</sup> and  $\rho_p^{\text{CD7}} = 1.84$  g/cm<sup>3</sup>.

This simplified approach estimates that CD1 bears  $\sim 2.5$  e/nm<sup>2</sup> ( $\sim 0.4$  C/m<sup>2</sup>) while CD7  $\sim 4.5$  e/nm<sup>2</sup> ( $\sim 0.72$  C/m<sup>2</sup>), corresponding respectively to  $\sim 32$  and  $\sim 89$  carboxyl groups per dot. These estimates confirm a few preconceived assumptions: (1) the N-CDs surface is densely covered by polar moieties; (2) CD7 shows a higher structural surface charge than CD1 as the measured values of Zeta potential indicated; (3) CD7 presents more chargeable sites per area, corroborating the greater reduction in density.

**Table 6** – Surface parameters determined by potentiometric-conductimetric titrations evaluated by the added titrant volume between the equivalence points using Equation 5.5 and 5.6.

Sample	Route	$H_{\text{add}}^+$ (mmol/g)	$\sigma_0^{\text{sat}}$ (e/nm <sup>2</sup> )	$\equiv\text{COOH}_{(\text{surf})}$ per particle
CD1	Acidic to Alkaline	$8.2 \pm 0.3$	$\sim 2.5$	$\sim 32$
	Alkaline to Acidic	$24.6 \pm 0.7$	$\sim 7.3$	$\sim 95$
CD7	Acidic to Alkaline	$9.8 \pm 0.2$	$\sim 4.5$	$\sim 89$
	Alkaline to Acidic	$23.0 \pm 0.6$	$\sim 10.2$	$\sim 208$

So, not only the profile of the alkaline to acidic route changed, but also the quantity of titrant added in the second region more than doubled as it increased to  $24.6 \pm 0.7$  mmol/g for CD1 and  $23.0 \pm 0.06$  mmol/g for CD7, as presented in Table 6. The increment in  $H_{\text{add}}^+$  can be at first attributed to the reduction of aggregates promoted by the stronger interparticle repulsion in alkaline medium, which increases the available completely solvated surface area as a higher number of particles are no longer inside compact agglomerated structures and/or in direct contact with each other. More insights about this issue will be provided in section 5.4.

Although the disaggregation effect should present an important impact in the added volume of titrant, the calculated amount of charge per area is over  $7$  e/nm<sup>2</sup> ( $> 1.0$  C/m<sup>2</sup>) and the number of sites per particle reaches extremely high values (up to  $\sim 210$ ) that are physically unreasonable, which should be an indicator that the calculated surface area could have been underestimated. Moreover, the variation in shape of the potentiometric curve suggests modifications in the pK of the surface as a consequence of some sort of pH-induced chemical reaction, that could have generated more chargeable functional groups. For this reasons, in the following section it will be discussed a possible explanation for this peculiar behavior.

### 5.3.3 Surface Charge

Based on the titrations results, the pH-dependence of the concentration of acidic surface groups of N-CDs can be approximately evaluated in a model considering that number

of carboxyl groups per gram [ $\equiv \text{COOH}_{(\text{surf})}\text{T}$ ] is constant until  $\text{EP}_1$ . Then, the deprotonation process begins and the concentration of carboxylate surface groups [ $\equiv \text{COO}^-_{(\text{surf})}$ ] progressively increases until the pH corresponding to  $\text{EP}_2$ , where its maximum value is reached. Then, by applying the proton balance equation in the region between  $\text{EP}_1$  and  $\text{EP}_2$ , the variation of [ $\equiv \text{COO}^-_{(\text{surf})}$ ] with pH can be expressed as [213]:

$$\begin{aligned} [\equiv \text{COO}^-_{(\text{surf})}] = \frac{1}{m_p} \left\{ (V_i + V_{\text{EP}_1}) \left( [\text{H}_3\text{O}^+]_{\text{EP}_1} - [\text{OH}^-]_{\text{EP}_1} \right) + V_t C_t \right. \\ \left. - (V_i + V_{\text{EP}_1} + V_t) \left( [\text{H}_3\text{O}^+]_f - [\text{OH}^-]_f \right) \right\}, \end{aligned} \quad (5.7)$$

where  $m_p$  is the mass of N-CDs sample,  $V_i$  is the initial volume of the N-CDs samples,  $V_{\text{EP}_1}$  and  $V_t$  are the volume of titrant added until  $\text{EP}_1$  and from  $\text{EP}_1$ , respectively,  $[\text{H}_3\text{O}^+]_{\text{EP}_1}$  and  $[\text{OH}^-]_{\text{EP}_1}$  are the molar concentration of  $\text{H}_3\text{O}^+$  ions and  $\text{OH}^-$  ions at  $\text{EP}_1$ ,  $C_t$  is the molar concentration of titrant and  $[\text{H}_3\text{O}^+]_f$  ( $[\text{OH}^-]_f$ ) are the equilibrium concentration of  $\text{H}_3\text{O}^+$  ( $\text{OH}^-$ ) ions. In this model, the surface charge density of carboxylate groups ( $\sigma_{\text{COO}^-}$ ) as a function of pH can be estimated as

$$\sigma_{\text{COO}^-} = [\equiv \text{COO}^-_{(\text{surf})}] N_A e, \quad (5.8)$$

where the surface charge is going to be expressed in Coulombs per unit of mass due to the uncertainty in the samples' surface area. In order to cross the analysis of the potentiometric-conductometric titrations with that of zeta potential measurements, we have calculated the electrokinetic charge density ( $\sigma_\zeta$ ) through the following empirical formula [214–216]:

$$\sigma_\zeta = \frac{\varepsilon_0 \varepsilon_r k T}{e} \kappa \left[ 2 \sinh \left( \frac{e \zeta \sigma}{2 k T} \right) + \frac{4}{\kappa r} \tanh \left( \frac{e \zeta \sigma}{4 k T} \right) \right], \quad (5.9)$$

where  $k$  is the Boltzmann constant and  $T$  the temperature. On one hand,  $\sigma_{\text{COO}^-}$  is directly proportional to the concentration of carboxylate groups onto N-CDs surface, therefore, in absence of specific adsorption, this parameter can be finely tuned by the pH. On the other hand,  $\sigma_\zeta$  is particularly dependent on the ionic strength of the dispersion since the electrokinetic charge density is defined as the effective electric charge normalized on the area of the slip plane in the electric double layer [217].

Figure 49 shows the pH-dependence of  $\sigma_{\text{COO}^-}$  and  $\sigma_\zeta$  evaluated using Equation 5.8 and 5.9, respectively. Note that the right and left vertical axis in Figure 49 (a) and (b) were aligned just for the convenience of the qualitatively analysis the pH-dependency – the two scales are *not* quantitatively comparable – as  $\sigma_\zeta$  is expressed in  $\text{C}/\text{m}^2$  while  $\sigma_{\text{COO}^-}$  was calculated in  $\text{C}/\text{mg}$  due to the mentioned experimental limitations.

Based on the acidity range of the carboxyl groups, the concentration of carboxylate groups at  $\text{pH} = 2.0$  is zero, leading to  $\sigma_{\text{COO}^-} = 0$ . However, the particles present a

negative electrokinetic charge density at this highly acidic pH ( $\sigma_{\zeta}^{\text{CD1}} = -0.016 \text{ C/m}^2$  and  $\sigma_{\zeta}^{\text{CD7}} = -0.019 \text{ C/m}^2$ ), which can be attributed to the presence of oxidized nitrogen functionalities, as already observed for similar carbon materials [188–190]. As a matter of fact, XPS studies of these CDs [170] revealed the presence of N–O bonds on the surface, confirming the present conclusion. This can also explain the reason why CD7 presents a slight more negative value throughout the whole range of pH, since the higher N-content in the synthesis precursor could have propitiated the formation of a few more N–O functionalities.

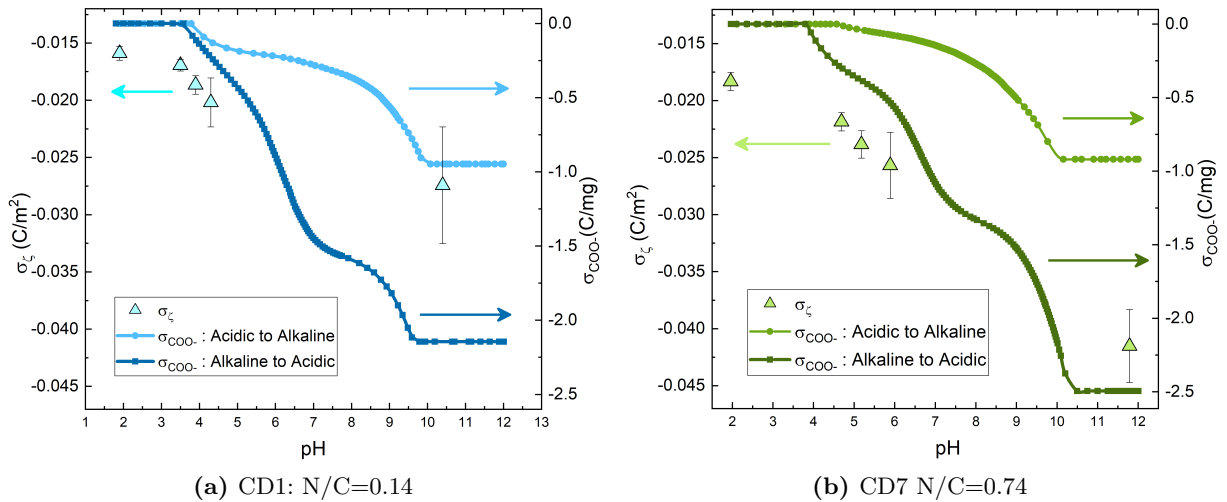


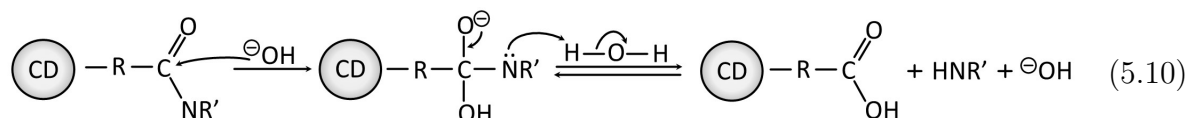
**Figure 49** – The pH-dependence of  $\sigma_{\text{COO}^-}$  and  $\sigma_{\zeta}$  evaluated using Equation 5.8 and 5.9, respectively. The right and left vertical axis are independent and the alignment was performed only for qualitative analysis.

The profiles of  $\sigma_{\zeta}$  and  $\sigma_{\text{COO}^-}$  exhibit the same general trend for both CD1 and CD7 samples, capturing also the deeper reduction at  $\text{pH} > 10.0$ . The fact that the zeta points concentrated at pHs between 3.5 – 4.5 for CD1 and 4.5 – 6 correlates with the beginning of the surface charging process. This effect is a consequence of the deprotonation of carboxyl surface groups being triggered off by the added base and – for the same reason – the  $\text{pH}_f$  of the buffering plateau (see Figure 46a) is located at similar values. Also, the pH-range of surface charging (i.e. the region in between the EPs of the acidic to alkaline route) follows the same  $\text{pH}_i$ -interval of the buffering region for both samples, confirming the starting and end points of the surface charge development.

Here, it is even more clear the already mentioned difference in saturation charge  $\sigma_{\text{COO}^-}^{\text{sat}}$  between the charging (acidic-alkaline) and the discharging (alkaline-acidic) routes. The charging curve starts with a gentle decay (more timid for CD7) and – after an inversion of the concavity – reaches the charge saturation. On the other hand, in the discharging curve the starting point of the first decay is dislocated towards lower values, with a more accentuated variation for CD7. It also shows a steeper behavior in this region between pHs 4.0 – 5.5 and an even steeper novel charge variation in pHs 5.5 – 8.0. The pK values between 6 and 8 have already been observed in carbonaceous particles where they were

attributed to hydrolyzed lactones or even carboxylic anhydride groups [208, 209]. However, considering that the appearance of this new features occurred after the sample was exposed to a highly alkaline condition, these variations suggest that the change in the overall pK of the surface could actually be in response to pH-induced chemical reactions that altered the nature of some surface groups.

We hypothesize that the hydrolysis of the amide functional groups could be the possible mechanism for this surface modifications, following the reaction [218]



where the conversion into  $\equiv\text{COOH}_{\text{surf}}$  groups would provide the additional charge in the first region and generate the weaker acidic character of the second region as a consequence of the diversity of the attached organic groups R.

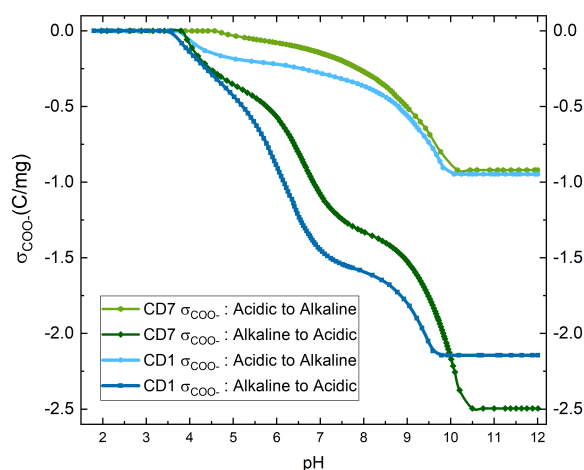


**Figure 50** – Comparison of the charge density development between samples CD1 and CD7 determined by the potentiometric-conductimetric titrations.

Figure 50 shows the comparison of the two samples where the superposition of a few regions are observed. The acidic to alkaline routes show a very similar behavior reaching almost the same saturation value, although for CD1 the surface charge develops in lower values of the pH, while CD7 balances out after pH 8.5. It is worth to remember that the actual value of charge per surface is most likely different between CD1 and CD7 because of the divergences in size, density, length and type of surface groups.

For the alkaline to acidic routes, the first decay is significantly more alike, but the intermediary region is once again more prominent for CD1. After pH 8.0 till the charge saturation, the variation  $\Delta\sigma_{\text{COO}^-}$  for CD1 does not show a significant difference between the two routes, remaining at  $\Delta\sigma_{\text{COO}^-} \sim -0.6$  C/mg in both situations. Nonetheless, for CD7 the value almost doubles, shifting from  $\Delta\sigma_{\text{COO}^-} = -0.65$  to  $-1.2$  C/mg. Therefore, the actual final difference in charge between CD1 and CD7 is mostly related to groups

with very weak acidity, that may undergo chemical alterations in alkaline media solely in sample CD7.

## 5.4 Nanoscale Organization

If the results obtained from the visual observations and the surface charge development in aqueous media are combined, we could already trace a general panorama on the macro to microscopical colloidal stability. Certainly, the eventually formed precipitate contains aggregated N-CDs, nonetheless, we are still not aware of the agglomeration state of the highly stable supernatant in lower scales.

Further, it was observed a variation of the surface composition between the two types of N-CDs, showing a considerable impact on the surface charge – specially in highly alkaline media. Taking into account that the surface charge development plays a critical role in the microscopical particle organization, the surface differences are likely to also influence the nanoscale structuration of the fluid, justifying the hereafter conducted investigation.

Consequently, we probe the nanoscale nanoparticle ordering using three different techniques: transmission electrons microscopy (TEM) provides some superficial insights of the possible particle aggregation states, keeping in mind that the images were acquired in dried sample; on the other hand, dynamic light scattering (DLS) was performed in the aqueous dispersion, thus providing an average hydrodynamic diameter in different pHs. Gravitation sedimentation and ultracentrifugations were investigated to determine a critical size limit that allows the sample separation via centripetal force; finally, small angle X-ray scattering (SAXS) measurements were performed in order to highlight the interparticle organization and nanoscale time evolution.

### 5.4.1 Transmission Electron Microscopy

Transmission electron microscopy images were acquired following the same procedure described previously when discussing the N-CDs size (see [section 4.2](#)), but here we explore a larger scale. Which means that the sample was initially diluted in aqueous media, but later deposited onto the substrate by means of the complete evaporation of the solvent. Thereupon, aggregation effects inevitably took place – even for well-dispersed N-CDs – yet two different conformations were noted, as in [Figure 51](#). The image of the CD1 sample shows lower density clusters formed by a single or just a few layers of aggregated N-CDs. They are observed concomitantly with higher density clusters displaying conspicuous three-dimensionality, which is evidenced by the increased contrast due to the superposition of the nanoparticles. This high density clusters were solely observed in CD1 images, while for CD7 they were not found, which does not rule out the possibility of their existence, after all they could just be more uncommon.

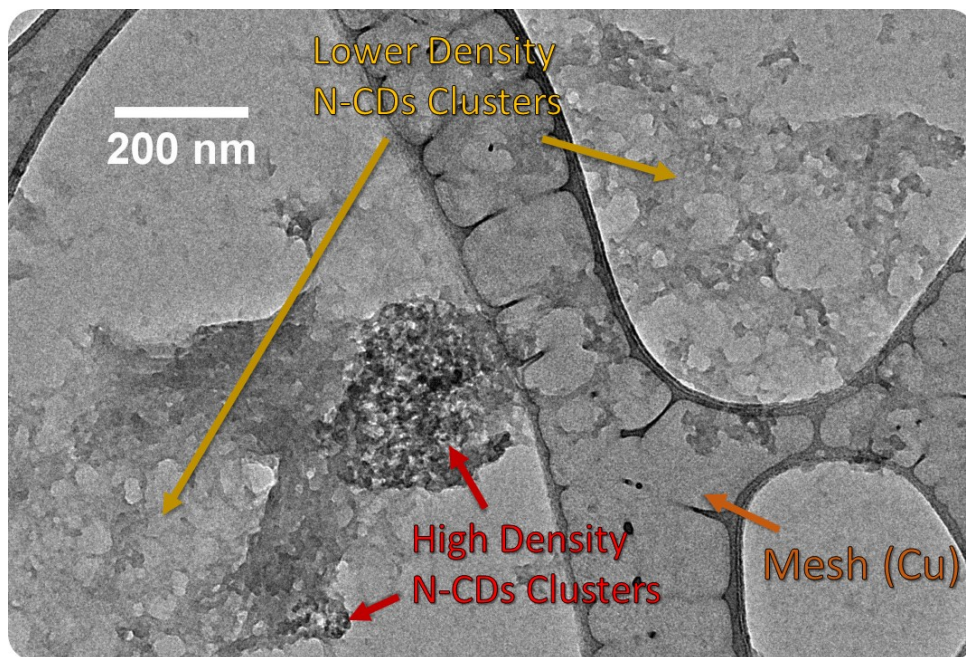


**Figure 51** – Transmission electron microscopy of sample CD1 evidencing different regimes of aggregation of the N-CDs.

Such heterogeneous pattern is visually alike to what was observed by optical microscopy of the precipitate, although in a few orders of magnitude lower. Here, the compact agglomerates were also realized isolated from other particle clusters as shown in [Figure 52](#). They exhibit irregular shapes with certain anisotropy as the thickness ranges from tens to a few hundreds of nanometers.

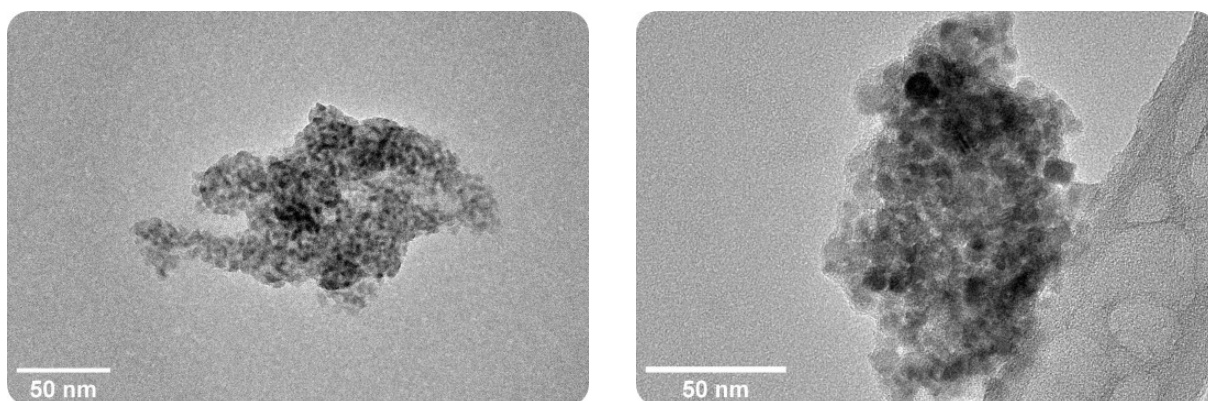


**Figure 52** – Transmission electron microscopy of CD1 sample evidencing two different isolated high density clusters.

Following the interpretation applied to the microscopical observations, we can presuppose that some of these aggregates were present before the solvent evaporation, as they were never broken apart in the dispersion process. On the other hand, they could have progressively grown in size as the interparticle distance was reduced and the overall interaction potential became attractive due the solvent removal. The first seems to be

more likely the case of the high density aggregates, while the latter situation could be associated with the the lower density, following the reasoning considered in [section 5.2](#).

Whereas in light of the exposed difficulties of correctly determining the previous dispersed state of the system, the next sections will be dedicated in probing the samples in liquid media by light and X-ray scattering techniques to gain deeper understanding in the particle organization of the supernatants at the nanoscale.

### 5.4.2 Dynamic Light Scattering (DLS)

Dynamic light scattering measurements were performed in a VASCO nanoparticle analyzer (Cordouan) to evaluate the hydrodynamic diameters ( $d_H$ ) of the supernatants of the samples. The size was measured at neutral pH in different particle concentrations (0.3, 1.0 and 10.0 g/L) which were subjected to natural gravitational sedimentation up to 14 days. Also, using a Optima 70 ultracentrifuge with a type 100 Ti fixed-angle rotor (Beckman Coulter) we checked by ultracentrifugation a higher separation force of  $\sim 10.000\times g$  in highly concentrated dispersions (30 g/L). The samples were dispersed in distilled water and in alkaline medium (with NaOH at pH 12.0) following the typical protocol (see [section 5.1](#)).

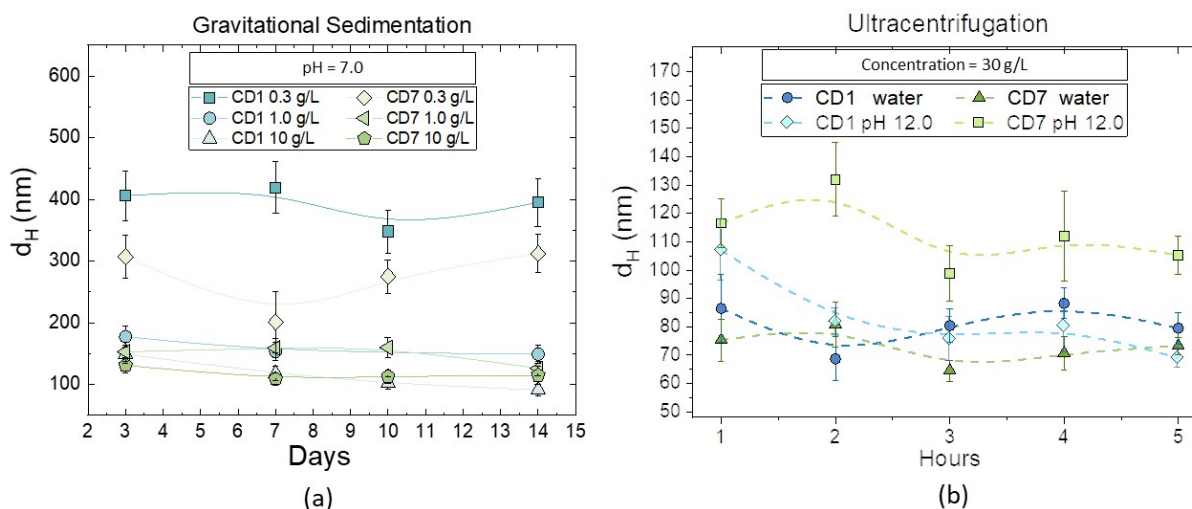


**Figure 53** – Hydrodynamic diameters determined by DLS measurements of (a) the supernatants removed after 3, 7, 10 and 14 days of gravitational sedimentation at different concentration dispersed in pure water and of (b) ultracentrifugation over 1, 2, 3, 4 and 5 hours of the supernatant of samples prepared at 30 g/L in pure water and at pH 12.

[Figure 53a](#) shows the results in which the samples were let at rest, thus, only subjected to the natural gravitational force ( $1.0 \times g$ ). The measured average size between  $100 < d_H < 500$  nm indicates the presence of nanoscale aggregates that does not significantly precipitate throughout the two weeks of observation. Although the supernatant presents N-CD's aggregates, the sub-micrometric diameter allows the visual homogeneity observed in the optical microscopy images (see [Figure 44](#)).

The DLS technique measures an average volume-based diameter, therefore, bigger particles present a higher signal compared to the smaller ones. With that in mind, we can assume that the decrease in diameter as the concentration increases could be associated with a statistical effect, because as the number of well-dispersed N-CDs and smaller aggregates in the supernatant increases, there is a higher significance of their optical signal in the auto-correlation function. The average diameter observed in higher concentrations  $d_H \sim 150$  nm presents a similar size of the high density aggregates observed in TEM images (see [Figure 52](#)), supporting the hypothesis that these type of aggregates were indeed already present in the aqueous dispersion.

The ultracentrifugation results exhibited in [Figure 53b](#) show that  $d_H$  can in fact be reduced to values close to 80 nm in pure water for both samples. It seems to be the critical diameter for this amount of force considering that the measured value only exhibits small fluctuations after the first hour, at least in this time window. The achieved  $d_H$  limit should be a consequence of the agglomerate's density<sup>5</sup> and the disassembly capacity in the medium, thus the obtained results reflect this expected sized variation due to the sample physico-chemical conditions.

At pH 12.0, the size reduction observed for CD1 presents similar values of the ones found at pure water, nonetheless for CD7  $d_H$  remains close to the 100 nm limit. This cannot be directly associated with an increase in surface charge as CD1 also presents a charge augmentation at alkaline conditions, hence an additional factor might influence in this effect. One hypothesis is that the difference in aggregate size is a consequence of the various surface states that change from dot to dot. The aggregates that are easily broken down by hydrophilic effects enter in dispersion at lower pH, as the less hydrophilic particles remain in clusters with average size higher above the critical diameter. The same reasoning can be reproduced considering the discrepancy in higher/lower chargeable surface groups per particle. As the surface charge increases in alkaline medium, these clusters gradually break apart with the aid of a stronger electrostatic repulsion, but since they are naturally more difficult to be reduced so their average size can be higher.

In the next section we present SAXS results that should provide useful information about the structural organization of these aggregates.

### 5.4.3 Small Angle X-ray Scattering (SAXS)

Small angle X-ray scattering (SAXS) measurements were performed at the Brazilian National Synchrotron Light Laboratory (LNLS) at the line SAXS01. This powerful X-ray source was essential to generate well-defined scattering profiles, since the experimental data naturally contains large amounts of noise as a consequence of the low water and carbon

<sup>5</sup> It will also depend on the temperature, gravity acceleration, viscosity and density of the solvent, but this parameters are fixed in each measurement series.

contrast. Nevertheless, these measurements were performed before the booster and storage ring were upgraded to the current SIRIUS facility, so at that moment, the beam intensity was still not capable to resolve very diluted samples in a reasonable exposure time. Hence, the following results are performed in moderate to high particle concentration (0.5–30 g/L) relative to the values usually employed in the literature when studying the fluorescence phenomenon ( $< 0.1$  g/L). The data was acquired in the  $0.14$  to  $0.52$   $\text{nm}^{-1}$   $Q$ -range, allowing us to obtain a reasonable portion of the curve profile. Our goal is to understand the particle organization of the well-dispersed portion of the sample, considering that the general condition of the precipitate can already be mostly observed in the microscopical range. Consequently, the following results are mainly focus on supernatants at different pH-values achieved by natural gravitational sedimentation or ultracentrifugation.

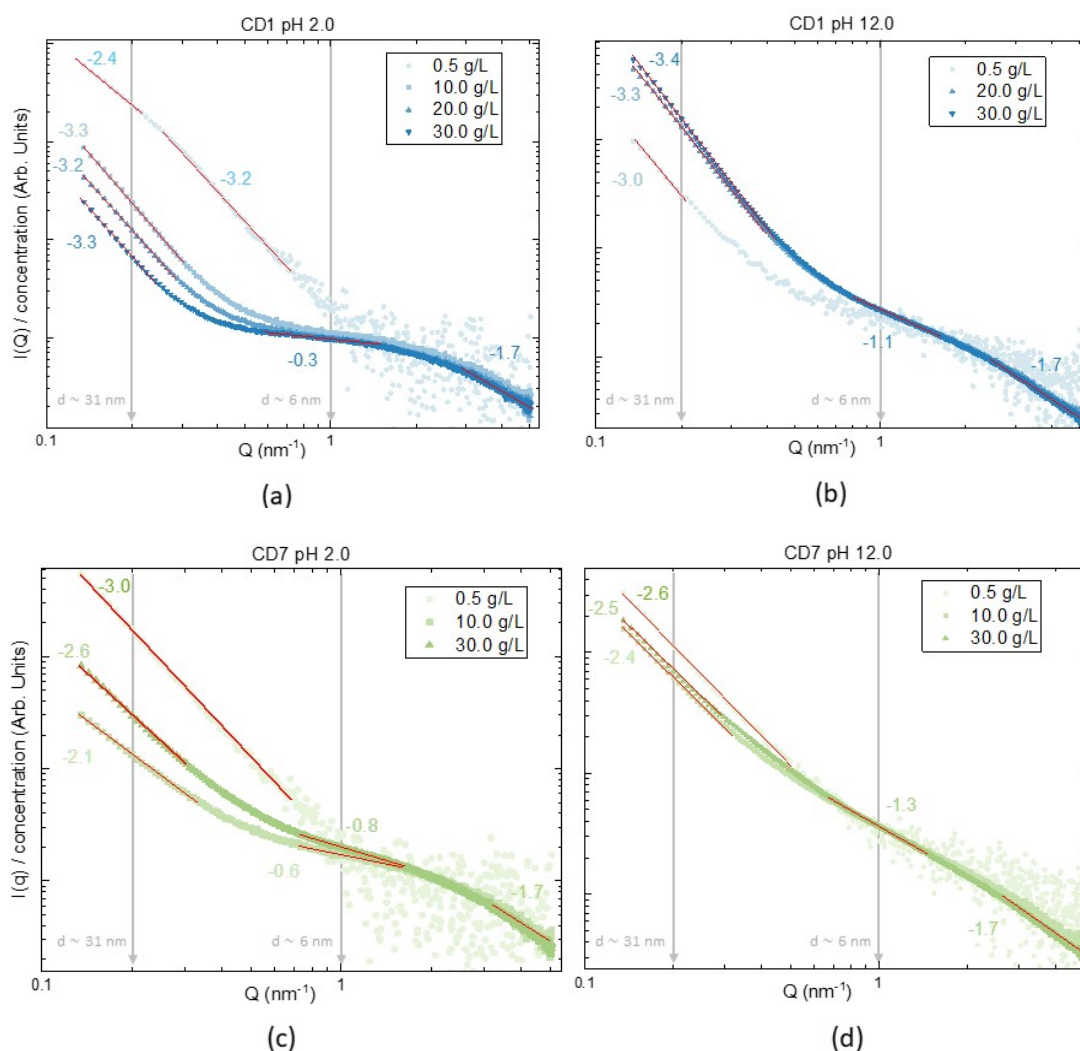


**Figure 54** – Normalized SAXS intensity profiles of CD1 and CD7 samples at different concentrations dispersed in acidic and alkaline media.

The intensity profiles of the supernatants obtained through gravitational sedimentation of CD1 and CD7 in different N-CDs concentrations at the extreme pHs 2.0 and 12.0 are exhibited in Figure 54. The curves were set at arbitrary units considering that

the present analysis do not required the intensity in absolute scale ( $\text{cm}^{-1}$ ), yet they were normalized by the mass concentration, so keep in mind that the more concentrated curves might be actually up to  $60\times$  more intense than the diluted ones. The previously mentioned statistical relevance of the smaller particles signal over the larger aggregates can be here observed through the noise reduction of the 0.5 g/L curve for values of  $Q > 1.0 \text{ nm}^{-1}$  as the N-CDs concentration increases. Note that the noise is also significantly reduced at pH 12.0, in agreement with the observed reduction of the precipitate, which increases the number of particles in the supernatant.

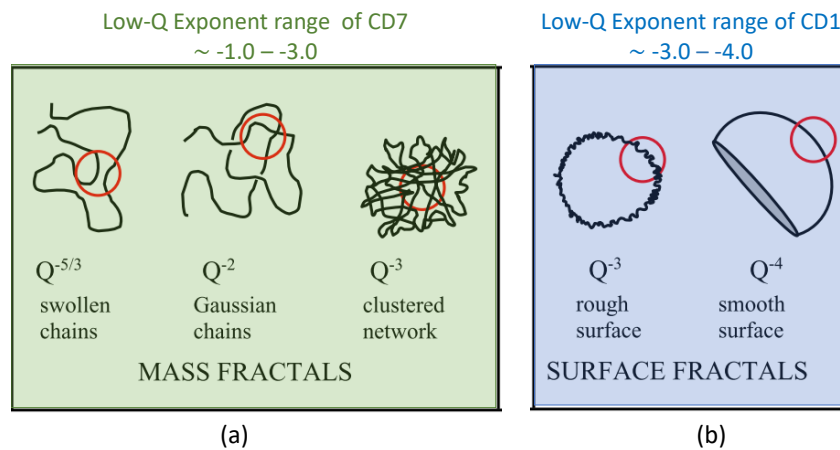


**Figure 55** – Exponent law of fractal structures: mass fractals range from  $-1.0$  low-density clusters to  $-3.0$  for condensed cluster networks, while surface fractals range from  $-3.0$  rough surfaces to  $-4.0$  to perfectly smooth ones. Figure adapted from ref.[219].

We start by acknowledging that the exponent of the intensity profiles at the Guinier region ( $Q \ll 2\pi/d_{\text{NP}}$ , where  $d_{\text{NP}}$  is the volume-averaged diameter) of non-interactive globular objects tends to zero, which is not the case observed here. The intensity increase in low- $Q$  values can thus be associated with the presence of aggregates, as already indicated by DLS measurements. These curve profiles are similar to the ones reported in SAXS studies performed with carbon blacks [220, 221] – the much larger ( $d_{\text{NP}} \sim 10 - 50 \text{ nm}$ ) predecessors of CDs – which also presented multiple shifts of the exponents due to aggregation effects. Interestingly, the range of the power law variation in the Guinier region ( $0.15 < Q < 0.6 \text{ nm}^{-1}$ ) is characteristic of each sample. For CD1 the exponent varies from  $-3.0$  to  $-3.4$  and for CD7 from  $-2.1$  to  $-3.0$ , characterizing the formation of surface fractals and mass fractals, respectively. Figure 55 illustrates the morphology of fractal structures due to the self-similarity behavior of the particle assembly. The exponent of the scattering vector  $Q^{-\alpha}$  varies from  $1 < \alpha < 3$  for mass fractals and from  $3 < \alpha < 4$  for surface fractals – determined by the fractal dimension  $D_f$  – which is  $D_f^m = 6 - \alpha$  for the former and  $D_f^s = \alpha$  for the latter.

Therefore, from this initial exponent analysis we can associate the general aggregate morphology of CD1 as globular rough objects, supporting the clusters configuration observed by TEM images (Figure 52), while CD7 presents a less dense configuration

transitioning from a clustered network towards possibly chain-like or lamellar configurations. A direct link between the aggregate structure and the surface charge cannot be established considering that the exponent does not present major changes from acidic to alkaline conditions, consequently, it is more likely that the difference arises from the nature of the surface groups and particle hydrophilicity. Besides the already considered greater density reduction, the higher pK of CD7 in comparison to CD1 could indicate a more extensive surface layer, since in general the pK increases with the enlargement of the alkyl chain [222]. These observations imply that a higher solvation combined with a longer steric repulsion could reduce the internal packing of the aggregates that remain dispersed.

The intermediary plateau observed in Figure 54a and 54c at  $0.5 < Q < 2.0 \text{ nm}^{-1}$  characterized by the change in concavity of the curve can be interpreted as the transition from the high- $Q$  Porod region dominated by N-CDs form factor  $P(Q)$  (since the structure factor  $S(Q) \rightarrow 1$ ) to the highly interacting Guinier region at low- $Q$  corresponding to the signal of the nanostructures assembled by the CDs. The greater the disparity in size and volume fraction between the large nanostructures in relation to the single CD particle, the broader is the plateau. The high- $Q$  exponent characteristic of the sphere's form factor ( $\alpha = 4$ ) cannot be observed, firstly, because of the experimental setup that limited the  $Q$ -range, but most importantly due to a background signal generated by the diffraction of the internal crystalline structure, as observed in refs. [220, 223] for carbonaceous materials. Saurel et al.[223] approaches the background reduction by fitting the first diffraction peak, but here higher angles were not probed, so this procedure could not be performed. Notwithstanding, this effect will not impact largely the following modeling of the system, as the implementation of a constant background will suffice to work around the issue.

A highly detailed modeling of systems presenting various degrees of organization – like the multi-scale structure here observed – is an analysis challenge due to a few reasons: If the approach is too general and implements a large number of adjusting parameters it can lose reliability as the fitting values are not sufficiently constrained, on the other hand, a deeply strict model might not capture the peculiarities of the structural organization and will not be able to adjust the experimental data at some point. For the moment, due to the limitations of the  $Q$ -range of experimental data, we are not able to precisely analyse the data quantitatively. Thus, the modeling of the system will be done in the future with additional results to be measured.

With that in mind, we consider the implementation of a binary hard sphere model to qualitatively analyse the system evolution over time. Considering that the aggregates behave as surface fractals, we can separate the experimental  $I(Q)$  in two Porod regions, one located at low- $Q$  (agglomerates) and one at high- $Q$  (single N-CDs) with respect to the intermediary plateau. This allows us to interpret the aggregates as a distribution of larger spheres composed by another distribution of smaller spheres, avoiding a direct

implementation of the structure factor of the internal structure. This simple non-interactive model will better reproduce the system's  $I(Q)$  profile as lower is the aggregate volume fraction, since this condition flattens the intermediary plateau as it reduces, proportionally, the structure factor contribution emerging from the nanoparticle correlation and ordering inside the agglomerates. The theoretical fits were generated by the software package developed by the NIST Center for Neutron Research (NCNR) [224] using a Bimodal Schulz Sphere Model in order to also incorporate the size polydispersity of the N-CDs and agglomerates. Considering the additive properties of the SAXS  $I(Q)$ , the total intensity in this binary model  $I_{\text{BM}}(Q)$  equals to

$$I_{\text{BM}}(Q) = I_{\text{BM}}^{\text{agg}}(Q) + I_{\text{BM}}^{\text{NP}}(Q) + bkg \quad (5.11)$$

where  $I_{\text{BM}}^{\text{agg}}(Q)$  and  $I_{\text{BM}}^{\text{NP}}(Q)$  are respectively the scattering intensity of the aggregated objects and of the individual N-CDs, that can be completely free or generating the larger nanostructures and  $bkg$  is a background signal. The independent intensities can then be written as

$$I_{\text{BM}}(Q) = \left[ \left( \frac{4\pi}{3} \right)^2 n_{\text{agg}} \Delta\rho^2 \int_0^\infty P_{\text{Schulz}}(R_{\text{agg}}) R_{\text{agg}}^6 P_{\text{sphr}}(QR_{\text{agg}}) dR_{\text{agg}} \right] + \left[ \left( \frac{4\pi}{3} \right)^2 n_{\text{NP}} \Delta\rho^2 \int_0^\infty P_{\text{Schulz}}(R_{\text{NP}}) R_{\text{NP}}^6 P_{\text{sphr}}(QR_{\text{NP}}) dR_{\text{NP}} \right] + bkg, \quad (5.12)$$

where  $R_{\text{NP}}$  ( $R_{\text{agg}}$ ) is the radius of the NPs (aggregates),  $n_{\text{NP}}$  ( $n_{\text{agg}}$ ) is the number of NPs (aggregates) per unit of volume and  $\Delta\rho$  is the contrast (difference in scattering length density between the CDs and the medium).  $P_{\text{sphr}}(Q)$  is the normalized form factor of a sphere with radius  $R$  [225]

$$P_{\text{sphr}}(Q) = \left[ 3 \cdot \frac{\sin(QR) - QR \cos(QR)}{(QR)^3} \right]^2 \quad (5.13)$$

and  $P_{\text{Schulz}}(R)$  is the normalized Schulz distribution [224] determined by

$$P_{\text{Schulz}}(R) = (s_0^{-2})^{s_0^{-2}} (R/r_0)^{(s_0^{-2}-1)} \cdot \frac{\exp[-s_0^{-2}(R/r_0)]}{r_0 \Gamma(s_0^{-2})}, \quad (5.14)$$

where  $s_0$  is the polydispersity,  $r_0$  is the median radius and  $\Gamma(x)$  is the gamma function. **Figure 56** shows the curve evolution for two variations: (a) the decrease in volume fraction of the aggregates creates a shift towards the left bottom corner due to an intensity reduction; (b) the increase in aggregate size creates a shift towards the left upper corner – since the scattered intensity increases with the particle volume and the Porod region gets dislocated towards lower  $Q$ -values (i.e. higher  $d$ 's).

The experimental challenges that hinders a proper fit of **Equation 5.12** to the data presented in **Figure 54** emerges from two issues: first, we need to be confident of the N-CDs form factor. The second matter lies on the fact that either decreasing the concentration or

increasing the size, both show a similar behavior in intermediary  $Q$ -values, as presented in Figure 56. The ambiguity can be observed at  $Q = 0.1 \text{ nm}^{-1}$  for the middle values of  $\Phi^{\text{agg}}/40$  and  $/100$  and the intermediary values of  $4 \times$  and  $8 \times d_0^{\text{agg}}$ . As a consequence, it is of paramount importance to have access to scattering vectors  $Q \ll 2\pi/d_0^{\text{agg}}$ , enabling the uniquely determination of the aggregate size and its volume fraction. Still, in this reduced range we can perform some qualitative analysis using the general curve behavior, which might provide a dynamic perspective on the  $\phi^{\text{agg}}$ -development in sedimentation effects.

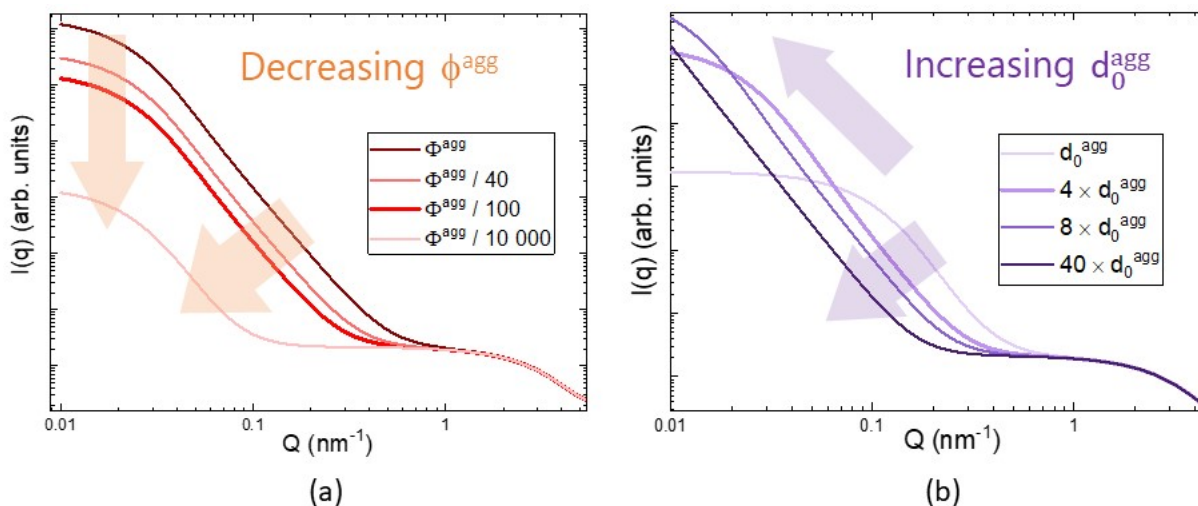


**Figure 56** – Theoretical  $I(Q)$ 's of a bimodal Schulz sphere model exemplifying curve developments by the reduction of the relative volume fraction of the aggregates  $\Phi^{\text{agg}}$  and the increase in their size  $d_0^{\text{agg}}$ .

At 30 g/L, a gradual precipitate formation can be promptly observed over the course of a few minutes at pH 2.0, while it is not completely evident at pH 12.0. Taking into account the mentioned surface charge development, one could have anticipated the visual nuances generated at these two pHs. Else, the substantial reduction in solubility is naturally expected to occur considering that 30 g/L is a fairly high particle concentration for this kind of N-CDs dispersions. Then, to check the evolution of the system at nanoscale, time-dependent SAXS measurements were performed by acquiring 60 subsequent shots of 1 minute – adding up to one complete hour – of the samples homogenized using the usual dispersion protocol. In addition, the samples were manually agitated immediately before the beginning of the measurement procedure, assuring the maximum amount of particles in suspension. Certainly, there are aggregates at the microscopical scale in the analysed samples, however, the focus of these measurements is to probe the unclear sedimentation effect at the sub-micrometric level, which cannot be detected in optical microscopy.

The evolution of the intensity profiles  $I(Q, t)$  are shown in Figure 57. Following the macroscopic observations, Figure 57a and 57c at pH 2.0 show stronger intensity changes over time if compared with 57b and 57d at pH 12.0, indicating an improvement of the colloidal stability as the general intensity reduction can be closely associated to

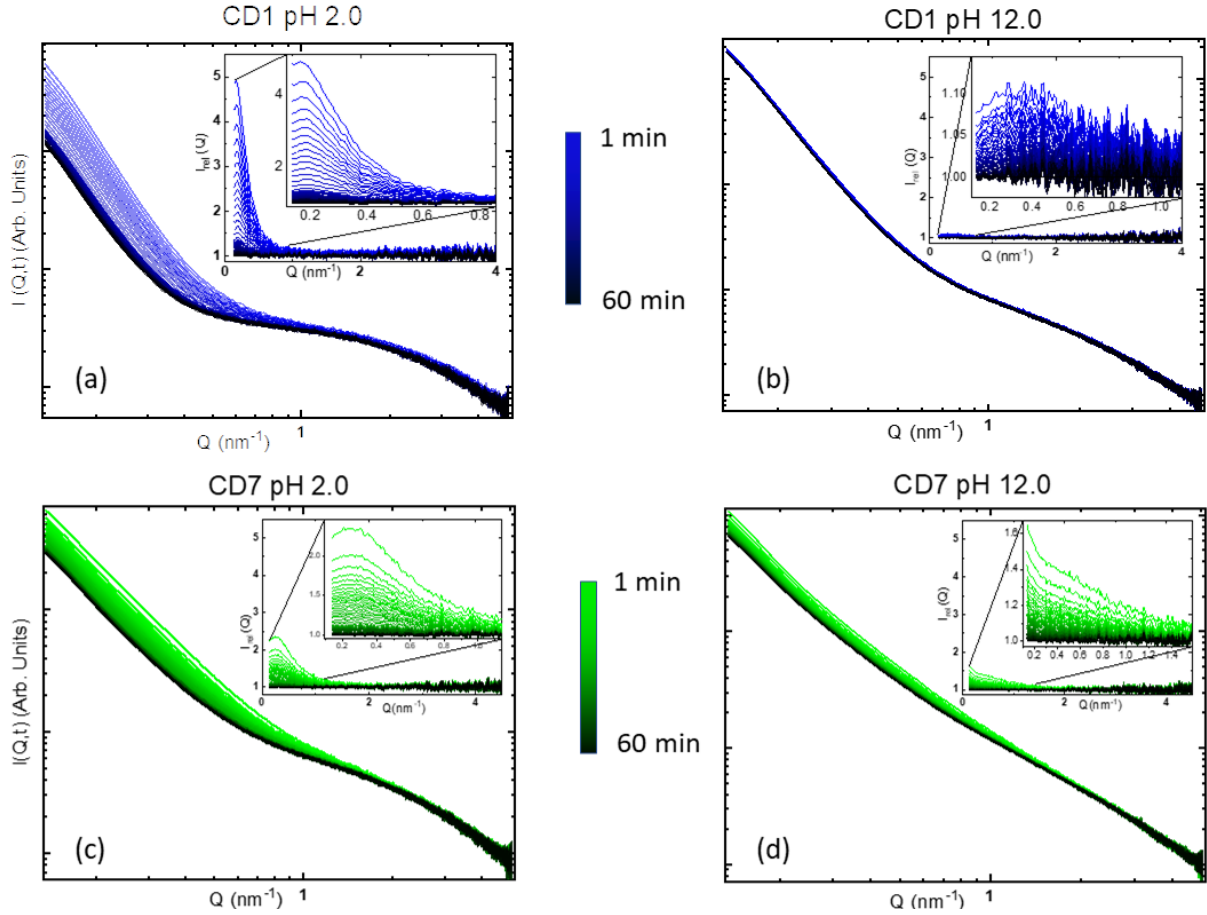


**Figure 57** – Evolution of the intensity profiles of samples CD1 and CD7 at pH 2.0 and 12.0. The curves were acquired by 1 minute shots over an hour immediately after manually agitating the samples. *Insets*: a relative experimental intensities of calculated by Equation 5.15.

the total number of particles in suspension. Experimentally, the observed intensity shift would thus correspond to the sedimentation of particles with dimensions above a critical diameter that move from the probing region of the X-ray beam to the bottom of the sample cell as a consequence of the gravitational potential. This description is supported by the theoretically calculated pattern exhibited in Figure 56a corresponding to a decrease in  $\Phi_{\text{agg}}$ .

The insets of the four graphs presented in Figure 57 exhibit an experimentally determined relative intensity  $I_{\text{rel}}(Q, t)$  calculated as a function of the last measured intensity profile  $I(Q, t_f = 60 \text{ min})$  as

$$I_{\text{rel}}(Q, t) = \frac{I(Q, t)}{I(Q, t_f)}. \quad (5.15)$$

This intensity relation comprehends the global variation in interparticle interactions and size distributions throughout the sedimentation process that occurred during the measured hour.

Hence, just a few speculations can be drawn out of the particularities observed on the behavior of these experimental curves. By this model, we can then attribute the

$Q > 2 \text{ nm}^{-1}$  range to the small particles Porod region where almost no variation in the shape is observed. The slight intensity reduction in  $I_{\text{rel}}(Q > 2 \text{ nm}^{-1})$  suggests that a portion of these smaller particles in fact sediment. Since this  $Q$ -range corresponds to a size of  $d_{\text{NP}} \lesssim 3 \text{ nm}$ , these NPs should not naturally sediment as they are sufficiently small to remain in solution due to thermal agitation. Therefore, the decrease in  $\Phi_{\text{NP}}$  observed in the high  $Q$ -range combined with the reduction of  $\Phi_{\text{agg}}$  attributed to the reduction of the signal in low  $Q$ -range support the hypothesis that the larger objects are at least partially constituted of the really small nanoparticles.

The maximum position of the  $I_{\text{rel}}$ , namely  $Q_{\text{max}}$ , does not present a large shift towards smaller or larger values as a function of time, only a progressive intensity reduction. In addition, the curves are always contained underneath the previous measurement profiles. Considering that DLS measurements show the persistence of  $\sim 100 \text{ nm}$  objects in solution even after centrifugation, the lower limit of the range (corresponding to distances  $< 62 \text{ nm}$ ) prevents a direct observation of the size distribution development. Still, it is clear that a reduction of  $\Phi_{\text{agg}}$  is most likely to occur as the intensity progressively decreases.

Figure 58 exhibits the evolution of  $I_{\text{rel}}(Q, t)$  in the two mentioned  $Q$  regions to provide an idea of the dynamics embedded in the  $\Phi$ -variations due to sedimentation. The Porod region is expressed by the mean value of  $I_{\text{rel}}(Q, t)$  at a given time  $t$  for  $Q_{\text{Porod}} > 2 \text{ nm}^{-1}$  and the Guinier portion by the intensity maximum located at  $Q_{\text{max}}$ . For a better visualization of the intensity decay these apparent structure factors were normalized by the first measured value, therefore, the insets in Figure 58 shows the evolution of  $I_{\text{rel}}(Q, t)/I_{\text{rel}}(Q, t = 1)$ .

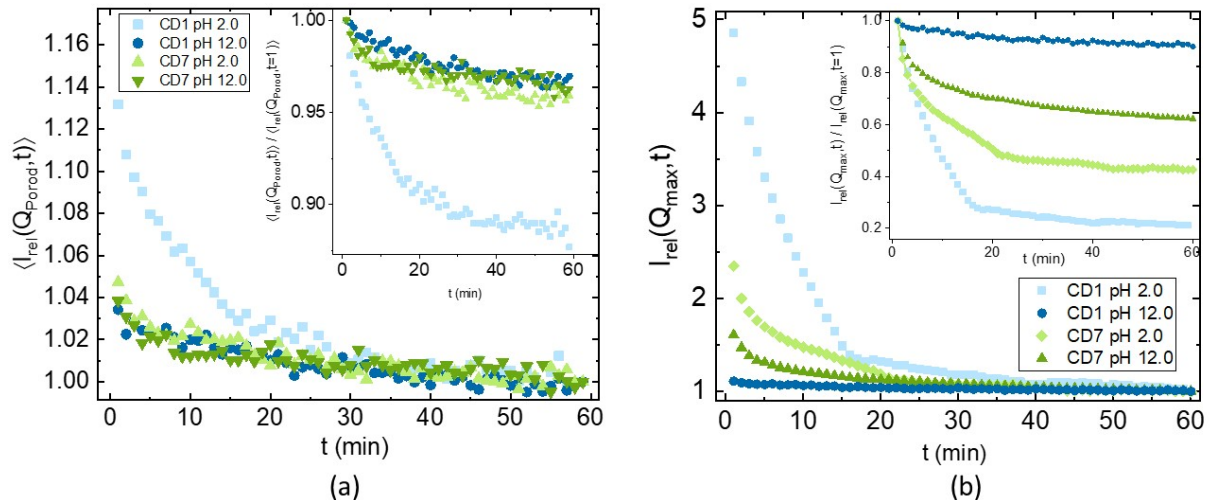


**Figure 58** – Time evolution of the experimental values of the apparent structure factors at (a) the Porod region ( $Q > 2 \text{ nm}^{-1}$ ) and (b) the Guinier region ( $Q_{\text{max}}$ ). *Insets:* Normalization by the first measured value ( $S_{\text{app}}(Q, t)/S_{\text{app}}(Q, t = 1)$ ) for better visualization of the curve profiles.

A steep decay within the initial 5 minutes is observed for all samples in Figure 58a and b. This reduction can be attributed to the exceedingly large aggregates that rapidly

sediment as they are way above the critical diameter. At the Porod region, CD1(pH 2.0) stands out as it presents the most sharp variation, while the other curves present a similar smoother evolution, despite of a small initial shift. This initial difference gets amplified in the Guinier region as it becomes evident the progression CD1(pH 2.0), CD7(pH 2.0), CD7(pH 12.0) and CD1(pH 12.0). This behavior follows the proposed idea that a higher surface charge reduces the particle sedimentation as the electrostatic repulsion increases. Note that although CD7(pH 12.0) presented the lowest Zeta potential and highest surface charge values it still presents a significant sedimentation effect if compared with CD1(pH 12.0). It shows that the increase in the surface charge alone is not a guarantee of eliminating particle sedimentation. This difference is likely to be related with the mentioned aggregate organization as the samples present distinct fractal dimensions.

Further, multiple sedimentation regimes are uncovered in [Figure 58b](#). At pH 2.0, in addition to the  $< 5$  min fast decay, both samples exhibit multiple changes in tendency over time, roughly in three regions: 5–20 mins, 20–40 mins and  $> 40$  mins. The slope variation can be attributed to the size heterogeneity of the aggregates. Moreover, this size polydispersity could still be kinetically driven to larger diameters if we consider the possibility of cluster coagulation due to insufficient electrostatic repulsion. In fact, this mixed aggregation and sedimentation behavior has been investigated in dispersions of magnetite nanoparticles, where similar sedimentation curves were obtained – except that the concentration variations were monitored over time by the absorbance at a specific wavelength in the visible spectrum [226]. Analogous interpretation of the sedimentation rate can be traced by both techniques, although the SAXS approach presents the possibility of conveniently selecting a size scale via the range of the scattering vector. Therefore, we can conclude that the particle sedimentation is partially reduced at alkaline medium in response to an increase of surface charge. At low pH, the sedimentation process is more heterogeneous, likely due to greater differences in aggregate size and the possibility of dynamic particle aggregation as the electrostatic repulsion is reduced in this condition.

In conclusion, these SAXS measurements indicate that even homogeneous macroscopic dispersions of N-CDs can still present a substantial amount of aggregates. The structure of agglomerates under a hundred nanometers varies between CD1 and CD7, while the former is mostly composed of surface fractal structures, the latter is dominated by mass fractals. At high concentrations, the multitude of aggregate sizes becomes evident by dynamically attesting the heterogeneity of sedimentation effects and by theoretically analysing ultracentrifugation size sorting procedures. The pH plays an important role in reducing the mean aggregate size, although at highly alkaline conditions it can increase their number in the dispersed phase.

## Chapter 6

# Photoluminescence (PL)

The photoluminescence effect (PL) is characterized by the emission of radiation from a material due to electronic excitations promoted by photo-absorption when exposed to a radiation source, usually ultraviolet (UV) or X-rays. Currently, the actual photoluminescence mechanisms of CDs are still under debate in the scientific community [227]. Some authors interpret the CD's fluorescence as an electronic transition within the crystalline nucleus, while others associate it with surface states, considering the decisive role of passivation in the generation of the PL [34]. Four mechanisms are strongly evidenced in carbonaceous-based nanoparticles [186]: the effect of quantum confinement ( $\pi$ -conjugated domains) associated with the nucleus; the surface state resulting from the hybridization of the carbon backbone and the functional groups bound on the surface; the molecule state determined only by the fluorescent molecules attached to the surface or interior of the carbon core; and the crosslink-enhanced emission effect (CEE).

Due to these multiple effects, the PL of CDs can be regulated by various parameters. For instance, size effects were evidenced by [Li et al.\[35\]](#) as CDs with an average size of 1.2 nm an emission in the UV range was observed, for sizes of 1.5–3.0 nm the emission was mostly composed of visible light, while for the 3.8 nm particle size the PL was close to the infrared. Therefore, the alteration of the PL is typically justified by confinement effects of the nucleus, nevertheless, there are several cases that the emission spectrum variation can be evidently related to the surface state, such as the results obtained by [Liu, Ye and Mao\[179\]](#) in which the different oxidation levels of the surface produced varied emissions from red to violet.

Independently of the generation mechanism, the photo-absorption of CDs usually covers both UV and visible range – which further combined with the already mentioned wide range of emission – allows the tuning the PL of CDs dispersion by the excitation wavelength. Thus, this kind of tunability is characterized by the shift of the emission peak as the excitation wavelength is altered. The high quantum yield, the sensitivity to the external environment and this multi-color emission tunability promotes the implementation

of these materials in combined applications, for example, performing cellular imaging and multidimensional sensing [228].

In the next sections, it will be provided a brief description of the difference in the PL mechanism of the blue-emitter (CD1) and green-emitter (CD7) N-CDs – unraveled in previous studies conducted with the same synthesis protocol – and a qualitative discussion of the alterations of the absorption and emission spectra at high alkaline medium previously observed in [section 5.2](#).

## 6.1 Nitrogen/Carbon Ratio Effect in Optical Properties

The structure and optical properties as a function of the nominal N/C ratios of the here studied N-CDs has been already comprehensively investigated by [Sciortino et al.](#)[38]. In this study, it was also considered intermediary and higher nitrogen contents other than the ones here reported (N/C = 0.14 and 0.74), comprehensively elucidating the mechanisms of the dual blue and green emission patterns. In this section we present a brief description of the optical properties already established in the literature which will serve as groundwork for the discussion of the qualitative results obtained in highly alkaline medium.

The mentioned study [38] probed two optical properties – the UV-vis optical absorption and the excitation-emission fluorescence – both are reproduced in [Figure 59](#). The investigated nominal N/C ratios are N1 (N/C = 0.14 equivalent to the here named CD1), N2 (N/C = 0.34), N3 (N/C = 0.58) and N4 (N/C = 0.74 equivalent to the here named CD7). The normalized optical absorption spectra is exhibited in [Figure 59a](#). Two prominent transitions can be observed at 340 nm (3.65 eV) and 410 nm (3.02 eV), which the former is regularly observed in CDs dispersions while the latter is less common. The higher-energy peak has been previously attributed to carboxyl moieties [229] and/or to aromatic conjugation [29], however, recent studies [196, 230] suggest that this absorption occurs in response to electronic transitions of small molecular fluorophores<sup>1</sup> attached to the surface of the N-CDs. On the other hand, the low-energy transitions are occasionally proposed to arise from nitrogen doping [231, 232], which is supported by the presented results as the peak gradually rises with the increase of the N/C ratio.

[Figure 59b](#) and [c](#) present the 2D excitation-emission fluorescence maps of samples CD7 and CD1, respectively, which shows significant differences between each other. Two well distinguishable fluorescence emission signals with similar intensities are observed in CD7, one located in the bottom-left (emission wavelength around 450 nm) corresponding to a violet-blue spectral region and a second maximum close to the center of the map

<sup>1</sup> These fluorescent molecules are produced as a side product in the synthesis process, as already pointed out in [section 4.4](#).

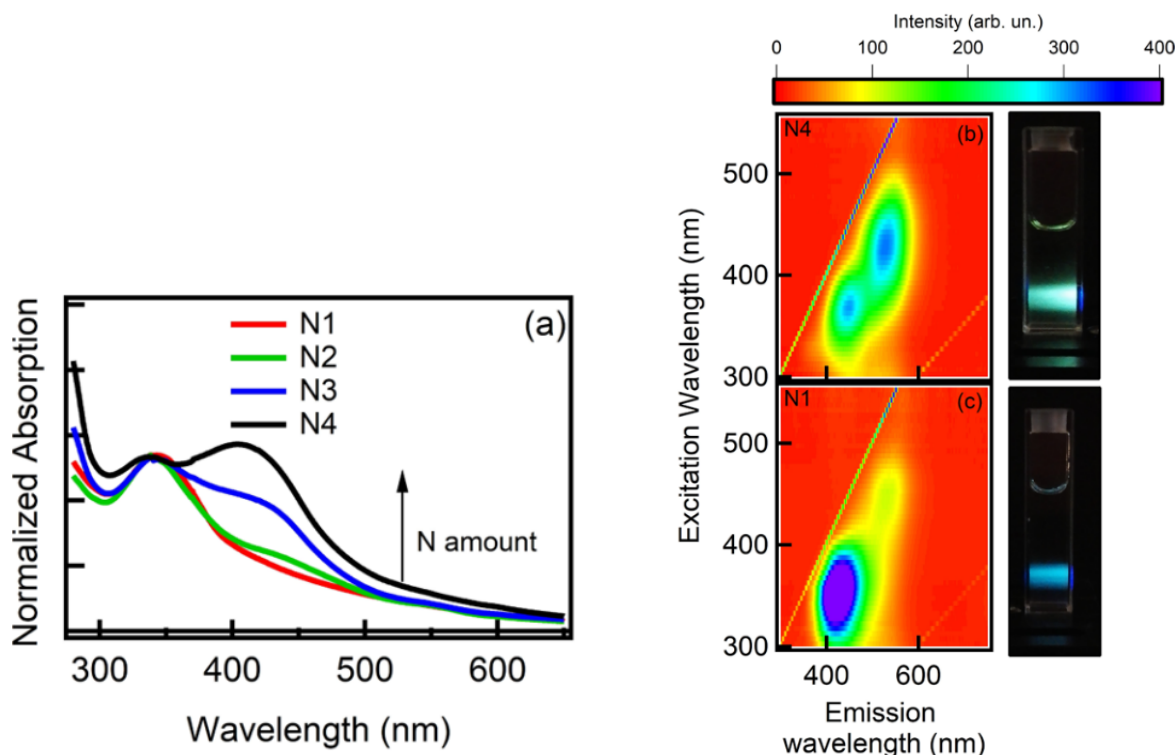


**Figure 59** – (a) Optical absorption spectra of sample N1 ( $N/C = 0.14$ ), red line, N2 ( $N/C = 0.34$ ), green line, N3 ( $N/C = 0.58$ ), blue line, N4 ( $N/C = 0.74$ ), black line. The arrow highlights the increase of the amount of nitrogen; (b) 2D excitation-emission fluorescence maps of N4 (in this thesis referred as CD7) with the respective photograph of a cuvette containing the N-CDs in water under excitation at 400 nm and (c) 2D excitation-emission fluorescence maps of N1 (in this thesis referred as CD1) with the respective photograph of a cuvette containing the sample in water under excitation at 400 nm. Figures reproduced from ref.[38]

(emission wavelength just above 500 nm) associated to a green spectral emission. The latter is almost absent in CD1, thus the broader violet-blue band is responsible for the majority of the emission signal. As a result, the overall emission color visually perceived – when exciting the samples at  $\sim 400$  nm – is green for the CD7 sample and blue for the CD1 sample. This visual observation was already asserted in the photos of Figure 41 and here once again in the cuvettes of Figure 59.

In this context, the green fluorescence signal could be associated with the core structure and the surface groups due to a number of reasons. First, this green emission is characteristic of the samples with the nominal  $N/C$  ratios above the threshold which the core undergoes the transition from the graphitic to the  $\beta\text{-C}_3\text{N}_4$  structure. Second, a previous study [34] with the high N-content CD7 sample suggested that the low-energy absorption band at  $\sim 410$  nm (see Figure 59a) arise from an electron transfer from the core to surface trapping states and the green emission results of the radiative recombination of the surface electrons with the core hole. In the framework of this model, the coupling between the core and surface structure requires a favorable alignment of their energy levels, imposing restrictions for this transitions to occur. Therefore, only certain structures, like the  $\beta\text{-C}_3\text{N}_4$ , would allow such kind of emission. In addition, as the emission is surface

dependent its intensity would be closely related to the amount of electron trapping surface states. As a matter of fact, the increased number of amide surface groups in higher N/C ratios (see [Figure 39](#) and the FTIR results of ref. [38]) correlates with the augmentation of the absorption band at 410 nm in [Figure 59a](#) between N3 and N4. The green emission is also enhanced as seen in the E.S.I. of ref. [38]. [Wang et al.\[233\]](#) also found a correlation between the density of N-related surface groups and the intensity of the green emission – at least for hydrothermal synthesis routes – supporting the initial hypothesis.

On the other hand, the violet-blue emission is equally observed in both C-graphitic and  $\beta$ -C<sub>3</sub>N<sub>4</sub> samples, therefore, it seems to be independent of the core electronic structure. This observation suggests that the emission transitions occur exclusively on the surface functional groups and, considering the low energy of the transitions, it is unlikely that they can be specifically localized on any specific group. Also, this fluorescence does not directly correlate with the abundance of surface amide groups, in fact, a slight intensity decrease of this fluorescence is observed when going from N/C = 0.58 to 0.74, despite the large increase of surface amide (see E.S.I. of ref. [38]). As a consequence, the blue emission seems to either originate from electronic transitions within a manifold of electronic states highly delocated on the surface shell (as observed in ref. [234]) or likely to arise from the side product fluorescent molecules adsorbed on the surface (as frequently observed in CDs obtained by the carbonization of citric acid [230, 232, 235]).

In conclusion, the emission and absorption properties of these N-CDs dispersed in ultra pure water have already been well characterized and its fluorescence mechanism comprehensively elucidated. However, time-dependent optical variations were qualitatively observed for aqueous dispersions at pH 12.0 in [section 5.2](#) (see [Figure 42](#)). Thus, in the next section we present a possible explanation for this evolution in alkaline medium.

## 6.2 Optical Absorption and Fluorescence in Highly Alkaline Medium

In order to quantitatively analyse the optical density reduction observed in [Figure 42](#) reported in [section 5.2](#) for the CD7 sample, a dispersion in ultrapure water with N-CDs concentration at 0.05 g/L was initially prepared following the dispersion protocol described in [section 5.1](#). The measured pH of the as-prepared solution is about 5.0 following the acidic behavior shown in [Figure 46](#) (see text of [subsection 5.3.1](#) for details). Then, we add sufficient NaOH to bring the dispersion to pH  $\sim$  11. From this moment on (named t=0) we follow in time the progressive modification of the optical absorption (OA) spectra by measurements at regular intervals by a double beam spectrophotometer (JASCO V-560) in the 270-600 nm range in a 1 cm quartz cuvette.

The OA results are shown in [Figure 60](#). It is clear that the alkaline medium triggers a progressive decrease of the longest wavelength absorption band around 400 nm,

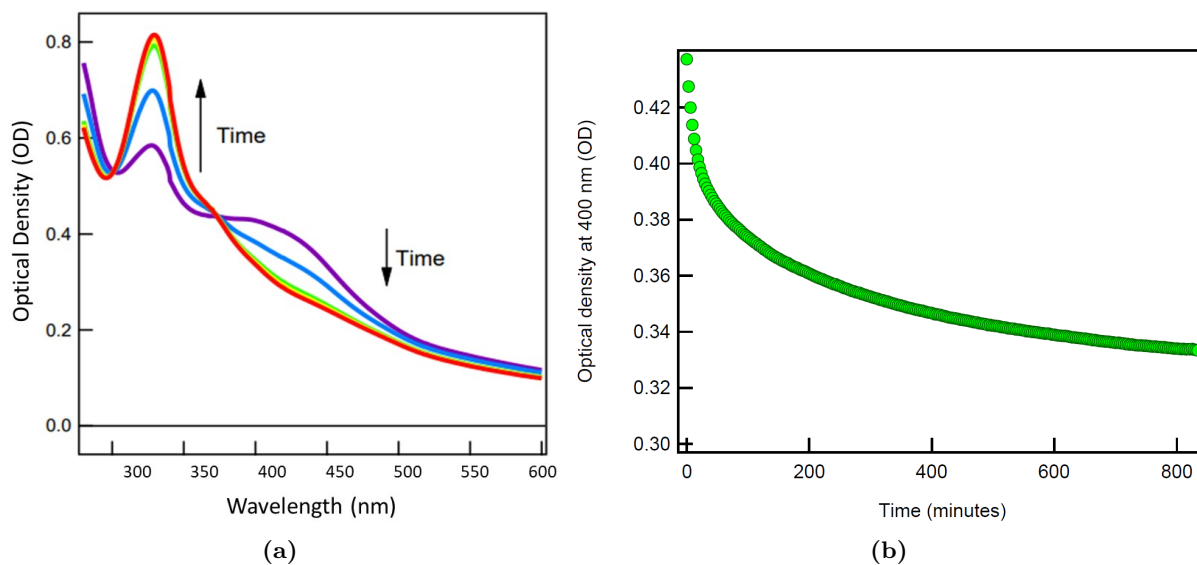


**Figure 60** – (a) Optical density variation as a function of the wavelength for an aqueous solution of CD7 sample right after it was alkalinized to  $\text{pH} \sim 11.0$  with NaOH. The initial N-CDs concentration was set as 0.05 g/L. (b) Time-dependency of the optical density at the absorption band around 400 nm.

accompanied by an anti-correlated increase of the band at 300–320 nm. The time scale of both processes is in the order of hours – as can be seen in the Figure 60b – where the OA at 400 nm is plotted vs time. The decrease seemingly shows a multiexponential kinetics, where the reduction begins immediately after the pH is increased. It turns out that this process is irreversible and leads to a permanent change of the OA spectrum, i.e., it cannot be reversed if going back to neutral or acidic pH. As mentioned in section 6.1, we have good reasons to attribute the 400 nm absorption band to amide surface groups and the band at 320 nm to the surface carboxylic groups, extending the results found on previous CDs studies [38, 229, 231, 232, 236]. If we accept this interpretation, the data would suggest the conversion from amide as the 400 nm band decreases to carboxylic group as the 320 nm band increases. The same hypothesis was already pointed out in section 5.3 considering the charge development, where the titration data indicated the surface chemical alteration which was attributed to the amide hydrolysis in alkaline medium.

The titration results of the alkaline to acidic route also indicate a surface alteration for the CD1 sample (see subsection 5.3.3 for details), which here is qualitatively confirmed by the absorption reduction in the visible range in Figure 61. However, considering that the fluorescence mechanism of this type of N-CDs are not directly related to the amide surface groups – but most likely related to carboxyl groups or adsorbed fluorophores – the color of the blue fluorescence remains mostly unchanged, apart from the intensity appearing slightly brighter and less opaque.

Contrarily, the CD7 sample at pH 12.0 shows an evident blue shift, meaning that the highly alkaline medium not only influences its optical absorption but also the dominant

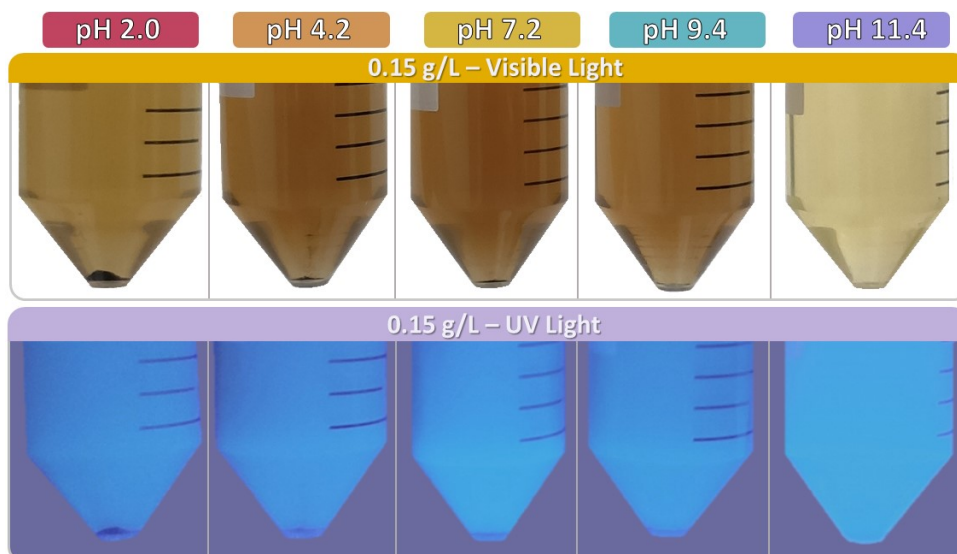


**Figure 61** – Visual aspects of sample CD7 after two weeks, observed under a commercial ultraviolet light (wavelength 480 – 320 nm).

wavelength of the fluorescence emission. In the previous section, it was established that the green emission mechanism correlates with the amount of amide surface groups, as the emission is enhanced with the increase of the N/C content. Therefore, the observed blue shift is actually a reduction of the green signal, as a consequence of the surface amide converting into carboxyl moieties due to the hydrolysis induced in alkaline medium. As a result, the coupling between the core and surface trapping states once generated by the amide groups is mostly lost. Thus explaining the reduction in both the optical low-energy absorption as well as the green emission. On the contrary, the blue emission is then again not majorly affected by the surface modification – as equivalently considered for the case of CD1.

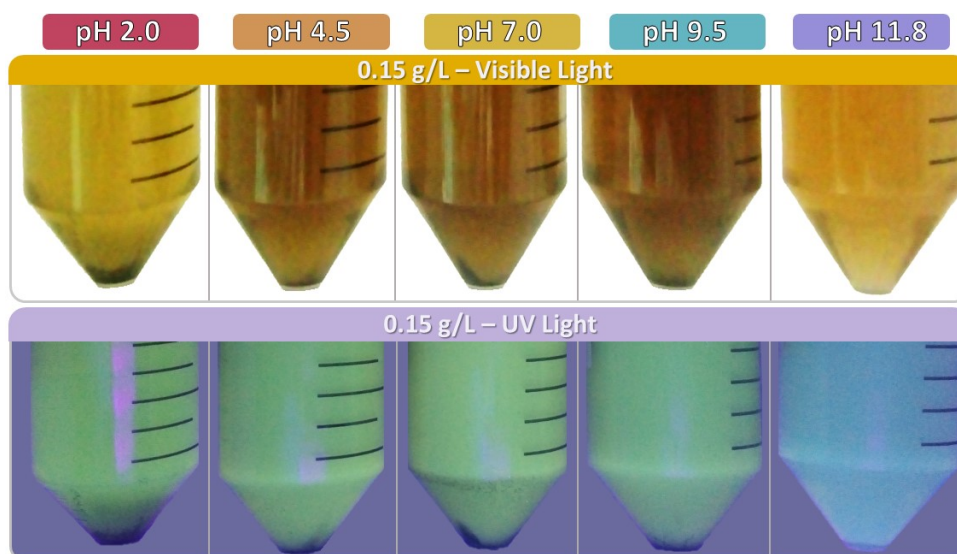


**Figure 62** – Visual aspects of sample CD7 after two weeks, observed under a commercial ultraviolet light (wavelength 480 – 320 nm).

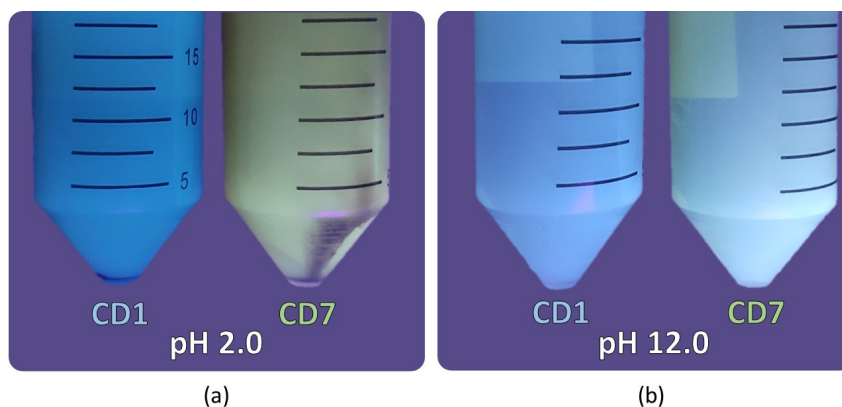


**Figure 63** – (a) A visual comparison between sample CD1 and CD7 in acidic medium (pH 2.0) at 0.15 g/L concentration after two weeks. The samples were photographed under a commercial ultraviolet light (wavelength 480 – 320 nm). (b) A visual comparison at equivalent conditions described in [Figure 63a](#), except they were dispersed in alkaline medium (pH 12.0).

[Figure 63](#) highlights the differences between the samples in pH 2.0 and 12.0 at a 0.15 g/L mass concentration. In pH 2.0, the green and blue emissions are strikingly noticeable, as the typical precipitate formation in acidic condition shows a reduction of the N-CDs concentration in the supernatant. At pH 12.0, even though the CD7 sample suffers a strong diminish of the green emission, it is still perceptible a persistent greenish hue when compared with the sample CD1. In both cases the samples appear more transparent as the absorption in longer wavelengths was reduced and presumably increased in the UV range. We cannot confirm a change in brightness by these qualitative results, therefore, in the near future we expect to perform quantitative fluorescence measurements fully characterizing these alkaline systems.

## Conclusions on N-CDs Aqueous Dispersions

In this part we studied aqueous dispersions of N-CDs synthesized with different nitrogen/carbon nominal ratios (N/C). The sample CD1 was prepared with a N/C = 0.14, while the sample CD7 was prepared with N/C = 0.74. The variations of the synthesis process were briefly described and their morphology, size distribution, surface structure and density were checked in order to provide support for the posterior analysis of the dispersions in aqueous medium in various pH's. An average diameter between 2 – 4 nm was measured by transmission electron microscopy (TEM) and X-ray diffraction (XRD), still, a large amount of particles with diameters < 2 nm were found by atomic force microscopy (AFM). The crystalline structure of the N-CDs have been previously determined as N doped C-graphite for CD1 and  $\beta$ -C<sub>3</sub>N<sub>4</sub> for CD7. Moreover, the presence of carboxyl and amide surface groups were here confirmed by Fourier-transform infrared spectroscopy (FTIR). The experimentally determined density of the N-CDs dry powder suggest that the surface is highly passivated as the measured value is considerably smaller (22 – 48%) if compared with the density of the crystalline core alone. We then focused on the charge development, colloidal stability and local ordering since these features are not deeply investigated in the current state of the art of N-CDs.

The N-CDs were dispersed in a wide range of pH (from 2.0 to 12.0) by the direct addition of the solid material in the acidic (NaNO<sub>3</sub>) and alkaline (NaOH) aqueous solutions. The sample was homogenized as much as possible via sonication in a ultrasound bath at 50°C for several hours. Nonetheless, as the pH shifts towards acidic conditions the solubility seemed to significantly reduce. The macroscopic visual aspects of the sample show that the N-CDs are partially well dispersed in solution, yet a portion of them sediment. The quantity of precipitated N-CDs correlates with the pH, such as, the amount of sediment is larger in acidic medium and it gradually reduces as the pH becomes alkaline. At pH 12.0 no precipitate is formed, however the sample shows modifications in its optical properties over time.

At the microscopic level, it is observed by optical microscopy that the precipitate presents aggregates in various orders of magnitude (from  $\sim 1 - 100 \mu\text{m}$ ). The larger aggregates were dense and compact lamellar structures, but as they get smaller, fractal structures were observed to be formed by a large number of sub  $10 \mu\text{m}$  clusters. Anyway,

the supernatant was highly homogeneous at the macro and microscopic scale in all of the probed pH's. This discrepancy between supernatant and precipitate was associated with the heterogeneity of the N-CDs properties, which should induce differences in solvation, interparticle interactions and nanoscale ordering in response to variations in size, surface structure and electric charge.

Therefore, we investigated the charge development of the N-CDs as a function of the pH. Zeta potential measurements indicated that the surface charge was always negative in the analyzed acid-base range and that its absolute value was higher for CD7 in comparison to CD1. The non-zero charge in highly acidic medium was associated with oxidized nitrogen groups while its progressive augmentation in magnitude towards alkaline conditions was attributed to the deprotonation of the carboxyl surface groups. Therefore, the better colloidal stability observed as the pH increases should arise from the additional electrostatic repulsion. The nitrogen to carbon ratio (N/C) seems to also affect the nature of the N-CDs surface, where the CD1 sample showed a more acidic character when compared with CD7. This result could be related to the proportion of carboxyl to nitrogen-based surface groups.

Potentiometric and conductimetric titrations allowed us to estimate the surface charge density arising from the carboxyl groups. The curves indicate a difference in behavior between the acidic-alkaline route and the inverse alkaline-acidic route. Not only the amount of titrant is altered as the shape of the curve is drastically modified. These results suggested that the observed hysteresis of the titration curves was likely to be a consequence of alkaline hydrolysis of the amide surface. This chemical reaction would explain the increase in surface charge as the amide groups are converted in carboxyl groups and the change in shape of the curve as the acidic nature of the particle surface is significantly modified.

Finally, the nanoscale organization of the N-CDs was probed by TEM, dynamic light scattering (DLS) and small angle X-ray scattering (SAXS) techniques. The results suggested the presence of aggregates also below 1  $\mu\text{m}$  in the supernatant, which was beyond the resolution of the optical microscope. DLS measurements indicated that the critical size of the aggregates were between 100-400 nm. Ultracentrifugation allowed us to reduce the hydrodynamic diameter to a window of 70-120 nm. The structure of this aggregates probed by SAXS indicated that it also differs with N/C. Once CD1 presented more densely packed clusters following surface fractal exponents, CD7 presented a less compact aggregated network with mass fractal exponents. Time-dependent measurements shed light in the sedimentation process at the nanoscale, confirming that the colloidal stability is indeed improved in alkaline medium. In addition, the dynamic measurement showed that the sedimentation process is heterogeneous, therefore, there is likely a size distribution of the aggregates at the nanoscale as well.

Lastly, a brief analysis of the optical properties of the samples at pH 12.0 was carried out. A blue-shift of the fluorescence of the green-emitting CD7 sample was observed, while CD1 remained blue. The optical absorption (OA) of the CD7 sample shows time-dependent variations, where the peak around 400 nm decreases while the band at 300-320 nm increases. This OA result – as well as the blue-shift in fluorescence – could be associated with the already conjectured amide hydrolysis. When considering the emission mechanism of these N-CDs, one can realize that the green emission is likely dependent of the amide surface groups, whereas the blue emission is not as substantially affected. Therefore, the green emission peak is reduced as a large portion of the surface amide is converted in carboxyl moieties.

## Part III

# Fluorescent Magnetic Liquids

## Chapter 7

# Magneto-Photoluminescent Systems based on Nanoparticles

Magnetic and fluorescent nanostructured materials have been envisioned to be applied in wide range of diverse applications. For example, it can be used in biomedical purposes such as bioimaging [40, 41, 43, 237] or industrial activities as in the quality of materials by non-destructive tests [238, 239]. In this sense, the design of more competitive fluorescent magnetic materials has been increasing in the past years, mostly in response to the marked demand. The majority of the currently available products are achieved via the combination of distinct magnetic and fluorescent components in a single structured material.

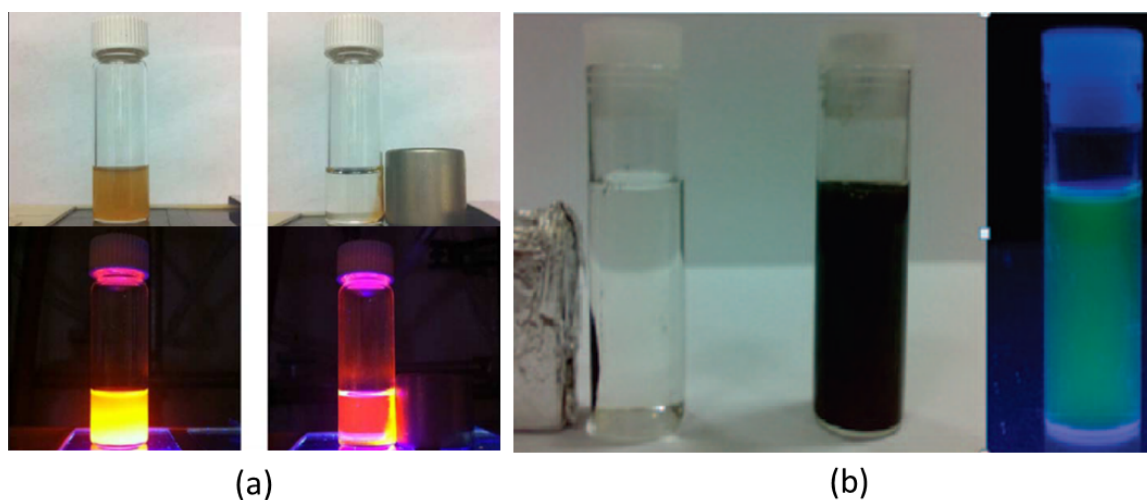


**Figure 64** – (a) Figure adapted from ref. [7] showing the the phase separation of magneto-fluorescent supernanoparticles upon exposure to visible (top) and UV light (bottom). (b) Figure adapted from ref. [240] exhibiting an aqueous solution of magnetic nanodiamonds with (left) and without (middle) an external magnet; (right) the fluorescence of the dispersion upon exposure to UV light.

In the specific case of magneto-fluorescent nanofluids, the majority of the currently available dispersions are achieved via the assembly of magnetic and fluorescent parti-

cles/molecules in a single structured particle, usually requiring some sort of encapsulating process. Therefore, the resulting nano-objects are typically larger than 100 nm (reaching up to microns) which makes the production of a stable colloidal dispersion almost impracticable in the presence of an external magnetic field (see [Figure 64](#)). The stability can be improved increasing the solvent viscosity (e.g in petroleum derivative oils) largely restricting their applicability range. In addition, the encapsulation of the nanostructures restricts several interesting properties that are sensitive to the particle/medium interface, limiting the potential of sensor applications.

In this chapter, we present the current state-of-the-art magneto-photoluminescent systems based in the combination of MNPs and CDs. Moreover, we introduce a proposed novel Fluorescent Magnetic Liquid (FML) and its possible industrial applications.

## 7.1 General Context and State of the Art

The conspicuous interest in magnetic and fluorescent nanomaterials is noticeable as the number of studies increases through the years – exploring the vast potential of these properties in contemporary applications. Combining both features in a single hybrid material presents multiple technological advantages, nonetheless, in most cases it is not an evident task as these properties can be strongly affect by the assembly procedure. To this extent, two approaches are generally applied in the current state of the art of magnetic and fluorescent nanofluids: (i) the functionalization of magnetic nanoparticles with fluorescent molecules, granting the magnetic core photoluminescent properties arising from the surface shell and (ii) the formation of nanocomposites through the agglomeration and/or confinement of magnetic and fluorescent nanoparticles.

Regarding the first strategy, recent publications [[237](#), [241–244](#)] have shown the possibility of producing magneto-photoluminescent particles using polymers and organic dyes. One of the major challenges and drawbacks of this technique is the potential toxicity due to the employed substances [[237](#)]. Also, the passivation of the MNP's surface in this approach requires complex and specific adaptations for each kind of fluorescent molecule. A common method to facilitate the adaptation and modification of the MNP's surface is first to grow a silica shell prior to the addition of the fluorescent molecules. The downside of this encapsulation procedure is the increase of particle size, which generally induces particle sedimentation in low viscosity media. In addition, the surface passivation does not generate an effective mid to long-range interparticle repulsion – giving the NPs at most a short-range steric component – and thus cannot effectively prevent particle aggregation over considerable periods of time. As a result, the dispersions do not show a long-term colloidal stability, even in the absence of an external magnetic field.

Following the second approach, the implementation of fluorescent carbon nanodots

(CDs) instead of typical fluorophore molecules confers some compelling technological enhancements to these hybrid magneto-fluorescent nanocomposites. For instance, the tunable full-color emission, the excellent biocompatibility, the facile/low-cost synthesis and the low environmental impact altogether compose an ensemble of assets that are exceedingly advantageous over regular fluorescent dyes. The combination of iron oxide nanoparticles and carbon based materials have been usually associated with nanoabsorbents [2,245–248] taking advantage of the extensive surface area of activated carbon and the convenient magnetic separation process – unfortunately, this form of carbon does not fluoresce. Thus, only after the discovery of the highly fluorescent carbon nanodots [31] that iron oxide/carbon combinations began to be explored as magneto-fluorescent systems.

Until the present moment, the CDs/MNPs nanocomposites reported in the literature [44,249–251] exhibit the recurrent lack of adequate colloidal stability. The fact that the current standard combination method focus on the encapsulation, agglomeration and/or attachment via binding molecules results in particle sizes always above the colloiddally stable threshold, where no effective particle repulsion mechanism is introduced. As a consequence, the particles eventually separate from the liquid phase with or without the application of an external magnetic field. In addition, the fact that in some cases the nanoparticles are encapsulated by a protective layer limits the benefits of particle-solvent interface effects, such as the solvatochromism [34]. In this context, we propose a new approach that solves the current colloidal stability issues, while maintaining to a great extent the main characteristics of each individual colloidal dispersion.

Here we present the merge of aqueous ferrofluids (described in Part I) and N-CDs aqueous dispersions (described in Part II) in a unique homogeneous, long-term colloiddally stable, fluorescent and magnetic nanofluid. In this method we avoid the encapsulation, aggregation and confinement of the NPs by finely controlling the physico-chemical conditions of the medium, consequently maintaining the mean size of the components (N-CDs and MNPs) under the critical diameter in which the gravitational precipitation would dominate. In fact, the interparticle repulsion is strong enough to prevent particle aggregation even in the presence of an external magnetic field, allowing the magnetic manipulation of the single phase fluorescent fluid. The combining method is practical, low-cost and easily reproducible. In addition, it is extremely versatile as it allows a wide variety of nanofluids, due to the extensive possibility of varying the magnetic and photoluminescent characteristics of each NP type independently.

The here achieved FML has a strong potential to be implemented in non-destructive quality control of forged parts and welds. This kind of smart materials are already applied in metallurgy in order to locate superficial discontinuities/defects, such as cracks, folds, inclusions, tears and seams in ferromagnetic materials (e.g iron, nickel and/or cobalt), specially in steel workpieces. Thus, this test is usually performed with magnetic particles

to both finished and semi-finished parts and, mainly, during the manufacturing stages as an essential procedure to assured the safety, quality and durability of the final product. The fluorescence of the inspection product detects smaller and finer indications, making the inspection process faster as the defects stand out under the UV light.

In a typical inspection test via magneto-fluorescent particles, the metal parts are first magnetized and subsequently the fluid is sprayed onto the parts to be examined. The presence of discontinuities will immediately drawn the particles to magnetic leaks on the surface of the test part, where the bright fluorescence clearly indicates of the shape and size of the fractures, cracks and others. Reducing particle aggregation and improving the fluid mobility presents a major benefit in this kind of tests, which the product currently available [239] in the market tries to achieve. The particle size of  $\sim 6$  microns requires the addition of conditioning agents in water as an attempt to improve particle suspendibility, mobility and surface wetting, even so, phase separation still occurs.

In the case of the proposed fluorescent magnetic liquid, the long-term stability, good mobility, low remanence and outstanding color would present a considerable improvement in comparison with the mentioned product. These features prevent the loss of the magnetic particles that might become trapped within the bath equipment inside the pipework, filters or the circulating pump. Therefore, this durable and reusable MFL could be a promising alternative to develop the current quality test of metal workpieces improving the identification of the discontinuities and reducing inspection time.

## Chapter 8

# N-CDs|MNPs Hybrid Nanocolloid

In this chapter we explore the possibility of achieving the conceptualized colloidally stable fluorescent magnetic liquid (FML) while mainly preserving the photoluminescent and magnetic properties provided by the N-CDs and MNPs, respectively. We here focus on core-shell MNPs with a cobalt ferrite ( $\text{CoFe}_2\text{O}_4$ ) core surrounded by a maghemite ( $\gamma\text{-Fe}_2\text{O}_3$ ) shell similar<sup>1</sup> to the NPs studied in [Part I](#) and the N-CDs studied in [Part II](#) in attempt to obtain a strong magnetic response and still have a bright tunable fluorescence.

In this chapter, it is first provided an overview of the different interparticle interactions depending on the pH of the medium, since this is the key parameter controlling the N-CDs and MNPs surface charge. Second, the acidic and neutral conditions are investigated probing the hybrid nanocolloids via the multi-scale techniques explored throughout this thesis: visual aspects, optical microscopy, transmission electron microscopy (TEM) and small angle X-ray scattering (SAXS). Finally, we check the magnetic and fluorescent properties in order to establish the possible modifications generated by combination of these two different type of NPs.

### 8.1 Overview: Acidic, Neutral and Alkaline Medium Conditions

In aqueous media, the here studied MNPs can be successfully dispersed in almost the entire pH-range thanks to the generation of a positive surface charge in acidic conditions, negative charge in alkaline conditions and – even though at  $\text{pH} \sim 7.0$  the MNPs reach their point of zero charge (PZC) – citrate functionalization can produce a negative surface charge providing an efficient electrostatic repulsion at neutral conditions (see [section 1.3](#)). The presented N-CDs can also be dispersed in almost the entire range of pH due to the negative electric charge development in aqueous medium, although, the heterogeneity of the particles' surface, size and aggregate structures only allows a portion of the added

---

<sup>1</sup> The synthesis of the core-shell magnetic nanoparticles follow an alternative method comprehensively described in ref. [\[51\]](#).

N-CDs powder to properly enter in suspension – which the quantity of well-dispersed particles increases towards alkaline conditions (see chapter 5).

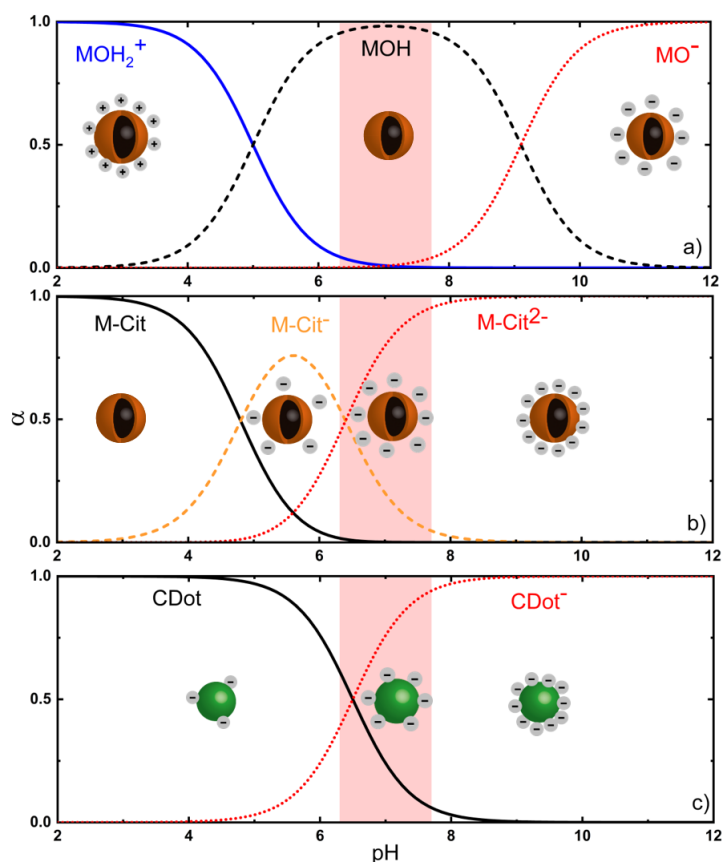


**Figure 65** – Speciation diagrams of: (a) bare iron oxide MNPs in aqueous dispersions with positive surface charge in acidic medium, zero charge around pH 7.0 and negative charge in alkaline medium; (b) citrate coated iron oxide MNPs in aqueous dispersions presenting increasingly negative surface charge as the pH shifts towards higher values; (c) N-CDs in aqueous dispersions presenting increasingly negative surface charge as the pH shifts towards alkaline values. This N-CDs’ diagram corresponds to the behavior of the initial amount of carboxyl surface groups, thus neglecting the small persistent negative surface charge in highly acidic conditions (provided by other functional groups) and the additional charge developed in highly alkaline medium (due to amide hydrolysis).

The pH-dependent speciation diagram summarizing the mentioned charge development is exhibited in Figure 65. Note that at acidic conditions the N-CDs and MNPs present a surface charge of opposite sign while in alkaline medium both NPs charges are negative. This means that introducing N-CDs in an acidic ferrofluid is likely to cause aggregation effects due to the strong attractive interactions between the components, consequently, inducing particle sedimentation over time.

On the other hand, the addition of N-CDs in alkaline medium should not significantly affect the ferrofluid stability as the nanoparticles present the same sign and would naturally repel each other. Nonetheless, in this condition the N-CDs surface undergoes the amide hydrolysis process causing the blue-shift of the fluorescence (see section 6.2). This effect would not only influence the emission color of the FML, as it should also reduce the

intensity of the photoluminescent emission since the absorption of the MNPs generally increases at smaller wavelengths in the visible range.

Anyway, we can achieve a similar repulsive interparticle regime by surface coating the MNPs with citrate ions. This procedure comes with the advantage of preserving the N-CDs emission spectrum, expanding the range of stability and bringing the pH to neutral conditions. Comparing the diagrams (b) and (c) in [Figure 65](#), we realize that the region highlighted in red between pH 6.0 and 8.0 is the most likely to achieve a stable FML. Yet, it might still be possible to accomplish a relative well-dispersed suspension in lower and higher pH's, if the surface charge is sufficiently high to provide a strong repulsion and the shielding by the increasing ionic strength is sufficiently low.

## 8.2 Combining N-CDs and Magnetic Fluids

The method to achieve the hybrid nanofluids consists of the direct mixture of stable colloidal dispersions of magnetic nanoparticles and fluorescent nanoparticles in specific physico-chemical conditions. This process allows the adjustment of the magnetic and fluorescent properties independently in each synthesis process, as well as in the final product by controlling the relative concentrations of each type of nanoparticles. In general, the process consists of the following steps:

Step 1 *Production of ferrofluids:*

- a) Synthesis of magnetic nanoparticles;
- b) Peptization and surface functionalization;

Step 2 *Production of fluorescent colloidal dispersions:*

- a) Synthesis of N-CDs;
- b) Dispersion of the dried N-CDs powder in aqueous medium;

Step 3 *Compatibility and mixture of the dispersions.*

An even more straightforward variation of this protocol can be also performed by directly adding the N-CDs powder to the ferrofluid, although this procedure is less efficient as it is more difficult to disassemble the N-CDs aggregates and the final pH of the dispersion might significantly change depending on the N-CDs concentration. Nonetheless, the pH can be readjusted with concentrated acidic/alkaline solution and any formed precipitate later removed.

The production of ferrofluids referred in [Step 1](#) was extensively described in [section 1.1](#) and [2.1](#), in which the acidic ferrofluid peptization is detailed in [subsection 2.1.1](#)

and neutral citrated ferrofluids functionalization and peptization are described in [subsection 2.1.2](#). The production of fluorescent colloidal dispersions referred in [Step 2](#) was presented in [chapter 4](#) and [5](#), where the synthesis was detailed in [section 4.1](#) and the aqueous dispersion protocol in different pH's was fully described in [section 5.1](#). Finally, [Step 3](#) is discussed in the following sections.

We investigated these N-CDs|MNPs hybrid nanocolloids in two distinct interparticle interactions: the attractive regime between N-CDs and MNPs in acidic medium; and the globally repulsive regime in neutral pH with citrated MNPs.

### 8.2.1 Colloidally Unstable Acidic Hybrid MNP|N-CD Suspension

Acidic Hybrid MNP|N-CD suspensions were prepared using  $\text{CoFe}_2\text{O}_4@-\gamma\text{-Fe}_2\text{O}_3$  MNPs. Two samples with different diameters were used in order to evaluate the possible size effects. The bigger one here named CoG was prepared by the standard coprecipitation method described in ref. [\[51\]](#) using sodium hydroxide as base, which results in mean particle diameters around 12.0 nm. The smaller one named CoP was prepared by the same synthesis method, but using methylamine as base, with which the usual particle diameter is around 7.0 nm.

The mixture procedure was performed combining equal volumes of the acidic ferrofluid at 1.0 – 2.0 vol% nanoparticle concentration with N-CDs dispersions of CD7 (N/C=0.74) at 1.0 g/L nanodots concentration both dispersed in aqueous  $\text{HNO}_3$  acidified medium set at pH 2.5. Therefore, the final particle concentration of the hybrid nanofluid is half of the precursor samples and the medium conditions remains nearly constant.

At the macroscopic level both samples look very similar and present equivalent unstable behavior. The MNPs can become suspended in the liquid phase if submerged for a few minutes in a ultrasound bath or just by manually agitating the eppendorf tubes, but the fluid does not significantly fluoresces under UV light. However, after a few hours the NPs gradually sediment independently of the “redispersion” method. The process can be sped up by placing the sample over a magnet as exhibited in [Figure 66](#) for CoG+CD7. During and after the magnetic separation it is also noticeable that the supernatant indeed shows a green emission, indicating the presence of well-dispersed N-CDs.

Interestingly, the precipitate does not look like the usual powder-like sediment observed at the point of zero charge (PZC), but it seems to be more alike to the highly concentrated phase formed when largely increasing of the ionic strength – for instance, as it is commonly observed in size sorting procedures via the addition of electrolytes [\[56, 57\]](#). Therefore, it is possible that the destabilization is a consequence of N-CDs decorating the MNPs surface, or vice-versa, due to a strong shielding of the electrostatic potential. TEM and SAXS measurements are presented in [subsection 8.3.1](#) in order to support this claim.

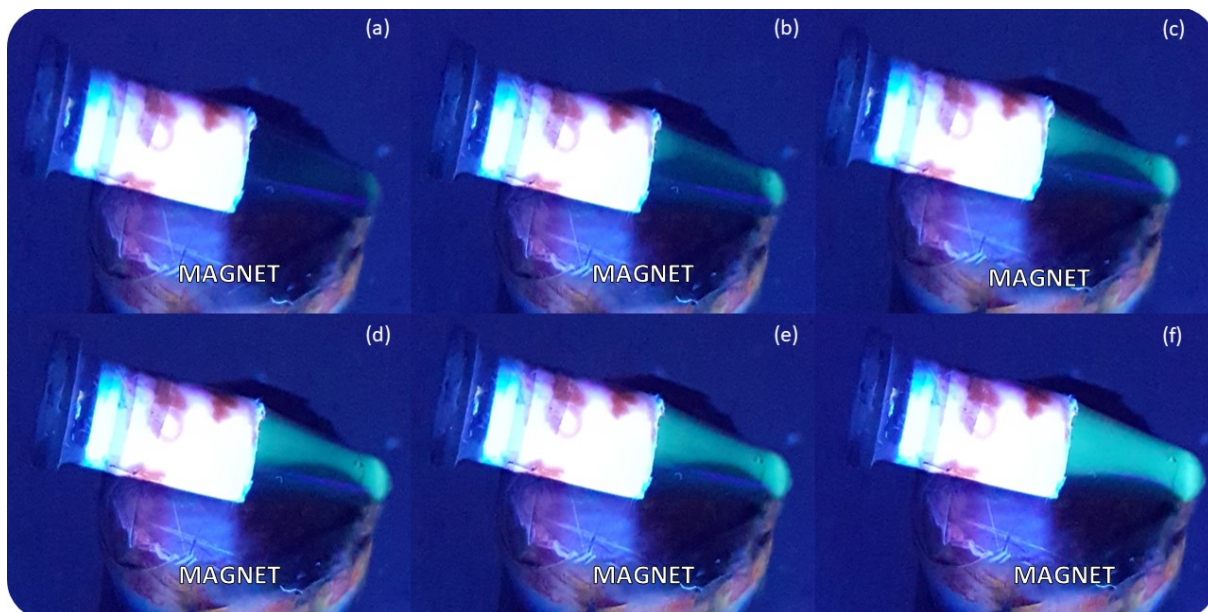


**Figure 66** – (a) An acidic hybrid nanofluid composed of 0.5% volume fraction of CoG MNPs and 0.5 g/L of CD7 N-CDs at pH 2.5 is positioned over a magnet after manually agitating the sample for a few seconds. (b)-(f) the MNPs concentrate closer to the magnet in a time interval of less than a minute. A considerable amount of N-CDs remain dispersed in solution evidenced by the green emission generated under UV light.

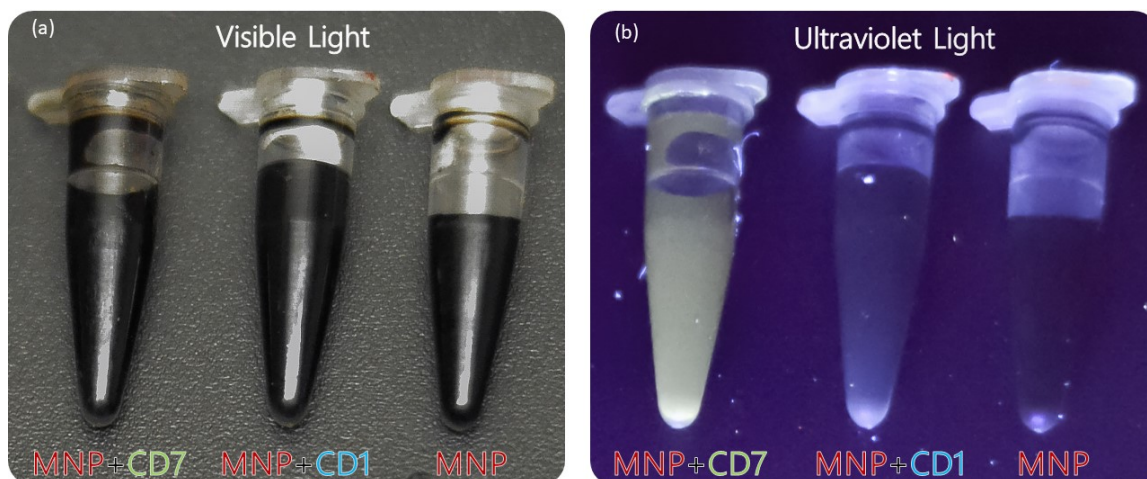
Thus, in acidic medium, the mixture would be equivalent to extremely increase the ionic strength of the systems, while the pH would not be significantly altered.

## 8.2.2 Colloidally Stable Fluorescent Magnetic Liquid

Neutral Hybrid MNP|N-CD dispersions were prepared using  $\text{CoFe}_2\text{O}_4@ \gamma\text{-Fe}_2\text{O}_3$  MNPs surface coated with citrate ions. The sample named Co6 was characterized in ref. [252] where the median diameter obtained by TEM was  $d_0^{\text{TEM}} = 6.4$  nm with a polydispersity of  $s_0^{\text{TEM}} = 0.3$  and the diameter extracted via XRD was  $d_{\text{XRD}} = 7.2$ . The ferrofluid ionic strength was set to  $10^{-2}$  mol/L in acidic medium and later the pH was adjusted to 7.0 via the controlled addition of NaOH.

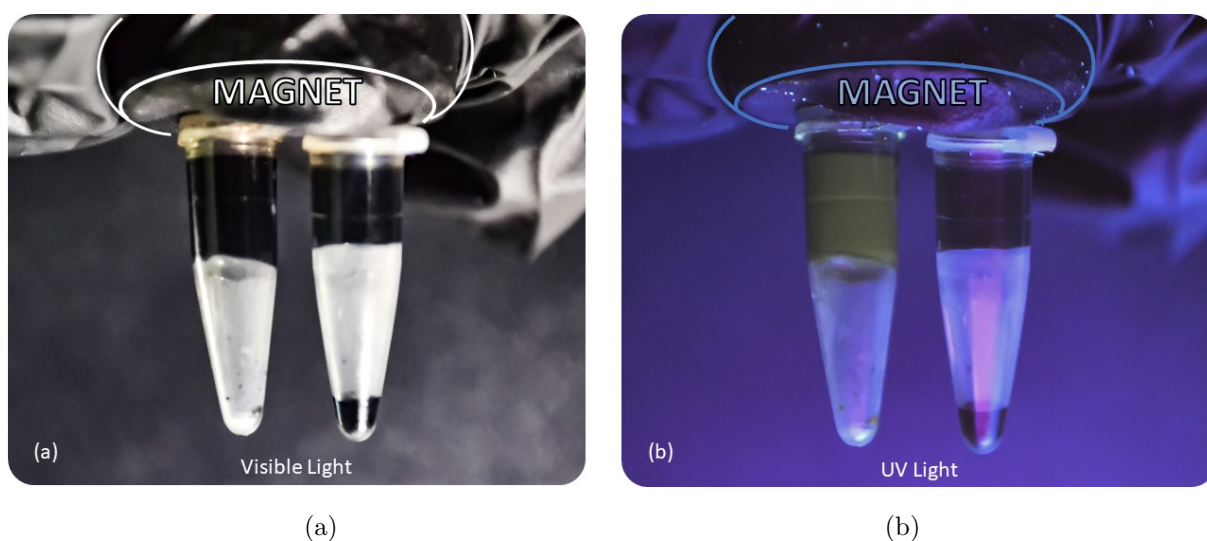
On the other hand, the N-CDs were initially added to a solution of citric acid at pH 2.0, subsequently adjusted to pH 7.0 in attempt to preserve the amount of free citrate in the final product, however the final ionic strength is not guaranteed due to the acidic character of the N-CDs (see subsection 5.3.1). The sample was homogenized following the dispersion protocol detailed in section 5.1.

Figure 67 exhibits the obtained stable fluorescent magnetic liquids based in CD1+Co6 and CD7+Co6 at a MNPs volume fraction of  $\phi = 0.5\%$  and a N-CD concentration of 5.0 g/L. The samples do not present significant differences when exposed to the visible light, but under an UV light the fluorescence emission produced by the N-CDs can be easily perceived. Note that the sample of just MNPs does not fluoresce, as expected.



**Figure 67** – Visual aspects of fluorescent magnetic liquids based in CD7+Co6 (left) and CD1+Co6 (middle) in comparison to the unmixed Co6 based ferrofluid (right) under (a) visible light and (b) UV light.

Unfortunately, the blue emission is considerably less intense if compared with the green emitter, likely due to the range of absorption of the MNPs and possible quenching effects. For this reason, from now on we focus on the characterization of the CD7+Co6 which presents the higher potential in future applications.



**Figure 68** – Fluorescent magnetic liquid based in CD7+Co6 samples (left) and the pure Co6 ferrofluid (right) being held by a magnet under (a) visible light and (b) UV light.

Figure 68 shows the samples previously presented in Figure 67 based in CD7+Co6 and the pure Co6 FF being held by a magnet against gravity – under visible and UV light. Note that no phase separation occurs, the manipulation of the fluid via magnetic forces is preserved and the fluorescence is not perceptibly affected when applying the external magnetic field.

The stability under external magnetic field generated by a magnet observed in the macroscopic level is also preserved in the microscopic scale as shown by the optical

microscopy images in Figure 69. No significant difference is observed from the pure FF in the left and the FML in the right, besides the fact that the mixed sample seems slightly darker.

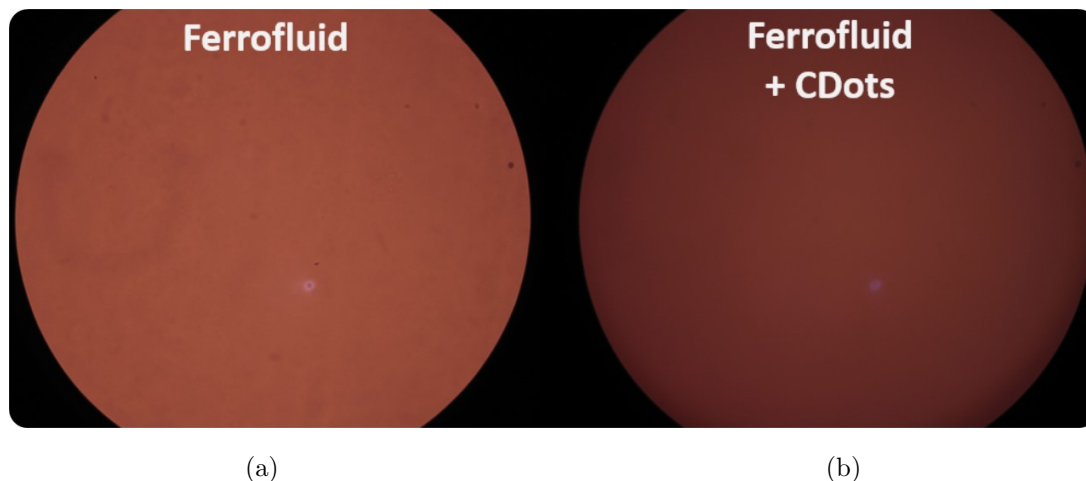


**Figure 69** – Optical microscopy images under an external magnetic field of (a) the neutral Co6 ferrofluid based in citrate coated MNPs and (b) the FML based in the CD7+Co6 samples.

These observations assure the macro and microscopic stability of this new nanocolloid based in MNPs and N-CDs. Still, in the next section we go one step further, thus examining the particle organization in this fluid at the nanometric scale.

### 8.3 Nanoscale Ordering

Small angle X-ray scattering (SAXS) measurements were performed at the Brazilian National Synchrotron Light Laboratory (LNLS) at the line SAXS01 and at the complex fluids group laboratory (GFC lab) at UnB with a XEUSS 2.0 (Xenocs). The data was acquired in the  $Q$ -range from 0.04 to 2.0  $\text{nm}^{-1}$  (XEUS) and 0.14 to 5.0  $\text{nm}^{-1}$  (LNLS) at room temperature and atmospheric pressure. Lastly, transmission electron microscopy (TEM) was performed in a JEM2100 electron microscope (JEOL) using an ultra thin carbon type-A 400 mesh Cu substrate (TED PELLA).

#### 8.3.1 Acidic Hybrid MNP|N-CD Suspension

The ferrofluid samples CoG and CoP were characterized prior and after the mixture with the N-CDs in order to probe the variations in interparticle interactions introduced by the coexistence of both NPs in the same acidic medium with opposite surface charge signs.

Figure 70 shows the scattering intensity  $I(Q)$  in absolute units ( $\text{cm}^{-1}$ ) of both ferrofluid samples sufficiently diluted such as the experimental structure factor  $S(Q) \sim 1$ . In this conditions, it was possible to adjust  $I(Q)$  with  $S(Q) = 1$  a form factor of log-normal polydisperse spheres using the software package developed by the NIST Center

for Neutron Research (NCNR) [224]. The obtained fitted values for the volume fraction were  $\Phi_{\text{SAXS}} = 0.51$  for CoG and  $\Phi_{\text{SAXS}} = 0.68$  for CoP, similar to the results  $\Phi_{\text{AAS}} = 0.53$  and  $\Phi_{\text{AAS}} = 0.89$  obtained by flame atomic absorption spectroscopy (AAS). The MNPs size parameters were  $d_0^{\text{SAXS}} = 10.6$  nm and  $s_0^{\text{SAXS}} = 0.41$  for CoG and  $d_0^{\text{SAXS}} = 6.1$  nm and  $s_0^{\text{SAXS}} = 0.40$  for CoP, as expected considering the base used in each synthesis protocol. The scattering length density (SLD) was theoretically calculated for water and cobalt ferrite as in ref. [253] and no background was added to the fit.

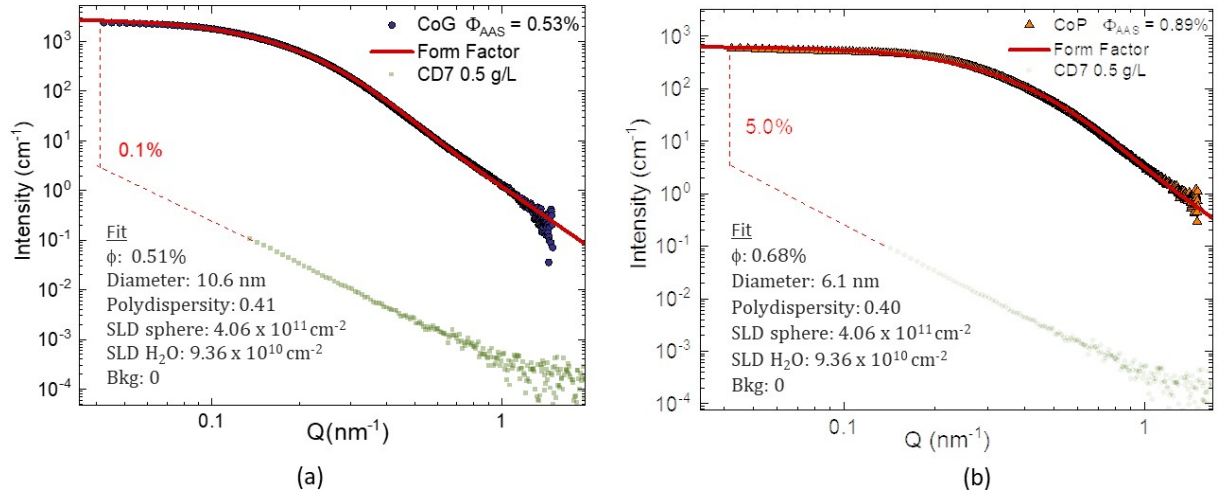


**Figure 70** – Scattered intensity  $I(Q)$  of the samples CoG, CoP and CD7 at diluted regimes. The ferrofluid data was fitted using a log-normal polydisperse sphere form factor in order to obtain the physical parameters written in red.

The signal of the sample CD7 at 0.5 g/L is also presented in Figure 70 to establish a comparison of the scattered intensity between these particles. The MNPs intensity is between  $20 - 1000\times$  more intense in the extrapolated  $0.04 < Q < 1.0$   $\text{nm}^{-1}$  region due to the higher contrast of the metallic material, if compared with the carbon based nanoparticles. For this reason, the simple addition of the signals would only result in a negligible modification of the ferrofluid curve in this range of  $Q$ , therefore, significant changes in the curve profile are expected to emerge mostly from alterations of local ordering of the MNPs.

The measurements of the mixed samples were performed at the LNLS as the high power of the X-ray beam allows us to have well resolved curves in just a matter of seconds of acquisition, avoiding particle sedimentation effects. The sample was sonicated and agitated immediately before insertion in the sample chamber, which from this point on took less than one minute till the end of the data acquisition. Figure 71 shows the profile of the both samples CoG and CoP before the mixture with CD7 and the corresponding FMLs, respectively, CoG+CD7 and CoP+CD7. Significant changes are observed in both cases, specially in the Guinier region.

For simplicity of the analysis, we will neglect the contribution of the N-CDs signal

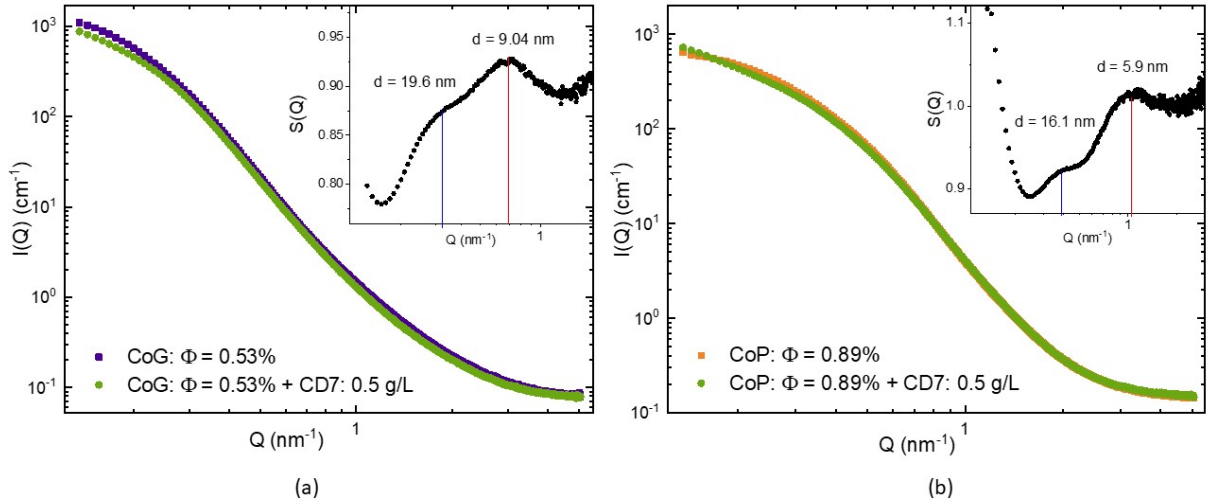


**Figure 71** – *Main figure*: Intensity profiles of the ferrofluids (a) CoG  $\Phi_{\text{AAS}} = 0.51$  and (b) CoP  $\Phi_{\text{AAS}} = 0.89$  before and after to the mixture with CD7 at 0.5 g/L. *Inset*: Experimental structure factor  $S(Q)$  estimated using Equation 8.1.

when considering the experimental structure factor  $S(Q)$  obtained by dividing the intensity of the mixture  $I_{\text{MIX}}(Q)$  by the intensity of the pure ferrofluid  $I_{\text{FF}}(Q)$

$$S(Q) = \frac{I_{\text{MIX}}(Q)}{I_{\text{FF}}(Q)}. \quad (8.1)$$

In this sense,  $S(Q)$  will be attributed mostly to the structuralization of the ferrofluid in response to the addition of the nanodots, as it would be unnecessarily complex to model both structure factor terms corresponding to the MNPs and N-CDs considering the intent of the present analysis.

Two main correlation peaks are observed in both cases. The peak located in larger  $Q$  correspond to distances ( $d = 2\pi/Q$ ) of 9.04 nm for CoG and 5.9 nm for CoP, which are very close to the particle size. This could be associated to particle aggregation considering that the observed correlation peak arises in response to MNPs now being at almost the contact distance – which is equal to twice the NPs mean radius. The peak at smaller  $Q$  corresponds to  $\sim 2 \times d_0^{\text{SAXS}}$  for CoG and  $\sim 2.6 \times d_0^{\text{SAXS}}$  for CoP, however from this results alone, its origin is not very clear. The attractive interparticle interactions are corroborated by the increase of  $S(Q \rightarrow 0)$  – despite the limited  $Q$ -range. In the case of CoG,  $S(Q \rightarrow \infty) < 1$  can be attributed to a small reduction of the number of MNPs in suspension due to sedimentation, as  $I(Q) \propto \Phi$ , causing an overall decrease in intensity of the curve profile of sample CoG+CD7 in relation to CoG.

In fact, TEM images<sup>2</sup> of sample CoG+CD7 presented in Figure 72 indicate that the N-CDs indeed decorate the MNPs. The bigger MNPs are surrounded by smaller nanoparticles with diameters around 2 nm, which thus we can assume to be the N-CDs. A size polydispersity of the N-CD coated MNPs is evident, as expected considering the

<sup>2</sup> Check section 4.2 for the procedure of sample deposition on the ultra-thin carbon substrate.

initial ferrofluid was already considerably polydisperse ( $s_0^{\text{SAXS}} = 0.4$ ). Diameters close to 10 nm, as well as around 20 nm can be observed, in agreement with the correlation lengths indicated by the SAXS curves.

The surface coating observed in Figure 72 for sample CoG was not as clear in TEM images captured for the CoP sample. This is probably due to the similarity in size distribution, as the number of MNPs in the 2 – 6 nm range is significantly higher in the case of CoP, which physically impairs the complete coverage of a MNP surface and, further, hinders the direct differentiation of N-CDs and MNPs in the TEM images by their diameter's gap.

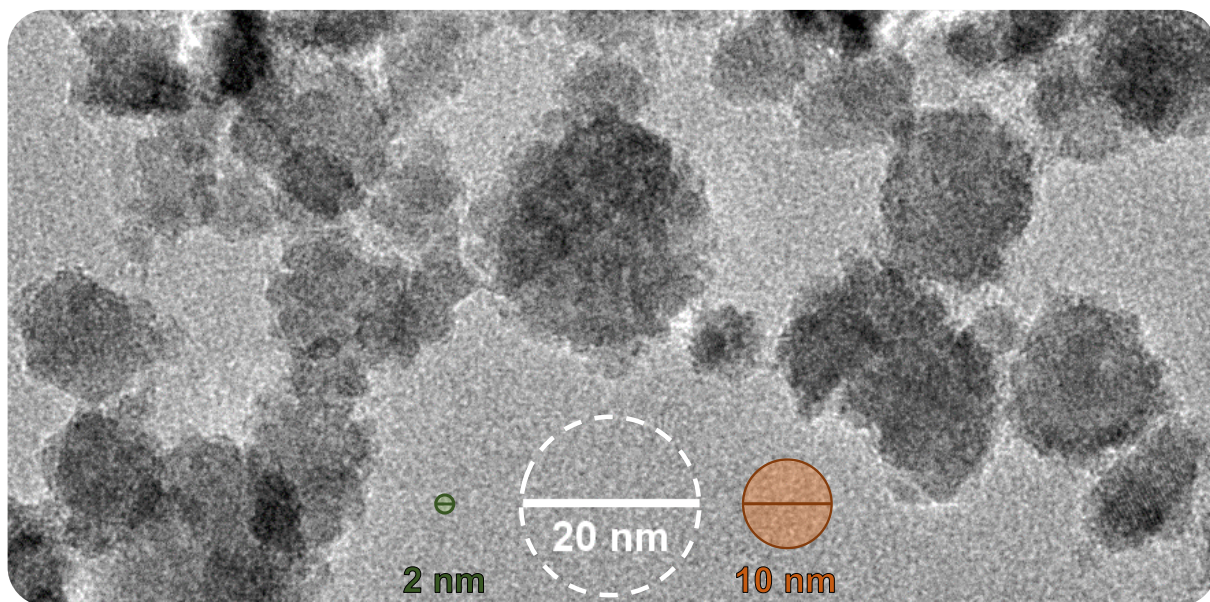


**Figure 72** – Transmission electron microscopy images of the FML composed of CoG and CD7. The scales of 2 nm, 10 nm and 20 nm are references to the sizes of N-CDs, MNPs and surface coated MNPs by N-CDs, respectively.

The ensemble of results from the macroscale to the nanoscale clarifies the impossibility of obtaining stable FMLs at highly acidic pH without additional surface functionalization. The main reason is the attractive electrostatic forces between the two types of NPs that induces the partial to complete surface coverage of the MNPs by N-CDs. The shielded electrostatic potential of the MNPs is insufficient to prevent flocculation then inducing particle sedimentation. The phase separation can be accelerated by an external magnetic field and, contrarily, it can be temporarily reversed by sonicating or manually agitating the sample. The excess of N-CDs can still remain dispersed in this condition, as indicated by the green emission in Figure 66. In opposition, the fluorescence seems to be mostly attenuated in the precipitate, in despite of the presence of numerous N-CDs that are covering the MNPs surface, suggesting a quenching effect due to the particle aggregation.

### 8.3.2 Fluorescent Magnetic Liquid

Alike the approach applied in previous section, we also performed SAXS measurements of the sample Co6 at  $\Phi = 1.02\%$  in order to obtain its intensity profile  $I(Q)$  at an approximately non-interacting regime. Indeed, it was possible to adjust a theoretical  $I(Q)$  based in the log-normal polydisperse form factor (and  $S(Q) = 1$ ), presented in Figure 73 which the obtained size parameters were  $d_0^{\text{SAXS}} = 5.8$  nm and  $s_0^{\text{SAXS}} = 0.44$ , similar to the values obtained by TEM measurements  $d_0^{\text{TEM}} = 6.4$  nm  $s_0^{\text{SAXS}} = 0.3$  and XRD  $d_{\text{XRD}} = 7.2$  nm [252].

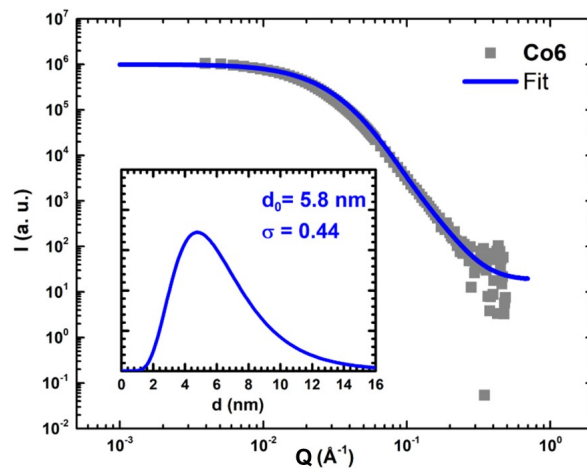


**Figure 73** –  $I(Q)$  of the ferrofluid sample Co6 at  $\Phi = 1.0\%$  adjusted by using a theoretical scattering intensity of log-normal polydisperse spheres. Figure reproduced from ref [252].

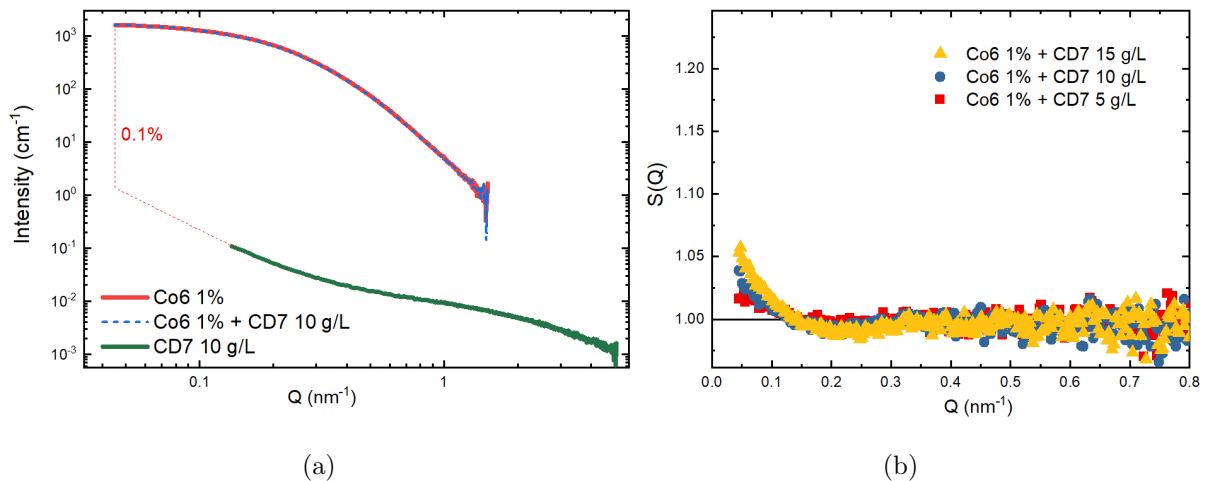


**Figure 74** – (a) Intensity profile  $I(Q)$  of the samples Co6, Co6+CD7 and aqueous dispersion of CD7. (b) Structure factor  $S(Q)$  of the FML Co6+CD7 with MNPs volume fraction  $\Phi = 1.0\%$  and in various concentrations of N-CDs 5, 10 and 15 g/L.

In subsection 8.2.2 it was attested that the FML is stable at the macroscopic and microscopic scale. Here, the stability at nanoscale can be also confirmed by the SAXS results. In Figure 74a, the mixture of N-CDs with the citrated ferrofluid (blue dashed curve) does not show critical changes if compared with the pure ferrofluid (red curve),

contrarily to what is observed for the acidic condition (see Figure 71). The experimental structure factors shown in Figure 74b for various N-CDs concentrations were calculated, as previously, following the relation established in Equation 8.1.

The  $S(Q)$  is very close to 1 for  $Q > 0.2 \text{ nm}^{-1}$ , but progressively increases with the concentration of N-CDs in smaller  $Q$ -values. Nevertheless, the observed increment at  $Q < 0.2 \text{ nm}^{-1}$  is almost negligible ( $S(Q \rightarrow 0) < 1.075$ ), which could be either associated to an increase in ionic strength originated from the N-CDs dispersion or the  $I(Q)$  signal of N-CDs aggregates themselves as it could introduce more than a 5% intensity increase if we consider a non-linear extrapolation. Either case, the stability is assured as the MNPs and N-CDs seem to effectively repel each other, despite of the minimal increase towards attractive interaction as the N-CDs concentration increases.

## 8.4 Magnetic and Photoluminescent properties

### 8.4.1 Magnetization and Magnetohypertermia

The nanofluids had their magnetic characterization carried out in a Cryogenic S700X-R SQUID Magnetometer at the GFC (UnB - Brasília). For the measurement, the samples were conditioned Plexiglas<sup>®</sup> sample holders sealed off with THF. Magnetization versus applied field was recorded both at room temperature (300 K) and at low temperature (5 K). Figure 75 shows the experimental results comparing the magnetic properties of the diluted FF ( $\Phi = 1\%$ ) (red line) and the mixed Co6[ $\Phi = 1\%$ ]+CD7[10 g/L] FML (blue circles).

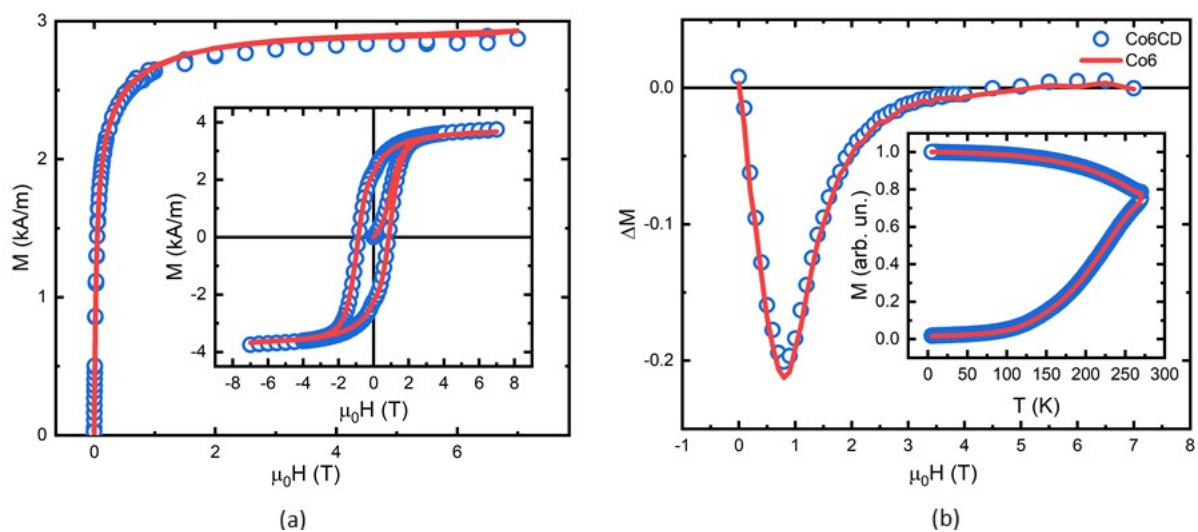


**Figure 75** – Comparison of the magnetic properties between the FML Co6[ $\Phi = 1\%$ ]+CD7[10 g/L] (blue circles) and the pure ferrofluid Co6 ( $\Phi = 1\%$ ) (red line): (a) *Main figure*: Room temperature (300 K) magnetization curves  $M(H)$ . *Inset*: Hysteresis loop at 5 K. (b) *Main figure*:  $\Delta M$  calculated by Equation 8.2 following the Thamm-Hesse formalism. *Inset*: Magnetization as a function of temperature  $M(T)$  curves following the ZFC/FC protocol.

The main graph in Figure 75a shows a typical room temperature magnetization curve ( $T = 300$  K) which allow us to assess  $M(H)$  in typical application temperatures. As mentioned in Part I, this curve highly depends on the size distribution of the sample, following the Langevin model (see Equation 1.2). Therefore, the superposition of the data indicates that the size distribution remained mostly unaffected, as well as the saturation magnetization.

In addition, the inset Figure 75a presents  $M(H)$  at 5 K, where the magnetic anisotropy and the effect of interparticle interactions are unraveled. Once again, the curves are superposed indicating no interference in  $M(H)$  by the introduction of the N-CDs. Moreover, while the low temperature coercivity could be used to characterize the anisotropy, the characterization of the interaction state of the colloids can be done applying the  $\Delta M$  Thamm-Hesse formalism [254].

In this approach, the experimental deviation from the expected on a noninteractive system by the Stoner-Wohlfarth model [255] is used as means to gauge the global interaction regime in the sample. In a non interactive regime, the remanence relations state that the initial magnetization curve at a given  $H$  value is expected to be the average between the upper and lower branches of the hysteresis loops. In this manner, the deviation  $\Delta M$  is written as

$$\Delta M(H) = M_{initial} - \frac{M_{upper} + M_{lower}}{2}, \quad (8.2)$$

where  $M_{\#}$  denotes the branches of the hysteresis loop analyzed. The main graph in Figure 75b shows that  $\Delta M$  is mostly negative, revealing that demagnetizing interactions (dipolar) are predominant. The FML presents equal behavior.

Finally, the blocking properties of the ferrofluids and the hybrid nanofluids are investigated by using low field thermal dependence of magnetization, employing the usual zero field cooling and field cooling (ZFC/FC) protocol. Unfortunately, the high values of the anisotropy and particle volume combined do not allow us to obtain a blocking temperature for this MNPs. Anyhow, we can attest that the magnetic behavior of the sample in both ZFC/FC protocols remains identical with the addition of the N-CDs.

Further, the magnetic nanoheating capabilities of the studied samples are investigated by magnetohyperthermia essays carried out in a nanoScale Biomagnetics D5 System. In an experiment, the sample is subjected to an AC magnetic field while the temperature increase is recorded.

The specific power absorption (SPA), expressed in W/g, quantifies the efficiency of the conversion of electromagnetic energy into heat by the nanoparticles. For a dispersion of magnetic nanoparticles with volume fraction  $\phi_{mnp_s}$ , SPA in the adiabatic regime is written as

$$SPA = \frac{1}{\Phi} \frac{\rho_s}{\rho_{MNP_s}} c_s \left( \frac{\partial T}{\partial t} \right)_{max}, \quad (8.3)$$

where  $\rho_s$  is the density of the solvent,  $\rho_{\text{MNPs}}$  the density of the magnetic nanoparticles and  $c_s$  the specific heat capacity of the solvent. The derivative  $\left(\frac{\partial T}{\partial t}\right)_{\text{max}}$  denotes the maximum variation of temperature recorded, characterizing the adiabatic regime.

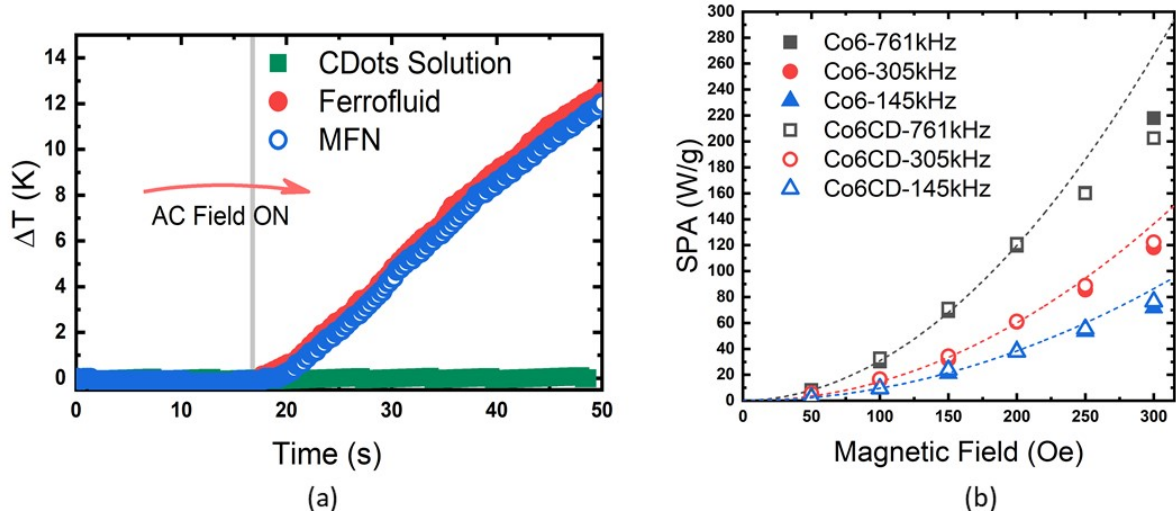


**Figure 76** – (a) Temperature variation over time for the CD7[10 g/L] aqueous solution (green squares) the sample Co6[ $\Phi = 1\%$ ] (red full circles) and for the magneto-fluorescent nanofluid (MFN) Co6[ $\Phi = 1\%$ ]+CD7[10 g/L] (blue circles). (b)  $SPA(H)$  comparison between the pure Co6 sample and the FML Co6+CD7 in various frequencies.

Figure 76a, as expected, the N-CDs dispersion alone does not show any temperature increase with the appliance of the AC magnetic field. On the other hand, both MNPs based samples present a significant temperature increase, while the FML shows just a slight delay in the heating process when comparing to the pure Co6. Indeed, no significant difference in the  $SPA(H)$ 's values can be observed in Figure 76b, regardless the frequency.

These results prove that the FML comprehensively retains the magnetic characteristics of the precursor ferrofluid, at 5 K and room temperature. Moreover, the conversion of electromagnetic energy into heat is also preserved as the SPA remains practically unchanged after the addition of the N-CDs. In the next section we probe the fluorescent properties, which are more likely to go through notable changes.

## 8.4.2 Photophysical effects

The FML samples based in Co6+CD7 were characterized by our Italian collaborators at UNIPA (Palermo) using steady-state and time-resolved spectroscopy. The emission spectra were recorded with a JASCO FP-6500 spectrofluorometer in a 1 cm cuvette. The time-resolved fluorescence measurements were carried out by a tunable laser system consisting in an optical parametric oscillator pumped by a Q-switched Nd:YAG laser (5 ns pulses at 10 Hz repetition rate). Fluorescence spectra were recorded on an intensified charge coupled device (CCD) camera, integrating the signal within temporal windows of 0.5 ns duration after variable delays from the laser pulse [183].

They chose two N-CDs concentrations of 1.0 g/L and 10 g/L to study the emission of the visible band in various concentrations of MNPs between  $\Phi = 0.1$  vol% and 1.0 vol%. In Figure 77a and b, it is reported the CDs emission band at 440 nm for the more diluted and more concentrated CDs dispersions, on increasing MNPs concentration. Moreover, it was checked that the magnetic nanoparticles with the  $\text{CoFe}_2\text{O}_4@ \gamma\text{-Fe}_2\text{O}_3$  iron oxide structure do not significantly emit in this spectral range (dashed line in Figure 77a).

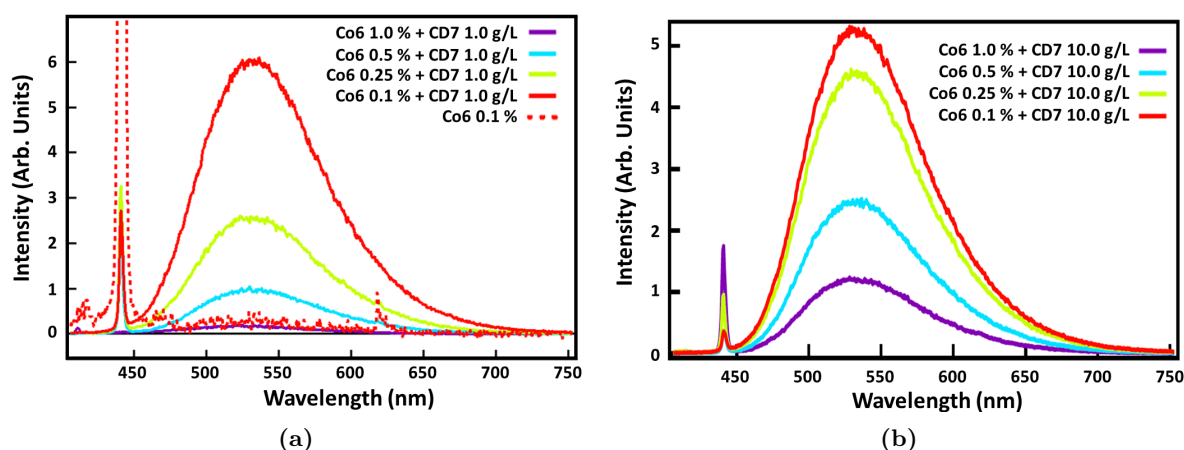


**Figure 77** – (a) Emission spectra of MFLs exciting at 440 nm at 1.0 g/L CDs concentration and different MPN's volume fractions (continuous curve) and the emission spectrum of bare MNPs (dashed curve); (b) Emission spectra of MFLs exciting at 440 nm at 10.0 g/L CDs concentration and different MPN's volume fractions.

Although the CD fluorescence remains well visible in almost any case, adding the MNPs produces a gradual quenching of the emission intensity, as it is clearly observed in both cases of Figure 77. The quenching occurs with almost no variations in the spectral shape.

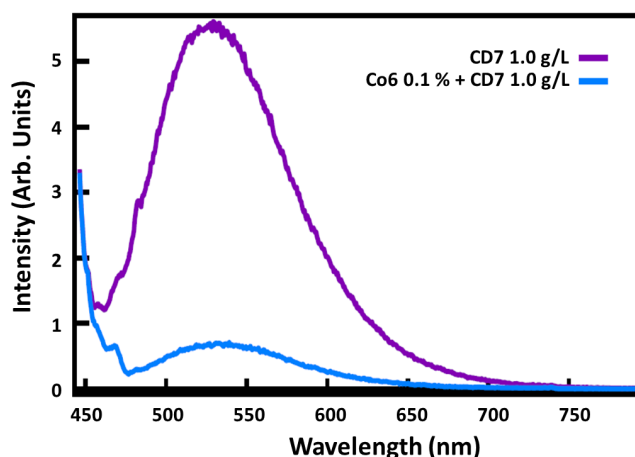


**Figure 78** – Emission spectra of aqueous solution at 1 g/L of bare N-CDs (purple curve) and of the same dispersion but with 0.1% of MNPs (blue curve).

To evaluate the degree of the emission reduction, Figure 78 exhibits a comparison between an aqueous solution of 1 g/L of bare CDs and with the FML containing 1.0 g/L of N-CDs and 0.1 vol% of MNPs. Indeed, the emission band intensity decreases of about

8 times in presence of just 0.1 vol% of MNPs. In this respect, it is worth noting that this quenching is not only due to an interaction between the two particles. Part of it is actually caused by the absorption of a fraction of the excitation beam from the MNPs. A rough estimation of this effect results concludes that out of the factor of 8, the “actual” quenching (i.e. due to the interactions between the NPs, and not just the MNPs absorbing the excitation beam) is about a factor of 3.2.

To deeply study the quenching of the emission, they also investigated and compared the decay kinetics of the emission band of CDs with or without the MNPs. The experimental lifetime of the emission ( $\tau$ ) was obtained by fitting an exponential function convoluted with a Gaussian instrumental response function (IRF) with a 5 ns full width at half maximum (FWHM), determined by the laser temporal profile. The accuracy on the time constant of the decays is about 0.2 ns.

The kinetics are reported in Figure 79. The emission lifetime of the bare N-CDs results in 5.7 ns, inside the typical range of this type of sample – from 4 to 7 ns depending on the excitation energy [34, 170]. On the contrary, the lifetime of the FML results 4.2 ns. The decrease of the emission lifetime indicates that part of the quenching is collisional, probably caused by the collision between N-CDs and MNPs particles. Despite this, the ratio between the lifetime values ( $5.7/4.2 = 1.36$ ) does not coincide with the total emission quenching observed in the steady-state experiments (3.2 vs 1.36) suggesting that the quenching is not only due to collisions, but it is also static, caused probably by the formation of stable ground-state CDs-MNPs complexes. This could justify the small attractive interaction observed in SAXS measurements (see Figure 74).

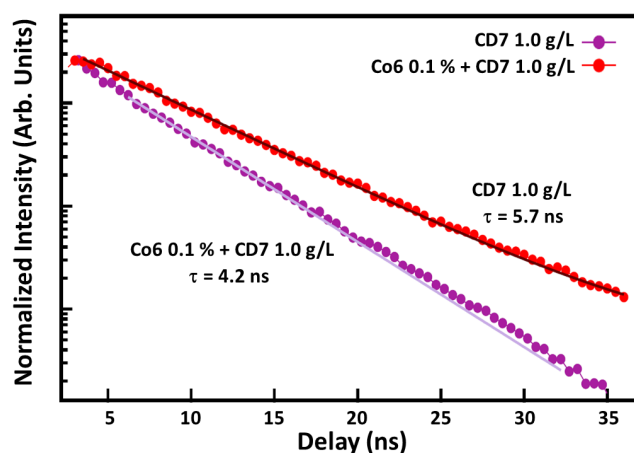


**Figure 79** – Decay kinetics of bare N-CDs (red) and the FML with 1 g/L of N-CDs and 0.1 vol% MNPs concentration. Lifetime values are  $\tau = 5.7$  ns for pure N-CDs and  $\tau = 4.2$  ns for the FML.

Overall, one may hypothesize that for a small fraction of the particles, the electrostatic repulsion is insufficient to keep them apart. Therefore, only a fraction of the NPs tend to form complexes (dynamically or statically), leading to a decrease of the emission intensity. Anyway, the lack of spectral changes of the fluorescence during the quenching

suggests that the interactions between the two types of NPs remain very weak except during their association into composites and/or collisions.

Further, it was also verified that the tunability of CDs emission – an important property for the potential applications of these FMLs – is mostly preserved by the addition of MNPs as shown in Figure 80.

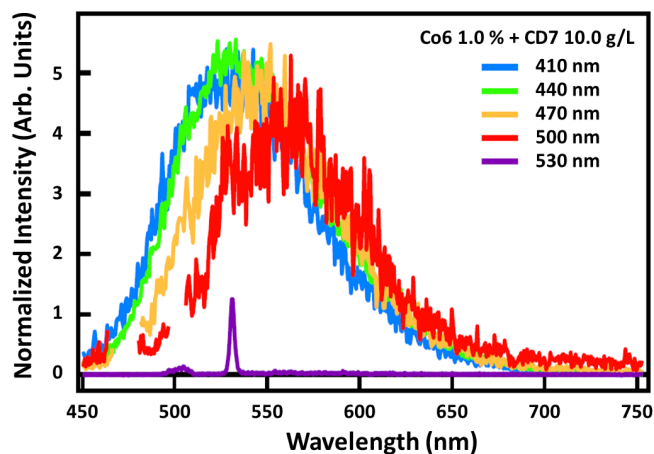


**Figure 80** – Emission spectra of FML composed of 10 g/L N-CDs and 1.0 vol% MNPs excited at different wavelengths.

Conclusively, the study of the synthesized FML by steady-state and time-resolved fluorescence spectroscopy confirms that the N-CDs retain their essential properties: fluorescence with nanosecond decay lifetimes; fluorescence tunability; and very similar spectral properties as compared to bare N-CDs aqueous dispersions, even in the co-presence of large concentrations of magnetic NPs. That being said, a closer look to the data reveals a significant degree of interaction between the two, which leads to fluorescence quenching. Based on lifetime measurements, the quenching occurs in part through a static mechanism (complex formation) and partly through a dynamic mechanism (collisions).

## Conclusions on Fluorescent Magnetic Liquids

In this part we have presented a novel fluorescent magnetic fluid based on magnetic iron oxide nanoparticles and carbon nanodots. The hybrid material was obtained with the use of the two nanomaterials described in [Part I](#) and [Part II](#) without any encapsulation or confinement of the components. The method used to combine the samples is practical, low-cost and reproducible. The advantage of using this type of MNPs is the possibility of tuning the magnetic properties through size, chemical composition and concentration. Moreover, the use of N-CDs allows to have a bright and tunable fluorescence by an abundant, non-toxic, low-cost and environmental friendly material. We probed two physico-chemical conditions: the aqueous dispersion of the bare iron oxide MNPs at acidic medium with the bare N-CDs; and the citrate coated MNPs with the bare N-CDs at neutral pH.

In the acidic condition, the hybrid dispersions were synthesized with core-shell  $\text{CoFe}_2\text{O}_4@ \gamma\text{-Fe}_2\text{O}_3$  MNPs with two different sizes (10 and 6 nm). Both dispersions were colloidally unstable, as the MNPs and N-CDs present opposite charge signals at pH 2.5, inducing particle aggregation. This clustering effect shields the initial repulsive MNPs-MNPs electrostatic potential, similarly to the effect of strongly increasing the ionic strength. The result was a slow phase separation by sedimentation or a fast one by the introduction of an external magnetic field. The concentrated phase composed of MNPs show almost no fluorescence (likely due to quenching) while the supernatant still emits due to an excess of well dispersed N-CDs. SAXS measurements indicated an attractive structure factor with two correlation lengths, one corresponding to distances of about the MNPs mean diameters and another a few times larger. Further, TEM images showed that the positively charge MNPs were indeed decorated by the negatively charge N-CDs in response to the attractive electrostatic forces.

On the other hand, highly stable fluorescent magnetic liquids (FMLs) were obtained mixing the bare N-CDs with citrate coated core-shell  $\text{CoFe}_2\text{O}_4@ \gamma\text{-Fe}_2\text{O}_3$  MNPs with an average diameter of 6 nm at pH = 7.0. The sample presented long-term colloidal stability at the macro and microscopic level, with and without the presence of an external magnetic field. The fluorescence was still noticeable after the mixture, however it was significantly brighter in the case of the green emitting CD7 sample.

Various magnetic characterizations were performed such as: magnetization at room

temperature, hysteresis loops at 5 K, Thamm-Hesse plots and ZFC/FC curves. All of them showed no significant changes from the pure FF sample and the hybrid FML. In addition, magnetohypertermia measurements were also carried out attesting that the presence of N-CDs did not affected the specific power absorption (SPA). In sum, the addition of the N-CDs in this physico-chemical condition does not actively influence the magnetic properties of the original ferrofluid.

Lastly, the photoluminescent properties were probed in order to quantitatively determine the modifications in the emission spectrum generated by the introduction of the MNPs into the N-CDs fluorescent nanofluid. First of all, the MNPs causes a reduction o the intensity of the PL, which could be linked to a few factors. In the specific case of  $\Phi = 0.1\%$  of MNPs and 1.0 g/L of N-CDs, the emission reduction in the 500 – 575 nm zone is about  $8\times$ . Since the MNPs partially absorb the excitation emission, the actual quenching from particle interactions is only a factor of 3.2. Moreover, measurements of the emission lifetime determine that the ratio between the lifetime values between the pure N-CDs dispersion and the FML is in fact 1.36. Therefore, the observed reduction of fluorescence signal ( $8\times$ ) is a combination of MNPs absorption (a factor of 4.8) of the excitation emission added to a collisional (a factor of 1.36) and a static (a factor of 1.84) quenching due to interactions between N-CDs and MNPs. Nonetheless, the intensity of the emission can be tailored by varying the concentration of each NP, as the addition of N-CDs increases the emission and an increase of MNPs reduces it. Anyway, the mentioned quenching does not fully eliminate the tunability of the N-CDs emission, which is mostly preserved till 500 nm.

These results confirm the possibility of obtaining a stable and microscopically homogeneous fluorescent magnetic fluid combining N-CDs and MNPs, where most of their individual properties are preserved in the final product. This nanofluid has a great potential in applications such as in quality tests of metal pieces used in industry.

## General Conclusions and Perspectives

## General Conclusions and Perspectives

On this thesis we studied ferrofluids based in ionic liquids, carbon nanodots aqueous dispersions and fluorescent magnetic fluids. The MNPs and N-CDs show great potential in applications involving energy conversion, where the former has shown to increase the efficiency in thermoelectric devices [16] while latter has been considered a promising candidate for “green” photovoltaic solar cells [256].

Regarding the ferrofluids based in room temperature ionic liquids (FFs-RTIL), we have focused on their stability and thermodiffusive properties. The investigation of the FF-RTIL based on EAN shed light on the influence of the initial counterions and water content by determining the interparticle interactions – via the compressibility  $\chi$  and the second virial coefficient  $A_2$  – and the thermodiffusion parameters  $S_T$  and  $D_m$  as a function of temperature and volume fraction of magnetic nanoparticles.

In addition, the study of the thermodiffusion under magnetic field in a broad range of temperatures performed with the FF-RTIL based in EMIM-TFSI demonstrates that the anisotropy of  $S_T$  and  $D_m$  can indeed be generated in such systems. Moreover, the effect is well adjusted by the theoretical model described in refs. [25, 127]. Therefore, this FF-RTIL is a promising candidate to make use of the magnetically induced enhancement of the Seebeck coefficient in thermoelectric applications.

The perspectives of future work with these FF-RTILs are:

- Systematic DLS measurements with the new device (Vasco Kin - Cordouan Technologies) have been also performed in many of the experimental situations described here, but a systematic comparison with the  $D_m$  determinations by FRS has not yet been conducted. This should be done in the near future to cleanly compare the two kinds of measurements, in order to clearly show in which situations the two determinations converge to comparable  $D_m$  values and when they are different and why.
- Up to this point, the theoretical adjustment of the  $\Phi$ -dependence of the Soret coefficient  $S_T$  with the model presented in [subsection 3.1.1](#) to deduce the NP’s Eastman entropy of transfer  $\hat{S}_{NP}$  has only been driven for ferrofluids based on EAN with  $\text{Na}^+$  counterions at room temperature. To analyse the ferrofluids based on

other RTIL systems, it would be necessary to evaluate the range of reasonable values of  $|\xi_0^{\text{eff}}|$  in these systems and how it can evolve with  $T$ . To obtain the sign of  $\xi_0^{\text{eff}}$ , complementary thermoelectric measurements are in progress, we do not yet have their result. Let us note however that some complementary measurement would be useful in the EMIM-TFSI system to extend the  $\Phi$ -range, with different NPs coatings (cf. the article to be published of Riedl J. et al. in Annex B). Complementary experiments would be also important in the water-EAN system at low proportion of EAN, focusing on the electrolyte-like area.

- From a more general point of view, for thermoelectric applications, it would necessary to obtain systems with a negative  $S_T$  stable up to high temperatures. All the RTILs probed up to now have given a positive  $S_T$ . A possibility, by analogy with the water-EAN system probed here, would be to use some mixtures of RTIL and organic solvent. Several candidates are presently under evaluation, anyway the study of such systems will concern another work.

The investigation of the N-CDs aqueous dispersions in different pH's focused on their colloidal stability, surface charge and local ordering. The experimental results showed that the stability is improved as the pH of the carrier liquid goes from acidic to alkaline. Zeta potential, potentiometric and conductimetric measurements established a correlation between the stability enhancement and the increase in the negative surface charge of the nanodots, indicating the fundamental role of the interparticle electrostatic repulsion.

However, in highly alkaline conditions an irreversible hydrolysis reaction occurs, further amplifying the negative surface charge of the N-CDs but also significantly altering their optical properties. This effect is critical for the green emitting CD7 sample as the fluorescence emission is strongly blue shifted.

Finally, a nanoscale examination by SAXS confirms the presence of aggregates that slowly sediment over time in acidic conditions. Surprisingly, the results indicated that a portion of the aggregates can still remain well dispersed in the supernatant, which can be partially removed by ultracentrifugation and can have their size, in some extent, reduced by elevating the pH.

The perspectives of future work with these N-CDs are:

- The charge determined by the potentiometric and conductimetric titrations could only be properly estimated in charge per unit of mass due to the lack of information regarding the N-CDs surface area. It would be of great benefit to experimentally determine the total surface area, thus being able to more precisely evaluate the number of sites per  $\text{nm}^2$ .

- The SAXS measurements performed at the LNLS could not resolve very small  $Q$ -values with sufficiently low amounts noise due to the lack intensity. However, the new SIRIUS facility have been recently inaugurated and the upgraded beam intensity is order of magnitude higher than the previous one. In the future it would be interesting to explore ultra small angles in order to precisely determine the aggregate sizes and fractal dimensions.
- The photoluminescence (PL) analysis of the N-CDs at highly alkaline medium (pH=12.0) was only qualitative. A dynamic quantitative analysis would allow us to evaluate the actual shift in the emission wavelength as well as determining the variation in the emission intensity. These results could provide new insights on the emission mechanisms extending the current understand of the N-CDs fluorescence.
- Now that the range of colloidal stability and optical properties were established, it is possible to study the thermodiffusion of N-CDs aqueous dispersions at higher concentrations by performing ultracentrifugation procedures – reducing aggregates and improving stability – while avoiding highly alkaline pH's (close to pH=12.0) – in order to maintain their strong optical absorption in the visible range.

We have shown that combining aqueous ferrofluids and N-CDs to produce a hybrid nanocolloid can either generate unstable suspensions or stable dispersions depending on the pH of the medium. At acidic conditions, the instability of the mixture arises from the fact that MNPs and N-CDs present opposite charges. For this reason, the N-CDs decorate the MNPs increasing in size and screening the repulsive MNPs-MNPs electrostatic potential. As a consequence, particle sedimentation and magnetic separation is observed to induce demixing of the magnetic and the fluorescent phases.

On the other hand, in an aqueous solution at pH = 7.0 with controlled free citrate ions, citrate-coated MNPs and N-CDs both present a negative surface charge, resulting in stable colloids to the microscopic level even under the application of an external magnetic field. We were able to confirm that the magnetic properties of the fluorescent magnetic liquid remains almost unchanged, however the fluorescence is partially quenched.

The perspectives of future work with these FML are:

- We here presented core-shell MNPs with a cobalt ferrite core and a maghemite shell. In the future we plan to vary the size and composition of the MNPs in order to explore the range of magnetic and fluorescent properties. Since its fluorescence emission is visible with the cobalt ferrite which has a strong optical absorption, better results are expected with maghemite, zinc or copper ferrites with emission in lower wavelengths.

- 
- Considering sensor applications, it would be interesting to test the limits in which the system undergoes phase separations, magnetic and/or fluorescence alterations depending on changes of medium, for instance pH, ionic strength or the introduction of contaminants.
  - Considering the quality of materials, we intend in the future to perform inspection tests in metallic parts in order to evaluate the efficiency of the nanomaterial in identifying the presence of discontinuities or fractures.
  - Since the material is stable and composed of two highly absorbing materials, thermodiffusion measurements via FRS would easily determine if this hybrid nanofluid is suitable for thermoelectric applications. Thus, we intend to perform in the near future thermodiffusive characterizations with and without an external magnetic field.

# Extended Abstracts

# Resumo Estendido em Português

## Introdução

Com o crescente consumo global de energia, a busca por fontes renováveis tornou-se uma das prioridades de pesquisa científica em nível mundial. Além das fontes de energia renováveis de larga escala (ex.: solar, eólica, hídrica e biomassa), a energia térmica residual é considerada uma promissora fonte de reaproveitamento de energia. Isso se deve ao fato da energia térmica representar uma considerável parcela do uso global de energia [13], sendo explorada principalmente pela indústria, onde grande parte dessa é desperdiçada via gases de exaustão e sistemas de resfriamento a água.

Um método direto de conversão do calor residual em uma forma reutilizável de energia é pelo uso de dispositivos termoelétricos, onde parte da energia térmica é convertida em energia elétrica. Os conversores termoelétricos mais eficientes atualmente são compostos de materiais semicondutores [15]. Porém, termocélulas baseadas em líquidos estão atraindo muita atenção por serem uma alternativa barata e escalável. Neste contexto, termocélulas baseadas em ferrofluidos são promissoras geradoras de energia limpa [16].

Os ferrofluidos (FFs), dispersões de nanopartículas magnéticas (NPMs) em meios líquidos, pertencem à crescente classe de materiais inteligentes por unirem propriedades físicas de materiais sólidos (como o ferrimagnetismo), às características físicas dos fluidos (como escoamento). Ferrofluidos baseados em líquidos iônicos são uma grande tendência atual por possuírem certas vantagens em relação a meios aquosos. Líquidos iônicos a temperatura ambiente (LITAs) são solventes compostos puramente de íons, sendo assim, são não inflamáveis, possuem alta estabilidade térmica e eletroquímica, insignificante pressão de vapor, além de serem uma ótima alternativa “verde” para substituir os clássicos e mais perigosos solventes orgânicos [17]. Nesta tese serão explorados dois tipos de ferrofluidos baseados em líquidos iônicos: o primeiro é composto de nanopartículas de maguemita recobertas por íons citrato dispersas em NEA (nitrato de etilamônio) [18]; o segundo também é composto de nanopartículas de maguemita, porém são recobertas por íons SMIM<sup>±</sup>-TFSI<sup>-</sup> (1-(4-sulfobutil)-3-metilimidazólio bistrifilimida desprotonada) dispersas em EMIM-TFSI (1-etil-3-metilimidazólio bistrifilimida) [19, 20].

O foco do estudo de ferrofluidos a base de NEA é investigar os efeitos termodifusivos

e de estabilidade coloidal com diferentes contra-íons e ainda com a crescente adição de água ao meio composto apenas de íons. Por outro lado, o ferrofluido em EMIM-TFSI é um ótimo sistema para avaliar a anisotropia causada pela aplicação de campo magnético externo nos efeitos termodifusivos em função da temperatura.

Nanodots de carbono (NCs) pertencem a uma outra classe de materiais nanoestruturados que também possuem alto potencial em aplicações relacionadas a geração de energia, principalmente em conversão de energia solar [27] devido a seu amplo espectro de absorção. Eles são uma interessante alternativa aos tradicionais *dots* quânticos baseados em semicondutores visto que apresentam vantagens como síntese direta, simples e barata [28], baixa toxicidade [29] e serem ecologicamente sustentáveis [30]. Nesta tese são estudados nanodots de carbono enriquecidos com nitrogênio (N-NCs) onde a dopagem com esse elemento aumenta significativamente a sua fluorescência [34], outra importante característica desses nanomateriais. Assim, foram investigadas duas amostras com quantidades nominais de nitrogênio/carbono (N/C) diferentes [38]: a primeira com uma baixa dopagem (N/C=0.14) é chamada de CD1 – possuindo uma fluorescência majoritariamente azul – e a segunda com uma quantidade de nitrogênio mais elevada (N/C=0.74) denominada CD7 – emitindo principalmente no verde.

Atualmente, pouco é reportado na literatura [197] a respeito da estabilidade de dispersões aquosas desse tipo de N-NCs, onde grande parte do foco é dado principalmente para as propriedades óticas. Sendo assim, nesse trabalho é investigado em profundidade a carga superficial, estabilidade coloidal e organização local dessas dispersões aquosas em função do pH – sem dúvida o principal parâmetro regulador dessas propriedades em macro e nano-escala. Além disso, em meios altamente alcalinos, a quantidade de carga superficial sofre uma significativa modificação sugerindo uma potencial hidrólise de grupos superficiais amida. Essa hipótese é sustentada por medidas óticas de absorção e fluorescência, onde a alta concentração de íons hidróxido causa um forte desvio para o azul na emissão verde da amostra CD7.

Por fim, na última parte desse estudo é sugerido um novo nanomaterial híbrido combinando os dois tipos de nanopartículas investigadas para produzir um líquido magnético fluorescente (LMFs). Em meio ácido, a combinação gera uma dispersão instável onde as NPMs são recobertas por N-NCs e podem ser separadas com o auxílio de um ímã. Já em meio neutro (pH~ 7.0), o nanofluido se difere dos demais sistemas magneto-fluorescentes reportados na literatura, pois apresenta alta estabilidade coloidal mesmo na aplicação de um campo magnético externo. Dessa forma, as propriedades individuais de cada uma das dispersões coloidais são em grande parte preservadas no produto final, sem que ocorra separação de fase por um longo período de tempo (> 1 ano).

## Capítulo 1: Nanopartículas Magnéticas (NPMs)

O processo utilizado para a produção de ferrofluidos segue o método de Massart [49, 50] composto de duas etapas: a primeira consiste na síntese química das NPMs por coprecipitação em meio alcalino; já a segunda etapa refere-se a peptização e funcionalização das nanopartículas em solventes mais complexos. No capítulo 1 é apresentado o processo referente a etapa 1 (exibido na Figura 1 da tese) referente a obtenção das nanopartículas magnéticas a base de maguemita, bem como suas principais características morfológicas e estruturais, sendo a etapa 2 descrita no capítulo 2.

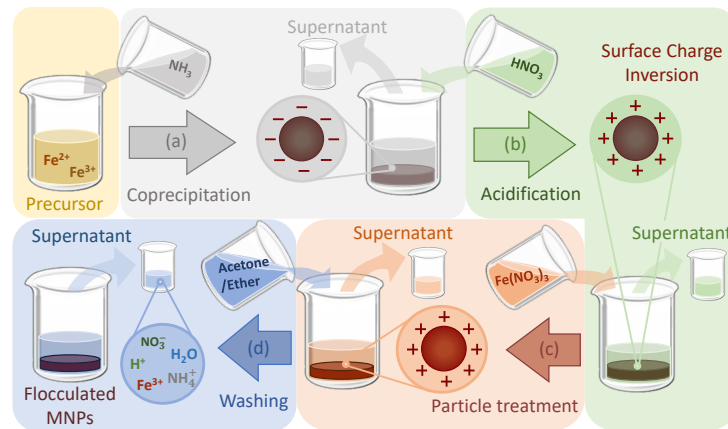


Figura 1 - Diagrama das quatro sub-etapas do processo de síntese de NPMs: (a) coprecipitação; (b) acidificação; (c) tratamento da partícula e (d) lavagem. A adição de soluções é representada pelas setas apontando para dentro enquanto a remoção de supernadantes é representada pela seta apontando para fora. A mudança de cor das NPMs representa a oxidação completa da estrutura cristalina.

A primeira etapa é subdividida em quatro sub-etapas: o processo se inicia pela coprecipitação (1a) ocorre a formação de NPs de magnetita ( $Fe_3O_4$ ) por nucleação e crescimento cristalino após a mistura da solução precursora de íons  $Fe^{+2}$  e  $Fe^{+3}$  com uma solução concentrada de  $NH_3$ . No processo de acidificação (1b) é adicionado  $HNO_3$  concentrado invertendo a carga superficial para valores positivos e dissolvendo possíveis subprodutos indesejáveis. A seguir, em (1c) é realizado um tratamento com  $Fe(NO_3)_3$  para oxidar completamente as NPs de magnetita para maguemita ( $\gamma-Fe_2O_3$ ). Finalmente, as partículas são lavadas com acetona/éter na sub-etapa (1d) reduzindo a força iônica e preparando o floculado para a futura dispersão e/ou funcionalização.

**Tabela 1 na tese** – Tamanhos determinados experimentalmente (referências [18, 19]) obtidos por MET ( $d_{0,MET}$ ,  $s_{0,MET}$ ) e magnetização a temperatura ambiente ( $d_{0,mag}$ ,  $s_{0,mag}$ ,  $d_{NP}$ ) das amostras dispersas em: EMIM-TFSI, NEA e meio aquoso.

Amostra	$d_{0,MET}$ (nm)	$s_{0,MET}$	$d_{0,mag}$ (nm)	$s_{0,mag}$	$d_{NP}$ (nm)
Água e NEA [18]	6.5	0.22	6.9	0.21	7.4
EMIM-TFSI [19]	8.7	0.3	8.9	0.23	9.6

Esse processo de síntese tipicamente produz NPs aproximadamente esféricas com

tamanhos médios de  $\sim 10$  nm. Entretanto, aplicando procedimentos de separação em tamanho por meio da variação da força iônica é possível reduzir a polidispersão e obter diferentes populações de NPs com diâmetros maiores ou menores. O tamanho das nanopartículas foi estimado por meio do ajuste de uma função lognormal nos histogramas obtidos a partir de medidas de microscopia eletrônica de transmissão (MET) e do ajuste da magnetização a temperatura ambiente ( $T = 300$  K) pelo modelo de Langevin. Os resultados são apresentados na tabela 1 da tese onde  $d_0$  é o diâmetro mediano,  $s_0$  a polidispersão e  $d_{NP}$  o diâmetro volumetricamente ponderado.

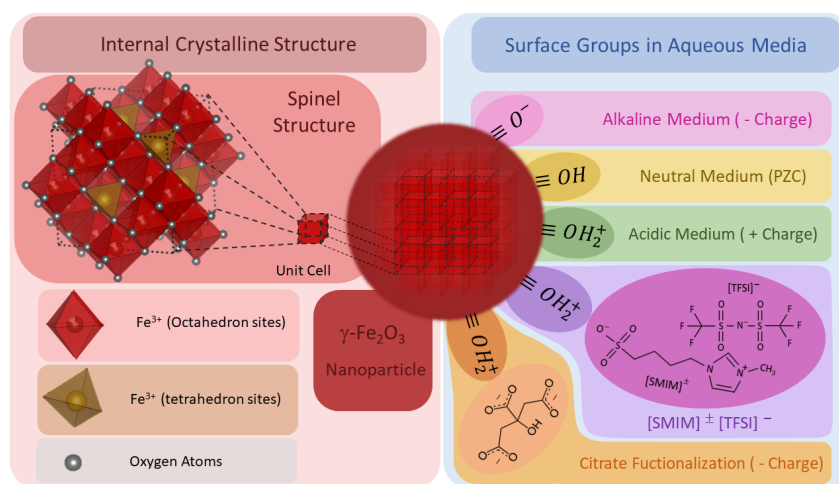


Figura 4 - Lado esquerdo em vermelho: Estrutura cristalina interna do tipo espinélio das NPMs exibindo os sítios octaedros (vermelho) e tetraedros (amarelo). Visualização da estrutura gerada usando ref. [64]. Lado direito em azul: Desenvolvimento dos grupos de superfície em diferentes meios aquosos: alcalino, neutro e ácido. A adição de dois ânions diferentes (citrato e  $[SMIM]^\pm$ - $[TFSI]^-$ ) a uma solução onde as nanopartículas têm carga altamente positiva pode induzir a funcionalização da superfície.

A maguemita pertence a classe das ferritas do tipo espinélio, sendo essa uma estrutura cúbica de empacotamento compacto pertencente ao grupo espacial  $Fd3m$  n° 227 ilustrada a esquerda da Figura 4 da tese. Devido ao tamanho reduzido e o formato aproximadamente esférico as NPMs podem ser consideradas monodomínios magnéticos uniaxiais com um alto momento magnético, porém com uma baixa energia de anisotropia. Assim, os ferrofluidos compostos por esse tipo de partícula apresentam características peculiares, como o superparamagnetismo de Néel [52].

A superfície dessas NPMs baseadas em óxidos metálicos ao entrar em contato com água sofrem reações que lhes conferem carga superficial positiva em meios aquosos ácidos, carga negativa em condições alcalinas e carga nula por volta de pH 7.0, como exibido a direita da Figura 4 da tese. Assim, partículas não funcionalizadas em meios aquosos são capazes de entrar em suspensão formando um coloide estável apenas perto dos extremos de pH ( $\sim 2.0$  ou  $\sim 12.0$ ). Em condições ácidas é possível realizar a funcionalização das NPs com citrato ou com  $SMIM^\pm TFSI^-$  devido a carga negativa desses íons e a carga positiva das NPMs. No capítulo 2 é relatado o processo de transferência dessas NPs funcionalizadas para os respectivos líquidos iônicos.

## Capítulo 2: Dispersões coloidais de NPMs

O protocolo de transferência das NPMs de dispersões aquosas para LITAs nos permite controlar parâmetros importantes como o revestimento da superfície e os contra-íons iniciais próximos a interface. Assim, as NPMs dispersas em NEA foram revestidas superficialmente com íons citrato e diferentes contra-íons iniciais, enquanto as partículas em EMIM-TFSI tiveram uma funcionalização de superfície com SMIM<sup>±</sup>-TFSI<sup>-</sup>. Em NEA, os contra-íons iniciais investigados foram Na<sup>+</sup>, Li<sup>+</sup> (ambos previamente estudados) e Rb<sup>+</sup> que nunca fora antes investigado. Medidas de compressibilidade por SAXS e SANS permitiram determinar em cada um destes casos o segundo coeficiente  $A_2$  do desenvolvimento de virial para a pressão osmótica. Assim, combinando várias titulações químicas (em particular utilizando espectrometro de massa) e considerações geométricas do arranjo iônico foi possível propor uma modelo de organização dos íons ao redor das NPMs caso a caso.

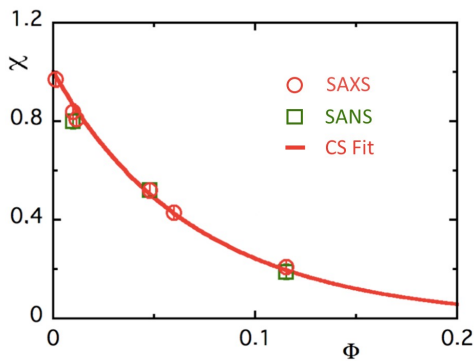


Figura 5a - Compressibilidade  $\chi$  de dispersões coloidais em EMIM-TFSI em função da sua fração volumétrica  $\Phi$ . Símbolos abertos: Dados experimentais em temperatura ambiente de SAXS e SANS (quadrados abertos) - Linha contínua: Ajuste de Carnahan-Starling com esferas duras [96, 98] de fração volumétrica  $\Phi_{\text{eff}}=1,82\Phi$  resultando em  $A_2 = 7,3$ .

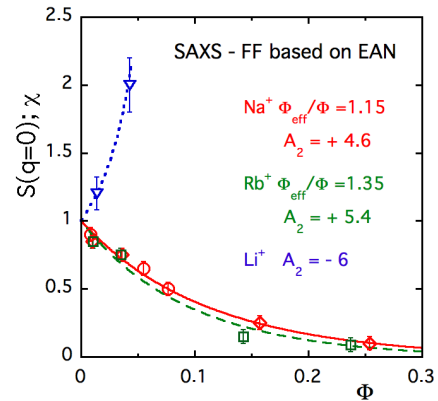


Figura 8 - Compressibilidade  $\chi$  de dispersões de NPMs determinadas por  $S(q=0)$  em experimentos de SAXS para amostras baseadas em NEA com Na<sup>+</sup> (círculos vermelhos referentes a este trabalho e diamantes vermelhos da ref. [58]) e Rb<sup>+</sup> (quadrados verdes) como contra-íons - Fits dos dados com a Equação 2.5 são obtidos usando  $\Phi_{\text{eff}}/\Phi = 1,15$  para Na<sup>+</sup> (linha contínua,  $A_2 = 4,6$ ) e  $\Phi_{\text{eff}}/\Phi = 1,35$  para Rb<sup>+</sup> (linha tracejada,  $A_2 = 5,4$ ). Para Li<sup>+</sup> (símbolos azuis) o desenvolvimento linear da Equação 2.4 é usado (linha pontilhada,  $A_2 = -6$ ).

Esses resultados são mostrados nas Figuras 5a e 8 onde as interações interpartícula são globalmente repulsivas para as NPMs revestidas por SMIM<sup>±</sup>-TFSI<sup>-</sup> dispersas em EMIM-TFSI (tipicamente até 11 vol% de NPs) e para NEA com contra-íons Na<sup>+</sup> e Rb<sup>+</sup> (até 25 vol% de NPs). Por outro lado, contra-íons Li<sup>+</sup> apresentam uma interações fracamente atrativas impedindo a obtenção de dispersões estáveis em altas concentrações de partículas. Os dados experimentais combinados ao entendimento atual da estruturação de LITAs sugerem que as interações repulsivas surgem da formação de camadas de contra-íons e co-íons induzidas pela superfície das NPs. O lítio, sendo um “quebrador” de estrutura do

NEA e estando em grande número na vizinhança da partícula (veja Figura 10 da tese), perturba a organização da primeira camada, resultando em dispersões menos estáveis.

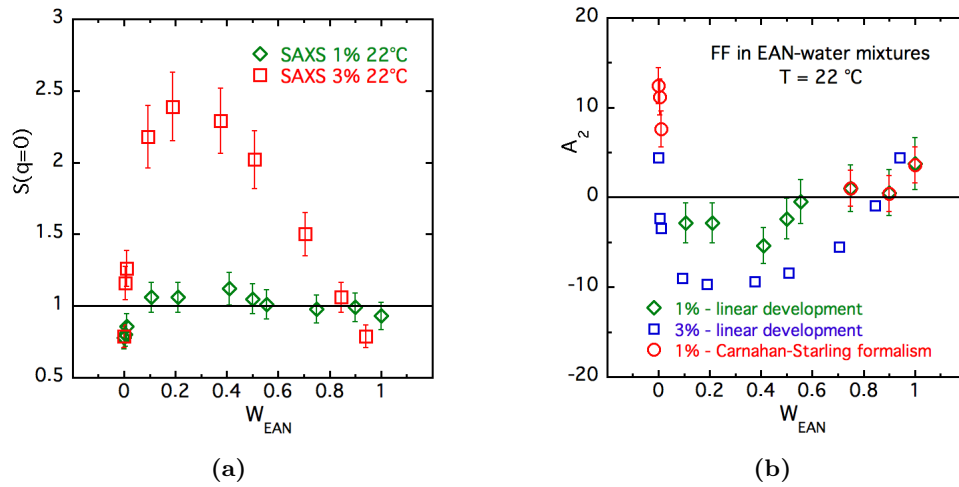


Figura 13 - (a) Valores de  $S(Q = 0)$  relacionados a compressibilidade  $\chi$  do sistema de NPMs por SAXS para amostras baseadas em misturas NEA/água com contra-íons  $\text{Na}^+$  em diferentes massa% de NEA ( $w_{NEA}$ ) a  $T = 22 \text{ }^\circ\text{C}$  em  $\Phi = 1.0\%$  and  $3.0\%$ . (b) Segundo coeficiente virial deduzido da figura (a) com a Equação 2.4 – Círculos abertos são deduzidos a  $\Phi = 1.0\%$  pela Equação 2.5 como na Figura 12b.

Indo um passo adiante, introduzimos um parâmetro adicional para a dispersão de NEA: o conteúdo de água no líquido iônico. Observações macroscópicas e microscópicas mostram que as dispersões de NPMs revestidas de citrato com contra-íons de  $\text{Na}^+$  permanecem estáveis pelo menos até  $\Phi = 3,0\%$  – com NPs de diâmetro médio da ordem de  $7,4 \text{ nm}$  – em toda a faixa de proporções de EAN e água (veja a Figura 11 da tese) e na presença de um campo magnético externo. Observe que esta estabilidade coloidal em toda a faixa da fração em massa de EAN  $w_{NEA}$  não seria observada com NPs do mesmo tamanho que as usadas em EMIM-TFSI com diâmetro médio de  $9,6 \text{ nm}$ . No entanto, com as NPs utilizadas, a transição entre um meio aquoso para um líquido iônico puro mostrou incluir uma gama de proporções em que as interações entre as partículas mudam de repulsivas para atrativas, e vice-versa. Este resultado foi inferido a partir de medidas SAXS em que  $A_2$  é negativo na faixa intermediária de  $w_{NEA}$  e  $A_2$  é positivo nos extremos. Esses resultados estão presentes na Figura 13 da tese. Graças a esta base de resultados abrangente, podemos então analisar profundamente a termodifusão dessas amostras por um experimento de espalhamento Rayleigh forçado (FRS).

### Capítulo 3: Propriedades termodifussivas

A influência da natureza dos contra-íons em ferrofluidos baseados em NEA foi analisada em função da fração volumétrica de NPs  $\Phi$  e da temperatura  $T$ . Na Figura 16, conforme esperado pelos desenvolvimentos teóricos de termodifusão, bem como observado em todo ferrofluido baseado em LITAs até agora, o coeficiente de Soret  $S_T$  é sempre

positivo e diminui com o aumento da temperatura  $T$ , independentemente da interação interpartículas. Em NEA observa-se que  $S_T$  também é positivo, mas apresenta diferentes comportamentos dependendo das interações interpartículas: nos sistemas repulsivos – onde  $A_2 > 0$  e a compressibilidade  $\chi < 1$  diminui com o incremento de  $\Phi$  –  $S_T$  diminui com o aumento de  $\Phi$ ; Em um sistema com interação interpartícula globalmente atrativa – onde  $A_2 < 0$  e  $\chi > 1$  vai aumentando conforme a amostra concentra – o coeficiente Soret  $S_T$  aumenta com  $\Phi$ , pelo menos na faixa de concentração disponível. Este resultado experimental ilustra o fato de que  $S_T$  é diretamente proporcional a  $\chi$ .

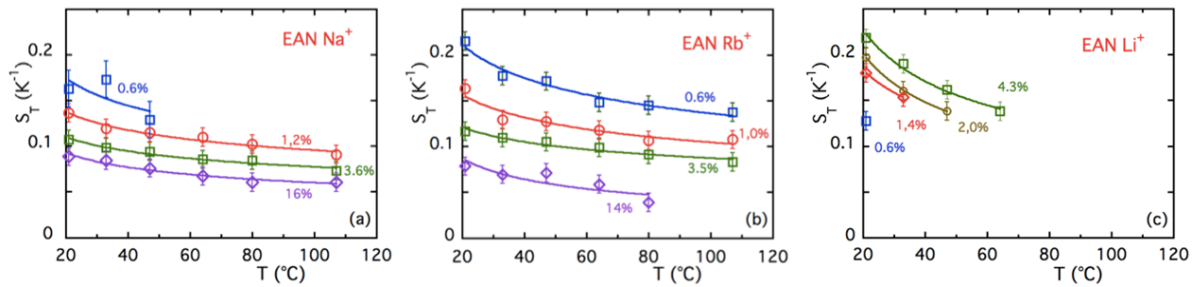


Figura 16 - Coeficiente Soret em função da temperatura e da concentração de partículas para os três tipos de contra-íons estudados  $\text{Na}^+$ ,  $\text{Rb}^+$  e  $\text{Li}^+$  em NEA. Linhas contínuas são guias para os olhos.

O coeficiente de difusão  $D_m$  também é afetado pelos diferentes regimes de interação e pela temperatura, como mostra a Figura 18. A  $T$ -dependência de  $D_m$  está fortemente relacionada com a viscosidade do meio líquido  $\eta_0(T)$ , enquanto a  $\Phi$ -dependência está em grande parte encapsulada em  $\chi(\Phi)$ . Em baixa concentração de NPs, é mostrado que a viscosidade efetiva experimentada pelas NPs é a viscosidade macroscópica do fluido carreador.

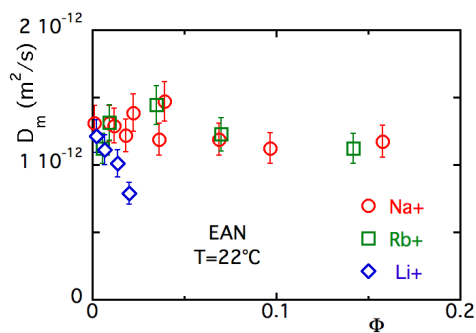


Figura 18 - Coeficiente de difusão  $D_m$  em função da fração volumétrica de NPs  $\Phi$  a  $T = 22^\circ\text{C}$  em FFs baseados em NEA com diferentes contra-íons iniciais  $\text{Na}^+$ ,  $\text{Rb}^+$  e  $\text{Li}^+$ .

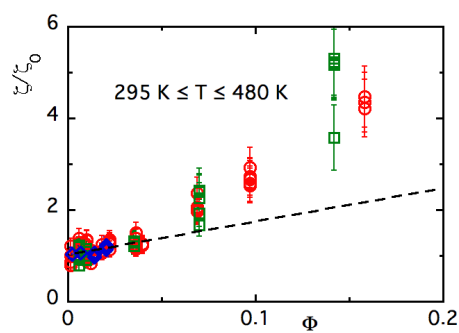


Figura 20 - Fricção reduzida  $\zeta/\zeta_0$  experienciada pelas NPs em função da sua fração volumétrica  $\Phi$  para os três contra-íons cíclicos vermelhos correspondem ao  $\text{Na}^+$ , quadrados verdes ao  $\text{Rb}^+$  e diamantes azuis ao  $\text{Li}^+$  em todo o intervalo de temperatura. As linhas pontilhadas correspondem à Eq.3.15 no caso do contra-íon  $\text{Na}^+$  ( $\Phi_{\text{eff}} = 1.15$ ).

Enquanto  $D_m$  permanece praticamente inalterado para os sistemas repulsivos  $\text{Na}^+$  e  $\text{Rb}^+$  (até  $\Phi \sim 15\%$ ),  $D_m$  reduz significativamente para  $\text{Li}^+$  à medida que a fração volumétrica  $\Phi$  aumenta ligeiramente. Para  $\text{Li}^+$ , isso pode ser associado ao aumento dos

valores de  $\chi$  como  $D_m \propto 1/\chi$ . Ainda assim,  $D_m$  depende da fricção  $\zeta(T, \Phi)$  que pode então ser deduzida das medidas de  $D_m$  e  $\chi$ . A fricção obtida em FFs diluídos ( $\Phi < 4,0\%$ ) é compatível com o desenvolvimento linear de Batchelor, no entanto, em concentrações mais altas, a fricção mostra um grande aumento. Embora não tenhamos uma descrição teórica para este desvio, ele certamente está relacionado à organização iônica local do NEA e à mencionada formação de camadas em torno das NPMs.

O NEA-FF com contra-íons  $\text{Na}^+$  pode ser considerado um sistema modelo versátil, portanto adequado para avaliar os efeitos do teor de água no líquido iônico. Desta forma,  $D_m$  e  $S_T$  foram ambos experimentalmente determinados por FRS como uma função da proporção de massa  $w_{\text{NEA}}$  de NEA na água,  $\Phi$  e  $T$ . Em  $\Phi = 1.0\%$ ,  $D_m$  aumenta em função da temperatura e diminui em relação a  $w_{\text{NEA}}$  conforme mostra a Figura 22a. Este comportamento pode ser principalmente – mas não exclusivamente, pois a compressibilidade depende claramente de  $w_{\text{NEA}}$  – atribuído a um aumento da viscosidade macroscópica  $\eta_0$  do fluido transportador conforme a quantidade de NEA é aumentada e, ao contrário, ocorre uma redução em  $\eta_0$  quando  $T$  aumenta. Além disso, uma vez que uma viscosidade efetiva  $\eta_{\text{eff}}$  pode ser calculada a partir do  $D_m$  medido em  $\Phi$  diluído, poderíamos comparar os valores determinados via FRS com os dados atualmente relatados na literatura [153]. Na Figura 23 é mostrado que os resultados obtidos estão de acordo para  $w_{\text{NEA}} = 1$  e 0 em toda a gama de  $T$  acessível e em qualquer  $w_{\text{NEA}}$  à temperatura ambiente. Em temperaturas mais altas para esses valores de  $w_{\text{NEA}}$  intermediários,  $\eta_{\text{eff}}$  segue a tendência mencionada anteriormente ( $\eta_{\text{eff}}$  diminui com  $T$  e aumenta com  $w_{\text{NEA}}$ ), todavia ainda não existem valores na literatura para serem comparados com estes resultados.

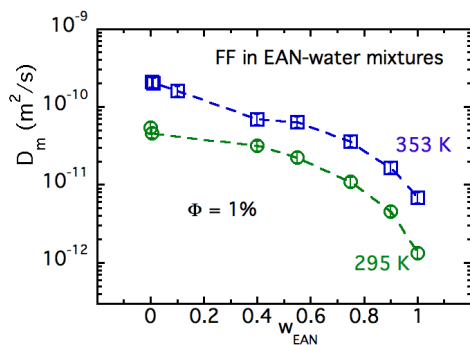


Figura 22a – Coeficiente de difusão  $D_m$  determinado por FRS à  $\Phi = 1.0\%$  em função de  $w_{\text{NEA}}$  nas duas temperaturas extremas. Linhas tracejadas são guias para os olhos.

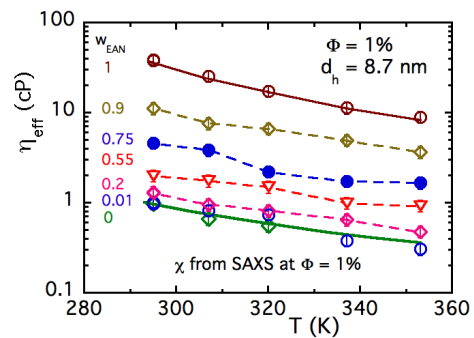


Figura 23 – Viscosidade efetiva  $\eta_{\text{eff}}$  deduzida a partir dos valores de  $D_m$  determinados à  $\Phi = 1.0\%$  da Fig. 22a em função de  $T$  em vários  $w_{\text{NEA}}$  - Alguns valores foram interpolados. Linhas contínuas são  $\eta_0$  para NEA (linha marrom da ref. [153]) e para água (linha verde). Linhas tracejadas são guias para os olhos.

Nas Figuras 24b e 25b da tese são apresentados os resultados de  $S_T$ . Nas misturas de água-NEA, em  $w_{\text{NEA}}$  pequeno e para  $\Phi = 1.0\%$  e  $\Phi = 3.0\%$ , observa-se que  $S_T$  aumenta com temperatura de um valor negativo para positivo, como é observado em ferrofluidos à base de água com NPs revestidas de citrato e contra-íons  $\text{Na}^+$ . Ao contrário,

em grande  $w_{NEA}$ ,  $S_T$  é medido positivamente e uma função decrescente de  $T$ , conforme observado anteriormente em NEA puro. Em  $\Phi = 3.0\%$ , os dois comportamentos opostos se encontraram em um ponto de inversão localizado em torno de  $w_{NEA} \sim 0.6$ , enquanto esta observação é menos precisa em  $\Phi = 1.0\%$ . Outra inversão também pode ser evidenciada por FRS em termos da  $\Phi$ -dependência de  $S_T$ . Em grande valores de  $w_{NEA}$ ,  $\Delta S_T/\Delta\Phi$  é negativo (como característico de sistemas LITA repulsivos), enquanto entre  $w_{NEA} = 0, 1$  e  $0,5$  é considerado positivo (uma marca de interações atrativas em sistemas de LITAs). Esta inversão de sinal de  $\Delta S_T/\Delta\Phi$  pode ser associada à mudança entre as interações interpartículas atrativas e repulsivas observadas em medidas de SAXS para as misturas de água e EAN.

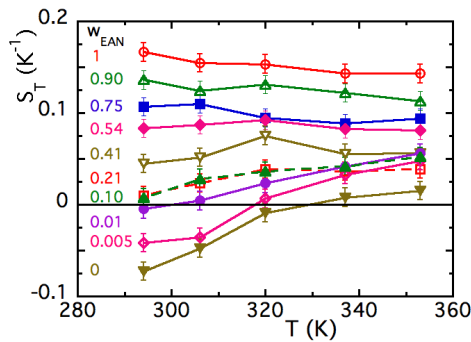


Figura 24b - (a) Medidas de FRS do coeficiente Soret  $S_T$  à  $\Phi = 1.0\%$  em função de  $T$  em varios  $w_{NEA}$  – Linhas contínuas são guias para os olhos.

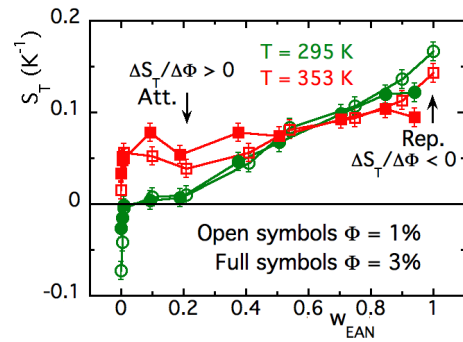


Figura 25b – Comparação do coeficiente Soret  $S_T$  à  $T = 295$  K and  $353$  K em função de  $w_{NEA}$  entre  $\Phi = 1.0\%$  and  $3.0\%$  – Linhas contínuas são guias para os olhos.

Uma análise em termos de  $TS_T/\chi$  em função de  $w_{NEA}$  mostra que o comportamento próximo ao de um ferrofluido em um eletrólito padrão com interações interpartículas repulsivas só é observado para  $w_{NEA}$  abaixo de  $0,01 - 0,1$ . Esta faixa de  $w_{NEA}$  mereceria no futuro uma análise mais sistemática. Além disso, em ferrofluidos aquosos com base em NPs revestidas com citrato (portanto, em  $w_{NEA} = 0$ ) à temperatura ambiente, o sinal do coeficiente Soret  $S_T$  foi mostrado inverter-se dependendo da hidroflicidade dos contra-íons livres. Em particular, se apenas contra-íons  $EA^+$  estivessem presentes e nenhum  $Na^+$ ,  $S_T$  seria positivo em  $w_{NEA} = 0$ . Ainda assim, neste caso, a carga superficial é das NPMs revestidas de citrato em água é sempre negativa, independentemente do tipo de contra-íons.

A inversão de sinal de  $S_T$  ocorrendo com o aumento de  $w_{NEA}$  pode, portanto, estar relacionada ao número crescente de íons  $EA^+$  na vizinhança da NP. Mas, curiosamente, os dados também podem sugerir que o efeito poderia ser associado a uma inversão de carga efetiva de negativa em  $w_{NEA} = 0$  (conforme medida experimentalmente) para positiva em  $w_{NEA} = 1$  (como deduzido para contra-íons  $Na^+$  em uma análise cruzada de FRS e medições termoeéticas). Uma possível rota poderia seguir a seguinte linha: a carga efetiva negativa  $\xi_0^{eff}$  dos NPs em  $w_{NEA} = 0$  diminui progressivamente em valor absoluto com  $w_{NEA}$ , reduzido a quase zero no intervalo intermediário  $0,01 \leq w_{NEA} \leq 0,2$ ; Para  $0,2 \leq w_{NEA} \leq 0,5 - 0,7$ , torna-se ligeiramente positiva, mas ainda não é capaz de produzir

uma repulsão interpartícula suficientemente forte; para  $0,7 \leq w_{\text{NEA}} \leq 1$ , a carga efetiva positiva torna-se grande o suficiente para produzir uma repulsão interpartícula global, decorrente da formação apropriada das mencionadas camadas iônicas.

Finalmente, a anisotropia do campo magnético da termodifusão foi investigada em um ferrofluido à base de IL pela primeira vez. A ampla faixa de  $T$  em que o FF baseado em EMIM-TFSI é estável nos permitiu sondar a resposta magnética de 295 K até 461 K em concentração moderada de  $\Phi = 5,95\%$ . Na ausência de um campo magnético externo,  $D_m$  e  $S_T$  se comportam como um típico FF-RTILs com interações repulsivas:  $D_m$  aumenta com a temperatura conforme a viscosidade macroscópica  $\eta_0$  do transportador de fluido diminui. Quanto ao FF baseado em EAN com contra-íons  $\text{Na}^+$ , o atrito é maior do que teoricamente previsto pelo desenvolvimento Batchelor (em 20 % a 40 %), provavelmente devido à organização estrutural iônica em torno dos NPMs. Além disso, os valores experimentais de  $S_T$  diminuem à medida que  $\Phi$  e  $T$  aumentam, seguindo a tendência característica dos ferrofluidos baseados em RTIL com interações interpartículas globalmente repulsivas.

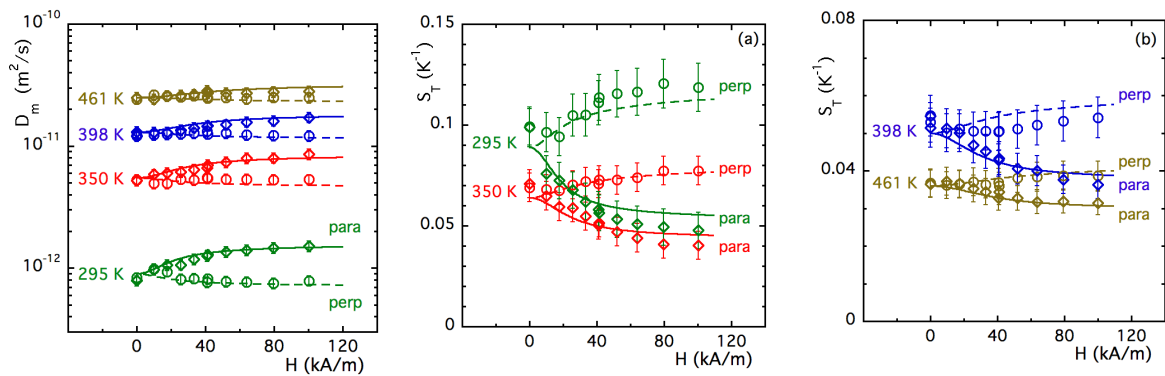


Figura 29 – Coeficiente de difusão  $D_m$  em função do campo aplicado  $H$  em diferentes temperaturas  $T$  (Fig. 30a à 295 e 350 K, Fig. 30b à 398 e 461 K); O rótulo perp (resp. para) e os círculos abertos representam medidas com  $H_{\perp}$  (resp.  $H_{\parallel}$ ); Símbolos correspondem a medidas de FRS, linhas tracejadas (resp. linhas contínuas) correspondem ao ajuste dos dados na direção  $H_{\perp}$  com a Eq. 3.24 (resp. na direção  $H_{\parallel}$  utilizando Eq. 3.25).

Uma anisotropia de campo aplicado de  $D_m$  e  $S_T$  é observada (Figuras 29 e 30) em todas as temperaturas sondadas. Como esperado, a resposta do sub-campo depende da direção (paralelo  $\vec{H}_{\parallel}$  ou perpendicular  $\vec{H}_{\perp}$  para  $\vec{\Delta}\Phi$ ) e a amplitude ( $0 \leq H \leq 100 \text{ kA m}^{-1}$ ) do campo magnético aplicado  $\vec{H}$ . Subcampo, o coeficiente de difusão  $D_m$  persiste em aumentar com  $T$  como no campo zero, no entanto, a anisotropia induzida magneticamente resulta em  $D_m(H_{\perp}) < D_m(H=0) < D_m(H_{\parallel})$ , onde este efeito diminui progressivamente à medida que a temperatura aumenta. Ao contrário,  $S_T$  reduz em função de  $T$  e o efeito de

anisotropia resulta em  $S_T(H_{\parallel}) < S_T(H = 0) < S_T(H_{\perp})$ , com aqui também uma redução progressiva do efeito à medida que  $T$  aumenta.

Os dados experimentais são bem ajustados em função de  $H$  e  $T$  pelo modelo teórico descrito nas refs. [25, 127] que já foi mostrado descrever adequadamente o efeito da anisotropia em ferrofluidos aquosos à temperatura ambiente. Aqui observamos que a modelagem também é válida para sistemas não-DLVO e em altas temperaturas. O ajuste usou valores de  $\chi$  determinados por SANS,  $m_s(T)$  usando a lei de Bloch e deixando  $d_{NP}$  e dois coeficientes de campo zero,  $D_m^*(T)$  e  $S_T^*(T)$  como parâmetros livres. É assumido aqui que  $\chi$  e  $\zeta$  mantiveram seus valores de campo zero como nas refs. [128, 129, 131]. Uma análise mais aprofundada foi aplicada aos diferentes termos do modelo. O parâmetro  $\alpha_{\lambda}$  está relacionado à interação dipolar em campo aplicado e é modelado aqui no contexto da aproximação de campo médio; É isotrópico e, portanto, existe em ambas as direções  $\vec{H}_{\perp}$  e  $\vec{H}_{\parallel}$ . O coeficiente  $\beta_{\lambda}$  modela a contribuição anisotrópica proveniente das inomogeneidades de concentração do sob campo magnético. Ambos os coeficientes são proporcionais ao parâmetro dipolar magnético  $\gamma(T)$ , tornando-se mais fracos à medida que  $T$  aumenta. Os dois próximos parâmetros  $S_1$  e  $S_2$  do modelo quase não têm contribuição na anisotropia gerada pelo campo aplicado do ponto de vista teórico, o que foi confirmado também nos resultados experimentais. A principal contribuição para a anisotropia de  $D_m$  e  $S_T$  surge, portanto, do parâmetro  $\beta_{\lambda}$ .

## Capítulo 4: Nanodots de Carbono Enriquecidos de Nitrogênio (N-NCs)

Nesta parte estudaremos dispersões aquosas de N-NCs sintetizados com diferentes razões nominais nitrogênio/carbono (N/C). A amostra CD1 foi preparada com N/C = 0,14, enquanto a amostra CD7 foi preparada com N/C = 0,74. O processo de síntese consiste de apenas uma etapa simples e direta (veja Figura 33). A morfologia, distribuição de tamanhos, estrutura superficial e densidade foram verificadas por múltiplas técnicas a fim de fornecer suporte para a posterior análise das dispersões em meio aquoso em vários pH's.

Um diâmetro médio entre 2 – 4 nm foi medido por microscopia eletrônica de transmissão (MET) e difração de raios X (DRX) como mostra a Tabela 4, porém, uma grande quantidade de partículas com diâmetros < 2 nm somente foram encontradas por microscopia de força atômica (AFM). Dessa forma a distribuição de tamanhos deve na realidade ser consideravelmente deslocada para tamanhos menores.

A estrutura cristalina dos N-NCs foi previamente determinada como carbono grafitico dopada com nitrogênio para CD1 e  $\beta$ -C<sub>3</sub>N<sub>4</sub> para CD7 como apresentado na Figura 38. Além disso, a presença de grupos de superfície carboxila e amida foi confirmada por espectroscopia de infravermelho (FTIR). A densidade determinada experimentalmente

Tabela 4 - Determinação experimental de tamanhos por MET ( $d_{0,MET}$ ,  $s_{0,MET}$ ) e por DRX ( $d_{DRX}$ ) das amostras CD1 e CD7.

Amostra	$d_{0,MET}$ (nm)	$s_{0,MET}$	$^1d_{DRX}$ (nm)	$^2d_{DRX}$ (nm)
CD1	$3.96 \pm 0.09$	$0.39 \pm 0.02$	$1.96 \pm 0.05$	$1.97 \pm 0.04$
CD7	$3.7 \pm 0.1$	$0.31 \pm 0.03$	$2.46 \pm 0.03$	-

do pó composto de N-NCs foi de  $1.53 \pm 0.01$  g/cm<sup>3</sup> para CD1 e  $1.84 \pm 0.04$  g/cm<sup>3</sup> para CD7 sugerindo que a superfície é altamente passivada, pois o valor medido é consideravelmente menor (22 – 48%) se comparado com a densidade do núcleo cristalino sozinho, 2.02 e 3.57 g/cm<sup>3</sup> respectivamente.

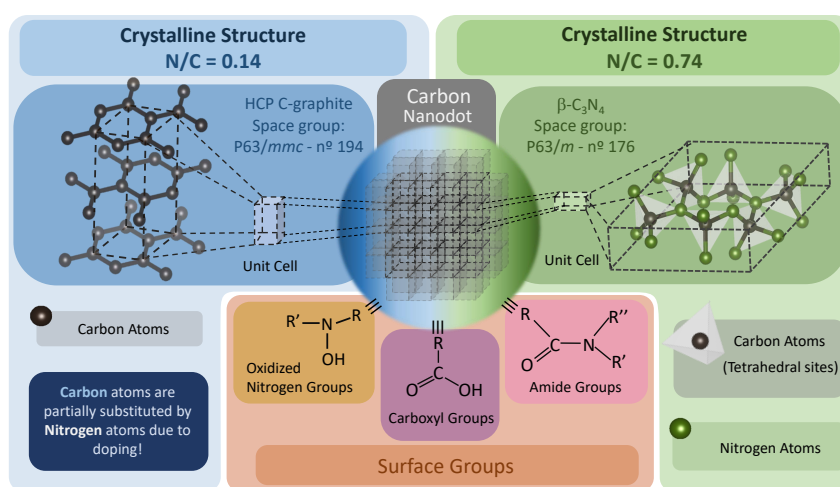


Figura 38 - Diagrama das características do núcleo e da superfície dos N-NCs estudados. As estruturas cristalinas internas mostradas correspondem às duas variantes da síntese hidrotérmica com diferentes razões N/C, denominadas aqui CD1 (*esquerda* - N/C=0,14) e CD7 (*direita* - N/C=0,74). Estruturas cristalinas (carbono grafitico e  $\beta$ -C<sub>3</sub>N<sub>4</sub>) e grupos de superfície (carboxila e amida) foram deduzidos de várias técnicas. Visualização da estrutura gerada usando a referência [64].

## Capítulo 5: Dispersões coloidais de N-NCs

Focamos no estudo do desenvolvimento da carga superficial, estabilidade coloidal e ordem local, uma vez que esses aspectos não são profundamente investigados no atual estado da arte desse tipo de nanodots. Os N-NCs foram dispersos em uma ampla faixa de pH (de 2,0 a 12,0) pela adição direta do material sólido nas soluções aquosas ácidas (NaNO<sub>3</sub>) e alcalinas (NaOH). A amostra foi homogeneizada tanto quanto possível por sonicção em um banho ultrassônico a 50°C por várias horas. No entanto, conforme o pH muda para condições ácidas, a solubilidade parece reduzir significativamente. Os aspectos visuais macroscópicos da amostra apresentados na Figura 42 mostram que os N-NCs estão parcialmente bem dispersos em solução, mas uma parte deles sedimenta. A quantidade de N-NCs precipitados se correlaciona com o pH, por exemplo, a quantidade de sedimento é maior em meio ácido e diminui gradativamente conforme o pH se torna alcalino. Em pH

12,0 nenhum precipitado é formado, entretanto, a amostra apresenta modificações em suas propriedades ópticas ao longo do tempo.

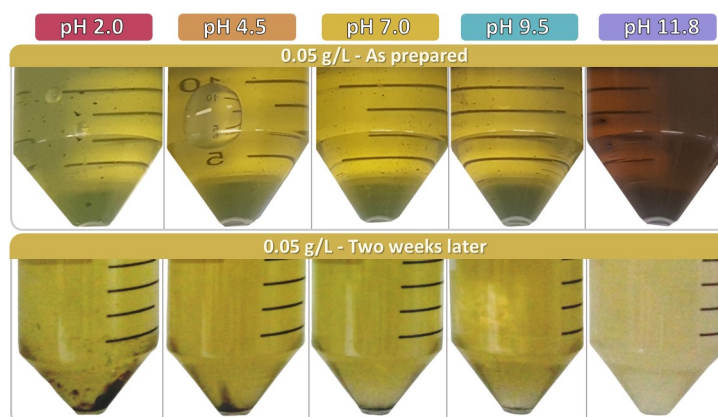


Figura 42 - Aspectos visuais da amostra CD7 dispersa em diferentes soluções de pH à 0,05 g/L. A primeira linha refere-se às fotos tiradas imediatamente posteriormente ao protocolo de dispersão e a segunda linha após a amostra ter sido deixada imobilizada por duas semanas.

Observa-se por microscopia óptica que o precipitado apresenta agregados em várias ordens de magnitude (de  $\sim 1 - 100 \mu\text{m}$ ). Os agregados maiores são estruturas lamelares densas e compactas, mas à medida que se tornam menores, observou-se que as estruturas fractais são formadas por um grande número de aglomerados abaixo de  $10 \mu\text{m}$ . De qualquer forma, o sobrenadante mostrou-se altamente homogêneo em escala macro e microscópica em todos os pHs sondados. Essa discrepância entre o sobrenadante e o precipitado foi associada à heterogeneidade dos N-NCs, que devem induzir diferenças na solvatação, interações interpartículas e ordenação em nanoescala em resposta às variações de tamanho, estrutura superficial e carga elétrica.

Assim, investigamos o desenvolvimento da carga superficial dos N-NCs em função do pH. As medidas de potencial zeta indicam que a carga superficial é sempre negativa na faixa ácido-base analisada e que seu valor absoluto foi maior para CD7 em comparação com a CD1. A carga não nula em meio altamente ácido foi associada a grupos superficiais de nitrogênio oxidado, enquanto seu aumento progressivo em magnitude para condições alcalinas foi atribuído à desprotonação dos grupos de superfície carboxila. Portanto, a melhora em estabilidade coloidal observada conforme o pH aumenta deve surgir da repulsão eletrostática adicional. A relação nitrogênio/carbono (N/C) parece afetar também a natureza da superfície dos N-NCs, onde a amostra CD1 apresenta um caráter mais ácido quando comparada com a CD7. Este resultado pode estar relacionado à proporção de grupos de superfície à base de carboxila e nitrogênio.

Titulações potenciométricas e condutimétricas apresentadas na Figura 49 nos permitiram estimar a densidade de carga superficial proveniente dos grupos carboxila. As curvas indicam uma diferença de comportamento entre a rota ácido-alcalina e a rota inversa, alcalina-ácida. Não apenas a quantidade de titulante é alterada como a forma da

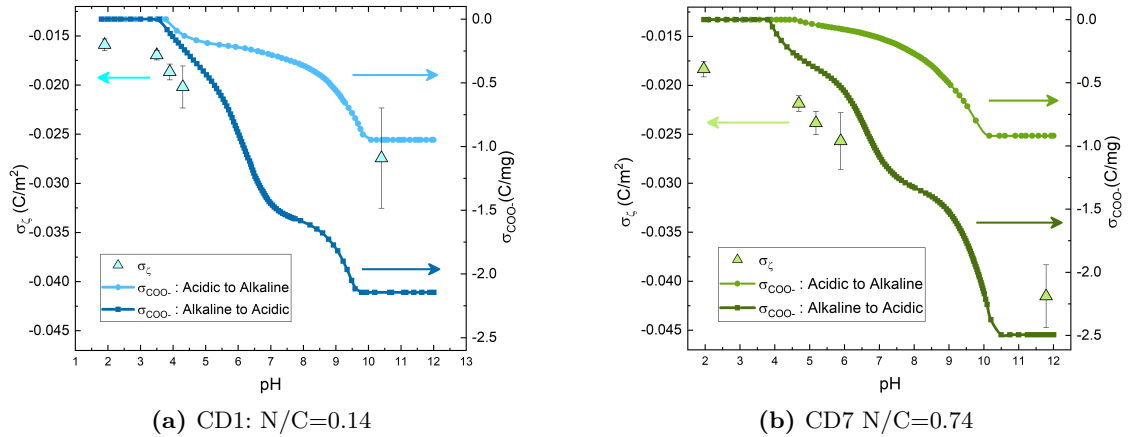


Figura 49 - A pH-dependência de  $\sigma_{\text{COO}^-}$  e  $\sigma_{\zeta}$  avaliadas utilizando Eq. 5.8 e 5.9, respectivamente. O eixo direto e esquerdo são independentes e o alinhamento foi realizado visando uma análise qualitativa.

curva é drasticamente modificada. Estes resultados sugeriram que a histerese observada nas curvas de titulação era provavelmente uma consequência da hidrólise alcalina da amida superficial. Esta reação química explicaria o aumento da carga conforme os grupos amida são convertidos em grupos carboxila, e ainda, a mudança na forma da curva em resposta a significativa mudança da natureza ácida da superfície da partícula.

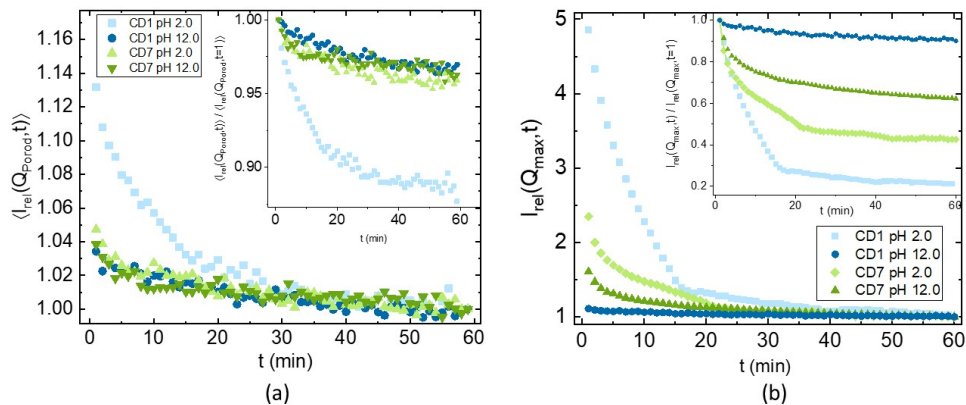


Figura 58 - Evolução temporal dos valores experimentais do fator de estrutura aparente (a) na região de Porod ( $Q > 2 \text{ nm}^{-1}$ ) e (b) na região de Guinier ( $Q_{\text{max}}$ ). *Insets*: Normalização pela intensidade do primeiro valor medido ( $S_{\text{app}}(Q, t)/S_{\text{app}}(Q, t = 1)$ ) para melhor visualização dos perfis das curvas.

Finalmente, a organização em nanoescala dos N-NCs foi testada por MET, técnicas de espalhamento dinâmico de luz (DLS) e de raios X em baixo ângulo (SAXS). Os resultados sugerem a presença de agregados também abaixo de  $1 \mu\text{m}$  no sobrenadante, o que estava além da resolução do microscópio óptico. As medidas de DLS indicam que o tamanho crítico dos agregados estava entre 100-400 nm. A ultracentrifugação nos permitiu reduzir o diâmetro hidrodinâmico para uma janela de 70-120 nm. A estrutura desses agregados sondados por SAXS também varia com N/C. Uma vez que CD1 apresentou clusters mais densamente compactados – seguindo expoentes de fractal de superfície – e CD7 apresentou uma rede agregada menos compacta – com expoentes de fractal de massa. Medidas de SAXS em função do tempo (figura 58) avaliaram o processo de sedimentação em nanoescala,

confirmando que a estabilidade coloidal é de fato melhorada em meio alcalino. Além disso, a medida dinâmica mostrou que o processo de sedimentação é heterogêneo, portanto, é provável que haja uma distribuição de tamanho dos agregados também em nanoescala.

## Capítulo 6: Fotoluminescência

Por fim, foi realizada uma breve análise das propriedades ópticas das amostras em pH 12,0. Foi observado um desvio para o azul da fluorescência da amostra CD7 de emissão verde, enquanto a CD1 permaneceu azul. A absorção óptica (AO) da amostra CD7 apresenta variações dependentes do tempo, onde o pico em torno de 400 nm diminui enquanto a banda em 300-320 nm aumenta. Este resultado da AO - assim como o desvio para o azul na fluorescência - deve estar associado à já conjecturada hidrólise da amida. Ao considerar o mecanismo de emissão desses N-NCs, pode-se perceber que a emissão verde é essencialmente dependente dos grupos amida, enquanto a emissão azul não é tão substancialmente afetada. Portanto, o pico de emissão verde é reduzido à medida que grande parte da amida superficial é convertida em grupos carboxila.

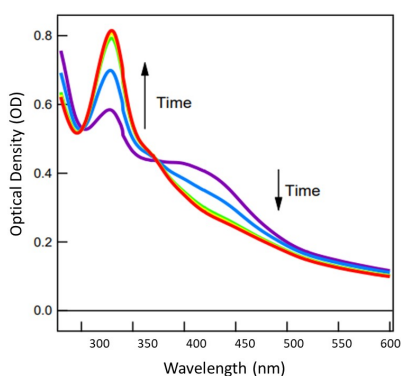


Figura 60a – Variação da densidade óptica em função do comprimento de onda para uma solução aquosa da amostra CD7 logo após ser alcalinizada a pH  $\sim 11,0$  com NaOH. A concentração inicial de N-NCs foi definida como 0,05 g/L.

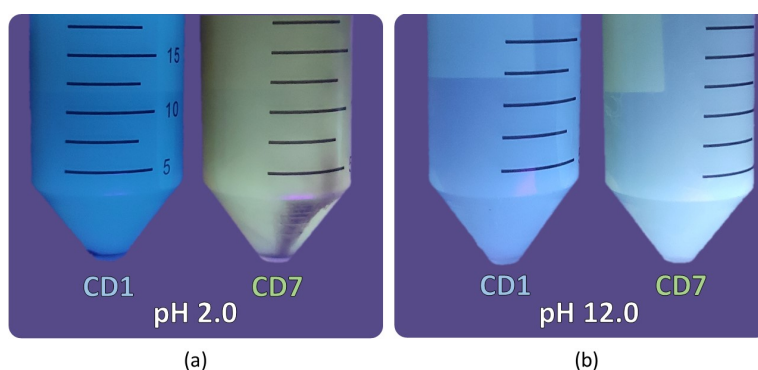


Figura 63 – (a) Uma comparação visual entre a amostra CD1 e CD7 em meio ácido (pH 2,0) na concentração de 0,15 g/L após duas semanas. As amostras foram fotografadas sob luz ultravioleta comercial (comprimento de onda 480 – 320 nm). (b) Uma comparação visual em condições equivalentes às descritas em [Figure 63a](#), exceto que elas estavam dispersas em meio alcalino (pH 12,0).

## Capítulo 7: Sistemas magneto fotoluminescentes

Neste capítulo foi abordado o estado da arte dos sistemas de nanoparticulados com propriedades magnéto-fluorescentes atualmente desenvolvidos na literatura. Nessa medida, duas abordagens são geralmente aplicadas no atual estado da arte de nanofluidos magnéticos e fluorescentes: (i) a funcionalização de nanopartículas magnéticas com moléculas fluorescentes, concedendo ao núcleo magnético propriedades fotoluminescentes decorrentes da casca da superfície e (ii) o formação de nanocompósitos por meio da aglomeração e/ou confinamento de nanopartículas magnéticas e fluorescentes.

A grande desvantagem de ambos os métodos se dá ao fato dos nano-objetos resultantes serem normalmente maiores do que 100 nm (atingindo até microns), o que torna a produção de uma dispersão coloidal estável quase impossível na presença de um campo magnético externo. A estabilidade pode ser melhorada aumentando a viscosidade do solvente (por exemplo, em óleos derivados de petróleo), restringindo amplamente sua faixa de aplicabilidade. Além disso, o encapsulamento das nanoestruturas restringe várias propriedades interessantes que são sensíveis à interface partícula/meio, limitando o potencial de aplicações como sensores. Dessa forma, foi proposto um novo tipo de fluido no qual ambas propriedades advindas de cada material são amplamente preservadas enquanto o colóide se mantém estável mesmo com campo magnético aplicado.

## Capítulo 8: Nanocolóide híbrido de N-NCs e NPMs

Nesse capítulo, apresentamos um novo fluido magnético fluorescente baseado em nanopartículas magnéticas de óxido de ferro e nanodots de carbono. O material híbrido foi obtido com a utilização dos dois nanomateriais descritos nas partes I e II sem qualquer encapsulamento ou confinamento dos componentes. O método utilizado para combinar as amostras é prático, de baixo custo e reproduzível. A vantagem de usar este tipo de NPMs é a possibilidade de ajustar as propriedades magnéticas do fluido através do tamanho, composição química e fração volumétrica. Além disso, o uso de N-NCs permite ter uma fluorescência brilhante e sintonizável sendo composto de um material abundante, atóxico, de baixo custo e biodegradável. Duas condições físico-químicas foram avaliadas: a dispersão em meio ácido e em pH neutro.

Na condição ácida, ferrofluidos estáveis à pH 2.5 baseados em NPMs do tipo núcleo-casca com um núcleo de ferrita de cobalto e uma casca de maguemita ( $\text{CoFe}_2\text{O}_4@ \gamma\text{-Fe}_2\text{O}_3$ ) são misturados a dispersões em mesmo pH de nanodots da amostra CD7. Dois tamanhos de nanopartículas magnéticas são investigados, isto é, uma amostra com tamanho médio de 10 nm (chamada CoG) e outra com um tamanho menor de 6 nm (CoP). Independente do tamanho, ambas misturas à pH ácido são coloidalmente instáveis. Isso ocorre pois nessas condições as NPMs são positivamente carregadas enquanto os N-NCs são negativamente carregados. Dessa forma, um potencial electrostático atrativo entre os componentes magnético e fluorescente é estabelecido induzindo a formação de aglomerados. O resultado macroscópico é uma separação de fase lenta por sedimentação que pode ser acelerada pela introdução de um campo magnético externo como mostra a Figura 66. A fase magnética concentrada próxima ao ímã não apresenta praticamente nenhuma fluorescência, enquanto o sobrenadante ainda fluoresce devido a presença de N-NCs que ainda se mantiveram bem dispersos. Medidas de SAXS indicam que de fato um fator de estrutura atrativo é gerado com comprimentos de correlação correspondentes à distância de contato das NPMs. Além disso, imagens de MET mostram que as NPMs são decoradas

pelos N-NCs devido ao potencial eletrostáticas atrativo.

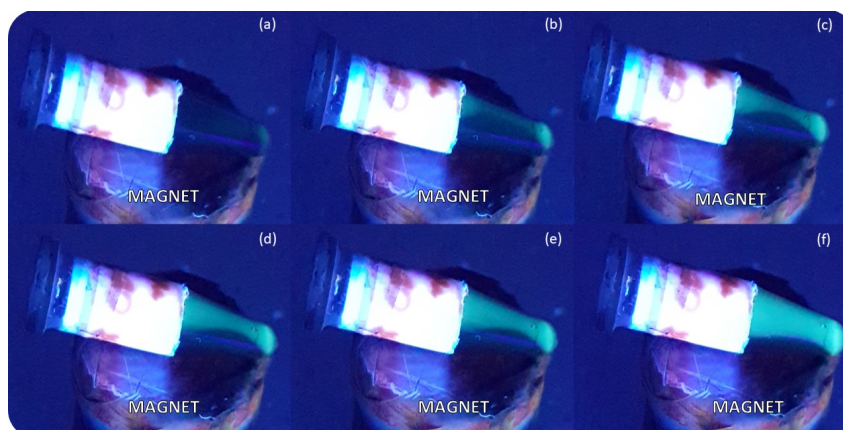


Figura 66 - (a) Um nanofluido híbrido ácido composto de 0,5% em fração volumétrica de CoG e 0,5 g/L de CD7 a pH 2,5 é posicionado sobre um ímã após ter sido agitado manualmente por alguns segundos. (b) - (f) as NPMs concentram-se mais perto do ímã em um intervalo de tempo de menos de um minuto. Uma quantidade considerável de N-NCs permanece dispersa em solução evidenciada pela emissão verde gerada sob a luz ultravioleta.

Por outro lado, líquidos magnéticos fluorescentes altamente estáveis (LMFs) foram obtidos misturando N-NCs CD1 e CD7 com nanopartículas magnéticas ( $\text{CoFe}_2\text{O}_4@ \gamma\text{-Fe}_2\text{O}_3$ ) funcionalizadas com íons citrato à pH = 7,0. As amostras apresentaram alta estabilidade coloidal de longa duração em nível macro e microscópico, com e sem a presença de campo magnético externo como mostra a Figura 68. A fluorescência ainda é perceptível após a mistura, com emissão de cor verde no caso da amostra CD7.

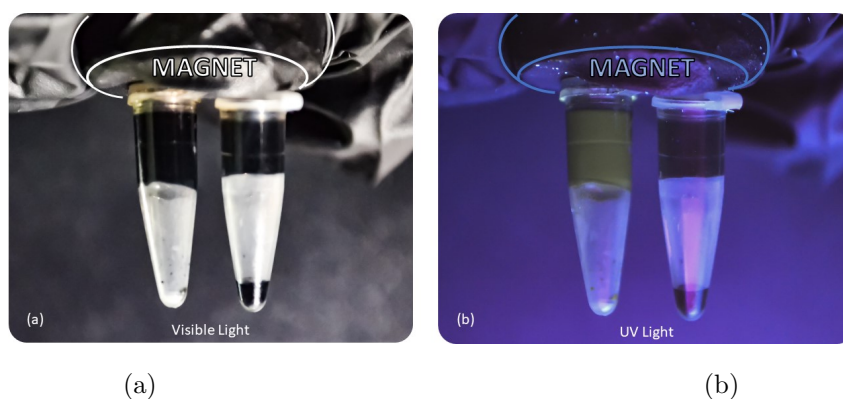


Figura 68 - Líquido magnético fluorescente baseado em amostras de CD7 + Co6 (à esquerda) e o ferrofluido Co6 puro (à direita) sendo mantido por um ímã sob (a) luz visível e (b) luz UV.

Várias caracterizações magnéticas foram realizadas e são apresentadas na Figura 75, tais como: magnetização em temperatura ambiente, loops de histerese à 5 K, gráficos de Thamm-Hesse e curvas ZFC/FC. Os resultados obtidos não apresentaram nenhuma alteração significativas quando comparada a amostra de FF puro e com o LMF híbrido. Além disso, medidas de magneto-hipertermia também foram realizadas atestando que a presença de N-NCs não afeta a taxa de absorção específica (SPA). Em suma, a adição de

N-NCs nesta condição físico-química não influencia ativamente as propriedades magnéticas do ferrofluido original.

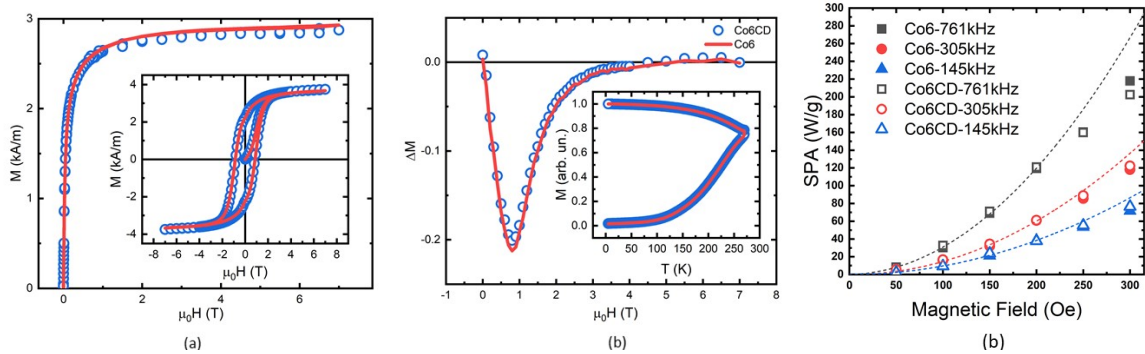


Figura 75 - Comparação das propriedades magnéticas entre o LMF Figura 76b - Comparação do  $\text{Co6}[\Phi = 1\%] + \text{CD7}[10 \text{ g/L}]$  (círculos azuis) e o ferrofluido puro  $\text{Co6}$  ( $\Phi = 1\%$ ) (linha vermelha): (a) *Figura principal*: Curvas de magnetização à temperatura ambiente (300 K)  $M(H)$ . *Inset*: Ciclo de histerese à rias frequências. 5 K. (b) *Figura principal*:  $\Delta M$  calculado pela Eq. 8.2 seguindo o formalismo de Thamm-Hesse. *Inset*: Magnetização em função da temperatura  $M(T)$  seguindo o protocolo ZFC/FC.

Por fim, as propriedades fotoluminescentes foram avaliadas a fim de determinar quantitativamente as modificações no espectro de emissão gerado pela introdução de NPMs na dispersão fluorescente de N-NCs. Em primeiro lugar, uma redução de intensidade da PL devido as NPMs pode estar ligada a mais de um fator, como indicado nos resultados das Figuras 77 e 79. No caso específico da concentração de NPMs à  $\Phi = 0,1\%$  e  $1,0 \text{ g/L}$  de N-NCs, a redução de emissão na zona  $500 - 575 \text{ nm}$  é de cerca de  $8 \times$  quando comparada a dispersão de N-NCs pura. Uma vez que as NPMs absorvem parcialmente a emissão de excitação, foi calculado que o *quenching* devido às interações entre as partículas é de um fator próximo à 3,2. Além disso, as medidas de tempo de vida da emissão determinam que a razão entre os valores obtidos para a dispersão de N-NCs puros e o LMF é na realidade de 1,36. Portanto, a redução observada do sinal de fluorescência ( $8 \times$ ) é primeiramente devida à absorção das NPMs da emissão de excitação (um fator de 4,8), somada a uma extinção colisional (um fator de 1,36) e uma extinção estática (um fator de 1,84) devido às interações entre N-NCs e NPMs. A intensidade da emissão pode ainda ser finamente ajustada variando a concentração de cada NP, visto que a adição de N-NCs aumenta a emissão e um aumento de NPMs a reduz. De toda forma, a atenuação mencionada não elimina a capacidade de sintonia da emissão de N-NCs, que é preservada em grande parte até  $500 \text{ nm}$  como mostra a Figura 80.

Estes resultados confirmam a possibilidade de obtenção de um LMF estável e homogêneo combinando N-NCs e NPMs, onde a maioria de suas propriedades individuais é preservada no produto final. Este nanofluido tem grande potencial em aplicações como em testes de qualidade de peças metálicas utilizadas na indústria.

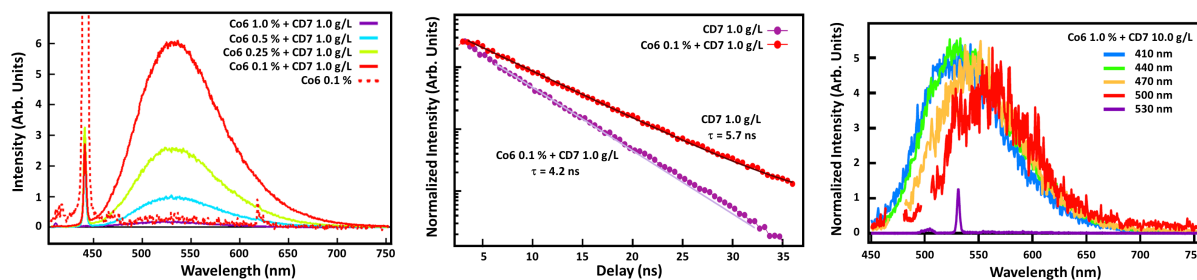


Figura 77a - Espectros de emissão de LMFs excitados à 440 nm em concentração de CDs à 1,0 g/L e diferentes frações volumétricas de NPMs. Figura 79 - Cinética de decaimento de N-NCs (vermelho) e de LMF com LMF compostos por 10 g/L de N-NCs e concentração de 0.1 vol% de NPMs. Os tempo de vida são  $\tau = 5.7$  ns para N-NCs e  $\tau = 4.2$  ns para LMF. Figura 80 - Espectros de emissão de LMF compostos por 10 g/L de N-NCs e 1,0 vol % NPMs excitados em diferentes comprimentos de onda.

## Conclusões Gerais

Nesta tese foram estudados ferrofluidos baseados em líquidos iônicos, dispersões aquosas de nanodots de carbono e fluidos magnéticos fluorescentes. As NPMs e N-NCs apresentam grande potencial em aplicações envolvendo conversão de energia, onde os ferrofluidos demonstram aumentar a eficiência em dispositivos termelétricos [16] enquanto os nanodots são considerado um candidato promissores para células solares fotovoltaicas “verdes” [256].

Em relação aos ferrofluidos à base de líquidos iônicos à temperatura ambiente (FFs-LITAs), nos concentramos em sua estabilidade e propriedades termodifusivas. A investigação do FF-LITA com base em EAN estabeleceu a grau de influência dos contra-íons iniciais e do teor de água determinando as interações interpartículas - via compressibilidade  $\chi$  e o segundo coeficiente virial  $A_2$  - e os parâmetros de termodifusão  $S_T$  e  $D_m$  em função da temperatura e fração de volume das nanopartículas magnéticas. Além disso, o estudo da termodifusão sob campo magnético aplicado em uma ampla faixa de temperaturas realizado com o FF-LITA baseado em EMIM-TFSI demonstra que a anisotropia de  $S_T$  e  $D_m$  pode de fato ser gerada em tais sistemas. Além disso, o efeito é bem ajustado pelo modelo teórico descrito nas refs. [25, 127]. Portanto, este FF-LITA é um candidato promissor para fazer uso do aprimoramento gerado por campo magnético externo no coeficiente de Seebeck em aplicações termoelétricas.

A investigação das dispersões aquosas de N-NCs em diferentes pHs expandiu o atual conhecimento de sua estabilidade coloidal, carga superficial e ordenação local. Os resultados experimentais mostraram que a estabilidade é melhorada à medida que o pH do líquido transportador passa de ácido para alcalino. Medidas de potencial zeta, titulações potenciométricas e condutimétricas estabeleceram uma correlação entre o aumento da estabilidade e o aumento da carga superficial negativa dos N-NCs, indicando o papel fundamental da repulsão eletrostática interpartículas. No entanto, em condições altamente alcalinas, ocorre uma reação de hidrólise irreversível, amplificando ainda mais

a carga superficial negativa dos N-NCs, mas também alterando significativamente suas propriedades ópticas. Este efeito é crítico para a amostra CD7 de emissão de verde, pois a emissão fluorescente é fortemente deslocada para o azul. Finalmente, um exame em nanoescala por SAXS confirma a presença de agregados que sedimentam lentamente ao longo do tempo em condições ácidas. Surpreendentemente, os resultados indicaram que uma porção dos agregados ainda pode permanecer bem dispersa no sobrenadante, podendo ser parcialmente removida por ultracentrifugação ou ao menos ter seu tamanho reduzido pela elevação do pH.

Mostramos que a combinação de ferrofluidos aquosos e N-NCs para produzir um nanocolóide híbrido pode gerar suspensões instáveis ou dispersões estáveis, dependendo do pH do meio. Em condições ácidas, a instabilidade da mistura decorre do fato de os NPMs e N-NCs apresentarem cargas opostas. Por esta razão, os N-NCs decoram as NPMs aumentando de tamanho e restringindo o potencial eletrostático repulsivo das interações NPM-NPM. Como consequência, a sedimentação de partículas e a separação magnética induzem o *demixing* das fases magnética e fluorescente. Por outro lado, em solução aquosa à pH=7,0 com citrato livre controlado, tanto N-NCs quanto as NPMs revestidas com citrato apresentam carga superficial negativa, resultando em coloides estáveis ao nível microscópico mesmo sob aplicação de campo magnético externo. Podemos confirmar que as propriedades magnéticas do líquido magnético fluorescente permanecem quase inalteradas, no entanto, a fluorescência está parcialmente reduzida.

# Résumé Long en Français

## Introduction

En réponse à l'augmentation de la consommation mondiale d'énergie, la recherche de sources renouvelables est devenue l'une des priorités de la recherche scientifique mondiale. En plus des sources d'énergie renouvelables à grande échelle (par exemple solaire, éolienne, hydraulique et biomasse), l'énergie thermique fatale est considérée comme une source prometteuse de réutilisation d'énergie, étant donné qu'elle représente une partie considérable de la consommation mondiale [13]. L'énergie thermique est utilisée principalement par l'industrie, dont une grande quantité est gaspillée via les gaz d'échappement et les systèmes de refroidissement par eau.

Une méthode directe de conversion de la chaleur résiduelle en une forme d'énergie réutilisable consiste à utiliser des dispositifs thermoélectriques, dans lesquels l'énergie thermique est convertie en énergie électrique. Les convertisseurs thermoélectriques les plus efficaces aujourd'hui sont composés de matériaux semi-conducteurs [15]. Toutefois les thermocellules à base de liquide attirent beaucoup d'attention car elles constituent une alternative moins chère et reproductible à grande échelle. Dans ce contexte, les thermocellules à base de ferrofluides ont un grand potentiel de génération efficace d'énergie renouvelable [16].

Les ferrofluides (FF), dispersions colloïdales de nanoparticules magnétiques (NPMs) dans les milieux liquides, appartiennent à la classe des matériaux intelligents puisqu'ils combinent les propriétés physiques de matériaux solides (comme le ferrimagnétisme) et les caractéristiques physiques des fluides (comme l'écoulement). Les ferrofluides à base de liquides ioniques (LIs) sont une forte tendance actuelle car ils présentent certains avantages par rapport aux milieux aqueux. Les liquides ioniques à température ambiante (LITA) sont des solvants composés uniquement d'ions, ainsi ils ne sont pas inflammables, ils ont une stabilité thermique et électrochimique élevée, une pression de vapeur saturante négligeable, en plus d'être une excellente alternative "verte" pour remplacer les classiques et plutôt dangereux solvants organiques [17]. Dans cette thèse, deux types de ferrofluides à base de liquides ioniques seront explorés : le premier est composé de nanoparticules de maghémite recouvertes d'ions citrate dispersés dans du nitrate d'éthylammonium (NEA) ; le second est

également composé de nanoparticules de maghémite, mais elles sont recouvertes par des ions  $\text{SMIM}^{\pm}\text{-TFSI}^{-}$  (1- (4-sulfobutyl)-3-méthylimidazole bistriflimide déprotoné) dispersés dans de l'EMIM-TFSI (1-éthyl-3-méthylimidazole bistriflimide).

L'objectif de l'étude des ferrofluides à base de NEA est d'étudier les effets thermomodifusifs et la stabilité colloïdale avec différents contre-ions et également avec l'ajout croissant d'eau au milieu composé uniquement d'ions. D'autre part, le ferrofluide dans EMIM-TFSI est un excellent système pour évaluer l'anisotropie provoquée par l'application d'un champ magnétique externe sur la thermodiffusion en fonction de la température.

Les nanodots de carbone (NCs) appartiennent à une autre classe de matériaux nanostructurés qui ont également un fort potentiel dans les applications liées à la production d'énergie, principalement dans la conversion d'énergie solaire [27] en raison de leur large spectre d'absorption. Ils constituent une alternative intéressante aux "quantum dots" traditionnels à base de semi-conducteurs car ils présentent des avantages tels qu'une synthèse directe, simple et pas chère [28], une faible toxicité [29] et le fait d'être écologiquement durable [30]. Dans cette thèse, des nanodots de carbone enrichis en azote (N-NCs) sont étudiés car le dopage avec cet élément augmente considérablement sa fluorescence [34], autre caractéristique importante de ces nanomatériaux. Ainsi, deux échantillons avec différents rapports azote/carbone (N/C) sont étudiés [38] : le premier avec un faible dopage (N/C=0,14) est appelé CD1 – ayant une fluorescence majoritairement bleue – et le second avec une plus grande quantité d'azote (N/C=0,74) appelé CD7 – émettant principalement dans le vert.

À l'heure actuelle, peu de résultats sont reportés dans la littérature [197] concernant la stabilité des dispersions aqueuses de ce type de N-NC, où l'attention est mise principalement sur les propriétés optiques. Par conséquent, ce travail étudie en profondeur la charge de surface, la stabilité colloïdale et l'organisation locale de ces dispersions aqueuses en fonction du pH - sans doute le principal paramètre de régulation de ces propriétés à l'échelle macro et nanométrique. De plus, dans les milieux hautement alcalins, la quantité de charge de surface subit un changement significatif suggérant une hydrolyse potentielle des groupes amides de surface. Cette hypothèse est étayée par des mesures optiques d'absorption et de fluorescence, où la forte concentration d'ions hydroxyde provoque un fort décalage de l'émission verte vers le bleu pour l'échantillon CD7 .

Enfin, dans la dernière partie de cette étude, un nouveau nanomatériau hybride est proposé qui combine les deux types de nanoparticules étudiées pour produire un liquide magnétique fluorescent (LMF). Dans un environnement acide, la combinaison génère une dispersion instable où les NPMs sont recouvertes par des N-NCs et peuvent être séparées à l'aide d'un aimant. En milieu neutre ( $\text{pH} \sim 7,0$ ), le nanofluide diffère des autres systèmes magnéto-fluorescents reportés dans la littérature et présente une stabilité colloïdale élevée même lors de l'application d'un champ magnétique externe. De cette

manière, les propriétés individuelles de chacune des dispersions colloïdales sont largement préservées dans le produit final, sans séparation de phase sur une longue période ( $> 1$  an).

## Chapitre 1 : Nanoparticules Magnétiques (NPMs)

La synthèse utilisée pour la production de ferrofluides suit la méthode de Massart [49, 50] composée de deux étapes : la première étape concerne la synthèse chimique des NPMs par coprécipitation en milieu alcalin ; la deuxième étape concerne la peptisation et la fonctionnalisation des nanoparticules dans des solvants plus complexes. Le chapitre 1 décrit le processus de l'étape 1 (représenté sur la Figure 1 de la thèse), c'est-à-dire l'obtention de nanoparticules magnétiques à base de maghémite, ainsi que ses principales caractéristiques morphologiques et structurales. En revanche, l'étape 2 est décrite au chapitre 2.

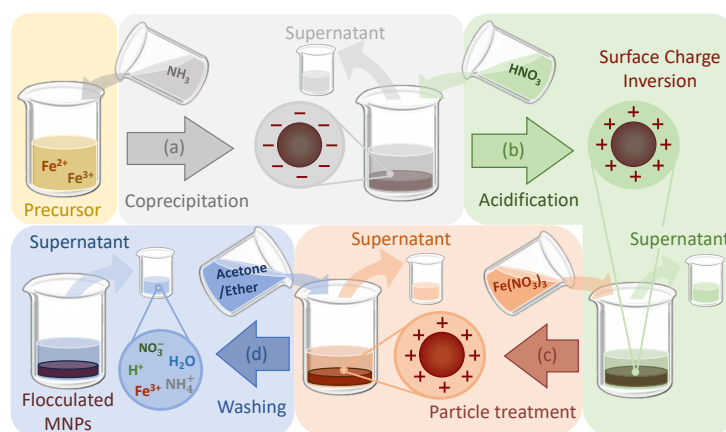


Figure 1 - Diagramme des quatre sous-étapes de la synthèse des NPMs : (a) coprécipitation ; (b) acidification ; (c) traitement des particules et (d) lavage. L'ajout des solutions est représenté par les flèches vers l'intérieur du bécher et l'élimination des surnageants par les flèches vers l'extérieur. Le changement de couleur des NPMs représente l'oxydation totale de la structure cristalline.

La première étape est subdivisée en quatre sous-étapes : le processus commence par la coprécipitation (1a) lorsque la formation de NPs de magnétite ( $Fe_3O_4$ ) par nucléation et croissance cristalline après le mélange de la solution d'ions précurseurs  $Fe^{2+}$  et  $Fe^{3+}$  avec une solution concentrée de  $NH_3$ . Dans le processus d'acidification (1b), du  $HNO_3$  concentré est ajouté, inversant la charge de surface en valeurs positives et dissolvant d'éventuels sous-produits indésirables. Puis, en (1c), un traitement avec  $Fe(NO_3)_3$  est effectué pour oxyder complètement les NPs de magnétite en maghémite ( $\gamma-Fe_2O_3$ ). Enfin, les particules sont lavées avec un mélange d'acétone et éther dans la sous-étape (1d) en réduisant la force ionique et en préparant le flocculat pour une future dispersion et/ou fonctionnalisation.

Ce processus de synthèse produit généralement des NPs approximativement sphériques avec des tailles moyennes de  $\sim 10$  nm. Cependant, en appliquant des procédures de tri en taille grâce à la variation de la force ionique, il est possible de réduire la polydispersité et d'obtenir différentes populations de NPs avec des diamètres plus ou moins grands. La

Table 1 – Tailles déterminées expérimentalement (refs. [18, 19]) obtenues par MET ( $d_{0,\text{MET}}$ ,  $s_{0,\text{MET}}$ ) et aimantation à température ambiante ( $d_{0,\text{mag}}$ ,  $s_{0,\text{mag}}$ ,  $d_{\text{NP}}$ ) des échantillons dispersés dans : EMIM-TFSI, NEA et eau.

Échantillon	$d_{0,\text{MET}}$ (nm)	$s_{0,\text{MET}}$	$d_{0,\text{mag}}$ (nm)	$s_{0,\text{mag}}$	$d_{\text{NP}}$ (nm)
Eau et NEA [18]	6.5	0.22	6.9	0.21	7.4
EMIM-TFSI [19]	8.7	0.3	8.9	0.23	9.6

taille des nanoparticules a été estimée avec l'ajustement par une fonction log-normale des histogrammes obtenus à partir de mesures de microscopie électronique à transmission (MET) et en ajustant l'aimantation à température ambiante ( $T = 300$  K) par le modèle de Langevin. Les résultats sont présentés dans la table 1 de la thèse où  $d_0$  est le diamètre médian,  $s_0$  la polydispersité et  $d_{\text{NP}}$  le diamètre volumétriquement pondéré.

La maghémite appartient à la classe des ferrites de type spinelle, avec une structure cubique compacte appartenant au groupe d'espace  $Fd3m$  n° 227 illustrée à gauche de la figure 4 de la thèse. En raison de leur petite taille et de leur forme approximativement sphérique, les NPMs peuvent être considérées comme des monodomains magnétiques uniaxiaux avec un moment magnétique élevé mais avec une faible énergie d'anisotropie. Ainsi, les ferrofluides composés de ce type de particule présentent des caractéristiques particulières, comme le superparamagnétisme de Néel [52].

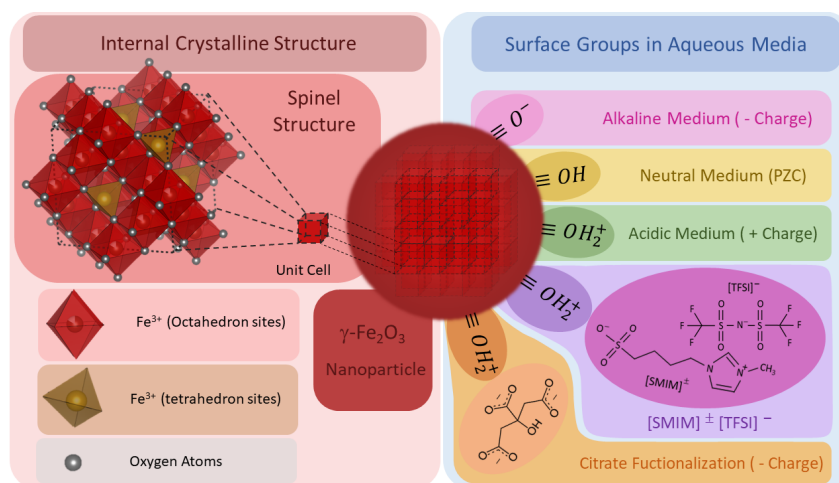


Figure 4 - *Panel gauche rouge* : Structure cristalline de type spinelle des NPMs exhibant les sites octaédriques (en rouge) et tétraédriques (en jaune). Visualisation générée avec ref. [64]. *Panel droit en bleu* : Développement des groupements de surface dans différents milieux aqueux : alcalin, neutre et acide. L'ajout de deux anions différents (citrate et  $[\text{SMIM}]^+[\text{TFSI}]^-$ ) à la solution où les nanoparticules ont une charge hautement positive peut induire une fonctionnalisation de surface.

La surface de ces nanoparticules à base d'oxydes métalliques dans l'eau subit des réactions qui leur confèrent une charge de surface positive en milieu aqueux acide, une charge négative en conditions alcalines et une charge nulle autour de  $\text{pH} \sim 7.0$ , comme indiqué à droite de la Figure 4 de la thèse. Ainsi, les particules non fonctionnalisées en milieu aqueux sont capables de rester en suspension pour former un colloïde stable

uniquement si proches des pH extrêmes ( $\sim 2.0$  ou  $\sim 12.0$ ). Dans les conditions acides, il est possible d'effectuer la fonctionnalisation des NPs avec du citrate ou avec  $\text{SMIM}^{\pm}\text{-TFSI}^{-}$  en raison de la charge négative de ces ions et de la charge opposée des NPMs. Le chapitre 2 décrit le processus de transfert de ces NPs fonctionnalisées vers les liquides ioniques respectifs.

## Chapitre 2 : Dispersions colloïdales de NPMs

Le protocole de transfert des NPMs des dispersions aqueuses vers les LITAs nous permet de contrôler des paramètres importants tels que le revêtement de surface et les contre-ions initiaux qui sont proches de l'interface. Ainsi, les NPMs dispersées dans NEA ont été recouvertes en superficie d'ions citrate et de différents contre-ions initiaux, tandis que les particules dans EMIM-TFSI avaient une fonctionnalisation de surface avec  $\text{SMIM}^{\pm}\text{-TFSI}^{-}$ . Dans NEA, les contre-ions initiaux étudiés étaient  $\text{Na}^{+}$ ,  $\text{Li}^{+}$  (tous deux précédemment étudiés) et  $\text{Rb}^{+}$  qui n'avait jamais été étudié auparavant. Les mesures de compressibilité par SAXS et SANS ont permis de déterminer dans chacun de ces cas le deuxième coefficient  $A_2$  du développement du viriel de la pression osmotique. Ainsi, en combinant plusieurs titrages chimiques (en particulier par spectrométrie de masse) et des considérations géométriques sur l'organisation ionique, il a été possible de proposer une organisation d'ions autour des NPMs au cas par cas.

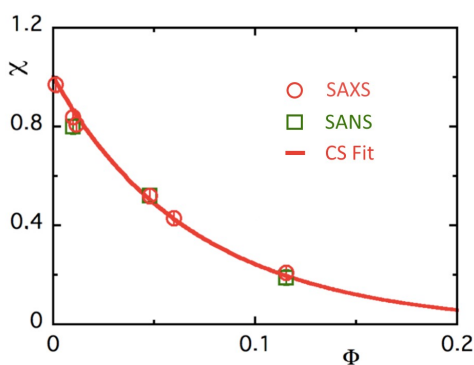


Figure 5a - Compressibilité osmotique  $\chi$  pour des suspensions colloïdales dans de l'EMIM-TFSI en fonction de leur fraction volumique  $\Phi$  - Symboles vides : Déterminations expérimentales à température ambiante par SAXS (cercles vides) et SANS (carrés vides) - Ligne : ajustement de Carnahan-Starling avec des sphères dures effectives [96,98] pour une fraction volumique  $\Phi_{\text{eff}} = 1.82 \Phi$  donnant  $A_2 = 7.3$ .

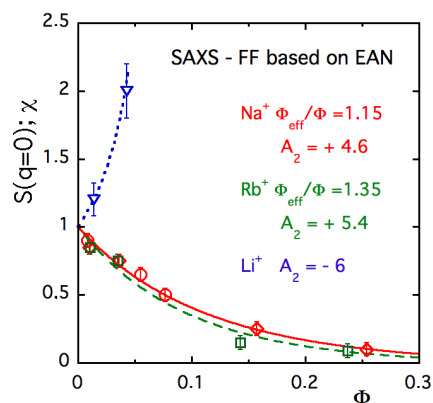


Figure 8 - Compressibilité  $\chi$  du système de NPs déterminée par  $S(q=0)$  dans les expériences de SAXS pour des dispersions dans NEA avec les contre-ions  $\text{Na}^{+}$  (ce travail (cercles rouges), ref [58] (diamants rouges)) et  $\text{Rb}^{+}$  (carrés verts) - Les fits des données avec Equation 2.5 sont obtenus en utilisant  $\Phi_{\text{eff}}/\Phi = 1.15$  pour  $\text{Na}^{+}$  (ligne continue,  $A_2 = 4.6$ ) et  $\Phi_{\text{eff}}/\Phi = 1.35$  pour  $\text{Rb}^{+}$  (ligne en tirets,  $A_2 = 5.4$ ). Pour  $\text{Li}^{+}$  (symboles bleus) le développement linéaire de Equation 2.4 est utilisé (ligne en pointillés,  $A_2 = -6$ ).

Ces résultats sont présentés dans les figures 5a et 8 où les interactions interparticulaires sont globalement répulsives pour les NPMs recouvertes de  $\text{SMIM}^{\pm}\text{-TFSI}^{-}$  dispersées

dans EMIM-TFSI (généralement jusqu'à 11 vol% NPs) et pour NEA avec des contre-ions  $\text{Na}^+$  et  $\text{Rb}^+$  (jusqu'à 25 vol% NPs). En revanche, les contre-ions  $\text{Li}^+$  présentent des interactions faiblement attractives qui empêchent l'obtention de dispersions stables à fortes concentrations de particules. Les données expérimentales combinées à la compréhension actuelle de la structure des LITAs suggèrent que les interactions répulsives proviennent de la formation de couches de contre-ions et de co-ions induites par la surface des NPs. Les ions lithium, étant des ions "briseurs" de la structure du NEA et ceux-ci se trouvant en grand nombre au voisinage de la particule (voir Figure 10 de la thèse), perturbe l'organisation de la première couche, entraînant des dispersions moins stables.

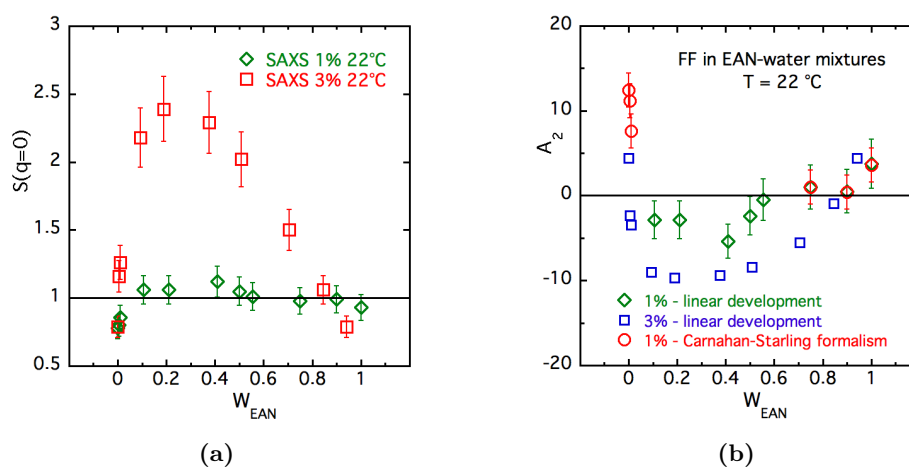


Figure 13 - (a) Valeurs  $S(Q = 0)$  assimilées à la compressibilité  $\chi$  du système de NPs déterminées par SAXS pour les échantillons avec un mélange NEA/eau avec des contre-ions  $\text{Na}^+$  à différents pourcentages en masse de NEA ( $w_{\text{NEA}}$ ) à  $T = 22$  °C pour  $\Phi = 1.0\%$  et  $3.0\%$ . (b) Deuxième coefficient du viriel déduit de la Figure (a) avec Equation 2.4 – Les cercles rouges vides sont déduits à  $\Phi = 1.0\%$  à partir de Equation.2.5 comme dans Figure 12b. Les Carrés bleus sont déduits (ici juste pour indication) d'un développement linéaire qui est faux à la concentration de  $3\%$ .

Pour aller plus loin, nous introduisons un paramètre supplémentaire pour la dispersion du NEA : la teneur en eau dans le liquide ionique. Les observations macroscopiques et microscopiques montrent que les dispersions de NPMs recouvertes de citrate avec des contre-ions  $\text{Na}^+$  restent stables au moins jusqu'à  $\Phi = 3,0\%$  - avec des NPs de diamètre moyen de l'ordre de  $7,4$  nm - dans toute la gamme des proportions de NEA et d'eau (voir Figure 11 de la thèse) et en présence d'un champ magnétique externe. Notez que cette stabilité colloïdale sur toute la fraction massique  $w_{\text{NEA}}$  ne serait pas observée avec des NPs de même taille que celles utilisées dans EMIM-TFSI avec un diamètre moyen de  $9,6$  nm. Cependant, avec les NPs utilisées, la transition d'un milieu aqueux à un liquide ionique pur s'est avérée inclure une gamme de proportions dans lesquelles les interactions entre les particules passent de répulsives à attractives, et vice versa. Ce résultat a été déduit par des mesures de SAXS dans lesquelles  $A_2$  est négatif pour les fractions massiques  $w_{\text{NEA}}$  intermédiaires et  $A_2$  est positif aux extrêmes. Ces résultats sont présentés sur la Figure 13 de la thèse. Grâce à cette base de résultats complète, nous pouvons ensuite analyser en

profondeur la thermodiffusion de ces échantillons par une expérience de diffusion Rayleigh forcée (FRS).

### Chapitre 3 : Propriétés thermodiffusives

L'influence de la nature des contre-ions sur les ferrofluides à base de NEA a été analysée en fonction de la fraction volumique des NPs  $\Phi$  et de la température  $T$ . Dans la Figure 16, comme attendu des développements théoriques sur la thermodiffusion, et comme on le voit dans tous les ferrofluides basés sur LITAs jusqu'à présent, le coefficient Soret  $S_T$  est toujours positif et diminue avec l'augmentation de la température  $T$ , quelle que soit l'interaction interparticulaire. Dans le NEA on observe que  $S_T$  est également positif, mais il présente plusieurs comportements en fonction de l'interaction interparticulaire : dans les systèmes répulsifs – où  $A_2 > 0$  et la compressibilité  $\chi < 1$  est décroissante avec  $\Phi$  –  $S_T$  diminue lorsque  $\Phi$  augmente ; Dans un système avec une interaction interparticulaire globalement attractive –  $A_2 < 0$  et  $\chi > 1$  augmentant à mesure que l'échantillon se concentre – le coefficient Soret  $S_T$  augmente avec  $\Phi$ , au moins sur les plages de concentration testées. Ce résultat expérimental illustre le fait que  $S_T$  est directement proportionnel à  $\chi$ .

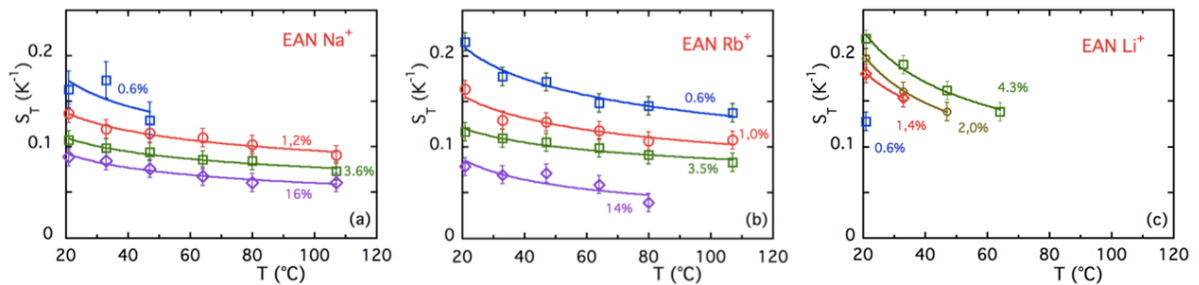


Figure 16 - Coefficient Soret en fonction de la température et de la concentration en particules pour les trois contre-ions étudiés  $\text{Na}^+$ ,  $\text{Rb}^+$  et  $\text{Li}^+$  dans NEA. Les lignes sont purement indicatives.

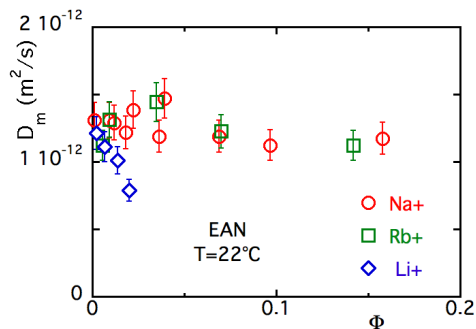


Figure 18 - Coefficient de diffusion  $D_m$  en fonction de la fraction volumique en NPs  $\Phi$  à  $T = 22^\circ\text{C}$  dans des ferrofluides à base de NEA avec différents contre-ions initiaux  $\text{Na}^+$ ,  $\text{Rb}^+$  et  $\text{Li}^+$ .

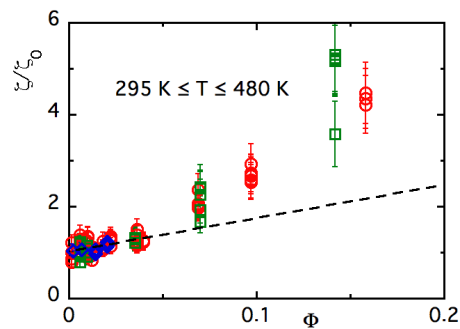


Figure 20 - Friction réduite  $\zeta/\zeta_0$  ressentie par les NPs en fonction de leur fraction volumique  $\Phi$  pour les trois contre-ions  $\text{Na}^+$  (cercles rouges),  $\text{Rb}^+$  (carrés verts) et  $\text{Li}^+$  (diamants bleus) sur toute la gamme expérimentale de température. La ligne pointillée correspond à Equation 3.15 dans le cas des contre-ions  $\text{Na}^+$  ( $\Phi_{\text{eff}} = 1.15$ ).

Le coefficient de diffusion  $D_m$  est également affecté par les différents régimes d'interaction et la température, comme le montre la figure 18. La dépendance en  $T$  de  $D_m$  est fortement liée à la viscosité du milieu liquide  $\eta_0(T)$ , tandis que la dépendance en  $\Phi$  est largement encapsulée dans  $\chi(\Phi)$ . À faible concentration de NPs, il est montré que la viscosité effective subie par les NPs est la viscosité macroscopique du fluide porteur.

Alors que  $D_m$  reste pratiquement inchangé pour les systèmes répulsifs  $\text{Na}^+$  et  $\text{Rb}^+$  (jusqu'à  $\Phi \sim 15\%$ ),  $D_m$  réduit considérablement pour  $\text{Li}^+$  lorsque la fraction volumique  $\Phi$  augmente légèrement. Pour  $\text{Li}^+$ , cela peut être associé à l'augmentation des valeurs de  $\chi$  comme  $D_m \propto 1/\chi$ . Pourtant,  $D_m$  dépend de la friction  $\zeta(T, \Phi)$  qui peut alors être déduite des mesures  $D_m$  et  $\chi$ . La friction obtenue dans les FF dilués ( $\Phi < 4,0\%$ ) est compatible avec le développement linéaire de Batchelor, cependant, à des concentrations plus élevées, la friction montre une forte augmentation. Bien que nous n'ayons pas de description théorique de cette déviation, elle est certainement liée à l'organisation locale des ions dans le NEA et à la formation de la couche susmentionnée autour des NPMs.

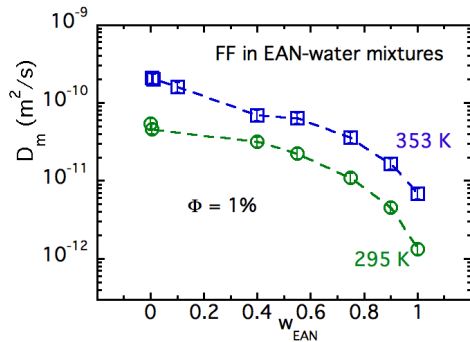


Figure 22a – Coefficient de diffusion  $D_m$  déterminé par FRS à  $\Phi = 1.0\%$  en fonction de  $w_{\text{NEA}}$  aux deux températures expérimentales extrêmes. Les lignes pointillées sont purement indicatives.

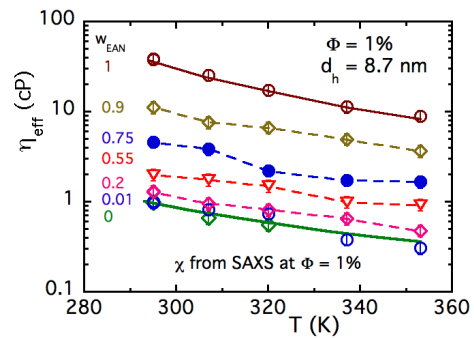


Figure 23 – Viscosité effective  $\eta_{\text{eff}}$  déduite des déterminations de  $D_m$  à  $\Phi = 1.0\%$  de la Figure 22a en fonction de  $T$  à différents  $w_{\text{NEA}}$  - Certaines valeurs ont été interpolées. Les lignes continues sont  $\eta_0$  pour NEA (ligne marron pour la ref. [153]) et pour l'eau (ligne verte). Les lignes pointillées sont purement indicatives.

Le NEA-FF avec les contre-ions  $\text{Na}^+$  peut être considéré comme un système modèle polyvalent, donc approprié pour évaluer les effets de la teneur en eau. De cette façon,  $D_m$  et  $S_T$  ont tous deux été déterminés expérimentalement par FRS en fonction du rapport pondéral de NEA dans l'eau  $w_{\text{NEA}}$ ,  $\Phi$  et  $T$ . À  $\Phi = 1.0\%$ ,  $D_m$  augmente en fonction de la température et diminue par rapport à  $w_{\text{NEA}}$  comme le montre la Figure 22a. Ce comportement peut principalement – mais pas exclusivement parce que la compressibilité des NPs dépend clairement de  $w_{\text{NEA}}$  – être attribué à une augmentation de la viscosité macroscopique  $\eta_0$  du fluide porteur à mesure que la quantité de NEA augmente et à une réduction de  $\eta_0$  qui se produit lorsque  $T$  augmente. De plus, comme une viscosité  $\eta_{\text{eff}}$  effective peut être calculée à partir du  $D_m$  mesuré aux petites valeurs de  $\Phi$ , nous pourrions comparer les valeurs déterminées via FRS avec les données actuellement reportées dans la littérature [153]. Dans la Figure 23 de la thèse, on montre que les résultats obtenus sont

en accord pour  $w_{\text{NEA}} = 1$  et 0 dans toute la plage de température accessible et en tout  $w_{\text{NEA}}$  à température ambiante dans la Figure 22b. À des températures plus élevées pour ces valeurs intermédiaires de  $w_{\text{NEA}}$ ,  $\eta_{\text{eff}}$  suit la tendance mentionnée ci-dessus ( $\eta_{\text{eff}}$  diminue avec  $T$  et augmente avec  $w_{\text{NEA}}$ ) mais il n'y a toujours pas de valeurs dans la littérature à comparer avec ces résultats.

Les figures 24b et 25b de la thèse montrent les résultats de  $S_T$ . Dans ces mélanges eau-NEA, aux petites valeurs de  $w_{\text{NEA}}$  et pour les deux  $\Phi = 1.0\%$  et  $\Phi = 3.0\%$ ,  $S_T$  augmente avec la température, d'une valeur négative vers une valeur positive, comme cela est observé dans les ferrofluides à base d'eau avec des NPs enrobées de citrate et des contre-ions  $\text{Na}^+$ . Au contraire, aux grandes valeurs de  $w_{\text{NEA}}$ ,  $S_T$  est positif et une fonction décroissante de  $T$ , comme précédemment observé dans le NEA pur. À  $\Phi = 3.0\%$  les deux comportements opposés se rencontrent clairement à un point d'inversion situé autour de  $w_{\text{NEA}} \sim 0.6$ , alors que cette observation est moins précise à  $\Phi = 1.0\%$ . Une autre inversion peut également être mise en évidence par FRS en termes de dépendance en  $\Phi$  de  $S_T$ . Aux grandes valeurs de  $w_{\text{NEA}}$ ,  $\Delta S_T/\Delta\Phi$  est négatif (ce qui est caractéristique des systèmes LITAs répulsifs), tandis qu'entre  $w_{\text{NEA}} = 0, 1$  et 0,5 il est trouvé positif (une marque d'interactions attractives dans les systèmes LITAs). Cette inversion de signe de  $\Delta S_T/\Delta\Phi$  peut en effet être associée à la bascule d'une interaction interparticule répulsive à attractive observée dans les mesures SAXS dans les mélanges eau-NEA pour  $w_{\text{NEA}}$  de l'ordre de 0,6 à  $\Phi = 1\%$ .

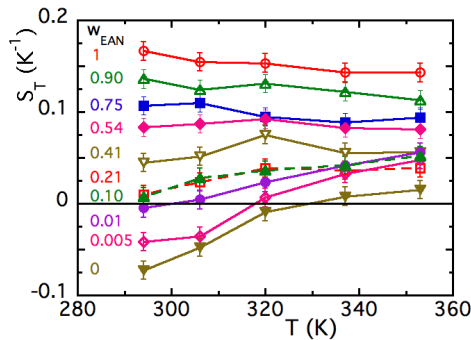


Figure 24b - (a) Coefficient Soret  $S_T$  mesuré par FRS à  $\Phi = 1.0\%$  en fonction de  $T$  aux différents  $w_{\text{NEA}}$  sondés.

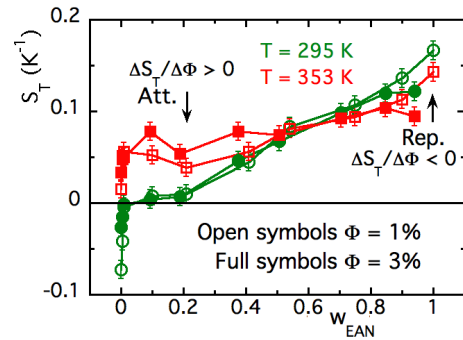


Figure 25b - Comparaison du coefficient Soret  $S_T$  à  $T = 295$  K and  $353$  K en fonction de  $w_{\text{NEA}}$  à  $\Phi = 1.0\%$  et  $3.0\%$ .

Une analyse en termes de  $TS_T/\chi$  en fonction de  $w_{\text{NEA}}$  montre qu'un comportement proche de celui d'un ferrofluide dans un électrolyte standard avec des interactions interparticulaires répulsives n'est observé que pour  $w_{\text{NEA}}$  inférieur à 0,01 – 0,1. Cette fourchette de  $w_{\text{NEA}}$  mériterait à l'avenir une analyse plus systématique. De plus, dans les ferrofluides aqueux à base de NPs enrobées de citrate (donc à  $w_{\text{NEA}} = 0$ ) à température ambiante, le signe du coefficient Soret  $S_T$  s'inverse en fonction du caractère hydrophile des contre-ions libres. En particulier, si seuls les contre-ions  $\text{EA}^+$  étaient présents et qu'il n'y avait pas de  $\text{Na}^+$ ,  $S_T$  serait positif à  $w_{\text{NEA}} = 0$ . Pourtant, dans ce cas, la charge de surface dans l'eau est toujours négative indépendamment du type de contre-ions.

L'inversion de signe de  $S_T$  qui se produit avec l'augmentation de  $w_{\text{NEA}}$  peut donc être liée au nombre croissant d'ions  $\text{EA}^+$  au voisinage des NPs. Mais il est intéressant de noter que les données pourraient également suggérer qu'il pourrait être associé à une inversion d'une charge effective négative pour  $w_{\text{NEA}} = 0$  (tel que mesuré expérimentalement) à positive pour  $w_{\text{NEA}} = 1$  (comme déduit pour les contre-ions  $\text{Na}^+$  d'une analyse croisée de FRS et de mesures thermoélectriques). Un développement possible pourrait respecter la ligne suivante : la charge effective négative  $\xi_0^{\text{eff}}$  des NPs à  $w_{\text{NEA}} = 0$  diminue progressivement en valeur absolue avec  $w_{\text{NEA}}$ , jusqu'à presque zéro dans la plage intermédiaire  $0,01 \leq w_{\text{NEA}} \leq 0,2$  ; Pour  $0,2 \leq w_{\text{NEA}} \leq 0,5-0,7$ , elle devient légèrement positive mais pas encore capable de produire une répulsion interparticulaire suffisamment forte ; pour  $0,7 \leq w_{\text{NEA}} \leq 1$ , la charge effective positive devient suffisamment grande pour produire une répulsion interparticulaire globale, résultant d'une structuration ionique en couches efficace.

Enfin, l'anisotropie de la thermodiffusion en présence d'un champ magnétique a été étudiée pour la première fois dans un ferrofluide à base de LITA. La large gamme de  $T$  dans laquelle le FF basé sur EMIM-TFSI est stable nous a permis de sonder la réponse magnétique de 295 K jusqu'à 461 K à une concentration modérée de  $\Phi = 5,95\%$ . En l'absence de champ magnétique externe,  $D_m$  et  $S_T$  se comportent comme des FF-LITA typiques avec des interactions répulsives :  $D_m$  augmente avec la température comme la viscosité macroscopique  $\eta_0$  du fluide porteur diminue. La friction est plus importante que prévu théoriquement par le développement de Batchelor (de 20% à 40%), probablement en raison de l'organisation structurale ionique autour des NPMs. De plus, les valeurs expérimentales de  $S_T$  diminuent à mesure que  $\Phi$  et  $T$  augmentent, suivant la tendance caractéristique des ferrofluides basés sur des LITA avec des interactions interparticulaires globalement répulsives.

Une anisotropie en présence de champ magnétique de  $D_m$  et  $S_T$  est observée (Figures 29 et 30) à toutes les températures sondées. Comme prévu, la réponse sous-champ dépend de la direction (parallèle  $\vec{H}_{\parallel}$  ou perpendiculaire  $\vec{H}_{\perp}$  à  $\vec{\Delta}\Phi$ ) et l'amplitude ( $0 \leq H \leq 100 \text{ kA m}^{-1}$ ) du champ magnétique appliqué  $\vec{H}$ . Sous champ le coefficient de diffusion  $D_m$  persiste à augmenter avec  $T$  comme sous champ nul. Cependant, l'anisotropie induite magnétiquement donne  $D_m(H_{\perp}) < D_m(H=0) < D_m(H_{\parallel})$ , où cet effet diminue progressivement à mesure que les températures augmentent. Au contraire,  $S_T$  se réduit en fonction de  $T$  et l'effet d'anisotropie se traduit par  $S_T(H_{\parallel}) < S_T(H=0) < S_T(H_{\perp})$ , avec ici aussi une réduction progressive de l'effet à mesure que  $T$  augmente.

Les données expérimentales sont bien ajustées en fonction de  $H$  et  $T$  par le modèle théorique décrit dans réfs. [25, 127] qui a déjà été utilisé pour ajuster correctement l'effet d'anisotropie dans les ferrofluides aqueux à température ambiante. On observe ici que la modélisation est également valable pour les systèmes non-DLVO et à des  $T$  élevées. L'ajustement a été réalisé avec des valeurs de  $\chi$  déterminées par SANS,  $m_s(T)$  en utilisant



vérifiées par de multiples techniques afin de fournir un support pour l'analyse ultérieure des dispersions en milieu aqueux à divers pH.

Un diamètre moyen entre 2 – 4 nm a été mesuré par microscopie électronique à transmission (MET) et diffraction des rayons X (DRX) comme indiqué dans la Table 4. Cependant, une grande quantité de nanoparticules avec des diamètres < 2 nm n'ont été trouvés que par microscopie à force atomique (AFM). Par conséquent, la distribution de taille devrait en fait être considérablement déplacée vers des tailles plus petites.

Table 4 - Détermination expérimentale des tailles par MET ( $d_{0,MET}$ ,  $s_{0,MET}$ ) et par XRD ( $d_{DRX}$ ) des échantillon CD1 e CD7.

Échantillon	$d_{0,MET}$ (nm)	$s_{0,MET}$	$^1d_{DRX}$ (nm)	$^2d_{DRX}$ (nm)
CD1	$3.96 \pm 0.09$	$0.39 \pm 0.02$	$1.96 \pm 0.05$	$1.97 \pm 0.04$
CD7	$3.7 \pm 0.1$	$0.31 \pm 0.03$	$2.46 \pm 0.03$	-

La structure cristalline des N-NC a été précédemment déterminée dans la réf. [38]. CD1 a une structure de carbone graphitique dopée à l'azote et CD7 a la structure  $\beta$ -C<sub>3</sub>N<sub>4</sub>, comme le montre la Figure 38. De plus, la présence de groupes de surface carboxyle et amide a été confirmée par spectroscopie infrarouge (FTIR). La densité déterminée expérimentalement de la poudre composée d'agrégats de N-NCs était de  $1,53 \pm 0,01$  g/cm<sup>3</sup> pour CD1 et  $1,84 \pm 0,04$  g/cm<sup>3</sup> pour CD7 suggérant que la surface est très passivée, car la valeur mesurée est considérablement inférieure (22 – 48%) par rapport à la densité du noyau cristallin seul, 2,02 et 3,57 g/cm<sup>3</sup> respectivement.

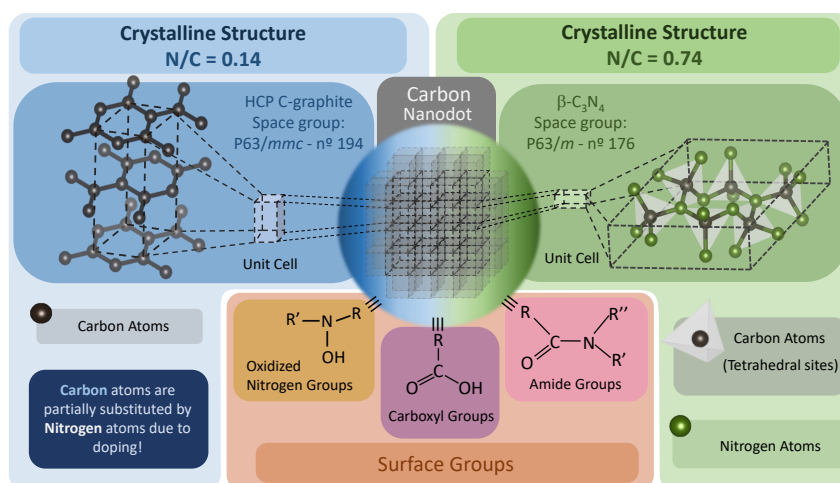


Figure 38 - Schéma des caractéristiques du noyau et de la surface des N-NC étudiés. Les structures cristallines internes présentées correspondent aux deux variantes de la synthèse hydrothermale avec différents rapports N/C, nommées ici CD1 (gauche - N/C=0,14) et CD7 (droite - N/C=0,74). Les structures cristallines (carbone graphitique et  $\beta$ -C<sub>3</sub>N<sub>4</sub>) et les groupes de surface (carboxyle et amide) ont été déduites de plusieurs techniques. Visualisation de la structure générée à l'aide de la référence [64].

## Chapitre 5 : Dispersions colloïdales de N-NCs

Nous nous concentrons sur l'étude du développement de la charge de surface, de la stabilité colloïdale et de l'ordre local, car ces aspects ne sont pas approfondis dans l'état de l'art de ce type de nanodots. Les N-NCs ont été dispersés sur une large gamme de pH (de 2,0 à 12,0) par l'addition directe de poudre dans les solutions aqueuses acides ( $\text{NaNO}_3$ ) et alcalines ( $\text{NaOH}$ ). L'échantillon a été homogénéisé autant que possible par sonication dans un bain à ultrasons à  $50^\circ\text{C}$  pendant plusieurs heures. Cependant, dans les conditions acides, la solubilité semble être considérablement réduite. Les aspects visuels macroscopiques de l'échantillon sont présentés sur la Figure 42 montrant que les N-NC sont partiellement bien dispersés en solution, mais qu'une partie d'entre eux se dépose au fond du tube. La quantité de N-NC précipités est en accord avec le pH, par exemple, la quantité de sédiment est plus élevée dans un milieu acide et diminue progressivement à mesure que le pH devient alcalin. À pH 12,0, aucun précipité ne se forme, mais l'échantillon montre des changements dans ses propriétés optiques avec le temps.

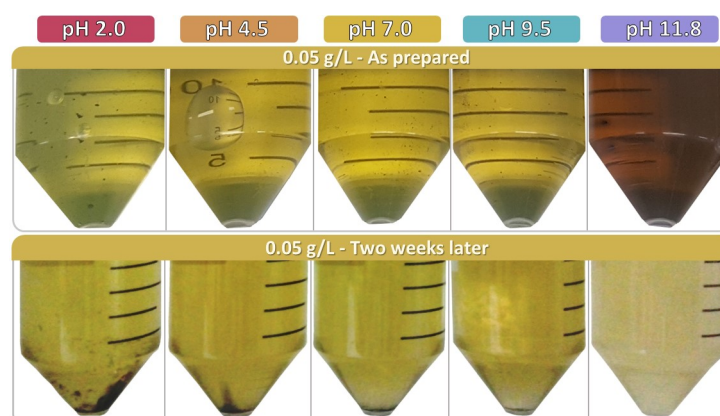


Figure 42 - Aspects visuels de l'échantillon CD7 dispersé en milieux aqueux dans différents pH à 0,05 g/L. La première ligne fait référence aux photos prises immédiatement après le protocole de dispersion et la deuxième ligne après que l'échantillon a été laissé immobilisé pendant deux semaines.

On observe par la microscopie optique que le précipité a des agrégats de divers ordres de grandeur (de  $\sim 1 - 100 \mu\text{m}$ ). Les plus gros agrégats sont des structures lamellaires denses et compactes, mais à mesure qu'ils deviennent plus petits, nous avons observé que les structures fractales sont formées par un grand nombre d'agglomérats inférieurs à  $10 \mu\text{m}$ . De toute façon, le surnageant s'est avéré être très homogène à une échelle macro et microscopique à tous les pH sondés. Cet écart entre le surnageant et le précipité était associé à l'hétérogénéité des N-NC, ce qui devrait induire des différences de solvation, d'interactions interparticulaires et d'ordre nanométrique en réponse aux variations de taille, de structure de surface et de charge électrique.

Ainsi, nous avons étudié le développement de la charge de surface des N-NC en fonction du pH. Les mesures du potentiel Zeta indiquent que la charge de surface est toujours négative dans l'intervalle acido-basique analysée et que sa valeur absolue était

plus élevée pour CD7 que pour CD1. La charge non nulle dans un milieu fortement acide était associée à des groupes de surface d'azote oxydé, tandis que l'augmentation progressive en valeur absolue de la charge pour les conditions alcalines était attribuée à la déprotonation des groupes de surface carboxyle. Par conséquent, l'amélioration de la stabilité colloïdale observée lorsque le pH augmente doit provenir de la répulsion électrostatique supplémentaire. Le rapport azote/carbone (N/C) semble également affecter la nature de surface des N-NC, où l'échantillon CD1 a un caractère plus acide par rapport au CD7. Ce résultat peut être lié à la proportion de groupes de surface à base de carboxyle et d'azote.

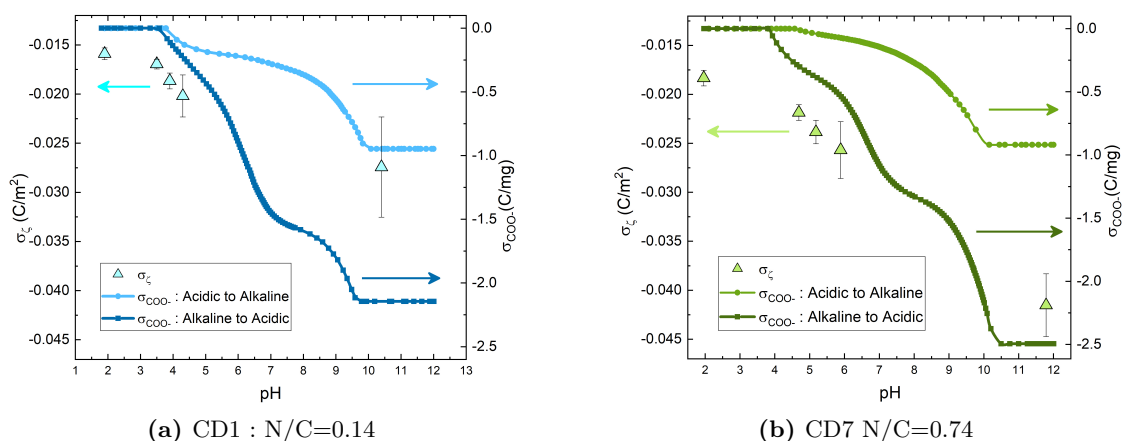


Figure 49 - Dépendance en pH de  $\sigma_{\text{COO}^-}$  et  $\sigma_z$  évaluée en utilisant Eq.5.8 et 5.9, respectivement. Les axes verticaux droit et gauche sont indépendants et l'alignement n'a été effectué que pour une analyse qualitative.

Les titrages potentiométriques et conductométriques montrés dans la Figure 49 nous ont permis d'estimer la densité de charge de surface à partir de la déprotonation de groupes carboxyle. Les courbes indiquent une différence de comportement entre la voie acide-alcaline et la voie inverse, alcaline-acide. Non seulement la quantité de titrant est modifiée, mais la forme de la courbe est radicalement changée. Ces résultats suggèrent que l'hystérésis observée dans les courbes de titrage est probablement une conséquence de l'hydrolyse alcaline de groupes amide. Cette réaction chimique expliquerait l'augmentation de la charge lorsque les groupes amide sont convertis en groupes carboxyle, ainsi que le changement de forme de la courbe arrive en réponse à un changement significatif de la nature acide de la surface des particules.

L'organisation nanométrique des N-NC a été testée par MET, techniques de diffusion dynamique de la lumière (DLS) et de rayons X aux petits angle (SAXS). Les résultats suggèrent la présence d'agrégats également inférieurs à 1  $\mu\text{m}$  dans le surnageant, ce qui était au-delà de la résolution du microscope optique. Les mesures DLS indiquent que la taille critique des agrégats était comprise entre 100 et 400 nm. L'ultracentrifugation nous a permis de réduire le diamètre hydrodynamique à une fenêtre de 70-120 nm. La structure de ces agrégats détectée par SAXS varie également avec N/C. Puisque CD1 présente des

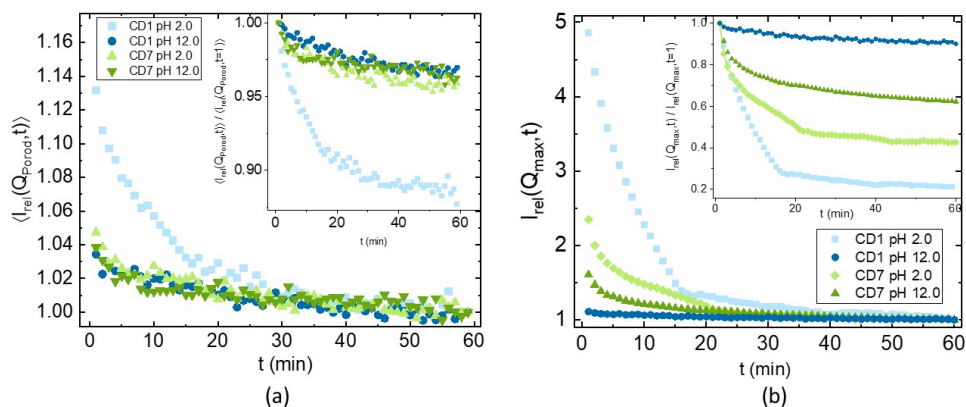


Figure 58 - Évolution temporelle des valeurs expérimentales des facteurs de structure apparents en (a) la région de Porod ( $Q > 2 \text{ nm}^{-1}$ ) et en (b) la région de Guinier ( $Q_{max}$ ). *Insets* : Normalisation par la première valeur mesurée ( $S_{app}(Q, t)/S_{app}(Q, t = 1)$ ) pour une meilleure visualisation des profils de courbes.

agglomérats plus dense et compacts - avec les exposants de fractales de surface - et CD7 présent un réseau d'agrégats moins compact - avec des exposants fractales de masse. Les mesures SAXS en fonction du temps (Figure 58) ont évalué le processus de sédimentation à l'échelle nanométrique, confirmant que la stabilité colloïdale est en fait améliorée dans un environnement alcalin. De plus, la mesure dynamique a montré que le processus de sédimentation est hétérogène, par conséquent, il est probable qu'il existe une distribution de taille des agrégats également à l'échelle nanométrique.

## Chapitre 6 : Photoluminescence

Enfin, une brève analyse des propriétés optiques des échantillons a été réalisée à pH 12,0. Un décalage de l'émission verte vers le bleu de la fluorescence de l'échantillon de CD7 a été observé, tandis que CD1 est resté bleue. L'absorption optique (AO) de

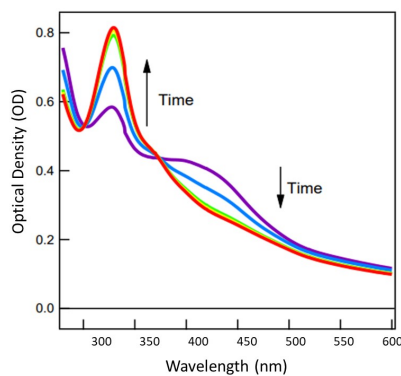


Figure 60a - Variation de densité optique en fonction de la longueur d'onde pour une solution aqueuse d'échantillon CD7 juste après avoir été alcalinisée à  $\text{pH} \sim 11,0$  avec NaOH. La concentration initiale de N-NCs a été fixée à 0,05 g/L.

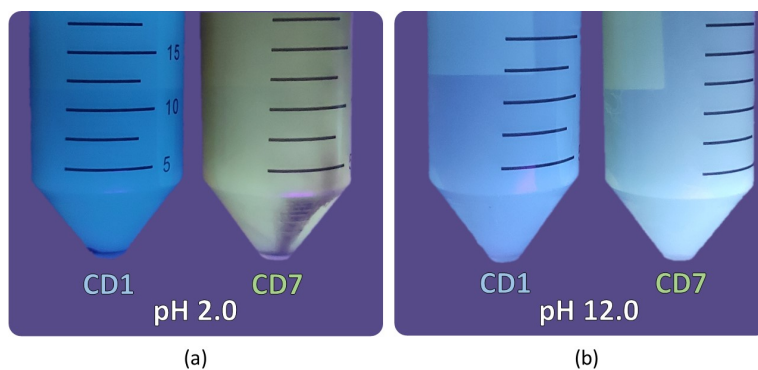


Figure 63 - (a) Une comparaison visuelle entre l'échantillon CD1 et CD7 en milieu acide (pH 2,0) à une concentration de 0,15 g/L après deux semaines. Les échantillons ont été photographiés sous une lumière ultraviolette du commerce (longueur d'onde 480–320 nm). (b) Une comparaison visuelle à des conditions équivalentes décrites dans Figure 63a, sauf qu'ils ont été dispersés dans un milieu alcalin (pH 12,0).

l'échantillon CD7 montre des variations dépendant du temps, où le pic autour de 400 nm diminue tandis que la bande à 300-320 nm augmente. Ce résultat d'absorption – ainsi que le décalage de la fluorescence vers le bleu – doit être associé à l'hydrolyse d'amide déjà conjecturée. En considérant le mécanisme d'émission de ces N-NCs, on peut voir que l'émission verte dépend essentiellement des groupes amide, alors que l'émission bleue n'est pas aussi sensiblement affectée. Par conséquent, l'émission verte maximale est réduite car une grande partie de l'amide sur la surface est convertie en groupes carboxyle.

## Chapitre 7 : Systèmes magnéto-photoluminescentes

Ce chapitre traite de l'état de l'art des systèmes nanoparticulaires aux propriétés magnéto-fluorescentes actuellement développés dans la littérature. Dans cette mesure, deux approches sont généralement appliquées dans l'état actuel de l'art des nanofluides magnétiques et fluorescents : (i) la fonctionnalisation de nanoparticules magnétiques avec des molécules fluorescentes, conférant au noyau magnétique des propriétés photoluminescentes issues de la coque de surface et (ii) la formation de nanocomposites par l'agglomération et/ou le confinement de nanoparticules magnétiques et fluorescentes.

Le grand inconvénient de ces deux méthodes est que les nano-objets résultants sont généralement supérieurs à 100 nm (atteignant quelques microns), ce qui rend presque impossible la production d'une dispersion colloïdale stable en présence d'un champ magnétique externe. La stabilité peut être améliorée en augmentant la viscosité du solvant (par exemple, dans les huiles dérivées du pétrole), ce qui restreint considérablement sa plage d'applicabilité. De plus, l'encapsulation des nanostructures restreint plusieurs propriétés intéressantes sensibles à l'interface particule/milieu, limitant le potentiel d'applications telles que les capteurs. Ainsi, un nouveau type de fluide a été proposé dans lequel les deux propriétés de chaque matériau sont largement préservées tandis que le colloïde reste stable même avec un champ magnétique appliqué.

## Chapitre 8 : Nanocolloïde hybride de NPMs et N-NCs

Dans ce chapitre, nous présentons un nouveau liquide magnétique fluorescent (LMF) à base de nanoparticules magnétiques d'oxyde de fer et de nanodots de carbone. Le matériau hybride a été obtenu en utilisant les deux nanomatériaux décrits dans les parties I et II sans aucune encapsulation ni confinement des composants. La méthode utilisée pour combiner les échantillons est pratique, peu coûteuse et reproductible. L'avantage d'utiliser ce type de NPM est la possibilité d'ajuster les propriétés magnétiques du fluide à travers de sa taille, sa composition chimique et sa fraction volumique. De plus, l'utilisation de N-NC permet d'avoir une fluorescence brillante et accordable se composant d'un matériau

abondant, non toxique, peu coûteux et biodégradable. Deux conditions physico-chimiques ont été évaluées : dispersion en milieu acide et pH neutre.

Dans les conditions acides, les ferrofluides stables à pH 2,5 sur la base de NPM noyau-coquille avec un noyau de ferrure de cobalt et une coquille de maghémite ( $\text{CoFe}_2\text{O}_4@ \gamma\text{-Fe}_2\text{O}_3$ ) sont mélangés avec des dispersions au même pH de nanodots de l'échantillon CD7. Deux tailles de nanoparticules magnétiques sont étudiées, à savoir un échantillon d'une taille moyenne de 10 nm (appelé CoG) et un autre d'une taille plus petite de 6 nm (CoP). Indépendamment de leur taille, les deux mélanges de pH acides sont instables colloïdalement. En effet, dans ces conditions, les NPM sont chargés positivement tandis que les N-NC sont chargés négativement. De cette manière, un potentiel électrostatique attractif entre les composants magnétiques et fluorescents est établi pour induire la formation d'agglomérats. Le résultat macroscopique est une séparation de phase lente par sédimentation qui peut être accélérée en introduisant un champ magnétique externe comme le montre la figure 66. La phase magnétique concentrée à proximité de l'aimant ne montre pratiquement aucune fluorescence, tandis que le surnageant est toujours fluorescent en raison de la présence de N-NC qui sont restés bien dispersés. Les mesures SAXS indiquent qu'en fait un facteur de structure attractif est généré avec des longueurs de corrélation correspondant à la distance de contact des NPM. De plus, les images MET montrent que les NPM sont décorés par des N-NC en raison du potentiel électrostatique attractif.

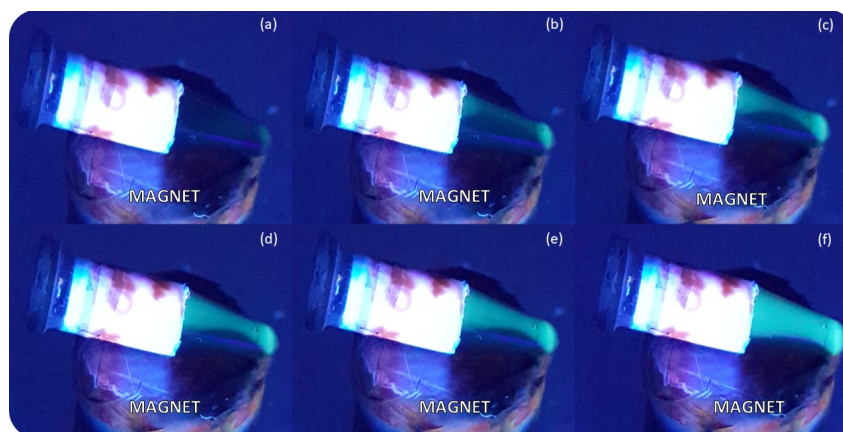


Figure 66 - (a) Un nanofluide hybride acide composé de 0,5% en fraction volumique de CoG (NPM) et 0,5 g/L de CD7 (N-NC) à pH 2,5 est positionné sur un aimant après avoir agité manuellement l'échantillon pendant quelques secondes. (b) - (f) les NPM se concentrent plus près de l'aimant dans un intervalle de temps inférieur à une minute. Une quantité considérable de N-NC reste dispersée dans la solution, ce qui est mis en évidence par l'émission verte générée sous la lumière UV.

D'autre part, des liquides magnétiques fluorescents très stables (LMF) ont été obtenus en mélangeant des N-NCs CD1 et CD7 avec des nanoparticules magnétiques ( $\text{CoFe}_2\text{O}_4@ \gamma\text{-Fe}_2\text{O}_3$ ) fonctionnalisées avec des ions citrate à  $\text{pH} = 7,0$ . Les échantillons ont montré une stabilité colloïdale élevée de longue durée au niveau macro et microscopique, avec et sans la présence d'un champ magnétique externe comme le montre la Figure 68. La fluorescence est toujours perceptible après le mélange, avec une émission verte dans le

cas de l'échantillon CD7.

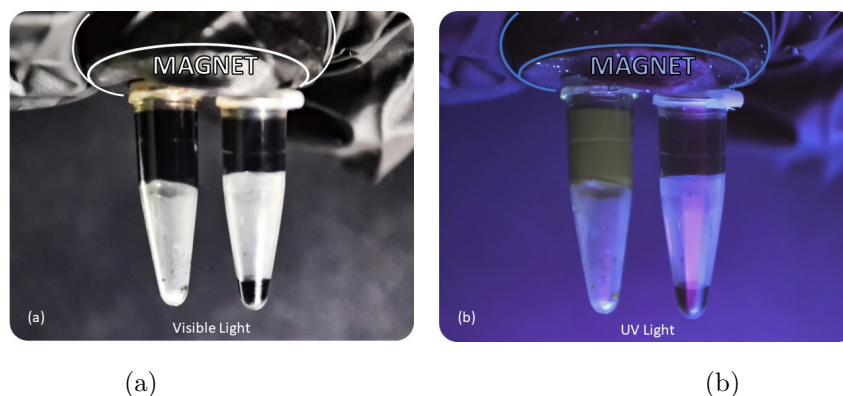


Figure 68 - Le liquide magnétique fluorescent à base d'échantillons CD7+Co6 (à gauche) et le ferrofluide Co6 pur (à droite) sont suspendus par un aimant sous (a) la lumière visible et (b) la lumière UV.

Plusieurs caractérisations magnétiques ont été réalisées et sont présentées sur la Figure 75, telles que : aimantation à température ambiante, boucles d'hystérésis à 5 K, graphes de Thamm-Hesse et courbes ZFC/FC. Les résultats obtenus n'ont pas montré de changements significatifs par rapport à l'échantillon de FF pur et de LMF hybride. De plus, des mesures de magnéto-hyperthermie ont également été réalisées attestant que la présence de N-NC n'affecte pas le taux d'absorption spécifique (SPA). En bref, l'ajout de N-NC dans cette condition physico-chimique n'influence pas activement les propriétés magnétiques du ferrofluide d'origine.

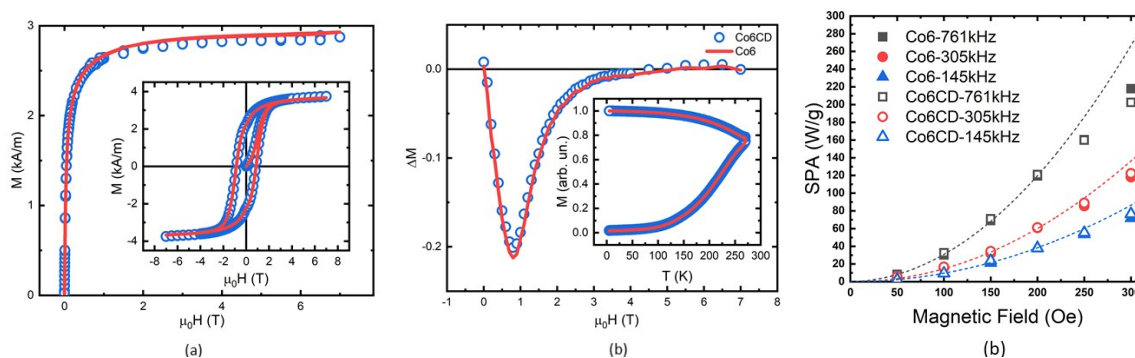


Figure 75 - Comparaison des propriétés magnétiques entre le LMF Co6[ $\Phi = 1\%$ ]+CD7[10 g/L] (cercles bleus) et le ferrofluide pur Co6 ( $\Phi = 1\%$ ) (ligne rouge) : (a) *Figure principale* : Courbes de aimantation  $M(H)$  à température ambiante (300 K). *Inset* : Cycle d'hystérésis à 5 K. (b) *Figure principale* :  $\Delta M$  calculé par Eq. 8.2 dans le cadre du formalisme de Thamm-Hesse. *Inset* : Courbes d'aimantation en fonction de la température  $M(T)$  suivant le protocole ZFC/FC.

Enfin, les propriétés photoluminescentes ont été évaluées afin de déterminer quantitativement les changements du spectre d'émission générés par l'introduction de NPM dans la dispersion fluorescente des N-NC. Premièrement, une réduction de l'intensité PL due aux NPM peut être liée à plus d'un facteur, comme indiqué dans les résultats des figures 77 et 79. Dans le cas particulier de la concentration de NPM à  $\Phi = 0, 1\%$  et 1,0 g/L de N-NC, la réduction des émissions dans la zone 500 – 575 nm est d'environ  $8 \times$  par

rapport à la dispersion N-NC pure. Puisque les NPM absorbent partiellement l'émission d'excitation, il a été calculé que le *quenching* dû aux interactions entre les particules est un facteur proche de 3,2. De plus, les mesures de durée de vie d'émission déterminent que le rapport entre les valeurs obtenues pour la dispersion des N-NC purs et le LFM est en réalité de 1,36. Par conséquent, la réduction observée du signal de fluorescence ( $8\times$ ) est principalement due à l'absorption des NPM de l'émission d'excitation (un facteur de 4,8), plus une extinction de collision (un facteur de 1,36) et une extinction statique (un facteur de 1,84) due aux interactions entre N-NC et NPM. L'intensité de l'émission peut également être finement ajustée en faisant varier la concentration de chaque NP, car l'ajout de N-NC augmente l'émission et une augmentation des NPM la réduit. Quoi qu'il en soit, l'atténuation mentionnée n'élimine pas la capacité d'accordabilité de l'émission N-NC, qui est largement conservée jusqu'à 500 nm comme le montre la Figure 80.

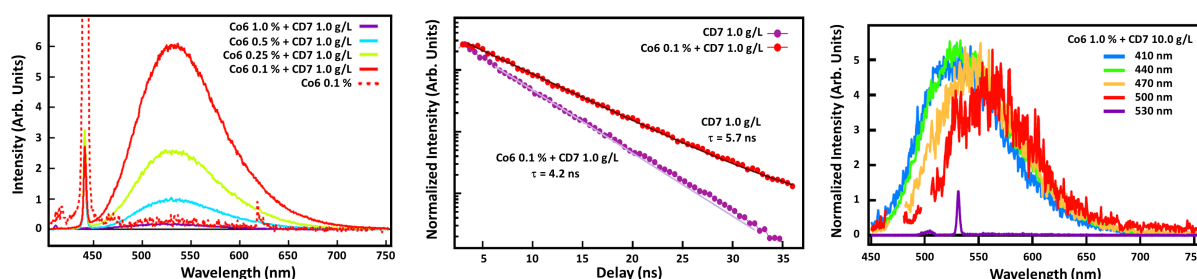


Figure 77a - Spectres d'émission de LMFs excités à 440 nm à une concentration de N-NC de 1,0 g/L et différentes fractions volumiques de NPM. Figure 79 - Cinétique de décroissance des N-NCs purs (rouge) et du LMF composé de 10 g/L N-NC avec 1 g/L de N-NCs et concentration de 0,1 vol% de NPMs. Les valeurs de durée de vie sont  $\tau = 5,7$  ns pour les N-NC purs et  $\tau = 4,2$  ns pour le LMF. Figure 80 - Spectres d'émission de LMF composés de 10 g/L N-NC et 1,0 vol% NPMs excités à différentes longueurs d'onde.

Ces résultats confirment la possibilité d'obtenir un fluide magnétique fluorescent stable et homogène combinant N-NC et NPM, où la plupart de ses propriétés individuelles sont conservées dans le produit final. Ce nanofluide a un grand potentiel dans des applications telles que les tests de qualité des pièces métalliques utilisées dans l'industrie.

## Conclusions Générales

Dans cette thèse, des ferrofluides à base de liquides ioniques, des dispersions aqueuses de nanodots de carbone et des fluides magnétiques fluorescents ont été étudiés. Les NPM et N-NC ont un grand potentiel dans les applications impliquant la conversion d'énergie, où il a été démontré que les ferrofluides augmentent l'efficacité des dispositifs thermoélectriques [16] tandis que les nanodots sont considérés comme un candidat prometteur pour les cellules solaires photovoltaïques "vertes" [256].

Concernant les ferrofluides à base de liquides ioniques à température ambiante (FFs-LITAs), nous nous sommes concentrés sur leur stabilité et leurs propriétés de thermodiffusion. L'étude du FF-LITA dans l'EAN a établi le degré d'influence des contre-ions

initiaux et de la teneur en eau déterminant les interactions interparticules - via la compressibilité  $\chi$  et le second coefficient viriel  $A_2$  - et les paramètres de thermiffusion  $S_T$  et  $D_m$  en fonction de la température et de la fraction volumique des nanoparticules magnétiques. De plus, l'étude de la diffusion thermique sous champ magnétique appliquée sur une large gamme de températures réalisée avec le FF-LITA basé sur EMIM-TFSI démontre que l'anisotropie de  $S_T$  et  $D_m$  peuvent en fait être générés dans de tels systèmes. De plus, l'effet est bien ajusté par le modèle théorique décrit dans les réfs. [25, 127]. Par conséquent, ce FF-LITA est un candidat prometteur pour tirer profit de l'amélioration générée par le champ magnétique externe dans le coefficient Seebeck dans les applications thermoélectriques.

L'étude des dispersions aqueuses de N-NC à différents pH a élargi les connaissances actuelles sur leur stabilité colloïdale, leur charge de surface et leur ordre local. Les résultats expérimentaux ont montré que la stabilité est améliorée lorsque le pH du liquide porteur passe de d'acide à alcalin. Les mesures du potentiel Zeta, les titrages potentiométriques et conductométriques ont établi une corrélation entre l'augmentation de la stabilité et l'augmentation de la charge de surface négative des N-NC, indiquant le rôle fondamental de la répulsion électrostatique interparticulaire. Cependant, dans des conditions hautement alcalines, une réaction d'hydrolyse irréversible se déroule, amplifiant davantage la charge de surface négative des N-NC, mais modifiant également de manière significative leurs propriétés optiques. Cet effet est critique pour l'échantillon de CD7 d'émission verte, car l'émission fluorescente est fortement décalée vers le bleu. Enfin, un examen à l'échelle nanométrique par SAXS confirme la présence d'agrégats qui se déposent lentement dans le temps dans des conditions acides. De manière surprenante, les résultats ont indiqué qu'une partie des agrégats peut encore rester bien dispersée dans le surnageant, et peut être partiellement éliminée par ultracentrifugation ou au moins réduite en taille en augmentant le pH.

Nous avons montré que l'association de ferrofluides aqueux et de N-NC pour produire un nanocolloïde hybride peut générer des suspensions instables ou des dispersions stables, en fonction du pH du milieu. En conditions acides, l'instabilité du mélange résulte du fait que les NPM et N-NC ont des charges opposées. Pour cette raison, les N-NC décoorent les NPM en augmentant leur taille et en limitant le potentiel électrostatique répulsif des interactions NPM-NPM. En conséquence, on observe que la sédimentation des particules et la séparation magnétique induisent le démixage des phases magnétique et fluorescente. D'autre part, en solution aqueuse à pH = 7,0 avec du citrate libre contrôlé, les N-NC et les NPM recouverts de citrate ont une charge de surface négative, ce qui entraîne des colloïdes stables au niveau microscopique même sous l'application d'un champ magnétique externe. Nous pouvons confirmer que les propriétés magnétiques du liquide magnétique fluorescent restent presque inchangées, cependant, la fluorescence est partiellement réduite.

## Bibliography

- 1 GUERRA, A. A. A. M. et al. Efficient uptake of phosphorus from water by core@shell bimagnetic nanoadsorbents. *Journal of Environmental Chemical Engineering*, Elsevier, v. 8, n. 4, p. 103888, 2020. Cited on page 10.
- 2 OLIVEIRA, L. C. A. et al. Activated carbon/iron oxide magnetic composites for the adsorption of contaminants in water. *Carbon*, v. 40, n. 12, p. 2177–2183, 2002. Cited 2 times on pages 10 and 136.
- 3 TRAN, N.; WEBSTER, T. J. Magnetic nanoparticles: biomedical applications and challenges. *Journal of Materials Chemistry*, The Royal Society of Chemistry, v. 20, n. 40, p. 8760, 10 2010. Cited on page 10.
- 4 LI, Q. et al. Photoluminescent Carbon Dots as Biocompatible Nanoprobes for Targeting Cancer Cells in vitro. *J. Phys. Chem. C*, v. 114, p. 12062–12068, 2009. Cited on page 10.
- 5 HUANG, X. et al. Effect of injection routes on the biodistribution, clearance, and tumor uptake of carbon dots. *ACS Nano*, v. 7, n. 7, p. 5684–5693, 2013. Cited on page 10.
- 6 DONG, X. et al. Carbon Dots' Antiviral Functions Against Noroviruses. *Scientific Reports*, Springer US, v. 7, n. 1, p. 1–10, 2017. Cited on page 10.
- 7 CHEN, O. et al. Magneto-fluorescent core-shell supernanoparticles. *Nature Communications*, Nature Publishing Group, v. 5, p. 5093, 2014. Cited 3 times on pages 10, 14, and 134.
- 8 NKURIKIYIMFURA, I.; WANG, Y.; PAN, Z. Heat transfer enhancement by magnetic nanofluids - A review. *Renewable and Sustainable Energy Reviews*, Elsevier, v. 21, p. 548–561, 2013. Cited on page 10.
- 9 SALINAS-CASTILLO, A. et al. Carbon dots for copper detection with down and upconversion fluorescent properties as excitation sources. *Chemical Communications*, v. 49, n. 11, p. 1103–1105, 2013. Cited on page 10.
- 10 PHILIP, J.; LASKAR, J. M. Optical Properties and Applications of Ferrofluids—A Review. *Journal of Nanofluids*, v. 1, n. 1, p. 3–20, 2012. Cited on page 10.
- 11 HAN, M. et al. Recent progress on the photocatalysis of carbon dots: Classification, mechanism and applications. *Nano Today*, Elsevier Ltd, v. 19, p. 201–218, 2018. Cited on page 10.
- 12 LI, X. et al. Carbon and Graphene Quantum Dots for Optoelectronic and Energy Devices: A Review. *Advanced Functional Materials*, v. 25, n. 31, p. 4929–4947, 2015. Cited on page 10.

- 13 BOR, D. M. van de; FERREIRA, C. A. I.; KISS, A. A. Low grade waste heat recovery using heat pumps and power cycles. *Energy*, Elsevier Ltd, v. 89, p. 864–873, 2015. Cited 3 times on pages [10](#), [163](#), and [183](#).
- 14 ANDREI, V.; BETHKE, K.; RADEMANN, K. Thermoelectricity in the context of renewable energy sources: Joining forces instead of competing. *Energy and Environmental Science*, v. 9, n. 5, p. 1528–1532, 2016. Cited on page [10](#).
- 15 ZHAO, L. D. et al. Ultrahigh power factor and thermoelectric performance in hole-doped single-crystal SnSe. *Science*, v. 351, n. 6269, p. 141–144, 2016. Cited 3 times on pages [10](#), [163](#), and [183](#).
- 16 SALEZ, T. J. et al. Can charged colloidal particles increase the thermoelectric energy conversion efficiency? *Physical Chemistry Chemical Physics*, Royal Society of Chemistry, v. 19, n. 14, p. 9409–9416, 2017. Cited 6 times on pages [10](#), [158](#), [163](#), [181](#), [183](#), and [201](#).
- 17 MAMUSA, M. *Colloidal interactions in ionic liquids*. Phd Thesis (PhD Thesis) — Université Pierre et Marie Curie - Sorbonne Universités, 2014. Cited 4 times on pages [11](#), [28](#), [163](#), and [183](#).
- 18 BHATTACHARYA, K. et al. Structural, Thermodiffusive and Thermoelectric Properties of Maghemite Nanoparticles Dispersed in Ethylammonium Nitrate. *ChemEngineering*, v. 4, n. 1, p. 5, 2020. Cited 17 times on pages [11](#), [21](#), [22](#), [23](#), [30](#), [31](#), [47](#), [55](#), [57](#), [59](#), [60](#), [66](#), [74](#), [75](#), [163](#), [165](#), and [186](#).
- 19 RIEDL, J. C. et al. Colloidal dispersions of oxide nanoparticles in ionic liquids: Elucidating the key parameters. *Nanoscale Advances*, v. 2, n. 4, p. 1560–1572, 2020. Cited 13 times on pages [11](#), [21](#), [23](#), [26](#), [28](#), [29](#), [30](#), [34](#), [35](#), [75](#), [163](#), [165](#), and [186](#).
- 20 RIEDL, J. C. *Dispersions of nanomagnets in ionic liquids for thermoelectric applications*. Phd Thesis (PhD Thesis) — Sorbonne Université, 2020. Cited 5 times on pages [11](#), [21](#), [28](#), [65](#), and [163](#).
- 21 DUBOIS, E. et al. Phase transitions in magnetic fluids. *Progress in Colloid & Polymer Science*, v. 104, n. 1, p. 173–176, 1997. Cited on page [11](#).
- 22 DUBOIS, E. et al. Structural analogy between aqueous and oily magnetic fluids. *The Journal of Chemical Physics*, v. 111, p. 7147, 1999. Cited 2 times on pages [11](#) and [40](#).
- 23 FRKA-PETESIC, B. *Agrégats de nanoparticules magnétiques auto-assemblées*. Phd Thesis (PhD Thesis) — Université Paris VI - UPMC, 2010. Cited on page [11](#).
- 24 SARKAR, M. et al. Inversion of thermodiffusive properties of ionic colloidal dispersions in water-DMSO mixtures probed by forced Rayleigh scattering. *Eur. Phys. J. E*, v. 42, p. 979–2989., 2019. Cited 4 times on pages [12](#), [50](#), [53](#), and [54](#).
- 25 KOUYATÉ, M. et al. Thermodiffusion of citrate-coated  $\gamma$ -Fe<sub>2</sub>O<sub>3</sub> nanoparticles in aqueous dispersions with tuned counter-ions-anisotropy of the Soret coefficient under a magnetic field. *Physical Chemistry Chemical Physics*, v. 21, n. 4, p. 1895–1903, 2019. Cited 15 times on pages [12](#), [46](#), [50](#), [55](#), [63](#), [64](#), [66](#), [67](#), [73](#), [78](#), [158](#), [173](#), [181](#), [192](#), and [202](#).
- 26 SALEZ, T. J. et al. Magnetically enhancing the Seebeck coefficient in ferrofluids. *Nanoscale Advances*, v. 1, n. 8, p. 2979–2989, 2019. Cited on page [12](#).

- 27 MIRTICHEV, P. et al. Solution phase synthesis of carbon quantum dots as sensitizers for nanocrystalline TiO<sub>2</sub> solar cells. *Journal of Materials Chemistry*, v. 22, n. 4, p. 1265–1269, 2012. Cited 4 times on pages 12, 13, 164, and 184.
- 28 ESSNER, J. B. et al. Pee-dots: biocompatible fluorescent carbon dots derived from the upcycling of urine. *Green Chemistry*, Royal Society of Chemistry, v. 18, n. 1, p. 243–250, 2016. Cited 3 times on pages 13, 164, and 184.
- 29 QU, S. et al. A biocompatible fluorescent ink based on water-soluble luminescent carbon nanodots. *Angewandte Chemie - International Edition*, v. 51, n. 49, p. 12215–12218, 2012. Cited 6 times on pages 13, 82, 94, 124, 164, and 184.
- 30 YUAN, Y. et al. Doxorubicin-loaded environmentally friendly carbon dots as a novel drug delivery system for nucleus targeted cancer therapy. *Colloids and Surfaces B: Biointerfaces*, Elsevier B.V., v. 159, p. 349–359, 2017. Cited 3 times on pages 13, 164, and 184.
- 31 SUN, Y.-P. et al. Quantum-Sized Carbon Dots for Bright and Colorful Photoluminescence. *Journal of the American Chemical Society*, v. 128, n. 24, p. 7756–7757, 2006. Cited 3 times on pages 13, 82, and 136.
- 32 NIE, H. et al. Carbon Dots with Continuously Tunable Full-Colour Emission and Their Application in Ratiometric pH Sensing. *Chemistry of Materials*, p. 3104–3112, 2014. Cited on page 13.
- 33 ZHANG, Q. et al. Improving the power conversion efficiency of carbon quantum dot-sensitized solar cells by growing the dots on a TiO<sub>2</sub> photoanode in situ. *Nanomaterials*, v. 7, n. 6, 2017. Cited on page 13.
- 34 SCIORTINO, A. et al. Solvatochromism Unravels the Emission Mechanism of Carbon Nanodots. *Journal of Physical Chemistry Letters*, v. 7, n. 17, p. 3419–3423, 2016. Cited 9 times on pages 13, 14, 81, 123, 125, 136, 153, 164, and 184.
- 35 LI, H. et al. Water-soluble fluorescent carbon quantum dots and photocatalyst design. *Angewandte Chemie - International Edition*, v. 49, n. 26, p. 4430–4434, 2010. Cited 4 times on pages 13, 89, 94, and 123.
- 36 LI, H. et al. One-step ultrasonic synthesis of water-soluble carbon nanoparticles with excellent photoluminescent properties. *Carbon*, Elsevier Ltd, v. 49, n. 2, p. 605–609, 2011. Cited 2 times on pages 13 and 94.
- 37 SCIORTINO, A.; CANNIZZO, A.; MESSINA, F. Carbon Nanodots: A Review—From the Current Understanding of the Fundamental Photophysics to the Full Control of the Optical Response. *C — Journal of Carbon Research*, v. 4, n. 4, p. 67, 2018. Cited 3 times on pages 14, 82, and 89.
- 38 SCIORTINO, L. et al. Tailoring the Emission Color of Carbon Dots through Nitrogen-Induced Changes of Their Crystalline Structure. *Journal of Physical Chemistry C*, American Chemical Society, v. 122, n. 34, p. 19897–19903, 2018. Cited 14 times on pages 14, 81, 83, 85, 86, 87, 89, 124, 125, 126, 127, 164, 184, and 194.
- 39 CORATO, R. D. et al. Multifunctional Nanobeads Based on Quantum Dots and Magnetic Cell Targeting and Sorting. *ACS Nano*, v. 5, n. 2, p. 1109–1121, 2011. Cited on page 14.

- 40 WU, Y. et al. A novel magneto-fluorescent nano-bioprobe for cancer cell targeting, imaging and collection. *Applied Biochemistry and Biotechnology*, v. 163, n. 7, p. 813–825, 2011. Cited 2 times on pages [14](#) and [134](#).
- 41 NAFIUJJAMAN, M. et al. Photosensitizer conjugated iron oxide nanoparticles for simultaneous in vitro magneto-fluorescent imaging guided photodynamic therapy. *Chem. Commun. Chem. Commun*, Royal Society of Chemistry, v. 51, n. 51, p. 5687–5690, 2015. Cited 2 times on pages [14](#) and [134](#).
- 42 XIA, H. et al. Synthesis and bio-applications of targeted magnetic-fluorescent composite nanoparticles. *Journal of Nanoparticle Research*, Journal of Nanoparticle Research, v. 19, n. 4, 2017. Cited on page [14](#).
- 43 RUAN, G. et al. Fluorescent–magnetic nanoparticles for imaging and cell manipulation. *Proceedings of the Institution of Mechanical Engineers, Part N: Journal of Nanoengineering and Nanosystems*, v. 223, p. 81–86, 2010. Cited 2 times on pages [14](#) and [134](#).
- 44 HE, X. et al. Photoluminescent Fe<sub>3</sub>O<sub>4</sub>/carbon nanocomposite with magnetic property. *Journal of Colloid and Interface Science*, Elsevier Inc., v. 356, n. 1, p. 107–110, 2011. Cited 2 times on pages [14](#) and [136](#).
- 45 FELD, A. et al. A Universal Approach to Ultrasmall Magneto-Fluorescent Nanohybrids. *Angewandte Chemie - International Edition*, v. 54, n. 42, p. 12468–12471, 2015. Cited on page [14](#).
- 46 BAAZIZ, W. et al. Microscopy investigations of the microstructural change and thermal response of cobalt-based nanoparticles confined inside a carbon nanotube medium. *J. Mater. Chem. A*, v. 3, n. 21, p. 11203–11214, 2015. Cited on page [14](#).
- 47 PAPELL, S. S. *Low Viscosity Magnetic Fluid Obtained By the Colloidal Suspension of Magnetic Particles*. [S.l.]: US Patent Office, 1965. 9–12 p. Cited on page [18](#).
- 48 ROSENSWEIG, R. E. *Ferrohydrodynamics*. [S.l.]: Cambridge University Press, 1985. Cited on page [19](#).
- 49 MASSART, R. Préparation de ferrofluides aqueux en l’absence de surfactant; comportement en fonction du pH et de la nature des ions présents en solution. *C. R. Acad. Sci. Paris*, v. 291, n. C1, p. 1–3, 1980. Cited 3 times on pages [19](#), [165](#), and [185](#).
- 50 MASSART, R. Preparation of aqueous magnetic liquids in alkaline and acidic media. *IEEE Transactions on Magnetics*, v. 17, n. 2, p. 1247–1248, 1981. Cited 3 times on pages [19](#), [165](#), and [185](#).
- 51 GOMES, J. D. a. et al. Synthesis of core-shell ferrite nanoparticles for ferrofluids: Chemical and magnetic analysis. *Journal of Physical Chemistry C*, v. 112, n. 16, p. 6220–6227, 2008. Cited 3 times on pages [21](#), [138](#), and [141](#).
- 52 BACRI, J.-C. et al. Magnetic colloidal properties of ionic ferrofluids. *Journal of Magnetism and Magnetic Materials*, v. 62, n. 1, p. 36–46, 1986. Cited 4 times on pages [21](#), [24](#), [166](#), and [186](#).
- 53 TOURINHO, F. A.; FRANK, R.; MASSART, R. Aqueous ferrofluids based on manganese and cobalt ferrites. v. 25, p. 3249–3254, 1990. Cited on page [21](#).

- 54 AQUINO, R. et al. Size control of MnFe<sub>2</sub>O<sub>4</sub> nanoparticles in electric double layered magnetic fluid synthesis. *Journal of Magnetism and Magnetic Materials*, v. 252, p. 23–25, 2002. Cited on page 21.
- 55 MASSART, R.; CABUIL, V. Effect of some parameters on the formation of colloidal magnetite in alkaline-medium-yield and particle-size control. *J. Chim. Phys.*, n. 84, p. 967, 1987. Cited on page 21.
- 56 MASSART, R. et al. Preparation and properties of monodisperse magnetic fluids. *Journal of Magnetism and Magnetic Materials*, v. 149, p. 1–5, 1995. Cited 2 times on pages 21 and 141.
- 57 LEFEBURE, S. et al. Monodisperse magnetic nanoparticles: Preparation and dispersion in water and oils. *Journal of Materials Research*, v. 13, p. 2975–2981, 1998. Cited 2 times on pages 21 and 141.
- 58 MAMUSA, M. et al. Microstructure of colloidal dispersions in the ionic liquid ethylammonium nitrate: Influence of the nature of the nanoparticles' counterion. *Journal of Physics Condensed Matter*, v. 26, n. 28, 2014. Cited 10 times on pages 21, 22, 24, 28, 36, 37, 38, 65, 167, and 187.
- 59 MAMUSA, M. et al. Concentrated assemblies of magnetic nanoparticles in ionic liquids. *Faraday Discuss.*, v. 181, p. 193–209, 2015. Cited 3 times on pages 22, 38, and 65.
- 60 RIEDL, J. C.; et al. To be published. *To be defined*. Cited 2 times on pages 21 and 28.
- 61 BERKOVSKY, B. (Ed.). *Magnetic Fluids and Applications Handbook*. New York: Begell House Inc. Publ., 1996. Cited 2 times on pages 23 and 65.
- 62 JOLIVET, J. P.; TRONC, E. Interfacial electron transfer in colloidal spinel iron oxide. Conversion of Fe<sub>3</sub>O<sub>4</sub>- $\gamma$ -Fe<sub>2</sub>O<sub>3</sub> in aqueous medium. *Journal of Colloid And Interface Science*, v. 125, n. 2, p. 688–701, 1988. Cited on page 23.
- 63 TESTA-ANTA, M. et al. Raman spectroscopy to unravel the magnetic properties of iron oxide nanocrystals for bio-related applications. *Nanoscale Advances*, v. 1, n. 6, p. 2086–2103, 2019. Cited on page 24.
- 64 MOMMA, K.; IZUMI, F. VESTA3 for three-dimensional visualization of crystal, volumetric and morphology data. *Journal of Applied Crystallography*, v. 44, n. 6, p. 1272–1276, 2011. Cited 6 times on pages 24, 90, 166, 174, 186, and 194.
- 65 ISRAELACHVILI, J. N. *Intermolecular and Surface Forces*. 3. ed. Santa Barbara: Academic Press, 2011. Cited 3 times on pages 25, 28, and 101.
- 66 CAMPOS, A. F. C. et al. Nanoparticles superficial density of charge in electric double-layered magnetic fluid: A conductimetric and potentiometric approach. *The European Physical Journal E*, v. 35, n. 2001, p. 29–35, 2001. Cited 2 times on pages 25 and 105.
- 67 ITRI, R. et al. Nanoparticle chain-like formation in electrical double-layered magnetic fluids evidenced by small-angle X-ray scattering. *The European Physical Journal E*, v. 4, n. 2, p. 201–208, 2001. Cited on page 25.

- 68 TOURINHO, F. A. et al. Surface charge density determination in electric double layers magnetic fluids. *Brazilian Journal of Physics*, v. 32, n. 2B, p. 501–508, 2002. Cited on page 25.
- 69 STUMM, W.; MORGAN, J. *Aquatic Chemistry: An Introduction Emphasizing Chemical Equilibria In Natural Waters*. New York: J. Wiley & Sons, 1981. Cited on page 25.
- 70 HIEMSTRA, T.; RIEMSDIJK, W. V.; BOLT, G. Multisite proton adsorption modeling at the solid/solution interface of (hydr)oxides: A new approach: I. Model description and evaluation of intrinsic reaction constants. *J. Colloid. Interface Sci*, n. 133, p. 91, 1989. Cited on page 25.
- 71 HASMONAY, E. et al. pH effect on an ionic ferrofluid: Evidence of a thixotropic magnetic phase. *Journal of Physical Chemistry B*, v. 103, p. 6421–6428, 1999. Cited on page 25.
- 72 CAMPOS, A. F. C. et al. X-DLVO Interactions between nanocolloidal magnetic particles: the quantitative interpretation of the pH-dependent phase diagram of EDL-MF. *Brazilian Journal of Physics*, v. 39, n. 1a, p. 230–235, 2009. Cited 2 times on pages 25 and 28.
- 73 CAMPOS, A. F. C. et al. Influence of the spatial confinement at nanoscale on the structural surface charging in magnetic nanocolloids. *European Physical Journal E*, v. 36, n. 4, 2013. Cited 2 times on pages 25 and 105.
- 74 GOODWIN, J. W. *Colloids and Interfaces with Surfactants and Polymers - An Introduction*. 1. ed. Portland: John Wiley & Sons, 2004. Cited on page 27.
- 75 SHLIOMIS, M. I. Magnetic Fluids. *Sov. Phys. Usp*, v. 17, p. 153, 1974. Cited on page 27.
- 76 DERJAGUIN, B.; LANDAU, L. Theory of the stability of strongly charged lyophobic sols and of the adhesion of strongly charged particles in solution of electrolytes. *Acta Physicochim*, v. 14, p. 633–662, 1941. Cited 2 times on pages 27 and 99.
- 77 VERWEY, E. J. W.; OVERBEEK, J. T. G. *Theory of the stability of lyophobic colloids - The Interaction of Sol Particles Having an Electrical Double Layer*. 1948. Cited 2 times on pages 27 and 99.
- 78 GOUY, G. Sur la constitution de la charge électrique à la surface d'un électrolyte. *J. Phys. Radium*, v. 9, p. 457, 1910. Cited on page 28.
- 79 CHAPMAN, D. L. LI. A contribution to the theory of electrocapillarity. *Phil. Mag.*, v. 25, n. 148, p. 475–481, 1913. Cited on page 28.
- 80 HERMANSSON, M. The DLVO theory in microbial adhesion. *Colloids and Surfaces B: Biointerfaces*, v. 14, n. 1-4, p. 105–119, 1999. Cited on page 28.
- 81 MAMUSA, M. et al. Tuning the colloidal stability in ionic liquids by controlling the nanoparticles/liquid interface. *Soft Matter*, v. 10, n. 8, p. 1097–1101, 2014. Cited 3 times on pages 28, 34, and 65.

- 82 FILOMENO, C. L. et al. Tuning the Solid/Liquid Interface in Ionic Colloidal Dispersions: Influence on Their Structure and Thermodiffusive Properties. *Journal of Physical Chemistry C*, v. 121, n. 10, p. 5539–5550, 2017. Cited 4 times on pages 29, 32, 33, and 46.
- 83 SOLVIONIC. *Family - Ionic Liquids*. 2020. Available at: <<http://en.solvionic.com/products/>>. Cited on page 29.
- 84 PADUSZYNSKI, K.; DOMANSKA, U. Viscosity of Ionic Liquids: An Extensive Database and a New Group Contribution Model Based on a Feed-Forward Artificial Neural Network. *J. Chem. Inf. Model.*, v. 54, p. 1311–1324, 2014. Cited 3 times on pages 29, 65, and 66.
- 85 CAO, Y.; MU, T. Comprehensive investigation on the thermal stability of 66 ionic liquids by thermogravimetric analysis. *Industrial and Engineering Chemistry Research*, v. 53, n. 20, p. 8651–8664, 2014. Cited on page 29.
- 86 WASSERSCHIED, P.; WELTON, T. (Ed.). *Ionic Liquids in Synthesis*. Weinheim, FRG: Wiley-VCH Verlag GmbH & Co. KGaA, 2002. Cited on page 29.
- 87 LAUX, E. et al. Novel Ionic Liquids for Thermoelectric Generator Devices. *Mater. Today Proc.*, v. 8, p. 672–679, 2019. Cited on page 29.
- 88 MOROZOV, K. I.; LEBEDEV, A. V. The effect of magneto-dipole interactions on the magnetization curves of ferrocolloids. *J. Magn. Magn. Mat.*, v. 85, p. 51, 1990. Cited 2 times on pages 30 and 49.
- 89 BENLHIMA, N.; LEMORDANT, D.; LETELLIER, P. Acidity scales in water-ethylammonium nitrate mixtures, at 298 K solubility of organic compounds. *Journal de Chimie Physique et de Physico-Chimie Biologique*, v. 86, p. 1919–1939, 1989. Cited on page 30.
- 90 KANZAKI, R. et al. Acid-Base Property of Ethylammonium Nitrate Ionic Liquid Directly Obtained Using Ion-selective Field Effect Transistor Electrode. *Chemistry Letters*, The Chemical Society of Japan, v. 36, n. 5, p. 684–685, 2007. Cited on page 30.
- 91 FUMINO, K.; WULF, A.; LUDWIG, R. Hydrogen Bonding in Protic Ionic Liquids: Reminiscent of Water. *Angewandte Chemie International Edition*, v. 48, n. 17, p. 3184–3186, 2009. Cited on page 30.
- 92 HAYES, R. et al. Amphiphilicity determines nanostructure in protic ionic liquids. *Phys. Chem. Chem. Phys.*, v. 13, p. 3237–3247, 2011. Cited 2 times on pages 30 and 39.
- 93 HAYES, R.; WARR, G. G.; ATKINA, R. At the interface: solvation and designing ionic liquids. *Phys. Chem. Chem. Phys.*, v. 12, p. 1709–1723, 2010. Cited 2 times on pages 31 and 34.
- 94 COUSIN, F. et al. Overview of the phase diagram of ionic magnetic colloidal dispersions. *Brazilian Journal of Physics*, v. 31, n. 3, p. 350–355, 2001. Cited on page 31.
- 95 COUSIN, F.; DUBOIS, E.; CABUIL, V. Tuning the interactions of a magnetic colloidal suspension. *Physical review E*, v. 68, p. 021405, 2003. Cited on page 32.

- 96 CARNAHAN, N. F.; STARLING, K. E. Thermodynamic Properties of a Rigid-Sphere Fluid. *The Journal of Chemical Physics*, v. 53, n. 2, p. 600–603, 7 1970. Cited 4 times on pages 33, 34, 167, and 187.
- 97 FILOMENO, C. L. et al. Ionic magnetic fluids in polar solvents with tuned counter-ions. *J. Magn. Magn. Mat.*, v. 431, p. 2–7, 2017. Cited on page 33.
- 98 GOMES, R. C. et al. Thermodiffusion of repulsive charged nanoparticles—the interplay between single-particle and thermoelectric contributions. *Physical Chemistry Chemical Physics*, v. 20, n. 24, p. 16402–16413, 2018. Cited 10 times on pages 33, 34, 40, 46, 53, 55, 64, 66, 167, and 187.
- 99 HORN, R. G.; EVANS, D. F.; NINHAM, B. W. Double-layer and solvation forces measured in a molten salt and its mixtures with water. *Journal of Physical Chemistry*, v. 92, p. 3531–3537, 1988. Cited on page 34.
- 100 CHENG, H.-W. et al. Characterizing the Influence of Water on Charging and Layering at Electrified Ionic-Liquid/Solid Interfaces. *Adv. Mater. Interfaces*, p. 1500159, 2015. Cited on page 34.
- 101 MEZGER, M. et al. Molecular Layering of Fluorinated Ionic Liquids at a Charged Sapphire (0001) Surface. *Science*, v. 322, p. 424–428, 2008. Cited on page 34.
- 102 VATAMANU, J.; BORODIN, O.; SMITH, G. D. Molecular Insights into the Potential and Temperature Dependences of the Differential Capacitance of a Room-Temperature Ionic Liquid at Graphite Electrodes. *J. Am. Chem. Soc.*, v. 132, p. 14825–14833, 2010. Cited on page 34.
- 103 MERLET, C. et al. Computer simulations of ionic liquids at electrochemical interfaces. *Phys. Chem. Chem. Phys.*, v. 15, p. 15781, 2013. Cited on page 34.
- 104 IVANIŠTŠEV, V.; O'CONNOR, S.; FEDOROV, M. Poly(a)morphic portrait of the electrical double layer in ionic liquids. *Interface Mag.*, v. 23, p. 65–69, 2014. Cited on page 34.
- 105 COLES, S. W. et al. Interfacial structure and structural forces in mixtures of ionic liquid with a polar solvent. *Faraday Discuss.*, v. 206, p. 427–442, 2018. Cited on page 34.
- 106 FENG, G. et al. The importance of ion size and electrode curvature on electrical double layers in ionic liquids. *Phys. Chem. Chem. Phys.*, v. 13, p. 1152–1161, 2011. Cited on page 34.
- 107 ZHANG, H. et al. Stable colloids in molten inorganic salts. *Nature*, v. 542, p. 328–331, 2017. Cited on page 34.
- 108 KAMYSBAYEV, V. et al. Nanocrystals in Molten Salts and Ionic Liquids: Experimental Observation of Ionic Correlations Extending beyond the Debye Length. *ACS Nano*, v. 13, n. 5, p. 5760–5770, 2019. Cited on page 34.
- 109 LARGEOT, C. et al. Relation between ion size and pore size for electric double layer capacitor. *J. Am. Chem. Soc.*, v. 130, p. 2730–2731, 2008. Cited on page 34.
- 110 BACRI, J.-C. et al. Ionic ferrofluids: a crossing of chemistry and physics. *J. Magn. Magn. Mat.*, v. 85, p. 27–32, 1990. Cited on page 35.

- 111 MÄHLER, J.; PERSSON, I. A Study of the Hydration of the Alkali Metal Ions in Aqueous Solution. *Inorganic Chemistry*, v. 51, p. 425–438, 2012. Cited on page 38.
- 112 HAYES, R. et al. Solvation of Inorganic Nitrate Salts in Protic Ionic Liquids. *The Journal of Physical Chemistry C*, v. 118, p. 21215–21225, 2014. Cited on page 39.
- 113 MÉNDEZ-MORALES, T. et al. Solvation of Lithium Salts in Protic Ionic Liquids: A Molecular Dynamics Study. *The Journal of Physical Chemistry B*, v. 118, p. 761–770, 2014. Cited on page 39.
- 114 D'ANGELO, P. et al. Structural characterization of zinc(II) chloride in aqueous solution and in the protic ionic liquid ethylammonium nitrate by X-ray absorption spectroscopy. *The Journal of Chemical Physics*, v. 135, p. 154509, 2011. Cited on page 39.
- 115 SERVA, A. et al. How Does Ce III Nitrate Dissolve in a Protic Ionic Liquid? A Combined Molecular Dynamics and EXAFS Study. *Chemistry - A European Journal*, v. 23, p. 8424–8433, 2017. Cited on page 39.
- 116 HAYES, R.; WARR, G.; ATKIN, R. At the interface: solvation and designing ionic liquids. *Phys. Chem. Chem. Phys.*, v. 12, p. 1709–1723, 2010. Cited on page 39.
- 117 PIAZZA, R.; GUARINO, A. Soret Effect in Interacting Micellar Solutions. *Physical Review Letters*, v. 88, n. 20, p. 4, 2002. Cited on page 45.
- 118 PIAZZA, R.; PAROLA, A. Thermophoresis in colloidal suspensions. *J. Phys.: Condens. Matter*, v. 20, n. 153102, 2008. Cited 2 times on pages 45 and 46.
- 119 BURELBACH, J. et al. A unified description of colloidal thermophoresis. *European Physical Journal E*, v. 41, n. 1, 2018. Cited on page 46.
- 120 MAJEE, A.; WÜRGER, A. Collective thermoelectrophoresis of charged colloids. *Physical Review E - Statistical, Nonlinear, and Soft Matter Physics*, v. 83, n. 6, p. 1–7, 2011. Cited on page 46.
- 121 WÜRGER, A. Transport in Charged Colloids Driven by Thermoelectricity. *Physical Review Letters*, American Physical Society, v. 101, n. 10, p. 108302, 9 2008. Cited on page 46.
- 122 AGAR, J. N.; MOU, C. Y.; LIN, J. L. Single-ion heat of transport in electrolyte solutions. A hydrodynamic theory. *Journal of Physical Chemistry*, v. 93, n. 5, p. 2079–2082, 1989. Cited on page 46.
- 123 PUTNAM, S. A.; CAHILL, D. G. Transport of Nanoscale Latex Spheres in a Temperature Gradient. *Langmuir*, v. 21, n. 12, p. 5317–5323, 2005. Cited on page 46.
- 124 HUANG, B. T. et al. Thermoelectricity and thermodiffusion in charged colloids. *The Journal of chemical physics*, v. 143, n. 5, p. 054902, 2015. Cited on page 46.
- 125 PHILLIES, G. D. Effects of intermacromolecular interactions on diffusion. I. Two-component solutions. *The Journal of Chemical Physics*, v. 60, n. 3, p. 976–982, 1974. Cited on page 47.

- 126 BATCHELOR, G. K. Sedimentation in a dilute polydisperse system of interacting spheres. Part 1. General Theory. *Journal of Fluid Mechanics*, v. 119, p. 379–408, 11 1982. Cited 2 times on pages 48 and 57.
- 127 SALEZ, T. J. et al. Thermoelectricity and Thermodiffusion in Magnetic Nanofluids: Entropic Analysis. *Entropy*, v. 20, p. 405, 2018. Cited 10 times on pages 48, 49, 50, 73, 78, 158, 173, 181, 192, and 202.
- 128 BACRI, J.-C. et al. Forces Rayleigh experiment in a Magnetic Fluid. *Phys. Rev. Lett.*, v. 74, p. 5032–5035, 1995. Cited 6 times on pages 48, 49, 67, 78, 173, and 193.
- 129 BACRI, J. C. et al. Transient grating in a ferrofluid under magnetic field: Effect of magnetic interactions on the diffusion coefficient of translation. *Phys. Rev. E*, v. 52, p. 3936–3942, 1995. Cited 6 times on pages 48, 49, 67, 78, 173, and 193.
- 130 MÉRIGUET, G. et al. Understanding the structure and the dynamics of magnetic fluids: coupling of experiment and simulation. *J. Phys. Cond. Matter*, v. 18, p. S2685–S2696, 2006. Cited 3 times on pages 48, 49, and 67.
- 131 MÉRIGUET, G. et al. What tunes the structural anisotropy of magnetic fluids under a magnetic field? *J. Phys. Chem. B*, v. 110, p. 4378–4386, 2006. Cited 5 times on pages 49, 67, 78, 173, and 193.
- 132 GAZEAU, F. et al. Static and quasi-elastic small angle neutron scattering on biocompatible ionic ferrofluids: magnetic and hydrodynamic interactions. *J. Phys. Cond. Matt*, v. 15, p. S1305–S1334, 2003. Cited 2 times on pages 49 and 67.
- 133 MÉRIGUET, G. et al. Magnetic fluids with tunable interparticle interaction : monitoring the under-field local structure. *Magnetohydrodynamic*, v. 48, n. 2, p. 415–426, 2012. Cited 2 times on pages 49 and 67.
- 134 IVANOV, A. O.; KUZNETSOVA, O. B. Magnetic properties of dense ferrofluids: An influence of interparticle correlations. *Phys. Rev. E*, v. 64, p. 041405., 2001. Cited on page 49.
- 135 LANDAU, L.; LIFSHITZ, E. *Electrodynamics of Continuous Media*. New York,: Pergamon Press, 1960. Cited on page 49.
- 136 WANDERSMAN, E. et al. Relaxation of the field-induced structural anisotropy in a rotating magnetic fluid. *Europhysics Lett.*, v. 86, p. 1–5, 2009. Cited on page 49.
- 137 BLUMS, E.; CEBERS, A.; MAIOROV, M. *Magnetic Liquids*. New York: W. de G. Gruyter, 1997. Cited on page 49.
- 138 NAGASAKA, Y. et al. Measurement of the thermal-diffusivity of liquids by the forced Rayleigh-scattering. *Rev. Sci. Instrum.*, v. 59, p. 1156–1168, 1988. Cited on page 50.
- 139 MEZULIS, A.; MAIOROV, M.; BLUMS, E. Transport properties of an ionic magnetic colloid: experimental study of increasing the ionic strength. *J. Magn. Magn. Mat.*, v. 252, p. 221–223, 2002. Cited on page 50.

- 140 ALVES, S. et al. Investigation of the sign of the Soret coefficient in different ionic and surfacted magnetic colloids using forced Rayleigh scattering and single-beam Z-scan techniques. *Philosophical Magazine*, v. 83, p. 2059–2066, 2003. Cited 2 times on pages 50 and 66.
- 141 DEMOUCHEY, G. et al. Diffusion and thermodiffusion studies in ferrofluids with a new two-dimensional forced Rayleigh-scattering technique. *Journal of Physics D: Applied Physics*, v. 37, n. 10, p. 1417–1428, 5 2004. Cited 2 times on pages 50 and 53.
- 142 NING, H.; WIEGAND, S. Experimental investigation of the Soret effect in acetone/water and dimethylsulfoxide/ water mixtures. *J. Chem. Phys.*, v. 125, p. 1–4, 2006. Cited on page 50.
- 143 NING, H.; DHONT, J. K. G.; WIEGAND, S. Thermal-Diffusive Behavior of a Dilute Solution of Charged Colloids. *Langmuir*, v. 24, p. 2426–2432, 2008. Cited on page 50.
- 144 LUDWIG, C. F. W. Diffusion zwischen ungleich erwärmten Orten gleich zusammengesetzter Lösungen. *Sitzungsberichte der Akad. der Wissenschaften Math. Klasse*, v. 20, p. 539, 1856. Cited on page 52.
- 145 SORET, C. Sur l'état d'équilibre que prend, au point de vue de sa concentration, une dissolution saline primitivement homogène, dont deux parties sont portées à des températures différentes. *Arch. Sci. Phys. Nat. Genève*, v. 3, p. 48, 1879. Cited on page 52.
- 146 BRUGGEMAN, D. A. G. Berechnung verschiedener physikalischer Konstanten von heterogenen Substanzen. I. Dielektrizitätskonstanten und Leitfähigkeiten der Mischkörper aus isotropen Substanzen. *Ann. Phys.*, v. 416, n. 7, p. 636–664, 1935. Cited on page 53.
- 147 SEKI, S. et al. Comprehensive Refractive Index Property for Room-Temperature Ionic Liquids. *J. Chem. Eng. Data*, v. 57, p. 221–2216, 2012. Cited on page 53.
- 148 CAPELO, S. B. et al. Effect of temperature and cationic chain length on the physical properties of ammonium nitrate-based protic ionic liquids. *Journal of Physical Chemistry B*, v. 116, n. 36, p. 11302–11312, 2012. Cited on page 53.
- 149 ABBATE, G. et al. Temperature Dependence of the Refractive Index of Water. *The Journal of Chemical Physics*, v. 11, p. 1167–1172, 8 1978. Cited on page 53.
- 150 LUO, W.; DU, T.; HUANG, J. Novel Convective Instabilities in a Magnetic Fluid. *Phys. Rev. Lett.*, v. 82, p. 4134–4137, 1999. Cited on page 54.
- 151 ZABLITSKY, D. *Microconvective effects in non-isothermal and inhomogeneous dispersions of magnetic nanoparticles*. Phd Thesis (PhD Thesis) — Faculty of Physics and Mathematics - Univ. of Latvia, Riga - Latvia, 2012. Cited on page 54.
- 152 ZABLITSKY, D.; MEZULIS, A.; BLUMS, E. Formation of magnetoconvection by photoabsorptive methods in ferrofluid layers. *C. R. Mec.*, v. 341, p. 449–454, 2013. Cited on page 54.
- 153 SMITH, J. A. et al. Rheology of Protic Ionic Liquids and Their Mixtures. *The Journal of Physical Chemistry B*, American Chemical Society, v. 117, n. 44, p. 13930–13935, 11 2013. Cited 6 times on pages 57, 58, 61, 77, 170, and 190.

- 154 SEGURA, J. J. et al. Adsorbed and near surface structure of ionic liquids at a solid interface. *Physical Chemistry Chemical Physics*, v. 15, n. 9, p. 3320, 2013. Cited on page 59.
- 155 ZARROUGUI, R.; DHAHBI, M.; LEMORDANT, D. Transport and Thermodynamic Properties of Ethylammonium Nitrate–Water Binary Mixtures: Effect of Temperature and Composition. *Journal of Solution Chemistry*, v. 44, n. 3, p. 686–702, 2015. Cited on page 61.
- 156 NIETHER, D. et al. Peptide model systems: Correlation between thermophilicity and hydrophilicity. *Journal of Chemical Physics*, v. 149, n. 4, 2018. Cited on page 62.
- 157 BLUMS, E. et al. Soret coefficient of nanoparticles in ferrofluids in the presence of a magnetic field. *Phys. Fluids*, v. 10, p. 2155–2163, 1998. Cited on page 67.
- 158 BLUMS, E. New transport properties of ferrocolloids: magnetic Soret effect and thermomagnetoosmosis. *J. Magn. Magn. Mat.*, v. 289, p. 246–249, 2005. Cited on page 67.
- 159 SPRENGER, L.; LANGE, A.; ODENBACH, S. Thermodiffusion in concentrated ferrofluids: Experimental and numerical results on magnetic thermodiffusion. *Phys. Fluids*, v. 26, p. 22001, 2014. Cited on page 67.
- 160 CREER, K.; HEDLEY, I.; O'REILLY, W. *Magnetic oxides*. London: J. Wiley, 1975. 649–688 p. Cited on page 69.
- 161 MURAD, E. *Properties and behaviour of iron oxides as determined by Mössbauer spectroscopy in "The Geobiochemical Cycle of Iron in Iron in Soils and Clay Minerals "*. Dordrecht, Holland: D. Reidel Publishing Company, 1988. 309–350 p. (NATO ASI Series). Cited on page 69.
- 162 TRONC, E. et al. Surface effects in noninteracting and interacting  $\gamma$ -Fe<sub>2</sub>O<sub>3</sub> nanoparticles. *J. Magn. Magn. Mat.*, v. 262, p. 6, 2003. Cited on page 69.
- 163 CULLITY, B. D.; GRAHAM, C. D. *Introduction to Magnetic Materials*. 2. ed. Hoboken, New Jersey, USA: John Wiley and sons, Inc. - IEEE Press, 2009. Cited on page 69.
- 164 KODAMA, R. H. Magnetic nanoparticles. *J. Magn. Magn. Mat.*, v. 200, p. 272–359, 1999. Cited on page 69.
- 165 BATTLE, X.; LABARTA, A. Finite-size effects in fine particles: magnetic and transport properties. *J. Phys. D: Appl. Phys.*, v. 35, p. R15–R42, 2002. Cited on page 69.
- 166 AQUINO, R. et al. Magnetization temperature dependence and freezing of surface spins in magnetic fluids based on ferrite nanoparticles. *Phys. Rev. B*, v. 72, p. 1–10, 2005. Cited on page 69.
- 167 SILVA, F. G. da et al. Structural and magnetic properties of spinel nanoparticles. *J. of Nanosci. Nanotechnol.*, v. 19, p. 4888–4902, 2019. Cited on page 69.
- 168 SALEZ, T. J. et al. Magnetically enhancing the Seebeck coefficient in ferrofluids. *Nanoscale Adv.*, v. 1, p. 2979–2989, 2019. Cited on page 73.

- 169 SILVA, J. C. Esteves da; GONÇALVES, H. M. Analytical and bioanalytical applications of carbon dots. *Trends in Analytical Chemistry*, v. 30, n. 8, p. 1327–1336, 2011. Cited on page [81](#).
- 170 MESSINA, F. et al. Fluorescent nitrogen-rich carbon nanodots with an unexpected  $\beta$ -C<sub>3</sub>N<sub>4</sub> nanocrystalline structure. *J. Mater. Chem. C*, Royal Society of Chemistry, v. 4, n. 13, p. 2598–2605, 2016. Cited 9 times on pages [81](#), [84](#), [86](#), [88](#), [90](#), [91](#), [103](#), [109](#), and [153](#).
- 171 MESSINA, F. et al. Photoluminescence of Carbon Dots Embedded in a SiO<sub>2</sub> Matrix. *Materials Today: Proceedings*, Elsevier Ltd., v. 3, n. March, p. S258–S265, 2016. Cited 4 times on pages [81](#), [82](#), [84](#), and [94](#).
- 172 SCIORTINO, A. et al.  $\beta$ -C<sub>3</sub>N<sub>4</sub> Nanocrystals: Carbon Dots with Extraordinary Morphological, Structural, and Optical Homogeneity. *Chemistry of Materials*, v. 30, n. 5, p. 1695–1700, 2018. Cited 4 times on pages [81](#), [82](#), [84](#), and [103](#).
- 173 SHARMA, A. et al. Origin of Excitation Dependent Fluorescence in Carbon Nanodots. *Journal of Physical Chemistry Letters*, v. 7, n. 18, p. 3695–3702, 2016. Cited on page [82](#).
- 174 ZHAI, D. et al. The role of "disaggregation" in optical probe development. *Chemical Society Reviews*, v. 43, n. 8, p. 2402–2411, 2014. Cited on page [82](#).
- 175 LIU, Z. X. et al. Carbon dots with aggregation induced emission enhancement for visual permittivity detection. *Chemical Communications*, v. 52, n. 10, p. 2063–2066, 2016. Cited on page [82](#).
- 176 DENG, L. et al. Development of hydrophilicity gradient ultracentrifugation method for photoluminescence investigation of separated non-sedimental carbon dots. *Nano Research*, v. 8, n. 9, p. 2810–2821, 2015. Cited 2 times on pages [82](#) and [103](#).
- 177 XU, X. et al. Electrophoretic Analysis and Purification of Fluorescent Single-Walled Carbon Nanotube Fragments. *Journal of the American Chemical Society*, v. 126, n. 40, p. 12736–12737, 2004. Cited on page [82](#).
- 178 YU, S.-J. et al. Bright Fluorescent Nanodiamonds: No Photobleaching and Low Cytotoxicity. *J. Am. Chem. Soc.*, v. 127, n. 50, p. 17604–17605, 2005. Cited on page [82](#).
- 179 LIU, H.; YE, T.; MAO, C. Fluorescent carbon nanoparticles derived from candle soot. *Angewandte Chemie - International Edition*, v. 46, n. 34, p. 6473–6475, 2007. Cited 2 times on pages [82](#) and [123](#).
- 180 ZHAO, Q.-L. et al. Facile preparation of low cytotoxicity fluorescent carbon nanocrystals by electrooxidation of graphite. *Chemical Communications*, v. 281, n. 41, p. 5116, 2008. Cited on page [82](#).
- 181 BOURLINOS, A. et al. Photoluminescent Carbogenic Dots. *Chem. Mater*, v. 20, n. 14, p. 4539–4541, 2008. Cited on page [82](#).
- 182 ZHAI, X. et al. Highly luminescent carbon nanodots by microwave-assisted pyrolysis. *Chemical Communications*, v. 48, n. 64, p. 7955–7957, 2012. Cited on page [82](#).

- 183 SCIORTINO, A. et al. The interaction of photoexcited Carbon nanodots with metal ions disclosed down to the femtosecond scale. *Nanoscale*, v. 1223, 2017. Cited 3 times on pages 82, 86, and 151.
- 184 CULLITY, B. D.; STOCK, S. R. *Elements of X-Ray Diffraction*. Upper Saddle River: Prentice Hall, 2001. 664 p. Cited on page 86.
- 185 HOLA, K. et al. Carbon dots - Emerging light emitters for bioimaging, cancer therapy and optoelectronics. *Nano Today*, Elsevier Ltd, v. 9, n. 5, p. 590–603, 2014. Cited on page 89.
- 186 ZHU, S. et al. The photoluminescence mechanism in carbon dots (graphene quantum dots, carbon nanodots, and polymer dots): current state and future perspective. *Nano Research*, v. 8, n. 2, p. 355–381, 2015. Cited 2 times on pages 89 and 123.
- 187 MARQUÉS, M. et al. Pressure effects on the structure and vibrations of  $\beta$ - and  $\gamma$ -C<sub>3</sub>N<sub>4</sub>. *Physical Review B - Condensed Matter and Materials Physics*, v. 70, n. 10, p. 1–11, 2004. Cited on page 89.
- 188 ONG, W.-J. et al. Surface charge modification via protonation of graphitic carbon nitride (g-C<sub>3</sub>N<sub>4</sub>) for electrostatic self-assembly construction of 2D/2D reduced graphene oxide (rGO)/g-C<sub>3</sub>N<sub>4</sub> nanostructures toward enhanced photocatalytic reduction of carbon dioxide to methane. *Nano Energy*, Elsevier, v. 13, n. August, p. 757–770, 2015. Cited 3 times on pages 91, 103, and 109.
- 189 DATTA, K. K. R. et al. Yellow emitting carbon dots with superior colloidal, thermal, and photochemical stabilities. *Journal of Materials Chemistry C*, Royal Society of Chemistry, v. 4, n. 41, p. 9798–9803, 2016. Cited 3 times on pages 91, 103, and 109.
- 190 XIAO, G. et al. Superior adsorption performance of graphitic carbon nitride nanosheets for both cationic and anionic heavy metals from wastewater. *Chinese Journal of Chemical Engineering*, Elsevier B.V., v. 27, n. 2, p. 305–313, 2019. Cited 3 times on pages 91, 103, and 109.
- 191 RESHAK, A. H.; KHAN, S. A.; AULUCK, S. Linear and nonlinear optical properties for AA and AB stacking of carbon nitride polymorph (C<sub>3</sub>N<sub>4</sub>). *RSC Advances*, v. 4, n. 23, p. 11967–11974, 2014. Cited on page 92.
- 192 HU, J.; YANG, P.; LIEBER, C. M. Nitrogen-driven sp<sup>3</sup> to sp<sup>2</sup> transformation in carbon nitride materials. *Physical Review B - Condensed Matter and Materials Physics*, American Physical Society, v. 57, n. 6, p. R3185–R3188, 2 1998. Cited on page 92.
- 193 PAPAGIANNOULI, I. et al. Depth Profiling of the Chemical Composition of Free-Standing Carbon Dots Using X-ray Photoelectron Spectroscopy. *Journal of Physical Chemistry C*, American Chemical Society, v. 122, n. 26, p. 14889–14897, 7 2018. Cited on page 93.
- 194 SONG, Y. et al. Investigation from chemical structure to photoluminescent mechanism: A type of carbon dots from the pyrolysis of citric acid and an amine. *Journal of Materials Chemistry C*, Royal Society of Chemistry, v. 3, n. 23, p. 5976–5984, 6 2015. Cited on page 93.

- 195 LIU, X. et al. Structure and photoluminescence evolution of nanodots during pyrolysis of citric acid: From molecular nanoclusters to carbogenic nanoparticles. *Journal of Materials Chemistry C*, Royal Society of Chemistry, v. 5, n. 39, p. 10302–10312, 10 2017. Cited on page [93](#).
- 196 SCHNEIDER, J. et al. Molecular fluorescence in citric acid-based carbon dots. *Journal of Physical Chemistry C*, v. 121, n. 3, p. 2014–2022, 2017. Cited 2 times on pages [93](#) and [124](#).
- 197 FIUZA, T. et al. On the Colloidal Stability of Nitrogen-Rich Carbon Nanodots Aqueous Dispersions. *C — Journal of Carbon Research*, v. 5, n. 4, p. 74, 11 2019. Cited 3 times on pages [99](#), [164](#), and [184](#).
- 198 SHAW, D. J. *Introdução à Química dos Colóides e de Superfícies*. São Paulo: Editora Blucher, 1992. Cited on page [100](#).
- 199 BHATTACHARJEE, S. DLS and zeta potential - What they are and what they are not? *Journal of Controlled Release*, Elsevier B.V., v. 235, p. 337–351, 2016. Cited on page [101](#).
- 200 OHSHIMA, H. A Simple Expression For Henry's Function for the Retardation Effect in Electrophoresis of Spherical Colloidal Particles. *Journal of Colloid and Interface Science*, v. 168, p. 269–271, 1994. Cited on page [102](#).
- 201 HUNTER, R. J. *Foundations of Colloid Science*. 2. ed. Oxford: Oxford University Press, 2001. Cited on page [102](#).
- 202 SIKORA, A. et al. A systematic comparison of different techniques to determine the zeta potential of silica nanoparticles in biological medium. *Analytical Methods*, Royal Society of Chemistry, v. 7, n. 23, p. 9835–9843, 2015. Cited on page [102](#).
- 203 SCIORTINO, A. et al. Disentangling size effects and spectral inhomogeneity in carbon nanodots by ultrafast dynamical hole-burning. *Nanoscale*, v. 10, n. 32, p. 15317–15323, 2018. Cited on page [103](#).
- 204 GAZZETTO, M. et al. Photocycle of Excitons in Nitrogen-Rich Carbon Nanodots: Implications for Photocatalysis and Photovoltaics. *ACS Applied Nano Materials*, v. 3, n. 7, p. 6925–6934, 2020. Cited on page [103](#).
- 205 STRELKO, V.; MALIK, D. J.; STREAT, M. Characterisation of the surface of oxidised carbon adsorbents. *Carbon*, v. 40, n. 1, p. 95–104, 2002. Cited on page [103](#).
- 206 CAMPOS, A. F. C. et al. Surface charge density determination in water based magnetic colloids: A comparative study. *Materials Research*, v. 20, n. 6, p. 1729–1734, 2017. Cited on page [105](#).
- 207 DEAN, J. A. *Lange's Handbook of Chemistry*. 16. ed. New York: McGraw-Hill Education, 2005. Cited on page [105](#).
- 208 ALVES, L. A. et al. Characterization of acid functional groups of carbon dots by nonlinear regression data fitting of potentiometric titration curves. *Applied Surface Science*, v. 370, p. 486–495, 2016. Cited 2 times on pages [106](#) and [110](#).

- 209 CONTESCU, A. et al. Acid buffering capacity of basic carbons revealed by their continuous pK distribution. *Carbon*, v. 36, n. 3, p. 247–258, 1998. Cited 2 times on pages 106 and 110.
- 210 GORGULHO, H. F. et al. Characterization of the surface chemistry of carbon materials by potentiometric titrations and temperature-programmed desorption. *Carbon*, v. 46, n. 12, p. 1544–1555, 2008. Cited on page 106.
- 211 CAREY, F. A.; GIULIANO, R. *Organic Chemistry*. 10. ed. New York: McGraw-Hill Education, 2017. Cited on page 106.
- 212 ESTES, C. S. et al. Preparation of highly functionalized carbon nanoparticles using a one-step acid dehydration of glycerol. *Carbon*, The Authors, v. 142, p. 547–557, 2019. Cited on page 106.
- 213 BANDOSZ, T. J. et al. Characterization of the surfaces of activated carbons in terms of their acidity constant distributions. *Carbon*, v. 31, n. 7, p. 1193–1202, 1993. Cited on page 108.
- 214 JALIL, A. H.; PYELL, U. Quantification of Zeta-Potential and Electrokinetic Surface Charge Density for Colloidal Silica Nanoparticles Dependent on Type and Concentration of the Counterion: Probing the Outer Helmholtz Plane. *Journal of Physical Chemistry C*, v. 122, n. 8, p. 4437–4453, 2018. Cited on page 108.
- 215 FOSDICK, L. D. et al. The Electrical Double Layer Around a Spherical Colloid Particle. *Math. Comput.*, v. 15, n. 76, p. 425, 1961. Cited on page 108.
- 216 RUSSEL, W. B.; SAVILLE, D. A.; SCHOWALTER, W. R. *Colloidal Dispersion*. [S.l.]: Cambridge University Press, 1992. Cited on page 108.
- 217 WIERSEMA, P.; LOEB, A.; OVERBEEK, J. Calculation of the electrophoretic mobility of a spherical colloid particle. *Journal of Colloid and Interface Science*, v. 22, n. 1, p. 78–99, 7 1966. Cited on page 108.
- 218 ROBERT, J. D.; CASERIO, M. C. *Basic Principles of Organic Chemistry*. 2nd editio. ed. Menlo Park, CA: W. A. Benjamin Inc, 1977. Cited on page 110.
- 219 HAMMOUDA, B. *Insight into the SANS Technique*. Gaithersburg, Maryland: Digital Media, 2016. Available at: <[https://www.ncnr.nist.gov/staff/hammouda/the\\_sans\\_toolbox.pdf](https://www.ncnr.nist.gov/staff/hammouda/the_sans_toolbox.pdf)>. Cited on page 116.
- 220 RIEKER, T. P.; MISONO, S.; EHRBURGER-DOLLE, F. Small-angle X-ray scattering from carbon blacks: Crossover between the fractal and porod regimes. *Langmuir*, v. 15, n. 4, p. 914–917, 1999. Cited 2 times on pages 116 and 117.
- 221 RIEKER, T. P.; HINDERMANN-BISCHOFF, M.; EHRBURGER-DOLLE, F. Small-Angle X-ray Scattering Study of the Morphology of Carbon Black Mass Fractal Aggregates in Polymeric Composites. *Langmuir*, v. 16, n. 13, p. 5588–5592, 6 2000. Cited on page 116.
- 222 CHEN, Y.; WANG, H.; WANG, J. Effects of alkyl chain length and solvents on thermodynamic dissociation constants of the ionic liquids with one carboxyl group in the alkyl chain of imidazolium cations. *Journal of Physical Chemistry B*, v. 118, n. 17, p. 4630–4635, 2014. Cited on page 117.

- 223 SAUREL, D. et al. A SAXS outlook on disordered carbonaceous materials for electrochemical energy storage. *Energy Storage Materials*, Elsevier Ltd, v. 21, n. May, p. 162–173, 2019. Cited on page [117](#).
- 224 KLINE, S. R. Reduction and analysis of SANS and USANS data using IGOR Pro. *Journal of Applied Crystallography*, v. 39, n. 6, p. 895–900, 2006. Cited 2 times on pages [118](#) and [145](#).
- 225 RAYLEIGH, L. The Incidence of Light upon a Transparent Sphere of Dimensions Comparable with the Wave-Length. *Proc. Roy. Soc. (London)*, A-84, n. 567, p. 25–46, 1910. Cited on page [118](#).
- 226 VIKESLAND, P. J. et al. Aggregation and sedimentation of magnetite nanoparticle clusters. *Environmental Science: Nano*, Royal Society of Chemistry, v. 3, n. 3, p. 567–577, 2016. Cited on page [122](#).
- 227 CAO, L. et al. Photoluminescence Properties of Graphene versus Other Carbon Nanomaterials. *Accounts of Chemical Research*, v. 46, n. 1, p. 171–180, 2013. Cited on page [123](#).
- 228 PAN, L. et al. Truly Fluorescent Excitation-Dependent Carbon Dots and Their Applications in Multicolor Cellular Imaging and Multidimensional Sensing. *Advanced Materials*, Wiley-VCH Verlag, v. 27, n. 47, p. 7782–7787, 2015. Cited on page [124](#).
- 229 YU, P. et al. Temperature-dependent fluorescence in carbon dots. *Journal of Physical Chemistry C*, v. 116, n. 48, p. 25552–25557, 2012. Cited 2 times on pages [124](#) and [127](#).
- 230 WANG, A. et al. Recent Advances of Graphitic Carbon Nitride-Based Structures and Applications in Catalyst, Sensing, Imaging, and LEDs. *Nano-Micro Letters*, v. 9, n. 4, p. 47, 2017. Cited 2 times on pages [124](#) and [126](#).
- 231 JIANG, K. et al. Red, Green, and Blue Luminescence by Carbon Dots: Full-Color Emission Tuning and Multicolor Cellular Imaging. *Angewandte Chemie*, v. 127, n. 18, p. 5450–5453, 4 2015. Cited 2 times on pages [124](#) and [127](#).
- 232 CAYUELA, A. et al. Semiconductor and carbon-based fluorescent nanodots: The need for consistency. *Chemical Communications*, v. 52, n. 7, p. 1311–1326, 2016. Cited 3 times on pages [124](#), [126](#), and [127](#).
- 233 WANG, H. et al. Fluorescently tuned nitrogen-doped carbon dots from carbon source with different content of carboxyl groups. *APL Materials*, v. 3, n. 8, p. 1–8, 2015. Cited on page [126](#).
- 234 SCIORTINO, A. et al. Different natures of surface electronic transitions of carbon nanoparticles. *Physical Chemistry Chemical Physics*, v. 19, n. 34, p. 22670–22677, 2017. Cited on page [126](#).
- 235 EHRAT, F. et al. Tracking the Source of Carbon Dot Photoluminescence: Aromatic Domains versus Molecular Fluorophores. *Nano Letters*, v. 17, n. 12, p. 7710–7716, 2017. Cited on page [126](#).
- 236 ZHANG, X. et al. Color-Switchable Electroluminescence of Carbon Dot Light-Emitting Diodes. *ACS Nano*, v. 7, n. 12, p. 11234–11241, 2013. Cited on page [127](#).

- 237 GARCÍA, R. S.; STAFFORD, S.; GUN'KO, Y. K. Recent Progress in Synthesis and Functionalization of Multimodal Fluorescent-Magnetic Nanoparticles for Biological Applications. *Appl. Sci.*, v. 8, n. 172, 2018. Cited 2 times on pages 134 and 135.
- 238 SHEN, M.; XU, A.; YAO, W. *Fluorescent oil-base magnetic suspension for magnetic particle inspection, and preparation method thereof*. [S.l.]: The State Intellectual Property Office of People's Republic of China, 2012. Cited on page 134.
- 239 MAGNAFLUX. *A14 Fluorescent Magnetic Particles - Spray, water and oil based dispersions*. 2020. Available at: <<https://www.magnaflux.com/Magnaflux/Products/Magnetic-Particle-Inspection/Consumables.htm>>. Cited 2 times on pages 134 and 137.
- 240 IN, P. C.; KUO, C. H.; CHIANG, C. S. Preparation of fluorescent magnetic nanodiamonds and cellular imaging. *Journal of the American Chemical Society*, v. 130, n. 46, p. 15476–15481, 2008. Cited on page 134.
- 241 ATWOOD, C. *Oriented magnetic particle-fluorescence detectable moiety compositions and methods of making and using the same*. 2007. Cited on page 135.
- 242 WEISS, C. K.; LANDFESTER, K. Miniemulsion polymerization as a means to encapsulate organic and inorganic materials. *Advances in Polymer Science*, v. 233, n. January, p. 185–236, 2010. Cited on page 135.
- 243 BAO, Y. et al. Magnetic nanoparticles: material engineering and emerging applications in lithography and biomedicine. *Journal of Materials Science*, Springer US, v. 51, n. 1, p. 513–553, 2015. Cited on page 135.
- 244 JIAO, J. et al. Mini-emulsion fabricated magnetic and fluorescent hybrid Janus micro-motors. *Micromachines*, v. 9, n. 2, 2018. Cited on page 135.
- 245 PENG, X. et al. Carbon nanotubes-iron oxides magnetic composites as adsorbent for removal of Pb(II) and Cu(II) from water. *Carbon*, v. 43, n. 4, p. 880–883, 2005. Cited on page 136.
- 246 ZHANG, G. et al. CuFe<sub>2</sub>O<sub>4</sub>/activated carbon composite: A novel magnetic adsorbent for the removal of acid orange II and catalytic regeneration. *Chemosphere*, v. 68, n. 6, p. 1058–1066, 2007. Cited on page 136.
- 247 SHAO, L. et al. Facile synthesis, characterization of a MnFe<sub>2</sub>O<sub>4</sub>/activated carbon magnetic composite and its effectiveness in tetracycline removal. *Materials Chemistry and Physics*, Elsevier B.V, v. 135, n. 1, p. 16–24, 2012. Cited on page 136.
- 248 WU, G. et al. Design of carbon sphere/magnetic quantum dots with tunable phase compositions and boost dielectric loss behavior. *Chemical Engineering Journal*, Elsevier, v. 333, n. September 2017, p. 519–528, 2018. Cited on page 136.
- 249 ZHANG, Y. et al. Mitochondria-targeting nanoplatfrom with fluorescent carbon dots for long time imaging and magnetic field-enhanced cellular uptake. *ACS Applied Materials and Interfaces*, v. 7, n. 19, p. 10201–10212, 2015. Cited on page 136.
- 250 HU, Y. et al. Preparation and optical properties of magnetic carbon/iron oxide hybrid dots. *RSC Advances*, Royal Society of Chemistry, v. 7, n. 65, p. 41304–41310, 2017. Cited on page 136.

- 251 LI, L. et al. Chitosan and carboxymethyl cellulose-multilayered magnetic fluorescent systems for reversible protein immobilization. *Carbohydrate Polymers*, Elsevier Ltd., v. 201, p. 357–366, 2018. Cited on page [136](#).
- 252 GOMIDE, G. S. *Uma contribuição ao nanomagnetismo : dependência térmica da coercividade e da anisotropia magnética em sistemas polidispersos de partículas ferrimagnéticas*. Phd Thesis (PhD Thesis) — Universidade de Brasília, 2018. Cited 2 times on pages [142](#) and [148](#).
- 253 FIUZA, T. *Estudo da Microestrutura de Nanocoloides Magnéticos por Espalhamento de Raio-X em Baixo Ângulo*. Brasília: UnB, 2016. Cited on page [145](#).
- 254 THAMM, S.; HESSE, J. A simple plot indicating interactions between single-domain particles. *Journal of Magnetism and Magnetic Materials*, v. 154, n. 2, p. 254–262, 1996. Cited on page [150](#).
- 255 STONER, E. C.; WOHLFARTH, E. P. A mechanism of magnetic hysteresis in heterogeneous alloys. *Philosophical Transactions of the Royal Society of London. Series A, Mathematical and Physical Sciences*, v. 240, n. 826, p. 599–642, 1948. Cited on page [150](#).
- 256 WANG, H. et al. Nitrogen-doped carbon dots for “green” quantum dot solar cells. *Nanoscale Research Letters*, Springer New York LLC, v. 11, n. 1, 2016. Cited 3 times on pages [158](#), [181](#), and [201](#).

# Annex



Article

# On the Colloidal Stability of Nitrogen-Rich Carbon Nanodots Aqueous Dispersions

Thiago Fiuza<sup>1,2</sup>, Guilherme Gomide<sup>1</sup> , Alex Fabiano Cortez Campos<sup>3</sup> , Fabrizio Messina<sup>4</sup>  
and Jérôme Depeyrot<sup>1,\*</sup>

<sup>1</sup> Instituto de Física, Universidade de Brasília, 70904-970 Brasília, DF, Brazil; thiagofiuza91@gmail.com (T.F.); guilhermegomide@unb.br (G.G.)

<sup>2</sup> Laboratoire PHENIX, Sorbonne Université, UPMC Univ Paris 06, CNRS, Case 51, 4 Place Jussieu, F-75005 Paris, France

<sup>3</sup> Faculdade UnB Planaltina, Universidade de Brasília, 73345-010 Planaltina, DF, Brazil; relex@unb.br

<sup>4</sup> Dipartimento di Fisica e Chimica—Emilio Segrè, Università degli Studi di Palermo, Via Archirafi 36, 90123 Palermo, Italy; fabrizio.messina@unipa.it

\* Correspondence: jerome@unb.br; Tel.: +55-613-107-7818

Received: 1 October 2019; Accepted: 13 November 2019; Published: 16 November 2019



**Abstract:** The present survey reports on the colloidal stability of aqueous dispersions of nitrogen-rich carbon nanodots (N-CDs). The N-CDs were synthesized by thermally induced decomposition of organic precursors and present an inner core constituted of a  $\beta$ - $C_3N_4$  crystalline structure surrounded by a surface shell containing a variety of polar functional groups. N-CDs size and structure were checked by combined analysis of XRD (X-ray Diffraction) and TEM (Transmission Electron Microscopy) measurements. FTIR (Fourier-Transform Infrared Spectroscopy) experiments revealed the presence of carboxyl and amide groups on N-CDs surface. Towards a better understanding of the relation between colloidal stability and surface charge development, zetametry experiments were applied in N-CDs dispersions at different pHs and constant ionic strength. The increase of the absolute values of zeta potential with the alkalization of the dispersion medium is consistent with the deprotonation of carboxyl groups on N-CDs surface, which agrees with the macroscopic visual observations of long-term colloidal stability at pH 12. The saturation value of N-CDs surface charge density was evaluated by means of potentiometric-conductometric titrations. The difference between carboxyl-related surface charge and the one determined by zeta potential measurements point to the presence of oxidized nitrogen functionalities onto the N-CDs surface in addition to carboxyl groups. These novel results shed light on the electrostatic repulsion mechanism that allows for the remarkable colloidal stability of N-CDs dispersions.

**Keywords:** carbon nanodots; colloidal stability; surface charge

## 1. Introduction

Carbon nanomaterials have been under the spotlight of scientific development in numerous distinct areas over the last decades, notably carbon nanodots (CDs), considered 0-dimensional nanoparticles, offer exceptional bright [1] and tunable photoluminescence in the visible range [2]. Additionally, these low-cost and easily synthesized nanostructured materials [3] also incorporate appealing biophysical-chemical characteristics such as biocompatibility [4], low toxicity [5], good electron donor/acceptor [6] and high sensitivity to the environment [7]. The combination of these properties makes them suitable for the use in industry as nanosensors [8], photocatalytic and optoelectronic components [9,10], as well as on the medical field in bioimaging [11], photo-activated antiviral/antibacterial agents [12] and targeting nanotools applied to cancer therapy [13–15].

Generally, CDs are quasi-spherical nanoparticles smaller than 10 nm constituted of a carbonaceous core and a densely passivated disordered surface. Depending on the synthesis particularities, the core carbon atoms can exhibit different degrees of hybridization producing amorphous or crystalline structures [16]. The surface shell is also synthesis-dependent presenting a wide range of possible surface groups from small to very long atomic chains with hydrophilic or hydrophobic properties.

One of the most interesting properties of CDs is that they can be easily dispersed in water and other polar solvents up to large concentrations, leading to colloids with long-term stability [17]. This exceptional colloidal stability is found in as-synthesized CDs, without the need of any post synthesis functionalization, and is achieved thanks to the singular characteristic of the CDs surface, where functional groups provide an electric charge density that leads to effective electrostatic repulsions between particles, avoiding agglomeration phenomena [18]. The type of charge (positive or negative) imparted by the surface functional groups depends mainly on their chemical nature, on the pH and the ionic strength of the medium [19]. Groups with acid-base properties, such as amine and carboxyl, generate surface charge through protonation-deprotonation process, therefore the magnitude of the charge can be controlled by pH. Other groups provide constant structural charge, such as quaternary ammonium [20] (positive) and oxidized nitrogen functionalities [21] (negative). Possible specific adsorption of cations or anions also affects the surface charge and can even result in charge reversal [19]. Thus, at a constant temperature, the electrostatic repulsion between CDs can be tuned by varying the pH and the ionic strength of the dispersion, which corresponds to control the surface charge of the nanodots and the rate of screening in the electric double layer, respectively.

Among the large quantity of different approaches to obtain CDs, the popular microwave decomposition method has the advantage of enabling the nanoparticles doping with other atoms. In the context of this study, nitrogen atoms were introduced in the CDs carbon matrix originating the so called nitrogen-rich carbon nanodots (N-CDs). This special family has attracted great attention because of their big fluorescence quantum yields [5,22–24]. This bottom-up method also has the special feature of controlling the internal and surface structure of the CDs by balancing the proportion of the carbon and nitrogen molecular precursors. In sufficiently high N-doping conditions, the formation of a  $\beta$ -C<sub>3</sub>N<sub>4</sub> crystalline core with a surface layer hosting amide, carboxyl and hydroxyl groups has been observed [4,25]. Thus, since amides and alcohols present pK<sub>a</sub> values in water usually higher than 15 [26], the charge of the N-CDs in aqueous colloidal dispersions arises mainly from deprotonation of surface carboxyl groups ( $\equiv$  COOH<sub>(surf)</sub>) into carboxylate ( $\equiv$  COO<sub>(surf)</sub><sup>-</sup>), in function of pH. The strength of acidity is related to the type of carboxyl group present at the N-CDs surface. pK values between 2.0 and 5.0 are typically associated with carboxylic acids [27], while pK values between 6 and 8 are attributed to hydrolyzed lactones or even carboxylic anhydride groups [28,29]. As a consequence of the heterogeneity of the carboxyl groups, the surface of N-CDs tends to exhibit pK values over a wide range, as commonly observed in carbon materials [30,31].

In previous studies [22,24,25,32], the structural and photoluminescent properties of N-CDs were extensively investigated, however very limited information is reported on the extent of the colloidal stability of these aqueous dispersions. The evaluation of the stability of the system presents major importance in order to appraise effects as local variations in nanoparticle concentration, change in interparticle interactions, aggregation and sedimentation processes. Understanding these phenomena should provide needful assistance, not only in the dispersibility, but also in the interpretation of the photoluminescence emission. As an example of the significance of this research, the origin of the CDs emission tunability has been a theme of intense debate in the literature [16], where aggregation effects are given a significant role on the data interpretation [33]. In this context, addressing the impact of physico-chemical parameters in surface properties would aid to clarifying interparticle interactions and ordering. Also, it could serve as an alternative or complementary procedure to the existing sorting methods (e.g. size exclusion chromatography [32] and ultracentrifugation [34]) to obtain more homogeneous characteristics making use of well controlled induced phase separations.

One of the key factors for stability in charged colloids is the development of the nanoparticles surface charge depending on the medium characteristics. Given the nature of the N-CDs charge mechanism in aqueous medium, we focused our attention on the pH-dependency, reasonably the most important parameter to monitor the surface charge. The limited range of studies on the stability of this material led us to develop a quantitative and qualitative analysis, by applying coupled experimental techniques to evaluate the surface charge density and link the results with the evolution over time of the macroscopical visual aspect of the samples. Also, a careful characterization of N-CDs in order to determine nanoparticles morphology, structure and sizes as well as to identify the nanoparticles main surface groups was required to guarantee a systematic and substantiated analysis.

The results reported on this study demonstrate the improvement of the colloidal stability in N-CDs dispersions as the pH of the aqueous medium undergoes a shift towards alkaline conditions. This response could be attributed to the increase in electrostatic repulsion based on the progression of the surface charge density. To fully comprehend the effect throughout the whole pH range, we propose a model combining potentiometric-conductometric titrations and zetametry results aiming the recognition of the different contributions to surface charge mechanism on the interface nanoparticle/solvent.

## 2. Materials and Methods

### 2.1. Reagents

The following pro analyse (P.A.) grade reagents, supplied from Sigma-Aldrich, Merck or Vetec Química Fina, were used for the nanoparticles synthesis and dispersion in aqueous media: citric acid monohydrate ( $C_6H_8O_7 \cdot H_2O$ ), urea ( $CH_4N_2O$ ), nitric acid ( $HNO_3$  63%), sodium hydroxide (NaOH) and sodium nitrate ( $NaNO_3$ ). The aqueous solutions were prepared with deionized water Type I (Millipore Milli-Q Gradient quality).

### 2.2. Synthesis of the N-CDots Colloidal Dispersions

The synthesis of the nitrogen enriched carbon nanodots follows a thermally microwave-induced decomposition protocol performed in a household microwave oven. The procedure consists in the carbonization (microwave power set at 700 W) of an aqueous solution with completely dissolved citric acid monohydrate and urea. The organic precursor is prepared by diluting in 10 mL of Type 1 water 3 g of citric acid monohydrate with 3 g of urea, so that a 0.74 molar ratio of nitrogen and carbon (N/C) is established. After the complete water evaporation, the system is brought back to room temperature and can yield up to 30% in weight of the initial precursors. The reaction produces a strongly hygroscopic black powder consisting of aggregated N-CDots, which is dried under vacuum for 90 minutes ensuring the removal of any remaining solvent. Thenceforth, the powder can be dispersed in different aqueous solutions with well controlled physico-chemical parameters. The dispersion medium is primarily Type I water ( $pH \approx 7$ ), which had its pH regulated with either the addition of nitric acid or sodium hydroxide. The dispersion is performed by the addition of a certain mass of CDs to the corresponding volume of adjusted aqueous medium solution. The dispersion process is finalized with the use of an ultrasound bath at 50 °C until the macroscopic visual aspect of the sample is homogeneous.

### 2.3. Physical and Chemical Characterization

#### 2.3.1. Transmission Electron Microscopy

Transmission electron microscopy images were obtained in a JEM2100 electron microscope (JEOL) using a carbon type-A 400 mesh Cu substrate (TED PELLA). The N-CDs were dispersed in deionized water type I following the procedure described above. The dispersion was then diluted in alcohol and then deposited over the substrate and let to dry. The histogram was obtained by pixel measuring the

diameter of the N-CDs. A lognormal and gaussian function fit was performed in order to obtain the mean diameter of the size distribution.

### 2.3.2. X-ray Diffraction

X-ray diffraction was performed on post-synthesis dried powder, prior to any dispersion in aqueous media. The measurements were carried out in a D8 Focus (Bruker) diffractometer with  $\text{CuK}\alpha$  radiation (wavelength  $\lambda = 1.5406 \text{ \AA}$ ). The sample was probed in a  $10^\circ$ – $90^\circ$  range of  $2\theta$  with a  $0.05^\circ$  step at  $0.1^\circ/\text{min}$ . A Si standard was used to obtain the instrumental line broadening  $\beta_{\text{ins}}$ . The nanoparticles mean size can be estimated by the broadening of the diffraction peaks using Scherrer's equation:

$$D_{\text{XR}} = \frac{k\lambda}{\beta \cos \theta'} \quad (1)$$

where  $k$  is the correlation factor (0.9 for spheres),  $\lambda$  the x-ray beam wavelength,  $\theta$  the incidence angle and

$$\beta = \sqrt{FWHM^2 - \beta_{\text{ins}}^2} \quad (2)$$

represents the line broadening coming from the dots characteristics determined with the full width at half maximum ( $FWHM$ ).

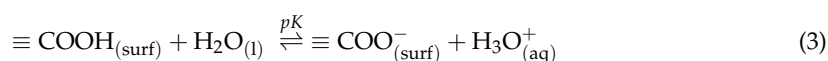
### 2.3.3. Fourier-Transform Infrared Spectroscopy

Fourier transform infrared spectroscopy (FTIR) measurements were performed using a Perkin Elmer FTIR spectrometer (model Frontier) to gain further structural insights about the prepared N-CDs. Pellets of  $KBr$ -sample were prepared by mixing sample and potassium bromide then pressing at 10 tons on a hydraulic press (Auto-CrushIR, Pike Technologies). Spectra were recorded in absorbance mode from  $4000$  to  $400 \text{ cm}^{-1}$  using 8 scans at  $4 \text{ cm}^{-1}$  resolution.

## 2.4. Colloidal Stability of Dispersions

### 2.4.1. Potentiometric and Conductimetric Titrations

The electrochemical measurements were acquired with a 713 Metrohm pHmeter with a pH glass double-junction electrode, a 712 Metrohm Conductimeter with a conductometer using a conductivity cell specially designed for colloidal dispersions and an electronic burette 665 Metrohm Dosimat. Potentiometric and conductimetric acid-base titrations were simultaneously performed on 35 mL of N-CDs dispersions at  $0.15 \text{ g/L}$  mass concentration in acidified ( $\text{HNO}_3$ ) pH 2 aqueous medium. This mass fraction was selected in order to generate a well-resolved conductimetric curve where the distinction of strong and weak acids is evident. The titrations were performed from pH 2 to 12 by controlling the titrant (standardized  $\text{NaOH}$  solution,  $0.01 \text{ mol/L}$ , stirred and degassed by purified nitrogen during 10 minutes to avoid carbonation) addition with an electronic burette. Both potentiometer and conductometer were gauged using appropriate templates. Upon addition of the titrant, the pH and the conductivity of the sample medium are measured after equilibrium is reached. Thermal compensation is automatically applied in the measured conductivity. The titrations were performed in triplicate as usual in analytical chemistry and the results of equivalence points determinations present very low standard deviations. The titration analysis were performed by considering the deprotonation equilibrium of surface carboxyl groups according to:



where  $K$  is the corresponding thermodynamic constant ( $pK = -\log K$ ).

#### 2.4.2. Zetametry

Zeta potential measurements were taken using a ZetaSizer (model NanoZS 90, Malvern Panalytical, Malvern, UK) with a disposable folded capillary cell (DTS 1070). The N-CDs were dispersed in five different acidified ( $\text{HNO}_3$ ) and alkalinized ( $\text{NaOH}$ ) aqueous solutions: pH 2.0, 4.5, 7.0, 9.5 and 11.8. The ionic strength of 0.01 mol/L was imposed by adding  $\text{NaNO}_3$  as a background electrolyte, avoiding the introduction of different ions to the system. The pH was measured before and after the addition of the N-CDs and in order to preserve the 0.15 g/L nanoparticles mass concentration, no adjustment of the physical-chemical parameters was performed after combining the N-CDs and the suited medium. Temperature variation/gradient effects were evaded by performing all measurements at 25 °C. The electrophoretic mobilities  $\mu$  values are obtained from measurements of particle velocity using Laser Doppler Velocimetry (LDV). Then, the corresponding zeta potentials ( $\zeta$ ) are calculated using the Henry's equation [35]

$$\mu = \frac{2}{3} \frac{\epsilon_0 \epsilon_r \zeta}{\eta} f(\kappa r), \quad (4)$$

where  $\eta$  and  $\epsilon_r$  are the viscosity and dielectric constant of the solvent, respectively, and  $\epsilon_0$  is the vacuum permittivity.  $f(\kappa r)$  is the Henry's function which depends on both Debye length  $\kappa^{-1}$  and particle radius  $r$ . The Debye length is given by the expression

$$\kappa^{-1} = \left( \frac{\epsilon_0 \epsilon_r k T}{2 N_A e^2 I} \right)^{1/2}, \quad (5)$$

where  $I$  is the ionic strength of the dispersion.  $f(\kappa r)$  varies from 1.0, for low values of  $\kappa r$  (Hückel model), to 1.5 as  $\kappa r$  approaches infinity (Smoluchowski model). For the transition range between low and high  $\kappa r$ , Ohshima [36] has provided an approximate analytical expression of  $f(\kappa r)$  as

$$f(\kappa r) = 1 + \frac{1}{2} \left[ 1 + \frac{2.5}{\kappa r (1 + 2e^{-\kappa r})} \right]^{-3}. \quad (6)$$

In addition, macroscopic visual observation of the evolution of the as prepared samples was carried out a week later. During this ageing process the samples were held motionless and at room temperature.

### 3. Results and Discussion

#### 3.1. Physical and Chemical Characteristics of N-CDs

The characterization methods here employed allowed to confirm the expected morphology of the nanomaterial produced by referred synthesis protocol. TEM imaging is able to resolve the N-CDs regardless the very small particle size, for instance, an aggregate of a few dots is exhibited in Figure 1 indicating the synthesis process successfully produced nanoparticles. Although the particles agglomerated due to the evaporation of the solvent, tracing boundaries is feasible owing to the internal structural organization of the N-CDs.

The crystalline structure is evidenced by the HRTEM measurements, where the lattice planes are visible and an almost spherical morphology is detected. TEM images are oftentimes not sufficient to determine the three-dimensionality of the particles, for example, it could be intricate to differentiate CDs from Graphene Quantum Dots (GQDs). However, the result here described is in strong agreement with high resolution transmission electron microscopy (HRTEM) combined with atomic force microscopy (AFM) reported in previous studies [22,24,32] with the same synthesis protocol, therefore endorsing the efficacy and reproducibility of the method. Due to their low contrast, it is a challenge to get enough images of N-CDs for size distribution histograms, but the observed N-CDs diameters lie mostly within the range of 2–4 nm.

Since TEM may have some limitations due to the nature of these nanoparticles, XRD was performed to obtain a mean size estimation by a different approach. The diffratogram presented

in Figure 2 shows one intense peak, with some lower intensity contributions that were subtracted since they were only slightly above noise level, and would not help from a quantitative point of view. The absence of very sharp peaks assures that microcrystalline structures were not formed, an issue observed in higher N/C ratios Sciortino et al. [22].

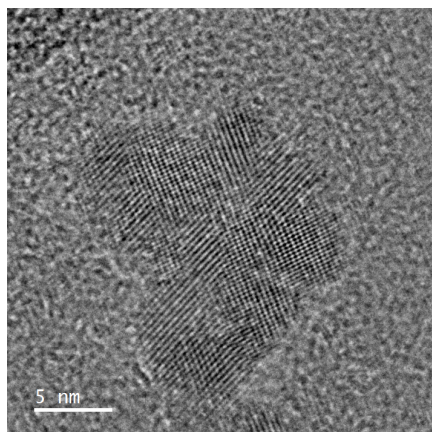


**Figure 1.** High resolution transmission electron microscopy of the studied sample, evidencing the crystalline structure of the dots.

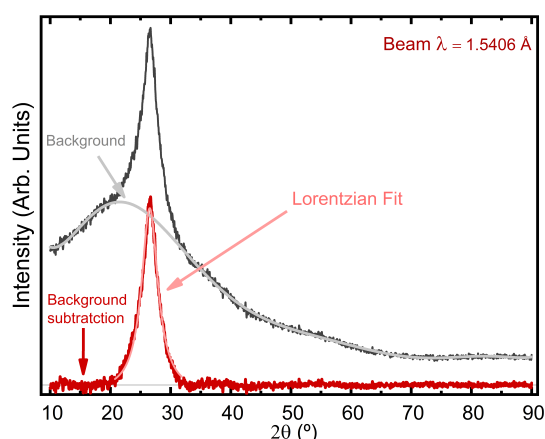


**Figure 2.** X-ray diffractogram of the investigated sample. Experimental values are shown in black and fitting results are shown in thinner solid lines.

The X-ray diffraction diameter ( $D_{XR}$ ) is determined using Scherrer's equation and a particle diameter of  $2.46 \pm 0.03$  nm is found. These results reinforce the already well established characterization of these nanoparticles as dots, namely, systems with really reduced particle size (1–8 nm) presenting a spherical symmetry. Thence, now the focus is directed over the surface features of this N-CDs, since the interface particle/solvent shall have a crucial role in the colloidal stability of these systems.

The mid-FTIR spectrum of the N-CDs is shown in Figure 3 and reveals their complex surface chemistry. The large broad band between  $2600$  and  $3400$   $\text{cm}^{-1}$  (A) are due to O–H, N–H and possibly C–H stretching vibrations. The peaks at  $1712$   $\text{cm}^{-1}$  (B) and  $1600$   $\text{cm}^{-1}$  (C) can be respectively attributed to carboxylic and amide C=O stretchings. The peak at  $1401$   $\text{cm}^{-1}$  (D) is characteristic of the O–H in plane bend while that at  $1357$   $\text{cm}^{-1}$  (E) can be assigned to the C–N stretching. Finally, the spectrum still shows characteristic H–O and H–N out of plane vibrations (F). These results are in agreement with the data presented on the article [24] upon the structural analysis of the N-CDs.

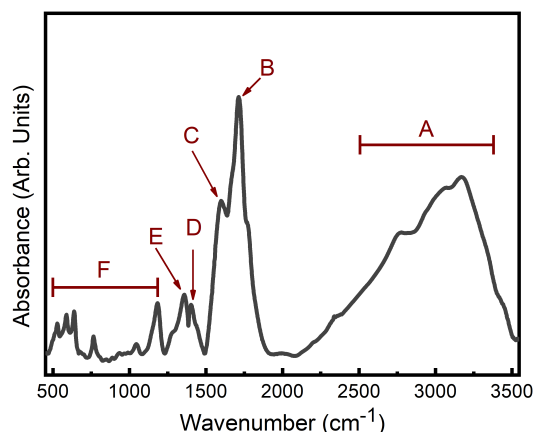


**Figure 3.** FTIR spectrum of the investigated sample, A-G areas illustrate the different regions of interest described in the text.

### 3.2. Colloidal Properties of N-CDs Aqueous Dispersions

Typical potentiometric-conductometric titration curves of N-CDs sample are presented in Figure 4, where the equivalence points  $EP_1$  and  $EP_2$  were determined by using direction lines applied to the conductometric curve [37–39]. These equivalence points delimit three distinct regions whose meaning can be described as follows. The first one corresponds to the strong acid titration (free  $H_3O^+$  ions from  $HNO_3$  in the bulk dispersion). The sharp decrease of the conductivity indicates the neutralization of  $H_3O^+$  ions, gradually substituted by  $Na^+$  ions from the titrant solution, which present lower specific molar conductivity [40]. After  $EP_2$ , the third region is related to the excess of titrant reagent, which increases the conductivity strongly due to the high specific molar conductivity of  $OH^-$  ions. The second region, between  $EP_1$  and  $EP_2$ , corresponds to the titration of N-CDs, i.e., the deprotonation of surface carboxyl groups. The contribution of N-CDs to the conductivity is negligible due to the mass of the particles, and the slight increase in conductivity can be more appropriately assigned to the increase of  $Na^+$  ions concentration from the titrant.

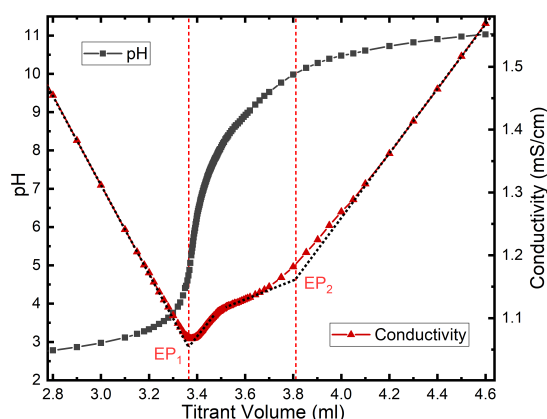


**Figure 4.** Potentiometric and Conductometric Titration showing the pH (in gray) and conductivity (in red) as a function of titrant volume. Vertical dashed lines indicate the equivalence points as determined from the conductivity curves.

As it can be observed, in this second region the potentiometric curve does not exhibit sharp changes, which is consistent with the presence of different surface carboxyl groups associated to various acidic constants [28,29,31]. Moreover, as previously mentioned, the protons of N–H and O–H bonds related amide and hydroxyl groups present at N-CDs surface are not titratable in the

investigated pH range [26]. Then, using the determined equivalence points and the mass balance, the total titratable acidity of the N-CDs surface could be calculated in terms of moles number of surface carboxyl groups per gram of N-CD sample ( $[\equiv \text{COOH}_{(\text{surf})}]_T$ ) leading to 9.8 mmol/g, a value similar to that of other carbon materials [41]. Considering the average diameter (2.46 nm) of our CDs, and the density of  $\beta\text{-C}_3\text{N}_4$  (3.57 g/cm<sup>3</sup>), one can calculate that this value of [COOH] corresponds to >100 carboxyl groups per dot, confirming the picture of CD surfaces very densely covered by such polar moieties.

The zeta potential of N-CDs dispersions obtained at different pH values are depicted in Figure 5 together with a picture that illustrates the macroscopic state of the colloidal systems after two weeks of preparation. As it can be seen, the zeta potential of N-CDs is strongly pH-sensitive. This behavior can be correlated with the deprotonation of carboxyl groups with increasing pH, which results in higher concentration of negatively charged surface groups and therefore more negative values of zeta potential. In charged colloids, as N-CDs, it is generally assumed that zeta potential higher than  $|30 \text{ mV}|$  indicates good stability against aggregation because of electrostatic repulsion between particles [42,43]. This is consistent with our experimental macroscopic observations of N-CDs dispersions at different pH values. Indeed, at pH = 11.8, the high negative zeta potential ensures a very stable sol and no phase separation is noted. For lower pH values, the zeta potential becomes less negative inducing coagulation and settling of nanoparticles at the bottom of the falcon tube. This aggregation effect is more pronounced at pH = 2.0, where a sharp precipitation of aggregated N-CDs can be observed.

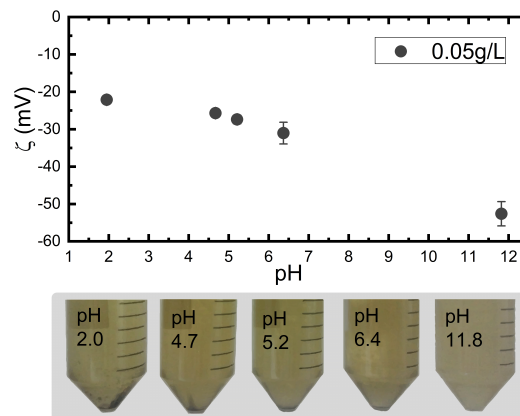


**Figure 5.** Top: Zeta potential as a function of the pH for the investigated N-CD sample in a concentration of 0.05 g/L. Bottom: Picture of the samples after two weeks in each pH, showing the reduction of precipitate amount with increasing pH.

Based on the titrations results, the pH-dependence of the concentration of acidic surface groups of N-CDs can be roughly evaluated in a model that considers that  $[\equiv \text{COOH}_{(\text{surf})}]_T$  is constant until  $\text{EP}_1$ . Then, the deprotonation process begins and the concentration of carboxylate surface groups  $[\equiv \text{COO}^-_{(\text{surf})}]$  progressively increases until the pH corresponding to  $\text{EP}_2$ , where its maximum value is reached. Then, by applying the proton balance equation in the region between  $\text{EP}_1$  and  $\text{EP}_2$ , the variation of  $[\equiv \text{COO}^-_{(\text{surf})}]$  with pH can be expressed as [44]:

$$[\equiv \text{COO}^-_{(\text{surf})}] = \frac{1}{m} \left\{ (V_0 + V_{\text{EP}_1}) \left( [\text{H}_3\text{O}^+]_{\text{EP}_1} - [\text{OH}^-]_{\text{EP}_1} \right) + V_t C_t - (V_0 + V_{\text{EP}_1} + V_t) \left( [\text{H}_3\text{O}^+]_f - [\text{OH}^-]_f \right) \right\}, \quad (7)$$

where  $m$  is the mass of N-CDs sample,  $V_0$  is the initial volume of the N-CDs samples,  $V_{EP_1}$  and  $V_t$  are the volume of titrant added until  $EP_1$  and from  $EP_1$ , respectively,  $[H_3O^+]$  and  $[OH^-]_{EP_1}$  are the molar concentration of  $H_3O^+$  ions and  $OH^-$  ions at  $EP_1$ ,  $C_t$  is the molar concentration of titrant and  $[H_3O^+]_f$  ( $[OH^-]_f$ ) are the equilibrium concentration of  $H_3O^+$  ( $OH^-$ ) ions. In this model, the surface charge density of carboxylate groups ( $\sigma_{COO^-}$ ) can be estimated as

$$\sigma_{COO^-} = \frac{[\equiv COO^-]_{(surf)} m N_A e}{A_T}, \quad (8)$$

where  $N_A$  is Avogadro's constant,  $e$  the elementary charge and  $A_T$  corresponds to the total surface area of nanoparticles, calculated considering spherical N-CDs of diameter  $D_{XR}$ . In order to cross the analysis of the potentiometric-conductometric titrations with that of zeta potential measurements, we have calculated the electrokinetic charge density ( $\sigma_\zeta$ ) through the following empirical formula [45–47]:

$$\sigma_\zeta = \frac{\epsilon_0 \epsilon_r k T}{e} \kappa \left[ 2 \sinh \left( \frac{e \zeta}{2 k T} \right) + \frac{4}{\kappa r} \tanh \left( \frac{e \zeta}{4 k T} \right) \right], \quad (9)$$

where  $k$  is the Boltzmann constant and  $T$  the temperature. On one hand,  $\sigma_{COO^-}$  is directly proportional to the concentration of carboxylate groups onto N-CDs surface, therefore, in absence of specific adsorption, this parameter can be finely tuned by the pH. On the other hand,  $\sigma_\zeta$  is particularly dependent on the ionic strength of the dispersion since the electrokinetic charge density is defined as the effective electric charge normalized on the area of the slip plane in the electric double layer [48].

Figure 6 shows the pH-dependence of  $\sigma_{COO^-}$  and  $\sigma_\zeta$  evaluated using Equations (8) and (9), respectively. As it can be seen, the profile of the curves obtained from the two measurements exhibits the same general trend, but the absolute value of the charge densities at a fixed pH shows a sharp difference. Based on the acidity of the particles surface, in the sample of N-CDs dispersed at pH = 2.0, the concentration of carboxylate groups is zero, leading to  $\sigma_{COO^-} = 0$ . However, the particles present a negative electrokinetic charge density at this pH ( $\sigma_\zeta = -0.019 \text{ C/m}^2$ ), which can be attributed to the presence of oxidized nitrogen functionalities onto N-CDs surface, as already observed for similar carbon materials [21,49,50]. As a matter of fact, XPS studies of these CDs [24] revealed the presence of N–O bonds on the surface, confirming the present conclusion. In the other samples, the N-CDs present increasing  $|\sigma_{COO^-}|$  values with pH, due to the deprotonation of carboxyl groups, as previously discussed. Nevertheless, the increase of  $|\sigma_\zeta|$  with pH is less significant because of the screening effect generated by the excess of counterions from the electrolytes (acid or base) used to adjust the pH of the medium [51].

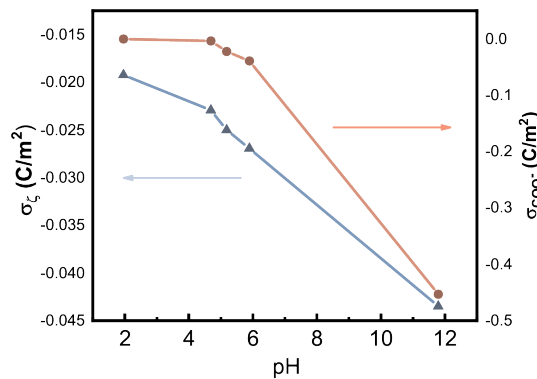


**Figure 6.** Electrokinetic charge density  $\sigma_\zeta$  (blue triangles) and calculated surface charge density of carboxyl groups  $\sigma_{COO^-}$  (red circles), both in  $C/m^2$ .

#### 4. Conclusions

We have successfully synthesized nitrogen-rich carbon nanodots (N-CDs) and dispersed them in water in order to investigate the mechanisms that play a role in their colloidal stability. The presence of carboxyl and amide groups on N-CDs surface were revealed by FTIR experiments. A well characterized sample of N-CDs with a  $\beta$ -C<sub>3</sub>N<sub>4</sub> core was used to maintain the focus on the surface charge mechanisms, which are responsible for controlling the aggregate formation and, therefore, affects the fluorescence tunability and efficiency.

Colloids zetametry in different pH was carried out to relate the colloidal stability to the development of surface charge due to the polar functional groups. The enhanced dispersibility of the N-CDs at high pH results from the high concentration of carboxylate groups on the surface that induces electrostatic repulsion between particles. The increase of the absolute value of the zeta potential with alkalinization is consistent with the deprotonation of these carboxyl groups on the N-CDs surface and explains the visual observations of improved colloidal stability at higher pH.

However, the carboxyl groups deprotonation alone cannot explain the negative zeta potential values we find at pH 2, since they do not contribute to the surface charge of N-CD at low pH. This negative electrokinetic charge density value determined at pH 2.0 can be attributed to the presence of oxidized nitrogen functionalities onto the N-CDs surface. The comparison of the electrokinetic charge density and the surface charge density of carboxyl groups allowed us to better understand the role of the surface groups on the pH-dependence of the zeta potential and, consequently, on the electrostatic repulsion mechanism that guarantees the colloidal stability of the investigated carbon nanodots dispersions.

**Author Contributions:** Conceptualization, T.F., G.G., A.F.C.C., F.M. and J.D.; methodology, T.F., G.G. and A.F.C.C.; validation, A.F.C.C., F.M. and J.D.; formal analysis, T.F., G.G., A.F.C.C.; investigation, T.F., G.G. and A.F.C.C.; resources, A.F.C.C., F.M. and J.D.; writing—original draft preparation, T.F. and A.F.C.C.; writing—review and editing, G.G., F.M. and J.D.; visualization, T.F. and G.G.; supervision, F.M. and J.D.; project administration, A.F.C.C. and J.D.; funding acquisition, A.F.C.C. and J.D.

**Funding:** Authors gratefully acknowledge the financial support of the Brazilian agencies: The Coordination for the Improvement of Higher Education Personnel (CAPES), the National Council for Scientific and Technological Development (CNPq – Grant Number 465259/2014-6 and 400849/2016-0), the National Institute of Science and Technology Complex Fluids (INCT-FCx) and the Distrito Federal Research Foundation (FAP-DF – Grant Number 0193.001569/2017, 0193.001194/2016 and 0193.001376/2016).

**Acknowledgments:** The authors would like to thank T. Oliveira dos Santos and Laboratório Multiusuário de Microscopia de Alta Resolução (LabMic) of University of Goiás, Brazil, for HRTEM measurements.

**Conflicts of Interest:** The authors declare no conflict of interest.

#### References

1. Sun, Y.P.; Zhou, B.; Lin, Y.; Wang, W.; Fernando, K.A.S.; Pathak, P.; Meziani, M.J.; Harruff, B.A.; Wang, X.; Wang, H.; et al. Quantum-Sized Carbon Dots for Bright and Colorful Photoluminescence. *J. Am. Chem. Soc.* **2006**, *128*, 7756–7757. [[CrossRef](#)] [[PubMed](#)]
2. Nie, H.; Li, M.; Li, Q.; Liang, S.; Tan, Y.; Sheng, L.; Shi, W.; Zhang, S.X.A. Carbon Dots with Continuously Tunable Full-Color Emission and Their Application in Ratiometric pH Sensing. *Chem. Mater.* **2014**, *26*, 3104–3112. [[CrossRef](#)]
3. Essner, J.B.; Laber, C.H.; Ravula, S.; Polo-Parada, L.; Baker, G.A. Pee-dots: Biocompatible fluorescent carbon dots derived from the upcycling of urine. *Green Chem.* **2016**, *18*, 243–250. [[CrossRef](#)]
4. Zhai, X.; Zhang, P.; Liu, C.; Bai, T.; Li, W.; Dai, L.; Liu, W. Highly luminescent carbon nanodots by microwave-assisted pyrolysis. *Chem. Commun.* **2012**, *48*, 7955–7957. [[CrossRef](#)] [[PubMed](#)]
5. Qu, S.; Wang, X.; Lu, Q.; Liu, X.; Wang, L. A Biocompatible Fluorescent Ink Based on Water-Soluble Luminescent Carbon Nanodots. *Angew. Chem. Int. Ed.* **2012**, *51*, 12215–12218. [[CrossRef](#)]
6. Wang, X.; Cao, L.; Lu, F.; Meziani, M.J.; Li, H.; Qi, G.; Zhou, B.; Harruff, B.A.; Kermarrec, F.; Sun, Y.P. Photoinduced electron transfers with carbon dots. *Chem. Commun.* **2009**, *25*, 3774–3776. [[CrossRef](#)]

7. Sciortino, A.; Marino, E.; Dam, B.V.; Schall, P.; Cannas, M.; Messina, F. Solvatochromism Unravels the Emission Mechanism of Carbon Nanodots. *J. Phys. Chem. Lett.* **2016**, *7*, 3419–3423. [[CrossRef](#)]
8. Salinas-Castillo, A.; Ariza-Avidad, M.; Pritz, C.; Campubí-Robles, M.; Fernández, B.; Ruedas-Rama, M.J.; Megia-Fernández, A.; Lapresta-Fernández, A.; Santoyo-Gonzalez, F.; Schrott-Fischer, A.; et al. Carbon dots for copper detection with down and upconversion fluorescent properties as excitation sources. *Chem. Commun.* **2013**, *49*, 1103–1105. [[CrossRef](#)]
9. Han, M.; Zhu, S.; Lu, S.; Song, Y.; Feng, T.; Tao, S.; Liu, J.; Yang, B. Recent progress on the photocatalysis of carbon dots: Classification, mechanism and applications. *Nano Today* **2018**, *19*, 201–218. [[CrossRef](#)]
10. Li, X.; Rui, M.; Song, J.; Shen, Z.; Zeng, H. Carbon and Graphene Quantum Dots for Optoelectronic and Energy Devices: A Review. *Adv. Funct. Mater.* **2015**, *25*, 4929–4947. [[CrossRef](#)]
11. Ruan, S.; Qian, J.; Shen, S.; Chen, J.; Zhu, J.; Jiang, X.; He, Q.; Yang, W.; Gao, H. Fluorescent carbonaceous nanodots for noninvasive glioma imaging after angioprep-2 decoration. *Bioconj. Chem.* **2014**, *25*, 2252–2259. [[CrossRef](#)] [[PubMed](#)]
12. Dong, X.; Moyer, M.M.; Yang, F.; Sun, Y.P.; Yang, L. Carbon Dots' Antiviral Functions Against Noroviruses. *Sci. Rep.* **2017**, *7*, 519. [[CrossRef](#)] [[PubMed](#)]
13. Li, Q.; Ohulchanskyy, T.Y.; Liu, R.; Koynov, K.; Wu, D.; Best, A.; Kumar, R.; Bonoiu, A.; Prasad, P.N. Photoluminescent Carbon Dots as Biocompatible Nanoprobes for Targeting Cancer Cells in Vitro. *J. Phys. Chem. C* **2010**, *114*, 12062–12068. [[CrossRef](#)]
14. Huang, X.; Zhang, F.; Zhu, L.; Choi, K.Y.; Guo, N.; Guo, J.; Tackett, K.; Anilkumar, P.; Liu, G.; Quan, Q.; et al. Effect of injection routes on the biodistribution, clearance, and tumor uptake of carbon dots. *ACS Nano* **2013**, *7*, 5684–5693. [[CrossRef](#)]
15. Zheng, M.; Liu, S.; Li, J.; Qu, D.; Zhao, H.; Guan, X.; Hu, X.; Xie, Z.; Jing, X.; Sun, Z. Integrating oxaliplatin with highly luminescent carbon dots: An unprecedented theranostic agent for personalized medicine. *Adv. Mater.* **2014**, *26*, 3554–3560. [[CrossRef](#)]
16. Sciortino, A.; Cannizzo, A.; Messina, F. Carbon Nanodots: A Review—From the Current Understanding of the Fundamental Photophysics to the Full Control of the Optical Response. *J. Carbon Res. C* **2018**, *4*, 67. [[CrossRef](#)]
17. Li, H.; Kang, Z.; Liu, Y.; Lee, S.T. Carbon nanodots: Synthesis, properties and applications. *J. Mater. Chem.* **2012**, *22*, 24230. [[CrossRef](#)]
18. Sachdev, A.; Gopinath, P. Green synthesis of multifunctional carbon dots from coriander leaves and their potential application as antioxidants, sensors and bioimaging agents. *Analyst* **2015**, *140*, 4260–4269. [[CrossRef](#)]
19. Chen, K.L.; Smith, B.A.; Ball, W.P.; Fairbrother, D.H. Assessing the colloidal properties of engineered nanoparticles in water: Case studies from fullerene C60 nanoparticles and carbon nanotubes. *Environ. Chem.* **2010**, *7*, 10–27. [[CrossRef](#)]
20. Bourlinos, A.B.; Zbořil, R.; Petr, J.; Bakandritsos, A.; Krysmann, M.; Giannelis, E.P. Luminescent surface quaternized carbon dots. *Chem. Mater.* **2012**, *24*, 6–8. [[CrossRef](#)]
21. Datta, K.K.R.; Qi, G.; Zboril, R.; Giannelis, E.P. Yellow emitting carbon dots with superior colloidal, thermal, and photochemical stabilities. *J. Mater. Chem. C* **2016**, *4*, 9798–9803. [[CrossRef](#)]
22. Sciortino, L.; Sciortino, A.; Popescu, R.; Schneider, R.; Gerthsen, D.; Agnello, S.; Cannas, M.; Messina, F. Tailoring the Emission Color of Carbon Dots through Nitrogen-Induced Changes of Their Crystalline Structure. *J. Phys. Chem. C* **2018**, *122*, 19897–19903. [[CrossRef](#)]
23. Krysmann, M.J.; Kelarakis, A.; Dallas, P.; Giannelis, E.P. Formation Mechanism of Carbogenic Nanoparticles with Dual Photoluminescence Emission. *J. Am. Chem. Soc.* **2012**, *134*, 747–750. [[CrossRef](#)] [[PubMed](#)]
24. Messina, F.; Sciortino, L.; Popescu, R.; Venezia, A.M.; Sciortino, A.; Buscarino, G.; Agnello, S.; Schneider, R.; Gerthsen, D.; Cannas, M.; et al. Fluorescent nitrogen-rich carbon nanodots with an unexpected  $\beta$ -C<sub>3</sub>N<sub>4</sub> nanocrystalline structure. *J. Mater. Chem. C* **2016**, *4*, 2598–2605. [[CrossRef](#)]
25. Messina, F.; Sciortino, L.; Buscarino, G.; Agnello, S.; Gelardi, F.; Cannas, M. Photoluminescence of Carbon Dots Embedded in a SiO<sub>2</sub> Matrix. *Mater. Today Proc.* **2016**, *3*, S258–S265. [[CrossRef](#)]
26. Carey, F.A.; Giuliano, R. *Organic Chemistry*, 10th ed.; McGraw-Hill Education: New York, NY, USA, 2017.
27. Strelko, V.; Malik, D.J.; Streat, M. Characterisation of the surface of oxidised carbon adsorbents. *Carbon* **2002**, *40*, 95–104. [[CrossRef](#)]

28. Alves, L.A.; De Castro, A.H.; De Mendonça, F.G.; De Mesquita, J.P. Characterization of acid functional groups of carbon dots by nonlinear regression data fitting of potentiometric titration curves. *Appl. Surf. Sci.* **2016**, *370*, 486–495. [[CrossRef](#)]
29. Contescu, A.; Vass, M.; Contescu, C.; Putyera, K.; Schwarz, J.A. Acid buffering capacity of basic carbons revealed by their continuous pK distribution. *Carbon* **1998**, *36*, 247–258. [[CrossRef](#)]
30. Kim, Y.S.; Park, C.R. One-pot titration methodology for the characterization of surface acidic groups on functionalized carbon nanotubes. *Carbon* **2016**, *96*, 729–741. [[CrossRef](#)]
31. Gorgulho, H.F.; Mesquita, J.P.; Gonçalves, F.; Pereira, M.F.R.; Figueiredo, J.L. Characterization of the surface chemistry of carbon materials by potentiometric titrations and temperature-programmed desorption. *Carbon* **2008**, *46*, 1544–1555. [[CrossRef](#)]
32. Sciortino, A.; Mauro, N.; Buscarino, G.; Sciortino, L.; Popescu, R.; Schneider, R.; Giammona, G.; Gerthsen, D.; Cannas, M.; Messina, F.  $\beta$ -C<sub>3</sub>N<sub>4</sub> Nanocrystals: Carbon Dots with Extraordinary Morphological, Structural, and Optical Homogeneity. *Chem. Mater.* **2018**, *30*, 1695–1700. [[CrossRef](#)]
33. Sharma, A.; Gadly, T.; Gupta, A.; Ballal, A.; Ghosh, S.K.; Kumbhakar, M. Origin of Excitation Dependent Fluorescence in Carbon Nanodots. *J. Phys. Chem. Lett.* **2016**, *7*, 3695–3702. [[CrossRef](#)] [[PubMed](#)]
34. Deng, L.; Wang, X.; Kuang, Y.; Wang, C.; Luo, L.; Wang, F.; Sun, X. Development of hydrophilicity gradient ultracentrifugation method for photoluminescence investigation of separated non-sedimental carbon dots. *Nano Res.* **2015**, *8*, 2810–2821. [[CrossRef](#)]
35. Bhattacharjee, S. DLS and zeta potential—What they are and what they are not? *J. Control. Release* **2016**, *235*, 337–351. [[CrossRef](#)]
36. Ohshima, H. A Simple Expression for Henry's Function for the Retardation Effect in Electrophoresis of Spherical Colloidal Particles. *J. Colloid Interface Sci.* **1994**, *168*, 269–271. [[CrossRef](#)]
37. Campos, A.F.C.; Aquino, R.; Tourinho, F.A.; Paula, F.L.O.; Depeyrot, J. Influence of the spatial confinement at nanoscale on the structural surface charging in magnetic nanocolloids. *Eur. Phys. J. E* **2013**, *36*, 42. [[CrossRef](#)]
38. Campos, A.; Tourinho, F.; da Silva, G.; Lara, M.; Depeyrot, J. Nanoparticles superficial density of charge in electric double-layered magnetic fluid: A conductimetric and potentiometric approach. *Eur. Phys. J. E* **2001**, *6*, 29–35. [[CrossRef](#)]
39. Campos, A.F.C.; De Medeiros, W.C.; Aquino, R.; Depeyrot, J. Surface charge density determination in water based magnetic colloids: A comparative study. *Mater. Res.* **2017**, *20*, 1729–1734. [[CrossRef](#)]
40. Dean, J.A. *Lange's Handbook of Chemistry*, 16th ed.; McGraw-Hill Education: New York, NY, USA, 2005.
41. Estes, C.S.; Gerard, A.Y.; Godward, J.D.; Hayes, S.B.; Liles, S.H.; Shelton, J.L.; Stewart, T.S.; Webster, R.I.; Webster, H.F. Preparation of highly functionalized carbon nanoparticles using a one-step acid dehydration of glycerol. *Carbon* **2019**, *142*, 547–557. [[CrossRef](#)]
42. Hunter, R.J. *Foundations of Colloid Science*, 2nd ed.; Oxford University Press: New York, NY, USA, 2001.
43. Sikora, A.; Bartczak, D.; Geißler, D.; Kestens, V.; Roebben, G.; Ramaye, Y.; Varga, Z.; Palmi, M.; Shard, A.G.; Goenaga-Infante, H.; et al. A systematic comparison of different techniques to determine the zeta potential of silica nanoparticles in biological medium. *Anal. Methods* **2015**, *7*, 9835–9843. [[CrossRef](#)]
44. Bandosz, T.J.; Jagiello, J.; Contescu, C.; Schwarz, J.A. Characterization of the surfaces of activated carbons in terms of their acidity constant distributions. *Carbon* **1993**, *31*, 1193–1202. [[CrossRef](#)]
45. Jalil, A.H.; Pyell, U. Quantification of Zeta-Potential and Electrokinetic Surface Charge Density for Colloidal Silica Nanoparticles Dependent on Type and Concentration of the Counterion: Probing the Outer Helmholtz Plane. *J. Phys. Chem. C* **2018**, *122*, 4437–4453. [[CrossRef](#)]
46. Fosdick, L.D.; Loeb, A.L.; Overbeek, J.T.G.; Wiersema, P.H. The Electrical Double Layer Around a Spherical Colloid Particle. *Math. Comput.* **1961**, *15*, 425. [[CrossRef](#)]
47. Russel, W.B.; Saville, D.A.; Schowalter, W.R. *Colloidal Dispersion*; Cambridge University Press: Cambridge, UK, 1992.
48. Wiersema, P.; Loeb, A.; Overbeek, J. Calculation of the electrophoretic mobility of a spherical colloid particle. *J. Colloid Interface Sci.* **1966**, *22*, 78–99. [[CrossRef](#)]
49. Xiao, G.; Wang, Y.; Xu, S.; Li, P.; Yang, C.; Jin, Y.; Sun, Q.; Su, H. Superior adsorption performance of graphitic carbon nitride nanosheets for both cationic and anionic heavy metals from wastewater. *Chin. J. Chem. Eng.* **2019**, *27*, 305–313. [[CrossRef](#)]

50. Ong, W.J.; Tan, L.L.; Chai, S.P.; Yong, S.T.; Mohamed, A.R. Surface charge modification via protonation of graphitic carbon nitride (g-C<sub>3</sub>N<sub>4</sub>) for electrostatic self-assembly construction of 2D/2D reduced graphene oxide (rGO)/g-C<sub>3</sub>N<sub>4</sub> nanostructures toward enhanced photocatalytic reduction of carbon dioxide to. *Nano Energy* **2015**, *13*, 757–770. [[CrossRef](#)]
51. Delgado, A.V.; González-Caballero, F.; Hunter, R.J.; Koopal, L.K.; Lyklema, J. Measurement and interpretation of electrokinetic phenomena. *J. Colloid Interface Sci.* **2007**, *309*, 194–224. [[CrossRef](#)]



© 2019 by the authors. Licensee MDPI, Basel, Switzerland. This article is an open access article distributed under the terms and conditions of the Creative Commons Attribution (CC BY) license (<http://creativecommons.org/licenses/by/4.0/>).

# Journal Name

## ARTICLE TYPE

Cite this: DOI: 00.0000/xxxxxxxxxx

## Colloidal and thermal stabilities of iron oxide nanoparticle dispersions in EMIM TFSI stabilised with sulfonate based imidazolium ions<sup>†</sup>

J. C. Riedl,<sup>a</sup> M. Sarkar,<sup>a</sup> T. Fiuza,<sup>a,b</sup> F. Cousin,<sup>c</sup> J. Depeyrot,<sup>b</sup> E. Dubois,<sup>\*,a</sup> G. Mériquet,<sup>a</sup> R. Perzynski,<sup>a</sup> V. Peyre<sup>a</sup>

Received Date

Accepted Date

DOI: 00.0000/xxxxxxxxxx

The use of ionic liquid-based colloids at elevated temperatures is one of their most promising fields of application. Long-term colloidal and thermal stability needs to be guaranteed at the application conditions for their practical use. Therefore, first the influence of the surface charge density of the nanoparticles as well as the nature and concentration of counterions on the colloidal stability is analysed in oxide nanoparticle dispersions in EMIM TFSI stabilised with sulfonate based imidazolium ions. An optimal surface charge density as well as the amount and nature of counterions are obtained. In a second step, the thermal stability of these nanoparticle dispersions is analysed on the short and long term up to 200°C combining dynamic light scattering (DLS), small angle X-ray/neutron scattering (SAXS/SANS) and thermogravimetric analysis (TGA). Long-term stable ionic liquid-based colloidal dispersions of iron oxide nanoparticles in EMIM TFSI can be obtained at least up to 200°C and nanoparticle concentrations of 12 vol% ( $\approx 30\text{wt}\%$ ).

## 1 Introduction

Ionic liquids (ILs) have a variety of properties such as high electrochemical and thermal stabilities, low vapour pressures, their abilities to dissolve many chemical species, and modest conductivities making them interesting for several fields of applications. Some examples are found in synthesis and catalysis processes<sup>1</sup>, seals and bearings<sup>2</sup>, as well as energy related applications<sup>3,4</sup> such as batteries, super-capacitors and thermoelectric applications<sup>5-7</sup>. However, ionic liquids also have some properties hindering their industrial employment in some fields. For example they generally show elevated viscosities compared to molecular solvents which is connected to poor mass transport properties limiting the performance in energy applications.<sup>3,7</sup> However, the viscosity reduces significantly when the ionic liquids are heated up whereby this disadvantage (almost) vanishes. Therefore, the use of ionic liquids at elevated temperatures is extremely interesting for applications. In addition, the performance of electrochemical devices is improved with increasing temperature. A way to further

improve the system's properties at low and higher temperatures can be the addition of nanoparticles to ionic liquids.<sup>8</sup> The addition of charged nanoparticles to electrolytes of electrochemical devices can, for instance, improve the thermoelectric properties compared to the solvent alone.<sup>9,10</sup>

Several approaches can stabilise nanoparticle dispersions in ionic liquids, ion layering of the ionic liquid around the nanoparticle being one possibility.<sup>11-16</sup> It leads to repulsive (oscillatory) forces that can outrank the attractive Van der Waals forces between the nanoparticles and therefore colloidal stability is obtained. This was shown by molecular dynamics (MD) simulations<sup>11</sup> and X-ray pair distribution analysis<sup>12</sup> of nanoparticle dispersions in molten salts\* and some ionic liquids.

MD simulations of ionic liquids on flat surfaces show that this ion layering at the interface is controlled by the ratio  $\kappa_{ion} = |\sigma / \Theta_{ion}^{max}|$  with  $\sigma$  being the solid's surface charge density and  $\Theta_{ion}^{max}$  being the maximum charge density of a densely packed counterion<sup>†</sup> monolayer.<sup>17</sup> A multilayered structure of ions is formed close to the solid surface if the ratio  $\kappa_{ion} = |\sigma / \Theta_{ion}^{max}|$  is close to 0.5.<sup>17,18</sup> The ion size thereby influences the threshold value  $\Theta_{ion}^{max}$  for the formation of a monolayer. Taking the example for small ions, the smaller the ion the more ions can fit in a monolayer and  $\Theta_{ion}^{max}$  increases. Consequently, a higher surface charge density

<sup>a</sup> Sorbonne Université, Laboratoire PHENIX, 4 place Jussieu, case 51, 75005, Paris, France.

<sup>b</sup> Inst. de Física, Complex Fluid Group, Universidade de Brasília, Brasília, Brazil

<sup>c</sup> Laboratoire Léon Brillouin, UMR 12 CNRS-CEA, CEA-Saclay, 91191, Gif-sur-Yvette, France.

\* Corresponding author: emmanuelle.dubois@sorbonne-universite.fr, veronique.peyre@sorbonne-universite.fr

† Electronic Supplementary Information (ESI) available: [details of any supplementary information available should be included here]. See DOI: 00.0000/00000000.

\* analogue of ionic liquids with a melting temperature above 100°C

† ions of opposite charge compared to the surface

$\sigma$  is needed to obtain a ratio  $\kappa_{ion} \approx 0.5$ . However, the range of variation of the surface charge density  $\sigma$  of nanoparticles is limited. It depends on the material as well as on the coating of the nanoparticles. For instance, the limits for citrate coated iron oxide nanoparticles are between 0 and  $32 \mu\text{C}/\text{cm}^2$ .<sup>19</sup> On the other hand, the counterions can be changed in the system, either by the choice of the ionic liquid itself or by additional ions.

Several works analysing ionic-liquid based colloids evidenced that these additional ions influence the colloidal stability despite their low concentration compared to the ions from the ionic liquid.<sup>14,15,20-22</sup> Furthermore, nanostructure modifications are observed in interface studies between ionic liquids and chargeable surfaces like graphite<sup>23</sup> and gold<sup>24</sup> when adding extra small ions like  $\text{Li}^+$  or  $\text{Cl}^-$ . These ions (even at low concentrations) have an influence as they can locate at the interface.

The use of ionic liquids at elevated temperatures is extremely interesting for applications. To be suitable, the ionic liquid-based systems need to be long-term stable in these application conditions. Some ionic liquids are only decomposed at  $400^\circ\text{C}$  and higher temperatures when analysed in the short term. EMIM TFSI has one of the highest values and is therefore chosen as the ionic liquid here.<sup>25</sup>

In this work, first the colloidal stability of nanoparticle dispersions in the ionic liquid EMIM TFSI is analysed changing the surface charge density as well as the nature and concentration of counterions. Choosing a system where it is possible, the optimal surface charge density as well as the amount and nature of counterions is obtained for charged (magnetic) iron oxide based systems using optical microscopy, dynamic light scattering (DLS) and small angle X-ray scattering (SAXS) measurements. The two best compositions are then analysed by transmission electron microscopy (TEM).

The second part of this work examines the long-term stability of colloids in optimal room temperature conditions found in the first part. As the long-term temperature stability of ionic liquids can be up to a factor two lower than the short term one<sup>26,27</sup>, long-term analysis is necessary to determine suitability for applications. The colloidal dispersions are analysed up to  $200^\circ\text{C}$  for hours combining dynamic light scattering (DLS), small angle X-ray/neutron scattering (SAXS/SANS) as well as thermogravimetric analysis (TGA) supported by DLS measurements over days.

## 2 Materials and Methods

### 2.1 Preparation of ionic liquid-based colloids

The products were purchased and used as received. They are listed in the ESI†. The same batch of maghemite ( $\gamma\text{-Fe}_2\text{O}_3$ ) nanoparticles was used for all experiments. The synthesis<sup>28,29</sup> and the sample characteristics are described in detail in ref.<sup>16</sup>. Briefly, sodium hydroxide solution was added to the initial acid ferrofluid stabilised with nitrate counterions till the point of zero charge was reached at  $\text{pH} \approx 7$ . The free ions were washed off several times with ultra-pure water. The particles can be charged by protonation of the oxide surface with four different strong acids to form hydroxyl groups: triflimidic acid (HTFSI), triflic acid (HTFO), 1-(4-Sulfobutyl)-3-methylimidazolium bistriflimide

(HSBMIM TFSI), and 1-(4-Sulfobutyl)-3-methylimidazolium triflate (HSBMIM TfO). The charge increases while decreasing the pH and it is compensated by the deprotonated form of these four acids, shown in Figure 1. Note that the acids HSBMIM TFSI and HSBMIM TfO are composed of two entities: the protonated cation HSBMIM<sup>+</sup> and the anion TFSI<sup>-</sup> or TfO<sup>-</sup>. The deprotonated form is thus composed of the zwitterion SBMIM<sup>±</sup> and the anion. In HSBMIM TFSI and HSBMIM TfO, the ratio of SBMIM<sup>±</sup> and TFSI<sup>-</sup> or TfO<sup>-</sup> can be varied by adding first HTFSI or HTFO and then SBMIM<sup>±</sup> (which is a powder).

All the initial aqueous dispersions were mixed with a similar volume of the ionic liquid EMIM TFSI (see Figure 1) and the water was removed by freeze-drying. The resulting nanoparticle volume fraction  $\Phi_{NP}$  in the ionic liquid of around 1vol% and the concentration of the initial counterions was hence kept.

The system with HSBMIM TFSI was centrifuged using an Optima 70 ultracentrifuge and a type 100 Ti fixed-angle rotor from the company Beckman Coulter, USA. The samples were centrifuged at 55 000 rpm (243 000g) for 24 hours at  $19^\circ\text{C}$ . Separating the clear supernatant led to concentrated samples with nanoparticle volume fractions  $\phi \approx 10\text{-}20\text{vol}\%$  which were diluted with their supernatant to appropriate concentrations.

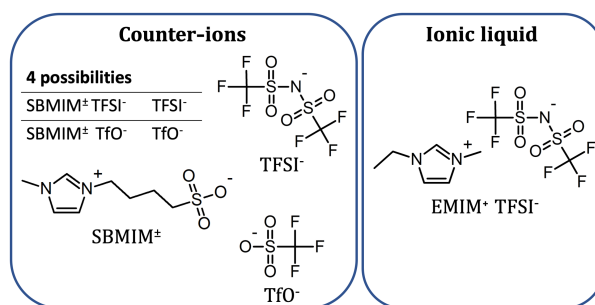


Fig. 1 Structures of the ions 1-(4-butylsulfonate)-3-methylimidazolium (SBMIM<sup>±</sup>), triflate (TfO<sup>-</sup>), bistriflimide (TFSI<sup>-</sup>), and 1-ethyl-3-methylimidazolium (EMIM<sup>+</sup>).

### 2.2 Analyses of the sample

The ionic liquid-based colloids were analysed by optical microscopy in order to detect agglomerates on the micrometre scale. They could also be analysed by transmission electron microscopy (TEM) using a JEOL-100 CX TEM. A droplet of the ionic liquid-based ferrofluids (diluted to around 0.01vol% with pure ionic liquid) was deposited on a carbon-coated copper grid and the backside of the grid was swiped over a paper to remove as much liquid as possible. However, the analysis with TEM needs to be complemented with other techniques as the preparation of the sample for the TEM measurements can affect the sample (e.g. interparticle interactions) due to dilution, exposure to humidity of the air and small analysed volumes (compared to the other techniques employed here). If no major agglomeration is observed in optical microscopy, the samples were analysed by dynamic light scattering (DLS). Light scattering measurements were performed using Vasco, VascoFlex or VascoKin DLS Particle Analyzers from Cor-

douan Technologies to study translational diffusion properties of the ionic liquid-based colloids. Note that the viscosity of the ionic liquid-based colloids is difficult to know accurately as it depends on water traces<sup>30</sup> and on the other additives in the dispersions. However, performed together with other techniques, DLS can give complementary information and the properties of the samples can be analysed in the long-term. As measurements are performed at 1vol% of NPs, only apparent hydrodynamic diameters  $d_H$  are given (see details in the ESI † section S2).

Light scattering was coupled with small angle neutron scattering (SANS) up to 200°C for hours. The setup and the details of the experiments performed on the PAXY spectrometer at the LLB facility (CEA Saclay, France) are described in detail in the ESI †. Three different configurations were used leading to an accessible Q-range of 0.005 Å<sup>-1</sup> to 0.2 Å<sup>-1</sup>.

SAXS experiments were carried out with a laboratory XEUSS 2.0 (W)SAXS. The beam energy was fixed at 8 keV and the wavelength at  $\lambda=1.54$  Å. The sample to detector distance was 3 m to yield an accessible Q-range of 0.005 Å<sup>-1</sup>-0.2 Å<sup>-1</sup>. The samples absorb X-rays due to the ionic liquid EMIM TFSI and due to the iron atoms. Therefore thin capillaries were needed and the best compromise between absorption and diffused signal was obtained with 0.1 mm thick borosilicate capillaries from Vitrocom®. However, the wall thickness of 0.07 mm has an error of ±20% and the interior thickness error is ±10%. As a consequence, absolute intensity could hardly be determined and the high Q region (> 0.1 Å<sup>-1</sup>) was rather noisy. As a conclusion, the nanoparticle volume fraction together with the SANS measurements were used to adjust the SAXS curves to absolute intensities.

The SAXS and SANS form factor  $P(Q)$  of the nanoparticles were obtained from several measurements at low nanoparticle volume fractions in water and these form factors were used to determine structure factors  $S(Q)$  from  $S(Q)=\frac{I(Q)}{\Delta\rho^2V\Phi_{NP}P(Q)}$ . The value of  $S(Q\rightarrow 0)$  therefore compares the studied dispersions to a "reference" dispersion of individual nanoparticles without interparticle interaction. The difference can be due to interparticle interaction or to a change of the scattering objects (for example formation of small aggregates).

Isothermal and ramped temperature thermogravimetric analysis (TGA) were performed with a TGA 550 from TA Instruments. All samples (about 10-20 mg with the mass precision ±0.1 µg) were measured in platinum pans and with a nitrogen gas flow of 40 mL/min. Short-term temperature stabilities were conducted with a heating rate of 10°C/min from room temperature up to 600°C. Long-term temperature stabilities were measured at isothermal mode for several hours at the specified isothermal temperature with a heating rate of 20°C/min from room temperature up to this temperature.

The nanoparticle volume fractions were deduced from the iron concentration determined by flame atomic absorption spectroscopy (FAAS) taking a density of 4.87 g/cm<sup>3</sup><sup>31</sup>.

The technical details and the implementation of the techniques are detailed in the ESI of ref<sup>16</sup>.

## 3 Results and discussion

### 3.1 Decoupled analysis of the optimal counterion concentrations at 1vol% of nanoparticles

In a recent publication<sup>16</sup> it was demonstrated that colloiddally long-term stable dispersions of oxide nanoparticles in EMIM TFSI can be prepared composed of positive nanoparticles with SBMIM<sup>±</sup> TFSI<sup>-</sup> assumed to be at the solid liquid interface. Here, the role of both counterions (the zwitterion SBMIM<sup>±</sup> and the anion TFSI<sup>-</sup>) is analysed in a decoupled way. In addition, SBMIM<sup>±</sup> TFSI<sup>-</sup> is replaced by SBMIM<sup>±</sup> TfO<sup>-</sup> in order to look at the influence of the anion, TfO<sup>-</sup> being smaller than TFSI<sup>-</sup>, its charge coming from a different chemical group.

For this purpose, in a first step the surface charge density is changed in water thanks to pH, beginning with dispersions at 1vol% of NPs. Adding HTFSI or HTfO to the neutral nanoparticles at the point of zero charge, the particles become positive with TFSI<sup>-</sup> or TfO<sup>-</sup> counterions, the charge increasing while pH decreases. The concentration of HTFSI and HTfO was adapted to reach pH values between 5 and 1.3 which convert to concentrations between 0.0035 and 0.075 mol/L. For the studied iron oxide nanoparticles and similar counterions, this converts to a surface charge between around 4 and 30 µC/cm<sup>2</sup>.<sup>19</sup> Note that lowering the pH too much can lead to dissolving of the particles. Therefore the minimum pH was set to pH=1.3 (equivalent of around 30 µC/cm<sup>2</sup>) to prevent particle dissolution.

Adding the zwitterion SBMIM<sup>±</sup> to these samples allows to introduce the second counterion independently so that the ratio of SBMIM<sup>±</sup> to TFSI<sup>-</sup> or TfO<sup>-</sup> can be adjusted.

After transfer to the ionic liquid keeping the NPs concentration at 1vol%, the samples are analysed by DLS measurements and the deduced apparent hydrodynamic diameter  $d_H$  are depicted in Figure 2. Note that the process can be performed in one step by simply adding HSBMIM TFSI or HSBMIM TfO, leading to a ratio SBMIM<sup>±</sup>/ TFSI<sup>-</sup> or TfO<sup>-</sup> equals one. These cases are shown as blue cones.

Several observations can be made with these experiments at a volume fraction  $\phi_{NP} \approx 1$  %.

- 1) Nanoparticles with TFSI<sup>-</sup> or TfO<sup>-</sup> counterions alone are flocculated systems whatever the surface charge densities analysed here (around 4 to 30 µC/cm<sup>2</sup>).
- 2) Adding SBMIM<sup>±</sup> to these systems can stabilise the nanoparticles if the concentration of TFSI<sup>-</sup> or TfO<sup>-</sup> counterions (the surface charge density) is high enough which means that SBMIM<sup>±</sup> localises at least partly at the solid liquid interface.
- 3) In these latter colloiddally stable systems, a higher surface charge density leads to a lower apparent hydrodynamic diameter  $d_H$  for the same SBMIM<sup>±</sup> concentration for both TfO<sup>-</sup> or TFSI<sup>-</sup> added ions.
- 4) In addition, the nature of the first ions introduced (TfO<sup>-</sup> or TFSI<sup>-</sup>) can influence the apparent hydrodynamic diameter  $d_H$  for the same counterion concentrations (surface charge density). For example for a surface charge density of 14 µC/cm<sup>2</sup> (0.014 mol/L TfO<sup>-</sup> or TFSI<sup>-</sup> introduced with the added acid) and a SBMIM<sup>±</sup> concentration of around 0.07 mol/l the apparent hydrodynamic

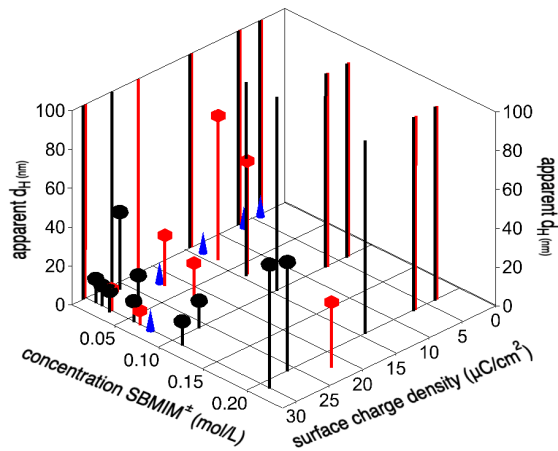


Fig. 2 DLS measurements at  $\phi_{NP}=1\%$  for nanoparticle dispersions in EMIM TFSI with  $\text{TfO}^-$  and  $\text{SBMIM}^+ \text{TfO}^-$  counterions (red boxes) as well as  $\text{TFSI}^-$  and  $\text{SBMIM}^+ \text{TFSI}^-$  counterions (black spheres). The blue cones correspond to a 1:1 ratio between  $\text{SBMIM}^+$  and  $\text{TFSI}^-$ . The corresponding ion structures are depicted in Figure 1. The surface charge density is introduced by the addition of HTFSI or HTFO to the nanoparticles. See text for more information. If only the drop line is visible it means that the apparent hydrodynamic diameter  $d_H$  is higher than 100 nm.

diameter for nanoparticle dispersions containing  $\text{TfO}^-$  is  $\approx 60$  nm, although it is bigger than 100 nm for dispersions with  $\text{TFSI}^-$ .

5) The apparent hydrodynamic diameter  $d_H$  is influenced by the added zwitterion  $\text{SBMIM}^+$  concentration. Starting from aggregated systems with only  $\text{TFSI}^-$  or  $\text{TfO}^-$  counterions, the addition of  $\text{SBMIM}^+$  first decreases the apparent hydrodynamic diameter  $d_H$ , which increases again at higher  $\text{SBMIM}^+$  concentrations. The lowest apparent hydrodynamic diameter  $d_H$  are observed at the maximum surface charge density  $\sigma \approx 30 \mu\text{C}/\text{cm}^2$  which corresponds to a counterion concentration of 0.075 mol/L. A 1:1 ratio of  $\text{SBMIM}^+$  to  $\text{TFSI}^-$  or  $\text{TfO}^-$  ions introduced leads to (one of) the lowest apparent hydrodynamic diameter  $d_H$  and can be added in one step in the form of HSBMIM TFSI or HSBMIM TfO. This makes the process easier and faster and it is thus used for further experiments as it is also more interesting for applications. According to the results presented above, the nanoparticles have thus  $\text{SBMIM}^+ \text{TFSI}^-$  or  $\text{SBMIM}^+ \text{TfO}^-$  counterions, in these two kinds of dispersions.

### 3.2 Room temperature colloidal stabilities

Among the nanoparticle dispersions with the lowest apparent hydrodynamic diameter  $d_H$  analysed in section 3.1 the most interesting for applications (easiest to prepare) are analysed with transmission electron microscopy (TEM) and the images are depicted in Figure 3. They show for both nanoparticles with  $\text{SBMIM}^+ \text{TFSI}^-$  and  $\text{SBMIM}^+ \text{TfO}^-$  counterions that the shape of the nanoparticles is not changed compared to the initial sample in water (TEM picture given in ref<sup>16</sup>). Figure 3 shows that the nanoparticles are not organized in the same way with

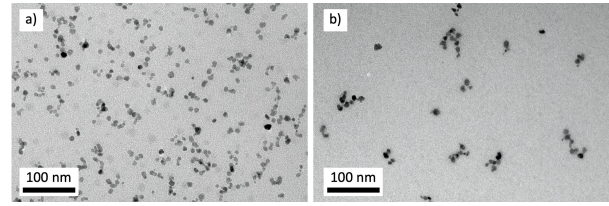


Fig. 3 TEM images of nanoparticles dispersed in the ionic liquid EMIM TFSI with a)  $\text{SBMIM}^+ \text{TFSI}^-$  and b)  $\text{SBMIM}^+ \text{TfO}^-$  counterions. The ion structures are depicted in Figure 1. Both samples were diluted to a nanoparticle volume fraction  $\phi_{NP} \approx 0.01$  vol% with pure EMIM TFSI before the deposition of the ionic liquid-based colloid on the TEM grid.

$\text{SBMIM}^+ \text{TfO}^-$  and  $\text{SBMIM}^+ \text{TFSI}^-$ : they appear rather well dispersed with  $\text{SBMIM}^+ \text{TFSI}^-$  although small loose clusters are observed with  $\text{SBMIM}^+ \text{TfO}^-$ . Although the observation is direct (no drying), the dispersion is highly diluted and the measure itself may modify the system, which does not allow us drawing a definite conclusion.

Figure 4 shows SANS measurements for bare nanoparticles dispersed in EMIM TFSI with  $\text{SBMIM}^+ \text{TFSI}^-$  and  $\text{SBMIM}^+ \text{TfO}^-$  counterions. The structure factors  $S(Q)$  of the samples are depicted which are defined by the ratio between their scattered intensity  $I_{\text{sample}}(Q)$  and the scattered intensity of the sample's form factor  $I_{\text{form factor}}(Q)$  which is equivalent to a sample without interparticle interaction<sup>‡</sup>. Interparticle interactions can be deduced from the value of the structure factor  $S(Q)$  extrapolated to  $Q=0 \text{ \AA}^{-1}$ . If  $S(Q \rightarrow 0)$  is bigger or smaller than 1, the system is attractive or repulsive, respectively. The values for  $S(Q \rightarrow 0)$  are given in the inset of Figure 4 as a function of the temperature and in Figure 5 as a function of the nanoparticle volume fraction  $\phi_{NP}$ . Figure 5 shows the values of  $S(Q \rightarrow 0)$  determined from SANS and SAXS measurements for the same sample batch. From both SAXS and SANS it can be deduced that the global interparticle interactions of the system with  $\text{SBMIM}^+ \text{TfO}^-$  counterions is attractive ( $S(Q \rightarrow 0) > 1$ ) and that of the system with  $\text{SBMIM}^+ \text{TFSI}^-$  counterions is repulsive ( $S(Q \rightarrow 0) < 1$ ). This shows that not only the zwitterion  $\text{SBMIM}^+$  stabilises the nanoparticles but that introducing the additional counterions  $\text{TfO}^-$  or  $\text{TFSI}^-$  also plays a role in the nanostructure at the nanoparticle interface. This means that they need to be situated at the interface (at least in parts) to influence the nanoparticle interactions.

Apparent hydrodynamic diameter  $d_H$  deduced from DLS measurements at  $\phi_{NP}=1\%$  for the nanoparticles with  $\text{SBMIM}^+ \text{TFSI}^-$  counterions is approximately 12 nm (as for the initial water samples,<sup>16</sup>) which proves that no aggregates are present. On the other hand, the sample with  $\text{SBMIM}^+ \text{TfO}^-$  counterions shows an average apparent hydrodynamic diameter  $d_H \approx 25$  nm, which suggests that small aggregates are present in the order of a few particles per aggregate.

Summarizing, the results obtained with small angle scattering,

<sup>‡</sup> The form factor is obtained from the extrapolation at 0 vol% of several dilute colloidal dispersions with low interparticle interactions. See the ESI of<sup>16</sup> for details and the corresponding curve

DLS and TEM at room temperature match well. In the sample with SBMIM<sup>±</sup> TFSI<sup>-</sup> counterions, the system's interparticle interactions are repulsive, which is consistent with the low apparent hydrodynamic diameter and the absence of aggregates in the TEM image (Figure 3). The sample with SBMIM<sup>±</sup> TfO<sup>-</sup> counterions is also colloidally stable, however, the interparticle interaction is slightly attractive as deduced from SANS and SAXS measurements. This is consistent with the higher average apparent hydrodynamic diameter at  $\phi_{NP}=1\%$   $d_H \approx 25$  nm representing around a few particles per cluster, and with the TEM image which shows small clusters. Besides their differences both samples are long-term stable at  $\phi_{NP}=1\%$  at least for one year as shown by SAXS measurements (Figure S2 of the ESI<sup>†</sup>).

However, at larger concentration, attractive ionic liquid-based

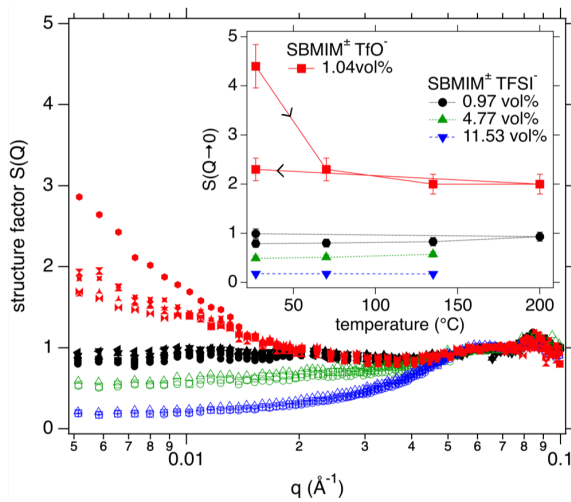


Fig. 4 Structure factors  $S(Q)$  at different temperatures (27°C (○), 70°C (□), 135°C (△), and 200°C (▽) and back at 27°C (◇)) obtained by small angle neutron scattering (SANS) as a function of the scattering vector  $Q$  for nanoparticle dispersions in EMIM TFSI. One sample with SBMIM<sup>±</sup> TfO<sup>-</sup> counterions at  $\phi_{NP}=1.04$  vol% (in red) and three samples with SBMIM<sup>±</sup> TFSI<sup>-</sup> counterions at  $\phi_{NP}=0.97$ , 4.77 or 11.53 vol% (in black, green, and blue, respectively) are shown. The ion structures are depicted in Figure 1. The inset gives the values for  $S(Q \rightarrow 0)$  as a function of temperature. The lines are shown for an optical guideline. Note that both concentrated sample cells leaked at 200°C. Therefore, no further SANS measurements could be obtained (SAXS and DLS could be performed with the remaining sample, the latter being plotted in the inset of Figure 5)

colloids can lead to a phase separation, as shown for citrated iron oxide nanoparticles with sodium counterions in another IL.<sup>32</sup> Hence, here only the nanoparticle system with SBMIM<sup>±</sup> TFSI<sup>-</sup> counterions is concentrated as it is repulsive. The interparticle interactions of the sample system as a function of the nanoparticle volume fraction  $\phi_{NP}$  is analysed by SAXS and SANS measurements. The deduced values of  $S(Q \rightarrow 0)$  are shown in Figure 5 for a repulsive system and equal osmotic compressibilities  $\chi$ . For individually dispersed particles,  $\chi$  is related to the osmotic pressure  $\Pi$ .

$$S(Q \rightarrow 0) = \chi(\phi_{NP}) = \frac{kT}{V_{NP}} \frac{\partial \Phi_{NP}}{\partial \Pi} \quad (1)$$

with  $V_{NP}$  the volume of the nanoparticles. At a low volume fraction  $\Phi_{NP}$ , the second order virial development of  $\Pi$  relates  $\chi(\Phi_{NP})$  with the second order virial coefficient  $A_2$  by:  $\chi(\Phi_{NP}) = (1 + 2A_2\Phi_{NP})^{-1}$ . The osmotic compressibility  $\chi(\Phi_{NP})$  decreases with increasing nanoparticle volume fraction  $\Phi_{NP}$  and therefore the two-bodies interparticle interaction in the dispersion.  $A_2$  is positive and the interparticle interaction is repulsive. In this case, the Carnahan-Starling expression for effective hard spheres<sup>33,34</sup> can be used to analyse the compressibility  $\chi$  up to large volume fractions as in references<sup>21,35-40</sup>. In this model an effective volume fraction  $\Phi_{eff}$  accounts for the decrease of the interparticle interaction through a characteristic length  $\kappa^{-1}$  which is the analogue of the Debye screening length of interparticle electrostatic repulsion in standard polar solvents. Equation (2) describes the compressibility

$$\chi(\Phi_{NP}) = \chi_{CS}(\Phi_{eff}) = \frac{(1 - \Phi_{eff})^4}{1 + 4\Phi_{eff} + 4\Phi_{eff}^2 - 4\Phi_{eff}^3 + \Phi_{eff}^4} \quad (2)$$

with

$$\Phi_{eff} = \Phi \frac{d_{eff}^3}{d_{NP}^3} = \Phi \left( 1 + \frac{2\kappa^{-1}}{d_{NP}} \right)^3 \quad \text{and} \quad d_{eff} = d_{NP} + 2\kappa^{-1} \quad (3)$$

and the two-bodies interparticle interaction  $A_2$  is then

$$A_2 = 4 \frac{\Phi_{eff}}{\Phi} \quad (4)$$

The experimental data of the compressibility is fitted in Figure 5 with the Equations (2) and (3). The best fit is obtained for a fitting parameter  $\kappa^{-1} \approx 1.0$  nm taking  $d_{NP}=8.7$  nm. The associated repulsive interparticle interaction range is 3-5  $\kappa^{-1}$ , hence 3-5 nm. The two-bodies interparticle interaction  $A_2$  is then  $A_2 = 7.8 \pm 0.5$  which is almost the double of the hard sphere value  $A_2^{HS} = 4^{33}$  and of the values obtained for citrate coated oxide nanoparticles in ethylammonium nitrate with sodium counterions and smaller NPs ( $A_2 = 4.6$ ).<sup>15,21</sup>

### 3.3 Thermal stabilities

The long-term stability of the samples needs to be guaranteed on a large range of temperatures to be suitable for applications. Therefore, the two best systems already studied in the previous sections are analysed at high temperatures. These systems are nanoparticles with SBMIM<sup>±</sup> TfO<sup>-</sup> counterions ( $\phi = 1.04$  vol%) and nanoparticles with SBMIM<sup>±</sup> TFSI<sup>-</sup> counterions ( $\phi = 0.97$  vol%, 4.77 vol%, and 11.53 vol%). Several techniques are coupled on different length scales.

Let us begin with the in-situ measurements of SANS and DLS up to 200°C. Given the limited SANS time, few temperatures were chosen (27°C, 70°C, 135°C, 200°C, and back at 27°C). For each step, DLS was performed after heating and enables checking that equilibrium is reached before measuring SANS. This is possible as the viscosity varies with temperature which influences the corre-

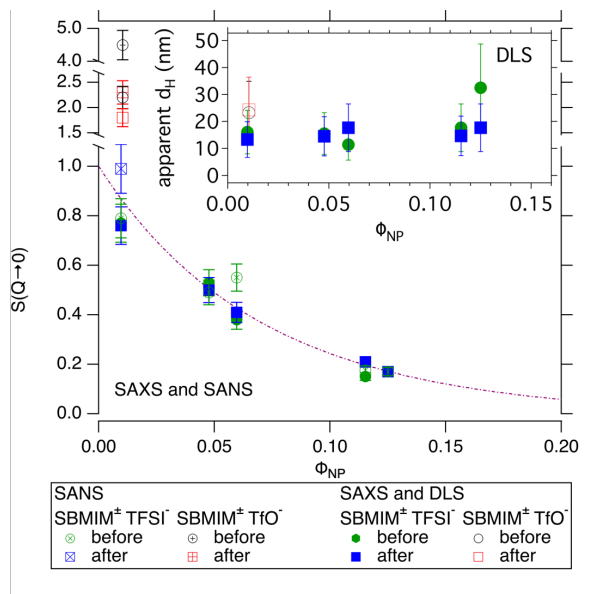


Fig. 5  $S(Q \rightarrow 0)$  deduced from SAXS and SANS measurements at room temperature for  $\text{SBMIM}^{\pm} \text{TFSI}^{-}$  counterions before and after heating the sample for several hours up to  $200^{\circ}\text{C}$  are depicted as a function of the nanoparticle volume fraction  $\phi_{NP}$ . The full line corresponds to the fit of the data with Equations (2) and (3) using  $\phi_{\text{eff}}/\phi = 1.82$  (two-bodies interparticle interaction quantified by the second virial coefficient  $A_2 = 7.8 \pm 0.5$ ). The inset shows apparent hydrodynamic diameter  $d_H$  at room temperature before and after heating the samples for several hours up to  $200^{\circ}\text{C}$  as a function of the nanoparticle volume fraction  $\phi_{NP}$  for both  $\text{SBMIM}^{\pm} \text{TFSI}^{-}$  and  $\text{SBMIM}^{\pm} \text{TfO}^{-}$  counterions. The ion structures are depicted in Figure 1.

lation function. Hence, stability of the correlation function means that the viscosity and temperature is stable. DLS performed after SANS tells us whether some change occurred. One T step lasts around two hours, the whole cycle from  $27^{\circ}\text{C}$  back to  $27^{\circ}\text{C}$  around 10 hours.

The structure factors are plotted in Figure 4 and the DLS is presented as an apparent  $d_H$  in the inset of Figure 5 at  $27^{\circ}\text{C}$  before and after the heating cycle up to  $200^{\circ}\text{C}$ . Note that SAXS before and after heating has also been performed (Figure 5) to complement the analysis.

Looking first at the two samples at  $\phi \approx 1$  vol% with different counterions shows a weak evolution at high temperature (Figure 4 and its inset showing  $S(Q \rightarrow 0)$ ). Indeed, the strong decrease of intensity for nanoparticles with  $\text{SBMIM}^{\pm} \text{TfO}^{-}$  counterions between  $27^{\circ}\text{C}$  and  $70^{\circ}\text{C}$  appears as an accident. The corresponding SAXS measurement at room temperature gives  $S(Q \rightarrow 0) = 2.2 \pm 0.2$ , which matches with the SANS after the cycle. Moreover, the DLS is similar before and after heating. This accident can be due to some pollution (water, solvent,...) that is removed reversibly while heating. Leaving aside this point, the values of  $S(Q \rightarrow 0)$  show that for these nanoparticles with  $\text{SBMIM}^{\pm} \text{TfO}^{-}$  counterions, the same small aggregates/weak attractions remain whatever the temperature. Both the repulsive and the attractive sample appear stable on the time scale of the experiment.

For the nanoparticles with  $\text{SBMIM}^{\pm} \text{TFSI}^{-}$  counterions, the interaction remains weakly repulsive whatever the temperature. However, due to a small increase of  $S(Q \rightarrow 0)$  at  $\phi_{NP} = 0.97\%$  from  $0.83 \pm 0.08$  to  $0.98 \pm 0.10$  after heating, a long-term experiment was performed. The sample was heated several days at three temperatures up to  $170^{\circ}\text{C}$  under vacuum and its state was checked with a DLS measurement at room temperature after each plateau. The results are summarised in Figure 6. The apparent hydrodynamic diameter is  $d_H = 12 \pm 2$  nm showing that the sample is long-term stable at high temperature, here during 18 days.

Analysing now by SANS, SAXS and DLS the behaviour of the con-

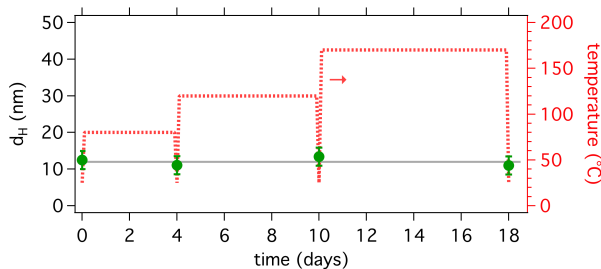


Fig. 6 DLS measurements at room temperature for the iron oxide nanoparticle dispersion with  $\text{SBMIM}^{\pm} \text{TFSI}^{-}$  counterions at a nanoparticle volume fraction  $\phi_{NP} = 0.97$  vol% shown in Figure 4 and 5. The sample was previously heated in a low vacuum of  $\approx 10$  mbar in an open bottle at the indicated temperatures for days. Note that the maximum temperature of the heating device is  $170^{\circ}\text{C}$ . These DLS measurements at room temperature give extra information about temperature cycling.

centrated samples based on nanoparticles with  $\text{SBMIM}^{\pm} \text{TFSI}^{-}$  counterions, the results are quite analogous. Note however that both concentrated sample cells leaked at  $200^{\circ}\text{C}$ , therefore no SANS could be performed. SAXS and DLS after heating were nevertheless measured with the remaining sample. Such a leak already appeared with dilute samples ( $\phi_{NP} \approx 1$  vol%) during the tests of the cell and was solved by adapting the nature of the ring spacer (and the nature of the materials). It appeared as a mixture of wetting phenomena and bubbling/degassing at high temperature, which was not occurring in the same way depending on the nature of the materials used to build the cell. This result shows however that these wetting phenomena and bubbling/degassing grow with  $\phi_{NP}$ .

At high temperature, the structure factors are close to those at room temperature and the compressibilities ( $S(Q \rightarrow 0)$ , Figure 5) after heating are also quite similar (Figure 4). The apparent  $d_H$  differ before and after heating for the concentrated samples (Figure 5, inset), some increasing others decreasing. This is probably due to an underestimated error bar on these values. Indeed, more concentrated samples are more difficult to measure and some pollution introduced by the cell or during the transfer to the oven may change the viscosity (water, solvent,...).

All these elements converge towards a good stability of these concentrated samples at high temperature, keeping the same nanostructure and interaction.

These analysis have been complemented by TGA, which brings an indirect and global information while heating. It elucidates

the maximum application temperatures of the samples in the short and long term. The weight losses and derivative weights of ramped TGA measurements up to 600°C are depicted in Figure 7 for ionic liquids without and with nanoparticles. Several values can be given for the thermal degradation, with  $T_{onset}$  and  $T_{start}$  being among the most popular.<sup>27,41</sup>  $T_{onset}$  is defined by the intersection of the linear extrapolation of the weight loss at decomposition to the baseline weight, either from the beginning of the experiment or after a drying step.<sup>41</sup> This value gives higher decomposition temperatures than  $T_{start}$  that is the temperature at which the sample starts to loose weight. It is here defined for a derivative mass loss of  $1.67 \times 10^{-2} \text{ \%}/^\circ\text{C}$  which represents a weight loss of 10%/1h (for a heating rate of 10°C/min) and is indicated in the graph. We will focus here on  $T_{start}$  values as this gives closer values to long-term applications.

Table 1 gathers the thresholds extracted from TGA either from our measurements (Figure 7) or from literature when available. For the ferrofluids with a nanoparticle volume fraction  $\phi_{NP} \approx 1$  vol%.  $T_{start} = 303 \pm 10^\circ\text{C}$  for both SBMIM<sup>±</sup> TFSI<sup>-</sup> and SBMIM<sup>±</sup> TfO<sup>-</sup> counterions although  $T_{onset}$  for SBMIM<sup>±</sup> TFSI<sup>-</sup> is around 20°C smaller than for the sample with SBMIM<sup>±</sup> TfO<sup>-</sup> counterions.

These curves can be compared to the data for pure EMIM TFSI. The literature values give  $T_{onset}$  in the range of 410 and 450°C and  $T_{start} \approx 320^\circ\text{C}$ ,<sup>26,42,43</sup> values higher than for the ferrofluids analysed here. However, the ferrofluids may contain some water around the nanoparticles which would correspond to 0.15-0.3 vol% if one or two water layers were present at the interface. EMIM TFSI left at air thus containing 0.5 wt% has been measured. It gives  $T_{onset} = 386 \pm 10^\circ\text{C}$  and  $T_{start} = 322 \pm 10^\circ\text{C}$ , lower than dry EMIM TFSI, however, higher than for the ferrofluids. The small difference between the nanoparticle dispersions could also be explained by the TfO<sup>-</sup> ions in the case of SBMIM<sup>±</sup> TfO<sup>-</sup> counterions. EMIM TfO is indeed less stable than EMIM TFSI according both to literature ( $T_{onset} = 348^\circ\text{C}$ ,<sup>44</sup>) and to our measurements with absorbed water ( $\approx 1.5$  wt%).

Another element is however present in the ferrofluids: SBMIM<sup>±</sup> with an amount of around 2.5 wt% for  $\phi \approx 1$  vol%. Hence, dry EMIM TFSI with this amount of HSBMIM TFSI is analysed and gives  $T_{onset} = 401^\circ\text{C}$  and  $T_{start} = 295 \pm 10^\circ\text{C}$ , a little smaller than pure dry EMIM TFSI. The sample with an elevated nanoparticle volume fraction ( $\phi_{NP} = 4.77$  vol%) gives  $T_{start} = 283 \pm 10^\circ\text{C}$ , 20°C lower than for both nanoparticle dispersions at around 1 vol% nanoparticles. Indeed, more concentrated ferrofluids contain more SBMIM<sup>±</sup> and SBMIM<sup>±</sup> appears to be the less stable component of the mixture when measured pure (Figure 7).

Note that partial evaporation of the sample also leads to a weight loss although the sample is not decomposed. EMIM TFSI for example is considered relatively volatile compared to other ionic liquids and its partial pressure at 200°C is 0.02 Pa (calculated with the values of ref<sup>44</sup>). This will be discussed in detail in the following section.

In addition, long term thermal stabilities are analysed in isothermal mode. Figure S5 of the ESI<sup>†</sup> shows that the weight loss for the ionic liquid EMIM TfO is smaller than 0.1% after 10 hours at 200°C (+3 hours at 160°C and 180°C each) however the losses

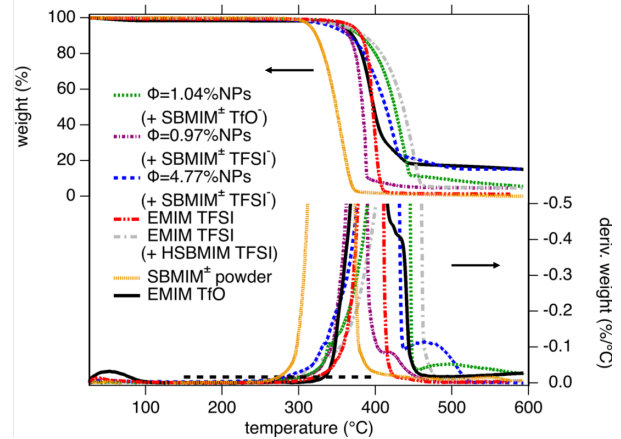


Fig. 7 Ramped thermogravimetric analysis (TGA) measurements for nanoparticle dispersions in EMIM TFSI are depicted with a nanoparticle volume fraction  $\phi_{NP} = 1.04$  vol% with SBMIM<sup>±</sup> TfO<sup>-</sup> counterions as well as  $\phi_{NP} = 0.97$  vol% and a concentrated sample with  $\phi_{NP} = 4.77$  vol% nanoparticles with SBMIM<sup>±</sup> TFSI<sup>-</sup>. Wet EMIM TFSI and wet EMIM TfO as well as dry SBMIM<sup>±</sup> and dry EMIM TFSI containing 2.5wt% HSBMIM TFSI are also depicted, 2.5wt% HSBMIM TFSI being the amount in nanoparticle dispersions with around 1 vol% nanoparticles.  $T_{start}$  is here defined for a derivative mass loss of  $1.67 \times 10^{-2} \text{ \%}/^\circ\text{C}$  representing a weight loss of 10%/1h and is indicated in the graph by the horizontal black dashed line.

for the ferrofluids in EMIM TFSI are larger. (data to complement with new measurements on EMIM TFSI alone to estimate evaporation, on SBMIM+/- TGA should work now. Discuss later when we have these results. )

### 3.4 Discussion

The colloidal stability of the analysed iron oxide nanoparticle dispersions is first discussed in general and then in regard of thermal stability.

A structuring of ions at the solid-liquid interface is proven to be the reason for colloidal stability in ionic liquids and molten salts.<sup>11,12</sup> Simulations of ionic liquids on flat surfaces show that this ion layering at the interface is controlled by the ratio  $\kappa_{ion} = |\sigma / \Theta_{ion}^{max}|$  with  $\sigma$  being the solid's surface charge density and  $\Theta_{ion}^{max}$  being the maximum charge density of a densely packed counterion monolayer.<sup>17</sup> A multilayered structure of positive and negative ions is formed close to the solid surface if the ratio  $\kappa_{ion}$  is close to 0.5.<sup>17,18</sup> Although a curvature of the nanoparticle surface and surface roughness influence the situation it is helpful for a discussion.

Experimentally, both  $\sigma$  and  $\Theta_{ion}^{max}$  are varied in the studied systems,  $\Theta_{ion}^{max}$  through the nature of the ions and  $\sigma$  through the pH of the surrounding medium. Assuming a similar behaviour for the nanoparticle charge for the different counterions<sup>19</sup>,  $\sigma$  is here tuned between 4 and 30  $\mu\text{C}/\text{cm}^2$ .

The  $\Theta_{ion}^{max}$  values of the analysed ions are  $|\Theta_{EMIM+}^{max}| \approx 45 \mu\text{C}/\text{cm}^2$ ,<sup>18</sup>  $|\Theta_{TFSI-}^{max}| \approx 50 \mu\text{C}/\text{cm}^2$ ,<sup>48</sup>  $|\Theta_{TfO-}^{max}| \approx 100 \mu\text{C}/\text{cm}^2$  assuming that it is around half the size of the TFSI<sup>-</sup> anion, and  $|\Theta_{SBMIM\pm}^{max}| \approx 35 \mu\text{C}/\text{cm}^2$  considering that SBMIM<sup>±</sup> is a BMIM<sup>±</sup>

Table 1 Critical temperatures ( $T_{start}$  and  $T_{onset}$ ) deduced from ramped thermogravimetric analysis (TGA) measurements.  $T_{start}$  gives the temperature at which the sample starts to loose weight, here defined for a derivative weight loss of  $1.67 \times 10^{-2} \%$ / $^{\circ}\text{C}$ .  $T_{onset}$  is defined by the linear extrapolation of the weight loss at decomposition to the baseline at zero weight loss. All temperatures are given in  $^{\circ}\text{C}$  and the error is  $\pm 10^{\circ}\text{C}$ . \* losses due to evaporation are removed;  $^i$  for ionic liquid containing water.

	measured		weight loss after 10h at 200 $^{\circ}\text{C}$	literature		$T_{0.01/10h}$ or $T_{0.02/10h}$	$T_{max0.01/year}$
	$T_{start}$	$T_{onset}$		$T_{start}$	$T_{onset}$		
$\phi_{NP}=1.04 \text{ vol}\%$ SBMIM $^{\pm}$ TfO $^{-}$	303	393		-	-		
$\phi_{NP}=0.97 \text{ vol}\%$ SBMIM $^{\pm}$ TFSI $^{-}$	303	374		-	-		
$\phi_{NP}=4.77 \text{ vol}\%$ SBMIM $^{\pm}$ TFSI $^{-}$	283	377		-	-		
EMIM TfO	333 $^i$	373 $^i$	<0.1%		348 <sup>44</sup>		185 <sup>44</sup> *
EMIM TFSI	322 $^i$	386 $^i$	<0.1% <sup>45</sup>	320 <sup>26</sup>	410-450 <sup>26,42,43</sup>	222 <sup>26</sup> or 252 <sup>45</sup>	286 <sup>44</sup> *
EMIM TFSI + 2.5 wt% HSBMIM TFSI	295	401		-	-		
SBMIM $^{\pm}$	274	325					
HSBMIM TFSI	30	305					
HSBMIM HSO $_4$					327 <sup>46</sup>		
HSPMIM TfO					288 <sup>47</sup>		

cation with an extra sulfonate group leading to a slightly smaller  $\Theta_{ion}^{max}$  value.

What can we learn from the results described above? Figure 8 shows two imaginable schemes of the nanoparticle (NP) ionic liquid (IL) interface for the case of SBMIM $^{\pm}$  TFSI $^{-}$  and SBMIM $^{\pm}$  TfO $^{-}$  counterions.

a) The zwitterions SBMIM $^{\pm}$  must locate at the solid-liquid interface as colloidal stability can only be achieved in their presence.

b) For the maximal surface charge density  $\sigma$  (here  $\approx 30 \mu\text{C}/\text{cm}^2$ ), the ratio  $\kappa_{ion} = |\sigma/\Theta_{ion}^{max}|$  for the zwitterion SBMIM $^{\pm}$  is close to 1 meaning that a structure close to a monolayer would be formed on the nanoparticle surface. As SBMIM $^{\pm}$  is a zwitterion this would not change the sign and value of the positive nanoparticle surface charge. The zwitterion SBMIM $^{\pm}$  could hence increase the distance of an ion layering to the nanoparticle surface leading to a bigger repulsion between the nanoparticles.

c) With the negative sulfonate group close to the positive nanoparticle surface, the imidazolium end shows away from the nanoparticle surface, providing a positive charge on the top of the SBMIM $^{\pm}$  layer, which can induce organisation. For this maximal surface charge, stable dispersions are obtained on a large range of SBMIM $^{\pm}$  concentrations (0.01-0.12 mol/L). Note that 0.01 mol/L corresponds to around half a monolayer of SBMIM $^{\pm}$  assuming all these zwitterions located at the nanoparticle interface, and that several hours of stirring are necessary to reach dispersions. This time decreases to a few seconds for higher concentration. The negative charge of the next layer can be the sulfonate of the SBMIM $^{\pm}$  or TfO $^{-}$  or TFSI $^{-}$  depending on the composition. As the properties of the two systems, with either SBMIM $^{\pm}$  TFSI $^{-}$  or SBMIM $^{\pm}$  TfO $^{-}$ , differ (SANS/SAXS, DLS, TEM), this suggests that the TfO $^{-}$  ions localise at least in parts close to the solid-liquid interface (shown in Figure 8b).

At the maximum surface charge density  $\sigma$ , the ratio  $\kappa_{ion} \approx 0.3$

in the case of introduced TfO $^{-}$  anions and  $\kappa_{ion} \approx 0.6$  in the case of TFSI $^{-}$  anions (with the values of ref<sup>18,48</sup>). The latter being closer to 0.5, this could explain the better colloidal stability seen in the experiments for this system, leading to 3-4 more ion layers.<sup>17,18</sup> Considering the size of the ions, this matches well with the value obtained for associated repulsive interparticle interaction in the range of 3-5 nm. The slightly lower colloidal stability of nanoparticle dispersions with SBMIM $^{\pm}$  TfO $^{-}$  counterions could also be explained by a disturbance of the SBMIM $^{\pm}$  monolayer. Both SBMIM $^{\pm}$  and TfO $^{-}$  contain a sulfonate group having an affinity for oxide surfaces.<sup>49,50</sup> A localisation of some TfO $^{-}$  ions would therefore disturb the monolayer of SBMIM $^{\pm}$  zwitterions due to their size difference and hence the multilayer structure formed behind, explaining the difference observed in the colloidal stability.

Looking now at lower surface charge densities  $\sigma$  on samples at 1vol% of NPs, the apparent  $d_H$  increases while the charge decreases until unstable systems are obtained. This is consistent with the decrease of the ratio  $\kappa_{ion} = |\sigma/\Theta_{ion}^{max}|$  far below 0.5, thus a decrease of the number of organised layers. However, there is a difference between SBMIM $^{\pm}$  TfO $^{-}$  and SBMIM $^{\pm}$  TFSI $^{-}$  counterions whatever the surface charge density  $\sigma$ . For lower  $\sigma$ , the behaviour is reversed compared to the one at the maximal charge as the NPs aggregate in smaller clusters with SBMIM $^{\pm}$  TfO $^{-}$  than with SBMIM $^{\pm}$  TFSI $^{-}$ . This result also indicates that TfO $^{-}$  anions are close to the solid-ionic liquid interface, maybe even in the first layer of the SBMIM $^{\pm}$ , modifying the organisation, producing dispersions of small aggregates instead of individual nanoparticles. Let us look now at the thermal stability, starting with the definition of used criteria. Many studies use TGA, and provide  $T_{onset}$ , sometimes  $T_{start}$ , both corresponding to short-term behaviour under gas flow. On the long term, several criteria have been defined, one example being 1% weight loss in 10 hours  $T_{0.01/10h}$ <sup>26</sup> and

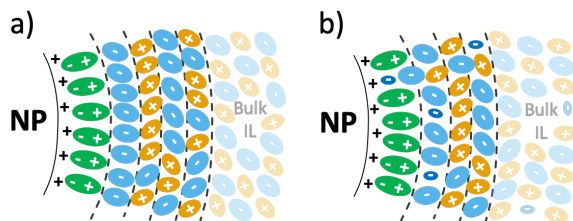


Fig. 8 Schemes of the nanoparticle (NP) ionic liquid (IL) interface for an imaginable case for a) SBMIM<sup>±</sup> TFSI<sup>-</sup> counterions and b) SBMIM<sup>±</sup> TfO<sup>-</sup> counterions. They are shown for a high surface charge density  $\sigma \approx 30 \mu\text{C}/\text{cm}^2$  illustrated by several "+" on the nanoparticle surface. The ions are represented as ellipsoids, the zwitterion SBMIM<sup>±</sup> in green, the cation EMIM<sup>+</sup> in yellow, and the anions TFSI<sup>-</sup> and TfO<sup>-</sup> in light and dark blue, respectively. Here  $\kappa_{\text{SBMIM}^\pm} = |\sigma / \Theta_{\text{SBMIM}^\pm}^{\text{max}}| \approx 1$  leading to a layer (or more) of SBMIM<sup>±</sup> zwitterions acting as a steric component not changing the absolute charge. After the SBMIM<sup>±</sup> zwitterion layer (possibly disturbed by TfO<sup>-</sup> counterions), a multilayer of the ionic liquid ions EMIM<sup>+</sup> and TFSI<sup>-</sup> (and possibly TfO<sup>-</sup> or SBMIM<sup>±</sup> ions) is shown which is obtained due to overscreening of the surface charge at a ratio of  $\kappa_{\text{ion}} = |\sigma / \Theta_{\text{ion}}^{\text{max}}| \approx 0.5$ . After some layers (around 3-4) the bulk ionic liquid structure is recovered, shown here with transparent ions (for more details see text).

another being the maximum operation temperature for an annual decomposition of 1%  $T_{\text{max},0.01/\text{year}}$ <sup>44,51</sup>, a value extrapolated from isothermal measurements on much shorter duration than 1 year. All these values are available here only for EMIM TFSI (see Table 1) and show that  $T_{\text{start}}$  and  $T_{\text{onset}}$  are much larger than  $T_{0.01/10h}$  or  $T_{\text{max},0.01/\text{year}}$ . Nevertheless, it is important to point out that evaporation can occur and is usually not taken into account (except for  $T_{\text{max},0.01/\text{year}}$  in table 1), so that the loss of mass measured is a mixture of evaporation and degradation. Let us consider the case of EMIM TFSI. At 200°C, its vapour pressure is 0.02 Pa (from ref<sup>44</sup>), however a high amount of gas passes in TGA. In 10 hour isothermal measurement, 24 L of gas pass on 30 micro litres (around 20 mg) of sample, thus  $8 \times 10^5 \text{ m}_{\text{gas}}^3 \text{ m}_{\text{ionliquid}}^{-3} \text{ h}^{-1}$ . If the gas saturated immediately (which is far from being the case) this would lead to complete evaporation of EMIM TFSI in around 1 minute which explains why evaporation can be observed in some ionic liquids if the carrier gas absorbs at least a bit. Note that for EMIM TfO, the vapour pressure is 0.002 Pa, 10 times lower.

It means that the degradation is usually overestimated from TGA measurements. Therefore at our maximal temperature of analysis for the ferrofluids here in SANS (200°C), EMIM TFSI can be considered as long-term stable, with no degradation and only evaporation. Another difficulty comes from the additives present in the ferrofluid, not only constituted of iron oxide and EMIM TFSI. SBMIM<sup>±</sup> and HSBMIM are present as well as TfO<sup>-</sup> anions in one of the samples. Such mixtures have never been studied and the only available data concern pure ionic liquids. HSBMIM TFSI was not studied, however some ionic liquids with other anions have been tested like HSBMIM HSO<sub>4</sub><sup>46</sup> and HSPMIM TfO<sup>47</sup>, the latter cation having one carbon separation less between the imidazolium and sulfonate functionalities. The average of their  $T_{\text{onset}}$  values compared to the experimental result here for HSB-

MIM TFSI are similar, however, the latter seeming to evaporate already near room temperature. In ionic liquids, the possible mechanisms of degradation have been explored. Chen *et al.*<sup>52</sup> analysed the temperature stability by TGA-MS of EMIM TFSI and found in their experiments that above 350°C first TFSI decomposes to more nucleophilic groups, such as F, CF<sub>3</sub> and NH<sub>2</sub> that mainly attack the ethyl group of the cation EMIM by elimination and nucleophilic substitution mechanisms. The same is observed for BMIM TfO that also decomposes to methylimidazolium (MIM) and HCF<sub>3</sub>.<sup>53</sup> Ethyl imidazols are the first species that are detected followed by methyl imidazoles. SO<sub>2</sub> is also detected for TFSI and as well for TfO based ionic liquids. Nakurte *et al.*<sup>54</sup> analysed the decomposition mechanisms of different zwitterions dissolved in water, one being close to the zwitterion SBMIM<sup>±</sup> analysed here but with a propyl instead of a butyl side chain. ESI-MS<sup>§</sup> for the compound shows protonation as the most probable. As observed in a lot of other studies for ionic liquids<sup>26,27,52</sup> it is the longer side chain of the imidazolium ring that is cleaved in the highest amount (here 60%) generating propane sulfonate and methylimidazolium. The second most probable mechanism is the elimination of sulfurous acid leaving methyl-propylene-imidazolium (10%).

From literature, it appears that the thermal stability of ionic liquids is governed by nucleophilic anion attack of the cation. Thermal stability is therefore higher for lower nucleophilicity (= higher lewis basicity).<sup>27</sup> As lewis bases (for the anion) lower the degradation temperature, it is assumed that lewis acids (for the cation) do as well. Hence, the (H)SBMIM could be causing the formation of neutral molecules that evaporate after.

From the measurements performed here on the components of the ferrofluids and on the ferrofluids, looking at  $T_{\text{start}}$  and  $T_{\text{onset}}$ , the colloidal dispersions appear less stable than pure EMIM TFSI (T shifted by 20-60°C) which seems to originate from HSBMIM. However the stability is kept at 200°C on the scale of hours from the SANS, SAXS, DLS experiments and TGA shows limits for short-term temperature stability of around 280 to 300°C.

## 4 Conclusions

This work examines charged (magnetic) iron oxide based colloidal systems probed by TEM, DLS, SAXS and SANS varying the (i) the surface charge of the nanoparticles (ii) the nature of the counterions and their concentration (iii) the particle volume fraction. The temperature stability is also explored.

Information could be obtained on the nanoparticle ionic liquid interface. The results indirectly prove that the zwitterions SBMIM<sup>±</sup> locate at the solid-liquid interface as colloidal stability can only be achieved in their presence and at elevated nanoparticle surface charge introduced by HTFSI or HTfO.

Despite the difference in nanostructure between the nanoparticle dispersions (well dispersed and repulsive interparticle interactions with SBMIM<sup>±</sup> TFSI<sup>-</sup> counterions or slightly attractive and having some small loose aggregates with SBMIM<sup>±</sup> TfO<sup>-</sup> counterions) both systems are colloidally stable at  $\phi_{\text{NP}}=1\%$  according

§ Electrospray ionization mass spectrometry

to all the techniques (small angle scattering (SANS and SAXS), dynamic light scattering (DLS)) also in the long term at least for one year. In addition, their colloidal stability is kept up to 200°C which is also the case for higher nanoparticle concentrations up to 12 vol% (for the well dispersed and repulsive interparticle interactions with SBMIM<sup>±</sup> TFSI<sup>-</sup> counterions). Hence, these long term stable ferrofluids are suited for the use in applications.

### Conflicts of interest

There are no conflicts of interest to declare.

### Acknowledgements

We thank Amandine Anfray for DLS measurements, Aude Michel for FAAS measurements, Arnaud Héлары for the design of the coupled DLS-SANS measurement setup at LLB (Laboratoire Léon Brillouin), and Sandra Casale for the TEM images taken at the IMPC (Institut des Matériaux de Paris-Centre). This work has been supported by the European Union Horizon 2020 research and innovation program under the grant number 731976 (MAGENTA). We also acknowledge funding from the Brazilian agency CNPq and the bilaterla program CAPES-COFEUCUB Ph 950/20.

### Notes and references

- 1 T. Welton, *Chemical Reviews*, 1999, **99**, 2071–2084.
- 2 L. Mestrom, J. J. M. Lenders, R. de Groot, T. Hooghoudt, N. A. J. M. Sommerdijk and M. V. Artigas, *Nanotechnology*, 2015, **26**, 285602.
- 3 D. R. MacFarlane, N. Tachikawa, M. Forsyth, J. M. Pringle, P. C. Howlett, G. D. Elliott, J. H. Davis, M. Watanabe, P. Simon and C. A. Angell, *Energy Environ. Sci.*, 2014, **7**, 232–250.
- 4 M. Armand, F. Endres, D. R. MacFarlane, H. Ohno and B. Scrosati, *Materials For Sustainable Energy: A Collection of Peer-Reviewed Research and Review Articles from Nature Publishing Group*, World Scientific, 2011, pp. 129–137.
- 5 M. Bonetti, S. Nakamae, B. T. Huang, T. J. Salez, C. Wiertel-Gasquet and M. Roger, *The Journal of Chemical Physics*, 2015, **142**, 244708.
- 6 E. Laux, S. Uhl, L. Jeandupeux, P. P. López, P. Sanglard, E. Vanoli, R. Marti and H. Keppner, *Journal of Electronic Materials*, 2018, 1–5.
- 7 M. Dupont, D. MacFarlane and J. Pringle, *Chem. Commun.*, 2017, **53**, 6288–6302.
- 8 Z. He and P. Alexandridis, *Advances in Colloid and Interface Science*, 2017, **244**, 54–70.
- 9 B. T. Huang, M. Roger, M. Bonetti, T. J. Salez, C. Wiertel-Gasquet, E. Dubois, R. Cabreira Gomes, G. Demouchy, G. Mériguet, V. Peyre, M. Kouyaté, C. L. Filomeno, J. Depeyrot, F. A. Tourinho, R. Perzynski and S. Nakamae, *The Journal of Chemical Physics*, 2015, **143**, 054902.
- 10 T. J. Salez, B. T. Huang, M. Rietjens, M. Bonetti, C. Wiertel-Gasquet, M. Roger, C. L. Filomeno, E. Dubois, R. Perzynski and S. Nakamae, *Physical Chemistry Chemical Physics*, 2017, **19**, 9409–9416.
- 11 H. Zhang, K. Dasbiswas, N. B. Ludwig, G. Han, B. Lee, S. Vaikuntanathan and D. V. Talapin, *Nature*, 2017, **542**, 328–331.
- 12 V. Kamysbayev, V. Srivastava, N. B. Ludwig, O. J. Borkiewicz, H. Zhang, J. Ilavsky, B. Lee, K. W. Chapman, S. Vaikuntanathan and D. V. Talapin, *ACS Nano*, 2019, **13**, 5760–5770.
- 13 F. C. C. Oliveira, L. M. Rossi, R. F. Jardim and J. C. Rubim, *The Journal of Physical Chemistry C*, 2009, **113**, 8566–8572.
- 14 M. Mamusa, J. Sirieix-Plénet, F. Cousin, E. Dubois and V. Peyre, *Soft Matter*, 2014, **10**, 1097.
- 15 M. Mamusa, J. Sirieix-Plénet, F. Cousin, R. Perzynski, E. Dubois and V. Peyre, *Journal of Physics: Condensed Matter*, 2014, **26**, 284113.
- 16 J. C. Riedl, M. A. Akhavan Kazemi, F. Cousin, E. Dubois, S. Fantini, S. Lois, R. Perzynski and V. Peyre, *Nanoscale Advances*, 2020, **2**, 1560–1572.
- 17 V. Ivaništšev, S. O'Connor and M. Fedorov, *Electrochemistry Communications*, 2014, **48**, 61–64.
- 18 V. Ivanistsev and M. V. Fedorov, *Interface magazine*, 2014, **23**, 65–69.
- 19 I. T. Lucas, S. Durand-Vidal, E. Dubois, J. Chevalet and P. Turq, *J. Phys. Chem. C*, 2007, **111**, 18568–18576.
- 20 C. Guibert, V. Dupuis, J. Fresnais and V. Peyre, *Journal of Colloid and Interface Science*, 2015, **454**, 105–111.
- 21 K. Bhattacharya, M. Sarkar, T. J. Salez, S. Nakamae, G. Demouchy, F. Cousin, E. Dubois, L. Michot, R. Perzynski and V. Peyre, *ChemEngineering*, 2020, **4**, 5.
- 22 J. Nordström, L. Aguilera and A. Matic, *Langmuir*, 2012, **28**, 4080–4085.
- 23 A. Elbourne, S. McDonald, K. Voichovsky, F. Endres, G. G. Warr and R. Atkin, *ACS Nano*, 2015, **9**, 7608–7620.
- 24 R. Hayes, N. Borisenko, B. Corr, G. B. Webber, F. Endres and R. Atkin, *Chemical Communications*, 2012, **48**, 10246.
- 25 S. Werner, M. Haumann and P. Wasserscheid, *ANNUAL REVIEW OF CHEMICAL AND BIOMOLECULAR ENGINEERING, VOL 1, ANNUAL REVIEWS*, 4139 EL CAMINO WAY, PO BOX 10139, PALO ALTO, CA 94303-0897 USA, 2010, vol. 1, pp. 203–230.
- 26 Y. Cao and T. Mu, *Ind. Eng. Chem. Res.*, 2014, **53**, 8651–8664.
- 27 C. Maton, N. D. Vos and C. V. Stevens, *Chemical Society Reviews*, 2013, **42**, 5963–5977.
- 28 R. Massart, *IEEE transactions on magnetics*, 1981, **17**, 1247–1248.
- 29 J.-P. Jolivet and E. Tronc, *Journal of Colloid and Interface Science*, 1988, **125**, 688–701.
- 30 K. Padaszyński and U. Domańska, *Journal of Chemical Information and Modeling*, 2014, **54**, 1311–1324.
- 31 U. Schwertmann and R. M. Cornell, *Iron Oxides in the Laboratory: Preparation and Characterization*, John Wiley & Sons, 2008.
- 32 M. Mamusa, J. Sirieix-Plénet, R. Perzynski, F. Cousin, E. Dubois and V. Peyre, *Faraday Discussions*, 2015, **181**, 193–209.
- 33 N. F. Carnahan and K. E. Starling, *The Journal of Chemical Physics*, 1970, **53**, 600–603.

- 34 J. A. Barker and D. Henderson, *The Journal of Chemical Physics*, 1967, **47**, 4714–4721.
- 35 M. Sarkar, J. C. Riedl, G. Demouchy, F. Gélébart, G. Mériquet, V. Peyre, E. Dubois and R. Perzynski, *Eur. Phys. J. E*, 2019, **42**, 72.
- 36 M. Kouyaté, C. L. Filomeno, G. Demouchy, G. Mériquet, S. Nakamae, V. Peyre, M. Roger, A. Cēbers, J. Depeyrot, E. Dubois and R. Perzynski, *Physical Chemistry Chemical Physics*, 2019, **21**, 1895–1903.
- 37 E. Wandersman, A. Cēbers, E. Dubois, G. Mériquet, A. Robert and R. Perzynski, *Soft Matter*, 2013, **9**, 11480.
- 38 C. L. Filomeno, M. Kouyaté, V. Peyre, G. Demouchy, A. F. C. Campos, R. Perzynski, F. A. Tourinho and E. Dubois, *The Journal of Physical Chemistry C*, 2017, **121**, 5539–5550.
- 39 C. Lopes Filomeno, M. Kouyaté, F. Cousin, G. Demouchy, E. Dubois, L. Michot, G. Mériquet, R. Perzynski, V. Peyre, J. Sirieix-Plénet and F. Tourinho, *Journal of Magnetism and Magnetic Materials*, 2017, **431**, 2–7.
- 40 R. Cabreira Gomes, A. Ferreira da Silva, M. Kouyaté, G. Demouchy, G. Mériquet, R. Aquino, E. Dubois, S. Nakamae, M. Roger, J. Depeyrot and R. Perzynski, *Phys. Chem. Chem. Phys.*, 2018, **20**, 16402–16413.
- 41 C. P. Fredlake, J. M. Crosthwaite, D. G. Hert, S. N. V. K. Aki and J. F. Brennecke, *J. Chem. Eng. Data*, 2004, **49**, 954–964.
- 42 W. H. Awad, J. W. Gilman, M. Nyden, R. H. Harris, T. E. Sutto, J. Callahan, P. C. Trulove, H. C. DeLong and D. M. Fox, *Thermochimica Acta*, 2004, **409**, 3–11.
- 43 H. L. Ngo, K. LeCompte, L. Hargens and A. B. McEwen, *Thermochimica Acta*, 2000, **357-358**, 97–102.
- 44 F. Heym, B. J. M. Etzold, C. Kern and A. Jess, *Green Chem.*, 2011, **13**, 1453.
- 45 M. Villanueva, A. Coronas, J. García and J. Salgado, *Ind. Eng. Chem. Res.*, 2013, **52**, 15718–15727.
- 46 J. Gui, H. Ban, X. Cong, X. Zhang, Z. Hu and Z. Sun, *Journal of Molecular Catalysis A: Chemical*, 2005, **225**, 27–31.
- 47 A. S. Amarasekara and O. S. Owereh, *J Therm Anal Calorim*, 2011, **103**, 1027–1030.
- 48 S. A. Kislenko, Y. O. Moroz, K. Karu, V. B. Ivaništšev and M. V. Fedorov, *Russian Journal of Physical Chemistry A*, 2018, **92**, 999–1005.
- 49 X. Lu, S. Deng, B. Wang, J. Huang, Y. Wang and G. Yu, *Journal of Colloid and Interface Science*, 2016, **474**, 199–205.
- 50 E. Potapova, R. Jolsterå, A. Holmgren and M. Grahn, *Journal of Surfactants and Detergents*, 2014, **17**, 1027–1034.
- 51 A. Seeberger, A.-K. Andresen and A. Jess, *Phys. Chem. Chem. Phys.*, 2009, **11**, 9375.
- 52 Y. Chen, Y. Cao, Y. Shi, Z. Xue and T. Mu, *Ind. Eng. Chem. Res.*, 2012, **51**, 7418–7427.
- 53 H. Ohtani, S. Ishimura and M. Kumai, *Anal. Sci.*, 2008, **24**, 1335–1340.
- 54 I. Nakurte, P. Mekss, K. Klavins, A. Zicmanis, G. Vavilina and S. Dubrovina, *Eur J Mass Spectrom (Chichester)*, 2009, **15**, 471–478.

## Journal Name

## ARTICLE TYPE

Cite this: DOI: 00.0000/xxxxxxxxxx

## Thermodiffusion anisotropy under magnetic field in ionic liquid-based ferrofluids

T. Fiuza,<sup>a,b</sup> M. Sarker,<sup>a</sup> J.C. Riedl,<sup>a</sup> A. Cēbers,<sup>c</sup> F. Cousin,<sup>d</sup> G. Demouchy,<sup>a,e</sup> J. Depeyrot,<sup>b</sup> E. Dubois,<sup>a</sup> F. Gélébart,<sup>a</sup> G. Mériquet,<sup>a</sup> R. Perzynski,<sup>a,\*</sup> and V. Peyre<sup>a</sup>

Received Date

Accepted Date

DOI: 00.0000/xxxxxxxxxx

Ferrofluids based on maghemite nanoparticles, typically 10 nm in diameter, are dispersed in an ionic liquid (1-ethyl 3-methylimidazolium bistriflimide - EMIM-TFSI). The average interparticle interaction is found repulsive by small angle scattering of x-rays and of neutrons, with a second virial coefficient  $A_2 = 7.3$ . A concentrated sample at  $\Phi = 5.95$  vol% is probed by forced Rayleigh scattering under an applied magnetic field (up to  $H = 100$  kA m<sup>-1</sup>) from room temperature up to  $T = 460$  K. The in-field anisotropy of the mass diffusion coefficient  $D_m$  and that of the (always positive) Soret coefficient  $S_T$  are well described by the presented model in the whole range of  $H$  and  $T$ . The main origin of the under-field anisotropy comes from the spatial inhomogeneities of concentration in the ferrofluid along the applied field. Being tightly connected with the magnetic dipolar interparticle interaction, the anisotropy of thermodiffusion progressively vanishes when temperature increases.

## 1 Introduction

Ferrofluids<sup>1–4</sup> based on Ionic Liquids (FF-ILs) are new colloidal materials, developed for improving thermoelectric low-grade energy harvesting<sup>5–9</sup>. In classical ionic ferrofluids based on polar solvents, it has been recently shown that the application of a magnetic field is able to improve the thermoelectric properties of the material<sup>10</sup>. The move here to a new family of solvents, Ionic Liquids (ILs) brings new properties, among which access to a wide range of temperatures  $T$ <sup>11</sup>. In these ionic liquids, which are molten salts at low  $T$ 's only composed of anions and cations, the colloidal dispersions of nanoparticles (NPs) has been shown to be possible despite the ILs' internal structure totally different from that of molecular solvents. NPs either coated by polymers,<sup>12–17</sup> or coated with shorter surfactant chains, or even bare charged NPs<sup>17–23</sup> have been dispersed. Among the extreme variety of room temperature ionic liquids<sup>24–26</sup>, EMIM-TFSI (1-Ethyl-3-methylimidazolium bistriflimide) which is a widely used IL in applications<sup>27–29</sup>, can be considered as an important model system, since it is not too viscous at room temperature and stable in a large range of  $T$ <sup>11,26,30,31</sup>. Hydroxyl-coated maghemite NPs, synthesized in water (diameter  $\sim 10$  nm) are modified in order

to adapt the NP/ solvent interface, i.e. the charge and the nature of the counterions, both shown to be crucial<sup>17,20,21</sup>. After a liquid-liquid transfer from water to the IL, stable dispersions are obtained, that can be concentrated up to  $\sim 12$  vol% in EMIM-TFSI<sup>17,32</sup>, these dispersions remaining stable (from both a chemical and a colloidal point of view) at least up to 473 K<sup>32</sup>.

Our aim is here to probe the under-field anisotropy of the NP's thermodiffusive properties at various temperatures, in terms of Soret coefficient  $S_T$  and diffusion coefficient  $D_m$ <sup>33</sup>. A Forced Rayleigh scattering experiment<sup>34–41</sup> is undertaken, under an applied magnetic field, in a wide range of temperatures  $T$  (from room temperature up to  $\sim 460$  K), using a moderately concentrated dispersion ( $\Phi = 5.95$  vol%) in order to render easier the under-field anisotropy measurement. As in<sup>33</sup> for aqueous ferrofluids at room temperature, the results are here analysed according to the model developed in<sup>42</sup>. To perform these adjustments, it is of paramount importance to probe independently the interparticle interaction in the colloidal dispersion. Small Angle Neutron Scattering (SANS) and Small Angle X-ray Scattering (SAXS) experiments are thus also undertaken to determine the osmotic compressibility  $\chi$  of the NP's system and the corresponding second virial coefficient in the colloidal dispersion<sup>23,43</sup>.

In the next section we present the colloidal system, briefly recalling how it is prepared and the proposed origin of its stability, together with the probing by SAXS and SANS measurements of the interparticle repulsion. The third section is devoted to the forced Rayleigh scattering experiments and the obtained results. The fourth section recalls the theoretical model used here to interpret the measurements. The last section presents a global dis-

<sup>a</sup> Sorbonne Université, CNRS, Lab. PHENIX, 4 Place Jussieu, F-75005 Paris, France.<sup>b</sup> Grupo de Fluidos Complexos, Inst. de Física, Univ. de Brasília, Brasília (DF), Brazil.<sup>c</sup> MML Lab, Faculty of Physics and Mathematics, University of Latvia, Zellu-8, LV-1002 Riga, Latvia.<sup>d</sup> Lab. Léon Brillouin - UMR 12 CNRS-CEA CEA-Saclay, 91191 Gif-sur-Yvette, France.<sup>e</sup> Dpt de physique, Univ. de Cergy Pontoise, 33 Bd du Port, 95011 Cergy-Pontoise, France.

\* corresponding author, regine.perzynskit@sorbonne-universite.fr

ussion of the whole study.

## 2 Magnetic Fluid samples

### 2.1 Synthesis

The magnetic nanoparticles used here are chemically synthesized using a well-known aqueous coprecipitation method<sup>44,45</sup>. From the analysis of magnetic measurements (VSM), their size distribution can be described by a log-normal distribution of median diameter 8.9 nm and a polydispersity index 0.23, leading to a volume-averaged diameter  $d_{NP} = 9.6 \text{ nm}^2$ . The details of the preparation of their dispersions in EMIM-TFSI are given extensively in<sup>17</sup>. Here is a short summary of the process. Firstly, the interface of the NPs is modified in water: a structural charge  $Z \sim +400 \pm 100$  is introduced. The species compensating their charge are deprotonated 1-(4-sulfobutyl)-3-methylimidazolium bistriflimide ( $\text{SMIM}^+ \cdot \text{TFSI}^-$ ) which has been shown to be close to the interface<sup>17</sup>. Secondly, the ionic liquid is added and the water removed by freeze-drying, leading to NPs in pure EMIM-TFSI. All the process is performed with a volume fraction of NPs around 1%.

EMI-TFSI is a room-temperature ionic liquid, here supplied by Solvionic, with a viscosity ranging from  $4 \times 10^{-2} \text{ Pa s}$  at 294 K down to  $3 \times 10^{-3} \text{ Pa s}$  at 460 K (following<sup>26</sup>). It presents a low vapor pressure, a low flammability, a high ionic conductivity and a wide electro-chemical window<sup>11,26,31</sup>. It is also chemically stable up to high temperature (long-term  $\sim 500 \text{ K}$  and up to  $\sim 700 \text{ K}$  for shorter times<sup>11</sup>), making it a good candidate for thermoelectrical applications<sup>46</sup>. The colloidal dispersions of the used maghemite NPs have been reported as being stable at room temperature in<sup>17</sup> with a repulsive interparticle interaction.

A series of samples at various volume fractions  $\Phi$  have been produced by ultracentrifugation of the initial dispersion at  $\Phi \sim 1\%$ , following the method described in<sup>32</sup>.

### 2.2 Colloidal stability - Interparticle interaction

Small Angle X-ray Scattering (SAXS) experiments were carried out with the XEUSS 2.0 (Xenocs) of LLB-Saclay at room temperature on dispersions at several volume fractions  $\Phi$ 's between 0.2 % and 12 %. Complementary Small Angle Neutron Scattering (SANS) experiments were performed at PAXY spectrometer in Orphée - LLB - Saclay at various  $T$ 's ranging between 293 K and 473 K. All these experiments were performed without applied magnetic field. The scattered intensity  $I(q)$ , analyzed as in<sup>47,48</sup>, shows that the interparticle interaction is repulsive indeed. The determination of the intensity at low scattering vector ( $q \rightarrow 0$ ) leads to the osmotic compressibility  $\chi$  of the NP's system, which is related to the osmotic pressure  $\Pi$  of the NP's system by the following relation:

$$\chi = \frac{kT}{\left(\frac{\partial \Pi_{v_{NP}}}{\partial \Phi}\right)_T}, \quad (1)$$

where  $v_{NP}$  is the NP's volume. The experimental results at room temperature and zero magnetic field are shown in Fig. 1. More-

over it has been checked that  $\chi$  does not present any temperature dependence in the experimental  $T$ -range. As shown by Fig. 1, the  $\Phi$ -dependence of  $\chi$  can be described by the Carnahan-Starling formalism<sup>43,49</sup> with effective hard spheres of volume fraction  $\Phi_{\text{eff}} = 1.82 \Phi$  and a second virial coefficient  $A_2 = 7.3$ .

The colloidal stability of the samples under-field up to  $H = 716 \text{ kA m}^{-1}$  ( $= 9000 \text{ Oe}$ ) has been checked optically, looking at the scattering pattern of a non-absorbing laser beam, as described in<sup>17,50</sup>.

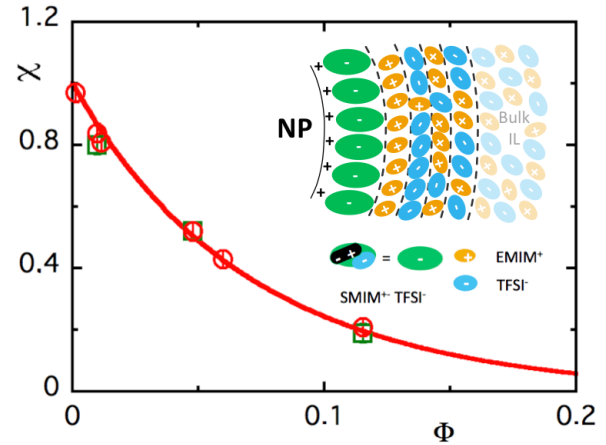


Fig. 1 Main figure: Osmotic compressibility  $\chi$  of the NPs in the colloidal dispersions as a function of their volume fraction  $\Phi$  - Open symbols: Experimental determinations at room temperature by SAXS (open circles) and SANS (open squares) - Full line: Carnahan-Starling adjustment with effective hard spheres<sup>43,49</sup> of volume fraction  $\Phi_{\text{eff}} = 1.82 \Phi$  leading to  $A_2 = 7.3$ ; Inset: Sketch of the ionic layering around the NPs responsible for the colloidal stability of the dispersion. The first layers close to NPs figure the hydroxyl ionic NP surface and some condensed  $\text{SMIM}^+ \cdot \text{TFSI}^-$  counterions, they initiate the long-range IL layering.

The colloidal stability of these samples, both in zero field and under-field, proves that a strong interparticle repulsion exists, which dominates the two kinds of interparticle attractions that are present here, van der Waals attraction (which is isotropic and is present in any colloid) and magnetic dipolar interaction (which is anisotropic and attractive on average, which is present in magnetic colloids such as those studied in the present work).

It has been proven both experimentally<sup>51-53</sup> and by numerical simulations<sup>54-58</sup> that along a flat and charged interface, Ionic Liquids can organize themselves as layers of ions, of alternate sign. Along a curved interface such as that of the present charged NPs<sup>22,59</sup>, long-range charge-density oscillations can be also formed, for given geometrical and charged conditions of the IL anions and cations<sup>17,57,60</sup>. If the number of organized layers is large enough, they are able to overcome attractive component of the interparticle interaction (usually van der Waals attraction) and stable colloidal dispersions can be obtained<sup>17,20,22</sup>. The colloidal stability of the present NPs in EMI-TFSI is thus proposed to come here from the "effective" interparticle repulsion, due to the regular layering of ions, of alternate sign, around the NPs (see the sketch in the inset of Fig. 1), which dominates both van der

Waals and magnetic dipolar interparticle attractions. Here the resultant screening  $\kappa^{-1}$  of the repulsive (on average) interparticle interaction can be extracted from the Carnahan-Starling adjustment of  $\chi(\Phi)$ , writing  $\Phi_{\text{eff}}/\Phi$  as  $[(d_{\text{NP}} + 2\kappa^{-1})/d_{\text{NP}}]^3$ <sup>23</sup>. It leads to  $\kappa^{-1} \sim 1.1$  nm, which means that the structure of the liquid is modified on few  $\kappa^{-1}$ , typically up to  $5 \kappa^{-1}$ , which corresponds to 6-7 layers of anions and cations from the IL<sup>28</sup>.

### 3 Forced Rayleigh Experiment

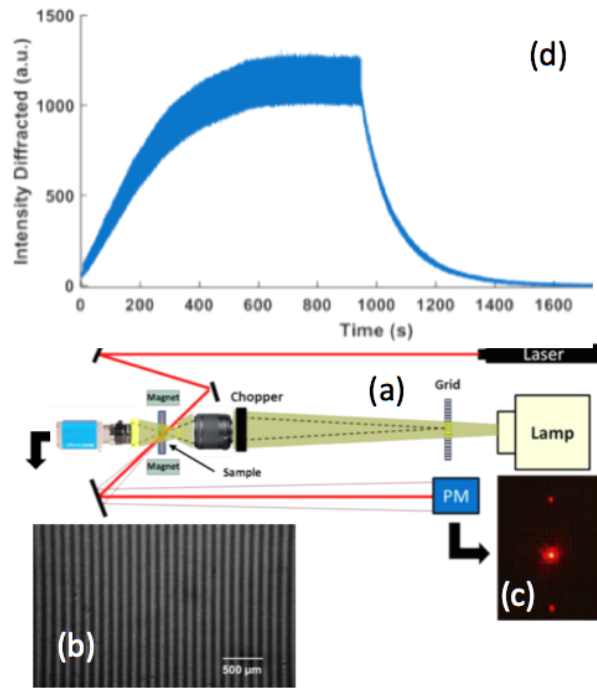


**Fig. 2** Forced Rayleigh scattering device: (a) Experimental set-up, seen from above; The Hg-lamp illuminates a grid, the image of which is made, periodically at a few Hz, in the thermalized sample, eventually submitted to an horizontal magnetic field  $\vec{H}$ ; Both a thermal and a concentration arrays are induced in the sample (for more details see text); Their temporal evolution is observed by the diffraction of a He-Ne laser beam; (b) Direct observation of the image of the grid in the sample; (c) Diffracted pattern of the He-Ne laser beam by the temperature and concentration arrays; (d) Recorded intensity of the first order diffraction at  $\Phi = 5.95\%$  as a function of time; When the heating beam is cut, the recorded intensity relaxes towards zero.

#### 3.1 Experimental device

The setup we use for these forced Rayleigh scattering\* (FRS) measurements (see Fig. 2) has been initially presented in ref.<sup>38</sup>. A high power lamp (Oriol 6285 - 500 W - Hg Arc Lamp) illuminates a grid, the image of which is made in the liquid sample, put in

a thin and thermalized optical cell (of thickness  $e = 25 \mu\text{m}$ ). Because of the strong optical absorption of the maghemite NPs a thermal grating of time-dependent amplitude  $\Delta T(t)$  and of spatial period  $\Lambda$  ranging between 88 and 145  $\mu\text{m}$ , is created in the NP dispersion. A concentration grating of amplitude  $\Delta\Phi(t)$  with the same spatial period  $\Lambda$  is then induced thanks to the Ludwig-Soret effect<sup>61,62</sup>. Both the thermal and the concentration gratings are here probed with the first order diffraction of a He-Ne laser beam, which is poorly absorbed by these dispersions. The Soret coefficient  $S_T$  links the applied temperature gradient  $\vec{\nabla}T$  and the induced volume-fraction gradient  $\vec{\nabla}\Phi$ , in the following way:

$$\vec{\nabla}\Phi = -\Phi S_T \vec{\nabla}T. \quad (2)$$

$S_T$  is obtained here by means of a modulation at 4 Hz of the Hg lamp intensity (the thermal response of the system being by orders of magnitude faster than the concentration one) and thanks to the knowledge of  $\partial n/\partial T$  and  $\partial n/\partial\Phi$ <sup>†</sup> (for details see<sup>41</sup> and its E.S.I.). If  $\Delta\Phi_{\text{St}}$  is the spatial modulation of volume fraction in stationary conditions, we obtain:

$$S_T = -\frac{\Delta\Phi_{\text{St}}}{\Phi\langle\Delta T\rangle}, \quad (3)$$

$\Delta\Phi_{\text{St}}$  being negative with the convention of<sup>41</sup> and  $\langle\Delta T\rangle$  being the time-averaged spatial modulation of temperature. As an example, at  $\Phi = 5.95\%$ , we obtain here  $|\Delta\Phi_{\text{St}}|/\Phi \leq 10^{-2}$  and  $\langle\Delta T\rangle \leq 0.1$  K whatever the amplitude and the direction of the applied field  $\vec{H}$  and whatever  $T$ .

Switching off the Hg lamp makes the concentration grating relax as well as the modulation of the optical index related to  $\Delta\Phi(t)$  and thus also the intensity of the diffracted beam (see Fig. 2(d)), allowing a determination of the mass diffusion coefficient  $D_m$  of the NPs.

$$\Delta\Phi(t) = \Delta\Phi_{\text{St}} e^{-q^2 D_m t} \quad (4)$$

with  $q = 2\pi/\Lambda$ .

The sample environment is thermo-regulated (here temperature  $T$  may vary from room temperature up to 460 K). It is also possible to apply an horizontal magnetic field  $\vec{H}$ , homogeneous at the scale of the sample, thanks to movable magnetic polar pieces (here  $H$  may vary from 0 up to 100  $\text{kA m}^{-1}$ ), making possible to determine both  $S_T(H, T)$  and  $D_m(H, T)$  in a large range of temperature and magnetic field. The under-field anisotropy of  $S_T(H, T)$  and  $D_m(H, T)$  is probed by orienting the temperature gradient (and thus also the concentration gradient) either horizontally or vertically, optical cell and grating being both in the vertical plane.

It is checked that the measured  $S_T$  is independent of  $\Lambda$  and of the power of the Hg lamp (the experimental range is limited to

\*Forced Rayleigh scattering implies forced inhomogeneities with respect to the spontaneous fluctuations observed in a classical Rayleigh scattering experiment<sup>34</sup>.

†The derivative  $\partial n/\partial T$  is taken equal  $-2.82 \times 10^{-4} \text{ K}^{-1}$  and independent of  $T$  in our range of  $T$  from the optical index measurement of<sup>63</sup> (even if only measured up to 353 K) and  $\partial n/\partial\Phi = 0.97$  as calculated from<sup>64</sup>.

the power linear regime<sup>65</sup>). In-field measurements are performed at ratios sample thickness  $e$  over spatial period  $\Lambda$ , such that  $0.17 < e/\Lambda < 0.28$ , thus in the 2D-array conditions. The experiments are also performed at magnetic fields  $\vec{H}$  below the threshold of 2D magnetoconvection<sup>66,67</sup>.

### 3.2 Experimental results in zero field

Fig. 3 presents the values of  $D_m$  (main figure) and  $S_T$  (inset) obtained experimentally in zero magnetic field at various temperatures  $T$  and volume fractions  $\Phi$ .

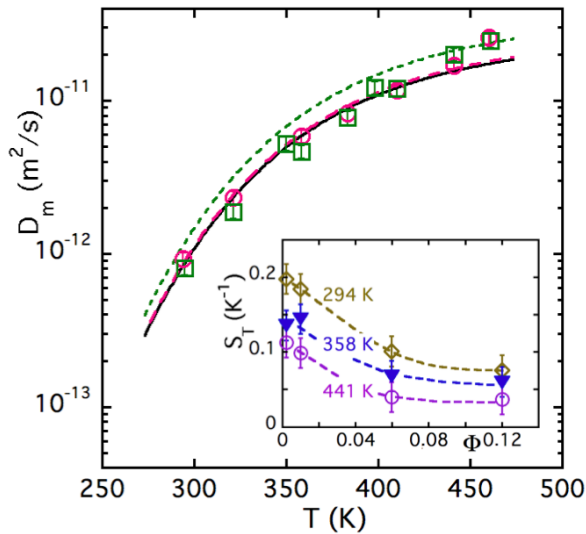


**Fig. 3** *Main figure*: Diffusion coefficient  $D_m$  as a function of  $T$  at  $\Phi = 1\%$  (open circles) and  $5.95\%$  (open squares); Full line corresponds to Eq. 7; Dashed (resp. dotted) line corresponds to Eq. 5 using  $\chi = 0.86$  (resp.  $0.43$ ) and Eq. 8 with  $\Phi_{HS} = \Phi_{\text{eff}} = 1.82 \Phi$  for  $\Phi = 1\%$  (resp.  $\Phi = 5.95\%$ ). *Inset*: Soret coefficient  $S_T$  at various  $T$ 's as a function of  $\Phi$ . Dashed lines are guide for the eye.

#### 3.2.1 Diffusion coefficient in zero field

In zero applied magnetic field, the mass diffusion coefficient  $D_m$  is isotropic and equals:

$$D_m(T) = \frac{1}{\zeta} \frac{\partial \Pi_{\text{NP}}}{\partial \Phi} = \frac{1}{\zeta} \frac{kT}{\chi} \quad (5)$$

where the compressibility  $\chi$  is given by Eq. 1 and Fig. 1;  $\chi$  has been shown experimentally to be  $T$ -independent. Oppositely the friction term  $\zeta$  is  $T$ -dependent.

In the absence of interparticle correlations,  $\chi = 1$  and the friction  $\zeta(T)$  writes as:

$$\zeta(T) = \zeta_0(T) = 3\pi\eta_0(T) d_H \quad (6)$$

where  $\eta_0(T)$  is the solvent viscosity and  $d_H$  the NP's hydrodynamic diameter. The mass diffusion coefficient  $D_{m,0}$  can then be written as :

$$D_{m,0}(T) = \frac{kT}{\zeta_0(T)} = \frac{kT}{3\pi\eta_0(T)d_H} \quad (7)$$

In the presence of interparticle correlations  $\chi \neq 1$  and  $\zeta(T) \neq \zeta_0(T)$ , these correlations modify  $D_m(T)$ . An expression for the friction  $\zeta(T)$  experienced by hard spheres in hydrodynamic interaction at a volume fraction  $\Phi_{HS}$  has been proposed in<sup>68</sup> for  $\Phi_{HS} \ll 1$ :

$$\zeta(T) = \zeta_0(T)(1 + k_F\Phi_{HS}) \quad \text{with} \quad k_F = 6.55 \quad (8)$$

The evolution of  $D_m(T)$  as a function of  $T$  is plotted in main Fig. 3. The full line is the computation of  $D_{m,0}(T)$  as a function of  $T$  taking  $\eta_0(T)$  as given by<sup>26</sup> and  $d_H = 13.6$  nm. As shown by this figure and Eq. 7, the strong temperature dependence of  $D_m(T)$  can be ascribed to the large decrease of the solvent viscosity  $\eta_0(T)$  as  $T$  increases. However, note that here, the NPs present strong interparticle repulsion (as shown by Fig. 1) and the interparticle correlations cannot be forgotten in the expression of  $D_m$  to take in account the NP's volume fraction influence.

Fig. 3 also presents  $D_m(T)$  as obtained from Eq. 5 using SAXS and SANS experimental  $\chi$  values and Eq. 8 with  $\Phi_{HS} = \Phi_{\text{eff}} (= 1.82 \Phi)$  for  $\Phi = 1\%$  (dashed line) and for  $\Phi = 5.95\%$  (dotted line). It matches correctly the experimental results at  $\Phi = 1\%$  - except at  $T \geq 420$  K, but it should be necessary to check that the viscosity values deduced from the calculations of Paduszynski and Domanska<sup>26</sup> are completely reliable in this range of  $T$ . On the contrary, a systematic discrepancy (by a constant factor  $\sim 1.6$  up to 420 K) is found at  $\Phi = 5.95\%$ , meaning that the friction  $\zeta$  is slightly larger than what is given by the development of Eq. 8 at this volume fraction and that the correction with respect to the ideal case is almost constant whatever  $T$  up to 420 K.

#### 3.2.2 Soret coefficient in zero field

Inset of Fig. 3 shows the evolution of the Soret coefficient  $S_T$  as a function of the volume fraction  $\Phi$  at three different temperatures. Let us note first that whatever  $\Phi$  and  $T$ , the measured  $S_T$  is here always positive, contrary to what is sometimes observed for ferrofluids in water<sup>33,37</sup> and similarly to what is observed with ferrofluids in another very different ionic liquid (ethylammonium nitrate, EAN)<sup>23</sup>. EAN is indeed hydrophilic and totally miscible with water, although EMIM-TFSI is hydrophobic<sup>‡</sup>.

Moreover the Soret coefficient  $S_T$  is a decreasing function of  $\Phi$ , which is expected as it has been shown in<sup>43</sup> that  $|S_T| \propto \chi$ , which is here a decreasing function of  $\Phi$  - see Fig. 1.  $S_T$  is also a decreasing function of  $T$ , which is also analogous to what is observed in EAN<sup>23</sup>. For a deeper analysis of the behaviour of  $S_T(\Phi, T)$  (as

‡ Moreover the NP/ liquid interface is not constituted of the same species and H-bonds can occur with EAN while only weaker ones can exist with EMIM-TFSI.

in<sup>23</sup> for example), a larger number of samples at various volume fractions  $\Phi$  should be investigated. It will be done in a forthcoming paper, we focus hereafter on the under-field behavior of the sample at  $\Phi = 5.95\%$  in the whole accessible  $T$ -range of the experiment.

### 3.3 Under-field experimental results

An anisotropy of both the diffusion coefficient  $D_m$  (see Fig. 4) and of the Soret coefficient  $S_T$  (see Fig. 5) is observed whatever  $T$  ranging between 295 K and 460 K, if an external magnetic field  $\vec{H}$  is applied to the sample during the FRS measurement ( $0 \leq H \leq 100 \text{ kA m}^{-1}$ ).  $D_m$  and  $S_T$  both depend on the amplitude of the applied field and on its direction, as it has been previously observed for  $D_m$  and/or  $S_T$  in non-ionic magnetic fluids<sup>69-71</sup> and in aqueous ferrofluids<sup>33,35,72,73</sup> at room temperature.

We limit ourselves here to gradients of temperature ( $\vec{\nabla}T$ ) and of concentration ( $\vec{\nabla}\Phi$ ) either horizontal (and thus parallel ( $\parallel$ ) to the applied field – direction denoted  $\vec{H}_{\parallel}$ ) or vertical (and thus perpendicular ( $\perp$ ) to the field – direction denoted  $\vec{H}_{\perp}$ ).

Fig. 4 and 5 show typical in-field anisotropies of  $D_m$  and of  $S_T$  observed at  $\Phi = 5.95\%$  and  $0 \leq H \leq 100 \text{ kA m}^{-1}$ , for both  $\vec{H}_{\parallel}$  and  $\vec{H}_{\perp}$ . As previously shown in main Fig. 3, the zero field value of  $D_m$  increases with  $T$ . Under-field  $D_m$  is anisotropic with  $D_m(H_{\perp}) < D_m(H=0) < D_m(H_{\parallel})$  and this anisotropy decreases with  $T$ . In an opposite manner (as also previously shown in inset of Fig. 3), the zero field value of  $S_T$  decreases with  $T$  with an under-field anisotropy of  $S_T$ , with  $S_T(H_{\parallel}) < S_T(H=0) < S_T(H_{\perp})$ . Let us note that, in the experimental range, whatever the amplitude of  $\vec{H}$  and whatever its direction with respect to  $\vec{\nabla}\Phi$  and  $\vec{\nabla}T$ ,  $S_T(H)$  remains always positive, as  $S_T(H=0)$ .

## 4 Under-field model and adjustment of the experimental results

### 4.1 Under-field model of diffusion coefficient

At room temperature, the in-field anisotropy of  $D_m$  in aqueous samples, measured in the absence of temperature gradient, has been extensively described with a mean-field framework in<sup>35,72,73</sup>. In this framework, the effective Langevin parameter  $\xi_e$  in the ferrofluid, based on NPs of magnetization  $m_S$  with a volume  $v_{\text{NP}}$  and a magnetic moment  $\mu_{\text{NP}} = m_S v_{\text{NP}}$ , is defined as :

$$\xi_e = \xi + \lambda \gamma L(\xi_e) \quad \text{with} \quad \xi = \frac{\mu_0 \mu_{\text{NP}} H}{kT} \quad (9)$$

$\xi$  is the Langevin parameter,  $\lambda$  the mean-field parameter,  $\gamma$  the magnetic dipolar interaction parameter and  $L(\xi) = \cotan(\xi) - 1/\xi$  the Langevin function. Here we use  $\lambda = 0.22$  as in<sup>35,72,74</sup>, value confirmed by the numerical simulations in water of ref.<sup>73</sup>. The magnetic dipolar interaction parameter is:

$$\gamma = \frac{\mu_0 m_S \mu_{\text{NP}} \Phi}{kT}. \quad (10)$$

Up to  $\gamma \sim 5$ , it has been shown (at room temperature) in ref.<sup>75,76</sup> that the simple mean-field model of Eq. 9 gives same initial magnetic susceptibility as the second order perturbation model of Ivanov and Kuznetsova<sup>77</sup> with  $\lambda = 1/3$  and as the mean-

spherical model of Morozov and Lebedev<sup>78</sup>, all the three being in good agreement with experiments.

The in-field diffusion coefficient  $D_m$  then writes with  $\vec{\nabla}T \parallel \vec{\nabla}\Phi$ , either perpendicular to the applied field  $\vec{H}$  ( $\vec{H}_{\perp}$ ) or parallel ( $\vec{H}_{\parallel}$ ):

$$D_m^{\vec{H}_{\perp}} = \frac{kT}{\zeta} \left( \frac{1}{\chi} - \alpha_{\lambda} \right) = D_m^* [1 - \chi \alpha_{\lambda}] \quad (11)$$

and

$$D_m^{\vec{H}_{\parallel}} = \frac{kT}{\zeta} \left( \frac{1}{\chi} + \beta_{\lambda} - \alpha_{\lambda} \right) = D_m^* [1 - \chi (\beta_{\lambda} - \alpha_{\lambda})] \quad (12)$$

where  $D_m^* = D_m(H=0) = kT/\zeta\chi$ , the parameters  $\alpha_{\lambda}$  and  $\beta_{\lambda}$  being given by :

$$\alpha_{\lambda} = \frac{\lambda \gamma L^2(\xi_e)}{1 - \lambda \gamma L'(\xi_e)} \quad (13)$$

and

$$\beta_{\lambda} = \frac{\gamma L^2(\xi_e)}{[1 - \lambda \gamma L'(\xi_e)][1 + (1 - \lambda) \gamma L'(\xi_e)]}. \quad (14)$$

$\alpha_{\lambda}$  is associated with the mean-field dipolar interaction, which is attractive on average. The term  $\beta_{\lambda}$  is anisotropic and due to the discontinuity of  $\vec{H}_{\parallel}$  in Maxwell equations along the spatial inhomogeneities<sup>§</sup> of concentration<sup>3,35,42,72</sup>.  $\beta_{\lambda}$  is maximum in the field direction parallel to  $\vec{\nabla}\Phi$  and null perpendicularly. The higher is the volume fraction  $\Phi$ , the larger are magnetic dipolar parameter  $\gamma$  and coefficient  $\beta_{\lambda}$ , and thus the larger is the anisotropy of  $D_m$ .

The adjustments of  $D_m^{\vec{H}_{\perp}}$  and  $D_m^{\vec{H}_{\parallel}}$  at room temperature are both presented in Fig. 4. They are made, assuming as in refs.<sup>35,72,74</sup> that  $\chi$  and  $\zeta$  keep under-field their zero field value. Using  $\chi = 0.43$  and  $m_S = 3.2 \times 10^5 \text{ A m}^{-1}$ , and letting in the fit  $d_{\text{NP}}$  as a free parameter, as well as  $D_m^*$  within the experimental error bar of  $D_m(H=0)$ , we obtain  $d_{\text{NP}} = 13.2 \text{ nm}$ , leading to  $\gamma = 2.3$  at room temperature. In the monodisperse model used here for the adjustment, the polydispersity in NP's diameter is not taken in account and the value of  $d_{\text{NP}}$  obtained is slightly larger than the volume average diameter obtained from magnetisation measurements. It is anyway reasonable as it corresponds to a reduced dipolar parameter  $\Psi_{\text{dd}} = \gamma/\Phi = 39$ , quite comparable to those previously obtained experimentally for aqueous samples based on maghemite NPs similar in diameter<sup>75,76</sup>.

At higher temperatures than 295 K, the osmotic compressibility  $\chi$ , as determined by SANS measurements at  $H=0$ , is observed to be independent of  $T$ <sup>32</sup>. The temperature dependence of  $\zeta(T)$  enters inside the fitting parameter  $D_m^*(T)$ , still kept within the experimental error bar of  $D_m(H=0)$  at the given  $T$ .

However two other parameters have to be modified in the model because of their  $T$ -dependence and that of the NP's magnetization  $m_S(T)$ . Namely these two parameters are the Langevin parameter  $\xi \propto \mu_{\text{NP}}/T \propto m_S(T)/T$  and the dipolar parameter  $\gamma \propto m_S \mu_{\text{NP}}/T \propto m_S^2(T)/T$ . In a first approximation, finite-size effects

§ Such under-field inhomogeneities of concentration are also present at the local scale as attested by small angle scattering<sup>74,79</sup>.

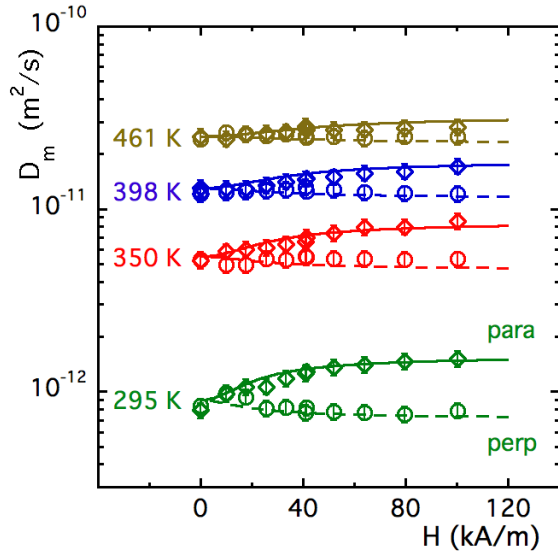


**Fig. 4** Under-field diffusion coefficient  $D_m$  as a function of the applied field for different temperatures  $T$  (from bottom to top: 295, 350, 398 and 461 K); The label perp (resp. para) and open discs (resp. open diamonds) mean measurements in  $H_{\perp}$  direction (resp.  $H_{\parallel}$ ); Symbols correspond to FRS measurements, dashed lines (resp. full lines) correspond to adjustment of the data in  $H_{\perp}$  direction with Eq. 11 (resp. in  $H_{\parallel}$  direction with Eq. 12). See the text for the detailed values of the parameters used.

and interface effects on the magnetization being small at the present NP diameters<sup>80–83</sup>, it is here proposed to approximate the temperature dependence of  $m_S$  with the following Bloch law of bulk maghemite<sup>84–87</sup>:

$$m_S(T) = 390 \left( 1 - 3.3 \times 10^{-5} T^{\frac{3}{2}} \right), \quad (15)$$

$m_S$  being expressed in  $\text{kA m}^{-1}$ ,  $T$  in K and this expression being only valid up to 723 K, temperature above which maghemite transforms in hematite.

Fig. 4 presents the adjustment of the in-field anisotropy of  $D_m$  at  $\Phi = 5.95\%$  and various  $T$ 's, with  $\chi$  kept independent of  $\vec{H}$  and  $T$  as said above, and  $D_m^*$  being the only  $T$ -dependent fitting parameter. At each  $T$ , the shape of the anisotropy of  $D_m$  is well adjusted with the model of Eqs. 11, 12, 13 and 14 with a dipolar interaction parameter  $\gamma(T)$  derived from Eqs. 10 and 15 given in Table 1. The model quite nicely reproduces the anisotropy of  $D_m$  in the experimental range of  $T$  and  $\vec{H}$ .

#### 4.2 Under-field model of Soret coefficient

The in-field anisotropy of the Soret coefficient  $S_T(\vec{H})$  can be expressed in the same framework as that of Eqs. 11 and 12 for  $D_m(\vec{H})$  but including derivatives of the NP's chemical potential

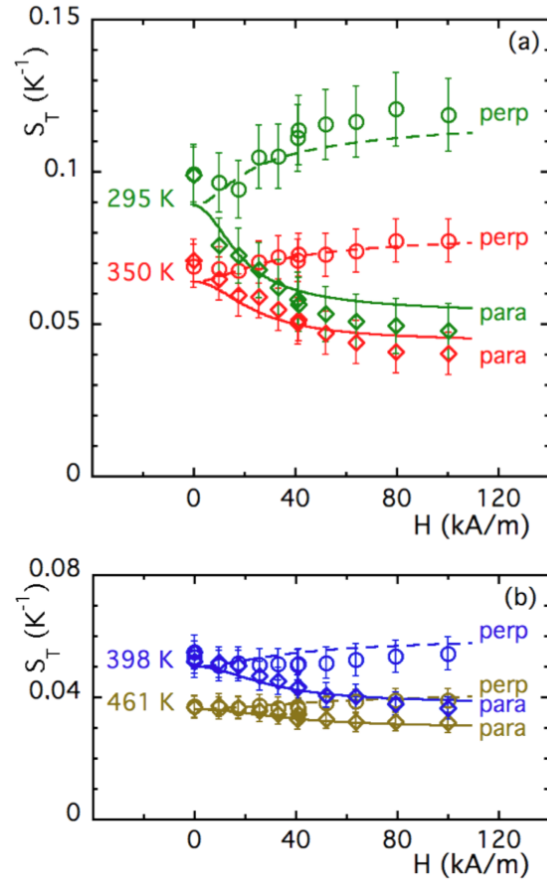


**Fig. 5** Under-field Soret coefficient  $S_T$  as a function of the applied field for different temperatures  $T$  (Fig. 5a at 295 and 350 K, Fig. 5b at 398 and 461 K); The label perp (resp. para) and open discs (resp. open diamonds) mean measurements in  $H_{\perp}$  direction (resp.  $H_{\parallel}$ ); Symbols correspond to FRS measurements, dashed lines (resp. full lines) correspond to adjustment of the data in  $H_{\perp}$  direction with Eq. 16 (resp. in  $H_{\parallel}$  direction with Eq. 17). See the text for the detailed values of the parameters used in the adjustments.

with respect to temperature<sup>33,42</sup>:

$$S_T^{\vec{H}_{\perp}} = \frac{1}{\frac{1}{\chi} - \alpha_{\lambda}} \left[ \frac{S_T^*}{\chi} + \frac{S_1}{T} \right] \quad (16)$$

and

$$S_T^{\vec{H}_{\parallel}} = \frac{1}{\frac{1}{\chi} + \beta_{\lambda} - \alpha_{\lambda}} \left[ \frac{S_T^*}{\chi} + \frac{S_1 - S_2}{T} \right], \quad (17)$$

where  $S_T^* = S_T(H=0, T)$ , the parameters  $S_1$  and  $S_2$  being given by :

$$S_1 = \frac{\xi_e L(\xi_e)}{1 - \lambda \gamma L'(\xi_e)} - \ln \frac{\sinh \xi_e}{\xi_e} \quad (18)$$

and

$$S_2 = \beta_{\lambda} \frac{\xi_e L'(\xi_e)}{L(\xi_e)}. \quad (19)$$

These equations involve the same parameters as Eqs. 11 and

**Table 1** Evolution of some fit parameters as a function of  $T$  (see text).

$T$ (K)	$\gamma$	$D_m(H=0)$ (m <sup>2</sup> /s)	$D_m^*$ (m <sup>2</sup> /s)	$\frac{D_m^* - D_m(H=0)}{D_m^*}$	$S_T(H=0)$ (K <sup>-1</sup> )	$S_T^*$ (K <sup>-1</sup> )	$\frac{S_T^* - S_T(H=0)}{S_T^*}$
295	2.3	$8.06 \cdot 10^{-13}$	$9.0 \cdot 10^{-13}$	+10	0.099	0.089	- 11
350	1.7	$5.24 \cdot 10^{-12}$	$5.5 \cdot 10^{-12}$	+ 6	0.070	0.064	- 9
398	1.3	$1.21 \cdot 10^{-11}$	$1.3 \cdot 10^{-11}$	+ 8	0.054	0.05	- 8
461	0.92	$2.45 \cdot 10^{-11}$	$2.5 \cdot 10^{-11}$	+ 4	0.037	0.036	- 3

12, in particular  $\xi_e$  (effective Langevin parameter given by Eq. 9),  $\lambda$  (mean field parameter, here fixed to 0.22),  $\gamma(T)$  (dipolar interaction parameter deduced from Eqs. 10 and 15),  $\alpha_\lambda$  and  $\beta_\lambda$  given by Eqs. 13 and 14. We use in Fig. 5 the same values of all these parameters as in Fig. 4 and only keep free  $S_T^*$  as a  $T$ -dependent parameter, adjusted within the experimental error bar of  $S_T(H=0)$  at the given temperature. A quite reasonable agreement with the experimental variation of in-field anisotropy of the Soret coefficient  $S_T(\vec{H})$  is obtained in the whole range of  $T$  and  $\vec{H}$ .

Let us note however a systematic small shift of  $D_m^*$  and  $S_T^*$  with respect to the direct experimental value of  $D_m$  and  $S_T$  in zero field at the same temperature (see Table 1). This shift, which is positive for  $D_m^*$  and negative for  $S_T^*$ , anyway always remain within the experimental error bar.

## 5 Discussion

In the under-field analysis the two main contributions to  $D_m(\vec{H})$  and  $S_T(\vec{H})$  come from the two parameters  $\alpha_\lambda$  and  $\beta_\lambda$ . The term  $\alpha_\lambda$  is related to the under-field dipolar interaction, modeled in the framework of a mean field approximation. It decreases as  $T$  increases. In this framework, it is isotropic and thus exists in both directions  $\vec{H}_\perp$  and  $\vec{H}_\parallel$ . In the model, the under-field anisotropic contribution to  $D_m(H)$  comes from the under-field inhomogeneities of concentration, modeled by  $\beta_\lambda$ . This anisotropic term, which is also proportional to the magnetic dipolar parameter  $\gamma(T)$ , becomes weaker as  $T$  increases. Let us first briefly discuss the influence of these two terms  $\alpha_\lambda$  and  $\beta_\lambda$  on the under-field variations of  $D_m(\vec{H})$  and  $S_T(\vec{H})$ . We then will focus on the influence of the two terms  $S_1$  and  $S_2$ .

The anisotropy of diffusion coefficient  $D_m$  is related to the terms  $\alpha_\lambda$  and  $\beta_\lambda$ . It is possible to compare the theoretical expressions of  $\alpha_\lambda$  and  $\beta_\lambda$  given by Eqs. 13 and 14 to experimental determinations, namely<sup>¶</sup>:

$$-\alpha_\lambda = \frac{1}{\chi} \frac{D_m^{\vec{H}_\perp} - D_m^*}{D_m^*} \quad (20)$$

and

$$\beta_\lambda = \frac{1}{\chi} \frac{D_m^{\vec{H}_\parallel} - D_m^*}{D_m^*}. \quad (21)$$

Fig. 6 presents at  $T = 295$  K and 461 K the experimental values of  $-\alpha_\lambda$  and  $\beta_\lambda$  deduced from Eqs. 20 and 21 using  $\chi = 0.43$  and  $D_m^*$  values obtained in Fig. 4 adjustments (see Table 1). Fig. 6

also compares these experimental determinations to the theoretical expressions of  $-\alpha_\lambda$  and  $\beta_\lambda$  deduced from Eqs. 13 and 14, using the same parameters values as in Fig. 4. There is a very good agreement between the theoretical and the experimental expressions of  $-\alpha_\lambda$  and  $\beta_\lambda$  as a function of  $H$  and  $T$ , within the error bar of the experiment.

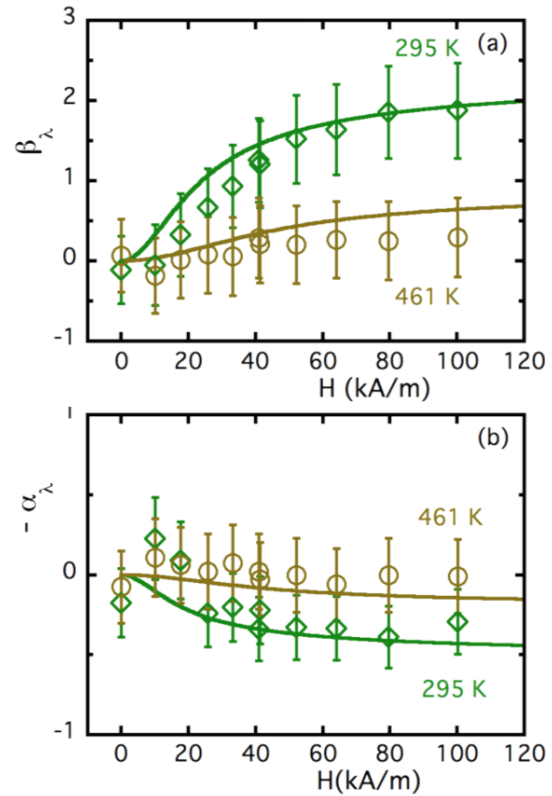


**Fig. 6** Field-dependence of parameters  $-\alpha_\lambda$  (b) and  $\beta_\lambda$  (a) at  $T=295$  K and 461K. Experimental values (see text for details) are obtained from Eqs. 20 and 21 (open diamonds at  $T=295$  K; open discs at  $T=461$  K). Theoretical adjustments (full lines) are deduced from Eqs. 13 and 14, using the same parameters values as in Fig. 4.

For its part, the anisotropy of the Soret coefficient  $S_T$  is also mainly related to the terms  $\alpha_\lambda$  and  $\beta_\lambda$ , which bring large contributions, larger than  $S_1$  and  $S_1 - S_2$ . In order to probe more

<sup>¶</sup>We use here the adjusted value of  $D_m^*$  and not the corresponding experimental value  $D_m(H=0)$  to reduce the error bar in Fig. 6

precisely the influence of the terms  $S_1$  and  $S_1 - S_2$ , we can remark that when looking at the product  $S_T D_m$  both  $\alpha_\lambda$  and  $\beta_\lambda$  contributions vanish. We obtain<sup>||</sup>:

$$\frac{S_T^{\vec{H}_\perp} D_m^{\vec{H}_\perp}}{D_m^*} = S_T^* + \chi \frac{S_1}{T} \quad (22)$$

and

$$\frac{S_T^{\vec{H}_\parallel} D_m^{\vec{H}_\parallel}}{D_m^*} = S_T^* + \chi \frac{S_1 - S_2}{T}. \quad (23)$$

Fig. 7 presents, at the various  $T$ 's, the experimental values of  $S_T^{\vec{H}_\perp} D_m^{\vec{H}_\perp} / D_m^*$  (open discs) and  $S_T^{\vec{H}_\parallel} D_m^{\vec{H}_\parallel} / D_m^*$  (open diamonds), using  $D_m^*$  values obtained in Fig. 4 adjustments (see Table 1). Fig. 7 also presents the expressions  $S_T^* + \chi S_1 / T$  (full lines) and  $S_T^* + \chi (S_1 - S_2) / T$  (dotted lines), using  $S_T^*$  values obtained in Fig. 5 adjustments (see Table 1),  $\chi = 0.43$  and theoretical expressions of  $S_1$  and  $S_2$ , given by Eqs. 18 and 19.

The first conclusions from this representation are that here:

$$\chi \frac{S_1(H, T)}{T} \ll S_T^*(T) \quad \text{and} \quad \chi \frac{[S_1(H, T) - S_2(H, T)]}{T} \ll S_T^*(T), \quad (24)$$

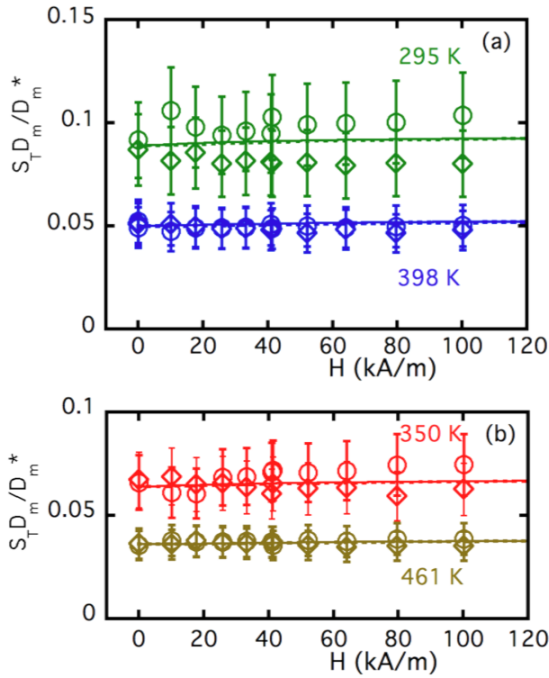


**Fig. 7** Under-field anisotropy of  $S_T D_m / D_m^*$  at various  $T$ 's; Experimental determinations (open discs symbols correspond to measurements in  $H_\perp$  direction and open diamonds to measurements in  $H_\parallel$  direction) are compared with theoretical expressions of Eqs. 22 (full line) and 23 (dotted line) - for details see text.

<sup>||</sup> We use here the adjusted value of  $S_T^*$  and not the corresponding experimental value  $S_T(H=0)$  to reduce the error bar in Fig. 7

which means that almost no under-field anisotropy is predicted in Eqs. 22 and 23 from a theoretical point of view, as well as a very weak field dependence of  $S_T D_m / D_m^*$ , weaker than the experimental error bar.

From an experimental point of view, similar conclusions are obtained. If a subsidiary field anisotropy of  $S_T D_m / D_m^*$  is observed (mainly at 295 K and 350 K), it however always remains smaller than the error bar. So within the error bar, which is here much larger than  $\chi S_1 / T$  and  $\chi (S_1 - S_2) / T$  variations, experimental values of  $S_T D_m / D_m^*$  can thus be adjusted by Eqs. 22 and 23. Then the main contribution to the under-field anisotropy of  $S_T$  is coming, as for  $D_m$ , from the term  $\beta_\lambda$ , which is associated to the under-field inhomogeneities of concentration.

Note that the small shift at  $H=0$  between experimental and adjusted values of  $D_m$  and  $S_T$ , almost completely compensate in  $D_m S_T$  representation of Fig. 7. It is also true for  $\beta_\lambda$  in Fig. 6a. On the contrary the term  $\alpha_\lambda$  in Fig. 6b, present small distortions at very low fields. This isotropic term  $\alpha_\lambda$ , associated to the modeling of the average magnetic dipolar interaction, is in fact responsible for the small, but systematic, positive shift obtained between  $D_m^*$  and the direct experimental value of  $D_m$  in zero field at the same temperature. It is as well responsible for the negative shift obtained between  $S_T^*$  and the direct experimental value of  $S_T$  in zero field at the same temperature.

We propose the following explanation; In fact, the right-hand term of Eq. 11 intrinsically supposes that the magnetic dipolar interparticle interaction vanishes in zero field, which is indeed not true. The approximation of Eq. 11 is very rough in low fields.  $D_m^*$  can be seen as the extrapolation of  $D_m(\vec{H})$  at  $H=0$  in the absence of magnetic dipolar interparticle interaction. The conclusion is equivalent for  $S_T^*$ .

We can then roughly evaluate at  $T = 295$  K the contribution in zero field  $\chi_{\text{dip}}$  of the magnetic dipolar interparticle interaction to the total compressibility  $\chi$  of the NPs' system to  $\sim 10\%$  of  $\chi$  measured by SAXS and SANS, as  $(D_m^* - D_m(H=0)) / D_m^* \sim (S_T(H=0) - S_T^*) / S_T^* \sim 10\%$ :  $\chi_{\text{dip}} \sim +0.04$ , which is of the order of magnitude of the error bar on  $\chi$  measurements at 295 K. This contribution would be smaller than the error bar at higher  $T$ 's.

## 6 Conclusions

Due to an efficient long-range ionic layering of the EMI-TFSI anions and cations around the maghemite NPs, the present synthesized ferrofluids are stable colloids in a large domain of temperatures  $T$  and applied magnetic fields  $\vec{H}$ , at least up to 460 K and 100 kA m<sup>-1</sup>. This stability will be very useful for their future thermoelectric applications. In zero applied field, the average interparticle repulsion is associated to a large second virial coefficient  $A_2 = 7.3$ , found experimentally independent of  $T$ . In FRS measurements performed with a fluid sample of thickness 25  $\mu\text{m}$  in gradients of temperature  $\vec{\nabla}T$  such as  $\Delta T \ll T$  over  $\sim 100 \mu\text{m}$ , the NPs always presents a positive Soret coefficient  $S_T$ , they are thus always migrating to the cold, whatever the mean temperature  $T$ . Increasing  $T$  lowers  $S_T$ , and it also increases  $D_m$ , as the EMI-TFSI viscosity decreases.

Under-field  $S_T$  and  $D_m$  coefficients are anisotropic.  $S_T$  is larger when  $\vec{\nabla}T$  and  $\vec{\nabla}\Phi$  are perpendicular to  $\vec{H}$ , while  $D_m$  reduces in this configuration, which is promising for thermoelectric applications<sup>10</sup>. The under-field anisotropy of  $S_T$  and  $D_m$  is well described, at the first order, by the model from<sup>33,42</sup> applied here in the whole range of  $T$  and  $\vec{H}$ , using the same values of the different parameters for the adjustment of both  $S_T$  and  $D_m$  at same  $\vec{H}$  and  $T$ .

The main cause of thermodiffusion anisotropy is attributed to under-field spatial inhomogeneities of NP's concentration, associated here to  $\beta_\lambda$  coefficient in the model. When  $T$  increases, the NP's magnetization  $m_S$  as well as the magnetic dipolar interaction parameter and  $\beta_\lambda$  coefficient decrease, the under-field anisotropy of both  $S_T$  and  $D_m$  coefficients then drastically reduces, as it is observed in the experiment.

### Conflicts of interest

There are no conflicts of interest to declare.

### Acknowledgements

We acknowledge funding from the Brazilian agency CNPq, the bilateral programs PHC OSMOSE 2018 No. 40033S and CAPES-COFECUB No. Ph 959/20 and the European Union's Horizon 2020 research and innovation programme under grant agreement No. 731976 (MAGENTA). We acknowledge the Laboratoire Léon Brillouin, CEA-Saclay, France for neutron beamtime at PAXY spectrometer.

### Notes and references

- 1 R. Rosensweig, *Ferrohydrodynamics.*, Cambridge University Press, Cambridge, 1985.
- 2 *Magnetic Fluids and Applications Handbook*, ed. B. Berkovsky, Begell House Inc. Publ., New-York, 1996.
- 3 E. Blums, A. Cēbers and M. Maiorov, *Magnetic Liquids*, W. de G. Gruyter, New York, 1997.
- 4 *Ferrofluids : Magnetically Controllable Fluids and Their Applications*, ed. S. Odenbach, Springer Verlag, Berlin, 2003.
- 5 B. Huang, M. Roger, M. Bonetti, T. J. Salez, C. Wiertel-Gasquet, E. Dubois, R. C. Gomes, G. Demouchy, G. Mériquet, V. Peyre, M. Kouyaté, C. L. Filomeno, J. Depeyrot, F. A. Tourinho, R. Perzynski and S. Nakamae, *J. Chem. Phys.*, 2015, **143**, 054902.
- 6 M. Bonetti, N. Nakamae, B. Huang, T. J. Salez, C. Wiertel-Gasquet and M. Roger, *J. Chem. Phys.*, 2015, **142**, 244708.
- 7 M. Dupont, D. MacFarlane and J. Pringle, *Chem. Commun.*, 2017, **53**, 6288–6302.
- 8 Z. He and P. Alexandridis, *Adv. Colloid Interface Sci.*, 2017, **244**, 54–70.
- 9 T. J. Salez, B. T. Huang, M. Rietjens, M. Bonetti, C. Wiertel-Gasquet, M. Roger, C. L. Filomeno, E. Dubois, R. Perzynski and S. Nakamae, *Phys. Chem. Chem. Phys.*, 2017, **19**, 9409–9416.
- 10 T. Salez, M. Kouyaté, C. L. Filomeno, M. Bonetti, M. Roger, G. Demouchy, E. Dubois, R. Perzynski, A. Cēbers and S. Nakamae, *Nanoscale Adv.*, 2019, **1**, 2979–2989.
- 11 Y. Cao and T. Mu, *Ind. Eng. Chem. Res.*, 2014, **53**, 8651–8664.
- 12 D. Zhao, Z. Fei, W. H. Ang and P. J. Dyson, *Small*, 2006, **2**, 879–883.
- 13 L. Rodríguez-Arco, M. T. López-López, F. González-Caballero and J. D. Durán, *Journal of Colloid and Interface Science*, 2011, **357**, 252–254.
- 14 N. Jain, X. Zhang, B. S. Hawkett and G. G. Warr, *ACS Applied Materials & Interfaces*, 2011, **3**, 662–667.
- 15 C. Guibert, V. Dupuis, J. Fresnais and V. Peyre, *J. Colloid Interface Sci.*, 2015, **453**, 105–111.
- 16 X. Shi, W. Huang and X. Wang, *Lubr. Sci.*, 2018, **30**, 73–82.
- 17 J. C. Riedl, M. A. Akhavan Kazemi, F. Cousin, E. Dubois, S. Fantini, S. Lois, R. Perzynski and V. Peyre, *Nanoscale Adv.*, 2020, **2**, 1560–1572.
- 18 G.-T. Wei, Z. Yang, C.-Y. Lee, H.-Y. Yang and C. R. C. Wang, *J. Am. Chem. Soc.*, 2004, **126**, 5036–5037.
- 19 K. Ueno, A. Inaba, M. Kondoh and M. Watanabe, *Langmuir*, 2008, **24**, 5253–5259.
- 20 M. Mamusa, J. Sirieux-Plénet, F. Cousin, E. Dubois and V. Peyre, *Soft Matter*, 2013, **10**, 1097–1101.
- 21 M. Mamusa, J. Sirieux-Plénet, F. Cousin, R. Perzynski, E. Dubois and V. Peyre, *J. Phys.: Condens. Matter*, 2014, **26**, 284113.
- 22 H. Zhang, K. Dasbiswas, N. B. Ludwig, G. Han, B. Lee, S. Vaikuntanathan and D. V. Talapin, *Nature*, 2017, **542**, 328–331.
- 23 K. Bhattacharya, M. Sarkar, T. J. Salez, S. Nakamae, G. Demouchy, F. Cousin, E. Dubois, L. Michot, R. Perzynski and V. Peyre, *ChemEngineering*, 2020, **4**, 5.
- 24 K. N. Marsh, J. Boxall and R. Lichtenthaler, *Fluid Phase Equilibria*, 2004, **219**, 93–98.
- 25 M. D. Fayer, *Chem. Phys. Lett.*, 2014, **616-617**, 259–274.
- 26 K. Padaszynski and U. Domanska, *J. Chem. Inf. Model.*, 2014, **54**, 1311–1324.
- 27 Y. Wakizaka, *PhD thesis*, University of Southampton - UK, 2007.
- 28 C. Largeot, C. Portet, J. Chmiolat, P. Taberna, Y. Gogotsi and P. Simon, *J. Am. Chem. Soc.*, 2008, **130**, 2730–2731.
- 29 R. Bhandary, J. G. Alauzun, P. Hesemann, A. Stocco, M. In and P. H. Mutin, *Soft Matter*, 2017, **13**, 8023–8026.
- 30 *Products | Solvionic*, 2020, <http://en.solvionic.com/products/>, Accessed: 2020-04-07.
- 31 *Ionic Liquids in Synthesis*, ed. P. Wasserscheid and T. Welton, Wiley-VCH Verlag GmbH & Co. KGaA, Weinheim, FRG, 2002.
- 32 J. C. Riedl and et al.
- 33 M. Kouyaté, C. Filomeno, G. Demouchy, G. Mériquet, S. Nakamae, V. Peyre, M. Roger, A. Cēbers, J. Depeyrot, E. Dubois and R. Perzynski, *Phys. Chem. Chem. Phys.*, 2019, **21**, 1895–1903.
- 34 Y. Nagasaka, T. Hatakeyama, M. Osuka and A. Nagashima, *Rev. Sci. Instrum.*, 1988, **59**, 1156–1168.
- 35 J.-C. Bacri, A. Cēbers, A. Bourdon, G. Demouchy, B. M. Heegaard and R. Perzynski, *Phys. Rev. Lett.*, 1995, **74**, 5032–5035.
- 36 A. Mezulis, M. Maiorov and E. Blums, *J. Magn. Magn. Mat.*, 2002, **252**, 221–223.

- 37 S. Alves, G. Demouchy, A. Bée, D. Talbot, A. Bourdon and A. M. Figueiredo Neto, *Philosophical Magazine*, 2003, **83**, 2059–2066.
- 38 G. Demouchy, A. Mezulis, A. Bée, D. Talbot, J. Bacri and A. Bourdon, *J. Phys. D: Appl. Phys.*, 2004, **37**, 1417–1428.
- 39 H. Ning and S. Wiegand, *J. Chem. Phys.*, 2006, **125**, 221102 1–4.
- 40 H. Ning, J. Dhont and S. Wiegand, *Langmuir*, 2008, **24**, 2426–2432.
- 41 M. Sarkar, J. C. Riedl, G. Demouchy, F. Gélébart, G. Mériduet, V. Peyre, E. Dubois and R. Perzynski, *Eur. Phys. J. E*, 2019, **42**, 979–2989.
- 42 T. Salez, S. Nakamae, R. Perzynski, G. Mériduet, A. Cēbers and M. Roger, *Entropy*, 2018, **20**, 405.
- 43 R. Cabreira-Gomes, A. da Silva, M. Kouyaté, G. Demouchy, G. Mériduet, R. Aquino, E. Dubois, S. Nakamae, M. Roger, J. Depeyrot and R. Perzynski, *Phys. Chem. Chem. Phys.*, 2018, **20**, 16402–16413.
- 44 R. Massart, *C. R. Acad. Sci. Paris*, 1980, **291**, 1–3.
- 45 R. Massart, *I.E.E.E., Trans. on Magn.*, 1981, **2**, 1247–1248.
- 46 E. Laux, L. Jeandupeux, S. Uhl, H. Keppner, P. P. López, P. Sanglard, E. Vanoli and R. Marti, *Mater. Today Proc.*, 2019, **8**, 672–679.
- 47 C. Filomeno, M. Kouyaté, V. Peyre, G. Demouchy, A. Campos, R. Perzynski, F. Tourinho and E. Dubois, *J. Phys. Chem. C*, 2017, **121**, 5539–5550.
- 48 C. Filomeno, M. Kouyaté, F. Cousin, G. Demouchy, E. Dubois, L. Michot, G. Mériduet, R. Perzynski, V. Peyre, J. Sirieix-Plénet and F. Tourinho, *J. Magn. Magn. Mat.*, 2017, **431**, 2–7.
- 49 N. Carnahan and K. Starling, *J. Chem. Phys.*, 1970, **53**, 600.
- 50 J.-C. Bacri, R. Perzynski, D. Salin, V. Cabuil and R. Massart, *J. Magn. Magn. Mat.*, 1990, **85**, 27–32.
- 51 R. G. Horn, D. F. Evans and B. W. Ninham, *Journal of Physical Chemistry*, 1988, **92**, 3531–3537.
- 52 R. Hayes, G. G. Warr and R. Atkina, *Phys. Chem. Chem. Phys.*, 2010, **12**, 1709–1723.
- 53 H.-W. Cheng, P. Stock, B. Moeremans, T. Baimpos, X. Banquy, F. U. Renner and M. Valtiner, *Adv. Mater. Interfaces*, 2015, 1500159.
- 54 M. Mezger, H. Schröder, H. Reichert, S. Schramm, J. S. Okasinski, S. Schöder, V. Honkimäki, M. Deutsch, B. M. Ocko, J. Ralston, M. Rohwerder, M. Stratmann and H. Dosch, *Science*, 2008, **322**, 424–428.
- 55 J. Vatamanu, O. Borodin and G. D. Smith, *J. Am. Chem. Soc.*, 2010, **132**, 14825–14833.
- 56 C. Merlet, B. Rotenberg, P. A. Madden and M. Salanne, *Phys. Chem. Chem. Phys.*, 2013, **15**, 15781.
- 57 V. Ivaništšev, S. O'Connor and M. Fedorov, *Interface Mag.*, 2014, **23**, 65–69.
- 58 S. W. Coles, A. M. Smith, M. V. Fedorov, F. Hausen and S. Perkin, *Faraday Discuss.*, 2018, **206**, 427–442.
- 59 G. Feng, R. Qiao, J. Huang, S. Dai, B. G. Sumpter and V. Meunier, *Phys. Chem. Chem. Phys.*, 2011, **13**, 1152–1161.
- 60 V. Kamysbayev, V. Srivastava, N. B. Ludwig, O. J. Borkiewicz, H. Zhang, J. Ilavsky, B. Lee, K. W. Chapman, S. Vaikuntanathan and D. V. Talapin, *ACS Nano*, 2019, **13**, 5760–5770.
- 61 C. F. W. Ludwig, *Sitzungsberichte der Akad. der Wissenschaften Math. Klasse*, 1856, **20**, 539.
- 62 C. Soret, *Arch. Sci. Phys. Nat. Genève*, 1879, **3**, 48.
- 63 S. Seki, S. Tsuzuki, K. Hayamizu, Y. Umebayashi, N. Serizawa, K. Takei and H. Miyashiro, *J. Chem. Eng. Data*, 2012, **57**, 221–2216.
- 64 D. A. G. Bruggeman, *Ann. Phys.*, 1935, **416**, 636–664.
- 65 W. Luo, T. Du and J. Huang, *Phys. Rev. Lett.*, 1999, **82**, 4134–4137.
- 66 D. Zablotsky, *PhD thesis*, Faculty of Physics and Mathematics - Univ. of Latvia, Riga - Latvia, 2012.
- 67 D. Zablotsky, A. Mezulis and E. Blums, *C. R. Mec.*, 2013, **341**, 449–454.
- 68 G. K. Batchelor, *J. Fluid Mech.*, 1982, **119**, 379–408.
- 69 E. Blums, S. Odenbach, A. Mezulis and M. Maiorov, *Phys. Fluids*, 1998, **10**, 2155–2163.
- 70 E. Blums, *J. Magn. Magn. Mat.*, 2005, **289**, 246–249.
- 71 L. Sprenger, A. Lange and S. Odenbach, *Phys. Fluids*, 2014, **26**, 022001.
- 72 J. C. Bacri, A. Cēbers, A. Bourdon, G. Demouchy, B. M. Heegaard, B. Kashevsky and R. Perzynski, *Phys. Rev. E*, 1995, **52**, 3936–3942.
- 73 G. Mériduet, E. Dubois, M. Jardat, A. Bourdon, G. Demouchy, V. Dupuis, B. Farago, R. Perzynski and P. Turq, *J. Phys. Cond. Matter*, 2006, **18**, S2685–S2696.
- 74 G. Mériduet, F. Cousin, E. Dubois, F. Boué, A. Cēbers, B. Farago and R. Perzynski, *J. Phys. Chem. B*, 2006, **110**, 4378–4386.
- 75 F. Gazeau, F. Boué, E. Dubois and R. Perzynski, *J. Phys. Cond. Matter*, 2003, **15**, S1305–S1334.
- 76 G. Mériduet, E. Wandersman, E. Dubois, A. Cēbers, J. de Andrade Gomes, G. Demouchy, J. Depeyrot, A. Robert and R. Perzynski, *Magneto-hydrodynamic*, 2012, **48**, 415–426.
- 77 A. O. Ivanov and O. B. Kuznetsova, *Phys. Rev. E*, 2001, **64**, 041405.
- 78 K. I. Morozov and A. V. Lebedev, *J. Magn. Magn. Mat.*, 1990, **85**, 51.
- 79 E. Wandersman, E. Dubois, F. Cousin, V. Dupuis, G. Mériduet, R. Perzynski and A. Cēbers, *Europhysics Lett.*, 2009, **86**, 10005 1–5.
- 80 R. Kodama, *J. Magn. Magn. Mat.*, 1999, **200**, 359–272.
- 81 X. Battle and A. Labarta, *J. Phys. D: Appl. Phys.*, 2002, **35**, R15–R42.
- 82 R. Aquino, J. Depeyrot, M. H. Sousa, F. A. Tourinho, E. Dubois and R. Perzynski, *Phys. Rev. B*, 2005, **72**, 184435 1–10.
- 83 F. G. da Silva, J. Depeyrot, A. Campos, R. Aquino, D. Fiorani and D. Peddis, *J. of Nanosci. Nanotechnol.*, 2019, **19**, 4888–4902.
- 84 *Magnetic oxides in geomagnetism* by K.M. Creer and I.G. Hedley and W. O'Reilly p.649-688 in "Magnetic oxides", ed. D. Craik, J. Wiley, London, 1975.
- 85 *Properties and behaviour of iron oxides as determined by Möss-*

- bauer spectroscopy by E. Murad p. 309-350 in "The Geobiochemical Cycle of Iron in Iron in Soils and Clay Minerals ", ed. J. Stucki, B. Goodman and U. Schwertmann, D. Reidel Publishing Company, Dordrecht, Holland, 1988.
- 86 E. Tronc, D. Fiorani, M. Nogues, A. M. Testa, F. Lucari, F. D'Orazio, J. M. Greneche, W. Wernsdorfer, N. Galvez, C. Chaneac, D. Maily and J. P. Jolivet, *J. Magn. Magn. Mat.*, 2003, **262**, 6.
- 87 B. Cullity and C. Graham, *Introduction to Magnetic Materials*, John Wiley and sons, Inc. - IEEE Press, Hoboken, New Jersey, USA, 2nd edn, 2009.



26/08/2020

870200107571

16:55



29409161916782999

## Pedido nacional de Invenção, Modelo de Utilidade, Certificado de Adição de Invenção e entrada na fase nacional do PCT

Número do Processo: BR 10 2020 017446 0

### Dados do Depositante (71)

---

#### Depositante 1 de 1

**Nome ou Razão Social:** FUNDAÇÃO UNIVERSIDADE DE BRASÍLIA

**Tipo de Pessoa:** Pessoa Jurídica

**CPF/CNPJ:** 00038174000143

**Nacionalidade:** Brasileira

**Qualificação Jurídica:** Instituição de Ensino e Pesquisa

**Endereço:** CENTRO DE APOIO AO DESENVOLVIMENTO TECNOLÓGICO -  
UNIVERSIDADE DE BRASÍLIA, CAMPUS UNIVERSITÁRIO DARCY  
RIBEIRO, EDIFÍCIO CDT, ASA NORTE

**Cidade:** Brasília

**Estado:** DF

**CEP:** 70904-970

**País:** Brasil

**Telefone:** (61)3107-4100/4137

**Fax:**

**Email:** nupitec@cdt.unb.br

---

**PETICIONAMENTO  
ELETRÔNICO**

Esta solicitação foi enviada pelo sistema Petição Eletrônica em 26/08/2020 às 16:55, Petição 870200107571

**Dados do Pedido**

---

**Natureza Patente:** 10 - Patente de Invenção (PI)

**Título da Invenção ou Modelo de Utilidade (54):** NANOFUIDOS MAGNÉTICOS FLUORESCENTES E SEU PROCESSO DE OBTENÇÃO

**Resumo:** A presente invenção situa-se no campo da nanotecnologia. Refere-se a nanofluidos compostos de nanopartículas magnéticas e nanopartículas fluorescentes que mantêm tanto propriedades magnéticas quanto fotoluminescentes sem perder a estabilidade de longo prazo, inclusive na presença de um campo magnético aplicado. As nanopartículas magnéticas utilizadas nas dispersões são compostas por ferritas de metal divalente e as propriedades de fluorescência advêm de nanopartículas carbonáceas. De forma geral, os nanofluidos apresentados no estado da técnica são obtidos a partir do encapsulamento e aglomeração de partículas magnéticas e fluorescentes, produzindo um fluido de baixa estabilidade. No entanto, na presente invenção os nanofluidos são estáveis devido à interação eletrostática repulsiva entre as partículas, maximizadas por meio do processo de compatibilização, sendo possível o controle das condições físico-químicas da dispersão variando a concentração relativa de material magnético e fluorescente.

**Figura a publicar:** 1